

**ÇUKUROVA UNIVERSITY
INSTITUTE OF NATURAL AND APPLIED SCIENCES**

PhD THESIS

Akın İLHAN

**AERODYNAMICS AND STATISTICAL ANALYSES OF
CONVENTIONAL AND DIFFUSER AUGMENTED WIND TURBINES**

DEPARTMENT OF MECHANICAL ENGINEERING

ADANA-2019

**ÇUKUROVA UNIVERSITY
INSTITUTE OF NATURAL AND APPLIED SCIENCES**

**AERODYNAMICS AND STATISTICAL ANALYSES OF
CONVENTIONAL AND DIFFUSER AUGMENTED WIND TURBINES**

Akın İLHAN

PhD THESIS

DEPARTMENT OF MECHANICAL ENGINEERING

We certify that the thesis titled above was reviewed and approved for the award of degree of the Doctor of Philosophy by the board of jury on 18/02/2019

.....
Prof. Dr. Beşir ŞAHİN
SUPERVISOR

.....
Prof. Dr. Hüseyin AKILLI
MEMBER

.....
Prof. Dr. Mehmet BİLGİLİ
MEMBER

.....
Prof. Dr. Muammer ÖZGÖREN
MEMBER

.....
Assoc. Prof. Dr. Coşkun ÖZALP
MEMBER

This PhD thesis was prepared at the Mechanical Engineering division of the Institute of Nature and Science of Çukurova University.

Registration Number:

**Prof. Dr. Mustafa GÖK
Director
Institute of Natural and Applied Sciences**

This thesis was supported by Scientific Researched Project Office of Çukurova University under Contract no: FDK-2016-7217.

Note: The usage of the presented specific declarations, tables, figures, and photographs either in this thesis or in any other reference without citation is subject to "The law of Arts and Intellectual Products" number of 5846 of Turkish Republic

ABSTRACT

Ph. D. THESIS

AERODYNAMICS AND STATISTICAL ANALYSES OF CONVENTIONAL AND DIFFUSER AUGMENTED WIND TURBINES

Akın İLHAN

DEPARTMENT OF MECHANICAL ENGINEERING
INSTITUTE OF NATURAL AND APPLIED SCIENCES
UNIVERSITY OF CUKUROVA

Advisor : Prof. Dr. Beşir ŞAHİN
Year: 2019, Pages: 428
Jury : Prof. Dr. Hüseyin AKILLI
Prof. Dr. Mehmet BİLGİLİ
Prof. Dr. Muammer ÖZGÖREN
Assoc. Prof. Dr. Coşkun ÖZALP

In this study; the wind energy production status of the World, Europe, and Turkey were reviewed in comparison with the other renewable energy sources. More specifically, wind energy situation of the World and Turkey was also examined in detail. Firstly, wind power estimation and analysis of a considered region in Turkey were conducted by statistical techniques. Secondly, the evaluation of the power generation and the efficiency of a wind farm located in Turkey were performed. Assessments of the aerodynamics of running wind turbines and evaluations of their operational procedure in the active wind farms in Turkey were conducted in the third and fourth stages of the study. The following three distinct studies include modeling and estimation of parameters such as aerodynamic structure, power output, and the power coefficient, utilizing artificial neural network (*ANN*) and adaptive neuro-fuzzy inference system (*ANFIS*). On the other hand, the comparisons by means of power generations and aerodynamics of currently operating selected wind turbines were reported in the eighth part of the study. In the following two parts of the study, it was focused on examining the increase of wind power output originated from the wind speed enhancement as a result of the innovative casing system of wind turbines. The most effective casing types and their related designs found in the literature are also evaluated within this thesis. Finally, the increase of wind speed in some designed wind turbine casing structures and flow characteristics inside these casing structures were investigated in detail, utilizing numerical and experimental methods.

Keywords: Aerodynamics of conventional bare wind turbines, analysis of wind power, design parameters of diffuser augmented wind turbines, wind energy

ÖZ

DOKTORA TEZİ

**GELENEKSEL VE YAYICI TAKVİYELİ RÜZGÂR TÜRBİNLERİNİN
AERODİNAMİK VE İSTATİSTİK AÇIDAN ANALİZLERİ**

Akın İLHAN

**ÇUKUROVA ÜNİVERSİTESİ
FEN BİLİMLERİ ENSTİTÜSÜ
MAKİNE MÜHENDİSLİĞİ ANABİLİM DALI**

Danışman : Prof. Dr. Beşir ŞAHİN
Sene: 2019, Sayfa: 428
Jüri : Prof. Dr. Hüseyin AKILLI
Prof. Dr. Mehmet BİLGİLİ
Prof. Dr. Muammer ÖZGÖREN
Doç. Dr. Coşkun ÖZALP

Bu çalışmada; Dünya'nın, Avrupa'nın ve Türkiye'nin rüzgâr enerji üretim durumu, diğer yenilenebilir enerji türlerine kıyasla ele alınmıştır. Ayrıca, Dünya'nın ve Türkiye'nin rüzgâr enerjisi durumu da ayrıntılı olarak incelenmiştir. Çalışmada ilk olarak, Türkiye'de göz önüne alınan bir bölgede, istatistik yöntemlerle rüzgâr gücü tahmini ve verimliliğinin değerlendirilmesi yapılmıştır. Çalışmanın üçüncü ve dördüncü safhalarında ise Türkiye'de çalışan rüzgâr çiftliklerinde yer alan rüzgâr türbinlerin aerodinamik yapıları incelenmiştir. Takip eden üç farklı çalışmada ise türbinlerin aerodinamik yapısı, güç çıktısı ve güç katsayısı gibi parametrelerinin, yapay sinir ağları ve uyarlamalı sinirsel bulanık çıkarım sistemi ile modellenmesi yapılmıştır. Diğer yandan, çalışmanın sekizinci bölümünde, seçilen ve halen çalışan rüzgâr türbinlerinin güç ve aerodinamik açıdan kıyaslanması üzerine çalışılmıştır. Çalışmanın takip eden iki bölümünde, yenilikçi sistem olan rüzgâr türbinlerinin kafeslenmesi sonucunda rüzgâr hızının artışına bağlı olarak güç üretiminde meydana gelen artışların incelenmesine odaklanılmıştır. Literatürde yer alan etkin kafesleme tipleri ve ilgili tasarımları da bu tez kapsamında değerlendirilmiştir. Son kısımda da, tasarlanmış bazı kafes yapılarında, rüzgâr hızının kafes içerisindeki artışı ve bu kafes sistemlerindeki akış karakteristikleri, nümerik ve deneysel yöntemler kullanılarak etraflıca araştırılmıştır.

Anahtar kelimeler: Geleneksel kafesiz rüzgâr türbinlerinin aerodinamiği, rüzgâr enerjisi, rüzgâr gücü analizi, yayıcı takviyeli rüzgâr türbinlerinin tasarım parametreleri

EXTENDED ABSTRACT

In this study, casing systems for the performance improvement of wind turbines were handled. Experimental and numerical analysis of designed linear and curved types of these systems were studied in order to configure wind speed increase, pressure changes, contours of the velocity component in the streamwise direction, pressure contours, velocity vectors, patterns of streamlines, and vorticity in the vicinity of these systems. Besides, dye observations of the particle image velocimetry (*PIV*) method were considered for the qualitative and quantitative flow visualizations downstream of the casing system with the flange.

The thesis included Bababurnu region of Turkey located in Çanakkale province in terms of wind energy potential assessment. In these regards, it was shown that this region was proper for new wind power plant installations. Based on the obtained results, annual average wind energy velocity and potential of this zone were demonstrated to correspond 6.01 m/s and 257 W/m², respectively.

Also, efficiency analysis of an installed wind farm in the South region of Turkey was also conducted in this thesis. Five wind turbines of this wind farm were used in this analysis. Monthly average wind speed values and hourly average energy generations for these wind turbines were determined in the scope of the analysis. On the other hand, wind directions of these considered turbines were reported. Average value air temperature data was also taken into account for the considered identical wind turbines. Based on the processed data obtained from this wind farm in 2010, 7.15 GWh of power at a mean wind speed value of 11.90 m/s was obtained in July. This value of power generation in July was conducted to be the highest energy generation for the whole year. Besides, 38.09 GWh of entire generations along the whole year of 2010 was obtained considering these five wind turbines.

Aerodynamic analysis of an operating wind farm located in Belen province of Turkey was also studied. The wind farm considered included 16 identical wind turbines in which 5 of 16 was chosen for the study. The mechanical output power of wind turbines, P , axial flow induction factor, a , power coefficient, C_p , thrust coefficient, C_T , and finally thrust force, T were obtained for whole chosen wind turbines presented with respect to the hub-height wind speed, U_D . Based on the most essential aerodynamic parameter, i.e. power coefficient, it was revealed that while wind turbine T2 generated a maximum peak power coefficient, C_p of 34%, it was concluded that turbine T4 generated a minimum peak power coefficient, C_p of 29%.

Another study was performed on aerodynamic analysis of horizontal axis wind turbines of a wind farm found in Hatay province of Turkey. Similarly, five of the same wind turbines were chosen. Blade Element Momentum Theory (*BEM*) was applied in order to obtain aerodynamic outputs of the mechanical output power of wind turbines, P , axial flow induction factor, a , power coefficient, C_p , thrust force coefficient, C_T , thrust force, T , and tangential flow induction factor, a' . All the cited parameters were defined according to the blade tip speed ratio, λ_R . In this study, maximum wind turbine output power of 2000 kW was reported to occur at a tip-speed ratio, λ_R of 2.81 and a rotational speed of $\Omega=16.40$ rpm. Besides, maximum wind turbine efficiency, C_p was determined to be $C_p=30\%$ at the tip speed ratio, λ_R of $\lambda_R=7.12$. Also, maximum thrust force, T was calculated at a tip speed ratio, λ_R of $\lambda_R=5.21$ to correspond $T=150$ kN.

Artificial Neural Network (*ANN*) prediction model was also applied in forecasting of aerodynamic parameters such as mechanical output power of wind turbines, P , axial flow induction factors, a , power coefficients, C_p , thrust coefficients, C_T , and thrust forces, T . Five identical wind turbines of an existing wind farm were studied in terms of obtaining the cited aerodynamic parameters by using only hub-height wind speed, U_D , and atmospheric air temperature, T_{atm} given

as inputs. Two distinct models were tested by the *ANN* tool. In these regards, in the first model, only hub-height wind speed, U_D was used in the prediction, whereas, in the second model, both hub-height wind speed, U_D and additionally atmospheric air temperature, T_{atm} were utilized for the predictions. This study revealed that utilized Model 2 gave better results than Model 1, due to having two aerodynamic input parameters given for the forecasting process.

Artificial Neural Network (*ANN*) was also studied for the determination of mechanical output power of wind turbines, P under the utilization of three input aerodynamic parameters including hub-height wind speed, U_D , atmospheric air temperature, T_{atm} , and turbine rotor rotational speed, Ω . *ANN* forecasting tool was shown to operate best during the case of optimum rotor rotational speeds, Ω , i.e., at $\Omega=16.14$ rpm of rotations.

On the other hand, Artificial Neuro-Fuzzy Inference System (*ANFIS*) was also studied for the mechanical output power of wind turbines, P configuration. Similarly, three input aerodynamic parameters including hub-height wind speed, U_D , atmospheric air temperature, T_{atm} , and turbine rotor rotational speed, Ω were considered for the output power determination. *ANFIS* forecasting tool was demonstrated to run best during the case of optimum rotor rotational speeds, Ω , i.e. at $\Omega=16.10$ rpm of rotor rotations.

Rotor diameter, D_{rotor} , rated power, P_r , and air density, ρ influences on aerodynamic parameters including mechanical output power of wind turbines, P , axial flow induction factor, a , power coefficient, C_p , and thrust force, T values were handled. Four different procedures were followed in the study. In the first procedure, the influence of only turbine rotor diameter, D_{rotor} was analyzed on the cited aerodynamic parameters. Secondly, the influence of the only turbine rated power, P_r on them was studied. The third procedure followed influences of both turbine rotor diameter, D_{rotor} and turbine rated power, P_r . Finally, the air density, ρ effect on aerodynamic outputs was investigated. Nine manufactured wind turbine types were

used in these researches. It was shown that moderate capacity of turbine rated power, P_r and turbine rotor swept area, A_d of V90-3 MW type resulted in the highest outcome of wind turbine power coefficient, C_p .

Enhancement of wind speed and power generation of wind turbines are generally obtained by the casing shroud system utilization. In these regards, this dissertation presented a large scale review of these systems. Besides, computational numeric analysis (*CFD*) and the particle image velocimetry (*PIV*) techniques were used for this purpose, in the investigation of inside and vicinity flows surrounding the designed types of linear and curved shrouding configurations. The numerical study covered 17 designed types of configurations prepared for the *CFD* study. It was shown that flange height ratio of $H/D=0.3$, half cone angle of the casing of $\theta=5^\circ$, and dimensionless casing full body length of $L/D=1.50$ gave superior performances of wind speed enhancement inside the casing body. The appropriate design of an inlet shrouding attached to the casing body was shown to increase the wind speed ratio by 16% compared concerning the non-inlet utilization. On the other hand, a curved type of casing configuration was designed for the test of *PIV* analysis for the flow visualization in the downstream rear area of the flange.

GENİŞLETİLMİŞ ÖZET

Bu çalışmada, rüzgâr türbinlerinin verimlerinin iyileştirilmesi için kullanılan kafes sistemleri ele alınmıştır. Bu sistemlerin yakınlarında meydana gelen rüzgâr hızı artışı, basınç değişimleri, akım içerisindeki hız bileşen kontürleri, basınç kontürleri, hız vektörleri, akım çizgisi desenleri ve girdapların belirlenmesi için tasarlanmış olan doğrusal ve kavisli yapıdaki bu sistemlerin deneysel ve nümerik analizleri üzerine çalışılmıştır. Diğer yandan, flanşlı kafes sisteminin aşağı akım yönündeki nitel ve nicel akış görüntüleri için *PIV* yönteminin boya gözlem sonuçları dikkate alınmıştır.

Bu tez, Türkiye'deki Çanakkale şehrinde yer alan Bababurnu yöresinin rüzgâr enerjisi potansiyeli açısından değerlendirilmesini içerir. Bu bölgenin yeni rüzgâr santrali inşaatı için uygun olduğu, bu kapsamda gösterilmiştir. Elde edilen sonuçlara dayanılarak, bu yörenin yıllık ortalama rüzgâr hızının ve potansiyelinin, sırasıyla, 6.01 m/s ve 257 W/m² ye karşılık geldiği gösterilmiştir.

İlaveten, Türkiye'nin güney bölgesinde yer alan kurulu bir rüzgâr çiftliğinin verim analizi de, bu tez kapsamında yürütülmüştür. Bu rüzgâr çiftliğinin beş adet rüzgâr türbini, ilgili analizde kullanılmıştır. Göz önüne alınan rüzgâr türbinlerinin aylık ortalama rüzgâr hızı değerleri ve saatlik ortalama enerji üretimleri, bu analiz kapsamında belirlenmiştir. Diğer yandan, ele alınan bu rüzgâr türbinlerinin, rüzgâr yönleri de raporlanmıştır. Değerlendirilen bu eşdeğer rüzgâr türbinlerinin ortalama hava sıcaklık veri değerleri de dikkate alınmıştır. Bu rüzgâr çiftliğinden, 2010 yılında, elde edilmiş ve işlenmiş olan veriler çerçevesinde; Temmuz ayı içerisinde 11.90 m/s'lik ortalama rüzgâr hızı değerine denk gelen 7.15 GWh'lik güç elde edildiği raporlanmıştır. Güç üretimine ilişkin Temmuz ayındaki ilgili bu değer; tüm yılın en yüksek enerji üretim değeri olduğu belirtilmiştir. Diğer taraftan, bu beş rüzgar türbini baz alındığında; tüm 2010 yılı boyunca, 38.09 GWh'lik toplam üretim sağlanmıştır.

Türkiye'nin Belen bölgesinde yer alan işletmedeki bir rüzgâr çiftliğinin aerodinamik analizi üzerine de çalışılmıştır. Göz önüne alınan bu rüzgâr çiftliği, 16 eşdeğer rüzgâr türbinini içermekte olup, 16 eşdeğer türbinin 5'i, bu çalışma için seçilmiştir. Seçilmiş olan tüm rüzgâr türbinleri için rüzgâr türbinleri mekanik çıkış gücü, P , aksenal akış indükleme katsayısı, a , güç katsayısı, C_p , itme katsayısı, C_T ve de itme kuvveti, T elde edilmiş ve bunlar göbek yüksekliği rüzgâr hızına (U_D) bağlı olarak da takdim edilmiştir. En başlıca aerodinamik parametre olan güç katsayısına dayanılarak; $T2$ türbininin %34'lük azami uç güç katsayısı, C_p değeri ürettiği gösterilirken, $T4$ türbininin ise %29'lük asgari uç güç katsayısı, C_p değeri ürettiği kararına varılmıştır.

Türkiye'nin Hatay ilinde bulunan bir rüzgâr çiftliğine ait yatay eksenli rüzgâr türbinlerinin aerodinamik analizi, başka bir çalışma kapsamında gerçekleştirilmiştir. Benzer şekilde, eşdeğer rüzgâr türbinlerin beşi seçilmiştir. Rüzgâr türbinleri mekanik çıkış gücü, P , aksenal akış indükleme katsayısı, a , güç katsayısı, C_p , itme kuvveti katsayısı, C_T , itme kuvveti, T ve de teğetsel akış indükleme katsayısı, a' gibi aerodinamik çıktıları elde etmek için Kanat Elemanı Momentum Teorisi (BEM) kullanılmıştır. Anılan tüm bu parametreler kanat uç hız oranına, λ_R göre tariflenmiştir. Bu çalışmada, 2.81'lik kanat uç hız oranında (λ_R) ve $\Omega=16.40$ rpm'lik dönüş hızında; 2000 kW'lık azami rüzgâr türbini çıkış gücünün meydana geldiği raporlanmıştır. Üstelik, azami rüzgar türbini verimi (C_p) olan $C_p=\%30$ değerinin ise $\lambda_R=7.12$ 'lik kanat uç hız oranı (λ_R) değerinde elde edildiği saptanmıştır. Ayrıca, $T=150$ kN'a karşılık gelen azami itme kuvveti (T) değeri ise $\lambda_R=5.21$ 'lik kanat uç hız oranı (λ_R) değerinde hesaplanmıştır.

Rüzgâr türbinleri mekanik çıkış gücü, P , aksenal akış indükleme katsayıları, a , güç katsayıları, C_p , itme kuvveti katsayıları, C_T ve itme kuvveti değerleri, T gibi aerodinamik parametrelerin tahmininde yapay sinir ağları (ANN) tahmin modeli uygulanmıştır. Varolan bir rüzgâr çiftliğinin beş eşdeğer rüzgâr türbini; anılan aerodinamik parametrelerin saptanmasında,

sadece girdi olarak verilen göbek yüksekliği rüzgâr hızına, U_D ve atmosferik hava sıcaklığına, T_{atm} bağlı olarak çalışılmıştır. İki ayrı model *ANN* aracı ile test edilmiştir. Bu açıdan, ilk modelde, tahmin için sadece göbek yüksekliği rüzgâr hızı (U_D) kullanılmışken; ikinci modelde, tahminlerde hem göbek yüksekliği rüzgâr hızı (U_D), hem de ek olarak atmosferik hava sıcaklığı, T_{atm} kullanılmıştır. Tahmin süreçlerinde iki adet aerodinamik parametrenin girdi olarak verilmesi sebebiyle, bu çalışma, 2. Modelin 1. Modele kıyasla daha iyi sonuçlar verdiğini göstermiştir.

Göbek yüksekliği rüzgâr hızını, U_D , atmosferik hava sıcaklığını, T_{atm} ve türbin rotor dönüş hızını, Ω içeren üç adet aerodinamik parametre girdilerinin, Yapay Sinir Ağları (*ANN*) ile çalışılarak kullanılmasıyla, rüzgâr türbinleri mekanik çıkış gücü, P belirlenmiştir. *ANN* tahmin aygıtının, ideal rotor dönüş hızlarında, Ω , yani, $\Omega=16.14$ rpm'lik dönüşlerde, en iyi çalıştığı gösterilmiştir.

Diğer yandan, rüzgâr türbinleri mekanik çıkış gücü, P yapılandırması kapsamında, Uyarlamalı Sinirsel Bulanık Çıkarım Sistemi (*ANFIS*) de çalışılmıştır. Benzer biçimde, çıkış gücünün belirlenmesinde; göbek yüksekliği rüzgâr hızını, U_D , atmosferik hava sıcaklığını, T_{atm} ve türbin rotor dönüş hızını, Ω kapsayan üç adet aerodinamik parametre girdileri göz önüne alınmıştır. *ANFIS* tahmin aygıtının, ideal rotor dönüş hızlarında, Ω , yani, $\Omega=16.10$ rpm'lik rotor dönüşlerinde, en iyi çalıştığı gösterilmiştir.

Rüzgâr türbinleri mekanik çıkış gücü, P , eksenel akış indükleme katsayısı, a , güç katsayısı, C_p ve itme kuvveti (T) değerlerini kapsayan aerodinamik parametreler üzerine, rotor çapının, D_{rotor} , anma gücünün, P_r ve hava yoğunluğunun, ρ etkileri incelenmiştir. Çalışmada, dört farklı yöntem takip edilmiştir. İlk yöntemde, sadece türbin rotor çapının (D_{rotor}), anılan bu aerodinamik parametrelere etkisi analiz edilmiştir. İkincil olarak, sadece türbin anma gücünün (P_r), bu parametrelerin üzerine etkisine çalışılmıştır. Üçüncü yöntem, hem türbin rotor

çapının (D_{rotor}), hem de türbin anma gücünün (P_r) etkilerinin incelenmesini kapsar. En sonunda, aerodinamik çıktılar üzerine, hava yoğunluğunun (ρ) etkisi araştırılmıştır. Bu araştırmalarda, dokuz adet imal edilmiş rüzgâr türbini türü kullanılmıştır. Türbin anma gücü (P_r) ve türbin rotor süpürme alanı (A_d) olarak orta derecede kapasiteye sahip olan V90-3 MW tipteki rüzgâr türbininin, en yüksek rüzgâr türbini güç katsayısına (C_p) sahip olduğu gösterilmiştir.

Rüzgâr türbinlerinin rüzgâr hızı ve güç üretimi artışı, genelde, kafes sistemi kullanımıyla elde edilir. Bu açıdan, bu tez, bu sistemlerin büyük ölçekli literatür taramasını da ortaya koymuştur. Diğer yandan, doğrusal ve kavisli tipte tasarlanmış kafes yapılarının içindeki ve etrafındaki akışların incelenmesinde, hesaplamalı sayısal analiz (CFD) ve parçacık görüntülemeli hız (PIV) teknikleri bu amaçla kullanılmıştır. Sayısal çalışma, CFD çalışması kapsamında hazırlanan 17 adet tipte tasarlanmış yapıları kapsar. Flanş yüksekliği oranının $H/D=0.3$, kafesin $\Theta=5^\circ$ 'lik yarım koni açısı ve de kafesin $L/D=1.50$ 'lik boyutsuz tam gövde uzunluğu değerleri; kafes gövdesi içerisindeki rüzgâr hızının artışı üzerine üstün performans sağlamışlardır. Kafes gövdesine eklenmiş olan ve uygun olarak tasarlanan bir kafes giriş ağzının, rüzgâr hızı oranını, giriş kullanılmadanki duruma kıyasla %16 civarında artırdığı gösterilmiştir. Diğer taraftan, flanşın aşağı akım arka bölgesindeki, akış görüntülenmesinin PIV analizi ile test edilebilmesi için kavisli tipte bir kafes yapısı tasarlanmıştır.

ACKNOWLEDGMENTS

I would like to offer my deepest respects and gratitude to my supervisor Prof. Dr. Beşir ŞAHİN, who continuously provided his support during the whole academic studies that we had conducted in order to be able to write this thesis. Since this thesis eventuated by the valuable overtime supports of my dear supervisor who spared his valuable time even out of office hours for every stages of my whole studies; I would like to further thank him personally for every extra moment he had reserved for me.

I would also like to thank to Prof. Dr. Mehmet BİLGİLİ who was assisting me in every moment of my studies and who helped me about every subjects relating with the thesis, and which I had fairly benefited from his knowledge.

Within the scope of my work with computer-aided simulation content, I would like to thank to Research Assistant Harun ZONTUL who spent his time and sacrifice that I had benefited about his knowledge and labor on this subject.

I would like to thank Project Assistant Mehmet Oğuz TAŞÇI and Research Assistant Sergen TŪMSE for their time and dedication for their information and efforts that I had referred in my studies including the *PIV* experiments.

Finally, I also thank to my dear precious family members for their continuous support and patience.

CONTENTS	PAGE
ABSTRACT.....	I
ÖZ	II
EXTENDED ABSTRACT	III
GENİŞLETİLMİŞ ÖZET	VII
ACKNOWLEDGMENTS	XI
CONTENTS.....	XII
LIST OF TABLES.....	XXII
LIST OF FIGURES	XXVI
NOMENCLATURE	XLII
1. INTRODUCTION	1
1.1. Overview of the Present Work	1
1.2. Energy Status in the World, Europe, and Turkey	2
1.2.1. Renewable Energy Sources and their Development in the World.....	7
1.2.2. Development of the Offshore Wind Power Technology in the World	11
1.2.3. Analysis of Turkey’s Electrical Energy Generation	14
1.2.4. Analysis of Turkey’s Renewable Energy Utilization	20
1.2.5. Analysis of Province Based Existing Wind Power Farms in Turkey	23
1.2.5.1. Turkey’s Cumulative Wind Power Capacity for Large Commercial Electricity Generations	26
1.2.5.2. Turkey’s Total Offshore Wind Power Capacity	27
1.2.6. Analysis of Turkey’s Present Situation in Wind Energy Generation	29
1.2.7. The Leading Countries of the World in Wind Power Generation	33
1.2.8. Turkey’s Future Prospect in Wind Energy	34
1.2.9. Turkey’s City Based Wind Farm Status	38
1.2.10. World’s and Turkey’s Current Wind Energy Situation	50

1.3. Wind Turbine Energy Generation	53
1.3.1. History of Wind Turbines	53
1.3.2. Rapid Shift of Energy Generation Using Wind Turbines Globally and in Turkey	53
1.3.3. Main Wind Turbine Aerodynamic Parameters	57
1.3.4. Wind Turbine Casing Studies and Classifications of Wind Turbines	60
1.3.5. Analysis of Casing Systems Applied to Horizontal Axis Wind Turbines.....	62
1.3.5.1. Horizontal Axis Wind Turbine with Exclusive Diffuser Components.....	62
1.3.5.2. Wind Turbine with Airfoil Shaped Diffuser Component.....	63
1.3.5.3. Wind Turbine with a Flange Component Introduced to the Diffuser Structure	65
1.3.5.4. Wind Turbine Casing Including Nozzle, Diffuser, and Flange Components Together	69
1.3.5.5. Smart Solutions to Cased Wind Turbines	71
1.3.5.5.(1). Flexible Flange Idea	71
1.3.5.5.(2). Wind Turbine Casing by Passive Flow Control Devices in Airfoil Cross-Section.....	74
1.3.5.5.(3). Truncated Nozzle-Diffuser Shaped Wind Turbine Casing.....	75
1.3.5.5.(4). Scoop Type of Wind Turbine Casing Configuration.....	76
1.3.6. Casing Systems Applied to Vertical Axis Wind Turbines.....	76
1.3.7. Shrouding of Savonius Wind Turbines.....	79
1.3.8. Recent Methods in Wind Energy Generation.....	81
1.3.8.1. Increased Velocity Wind Turbines (<i>INVELOX</i>).....	81

1.3.8.2. Neodymium Magnetic Wind Turbines.....	82
1.3.8.3. Vortex Bladeless Wind Turbines	83
2. LITERATURE SURVEY AND OUTLINE OF THE PRESENT STUDY	89
2.1. Literature Survey	89
2.1.1. Aerodynamic Characteristic Concept of Horizontal Axis Wind Turbines.....	89
2.1.1.1. Efficiency Analysis of Operating Wind Farms.....	89
2.1.1.2. Aerodynamic Parameter Analysis.....	90
2.1.2. Estimation of Aerodynamic Characteristics for Horizontal Axis Wind Turbines.....	92
2.1.2.1. Wind Energy Density Forecast by Statistical Analysis.....	92
2.1.2.2. Wind Power Output and Aerodynamic Forecasts through Artificial Neural Networks (<i>ANN</i>).....	94
2.1.2.2.(1). Wind Power Output Curve Determination by ANN	94
2.1.2.2.(2). Determination of Aerodynamic Parameters by ANN	97
2.1.2.3. Wind Power Output Curve Determination by Adaptive Neuro-Fuzzy Inference System (<i>ANFIS</i>).....	99
2.1.3. A Novel Concept of Wind Turbine Shrouding Systems.....	102
2.1.3.1. History of Wind Power Generation Systems and their Shroudings.....	102
2.1.3.2. Developments of Wind Turbine Capacity and Installations	103
2.1.3.3. Wind Turbines with Diffuser	104
2.1.3.4. Wind Turbine with a Nozzle-Diffuser-Flange Components	107
2.1.3.5. Vertical Axis Wind Turbines	110

2.1.4. Numerical CFD Analysis of Wind Turbine Shrouding Systems	111
2.1.5. Experimental PIV Analysis of Wind Turbine Shrouding Systems..	116
2.2. Outline, Objective, and Scope of the Dissertation.....	116
3. MATERIALS AND METHODS.....	125
3.1. Statistical Analysis for the Determination of Wind Energy Density.....	125
3.2. Calculation of Wind Power and Efficiency	127
3.3. Aerodynamics of Horizontal Axis Bare Wind Turbines	128
3.3.1. Blade Element Momentum Theory	129
3.3.2. Blade Element Angular Momentum Theory	134
3.3.3. Output Power Estimations of Bare Wind Turbines	136
3.3.3.1. Utilization of Artificial Neural Networks	136
3.3.3.2. Utilization of Adaptive Neuro-Fuzzy Inference System....	142
3.4. Aerodynamics of Shrouded Horizontal Axis Wind Turbines.....	149
3.4.1. Blade Element Momentum Theory for Wind Turbines with Diffuser Constructed	153
3.4.2. CFD Analysis of Wind Turbine Casing Shrouds.....	156
3.4.2.1. Definition of CFD Parameters	156
3.4.2.2. Standard k- ϵ Model	157
3.4.2.3. Physics of Standard k- ϵ Model.....	158
3.4.3. PIV Analysis of Wind Turbine Shrouds	160
3.4.3.1. Particle Image Velocimetry (<i>PIV</i>) Channel System.....	160
3.4.3.2. Experimental Aperture	161
3.4.3.3. Dye for Particle Image Velocimetry (<i>PIV</i>) Experiments ...	162
3.4.3.3.(1). Dye Visualization Experiments.....	162
3.4.3.4. Particle Image Velocimetry (<i>PIV</i>) Experiments.....	163
3.4.3.4.(1). Measurement Principle.....	163
3.4.3.5. Illumination	165

3.4.3.6. Adaptive Cross-Correlation Technique and Further Analysis	166
3.4.3.7. Experimental System.....	167
4. RESULTS AND DISCUSSIONS.....	171
4.1. Statistical Analysis of Wind Energy Density in the Babuburnu – Çanakkale Region of Turkey	171
4.1.1. Introduction	171
4.1.2. The Objective of the Present Work.....	171
4.1.3. Results and Discussions.....	173
4.1.4. Concluding Remarks.....	182
4.2. Efficiency Analysis of an Installed Wind Farm Located in South of Turkey .	183
4.2.1. Introduction	183
4.2.2. The Objective of the Present Work.....	183
4.2.3. Results and Discussions.....	185
4.2.3.1. Identification of Wind Directions for Considered Wind Turbines.....	185
4.2.3.2. Introduction of Cut-in and Cut-out Speeds	190
4.2.4. Concluding Remarks	198
4.3. Aerodynamic Characteristics of a Horizontal Axis Wind Turbine in Belen-Hatay, Turkey	199
4.3.1. Introduction	199
4.3.2. The objective of the Present Work	200
4.3.3. The Technique of the Study.....	201
4.3.3.1. Study Area and Data Description.....	201
4.3.3.2. Aerodynamic Concept.....	202
4.3.4. Results and Discussions.....	203
4.3.5. Concluding Remarks	207

4.4. Analysis of Aerodynamic Characteristics of 2 MW Horizontal Axis Large Wind Turbine.....	208
4.4.1. Introduction.....	208
4.4.2. The Objective of this Part of the Work.....	208
4.4.3. Examination of the Location of the Wind Farm and Analysis of the Working Efficiency of the Turbines.....	209
4.4.4. Results and Discussions.....	213
4.4.5. Concluding Remarks.....	220
4.5. Estimation of Aerodynamic Characteristics for a Horizontal Axis Wind Turbine.....	222
4.5.1. Introduction.....	222
4.5.2. The Objective of the Present Work.....	222
4.5.3. The Technique of the Study.....	223
4.5.3.1. Feasibility of Wind Farm Locations and Technical Specifications of Wind Turbines.....	223
4.5.3.2. ANN Forecasting Model Concept.....	225
4.5.4. Results and Discussions.....	228
4.5.5. Concluding Remarks	233
4.6. Estimation of Wind Power Output Curve using Artificial Neural Network....	233
4.6.1. Introduction.....	233
4.6.2. The Objective of the Present Work.....	234
4.6.2.1. Regional Feasibility Study for the Installation of the Wind Farm and Technical Specifications of Wind Turbines	234
4.6.2.2. ANN Forecasting Method.....	239
4.6.3. Results and Discussions.....	241
4.6.3.1. ANN Results	241

4.6.3.2. Errors in the Results of <i>ANN</i> Method with Reference to the Actual Power Output (<i>P</i>).....	245
4.6.4. Concluding Remarks.....	247
4.7. Wind Power Curve Estimation by Adaptive Neuro-Fuzzy Inference System.	248
4.7.1. Introduction	248
4.7.2. The Objective of the Present Work.....	249
4.7.2.1. Study Region, Data, and Turbine Technical Specifications	249
4.7.2.2. <i>ANFIS</i> Forecasting Method.....	254
4.7.3. Results and Discussions.....	259
4.7.4. Concluding Remarks.....	263
4.8. Theoretical Analysis of Different Capacity Wind Turbines Using the Blade Element Momentum Theory.....	264
4.8.1. Introduction.....	264
4.8.2. The Objective of the Present Work.....	265
4.8.3. Results and Discussions.....	269
4.8.4. Concluding Remarks	274
4.9. Wind Turbine Shrouding Systems.....	276
4.9.1. Comparison of Theoretical and Actual Power Coefficients	276
4.9.2. Variation of Wind Speed through the Rotor Cross-Section Placed in Diffuser with Different Geometrical Parameters	277
4.9.3. The Progress of Wind Speed in the Airfoil Structured Casing System	279
4.9.4. Comparison of Airfoil Structured Casing System with respect to the Conventional Linear Diffuser Casing Systems	281
4.9.4.1. Case Study 1.....	281
4.9.4.2. Case Study 2	282

4.10. Comparison of the Casing Advantages Described by the main Aerodynamic Characteristics.....	284
4.10.1. A Short Review of the Influence of Wind Turbine Shrouding Systems	321
4.11. Numerical and Experimental Performance Analyze of Wind Turbine Shrouding Systems	325
4.11.1. Introduction	325
4.11.2. The Objective of the Present Work	326
4.11.2.1. Linear Optimized Configurations	329
4.11.2.2. Curved Type Optimization.....	330
4.11.3. Results and Discussions.....	332
4.11.3.1. Results of Linear Optimizations.....	332
4.11.3.1.(1). Analysis of the Flange Component Influence ..	337
4.11.3.1.(2). Analysis of the Diffuser Opening Angle Influence	341
4.11.3.1.(3). Analysis of the Casing Length Influence ...	343
4.11.3.1.(4). Analysis of the Inlet Shrouding Component Influence	345
4.11.3.2. Results of Curved Optimizations	347
4.11.4. Concluding Remarks	357
5. OVERALL CONCLUSIONS AND RECOMMENDATIONS.....	361
5.1. Overall Conclusions	361
5.2. Resultant Outputs of the Conducted Studies in the Dissertation	361
5.2.1. Conclusions for Wind Energy Density Statistical Analysis.....	361
5.2.2. Conclusions for Installed Wind Farm Efficiency Analysis.....	362
5.2.3. Conclusions for Horizontal Axis Wind Turbine Aerodynamic Characteristics	364

5.2.4. Conclusions for 2.0 MW Horizontal Axis Large Wind Turbine Aerodynamic Characteristics	365
5.2.5. Conclusions for Horizontal Axis Wind Turbine Aerodynamic Characteristics Estimation.....	366
5.2.6. Artificial Neural Network Estimation of Wind Power Output Curve	368
5.2.7. Adaptive Neuro-Fuzzy Inference System Estimation of Wind Power Curve	369
5.2.8. Blade Element Momentum Theory Analysis Applied to Different Capacity Wind Turbines.....	369
5.2.9. Wind Turbine Shrouding System Flow and Performance Analyses through Utilizations of Numerical CFD and Experimental PIV Methods.....	372
5.3. Recommendations for Future Work	373
REFERENCES	375
CURRICULUM VITAE.....	405
APPENDICES	407



LIST OF TABLES**PAGE**

Table 1.1.	Comparison of the offshore versus onshore wind technologies by presenting the advantages and disadvantages of offshore technology (Bilgili et al., 2011)	12
Table 1.2.	Regional based all electric distribution companies operating in Turkey.....	18
Table 1.3.	Daily average electricity generation in Turkey in 2017, based on the electricity generating plant types	18
Table 1.4.	Average daily electricity generation in Turkey in 2017, based on the national and imported energy sources.....	19
Table 1.5.	Turkey's total available theoretical wind energy potential and its current production	24
Table 1.6.	Turkey's cumulative wind power capacity for large commercial electricity generations	27
Table 1.7.	Turkey's offshore wind power potential.....	28
Table 1.8.	Installed wind farm information considering Northwest of Turkey.....	41
Table 1.9.	Installed wind farm information considering Northwest of Turkey (Continuing)	42
Table 1.10.	Installed wind farm information considering North of Turkey.....	44
Table 1.11.	Installed wind farm information considering the South and Middle regions of Turkey	46
Table 1.12.	Installed wind farm information considering the West of Turkey.....	48

Table 1.13.	Installed wind farm information considering the West of Turkey (Continuing)	49
Table 1.14.	Classification of horizontal axis wind turbines categorized by the rotor diameters and the power rating data (Tummala et al., 2016)	61
Table 1.15.	The utilities of vertical axis wind turbine (<i>VAWT</i>) and enclosure applications placed at the cooling tower exit (Chong et al., 2014a; Chong et al., 2014b)	79
Table 1.16.	Comparison of bladeless wind turbine advantages and disadvantages (Demirbas and Andejany, 2017).....	87
Table 4.1.	Seasonal and yearly Weibull parameters for Bababurnu station.....	176
Table 4.2.	Seasonal and yearly average wind speed and wind energy potential for the Bababurnu station.....	182
Table 4.3.	Monthly average wind speed data (<i>Considering the boundary values</i>).....	185
Table 4.4.	Monthly average electricity generations per hour (<i>Considering the boundary values</i>).....	186
Table 4.5.	Monthly average wind direction data (<i>Considering the boundary values</i>).....	186
Table 4.6.	Monthly average air temperature data (<i>Considering the boundary values</i>).....	187
Table 4.7.	Power efficiencies of wind turbines including T01, T03, T04, and T05.....	192
Table 4.8.	Wind turbine technical specifications.....	202
Table 4.9.	Technical properties of wind turbines (<i>VESTAS</i> 2017)	211
Table 4.10.	Wind turbine technical properties.....	224

Table 4.11.	The input combinations and obtained equations of <i>ANN</i> models.....	232
Table 4.12.	The training and testing results of Models 1 and 2.....	232
Table 4.13.	Technical properties of wind turbines.....	235
Table 4.14.	Variation range of variables and related to statistical parameters.....	236
Table 4.15.	<i>MAPE</i> and <i>R</i> results of the forecasting model estimations	245
Table 4.16.	Technical properties of the considered wind turbines	249
Table 4.17.	Variation of variables and related statistical parameters	251
Table 4.18.	Basic linkage relations to the first layer (i.e., <i>premise</i>) using three inputs (U_D , T_{atm} , and Ω).....	256
Table 4.19.	Gaussian curve membership (i.e., <i>gaussmf</i>) functional relations of the first layer (i.e., <i>premise</i>).....	257
Table 4.20.	<i>MAPE</i> and <i>R</i> statistical results of the <i>ANFIS</i> forecasting model estimations	263
Table 4.21.	Wind turbines considered for the analysis of aerodynamic parameters (WP, 2018)	267
Table 4.22.	Wind turbines considered for the analysis of aerodynamic parameters (<i>Continuing</i>) (WP, 2018).....	268
Table 4.23.	Related reference names, the symbols relating to the results given in Figure 4.63, the relevant casing geometries of wind turbines, the type of studies, related other data and information	286
Table 4.24.	Related reference names, the symbols relating to the results given in Figure 4.64, the relevant casing geometries of wind turbines, the type of studies, related other data and information	292

Table 4.25.	Related reference names, the symbols relating to the results given in Figure 4.66, the relevant casing geometries of wind turbines, the type of studies, related other data and information	299
Table 4.26.	Related reference names, the symbols relating to the results given in Figure 4.67, the relevant casing geometries of wind turbines, the type of studies, related other data and information	304
Table 4.27.	Related reference names, the symbols relating to the results given in Figure 4.68, the relevant casing geometries of wind turbines, the type of studies, related other data and information	310
Table 4.28.	Related reference names, the symbols relating to the results given in Figure 4.69, the relevant casing geometries of wind turbines, the type of studies, related other data and information	318
Table 4.29.	Optimized linear casing shrouds.....	335
Table 4.30.	Coordinates of the optimized casing shroud cases	336

LIST OF FIGURES**PAGE**

Figure 1.1.	Global energy generation and World's total installed power capacity between 2000 and 2017, a) total energy generation of <i>OECD</i> countries, b) World's monthly total energy generation, c) Electricity production from different energy sources, d) Total global installed power generation using different energy resources.....	6
Figure 1.2.	All renewable energy sources and their sub-groups (Bilgili et al., 2015a)	8
Figure 1.3.	Offshore wind farm status in Europe, a) Number of offshore wind farms and grid-connected offshore wind turbines in Europe, b) Offshore wind power capacities of the leading European countries and the total installed power of the continent	13
Figure 1.4.	a) Total energy generations of Turkey and source-based shares between 1970 and 2017, b) Total installed power and its energy consumptions between 1975 and 2017 in Turkey	16
Figure 1.5.	The primary sectoral based electricity consumption items of Turkey.....	19
Figure 1.6.	Renewable installed power of Turkey and its source based shares	22
Figure 1.7.	Total electricity generation using only renewable energy sources in Turkey.....	22
Figure 1.8.	The map indicating those regions where desirable theoretical wind power potential exists for electricity generation in Turkey.....	24

Figure 1.9.	Wind speed distribution of Turkey at 50 m altitude	27
Figure 1.10.	Present situation of wind power capacities in Turkey expressed by the geographical territories and current types of installations.....	31
Figure 1.11.	Distributions of installed power of wind farms according to provinces of Turkey	32
Figure 1.12.	Total installed wind power capacity of Turkey between 2001 and 2018.....	33
Figure 1.13.	Installed power capacities of wind farms considering World's all leading countries.....	34
Figure 1.14.	Variation of the source based installed power (<i>GW</i>) in Turkey based on the current state politics scenario	37
Figure 1.15.	Locations of the installed wind farms in the Northwest region of Turkey	40
Figure 1.16.	Locations of the installed wind farms in the North region of Turkey.....	43
Figure 1.17.	Locations of the installed wind farms in the South and Middle regions of Turkey	45
Figure 1.18.	Locations of the installed wind farms in the West region of Turkey.....	47
Figure 1.19.	Statistical comparison of installed wind power capacity between Europe and the World (<i>GWEC</i> , 2016; <i>GWEC</i> , 2017).....	55
Figure 1.20.	Power coefficient, C_p ranges of different wind turbine designs available in the practical applications (Hau, 2006).....	59

Figure 1.21.	Illustration of the axial velocity distribution profile, $u(x)$ on the symmetry axis of an airfoil structured diffuser casing without an installed wind turbine (Rio Vaz et al., 2014).....	64
Figure 1.22.	Blade profiled diffuser shrouding configurations (Shives and Crawford, 2011), and a double airfoil shaped diffuser casing system, 8 th configuration (Bet and Grassmann, 2003)...	64
Figure 1.23.	Diffuser casing configuration of (Matsushima et al., 2006), only including a flange component at downstream	67
Figure 1.24.	Variation of maximum wind speed ratio, K along the diffuser central axis as a function of diffuser casing full-body length, L/D studied under a free-stream wind speed of $U_\infty=5$ m/s, (Matsushima et al., 2006).....	67
Figure 1.25.	Variation of maximum wind speed ratio, K along the diffuser central axis as a function of diffuser casing full cone angle, 2θ studied under a free-stream wind speed of $U_\infty=5$ m/s, (Matsushima et al., 2006).....	68
Figure 1.26.	Variation of maximum wind speed ratio, K along the diffuser central axis as a function of flange height ratio, H/D studied under a free-stream wind speed of $U_\infty=5$ m/s, (Matsushima et al., 2006)	68
Figure 1.27.	Flow structures around wind turbine with a nozzle, diffuser, and flange components, all together (Ohya and Karasudani, 2010).....	70
Figure 1.28.	Wind turbine output power, P depending on free-stream wind speed, U_∞ (Ohya and Karasudani, 2010)	70
Figure 1.29.	a) Conventional rigid flanged casing, b) general flexible flanged casing idea (Hu and Wang, 2015).....	71

Figure 1.30.	Curves of open gap with threshold of free-stream wind velocity, V_r (Hu and Wang, 2015)	72
Figure 1.31.	Wind loads acting on two kinds of wind turbines with and without a flanged casing at 60 m/s for various rated powers, P_r (Hu and Wang, 2015)	72
Figure 1.32.	The casing configuration to conduct drag comparison based on casing components, a) dimensions of a smart flanged casing, b) side view of the flexible flange component and related dimensions (Hu and Wang, 2015).....	73
Figure 1.33.	Drag forces, F_D of the casing components (Hu and Wang, 2015).....	73
Figure 1.34.	Drag coefficients, C_d of the casing components (Hu and Wang, 2015)	74
Figure 1.35.	The airfoil type casing appropriate for small scale wind turbines with passive control devices (Coşoiu et al., 2013).....	75
Figure 1.36.	Cross-section of a truncated triangle used for wind turbine shrouding (Setoguchi et al., 2004).....	75
Figure 1.37.	General schematic scoop optimization concept (Wang et al., 2008).....	76
Figure 1.38.	Samples of mostly used vertical axis wind turbines available in the industry.....	77
Figure 1.39.	The earliest known vertical axis windmills built initially by Persians in Nashtifan region in the east province of Khorasan of Iran (Sahin et al., 2017).....	78
Figure 1.40.	Vertical axis wind turbine shrouding application for the cooling tower, a) cooling tower with the other auxiliary equipment, b) dimensioning of <i>VAWT</i> settlement in diffuser	

	shaped shroud and guide vane locations (Chong et al., 2014a; Chong et al., 2014b).....	78
Figure 1.41.	The concentrator arrangement optimization for <i>VAWT</i> ($\alpha=45^\circ$, $\beta=52^\circ$, $\gamma=45^\circ$, and $\delta=15^\circ$) (Altan et al., 2008) ...	80
Figure 1.42.	<i>INVELOX</i> type energy generation method, a) schematic view to represent the main components of the <i>INVELOX</i> body, b) an installed, energy generating <i>INVELOX</i> type of wind turbine (Allaei and Andreopoulos, 2014)	82
Figure 1.43.	A miniature type of wind turbine, a) exploded components, and b) its shrouding (Howey et al., 2011).....	83
Figure 1.44.	A view of vortex bladeless wind turbine generating power.....	84
Figure 1.45.	An optimized configuration and its dimensions for numerical and experimental testing (Cajas et al., 2017).....	85
Figure 1.46.	Gyroscopic electric generator (Mane et al., 2017).....	86
Figure 2.1.	Opposite influences of either sole nozzle and diffuser casing applications (Ohya and Karasudani, 2010).....	105
Figure 2.2.	Diffuser geometry with straight wall (Jafari and Kosasih, 2014).....	107
Figure 2.3.	Flow around a wind turbine with a brimmed diffuser including nozzle-diffuser-flange components all together (Ohya and Karasudani, 2010)	108
Figure 2.4.	Illustration of a curved nozzle-diffuser casing structure including also a brim (Wang et al., 2015).....	109
Figure 2.5.	Propeller placed inside the shrouding form composed of double airfoil structures (Bet and Grassmann, 2003)	109

Figure 2.6.	a) Samples of vertical axis wind turbines, b) The earliest known vertical axis windmills built by the Persians in Nashtifan located in the east provinces of Khorasan of Iran	110
Figure 3.1.	Relation of wind power potential with respect to the wind speed (Tanrioven, 2011)	127
Figure 3.2.	Actuator disc and stream-tube representation for a wind turbine	129
Figure 3.3.	Energy interaction of the rotor disc that is rotating inside the stream tube (Burton et al., 2011).....	130
Figure 3.4.	Variation of turbine rotor angular speed, Ω on the rotary disc	135
Figure 3.5.	A multi-layer perceptron.....	138
Figure 3.6.	Schematic <i>ANFIS</i> structure representation with “ <i>n</i> ” inputs, “ <i>X</i> ” linguistic labels, and “ <i>t</i> ” nodes.....	147
Figure 3.7.	Wind turbine casings mainly available in the literature.....	151
Figure 3.8.	Along with the casing dimensionless axial coordinate system defined with respect to the cross-sectional diameter of the wind turbine location, x/D ; a) increase of wind speed shown by wind speed ratio inside and in the vicinity of casing, u/U_∞ ; b) decrease of dimensionless pressure coefficient, C_{pr} (Mansour and Meskinkhoda, 2014)	152
Figure 3.9.	Energy interaction within the control volume obtained from the wind turbine with diffuser constructed	153
Figure 3.10.	Schematic representation of the water channel used for <i>PIV</i> analysis	160

Figure 3.11.	Designed wind turbine shrouding configuration a) upstream side of configuration b) downstream side of the configuration.....	161
Figure 3.12.	Fixing equipment of designed wind turbine shrouding configuration.....	161
Figure 3.13.	Wind turbine casing system located inside the <i>PIV</i> water channel.....	162
Figure 3.14.	Channel schematics and its working mechanism.....	163
Figure 3.15.	3D <i>PIV</i> representation of illumination and camera system.....	164
Figure 3.16.	Source of a Nd. YAG Laser used in <i>PIV</i> experiments.....	165
Figure 3.17.	The location side of the flow viewer camera, i.e., at the right-hand side of the upstream flow direction.....	168
Figure 3.18.	Wind turbine shrouding system and flow monitoring camera.....	169
Figure 4.1.	Map of the region and location of the station (REGD, 2017)...	172
Figure 4.2.	Wind direction and frequency distribution for Bababurnu station, considering (a) 1 st (Top - left), (b) 2 nd (Top - right), and (c) 3 rd years of measurement time (Bottom)	173
Figure 4.3.	Hourly variation of the mean wind speed for Bababurnu station.....	175
Figure 4.4.	Wind speed frequency distributions for Bababurnu station, considering (a) 1 st , (b) 2 nd , and (c) 3 rd years of measurement time	178
Figure 4.5.	Monthly variations of mean wind speed values for Bababurnu station, considering (a) 1 st , (b) 2 nd , and (c) 3 rd years of measurement time	180

Figure 4.6.	Monthly variations of wind power potential for Bababurnu station, considering (a) 1 st , (b) 2 nd , and (c) 3 rd years of measurement time.....	181
Figure 4.7.	Distributions of wind directions for turbines T01, T02, T03, T04, and T05.....	188
Figure 4.8.	Monthly distributions of wind direction for wind turbines T01, T02, T03, and T04.....	189
Figure 4.9.	Monthly distributions of wind direction for wind turbine T05.....	190
Figure 4.10.	$C_p - \lambda$ distribution.....	194
Figure 4.11.	$C_T - \lambda$ distribution.....	194
Figure 4.12.	$C_p - a$ distribution.....	195
Figure 4.13.	$C_T - a$ distribution.....	195
Figure 4.14.	$U_w - U_\infty$ distribution.....	196
Figure 4.15.	$U_D - U_\infty$ distribution.....	196
Figure 4.16.	Power - U_∞ distribution.....	197
Figure 4.17.	Thrust - U_∞ distribution.....	197
Figure 4.18.	Monthly total electric generations and average wind speeds....	198
Figure 4.19.	Distribution of power generation, P with hub-height wind speed, U_D	203
Figure 4.20.	Variation of flow induction factor, a with hub-height wind speed, U_D	204
Figure 4.21.	Relation of power coefficient, C_p with hub-height wind speed, U_D	205
Figure 4.22.	Distribution of thrust coefficient, C_T with hub-height wind speed, U_D on the impeller.....	205

Figure 4.23.	Variation of thrust force, T with hub-height wind speed, U_D ...	206
Figure 4.24.	Sebenoba wind power plant in Hatay province (<i>REGD</i> , 2017).....	210
Figure 4.25.	Probability density of rotational speed, Ω	212
Figure 4.26.	Variation of turbine output power, P with hub-height wind speed, U_D at varied rotational speeds, Ω considering wind turbine TI	213
Figure 4.27.	Variation of turbine output power, P with the tip speed ratio, λ_R for five wind turbines.....	216
Figure 4.28.	Variation of flow induction factor, a with the tip speed ratio, λ_R for five wind turbines.....	217
Figure 4.29.	Variation of power coefficient, C_p with the tip speed ratio, λ_R for five wind turbines.....	218
Figure 4.30.	Variation of thrust coefficient, C_T with the tip speed ratio, λ_R for five wind turbines.....	219
Figure 4.31.	Variation of thrust force, T with the tip speed ratio, λ_R for five wind turbines.....	219
Figure 4.32.	Variation of angular flow induction factor, a' with the tip speed ratio, λ_R for five wind turbines.....	220
Figure 4.33.	The location of Belen <i>WPP</i> in Hatay province of Turkey.....	224
Figure 4.34.	<i>ANN</i> architecture used in this part of the dissertation.....	227
Figure 4.35.	Comparison between prediction and actual results for power, P	229
Figure 4.36.	Comparison between prediction and actual results for axial flow induction factor, a	229
Figure 4.37.	Comparison between prediction and actual results for power coefficient, C_p	230

Figure 4.38.	Comparison between prediction and actual results for thrust coefficient, C_T	230
Figure 4.39.	Comparison between prediction and actual results for thrust force, T	231
Figure 4.40.	Probability density representation of rotational speed (Ω)	239
Figure 4.41.	Schematic representation of the <i>ANN</i> frame-work used in the present study denoting of layers and nodes	240
Figure 4.42.	Comparison between the prediction of <i>ANN</i> forecasting method and measured results for the training data set in terms of studied data	242
Figure 4.43.	Comparison of actual and predicted output power, P values for the training data set	243
Figure 4.44.	Comparison of the actual output power (P) and the forecasted computational results at 12.44 rpm	243
Figure 4.45.	Comparison of the actual output power (P) and the forecasted computational results at 13.94 rpm	244
Figure 4.46.	Comparison of the actual output power (P) and the forecasted computational results at 16.14 rpm	244
Figure 4.47.	Probability density representation of the rotational speed (Ω).....	253
Figure 4.48.	Schematic <i>ANFIS</i> representation with three inputs, three linguistic labels, and a total of 27 nodes	254
Figure 4.49.	Comparison between the prediction of <i>ANFIS</i> forecasting model and actual measured results for the training data set	259
Figure 4.50.	Comparison of actual and predicted generated power, P values for the training data set	260

Figure 4.51.	Comparison of output power (P) to the hub-height wind speed (U_D) at $\Omega=12.44$ rpm using <i>ANFIS</i> forecasting model ...	261
Figure 4.52.	Comparison of power (P) to the hub-height wind speed (U_D) at $\Omega=13.94$ rpm using <i>ANFIS</i> forecasting model	261
Figure 4.53.	Comparison of power (P) to the hub-height wind speed (U_D) at $\Omega=16.1$ rpm using <i>ANFIS</i> forecasting model	262
Figure 4.54.	Wind turbine output power, P defined by the free-stream wind speed, U_∞ , according to the influences of a) wind turbine rotor diameter, D_{rotor} , b) turbine rated power, P_r , c) both rotor diameter and turbine rated power, and d) air density, ρ	270
Figure 4.55.	Axial flow induction factor, a expressed by free-stream wind speed, U_∞ , according to the influences of a) wind turbine rotor diameter, D_{rotor} , b) turbine rated power, P_r , c) both rotor diameter and turbine rated power, and d) air density, ρ	271
Figure 4.56.	Power coefficient, C_p presented as a function of free-stream wind speed, U_∞ , for the analysis of a) wind turbine rotor diameter, D_{rotor} , b) turbine rated power, P_r , c) both rotor diameter and turbine rated power, and d) air density, ρ	272
Figure 4.57.	Thrust force, T values of the chosen wind turbines shown depending to free-stream wind speed, U_∞ , in the analysis of a) wind turbine rotor diameter, D_{rotor} , b) turbine rated power, P_r , c) both rotor diameter and turbine rated power, and d) air density, ρ	274

Figure 4.58.	Theoretical expressions of power coefficient, C_p compared to an installed wind farm results (Sørensen, 2011; Burton et al., 2011; Ilhan et al., 2018a)	277
Figure 4.59.	Distributions of wind speed ratio, u/U_∞ in four different diffuser configurations, a) four different diffuser configurations, b) corresponding wind speed ratio, u/U_∞ (Disterfano et al., 2015; Ohya and Karasudani, 2010).....	279
Figure 4.60.	Axial, u and radial, v experimental wind speed measurements inside the casing shroud bodies (Nasution and Purwanto, 2011).....	280
Figure 4.61.	Rotor power coefficients, C_p expressed as the function of thrust coefficients, C_T (Hansen et al., 2000; Disterfano et al., 2015).....	282
Figure 4.62.	Power coefficient, C_p comparisons for the wind turbines equipped with and without shrouding utilizations, and application of shroudings utilizing a flanged diffuser and an airfoil casing types (Ohya et al., 2008; Grassmann et al., 2003).....	284
Figure 4.63.	Power coefficient, C_p expressions against tip speed ratio, λ_R for different literature studies of wind turbines with and without a casing shroud utilization, reviewed in Table 4.23	285
Figure 4.64.	Wind speed ratio, u/U_∞ distributions along the central axis of the casing for different literature studies, reviewed in Table 4.24	291
Figure 4.65.	Passive control devices including five separate airfoil sections attached to allow the air injection inside (Coşoiu et al., 2013).....	297

Figure 4.66.	Distributions of dimensionless pressure coefficient, C_{pr} expressions along the central axial axis of the casing for different literature studies, reviewed in Table 4.25	298
Figure 4.67.	Distributions of dimensionless pressure coefficient, C_{pr} values along the central axis of the casing for different literature studies, reviewed in Table 4.26	303
Figure 4.68.	Distributions of power coefficient, C_p to the thrust coefficient, C_T values considering different studies in the literature, indicated in Table 4.27	310
Figure 4.69.	Variations of torque, C_Q and thrust coefficients, C_T defined to the tip speed ratio, λ_R values considering different literature studies found in the scientific studies, reviewed in Table 4.28	317
Figure 4.70.	The schematic representation of a shrouded wind turbine and its performance analysis (a) a model of a micro wind turbine located in a shroud having a diffuser and a flange component (b) The performance of a shrouded micro wind turbine in terms of power generation enhancement (Ohya and Karasudani, 2010)	327
Figure 4.71.	Linear shrouding profile structure	330
Figure 4.72.	The curved type of casing geometric configuration used for <i>PIV</i> analysis	331
Figure 4.73.	Computational conditions (Abe and Ohya, 2004)	332
Figure 4.74.	Steady and unsteady state validation of the <i>CFD</i> study in this part of the dissertation and comparison with the study of (Abe and Ohya, 2004)	333

Figure 4.75.	Coordinate representation of the vertex points of the shrouding cases; a) shroud without a flange and b) shroud having the flange component.....	335
Figure 4.76.	Flange component performance analysis in the unsteady case revealing wind speed ratio, u/U_∞ in the vicinity of the casing shroud profiles	338
Figure 4.77.	Flange component performance analysis in the unsteady case revealing pressure drop, C_{pr} in the vicinity of the casing shroud profiles	339
Figure 4.78.	Diffuser opening angle performance analysis in the unsteady case revealing wind speed ratio, u/U_∞ in the vicinity of the casing shroud profiles.....	342
Figure 4.79.	Diffuser opening angle performance analysis in the unsteady case revealing pressure drop, C_{pr} in the vicinity of the casing shroud profiles	343
Figure 4.80.	Casing length performance analysis in the unsteady case revealing wind speed ratio, u/U_∞ in the vicinity of the casing shroud profiles	344
Figure 4.81.	Casing length performance analysis in the unsteady case revealing pressure drop, C_{pr} in the vicinity of the casing shroud profiles	345
Figure 4.82.	Casing inlet shrouding component performance analysis in the unsteady case revealing wind speed ratio, u/U_∞ in the vicinity of the casing shroud profiles.....	346
Figure 4.83.	Casing inlet shrouding component performance analysis in the unsteady case revealing pressure drop, C_{pr} in the vicinity of the casing shroud profiles.....	347

Figure 4.84.	Low pressure zone resulting enhanced mass flow rate of Ohya et al. (2004) study.....	348
Figure 4.85.	Vortices generations at up radial and down radial regions at a chosen variety of instances (Ohya et al., 2004).....	348
Figure 4.86.	Low pressure concept of up flange side images of Ohya et al. (2008) and the current study, a) Ohya et al. (2008) up flange dye visualization, b) first view of current study up flange dye visualization, c) the second view of current study up flange dye visualization, d) the third view of current study up flange dye visualization	349
Figure 4.87.	Low pressure concept of up flange side images of Ohya and Karasudani (2010) and the current study, a) Ohya and Karasudani (2010) up flange dye visualization, b) first view of current study up flange dye visualization, c) the second view of current study up flange dye visualization, d) the third view of current study up flange dye visualization.....	350
Figure 4.88.	Up flange wake side images of Ohya et al. (2002) and the current study, a) Ohya et al. (2002) up flange wake dye visualization, b) first view of current study up flange wake dye visualization, c) the second view of current study up flange wake dye visualization, d) the third view of current study up flange wake dye visualization	351
Figure 4.89.	Up flange wake side images of Ohya et al. (2006) and the current study, a) Ohya et al. (2006) up flange wake dye visualization, b) first view of current study up flange wake dye visualization, c) the second view of current study up	

	flange wake dye visualization, d) the third view of current study up flange wake dye visualization	351
Figure 4.90.	Hub side images of the current study at a chosen variety of instances.....	352
Figure 4.91.	Hub side images of the current study at a chosen variety of instances for the developed flow.....	352
Figure 4.92.	Streamlines shown at downstream and up radial regions of the curved type of wind turbine casing configuration.....	353
Figure 4.93.	Vorticity results shown at downstream and up radial regions of the curved type of wind turbine casing configuration (I/s).....	354
Figure 4.94.	The dimensionless magnitude of the resultant velocity, $ V /U_{\infty}$ outputs shown at downstream and up radial regions of the curved type of wind turbine casing configuration	355
Figure 4.95.	Streamlines shown at flange downstream of the curved type of wind turbine casing configuration	356
Figure 4.96.	Vorticity results shown at flange downstream of the curved type of wind turbine casing configuration (I/s).....	356
Figure 4.97.	The dimensionless magnitude of the resultant velocity, $ V /U_{\infty}$ outputs shown at flange downstream of the curved type of wind turbine casing configuration	357

NOMENCLATURE

Parameters of Statistical Analysis

k	: Weibull shape parameter
$f_w(v)$: The probability of observing wind velocity v
c	: Weibull scale parameter
$F_w(v)$: The cumulative probability function of the Weibull distribution
v_m	: Mean wind speed
σ	: Standard deviation
$\Gamma()$: Gamma function
n	: Sample number of hours in considered wind speed amounts in statistical analysis
v_i	: Observed i^{th} sample of the wind speed in statistical analysis
$f_R(v)$: The Rayleigh probability density function

Parameters of ANN

T_{atm}	: Atmospheric air temperature
ε	: Error - energy at the output layer of an ANN structure
k	: Designation presented in the summation formula demonstrating subsequent numbers between 1 to N
$\nabla \varepsilon_k$: The gradient on the error-energy at the output layer
w_{kj}	: Steepest gradient procedure
Δw_{kj}	: Steepest descent procedure
z_k	: k 's perceptron's node-output
x_j	: The j^{th} input to that neuron
y_k	: Perceptron's output
F_N	: Nonlinear function
p	: The output layer
j	: Shows the j^{th} input to the neuron k of the output (p) layer
Φ_k	: Presented to complete the derivation of the setting of output layer weights
MAPE	: The mean absolute percentage error
R	: The correlation coefficient

Parameters of ANFIS

T_{atm}	: Atmospheric air temperature
m	: Total number of ANFIS rules to be constructed
f	: Functional designation of ANFIS rule with the subscript and the final ANFIS function in the case without subscript
p	: First coefficient of ANFIS linear equation
q	: Second coefficient of ANFIS linear equation
r	: Constant of ANFIS linear equation
i	: The i^{th} node for each linguistic label in ANFIS for the first layer and also denotes the node number for the other layers
k	: The maximum number of node for each linguistic label in ANFIS
X	: Total number of linguistic labels in ANFIS structure and variable relating the last input to last linguistic label in ANFIS
j	: Layer indicating variable
O_i	: Functions for the i^{th} node in the considered layer of ANFIS
μ	: Multiplied coefficient of ANFIS function structure
A	: First linguistic label of ANFIS
B	: Second linguistic label of ANFIS
C	: Third linguistic label of ANFIS
x	: Variable relating first input to first linguistic label in ANFIS
y	: Variable relating second input to second linguistic label in ANFIS
z	: Variable relating third input to third linguistic label in ANFIS
a_i	: First coefficient of Bell-shaped and Gaussian Curve Membership function for linguistic label A
b_i	: Second coefficient of Bell-shaped Membership function for linguistic label A
c_i	: Third coefficient of Bell-shaped Membership function for linguistic label A
c	: Second coefficient of Gaussian Curve Membership function for linguistic label A
d_i	: First coefficient of Gaussian Curve Membership function for linguistic label B
f'	: Second coefficient of Gaussian Curve Membership function for linguistic label B

- g_i : First coefficient of Gaussian Curve Membership function for linguistic label C
 j' : Second coefficient of Gaussian Curve Membership function for linguistic label C
 C_{1i} : First coefficient of Gaussian Curve Membership function for linguistic label X
 C_2 : Second coefficient of Gaussian Curve Membership function for linguistic label X
 w : The weight calculated in second layer of ANFIS
 n : Total number of inputs in the ANFIS structure
 \bar{w}_i : The normalized firing strength in third layer of ANFIS
 $\bar{w}_i f_i$: Normalized firing strength with the linear function attached
 $\sum_i \bar{w}_i f_i$: Overall output of ANFIS in fifth layer
 O_i^1 : First layer function of ANFIS for i^{th} node
 O_i^4 : Fourth layer function of ANFIS for i^{th} node
 O_i^5 : Fifth layer function of ANFIS for i^{th} node

Parameters of Wind Turbine Aerodynamics and Wind Turbine Casing Shrouds

- P_{av} : Maximum wind power that is available to be converted into electric power
 V_i : Wind speed having the potential of available wind power
 P_{th} : Theoretical power delimited by the Betz limit, maximum accessible turbine power
 P : Mechanical output power of the wind turbine, also referred as rotor shaft power
 P_r : Rated power of a wind turbine (or power rating), or simply wind turbine capacity
 P_{rt} : Power rate of a wind turbine, i.e., power per unit area
 \dot{m}_{in} : Mass flow rate of air running through control volume of a stream tube
 \dot{m}_{out} : Mass flow rate of air leaving control volume of the stream tube
 T_{atm} : Atmospheric air temperature
 p : Local pressure in the vicinity of the casing shroud
 P_{atm} : Atmospheric pressure
 ρ : Air density
 A_{in} : Inlet area of the stream tube at far upstream

A_{rotor}	: Area of the rotor disc or called as the rotor swept area (A_d)
D_{rotor}	: Rotor diameter
d	: Diameter of a single Savonius blade
Φ_p	: The diameter of the pivot axle in which both Savonius blades rotate around it
s	: Piece of diameter length in a Savonius rotor intersected by both blades
α	: The angle formed in clockwise direction between the diameter line of a single Savonius blade with the axial axis
Π	: Length of “a curtain” for Savonius rotor
ξ	: Angle of “a curtain” for Savonius rotor
π	: Length of “b curtain” for Savonius rotor
ζ	: Angle of “b curtain” for Savonius rotor
A_w	: Exit area of the stream tube at far wake
U_∞	: Free-stream wind speed
U_{rotor}	: Wind speed at the rotor disc (U_D), hub-height wind speed
U_w	: Wind speed at far wake
P_1	: Pressure at the immediate upstream of the rotor disc
P_2	: Pressure at the immediate downstream of the rotor disc
U_1	: Fluid velocity at the immediate upstream of the rotor disc
U_2	: Fluid velocity at the immediate exit after the rotor contact, existed in the plane where P_2 is existed
E_0	: Energy of the wind flow at far upstream of the rotor
E_1	: Energy of the wind flow at the rotor location
E_2	: Energy of the wind flow at far downstream of the rotor
F_{rotor}	: Thrust force of the rotor disc
ΔM	: Momentum transfer along the considered stream tube, i.e., change of the momentum
T	: Thrust force occurred by the pressure drop in the control volume
a	: Axial flow induction factor
λ	: Coefficient to relate wake and free-stream wind speeds
C_p	: Power coefficient, also referred as the efficiency
η_{mech}	: dimensionless overall efficiency including mechanical and electrical efficiencies of the wind turbine

C_{pmax}	: Betz limit
C_{pmax}^*	: Theoretical estimation of the maximum power coefficient
n	: Number of blades in a wind turbine
F_D	: Drag force
C_d	: Drag coefficient
F_l	: Lift force
C_l	: Lift coefficient
X	: Coefficient required in calculation of power coefficient in the case of hub-height wind speed is known
C_T	: Thrust coefficient
Q	: Torque origination on the rotor disc
C_Q	: Torque coefficient
Ω	: Angular speed of the turbine rotor or turbine rotor rotational speed
a'	: Angular flow induction factor (tangential flow induction factor)
r	: Radial radius of the rotor
R	: Full radius of the rotor
λ_r	: Blade speed ratio
λ_R	: Blade edge speed ratio (Blade tip speed ratio)
η_r	: Efficiency of blade element based on radial radius
η_R	: Efficiency of blade based on full radius
C_t	: Loading coefficient
G.M.T.	: General momentum theory
β	: Rotor position angle defined on clockwise direction measured with respect to the axial axis
F_h	: Harmonic motion force
k	: Spring constant
y	: The displacement of the oscillating body measured on equilibrium point
m	: Mass of the oscillating body
t	: Time
C_1, C_2	: Constants of the harmonic motion special to the optimized configurations and initial conditions
w	: Angular frequency considered in the harmonic motion
ν	: Frequency considered in the harmonic motion

A	: Amplitude, i.e., the maximum displacement measured according to the equilibrium point
φ	: The phase
v_{ob}	: Speed of an oscillating body
KE	: Kinetic energy of a harmonic motion
PE	: Potential energy of a harmonic motion
TE	: System's total energy of a harmonic motion
L	: Casing full body length, as well referred as full body length of a diffuser in the case of not nozzle utilization; scoop full body length
L_1	: Nozzle length of the casing; entrance axial length of a scoop
L_y	: Diffuser length of the casing
L_{st}	: Axial length to measure the distance of the point where the truncated triangle shroud is cut, measured with respect to the flange cross-sectional plane
L_{tr}	: Length of the triangular section of the diamond cross sectional shroud
L_s	: Turbine axial length including whole mechanical mechanism
H	: Flange height
D_1	: Casing inlet diameter in the case of nozzle utilization or diffuser inlet diameter in the case of not nozzle utilization
D_2	: Casing exit diameter
D	: Diameter of the casing where the wind turbine is installed (For the narrowest cross-sectional diameter; also, referred as the throat diameter, D_t)
D_h	: Turbine hub diameter
D_1/D	: Dimensionless casing inlet diameter normalized on turbine location diameter
D_2/D	: Dimensionless casing exit diameter normalized on turbine location diameter
L_1/D	: Dimensionless nozzle axial length
L_y/D	: Dimensionless diffuser axial length
D_0	: Exit diameter of the casing, including the flange heights
Φ_1	: Entrance diameter of a scoop
Φ_2	: Exit diameter of a scoop
L_2	: Exit axial length of a scoop

Φ_c	: Diameter of the cylindrical section of the scoop
R_c	: Radius of the cylindrical section of the scoop without the thickness
R_{ct}	: Radius of the cylindrical section of the scoop including the thickness
L_c	: Axial length of the cylindrical section of the scoop
C_{pr}	: Pressure drop along the casing body, dimensionless pressure coefficient
C_{prmax}	: Maximum pressure drop ratio
L/D	: Dimensionless casing full body length
H/D	: Flange-height ratio, dimensionless flange height
U_{max}/U_∞	: Maximum wind speed enhancement along the casing body (K), maximum wind speed ratio
U_{max}	: Maximum axial wind speed obtained inside the casing body
V_{max}	: Maximum radial wind speed obtained inside the casing body
u	: Axial wind speed
v	: Radial wind speed
u/U_∞	: Wind speed ratio inside and in the vicinity of casing
U_{uv}	: Wind velocity axis including the representation of the magnitudes of u and v together, i.e., the representation of V_x and V_y together
U_{uv}/U_∞	: The axis demonstrating u and v wind speeds normalized by U_∞
V_x	: Magnitude of the axial wind velocity, u
V_y	: Magnitude of the radial wind velocity, v
$ V $: Magnitude of the resultant wind velocity including u and v
$ V /U_\infty$: Dimensionless magnitude of the resultant velocity normalized by free-stream wind speed
U_{out}	: Wind speed at the diffuser exit plane (U_b)
A_{exit}	: Area of the diffuser exit plane without including the flange heights
P_{exit}	: Pressure at the diffuser exit plane (P_b)
P_0	: Pressure at far upstream, i.e., before the casing interaction
ε	: Dimensionless area ratio to relate area of the diffuser exit plane, A_{exit} and area of the rotor disc, A_{rotor}
μ	: Dimensionless area ratio to relate inlet area of the stream tube, A_{in} and area of the diffuser exit plane, A_{exit}
$\mu\varepsilon$: Dimensionless area ratio to relate inlet area of the stream tube, A_{in} and area of the rotor disc, A_{rotor}

P_{total}	: Total pressure in a stream tube including static and dynamic pressures
$C_{T,\text{rotor}}$: Thrust coefficient of only rotor component in the case of casing utilization
$C_{P,\text{rotor}}$: Power coefficient of the rotor with turbine in the case of casing utilization
$C_{T,\text{total}}$: Total thrust coefficient of the casing and rotor system
$C_{T,\text{diffuser}}$: Thrust coefficient of only diffuser casing shroud component in the case of rotor assembled inside the casing body
F_{diffuser}	: Thrust force of the diffuser excluding the rotor
Θ	: Half cone angle of the casing
2Θ	: Full-cone angle of the casing, diffuser opening or included angle
γ	: Nozzle contraction angle of the casing
\dot{m}	: Mass flow rate of the air passing through the rotor disc
$u(x)$: Axial velocity distribution determined as the function of axial location inside the casing body
x/L	: Dimensionless axial coordinate defined with respect to the full body length of the casing shroud
x/D	: Dimensionless axial coordinate system defined with respect to the cross sectional diameter of the wind turbine location
L/D_1	: Dimensionless casing axial full body length normalized on inlet diameter of the casing, or diffuser length ratio in the case of no nozzle
L/D_2	: Dimensionless casing axial full body length normalized on exit diameter of the casing
μ^*	: The diffuser exit to inlet area ratio, i.e., D_2^2/D_1^2 (For this expression to be valid for this definition of μ^* ; the diffuser casing should not involve an inlet shrouding and the condition $D_1=D=D_t$ should be satisfied)
A_1	: Inlet area of the casing
x	: Axial coordinates aligned with the shroud full body length
r_{dir}	: Radial coordinates perpendicular to the shroud full body length
x_t	: Location of the wind turbine inside the casing shroud
V_r	: Threshold value of free-stream wind speed at which a self-adaptive flange opens itself to prevent the damage of casing shroud
n_d	: Diffuser efficiency, defined with respect to the rotor exit wind speeds and pressures; i.e., $n_d=(P_b-P_2)/(0.5\rho(U_2^2-U_b^2))$
t_s	: Thickness of the casing shroud

- r_{dir}/D : Dimensionless radial coordinates normalized by wind turbine location diameter
- AFSCS : Airfoil structured casing system

Parameters of CFD

- Re : Reynolds number
- ν : Kinematic viscosity
- I : Turbulence intensity
- k : Turbulent kinetic energy
- l : Turbulent length scale
- ε : Turbulent kinetic energy dissipation rate
- μ : Dynamic viscosity
- C_μ : Constant of turbulent/eddy viscosity, or also referred as the empirical constant that is specified in the turbulent model
- t : Time parameter of unsteady flow
- x_i : x - coordinate direction in the x-y plane coordinate system
- u_i : Fluid speed at the x - coordinate direction in x-y plane coordinate system
- x_j : y - coordinate direction in the x-y plane coordinate system
- μ_t : Turbulent/eddy viscosity
- σ_k : Prandtl number for turbulent kinetic energy, k
- G_k : Turbulent kinetic energy generation occurred by the mean velocity gradients
- G_b : Turbulent kinetic energy formation depending on the buoyancy
- S_k : Source term defined by users for k
- S_ε : Source term defined by users for ε
- σ_ε : Prandtl number for turbulent kinetic energy dissipation rate, ε
- $C_{1\varepsilon}$: First constant in k- ε model
- $C_{2\varepsilon}$: Second constant in k- ε model
- $C_{3\varepsilon}$: Third constant in k- ε model

1. INTRODUCTION

1.1. Overview of the Present Work

Fossil energy resources have declined rapidly over the past decade; on the other hand, the frequent increasing population and technological developments have substantially increased the demand for energy. Thus, the use of fossil energy sources and the ever-increasing global warming associated with the greenhouse gas emissions are the most critical and urgent global problems at the present time. According to a report released by the International Energy Agency (*IEA*), unless any precautions are not taken; greenhouse gas emissions are foreseen to be doubled by 2050 (*IEA, 2015*). Therefore, it is quite essential to shift from the utilization of fossil fuels to renewable energy sources in order to meet this demand and to simultaneously reduce global CO_2 emissions to tolerable levels.

As a renewable energy source, the global installed capacity of 994 GW in 2007 rapidly increased by 86% and reached the total capacity of 1849 GW in 2015, considering the global situation. On the other hand, energy generation from renewable sources reached the largest annual increase by 2016; i.e., approximately 161 GW of recent capacity in this sector was introduced to the global system. This amount of renewable power corresponded to rise around 9% compared to the former case of 2015 and exhibited an overall enhancement of renewable power generation reaching to the value of 2,017 GW at the end of 2016. These installations of new renewable energy sources throughout 2016 contributed with percentages of 47%, 34%, and 15.5% by means of solar PV technology, wind energy, and hydropower, respectively to the total installed renewable energy capacity worldwide. On the other hand, further increase of global installed capacity of the 2017 year was reported as to correspond 2195 GW of installations (*WE, 2018; REN21, 2018*).

Considering the importance of energy, especially renewable energy generation methods; the dissertation was also aimed to focus on energy situation of the World, Europe, and Turkey; however, it mainly covers the status of the wind energy. A novel concept including the shrouding of wind turbines to increase the wind turbine performances, and relating literature studies of casing shroud systems are discussed. A regional study including a statistical analysis of a considered location, i.e., Bababurnu region of Turkey was taken into consideration to forecast power density of the cited zone. On the other hand, wind power and efficiency analysis of an operating wind farm in the South region of Turkey were conducted. Theoretical aerodynamic analysis of another operating wind farm was executed in order to configure the aerodynamic parameters and their variations of the considered wind turbines. Besides, Artificial neural network (*ANN*) and adaptive neuro-fuzzy inference system (*ANFIS*) were also studied in the prediction of wind turbine output power and power coefficients. Additionally, other aerodynamic parameters were also studied. Besides, the design of casing configurations and aerodynamics of wind turbine blades were investigated in detail to reveal flow characteristics inside the casing shroud systems.

1.2. Energy Status in the World, Europe, and Turkey

Persistent development of industrial and social life definitely needs energy utilization. Thus, this situation carries energy to be an inevitable key sector for the present time as well as the future of the World. In this context, the energy sector including the energy generation, its distributions, and management has been becoming more important day by day. Unless the continuous trend of the energy utilization changes, more than 90% enhancement of the global energy demand is projected to take place by 2035 as reported by (IEA, 2015). However, the main problems that arise from the use of the traditional carbon-based products are

unfortunately greenhouse gas emissions and ultimately the global warming (Ilhan and Bilgili, 2016).

The concentration of CO_2 in the atmospheric air was reported to be 405.14 ppm in November 2017 (GE, 2017). On the other hand, according to the US National Oceanic and Atmospheric Administration's Mauna Loa Station in Hawaii, the considered concentration was 403.53 ppm in November of 2016 (Loa, 2016). More than 350 ppm of the CO_2 concentration in the atmospheric air indicates the exceeding of safe limit in terms of the climate changes (GE, 2017). However, this value was only 317.71 ppm in March of 1958 when the first measurement was taken at this station (Loa, 2016). The reliable limit of 350 ppm was unfortunately exceeded with the monthly average value of 350.39 ppm for the first time in January 1988. The concentration of carbon dioxide, CO_2 , which was 280 ppm before industrialization, has not exceeded 300 ppm for the last 800 thousand years (GE, 2017). On the other hand, by May 2018; the concentration of CO_2 was reported to exceed 414.7 ppm, which was also forecasted to be increased by an average of 2.75 ppm more by 2019 (CN, 2019). In 2016, it was reported that incentives of \$ 261 billion were provided in global fuel consumption. According to the IEA's 2017 World Energy Outlook Report, this figure was 15% lower than the previous year, and also this incentive was the lowest figure in the last ten years period. In summary, \$49 billion of this total incentive was provided for the natural gas consumption, \$105 billion for petroleum consumption, and \$107 billion for fossil fuel-based electricity generation. However, according to the IEA's calculations, the amount of incentive for the renewable energy-based electricity generation in 2016 corresponded to \$ 140 billion (GE, 2017).

On the other hand, the World Bank announced that it would not be provided any incentive scheme for oil and natural gas projects after 2019, except for the exceptional circumstances (WB, 2017). The statement was executed during the “*One Planet Summit*” performed in Paris. In the banking statement, it was also

reported that only the poorest countries would be subjected to exceptions for the fossil fuel based projects where reaching the energy is clearly beneficial for those countries, and whose projects meet the situations of the Paris Climate Treaty objectives. For example, World Bank lastly provided a financed credit for the Trans Anatolian Natural Gas Pipeline Project and the Bank had also declared in 2017 that the Salt Lake natural gas storage facility of Turkey would be financed by an additional new credit (GE, 2017). This situation was later approved by the Bank in 2018, and 600,000,000 Euros of credits were given to Turkey.

On the other hand, The Climate Act, which passed in the Swedish parliament in June of 2017, entered into the force on 1 January 2018. By this law, it was aimed to reset the country's net carbon emissions by 2045, and then to reach negative values after that date. In the framework of the explanation made by the Ministry of International Cooperation, Development and Climate of the Swedish country, it has been noted that this law will criminalize the situation of not giving priority to the climate (GE, 2017).

There are several studies in the literature involving in researching the status and negative features of rapidly increasing energy demand, analysis of the present situation of fossil fuel potential, and also dealing of the alternative energy generation methods. On the other hand, the continuous trend of global energy generation, unfortunately, requires huge investments for new production, its electricity transmission, and distribution network as well as the management of the whole (Tanrioven et al., 2011; Palensky, 2011). The rapid development of the World and Turkey causes tremendous energy consumptions both on a global scale and in Turkey (EP, 2017; Kakturk and Tokuc, 2017). If the necessary precautions are not taken to compensate these energy demands especially providing incentive schemes for the development of renewable energy technologies, the shortage of the energy supply will soon, unfortunately, be faced. In the global scale, the total energy generation of the World based on the most developed countries reached an

average value of 10,053.42 TWh/year in 2017 as presented in Figure 1.1a. These *OECD* (the Organization for Economic Co-operation and Development) countries, which absolutely produce and consume the majority of the World's energy, have a tendency to increase both energy production and consumption in the near future. Besides, the World's total energy generation by 2017 reached a total of 25,570 TWh (IEA, 2017b).

Monthly energy production of *OECD* countries, considering years between 2014 and 2017, is shown in Figure 1.1b for comparison purposes. This figure shows the average monthly energy production of the World in four separate years and the annual average value is equivalent to 870.12 TWh/month, considering the averages of these years. Besides, it is evident from this figure that the highest energy generations for the considered years mainly occur in winter or summer seasons reaching their peak values. Additionally, electricity production depending on the fuel type demonstrates CO_2 based energy generations, unfortunately, constitute the highest rate of total energy generations with a 59.70% in the *OECD* countries, shown in Figure 1.1c, regarding first eight months of 2014, 2015, 2016, and 2017 years (IEA, 2017c). Finally, the World's total installed power in terms of different energy resources is shown separately in Figure 1.1d. It is clear from this figure that the share of renewable energy installations is still pretty less compared to the total installed global power. The ratio corresponding to 15.82% of hydraulic energy, nuclear energy, and other renewable installed power measured with respect to the total installed power indicates that there is a still significant lack in renewable energy technologies applied in a global scale. Since the World still produces a large part of its energy from those carbon-based combustible fuels (*CF*) (IHA, 2017; MENR, 2015a; MENR, 2015b; WEC, 2016a; Karagol and Kavaz, 2017; EM, 2017a; MENR, 2017a; MENR, 2017b; EM, 2017b; REN21, 2017; CIA, 2017; MENR, 2017c).

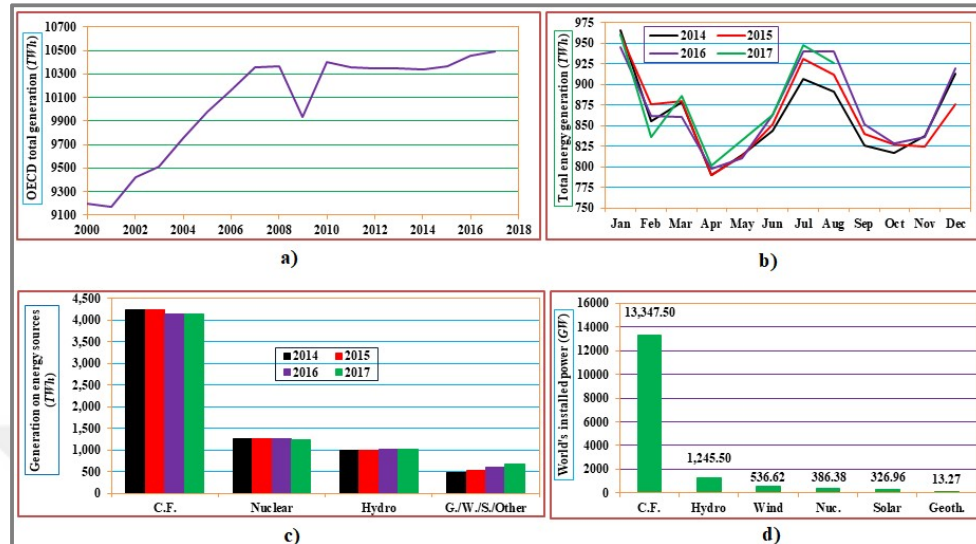


Figure 1.1. Global energy generation and World's total installed power capacity between 2000 and 2017, **a)** total energy generation of *OECD* countries, **b)** World's monthly total energy generation, **c)** Electricity production from different energy sources, **d)** Total global installed power generation using different energy resources

Alternative sources of energy are initially divided into two main categories as non-renewable and renewable energy resources (Sahin, 2004; Sahin, 2008). The first one covers the energy sources which deliver pollutions to the nature such as coal, fuel oil, and more recently the natural gas. On the other hand, the second one consists of the solar, wind, hydro, and wave energies, which are nonpolluting. Wind power nowadays is being the most demanding renewable energy source, and also it is expected to be the most challenging energy source in the near future since the capacity and installations of wind turbine technology have been improving rapidly (Bilgili, 2009; EWEA, 2016a; Ilhan et al., 2017a; Ilhan et al., 2017b). Thus, in this dissertation, the importance of renewable energy sources especially wind energy are aimed to be focused on. In this context, Turkey's current installed wind power, its available wind power, the locations of the wind farms are

comprehensively reviewed. Additionally, the wind installations compared with the installations of the World leading countries on a global scale is also discussed.

1.2.1. Renewable Energy Sources and their Development in the World

The adverse effects of fossil fuels can be alleviated over the long term at a tolerable level when renewable energy sources are used. As presented in Figure 1.2, renewable energy can be generated using a variety of resources such as bioenergy, geothermal, wind, ocean, hydro, and solar sources (Bilgili et al., 2015a). Especially biofuels are suitable to be used in the transportation sector (IEA, 2015; Chen et al., 2010). Renewable energy sources including geothermal and hydro energies are grown substantially in terms of technical point of view. On the other hand, ocean sources and biofuel technologies are the recent developing technologies. The global deployment of both technologies on a large scale is being observed.

Renewable energy generation methods shown in Figure 1.2 are also classified in terms of the environmental influences. In this regards, Atilgan and Azapagic (2016) conducted a study to reveal the environmental impacts of renewable energy generation methods. The environmental impacts that they dealt included abiotic depletion of elements, abiotic depletion of fossil resources, acidification potential, eutrophication potential, freshwater aquatic ecotoxicity potential, global warming potential, human toxicity potential, marine aquatic ecotoxicity potential, ozone layer depletion potential, photochemical oxidants creation potential, and terrestrial ecotoxicity potential. However, in terms of global warming potential, it is demonstrated that offshore wind is 88% lower than geothermal energy sources and 11% lower than hydropower sources. On the other hand, the acidification potential of the geothermal energy sources was unfortunately reported to be 281 times more than wind power.

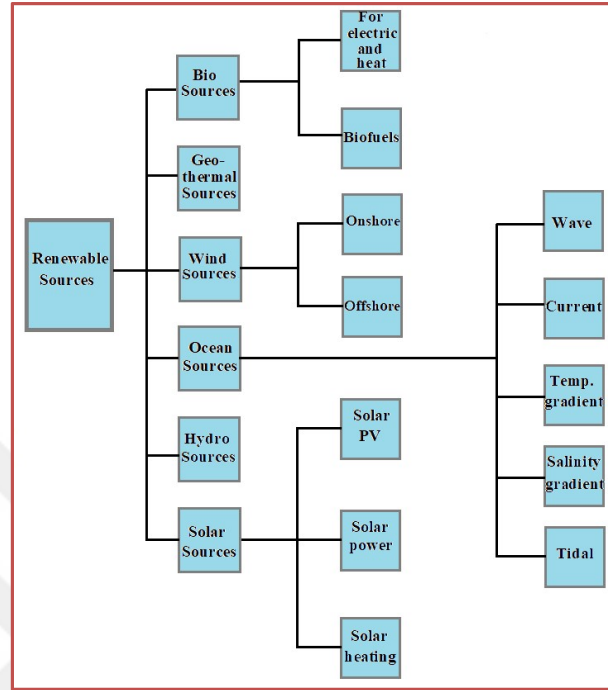


Figure 1.2. All renewable energy sources and their sub-groups (Bilgili et al., 2015a)

Renewable energy generating countries globally have already adopted some types of policies for the promotion of renewable power generations, since renewable generations are comparatively less harmful to nature. In this context, the renewable generation promotion policies mainly included feed-in tariff, renewable portfolio standards, capital subsidies, grants, rebates, investment excise, tax credits, loans, and financing as reported by (Simsek and Simsek, 2013).

The prominent countries in Europe in this sector mainly include Denmark, Germany, the United Kingdom (UK), and Spain. Denmark has set a considerable new record in the field of wind energy. The wind power plants of this country produced 14,700 GWh of electricity equivalent to 43.6% of the country's total electricity consumption in 2017 (GE, 2017). It is reported that this ratio is the highest level ever seen (DEA, 2017). On the other hand, Denmark aims to be able

to meet 50% of the electricity generation from wind energy utilization by the year 2020. Meanwhile, the share of the renewable energy sources including solar, biomass, and others in total electricity production of Denmark is expected to reach 80% (GE, 2017). In these regards, by 2018, Denmark executed capacity allocation for 6 sun projects constituting a total of 269 MW of new installations (GE, 2019a).

In Germany, new records were broken in the field of wind and solar energy applications in 2017. For the first time in the history of this country, the sum of electricity generated from the wind and solar energy has remained the lignite, coal, and nuclear power generation, behind (GE, 2017). According to the German Fraunhofer Institute data measured in 2017, the total electricity generation was 546.71 TWh (GFI, 2017). The share of the renewable energy sources in power production increased by 15% compared to the year before, reaching 210.02 TWh of total renewable energy equivalent to 38.5% of total electricity production of Germany. On the other hand, electricity generated from only wind and solar energy is reported to be 142 TWh, and this situation also showed that most of the total renewable energy generations were based on these two renewable energy sources. On the other hand, electricity production in natural gas power plants was reported not to increase any more after 2016 and stay in the same level by 2017 and 2018 (GE, 2017; GE, 2018). Solar energy is the fastest growing energy type in terms of total installations of Germany presented an annual growth of 2,960 MW of new installations by 2018, reaching 45,929 MW of total installations in this sector. On the other hand, Germany aims to increase its total wind power installations reaching 30 GW by 2035 (GE, 2019b).

In the UK, electricity generated from coal, natural gas, and nuclear power plants declined in 2017; while wind and solar energy-based renewable power production continued in a rapid increase. On the other hand, the fastest decline was observed in coal, and the amount of coal-based electricity production in the UK fell behind that of 1928 (GE, 2017). According to the reports of Durham University

Energy Institute, the energy consumption of the *UK* was 275 TWh in 2017 (BEG, 2017; DEI, 2017). The energy generations obtained using renewable sources exceeded 42 TWh corresponding to the 15% of total power generations (GE, 2017). Besides, *UK*'s electricity generation by 2018 reached a total of 335 TWh in which the energy generations obtained by renewable sources constituted 31.7% of these total generations (CN, 2019).

The wind power situation of the *USA* demonstrated an increase in installed wind power capacity greater than 7 GW in 2017. According to the declaration revealed by the American Wind Energy Association (*AWEA*), an increase of wind power capacity of the *USA* because of an additional 11 billion fund resulted in the total electricity generation by an amount of 89 GW. A total of 2,136 MW of wind turbines in 15 different projects were replaced with better ones based on the improvement studies conducted in 2017. New farms with a total of 13,332 MW wind power is under construction, and additional investment with total wind power with 15,336 MW of capacity is in the stage of projects (GE, 2017). Besides, *USA* exceeded 161 GW of total renewable power installations (REN21, 2018), in which accelerated especially the solar and wind energy installations where in terms of solar power plant installations are predicted to exceed 32 GW by 2019 (Solarist, 2018).

According to the declaration given by the Chinese National Energy Administration, the total electricity production capacity of the country increased by 133 GW in 2017. Besides, electricity generation capacity of the country based on the wind energy exhibited a 15.03 GW of increase which reached a total of 163.67 GW energy, in the same period (WI, 2017; Howey et al., 2011; Lilley and Rainbird, 1956; Manwell et al., 2009; Wood, 2011; Shonhiwa and Makaka, 2016). Further increase of wind power installations by 2018 resulted in *China*'s total wind energy power generation capacity has reached 171.6 GW (GE, 2018). On the other hand, arriving in 2019, *China*'s total installed wind power reached a level of

188.232 GW of installations (EPR, 2019). Besides, its total solar installations approached 131.1 GW by the same period (REN21, 2018).

1.2.2. Development of the Offshore Wind Power Technology in the World

Developed countries realized the benefit and importance of offshore wind energy technology. Therefore, coastal wind energy technology which is a traditional energy extraction method is now being replaced by offshore installations. In general, offshore wind power generation has so many advantages compared to the onshore wind power technology. But, offshore wind power generations are usually more complex and have higher installation expenses and maintenance costs; but some important key advantages are also presented about the offshore wind farms. For example, winds are especially quite stronger and stable at immense sea which yield higher generations of electrical energy per unit time. Also, substantial wind turbines can be installed more efficiently at the sea wind farms since the transportation of those components via marina transport is much easier. Besides, sea farms are installed far from coast resulting in the elimination of the negative visual impact and severe noise effects. Thus, testing of different wind turbine designs to improve the overall efficiency, is also much easier in the sea wind farms. Additionally, no space problem is valid at sea wind farms; thus, vast areas are already available without any limitations.

Utilization of the offshore wind power technology provides the transportation and component installations of the wind turbines to be executed in the sea more easily. Thus, this situation eliminates the limit in wind turbine sizes, unlike the case of onshore wind turbine installations. In the onshore wind power technology, one of the major problems arising during the forwarding of the turbine components is, unfortunately, the confrontation of the road restrictions. On the other hand, generated energy in offshore wind farms is carried directly by

transmission lines to urban centers. In this way, markets which require a large amount of energy in these centers can reduce the energy cost through obtaining this clean energy more speedily (Breton and Moe, 2009). In this context, the main advantages of the offshore wind power generation are given in Table 1.1 (OWE, 2009);

Table 1.1. Comparison of the offshore versus onshore wind technologies by presenting the advantages and disadvantages of offshore technology (Bilgili et al., 2011)

ADVANTAGES	DISADVANTAGES
Huge continuous zones in offshore technology are easily available especially for the grand projects,	Marine installations are usually more expensive in offshore technology,
Negative impacts due to visual and noise pollutions of onshore farms can be eliminated,	Integration of output power to the electric network is more expensive and sometimes the weak coastal grid capacity should be increased,
Free-stream wind speeds on the sea zones are usually much higher, and increase rapidly as drawn away from the shore,	Installation procedures are expensive and limited access in constructions are faced due to unfavorable conditions of the weather,
Wind turbulence is reduced to harvest more wind energy resulted by the elimination of the obstacles and barriers not found in the sea,	During wind farm operations, restricted access for wind farm executions and maintenances is usually encountered.
Wind shear is also reduced which allows to use short wind towers, eliminating of high costs of tower and other difficulties.	

Offshore wind technology grows rapidly; especially in the European Continent due to the high efficiency available over the sea. Figures 1.3a and 1.3b present grid connected numbers of offshore wind farms and grid-connected offshore wind turbines, and installed wind power capacity of offshore power plants, respectively for the European countries (GWEC, 2016). As seen from Figures 3a and 3b, a number of offshore wind farms, grid-connected offshore wind turbines, and offshore installed wind power are indeed highest in the United

Kingdom. The United Kingdom, being the leader in offshore technology and involving the highest numbers of installed wind farms and turbines, has a corresponding installed offshore wind power of 5,156 MW. On the other hand, the total number of offshore wind farms in Europe is 81, whereas, the number of grid-connected wind turbines is 3589 corresponding to a total installed offshore wind power of 12.6 GW.

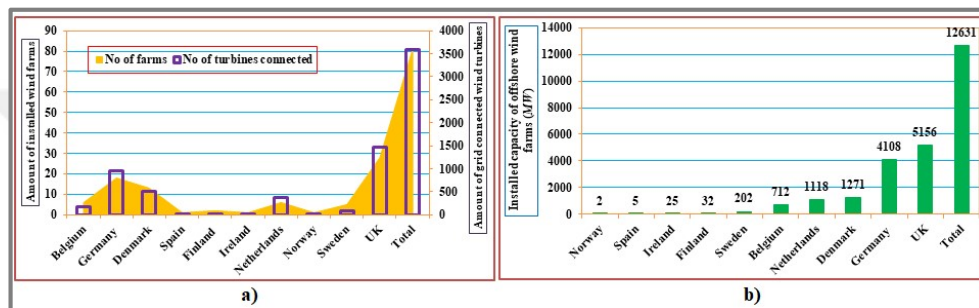


Figure 1.3. Offshore wind farm status in Europe, **a)** Number of offshore wind farms and grid-connected offshore wind turbines in Europe, **b)** Offshore wind power capacities of the leading European countries and the total installed power of the continent

The figure in 2017 on offshore wind power installations was further increased. For instance, based on the summary of work carried out at European offshore wind farms revealed that 17 additional wind farms were constructed at sea. In these regards; 8, 5, 1, 2, 1 additional offshore installations were carried out in the UK, Germany, Belgium, Finland, and France, respectively. These power installations correspond to 1,680 MW, 1,247 MW, 165 MW, 60 MW, and 2 MW of new constructions, respectively in those countries. On the other hand, the final situation of Europe offshore wind farm installations expressed based on sea basins reveal that, a total of wind farm installations in North Sea, Irish Sea, Baltic Sea, and Atlantic Ocean coasts were reported to be 11,111 MW, 2,430.556 MW, 1736.111 MW, and 138.889 MW, respectively (GWEC, 2017).

1.2.3. Analysis of Turkey's Electrical Energy Generation

Total energy generation of Turkey has increased by more than 35 times only in 47 years as clearly indicated in Figure 1.4a. Industrial and social developments, as well the population growth of Turkey resulted in increasing the total electric generation rapidly from 8 TWh to 274 TWh in between 1970 and 2016. Considering these rapid increases in electricity generation and consumption in Turkey, the Strategic Energy Efficiency Plan executed by the Turkish government demonstrated that reaching 2030; 10 TWh of electricity savings are required to be obtained compared to the reference scenario as reported by (Elsland et al., 2014). Besides, Turkish electricity generation depending on the energy source indicates that the highest power generations are still obtained from natural gas, followed by coal and hydropower as reported by (Austvik and Rzayeva, 2017; Baris and Kucukali, 2012; Melikoglu, 2016). This total electricity generation distributed over the whole country through the transmission lines with 62,636 km long (TEIAS, 2017). On the other hand, Turkey's total energy generation exceeded 297 TWh by 2017. This amount of generation was based depending on coal, natural gas, hydraulic, liquid fuel, and renewable sources with percentages of 32.8, 37.17, 19.59, 0.40, and 10.05, respectively (TEIAS, 2018).

Coal is unfortunately considered to be the most important indigenous energy source of Turkey. In this regards, the current and future role of fossil fuels in energy generations of Turkey, and compatibility of policies to the *EU*, and global energy policy and strategy should be clearly identified. For example, the Turkish government has unfortunately targeted to utilize the coal reserves entirely in the next decades. However, since Turkey has been trying hard to become an *EU* member, as well as in order to be compatible with the Kyoto Protocol, the country is needed to limit CO_2 emissions resulted from fossil fuel utilization (Baris, 2011). In this context, Turkey tried to increase installations of renewable power plants

considering the years between 1970 and 2017. Apart from the hydraulic energy, the percentage of energy generations using other renewable energy sources compared to the total electricity generations of Turkey was less than 2% by 1970. However, the ratio exceeding 6.5% by 2015 demonstrates that Turkey performed an excellent attack in energy generations using other renewable energy sources in 47 years period (TUIK, 2017). Additionally, this performance of Turkey even further enhanced reaching a higher level by 2016 almost attaining 9% in electrical generations from renewable energy sources apart from the hydraulic energy utilization. Finally, 2017 demonstrated the highest generations based on renewable sources apart from hydraulic energy corresponding to 10.05% of electricity production (TEIAS, 2018).

Figure 1.4b presents Turkey's total installed power generation and net total energy consumptions considering the range of years between 1975 and 2017. Thus, the total installed power of Turkey with 73.15 GW by the year of 2015 was further boosted in 2016, reaching 78.6 GW of the total installed power. On the other hand, by 2017, the total installed power of Turkey reached 85.2 GW (TUIK, 2018). This figure also indicates the difference of Turkey's gross total power generation and its net total energy consumption presented for the period between 1970 and 2017. Considering this period of time, the energy losses including the distributions and the other losses constitute unfortunately a considerable amount of underutilized energy equivalent to 902.4 TWh of energy (EI, 2017). On the other hand, in this period, based on the reports of regional electrical distribution companies of Turkey; unfortunately, 16.67% of lost energy is reported for each year corresponding to an energy loss of 31.19 TWh/year as shown in Table 1.2. The ratio of lost energy at this percentage of the total electric generation which was reported by these 21 regional electric distribution companies of Turkey are shown separately in this table to indicate the name of the companies and the regional energy losses (EMO, 2017).

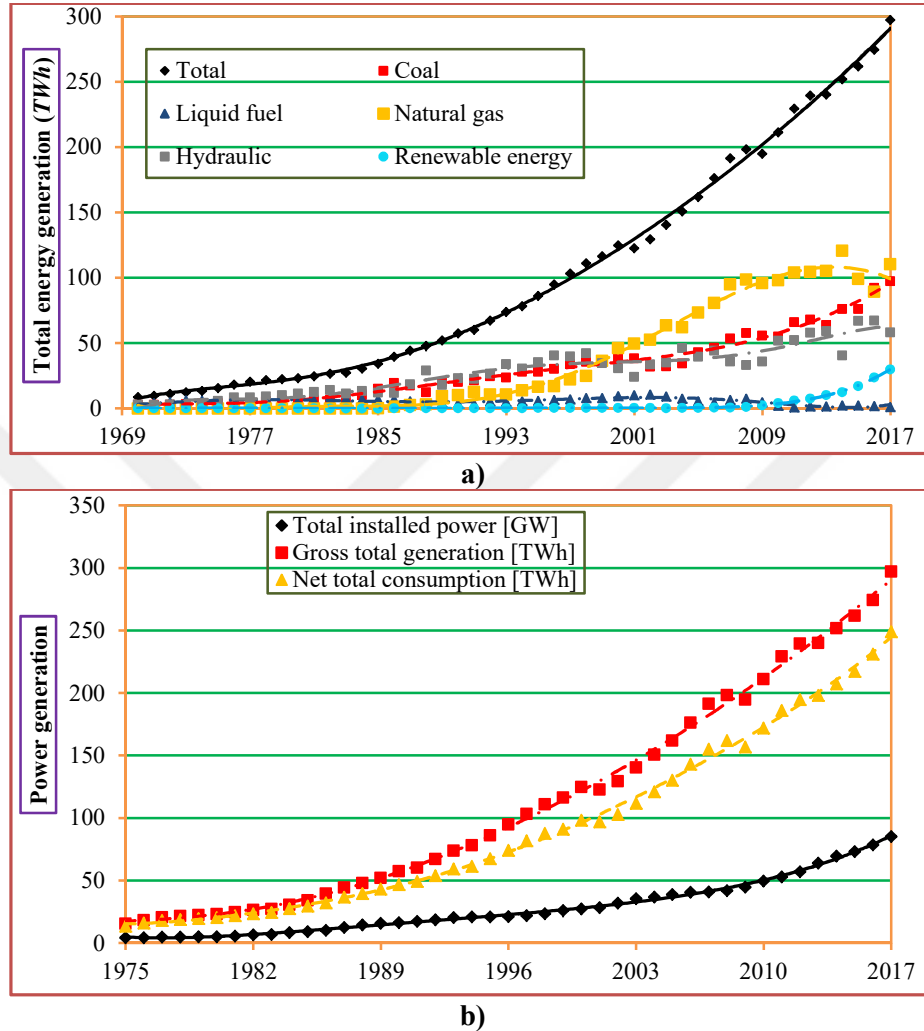


Figure 1.4. a) Total energy generations of Turkey and source-based shares between 1970 and 2017, b) Total installed power and its energy consumptions between 1975 and 2017 in Turkey

The electricity distribution infrastructure of Turkey which was divided into 21 different regions, was initially started to be customized by the *TEDAŞ* (*Turkish Electricity Distribution Company*). However, today, this distribution infrastructure is operated entirely by the private sector. In this context, Table 1.2 provides a chart for the electricity distribution companies, and detailed information are also

presented in this table. For which city and how much population each company serves are indicated in this table as well (EM, 2017c). Thus, total lost energy and its corresponding ratio are determined for Turkey from the reports of the distribution companies. While the total population exceeding 76,000,000 of Turkey purchases a mean value of 187.15 TWh of energy; a mean value of 31.19 TWh of the total generated energy is unfortunately lost, approximately reported for each year (EM, 2017c; EM, 2017d).

On the other hand, the present electrical energy generation taken into account which exceeded with an average of 840.59 GWh/day in 2017 reveals the following approximate production by those institutions, that is shown in Table 1.3:

On the other hand, the domestic ratio in electricity generation in Turkey is shown in Table 1.4. The utilization from the domestic resources in electricity generation for Turkey is, unfortunately, less compared to the imported resources. Thus, power generations from renewable energy sources, especially wind energy utilization must be increased in order to reduce the ratio of electricity generations depending on the imported fossil fuel sources. The recent results indicating that electricity generations based on the imported sources constitute the high rate of the total generations of Turkey cause, unfortunately, financial loss to this country (EBRD, 2017).

Table 1.2. Regional based all electric distribution companies operating in Turkey

No	Electric distribution company	Operating company	Served for the cities	Total population of the region	Purchased energy (MWh)	Energy sold (MWh)	Lost energy (MWh)	Ratio of lost energy (%)
1	Dicle Edaş	Eksim Holding Energy Group	Şanlıurfa, Diyarbakır, Mardin, Batman, Şırnak, and Siirt	5,526,144	21,053,332	5,612,523	15,440,809	73.34
2	Vangözü (Vedaş)	Türkerler Holding	Van, Muş, Bitlis, and Hakkari	2,092,863	3,865,646	1,557,805	2,307,841	59.70
3	Aras Edaş	Çalık Holding and Kiler Holding	Erzurum, Ağrı, Kars, Erzincan, Iğdır, Ardahan, and Bayburt	2,207,602	2,754,361	2,043,159	711,202	25.82
4	Çoruh Edaş	Aksa Energy	Trabzon, Giresun, Rize, Artvin, and Gümüşhane	1,822,195	3,583,289	3,250,900	332,389	9.28
5	Fırat Edaş	Aksa Energy	Malatya, Elazığ, Bingöl, and Tunceli	1,681,719	2,567,802	2,299,737	268,065	10.44
6	Çambel (Çedaş)	Kolin Construction, Limak Holding, and Cengiz Holding	Sivas, Tokat, and Yozgat	1,666,743	2,438,704	2,266,522	172,182	7.06
7	Toroslar Edaş	Enerjisa	Adana, Gaziantep, Mersin, Hatay, Osmaniye, and Kilis	7,830,105	15,723,489	13,757,500	1,965,989	12.50
8	Meram (Medaş)	Alarko Holding and Cengiz Holding	Konya, Aksaray, Niğde, Nevşehir, Karaman and Kırşehir	3,552,586	8,084,105	7,493,854	590,251	7.30
9	Başkent Edaş	Enerjisa	Ankara, Zonguldak, Kastamonu, Kırıkkale, Karabük, Çankırı, and Bartın	6,899,700	14,974,788	13,926,933	1,047,855	7.00
10	Akdeniz Edaş	Cengiz Holding, Kolin Construction, and Limak Holding	Antalya, Isparta, and Burdur	2,833,306	8,491,825	7,896,053	595,772	7.02
11	Gediz Edaş	Bereket Energy	İzmir and Manisa	5,420,537	14,287,404	13,235,449	1,051,955	7.36
12	Uludağ Edaş	Limak Holding, Cengiz Holding, and Kolin Construction	Bursa, Balıkesir, Çanakkale, and Yalova	4,626,181	11,169,659	10,394,648	775,011	6.94
13	Trakya (Tredaş)	IC İçtaş Energy	Tekirdağ, Kırklareli, and Edirne	1,613,616	6,472,516	5,994,530	477,986	7.38
14	Ayedaş	Enerjisa	İstanbul Anatolian Side	4,997,548	11,596,394	10,784,202	812,192	7.00
15	Sakarya (Sedaş)	Akenerji and Cez Energy	Kocaeli, Sakarya, Düzce, and Bolu	3,228,580	9,105,588	8,497,401	608,187	6.68
16	Osmangazi (Oedaş)	Zorlu Energy	Eskişehir, Afyon, Kütahya, Uşak, and Bilecik	2,634,302	6,199,085	5,726,404	472,681	7.63
17	Boğaziçi (Bedaş)	Cengiz Holding, Limak Holding, and Kolin Construction	İstanbul European Side	9,162,919	25,298,793	22,910,634	2,388,159	9.44
18	Kcetas	Kayseri Metropolitan Municipality	Kayseri	1,295,355	2,209,610	2,090,192	119,418	5.40
19	ADM (Menderes)	Bereket Energy	Aydın, Denizli, and Muğla	2,851,086	8,140,295	7,705,535	434,760	5.34
20	Akedaş (Göksu)	Kipaş	Kahramanmaraş and Adıyaman	1,672,890	3,811,201	3,621,508	189,693	4.98
21	Yeşilirmak (Yedaş)	Çalık Holding	Samsun, Ordu, Çorum, Amasya, and Sinop	3,051,887	5,322,363	4,894,555	427,808	8.04
TOTAL				76,667,864	187,150,249	155,960,044	31,190,205	16.67

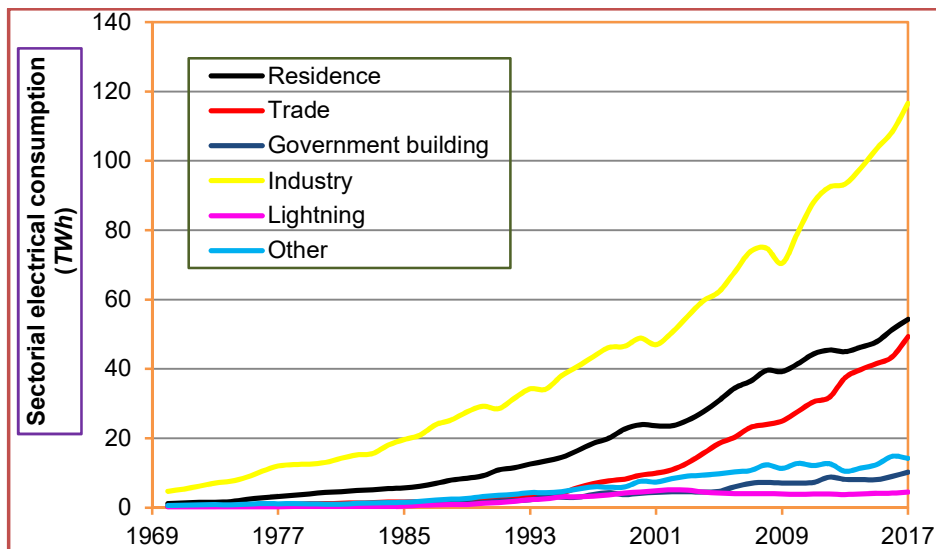
Table 1.3. Daily average electricity generation in Turkey in 2017, based on the electricity generating plant types

Plant type	Daily generation (kWh/day)	Share (%)
Private sector power plants	595,554,890	70.62
Plants of electricity generation joint-stock companies	123,849,320	14.69
Build-operate plants	92,654,000	10.99
Operating right transfer plants	15,443,310	1.83
Build-operate-transfer plants	13,086,600	1.55
Total of the above shares	840,588,120	100

Table 1.4. Average daily electricity generation in Turkey in 2017, based on the national and imported energy sources

Source type	Daily generation (kWh/day)	Share (%)
Electricity generation from the national energy resources	316,460,500	37.5238576
Electricity generation from imported energy resources	526,897,620	62.4761424

Figure 1.5 exhibits the distribution of net electricity consumption based on the primarily available energy consuming sectors in Turkey. It is clear from the figure that the most consumption of the energy depends on the industrial and residential demands regarding 47 years period of time. In additions, city and street lightning also consume a certain amount of electricity slightly exceed a total of 110 TWh of power considering the period between 1970 and 2017. The consumption item presented in this figure as “Other” particularly involves sub-items of consumptions in the agriculture, livestock, fishery sector, and municipal water abstraction pumping facilities, and also other public services, etc. (TUIK, 2017; TUIK, 2018).

**Figure 1.5.** The primary sectoral based electricity consumption items of Turkey

1.2.4. Analysis of Turkey's Renewable Energy Utilization

According to the regulation published by the Ministry of the Environment and Urbanization, it is aimed to control the emissions originated from the harmful fluorinated greenhouse gases. Turkey is also a side as a signatory to the *UN* Climate Change Framework Convention. Thus, the aim of the ministry is to establish the regulation of the principles and procedures on the harmful fluorinated greenhouse gases listed in the Kyoto Protocol which is intended for this framework convention to conduct the regulations for the use of the products or the equipment containing fluorinated greenhouse gases. In this regard, Turkey gave significant attention to the renewable energy generation as much as possible in order to be compatible with the cited Kyoto Protocol.

Moreover, the European Bank for Reconstruction and Development (*EBRD*) announced that it provides a new additional financial source for Industrial and Development Bank of Turkey. According to the statement revealed by the *EBRD*, an 85 million dollars financial source was provided in line with the growing demand for green energy in Turkey. Industrial and Development Bank of Turkey is able to use this financial source for the solar, hydropower, wind, geothermal, energy efficiency, water saving, and waste reduction projects. In the *EBRD* statement, it was also informed that within the framework of the 1.6 billion Euros Midseff program, 60 projects were financed by seven Turkish banks, with total installed capacity exceeding 1 GW of power ([MENR, 2017d](#)).

The utilized renewable energy technologies in Turkey essentially include solar energy, biomass, geothermal, wind, and hydraulic energies. In parallel with this, shares of renewable installed power; and energy generations between 2007 and 2018 period and thus its contribution to the total electricity generation are shown in Figures 1.6 and 1.7, respectively. The maximum installed renewable power of Turkey in this period of time reached 38.9 GW by 2017. It is further

enhanced to 41.4 GW by 2018. Also, analyzing this period demonstrates that the highest rate of renewable energy is always constituted by the hydraulic source as shown in Figure 1.6. Regarding the total installed power of Turkey corresponding to 87.7 GW of energy by August 2018, the share of renewable energy capacity including the hydraulic source measured with respect to the total capacity has reached 47.2% during this year. A rapid rise in the total installed renewable energy capacity is observed during this period of time, as shown in Figure 1.6 (MENR, 2017e; EPR, 2018). Also, the shares of other renewables especially wind energy applications have been increased starting from the 2010's.

While the cumulative installed power of Turkey reached 87.7 GW, the renewable installed power shares 41.4 GW of total power installations. In these regards, the contribution of renewable power to the cumulative power installations is nowadays quite sufficient for Turkey. But, its future plan of the 2023 year involves many further developments in renewable power installations.

On the other hand, the ratio of the total electricity generations using only renewable energy sources compared to the total power generations using all available sources by 2017 reached 32.6% as presented in Figure 1.7. Besides, by 2018, this ratio is reported to stay approximately at the same level and conducted to be 32.4%. Power generations from hydraulic and other renewable power sources including solar, wind, and geothermal, etc. were considered in this regard to reporting contributions of them to these yearly electricity generations. In the period of 2007 to 2018, it is also reported that the highest total electricity generation from only renewable energy sources was observed in 2018, corresponding to 97.2 TWh of generations (TEIAS, 2018).

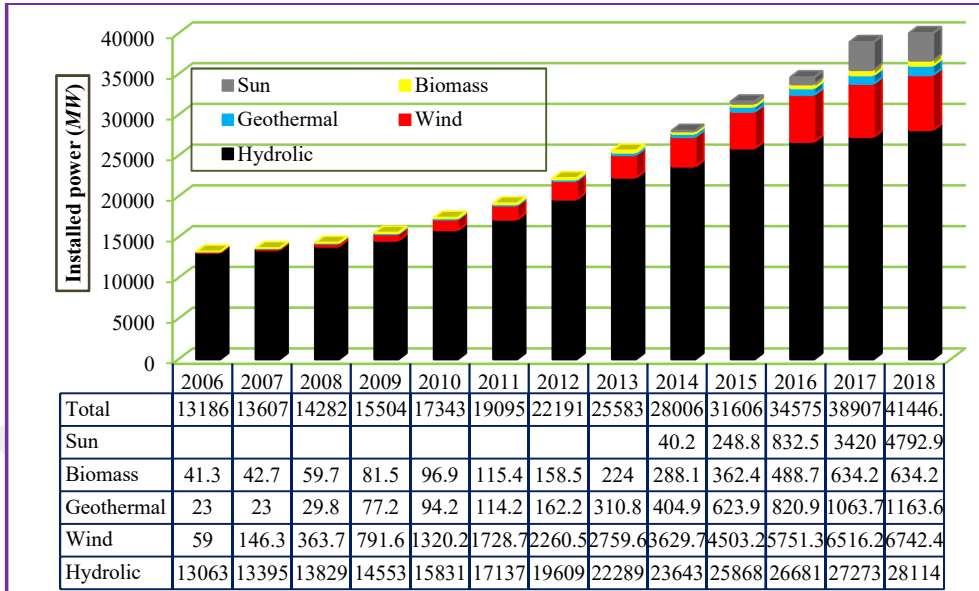


Figure 1.6. Renewable installed power of Turkey and its source based shares

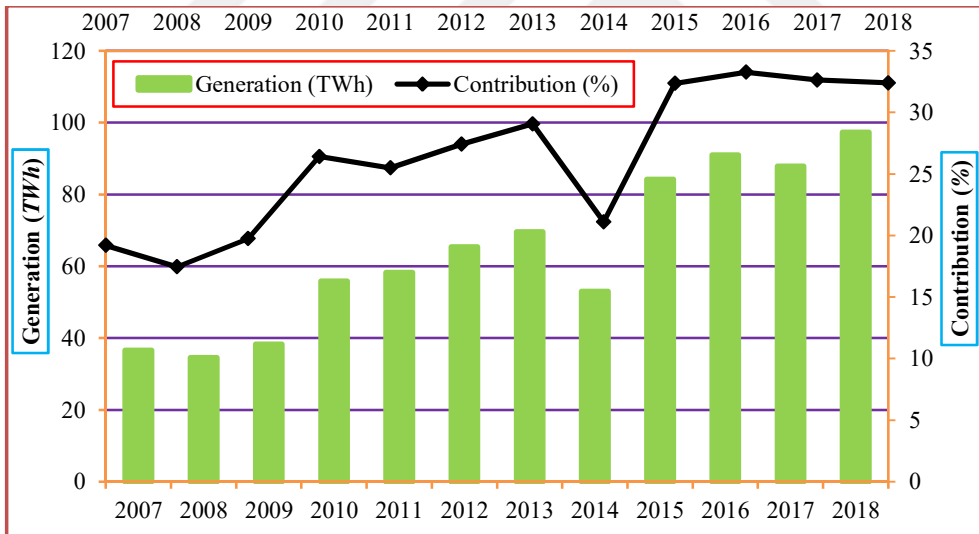


Figure 1.7. Total electricity generation using only renewable energy sources in Turkey

Ministry of the Energy and Natural Resources of Turkey prepared a strategic plan for power installations based on the renewable energy sources until

2020. According to this plan, until 2020, the electricity production planned to be produced from different renewable energy sources has been projected according to the performance of each renewable energy source. The ministry forecasts a total of 46,400 MW of renewable energy installations until 2020. On the other hand, considering the strategic plan of 2023, the total renewable energy installations are predicted to be beyond 50,000 MW (GDRE, 2017; MTA, 2017; TEMR, 2017).

1.2.5. Analysis of Province Based Existing Wind Power Farms in Turkey

Turkey's theoretical potential of the wind power is expressed in terms of the provinces as well the power extraction of each province is shown to reveal how much the total theoretical potential of the provinces have turned into reality (TWEA, 2017a; TWEA, 2019; EM, 2017d, EM, 2018). According to the Turkish Wind Energy Association (TWEA), total available wind power potential of Turkey corresponding to 115,329 MW is quite higher than the current cumulative installed power of this country. In the case of utilizing the remaining 87% of the theoretical wind potential of Turkey, the greenhouse gas emissions in this country can be reduced to a quite tolerable level. Secondly, the significant reduction in energy generations from the carbon-based fuels would be reduced. In this perspective, the theoretical wind power potential map and province-based wind power analysis of Turkey are reported in detail as indicated in Figure 1.8 and Table 1.5, respectively. The available data presented for the theoretical potential of Turkey indicates the total wind potential of Turkey even including wind speeds properly considering micro-scale wind turbines for power generations under, wind speeds of 3-4 m/s. On the other hand, for power generation using larger wind turbines, the wind speed is required to exceed 7 m/s resulting the theoretical potential of Turkey to be less than half of the cited 115,329 MW of projected power as seen in Table 1.5.

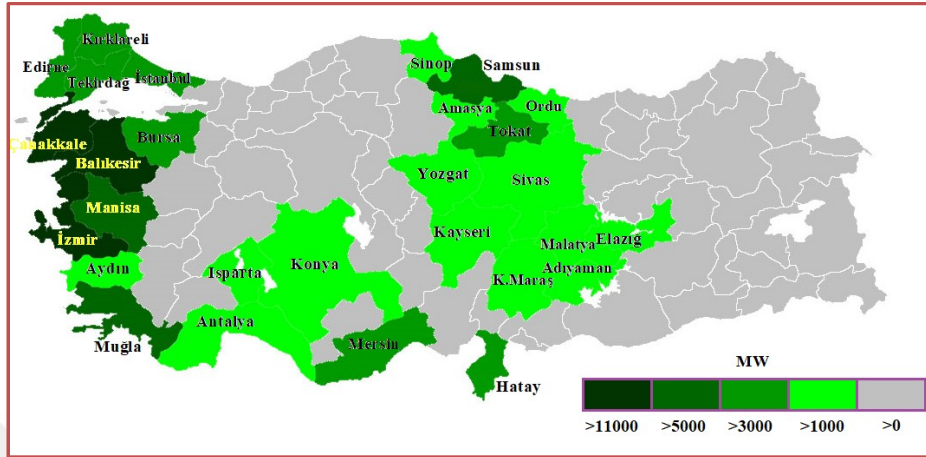


Figure 1.8. The map indicating those regions where desirable theoretical wind power potential exists for electricity generation in Turkey

Table 1.5. Turkey's total available theoretical wind energy potential and its current production

No	City	Theoretical potential (MW)	Operational (MW)	Under construction (MW)	Licensed (MW)	Pre-licensed (MW)	Total process (MW)	Process/theoretical (%)
1	Balıkesir	13,827	1,079	173	74	478	1,804	13.0
2	Çanakkale	13,013	323	70	425	501	1,319	10.1
3	İzmir	11,854	1,291	268	62	73	1,694	14.3
4	Manisa	5,302	640	58	10	30	738	13.9
5	Samsun	5,222	0	52	9	49	110	2.1
6	Muğla	5,171	196	59	0	275	530	10.2
7	Tekirdağ	4,627	153	49	19	60	281	6.1
8	İstanbul	4,177	231	108	277	250	866	20.7
9	Bursa	3,882	119	4	0	130	253	6.5
10	Mersin	3,531	173	0	0	30	203	5.7
11	Edirne	3,470	167	27	0	344	538	15.5
12	Hatay	3,414	360	27	33	30	450	13.2
13	Kırklareli	3,079	116	11	150	145	422	13.7
14	Tokat	3,002	128	1	0	40	169	5.6
15	Aydın	2,524	250	2	184	250	686	27.2
16	Ordu	2,276	0	0	10	50	60	2.6
17	K. Maraş	2,072	82	36	0	40	158	7.6
18	Kayseri	1,885	264	8	0	80	352	18.7
19	Konya	1,860	130	71	60	48	309	16.6
20	Sivas	1,642	150	0	37	240	427	26.0
21	Sinop	1,491	0	0	5	5	10	0.7
22	Isparta	1,423	60	0	0	0	60	4.2
23	Malatya	1,395	0	0	10	80	90	6.5

24	Amasya	1,200	120	10	0	60	190	15.8
25	Adıyaman	1,197	25	0	0	40	65	5.4
26	Antalya	1,170	0	0	0	100	100	8.5
27	Yozgat	1,076	0	5	0	0	5	0.5
28	Elazığ	1,028	0	0	0	40	40	3.9
29	Karaman	934	7	0	40	0	47	5.0
30	Adana	899	0	0	0	120	120	13.3
31	Afyonkarahisar	860	263	0	88	0	351	40.8
32	Osmaniye	718	235	0	0	0	235	32.7
33	Diyarbakır	635	0	0	0	0	0	0.0
34	Yalova	533	84	50	32	110	276	51.8
35	Kastamonu	515	0	0	0	0	0	0.0
36	Mardin	509	0	0	0	0	0	0.0
37	Erzincan	383	0	0	0	50	50	13.1
38	Kocaeli	334	10	294	0	30	334	100.0
39	Çankırı	315	0	0	0	50	50	15.9
40	Bilecik	309	39	41	90	0	170	55.0
41	Gaziantep	267	86	0	0	0	86	32.2
42	Denizli	239	0	0	66	0	66	27.6
43	Kütahya	190	0	0	0	50	50	26.3
44	Sakarya	180	0	0	70	110	180	100.0
45	Kırşehir	168	168	0	0	0	168	100.0
46	Giresun	160	0	0	0	0	0	0.0
47	Çorum	156	0	0	0	65	65	41.7
48	Zonguldak	120	0	0	120	0	120	100.0
49	Bolu	117	0	0	0	0	0	0.0
50	Eskişehir	89	0	39	0	50	89	100.0
51	Ankara	80	0	0	0	80	80	100.0
52	Karabük	73	0	0	0	30	30	41.1
53	Bartın	62	0	0	0	0	0	0.0
54	Niğde	62	0	0	0	0	0	0.0
55	Bingöl	61	0	0	0	50	50	82.0
56	Burdur	58	0	1	0	0	1	1.7
57	Uşak	57	54	3	0	0	57	100.0
58	Ağrı	50	0	0	0	50	50	100.0
59	Erzurum	50	0	0	0	50	50	100.0
60	Van	50	0	0	0	50	50	100.0
61	Bitlis	40	0	0	0	40	40	100.0
62	Kars	40	0	0	0	40	40	100.0
63	Kilis	40	0	0	0	40	40	100.0
64	Kırıkkale	40	0	0	0	40	40	100.0
65	Trabzon	30	0	0	0	30	30	100.0
66	Hakkâri	29	0	0	0	0	0	0.0
67	Siirt	15	0	0	0	0	0	0.0
68	Tunceli	13	0	0	0	0	0	0.0
69	Artvin	10	0	0	0	0	0	0.0
70	Ardahan	9	0	0	0	0	0	0.0
71	Batman	8	0	0	0	0	0	0.0
72	Nevşehir	8	0	0	0	0	0	0.0
73	İğdır	2	0	0	0	0	0	0.0
74	Gümüşhane	1	0	0	0	0	0	0.0
75	Şanlıurfa	1	0	0	0	0	0	0.0
76	Aksaray	0	0	0	0	0	0	0.0
77	Bayburt	0	0	0	0	0	0	0.0

78	Düzce	0	0	0	0	0	0	0.0
79	Muş	0	0	0	0	0	0	0.0
80	Rize	0	0	0	0	0	0	0.0
81	Şirnak	0	0	0	0	0	0	0.0
TOTAL		115,329	7,003	1,467	1,871	4,603	14,944	13.0

Based on the data presented in Table 1.5, it is reported that the total process of wind farm applications increased from 10,774 MW to 14,944 MW from 2017 to 2018. On the other hand, other data revealed that operational, under construction, licensed, and pre-licensed installations also shifted from 6,413 MW to 7,003 MW, 1,785 MW to 1,467 MW, 1,926 MW to 1,871 MW, and 652 MW to 4,603 MW, respectively, in this period. These alterations of power installations report that while operational and pre-licensed wind farm installations increased, under construction and licensed installations decreased, which resulted increase of active power-generating wind farms, as well as constituting process/theoretical applications to increase from 9.4% initially in 2017 to 13.0% following in 2018 (EM, 2017d, EM, 2018; TWEA, 2019).

1.2.5.1. Turkey's Cumulative Wind Power Capacity for Large Commercial Electricity Generations

In determining the characteristics and the distribution of the wind resources of Turkey, the Wind Energy Potential Atlas of Turkey (*REPA*) was developed by the General Directorate of Electrical Power Resources (*EIE*) in 2006 (Unlu, 2012). Figure 1.9 shows Turkey's wind speed map according to the yearly average at 50 m height. As clear from the map that the high wind potential shores generally lay along the Aegean Sea shore, followed by the central Black Sea, and the eastern Mediterranean Sea (Unlu, 2012). Besides, Table 1.6 gives the wind power capacity of Turkey defined with respect to the different degrees of wind resources, wind classes, power densities, and wind speeds (Unlu, 2012). According to the reports of

REPA presents that Turkey's total technical wind power potential at 50 m altitude is estimated to exceed 47 GW.

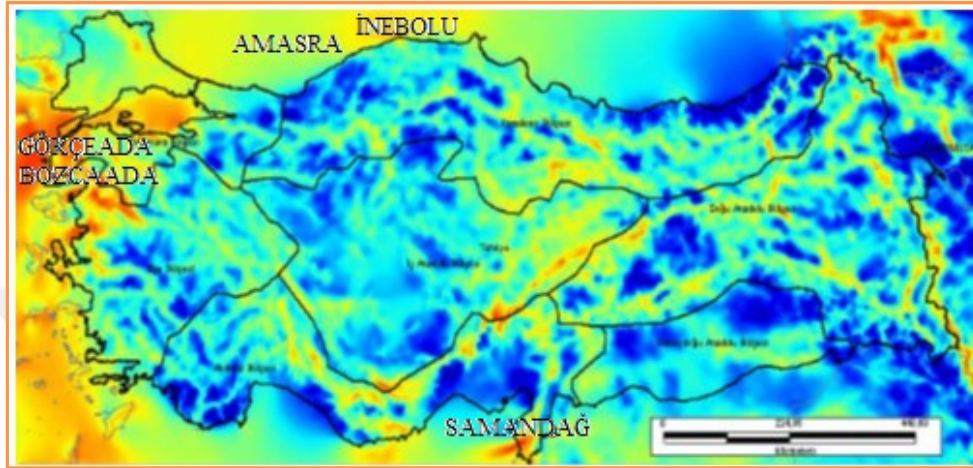


Figure 1.9. Wind speed distribution of Turkey at 50 m altitude

Table 1.6. Turkey's cumulative wind power capacity for large commercial electricity generations

Yearly average wind speed (m/s)	Power density (W/m^2)	Power potential (MW)
7.0 - 7.5	400 - 500	29,259.36
7.5 - 8.0	500 - 600	12,994.32
8.0 - 9.0	600 - 800	5,399.92
> 9.0	> 800	195.84
	Total	47,849

1.2.5.2. Turkey's Total Offshore Wind Power Capacity

The offshore wind energy advantages have made this technology to become extremely attractive; thus it is considered as a new potential resource (Zheng et al., 2016). Turkey is surrounded with seashore by three sides, named Anatolian peninsula, including the Mediterranean Sea in the south, the Aegean Sea in the west,

and the Black Sea in the North. Accordingly, Turkey can appreciate good wind potential of the windy shores (Unlu, 2012). On the other hand, offshore wind power technology has yet unfortunately not gone in action (Argin and Yerci, 2015). As of 2015, the installed wind power capacity of Turkey is 4,718 MW; this installed power further accelerated to 7,369 MW of total wind power installations by 2018; and finally, by the end of 2023, it is scheduled to approach 20,000 MW. In this respect, smart wind resource plan evaluation is vital to make a great deal of profit by optimization of land use and other related effects. Therefore, offshore wind farm investments for which Turkey is a peninsula surrounded on three sides by the sea will be inevitable (Tan, 2015).

Moreover, Turkey's offshore wind power potential exceeds 10 GW, which corresponds to 22% of the cumulative wind power capacity presented for large commercial electricity generations. In this context, Turkey's offshore wind power potential defined with respect to the different wind classes is demonstrated in Table 1.7 (Unlu, 2012).

Table 1.7. Turkey's offshore wind power potential

Wind resource degree	Wind class	Yearly average wind speed (m/s)	Power density (W/m^2)	Power potential (MW)
Good	4	7.0 - 7.5	400 - 500	5,133
High	5	7.5 - 8.0	500 - 600	3,444
Excellent	6	8.0 - 9.0	600 - 800	1,742
Extraordinary	7	> 9.0	> 800	142
			Total	10,463

Although other developed countries investigate on offshore wind power production and install wind power plants, no attempt in offshore wind power plant

installations in Turkey has yet started. Even studies regarding offshore wind power are very new in Turkey. In this context, (Argin and Yerci, 2015) studied on the offshore wind power potential evaluation of Turkey. They reported the related assessments based on the criteria such as wind potential, territorial waters, military zones, civil aviation, maritime traffic, pipelines, and underground cables according to the selected regions. Due to the high costs of offshore wind power plants, Gökçeada, Bozcaada, Samandağ, Amasra and İnebolu regions, which have high wind energy potential, are required to be initially taken into consideration as offshore wind power plant installation as seen in Figure 1.9. Inclusive factors such as sea depth, sea basement structure, distance to the land, and to the nearest transformer station of a possible plant location in these regions must also be examined, carefully. Furthermore, long term wind speed and wind power potential coinciding higher altitudes on the sea must be especially obtained before giving the final decision (Argin and Yerci, 2015).

1.2.6. Analysis of Turkey's Present Situation in Wind Energy Generation

Figure 1.10 presents the power capacities of the operating, under construction, and licensed wind farms in Turkey with seven different territorial comparison. It is specified in this figure that the main operating wind farms are mainly constructed in the West and South parts of Turkey. Thus, the leader region in terms of the operating wind power in Turkey is reported to be the Aegean region having the largest wind farm installations by the end of 2016, corresponding to a total installed wind power of 2.38 GW. These installations further increased to 2.83 GW in this region by 2018. On the other hand, this part of the dissertation also reports that the fastest construction site in the wind power sector was also observed to be located in the Aegean region by 2016. The additional wind power capacity of this territory exceeded 332.6 MW which also included under constructional wind

power capacity in this year. However, the least regional based wind power under construction was observed in the Mediterranean region with the maximum capacity of 32.75 MW by 2016. But, most of these installations in these provinces were reported to be completed, i.e., most of under construction wind farms in Aegean region is completed by 2018 resulting 138.90 MW of installations are currently under construction, and, total of 32.75 MW of under construction installations in Mediterranean region of 2016 is completed totally in 2018. At present, the fastest construction site in the wind power sector is reported to be the Marmara region with 398.60 MW of new installations by 2018. Finally, the territory where the installed licensed wind farms were most concentrated was conducted to be Marmara region in 2016, exceeding 1640 MW of wind power. As well as, the region where the licensed wind farms were least concentrated was the Southeastern Anatolia Region corresponding to only 10 MW of wind power installations in this year, since Southeastern Anatolia region of Turkey is generally extremely weak in terms of wind power applications (BNEF, 2014). Besides, by 2018, installed licensed wind farms are most concentrated also in Marmara region with a little decline to 1323.81 MW of installations. And, in Southeastern Anatolia, whole installed wind farms of 10 MW by 2016 has shifted to operating wind farms, since never left behind in terms of licensed installed wind farms in this region by 2018 (TWEA, 2018). The increase of installed power of operating wind farms between 2016 and 2018, and similarly decrease of installed power of under construction and licensed wind farms in the same period demonstrate that Turkey is performing an essential attack in terms of wind power applications. Additionally, it is glamorous to report that in Eastern Anatolia region of Turkey, an under construction wind farm with a power capacity of 11.70 MW is conducted as a new improvement, since this wind farm located in Malatya province of Turkey will be the first completed wind farm of this Eastern Anatolia region. This situation is as well

conducted to be a new development by 2018 as distinct from the situation of 2016 (TWEA, 2019).

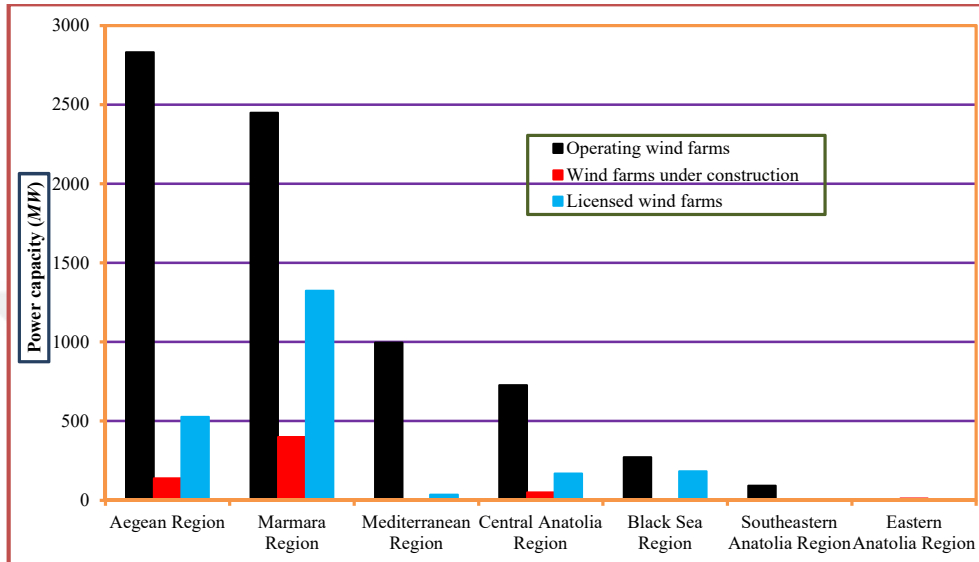


Figure 1.10. Present situation of wind power capacities in Turkey expressed by the geographical territories and current types of installations

Moreover, province-based installed wind power in Turkey is demonstrated in Figure 1.11. This figure also includes cumulative wind power capacities expressed in terms of the provinces of Turkey. The share of the wind power for leading ten provinces of Turkey, and the rest indicated small shares demonstrated as using the word “*others*” as a designation symbol in this figure. İzmir is one of the richest cities in terms of wind power potential and wind power generation and has the greatest share of wind power generation of Turkey corresponding to the value of 1,632.3 MW. On the other hand, minimum installed wind power among the ten leading provinces is in Kayseri having only 275.1 MW of capacity. The total of small shares of the province based installed wind power beyond ten leading provinces of Turkey designated with “*Others*” designation is equivalent to a total power of 3,245.3 MW (BNEF, 2014; TWEA, 2018; TWEA, 2019).

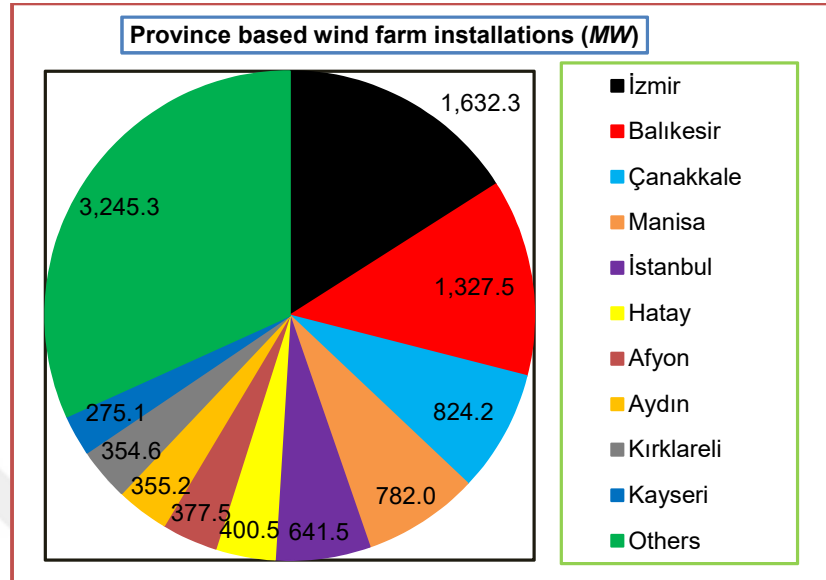


Figure 1.11. Distributions of installed power of wind farms according to provinces of Turkey

On the other hand, Figure 1.12 presents the total and annual wind farm installed capacities in whole Turkey considering a year range between 2001 and 2018. This figure indicates that although the total and annual wind power installations at the beginning of 2000 were so poor, this situation rapidly accelerated in the last ten years reaching 7300 MW of the total wind power. The total installed capacity of wind power plants was only 19 MW during 2001. However, at the present time, the total installed capacity of wind farms reached a total installed power capacity of 7369.35 MW by the end of 2018, exhibiting a superior performance of wind farm installations in last five years. On the other hand, the maximum annual installation took place in 2016 corresponding to a yearly installation of 1387.75 MW of wind power construction (TWEA, 2018; TWEA, 2019).

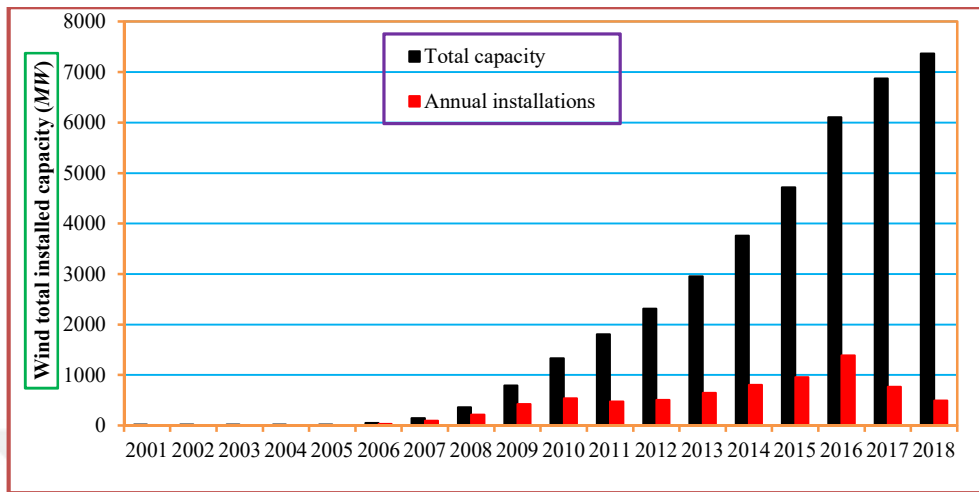


Figure 1.12. Total installed wind power capacity of Turkey between 2001 and 2018

1.2.7. The Leading Countries of the World in Wind Power Generation

Figure 1.13 presents the total installations of the leading countries all over the World and the including position of Turkey among these countries in terms of the available wind farm installed capacity is also shown (GWEC, 2016). Thus, Turkey today is the 7th country among other leading countries in the wind power sector as presented in this figure. It is also expected that the rate of wind turbine installations rises further in coming five years until the year 2023. The leader of the World in terms of wind power generation is obviously Republic of China having a huge total installed capacity of 187.730 GW of wind power. On the other hand, the least wind power generation in the World leading countries was reported to be Taiwan corresponding to only 682 MW of wind farm installations by 2016 (GWEC, 2016; EM, 2018). However, recently this country also accelerated its investments in this field reaching 744 MW of additional installations by 2018; and its plan till 2022 firstly involves additional 920 MW in offshore installations and

aims in offshore installations totally to be reached to 5 GW of total installations by 2022 (EL, 2018).

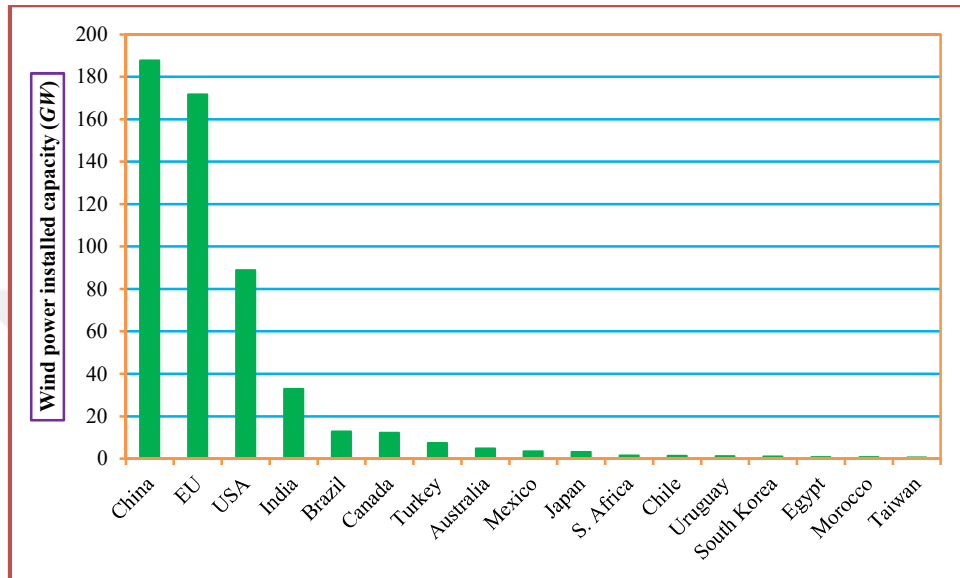


Figure 1.13. Installed power capacities of wind farms considering World's all leading countries

1.2.8. Turkey's Future Prospect in Wind Energy

2023 renewable vision plans of Turkey for hydroelectricity, wind power, solar energy, geothermal, and biomass were expected to reach 36 GW, 20 GW, 3 GW, 0.6 GW, and 2 GW of power, respectively. On the other hand, the total installed power capacity of Turkey considering whole resources were expected to exceed 120 GW according to this vision plan by 2023 (Melikoglu, 2016). Similarly, with a slight difference, Ozcan (2018) reported the forecasted installations for the same renewable resources were expected to be 34 GW, 20 GW, 5 GW, 1 GW, and 1 GW of power, respectively by 2023. However, as reported in Figure 1.6, it is shown that Turkey is in a better situation by 2018 compared with respect to the forecasted plans constituted earlier. Since, these values of two model

forecasting data are already exceeded, especially in the case of solar and geothermal power installations, as shown in this figure.

Similarly, another forecasting model of power generation of Turkey till the year 2030 is shown in Figure 1.14 considering the annual source-based installations which have rapidly accelerated since 2014. This figure involves the situation of the whole source-based power generations depending on the current politics scenario including the period of 2014-2030. This forecasting scenario was structured based on the state politics of Turkey. Thus, the relevant institution that conducts the task of related matters; i.e., Energy Marketing Regulation Board of Turkey performed the study of the estimations till the year 2030 (TWEA, 2017a).

Eight different energy sources are compared in this figure to reveal the situation of the wind energy source on the total generated power of Turkey based on the state forecasting results. In these regards, the eight sources including the stone coal, lignite, oil, natural gas, nuclear, hydroelectric, wind, and solar types are considered in this part of the dissertation; however, due to the low shares of the geothermal and biomass renewable sources, the relevant sources are not demonstrated in this figure.

The total of the eight sources indicates that the total installations currently is expected to rise from the vicinity of 80 GW to reach 120 GW of cumulative installations by the end of 2030. In this context, in this part of the dissertation, it is reported that at least 50% enhancement in total installed power of Turkey is necessarily required in forthcoming 15 years based on this forecasting model, due to the rapid social, industrial, and technological developments, as well the population rise.

It is clear from this figure that additional coal installations are forecasted to reach 19 GW by the end of 2030. On the other hand, based on the current plans, a total of 3 GW of new installations depending on the natural gas are expected to be realized in this range of time as well. The most important item on Turkey's energy

production, i.e., hydropower resources according to the current state policy indicates that 5 GW of additional installations is required to be realized in this renewable sector till the year 2022. However, the scenario estimates that no more additional applications will be executed in terms of the hydraulic power in the year range from 2022 to 2030. Besides, a total of 4.8 GW of installations in nuclear energy for the first time in Turkey are required to start running the nuclear power plant until the end of 2025. But, beyond the year of 2025, in terms of nuclear energy, no more installations will take place until 2030 as reported in the current state politics of Turkey. On the other hand, after 2022, nuclear energy will undoubtedly take over some share of electric generations obtained from the natural gas. In this context, the annual utilization of natural gas power plants will drop to lower levels, resulting in some of them to be even closed after the year of 2022. The main reason behind this situation is that natural gas power plants have higher marginal costs as a result of the expensive fuel usage as well as the CO_2 emissions. Although the initial investments of nuclear power plants are quite expensive, electricity can undoubtedly be generated at a lower running cost.

Finally, the most essential items presented in Figure 1.14 are obviously wind and solar energy sources, since they are indeed the saviors of World's future life. Current state policies pointing out the target of 2023 which forecasted a total of 3 GW additional installations in solar energy should be even surpassed. In this respect, a total of 5.5 GW solar power should be reached by 2023. Although the development of the wind power reported with respect to other sources is much better, the situation of wind installed power development with respect to the solar installations is weak. Since the current state wind policy requires the total installed power in terms of wind source should reach 20 GW by the year 2023. However, according to the current progress, only 10.8 GW of total wind power installations will be obtained until the end of 2023. This situation is unfortunately only half of the initial state target of Turkey. The state scenario absolutely requires 800

MW/year and 650 MW/year annual renewable installations for wind and solar energy, respectively in the period between 2018 and 2030 (TWEA, 2017b).

On the other hand, beyond the plans of Energy Marketing Regulation Board of Turkey, the Ministry of Energy and Natural Resources of Turkey also forecasts a strategic plan of wind power installations till the end of 2020 to reach in the total of 10000 MW power generations. The related prediction is performed according to the current performance indicators of wind power installations eventuated up to the present time. However, the ministry also declares that the necessary annual investment has to be done according to the annual plan of the ministry to exceed 20 GW of installations until the end of 2023 in order to achieve the Turkish Republic policy planned initially (GDRE, 2017; MTA, 2017; TEMR, 2017).

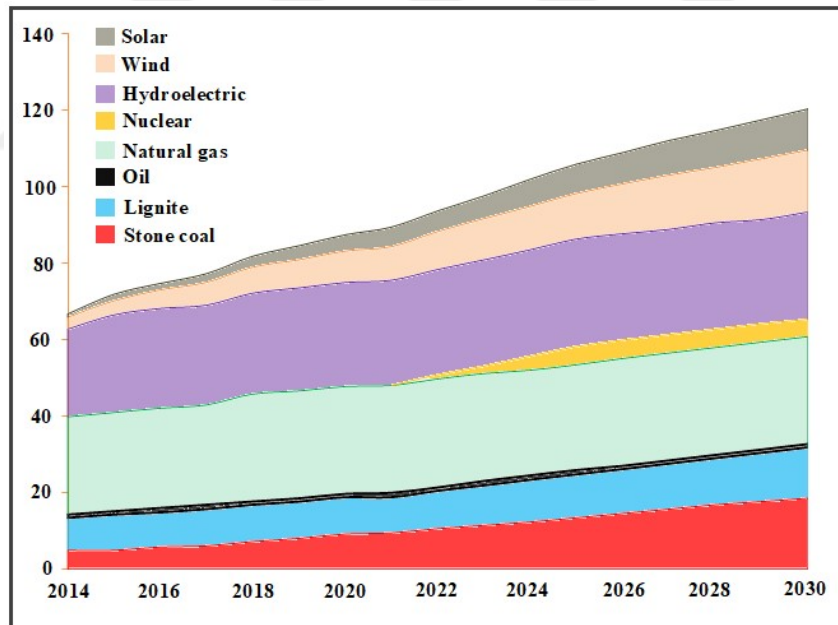


Figure 1.14. Variation of the source based installed power (GW) in Turkey based on the current state politics scenario

1.2.9. Turkey's City Based Wind Farm Status

This part of the dissertation also deals with the exact locations of the wind farms presented separately for four locations including the Northwest region, North region, South and Middle regions, and West region of Turkey, shown separately in Figures 1.15, 1.16, 1.17, and 1.18, respectively, in 2017. The detailed information regarding these wind farms including the project names, installed power of the wind farms, turbine models, types, turbine rated powers, commissioning dates of wind farms, type of wind farms, and location of the wind farms are clearly shown for these regions in Tables 1.8 and 1.9, 1.10, 1.11, and 1.12 and 1.13, respectively, in 2017.

Among the presented four provinces of Turkey, the highest wind farm installations have absolutely been executed in Northwest and West regions as presented in Figures 1.15 and 1.18, respectively, by 2017. Thus, this situation demonstrates that a high share of the available power potential in those regions has successfully turned into useful and beneficial power. On the other hand, comparatively fewer installations were applied in the South and Middle regions of Turkey by 2017, as shown in Figure 1.17. Finally, Figure 1.16 shows, unfortunately, the least installations observed in the North region of Turkey, by 2017.

Although larger installations were planned for the Northwest region comparing to the West region of Turkey reported with respect to the total installations; the operating and under constructional capacities of the wind farms of the West region were higher than the Northwest region, in 2017. However, the Northwest region was quite superior in terms of the licensed wind farm installations capacity providing that the total capacity of wind farm installations exceeded the West region of Turkey, in 2017.

On the other hand, the applied wind potential of the North, and South and Middle regions of Turkey were less compared to the applied wind potential available in the Northwest and West regions by 2017, as shown in Figures 1.16 and 1.17, compared with respect to the Figures 1.15 and 1.18. However, this part of the dissertation reports that especially in the North region of Turkey, Samsun province was unfortunately so poor of wind farm installations, by 2017, although high available wind energy potential is quite available in this province. On the other hand, Tokat province having comparatively less available wind energy potential had higher applications of wind farm installations, by 2017. However, this was still fewer, by 2017, according to its all available theoretical wind power potential. Since, both Tokat and Samsun provinces had only 4.3% and 1.2% shares of processed wind potential, respectively, referenced according to the total available theoretical wind energy potential. This situation is a little improved in 2018, i.e., cited Tokat and Samsun provinces have 5.6% and 2.1% shares of processed wind potential, respectively in this year, as observed in Table 1.5. Besides, Yozgat and Elazığ provinces also have enough available wind energy potentials for wind power generations as shown in the wind power potential map of Turkey presented in Figure 1.8. But, almost no wind farms had been constructed in those provinces, by 2017. However, in 2018, although Elazığ province performed wind power installations reaching 3.9% share of processing, Yozgat province remained in the same share of 0.5% of processing in 2018 as in the case of 2017. Additionally, considering the South of Turkey; Konya, Isparta, and Antalya provinces were quite poor in terms of the wind farm applications although a total of 4,453 MW of total available theoretical wind power potential is available in these regions. In this context, while the remaining 92.5% of available theoretical wind power potential existed as an unused source in these cited provinces, in 2017; this is improved in 2018, i.e., remaining 89.5% of available theoretical wind power potential exists as an unused source in these provinces by this year.

When all provinces of Turkey are considered, the present capacity of 14,944 MW of applied installations, by 2018, is still meager comparing to the total available theoretical wind power capacity of 115,329 MW. This applied share only corresponds to 13.0% of the total available theoretical wind power potential, in 2018. The rest of the other share is, unfortunately, the non-utilized available wind energy. In this regards, Turkey's 2023 future wind power strategy is aimed to convert the rest of the available wind power into electricity as much as and as soon as possible (TWEA, 2017b; TWEA, 2019).

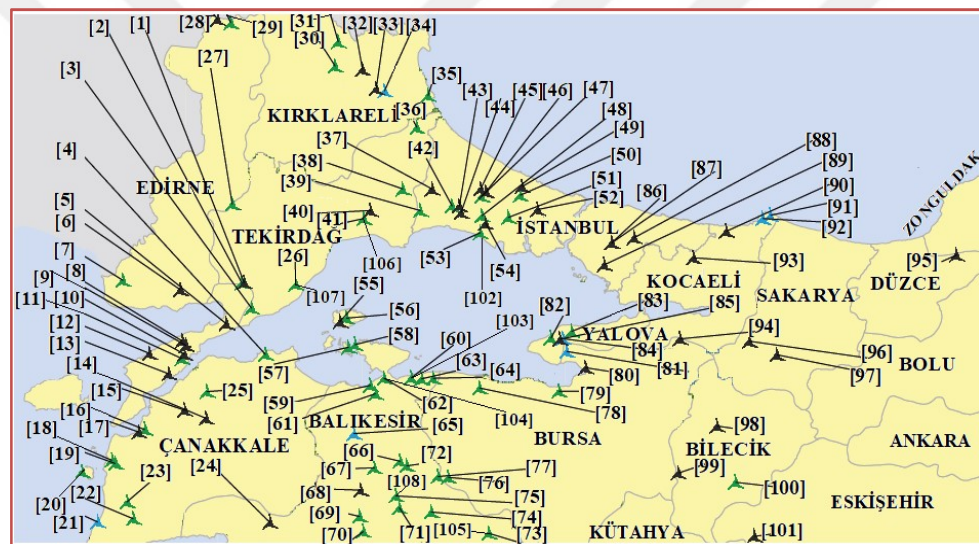


Figure 1.15. Locations of the installed wind farms in the Northwest region of Turkey

Table 1.8. Installed wind farm information considering Northwest of Turkey

Row No	Name of the project	Installed power or capacity (MW)	City	Turbine company	Turbine model	Turbine power (MW)	Commissioning of operation	Wind farm type
1	Konudağ	3.00	Tekirdağ					Licensed
2	Şadıllı	38.50	Çanakkale	GE	GE2.75-100	2.75	2014	Operating
3	Sarkaya	30.00	Tekirdağ	Enercon	E-82/E-70/E-48	2/0.8	2009	Operating
4	Biga	60.80	Çanakkale	GE	GE3.2-103	3.2	2015	Operating
5	Maslaktepe	20.00	Çanakkale					Licensed
6	Kızılcaerzi	12.00	Edirne					Licensed
7	Enez	21.60	Edirne	Nordex	N90/N100	2.5/3.3	2008/2016	Operating
8	Yeniköy	15.00	Çanakkale					Licensed
9	G	5.00	Çanakkale					Licensed
10	Yeniköy	48.00	Çanakkale					Licensed
11	Burgaz	14.90	Çanakkale	Enercon	E-48/E-44	0.8/0.9	2007	Operating
12	Saros	138.00	Çanakkale					Licensed
13	Çazi-9	51.00	Çanakkale					Licensed
14	Kocalar	26.00	Çanakkale					Licensed
15	Üçpınar	99.00	Çanakkale					Licensed
16	İntepe	55.70	Çanakkale	Enercon	E-48/E-82	0.8/2	2007/2014/2016	Operating
17	Hasanoba	51.00	Çanakkale					Licensed
18	Çamsöki	20.80	Çanakkale	Enercon	E-82/E-48	2/0.8	2009	Operating
19	Mahmudiye	29.90	Çanakkale	Siemens	SWT-2.3-101	2.3	2010	Operating
20	Bozcaada	10.20	Çanakkale	Enercon	E-40	0.6	2000	Operating
21	Göztepe	3.00	Çanakkale	Senvion	3.4M114	3.4		U.C.
22	AyRES	5.40	Çanakkale	Vestas	V90-1.8	1.8	2011	Operating
23	SaRES	27.50	Çanakkale	GE	GE2.75-100	2.75	2010/2011	Operating
24	Şapdağı	55.00	Balıkesir					Licensed
25	Koru	52.80	Çanakkale	Vestas	V112-3.3	3.3	2015	Operating
26	Barbaros	2.85	Tekirdağ	GE	GE2.85-103	2.85	2016	Operating
27	Kanije	64.00	Edirne	Siemens	SWT-3.2-113	3.2	2016	Operating
28	Hamzabeyli	3.00	Edirne					Licensed
29	Süloğlu	66.00	Kırklareli	Vestas	V126-3.3	3.3	2015	Operating
30	Zelha	25.60	Kırklareli	Siemens	SWT-3.2-113	3.2	2016	Operating
31	Karadere	19.20	Kırklareli	GE	GE1.6-100	1.6	2014/2016	Operating
32	Yeni	30.00	Kırklareli					Licensed
33	Evrencik	120.00	Kırklareli					Licensed
34	AirRES-4	60.80	Kırklareli	Siemens	SWT-3.2-113	3.2		U.C.
35	Kıyıköy	28.00	Kırklareli	Gamesa	G90/G97	2	2014	Operating
36	Kıyıköy	45.00	Tekirdağ	Nordex	N117	3	2015	Operating
37	Ertan	3.00	İstanbul					Licensed
38	Saray	6.95	Tekirdağ	Enercon	E-82/E-92	2.3/2.35	2012/2016	Operating
39	Çanta	47.50	İstanbul	Nordex	N100	2.5	2013/2014	Operating
40	Karatepe	13.00	Tekirdağ					Licensed
41	Balabanlı	50.60	Tekirdağ	Siemens	SWT-2.3-108	2.3	2014	Operating
42	Silivri	45.00	İstanbul	Nordex	N100	2.5	2014	Operating
43	Sakarbayır	3.00	İstanbul					Licensed
44	Çazi	5.00	İstanbul					Licensed
45	Yamaçtepe-2	30.00	İstanbul					Licensed
46	Küptepe	10.00	İstanbul					Licensed
47	Çataltepe	12.00	İstanbul	Nordex	N117	3	2016	Operating
48	Çataca	93.00	İstanbul	Vestas	V90-3.0/V126-3.3	3	2008/2016	Operating
49	Tayakadın	50.00	İstanbul					Licensed
50	Kemerburgaz	24.00	İstanbul	Enercon	E-82	2	2008	Operating
51	Sunçüt	1.20	İstanbul	Enercon	E-40	0.6	2006	Operating
52	Gaziosmanpaşa	50.00	İstanbul					Licensed
53	TepeRES	0.85	İstanbul	Vestas	V52-850	0.85	2006	Operating
54	Çakıl	52.50	İstanbul					Licensed
55	Marmara	10.00	Balıkesir					Licensed
56	Ada 2	4.60	Balıkesir	Enercon	E-70	2	2015	Operating
57	Paşalimanı	0.80	Balıkesir	Enercon	E-53	0.8	2013	Operating
58	Kapıdağ	28.00	Balıkesir	Vestas	V80-2.0	2	2013/2014	Operating
59	Edincik	77.40	Balıkesir	Nordex	N100/N117	2.5/2.4/3	2013/2015/2016	Operating

Table 1.9. Installed wind farm information considering Northwest of Turkey
(Continuing)

60	Bandırma	30.00	Balıkesir	GE	GE1.5se	1.5	2006	Operating
61	Bandırma-3	41.80	Balıkesir	Nordex	N90-N117	2.5/2.4	2008/2016	Operating
62	Ayyıldız	15.00	Balıkesir	Vestas	V90-3.0/V112-3.3	3/3.3	2009/2016	Operating
63	Bandırma	89.70	Balıkesir	Vestas	V90-3.0/V112-3.3	3/3.3	2009/2010/2014	Operating
64	ŞahRES	105.00	Balıkesir	Vestas	V90-3.0	3	2011/2013	Operating
65	Kalfaköy	10.20	Balıkesir	GE	GE1.7-103	1.7	-----	U.C.
66	Günaydın	20.75	Balıkesir	GE	GE2.5-100/GE2.75-100	2.5/2.75	2012/2014	Operating
67	Şamlı	113.40	Balıkesir	Vestas	V90-3.0/V90-1.8	3/1.8	2008/2010	Operating
68	Tatlıpınar	108.00	Balıkesir	-----	-----	-----	-----	Licensed
69	Kavaklı	52.80	Balıkesir	Vestas	V112-3.3	3.3	2014	Operating
70	Ortamandıra	11.20	Balıkesir	GE	GE1.6-100	1.6	2015	Operating
71	Balıkesir	143.00	Balıkesir	GE	GE2.75-103	2.75	2012	Operating
72	Keltepe	29.90	Balıkesir	Enercon	E-44/E-70	0.9/2	2009/2014/2016	Operating
73	Umurlar	10.00	Balıkesir	Vestas	V100-2.0	2	2014	Operating
74	Poyraz	77.10	Balıkesir	Enercon	E-82/E-44/E-92	2/0.9/2.35	2012/2013/2016	Operating
75	Susurluk	60.00	Balıkesir	Nordex	N100/N90	2.5	2012	Operating
76	Poyrazgözü	34.50	Balıkesir	Enercon	E-70/E-82	2	2015	Operating
77	Poyraz	32.00	Balıkesir	Siemens	SWT-3.2-108	3.2	2016	Operating
78	Harmanlık	52.80	Bursa	Vestas	V112-3.3	3.3	2015	Operating
79	Gündoğdu	9.60	Bursa	Nordex	N117	2.4	2016	Operating
80	Yalova	50.00	Bursa	-----	-----	-----	-----	Licensed
81	Kürekdagi	36.00	Bursa	Nordex	N117	3.6	-----	U.C.
82	Yalova	54.00	Yalova	Sinovel	SL1500/90 SL1500/82	1.5	2016	Operating
83	Karacabey	30.00	Yalova	Nordex	N100	2.5	2016	Operating
84	Esenköy	32.40	Yalova	Nordex	N117	3.6	-----	U.C.
85	Manastır	12.00	Yalova	-----	-----	-----	-----	Licensed
86	Çataltepe	2.00	İstanbul	-----	-----	-----	-----	Licensed
87	Mahmut Şevket Paşa-1	8.00	İstanbul	-----	-----	-----	-----	Licensed
88	Ömerli	100.00	İstanbul	-----	-----	-----	-----	Licensed
89	Aydos	14.00	İstanbul	-----	-----	-----	-----	Licensed
90	Kandıra	49.00	Kocaeli	-----	-----	-----	-----	Licensed
91	Dikili	5.00	Kocaeli	Senvion	3.6M140	3.6	-----	U.C.
92	Gökdağ	10.20	Kocaeli	GE	GE1.7-103	1.7	-----	U.C.
93	Şile	50.00	Kocaeli	-----	-----	-----	-----	Licensed
94	Yuvaçık	120.00	Bursa	-----	-----	-----	-----	Licensed
95	Zonguldak	120.00	Düzce	-----	-----	-----	-----	Licensed
96	Pamukova	20.00	Sakarya	-----	-----	-----	-----	Licensed
97	Geyve	50.00	Sakarya	-----	-----	-----	-----	Licensed
98	Meryem	30.00	Bilecik	-----	-----	-----	-----	Licensed
99	Bozüyük	90.00	Bilecik	-----	-----	-----	-----	Licensed
100	Metristepe	40.00	Bilecik	Nordex	N100	2.5	2011	Operating
101	Kartal	39.00	Eskişehir	-----	-----	-----	-----	Licensed
102	Teperes Ext.	5.00	İstanbul	Nordex	N90	2.5	2016	Operating
103	Bandırma Ext.	21.50	Balıkesir	Nordex	N90	2.5	2012	Operating
104	Ayyıldız Ext.	13.20	Balıkesir	Vestas	V112-3.3	3.3	-----	U.C.
105	Umurlar Ext.	26.40	Balıkesir	Vestas	V126-3.3	3.3	-----	U.C.
106	Balabanlı Ext.	36.00	Tekirdağ	Siemens	SWT-3.6-130	3.6	-----	U.C.
107	Barbaros	9.60	Tekirdağ	GE	GE3.2-103	3.2	-----	U.C.
108	Susurluk Ext.	15.00	Balıkesir	Nordex	N117	3	-----	U.C.

This part of the dissertation also reports that in the Northwest region of Turkey, a total of 108 wind farms were constructed consisting of 55 operating, 41 licensed, and 12 under construction, by 2017, as seen in the map indicated in Figure 1.15, and other detailed information is given in Tables 1.8 and 1.9. These wind farms included capacities corresponding to 2089.70 MW, 1764.50 MW, and 257.80 MW of installed power, respectively by 2017, which were reported to constitute a total of 4112.00 MW of installations in the near future, as long as construction of whole remaining wind farms was completed (TWEA, 2017b).

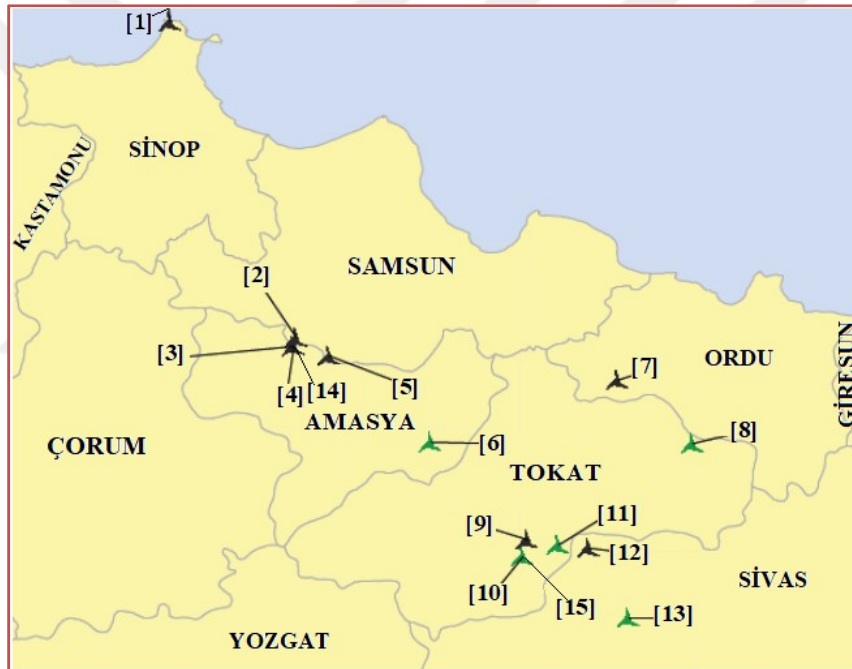


Figure 1.16. Locations of the installed wind farms in the North region of Turkey

Table 1.10. Installed wind farm information considering North of Turkey

Row No	Name of the project	Installed power or capacity (MW)	City	Turbine company	Turbine model	Turbine power (MW)	Commissioning of operation	Wind farm type
1	Fener	5.00	Sinop					Licensed
2	Havza	48.00	Samsun					Licensed
3	Kayadüzü	75.00	Amasya					Licensed
4	Amasya	40.00	Amasya	Nordex	N100	2.5	2008	Operating
5	Polat 2	9.00	Samsun					Licensed
6	Amasya	46.20	Amasya	Vestas	V126-3.3	3.3	2016	Operating
7	Akkuş	10.00	Ordu					Licensed
8	Bereketli	32.00	Tokat	Siemens	SWT-3.2-113	3.2	2016	Operating
9	Kılık	85.00	Tokat					Licensed
10	Tokat	40.00	Tokat	Nordex	N100	2.5	2010/2011	Operating
11	Akyurt	14.70	Tokat	Gamesa	G114	2.1	2016	Operating
12	Demirözü	37.00	Sivas					Licensed
13	Karacayır	12.60	Sivas	Gamesa	G114	2.1	2016	Operating
14	Amasya Ext.	42.00	Amasya	Nordex	N117	3		U.C.
15	Tokat Ext.	54.00	Tokat	Nordex	N117	3		U.C.

Considering the provinces of the North region of Turkey; a total of 15 wind farms were available including 6 of them in operation, 7 of them licensed, and 2 of them under construction, by 2017, as presented with the map shown in Figure 1.16, and other detailed information is given in Table 1.10. These wind farms had capacities equivalent to 185.50 MW, 269.00 MW, and 96.00 MW of installed power, respectively by 2017, which were reported to constitute a total of 550.50 MW of installations in the near future, as long as the whole remaining wind farm constructions were completed (TWEA, 2017b).



Figure 1.17. Locations of the installed wind farms in the South and Middle regions of Turkey

Table 1.11. Installed wind farm information considering the South and Middle regions of Turkey

Row No	Name of the project	Installed power or capacity (MW)	City	Turbine company	Turbine model	Turbine power (MW)	Commissioning of operation	Wind farm type
1	Çamınbaşı	27.00	Antalya					Licensed
2	Kuyulukoyak	16.00	Antalya					Licensed
3	Akdağ	23.63	Konya	Gamesa	G126	2.625		U.C.
4	Mutlu	44.00	Konya					Licensed
5	Bağlar	100.00	Konya					Licensed
6	Alibeyhüyüğü	3.00	Konya					Licensed
7	Hilal-2	9.90	Karaman	Vestas	V112-3.3	3.3	2015	Operating
8	Mut	52.80	Mersin	Vestas	V112-3.3	3.3	2015	Operating
9	Dağpazan	39.00	Mersin	Siemens	SWT-3.0-101	3.0	2011	Operating
10	Mersin Ext.	10.35	Mersin	Vestas	V112-3.45	3.45		U.C.
11	Mersin Mut	42.00	Mersin	Vestas	V90-3.0	3.0	2010/2013	Operating
12	Elmalı	9.90	Mersin	Vestas	V112-3.45	3.45		U.C.
13	Elmalı	30.00	Mersin	Vestas	V100-2.0	2.0	2016	Operating
14	Kurtini	14.00	Mersin					Licensed
15	Geycek	168.00	Kırşehir	Enercon	E-82	2/3	2013/2014	Operating
16	Zincirli	12.00	Kayseri	Nordex	N117	2.4	2016	Operating
17	Kurtkayası	45.60	Kayseri	Nordex	N117	2.4	2016	Operating
18	Yahyalı	52.80	Kayseri	Nordex	N117	2.4	2015	Operating
19	Yahyalı	79.20	Kayseri	Nordex	V126-3.3	3.3	2016	Operating
20	Aksu	72.00	Kayseri	Vestas	V100-2.0	2	2012	Operating
21	Kangal Ext.	50.00	Sivas	Gamesa	G114	2/2.1		U.C.
22	Kangal	78.00	Sivas	Vestas	V100-2.0/V110-2.0	2.0	2014/2015	Operating
23	Konakpınarı	14.70	Sivas	Gamesa	G114	2.1	2016	Operating
24	Arapkir	10.00	Malatya					Licensed
25	Cerit	90.00	K. Maraş					Licensed
26	Sincik	27.50	Adıyaman	Nordex	N100	2.5	2013	Operating
27	Dilek	24.00	K. Maraş	Nordex	N117	2.4	2015	Operating
28	Sartepe	57.00	Osmaniye	GE	GE2.85-103	2.85	2016	Operating
29	Demirciler	23.30	Osmaniye	GE	GE1.7-100/GE2.85-103	1.7/2.85	2016	Operating
30	Kartaldağı	65.55	Gaziantep	Vestas	V126-3.45	3.45		U.C.
31	Gökçadağ	135.00	Osmaniye	GE	GE2.5-100	2.5	2009	Operating
32	Hasanbeyli	50.00	Osmaniye	Nordex	N100	2.5	2014	Operating
33	Atık Belen	18.00	Hatay	Gamesa	G90	2.0	2014	Operating
34	Çerçikaya	57.00	Hatay	Acciona	AW125	3.0	2015	Operating
35	Sebonoba	63.70	Hatay	Vestas	V80-2.0/V112-3.0	2/3	2008/2015	Operating
36	Şenköy	36.00	Hatay	Alstom	ECO100	3.0	2012/2014	Operating
37	Ziyaret	76.00	Hatay	GE	GE2.5-100/GE2.75-100	2.5/2.75	2010/2011/2014	Operating
38	Özbek	24.00	Hatay					Licensed
39	Orhanlı	9.00	Hatay					Licensed
40	Şenbük	27.70	Hatay	Vestas	V112-3.0	3.0	2013	Operating
41	Şenbük	38.10	Hatay	Vestas	V90-3.0/V112-3.3	3/3.3	2010/2014	Operating
42	Belen	48.00	Hatay	Vestas	V90-3.0	3.0	2009/2010/2012	Operating
43	Ardıçlı	50.00	Konya					Licensed
44	Atık Belen	12.50	Hatay	Gamesa	G114	2.5		U.C.
45	Yahyalı	3.30	Kayseri	Vestas	V126-3.3	3.3		U.C.

On the other hand, in the South and Middle regions of Turkey, a total of 45 wind farms included 27 operating wind farms, 11 licensed wind farms, and 7 wind farms which were under construction, by 2017, as seen with the map shown in Figure 1.17, and other detailed information is presented in Table 1.11. These wind farms with different status had capacities of 1377.30 MW, 387.00 MW, and 175.23 MW, respectively by 2017, which were reported to constitute a total of 1939.53 MW of installations, as long as construction of whole remaining wind farms was completed (TWEA, 2017b).

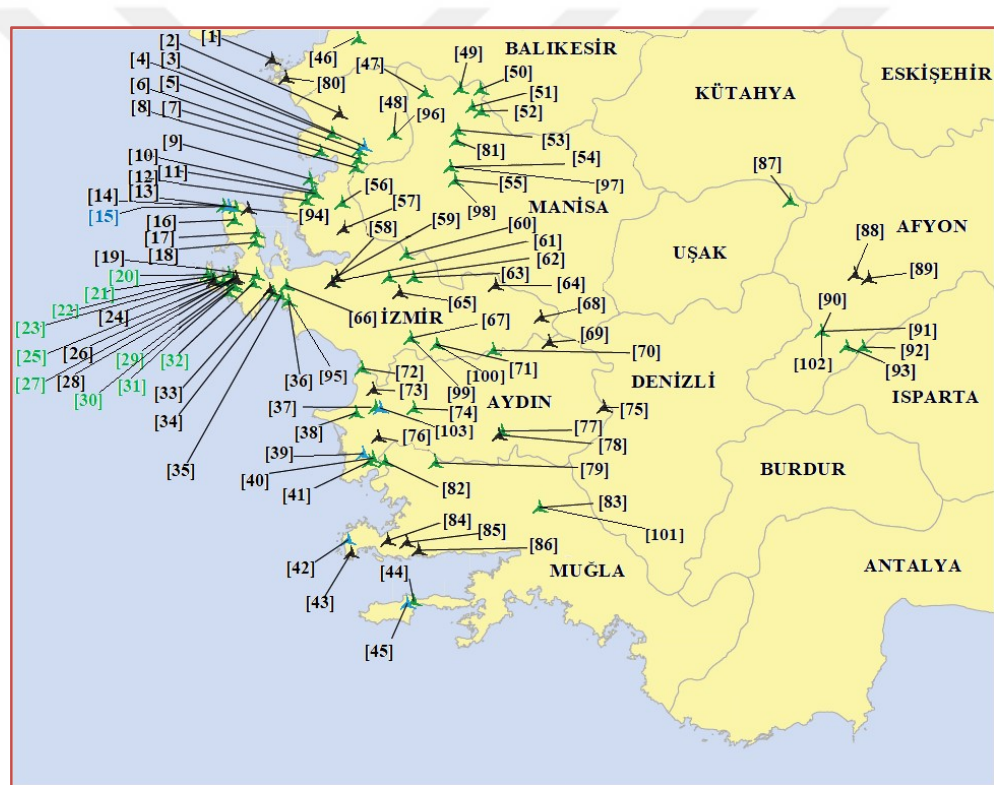


Figure 1.18. Locations of the installed wind farms in the West region of Turkey

Table 1.12. Installed wind farm information considering the West of Turkey

Row No	Name of the project	Installed power or capacity (MW)	City	Turbine company	Turbine model	Turbine power (MW)	Commissioning of operation	Wind farm type
1	Alibey Adası	30.00	Balıkesir					Licensed
2	Bergama	26.40	İzmir					Licensed
3	BergRES	69.95	İzmir	GE	GE3.2-103/GE2.75-103	3.2/2.75		U.C.
4	Düzova	51.50	İzmir	GE	GE2.5-100/GE2.75-100	2.5/2.75	2009/1010/2013/2014	Operating
5	Yuntdağ	60.00	İzmir	Nordex	N90/N100	2.5	2011/2014	Operating
6	Bergama	120.00	İzmir	Nordex	N90/N117	2.5/3	2007/2016	Operating
7	Pitane	4.80	İzmir	Nordex	N117	2.4	2014	Operating
8	Seyitali	41.50	İzmir	Enercon	E-70/E-92	2.3/2.35	2011/2015/2016	Operating
9	Petkim	51.00	İzmir	Alstom	ECO110	3.0	2016	Operating
10	Karadağ	10.00	İzmir	GE	GE2.5-100	2.5	2012	Operating
11	Bozyaka	19.70	İzmir	Nordex	N100/N117	2.5/2.4	2012/2016	Operating
12	Kozbeyli	32.20	İzmir	Enercon	E-70	2.0	2012/2013	Operating
13	Karaburun	120.00	İzmir	Enercon	E-82	2/3	2013	Operating
14	Salman	27.50	İzmir	GE	GE2.75-100	2.75	2014	Operating
15	Sarpineik	32.50	İzmir	Nordex	N90/N100	2.5		U.C.
16	Yaylaköy	15.00	İzmir	Enercon	E-82	3.0	2016	Operating
17	Mordoğan	31.50	İzmir	Suzlon	S88	2.1	2014	Operating
18	Mordoğan	15.00	İzmir	Enercon	E-82	3.0	2016	Operating
19	Urla	15.00	İzmir	Enercon	E-82	3.0	2016	Operating
20	Karadağ	18.00	İzmir	Nordex	N117	3.0	2016	Operating
21	Çeşme	18.00	İzmir	Nordex	N117	3.0	2015	Operating
22	Alaçatı	16.00	İzmir	Enercon	E-82	2.0	2016	Operating
23	Gemiyân	12.00	İzmir	Enercon	E-82	2.0	2016	Operating
24	Ovacık	18.00	İzmir					Licensed
25	Ares	7.20	İzmir	Vestas	V44-600	0.6	1998	Operating
26	Gemiyân	10.70	İzmir					Licensed
27	Çeşme	1.50	İzmir	Enercon	E-40	0.5	1998	Operating
28	Gemiyân	9.60	İzmir					Licensed
29	Mare Manastır	56.20	İzmir	Enercon	E-48/E-44/E-82 E2	0.8/0.9/2.3	2006/2007/2016	Operating
30	Zeytineli	50.00	İzmir	Nordex	N100/N90	2.5	2013	Operating
31	Mazı-3	30.00	İzmir	Nordex	N90	2.5	2011	Operating
32	Kores	25.00	İzmir	Nordex	N90/N100	2.5	2012/2015	Operating
33	Yağcılar	10.00	İzmir					Licensed
34	Demirelli	40.00	İzmir	Nordex	N90(3)+N100(13)	2.5	2016	Operating
35	Korkmaz	25.20	İzmir	Suzlon	S88	2.5	2014	Operating
36	Seferihisar	21.00	İzmir	Nordex	N117	3.0	2016	Operating
37	Söke	30.00	Aydın	Gamesa	G90	2.0	2010	Operating
38	Söke	49.50	Aydın	Vestas	V112-3.3	3.3	2015	Operating
39	Yenihisar	21.60	Aydın	Nordex	N117	2.4		U.C.
40	Akbük	9.60	Aydın	Nordex	N117	2.4	2015	Operating
41	Akbük	31.50	Aydın	Suzlon	S88	2.1	2009	Operating
42	Geniş	12.00	Muğla	Nordex	N117	3.0		U.C.
43	Akyar	15.00	Muğla					Licensed
44	Dares Datça	29.60	Muğla	Enercon	E-48/E-44	0.8/0.9	2008	Operating
45	Datça	12.50	Muğla	Gamesa	G114	2.5		U.C.
46	Çataltepe	16.00	Balıkesir	Enercon	E-82	2.0	2010	Operating
47	Soma	120.00	Manisa	Nordex	N90/N117	2.5/3	2007/2016	Operating
48	Kınık	51.20	İzmir	Siemens	SWT-3.2-108	3.2	2016	Operating
49	Soma	264.10	Manisa	Enercon	E-70/E-44	2/0.9	2011/2012/2014/2015	Operating
50	Kuyucak	40.90	Manisa	Enercon	E-44/E-70/E-82	0.9/2	2010/2015	Operating
51	Geres	30.00	Manisa	Nordex	N90	2.5	2014/2015	Operating
52	Sayalar	57.20	Manisa	Enercon	E-82/E-70/E-44	2/0.9	2008/2013	Operating
53	Karakurt	12.00	Manisa	Vestas	V90-2.0	2.0	2007	Operating
54	AkRES	45.00	Manisa	Nordex	N90	2.5	2000	Operating
55	Kırkağaç	34.20	Manisa	GE	GE2.85-103	2.85	2016	Operating
56	Samurlu	34.50	İzmir	Enercon	E-70	2.0	2012/2013	Operating
57	Yılmaz	12.50	İzmir					Licensed
58	Gaziemir	20.00	İzmir					Licensed
59	Emres	2.00	İzmir					Licensed

Table 1.13. Installed wind farm information considering the West of Turkey
(Continuing)

60	Ege	9.20	İzmir	Enercon	E-70	2.0	2015	Operating
61	Aliağa	19.20	İzmir	Nordex	N117	2.4	2014/2016	Operating
62	Karabel	3.00	İzmir	Senvion	3.4M104	3.4	2016	Operating
63	Fuat	33.00	İzmir	Vestas	V112-3.3	3.3	2015/2016	Operating
64	Gündalan	5.00	İzmir	-----	-----	-----	-----	Licensed
65	Mersinli	55.00	İzmir	-----	-----	-----	-----	Licensed
66	Urla	18.00	İzmir	Nordex	N117	3.0	2016	Operating
67	Tire	8.50	İzmir	GE	GE1.7-103	1.7	2016	Operating
68	Alares	10.00	İzmir	-----	-----	-----	-----	Licensed
69	Kirazlı	50.00	Aydın	-----	-----	-----	-----	Licensed
70	OvaRES	18.00	Aydın	Gamesa	G97	2.0	2016	Operating
71	Ödemiş	21.00	İzmir	Nordex	N117	3.0	2015	Operating
72	AdaRES	10.00	İzmir	Gamesa	G97	2.0	2015	Operating
73	Söke	104.00	Aydın	-----	-----	-----	-----	Licensed
74	Bağarası	48.00	Aydın	Nordex	N117	2.4	2015	Operating
75	Denizli	66.00	Aydın	-----	-----	-----	-----	Licensed
76	Bafa	35.00	Aydın	-----	-----	-----	-----	Licensed
77	Madranbaba	20.00	Aydın	Gamesa	G90	2.0	2013	Operating
78	Çataltepe-Hisarardı	45.00	Aydın	-----	-----	-----	-----	Licensed
79	Turguttepe	24.00	Muğla	Vestas	V90-2.0	2.0	2010	Operating
80	Ayvalık-1	9.00	Balıkesir	-----	-----	-----	-----	Licensed
81	GökRES	35.75	Manisa	GE	GE2.75-103	2.75	2014	Operating
82	Akbük 2	21.00	Muğla	Suzlon	S95	2.5	2016	Operating
83	Fatma	38.40	Muğla	Siemens	SWT-3.2-113	3.2	2016	Operating
84	Güllük	33.00	Muğla	-----	-----	-----	-----	Licensed
85	Karova	30.00	Muğla	-----	-----	-----	-----	Licensed
86	Alapınar	0.80	Muğla	-----	-----	-----	-----	Licensed
87	Uşak	54.00	Uşak	Sinovel	SL1500/90	1.5	2013	Operating
88	Afyon 2	88.00	Afyon	-----	-----	-----	-----	Licensed
89	Eber	36.00	Afyon	-----	-----	-----	-----	Licensed
90	Dinar	115.00	Afyon	Siemens	SWT-2.3-108	2.3	2013	Operating
91	Dinar Ext	77.00	Afyon	GE	GE2.75-120	2.75	2016	Operating
92	Uluborlu	61.20	Isparta	GE	GE1.7-103	1.7	2016	Operating
93	İncesu	29.20	Afyon	Vestas	V112-3.3/V100-2.0	3.3/2	2014/2016	Operating
94	Salman	20.00	İzmir	-----	-----	-----	-----	Licensed
95	Seferhisar 2	21.00	İzmir	Nordex	N117	3	-----	U.C.
96	Kınık	3.20	İzmir	Siemens	SWT-3.2-108	3.2	-----	U.C.
97	Akres Ext.	10.00	Manisa	Nordex	N100	2.5	-----	U.C.
98	Kırkağaç	11.40	Manisa	GE	GE2.85-103	2.85	-----	U.C.
99	Tire	42.40	İzmir	GE	GE1.7-103/GE3.2-103	1.7/3.2	-----	U.C.
100	Ödemiş Ext.	21.00	İzmir	Nordex	N117	3.0	-----	U.C.
101	Fatma	41.60	Muğla	Siemens	SWT-3.2-113	3.2	-----	U.C.
102	Dinar 4	8.25	Afyon	GE	GE2.75-120	2.75	-----	U.C.
103	Çatalbük	25.20	Aydın	Gamesa	G114	2.1	-----	U.C.

In the West region of Turkey; a total of 103 wind farms were constructed including 64 operating, 25 licensed, and 14 under construction wind farms, by 2017, as seen in the map indicated in Figure 1.18, and other detailed information is provided in Tables 1.12 and 1.13. These wind farms included capacities corresponding to 2453.55 MW, 741.00 MW, and 332.60 MW of installed power, respectively by 2017, which were reported to constitute a total of 3527.15 MW of installations in the near future, as long as whole remaining wind farms were constructed in these provinces (TWEA, 2017b).

Total wind power installations based on the above-cited geographical locations in 2017 was expected to be a total of 10,129.18 MW of power installations in the near future, as long as whole remaining wind farms were constructed. Besides, this report included the discrete data of operating, licensed, and under construction wind farm capacities of Turkey (TWEA, 2017). Similarly, in 2019; total expectations based on the cited four geographical regions are 10,215.51 MW of power installations. However, operating wind farm capacities in 2019 are reported to be 7,369.35 MW. Whereas, licensed and under construction wind farms capacities are reported to be 2,239.96 MW and 606.20 MW, respectively in 2019, demonstrating around 3 GW of wind power installations are needed to be enacted as soon as possible based on the initial scheme of wind power installation plan executed in 2017, and shown above (TWEA, 2019).

1.2.10. World's and Turkey's Current Wind Energy Situation

The total energy generations of Turkey based on carbon-based fuels constitute only 2.84%, 2.94%, and 3.37% of *OECD's* total energy generations based on carbon-based fuels by 2015, 2016, and 2017, respectively. Fortunately, Turkey is quite prominent in renewable energy installations reaching 43.20%, 44.05%, and 45.67% of its total energy installations by 2015, 2016, and 2017,

respectively. Besides, in terms of the real energy generations, renewable energy sources constitute 33.16% of total energy generations by the end of 2016. This percentage declined to 29.64% by the end of 2017 in Turkey. Whereas, in terms of the current installed power situation of the renewable energy for the whole World is 13.4% corresponding to 2122 GW of renewable installed power plants by 2018. Similarly, considering the *OECD* countries, it is seen that the rate of electricity generations from the renewable energy sources including the hydropower constitute 17.4% of total energy generations considering the period between 2000 and 2017 in the global scale. Presently, the highest electricity generations of the World are unfortunately obtained firstly from the combustible fuels and subsequently from nuclear energy sources. This situation is also, unfortunately, the case for most of the *OECD* countries.

In this part of the dissertation, Turkey's total renewable energy installations are compared with respect to the status of the World. The comparisons reveal that Turkey reaches 1.83% of the World's total renewable installed power. Also, it is reported in this part of the dissertation, that the ratio of the installed power of wind energy in Turkey to the situation of the World is also in a parallel line. For example, Turkey's wind power installations compared with respect to the World's situation is 1.21% by 2017. In these respects, Turkey, on this issue, has arrived at a good position. That is to say; Turkey has been performing significant progress on renewable energy generation issues, especially on the solar and wind power applications (TWEA, 2017b). When the total process of installations with respect to the cumulative theoretical wind power potential of Turkey is considered, it is conducted that only 13.00% of wind energy is, unfortunately, being used for electricity generation. So, the current situation indicates that much more steps must be taken immediately in this regard. Aegean and secondly Marmara regions are the leaders in using wind energy sources in Turkey. Besides, İzmir and Balıkesir provinces belonging to these geographical regions of Turkey, and they are reported

to be the leading cities in these respects. When Turkey's place in the World in terms of wind energy generation is examined; available literature reveals that the wind energy application has been rapidly progressing, and today, it's the 7th country in wind farm installations among World's other leading countries.

In other respects, analysis of Turkey's future prospect in electrical generations utilizing wind energy is officially conducted. Turkey's wind energy production is expected to exceed 20 GW, based on the reports of the Energy Marketing Regulation Board of Turkey. This situation has already been observed to be consistent with Turkey's wind politics of 2023 based on the reports of the Ministry of Energy and Natural Resources of Turkey. But, according to the current progress, only 10.8 GW of total wind power installations will be obtained until the end of the 2023 year. Unfortunately, this is only half of the initial state target of Turkey. Thus, the state scenario absolutely requires 800 MW/year of annual installations for wind energy in the time range from 2018 to 2030. Province-based exact locations and types of wind farms located in the Republic of Turkey are separately examined in detail according to the four different geographical regions where wind farms are rather intense. In this context, detailed information covering wind farm project names, locational installed power, the city of the installations, names of turbine companies, turbine models, turbine rated powers, commissioning dates of the farms, and wind farm types were performed. Considering these frameworks; the current part of the dissertation reports that the most intense and proper locations of Turkey certainly include West, Northwest, and South regions.

1.3. Wind Turbine Energy Generation

1.3.1. History of Wind Turbines

More specifically, wind power is one of the most important and harmless, thus nature-friendly type of whole available renewable energy generation methods. Considering the historical situation of wind utilization; it is known that more than 3000 years, wind power generation systems have certainly been in use. Thus, several different types of wind-mills have been invented starting from 3000 years ago by the initial appearance of the ancient Persian vertical axis wind-mills. However, a starting point of wind power generation system intended to be employed in electrical power generation started in the late 1800s and the early 1900s. Nevertheless, wind turbines mainly started to spread across the whole World mainly in the last three decades, especially depending on the global energy crises and rapid changes of political and social climates (Sørensen, 2011).

1.3.2. Rapid Shift of Energy Generation Using Wind Turbines Globally and in Turkey

Global installed wind energy generation capacity has been enhanced nearly 72 times in the last two decades, i.e., from 7.5 GW in 1997 to 539.123 GW in 2017. Nowadays, wind power is reported to be the fastest growing sector among the others in terms of electricity generation. In additions, it has also been observed that wind power has the fastest growing capability among whole renewable energy sources, especially in recent years (Bilgili et al., 2015a). In this context, the total wind power installed capacity in Europe and the World between 2000 and 2017 is reported in Figure 1.19, in order to reveal both Europe's and World's accelerated interest in wind energy utilization. As clearly seen, the capacity of wind

energy installation within this given time period has a rapid increasing trend both in Europe and the World. The cumulative installed wind power capacity in 2000 was only 17.40 GW, globally, but at the end of 2016, the total worldwide wind power capacity reached 487.279 GW (*GWEC, 2016*). These wind power installations further increased to 539.123 GW by 2017 with a very high development (*GWEC, 2017*). On the other hand, Europe owned almost one-thirds of global share corresponding to 154.0 GW of World's total installed wind power capacity by 2016. Onshore and offshore wind farms in Europe shared out of this amount which were 141.0 GW and 13.0 GW, respectively by 2016. Presently, the total installed wind power of Europe reached 168.8 GW of installations by 2017. Similarly, onshore and offshore installations share out of this amount which are 153.0 GW and 15.8 GW, respectively by 2017. However, the offshore wind farm installations are needed to be rapidly improved in the near future (*EWEA, 2016b; GWEC, 2017*).

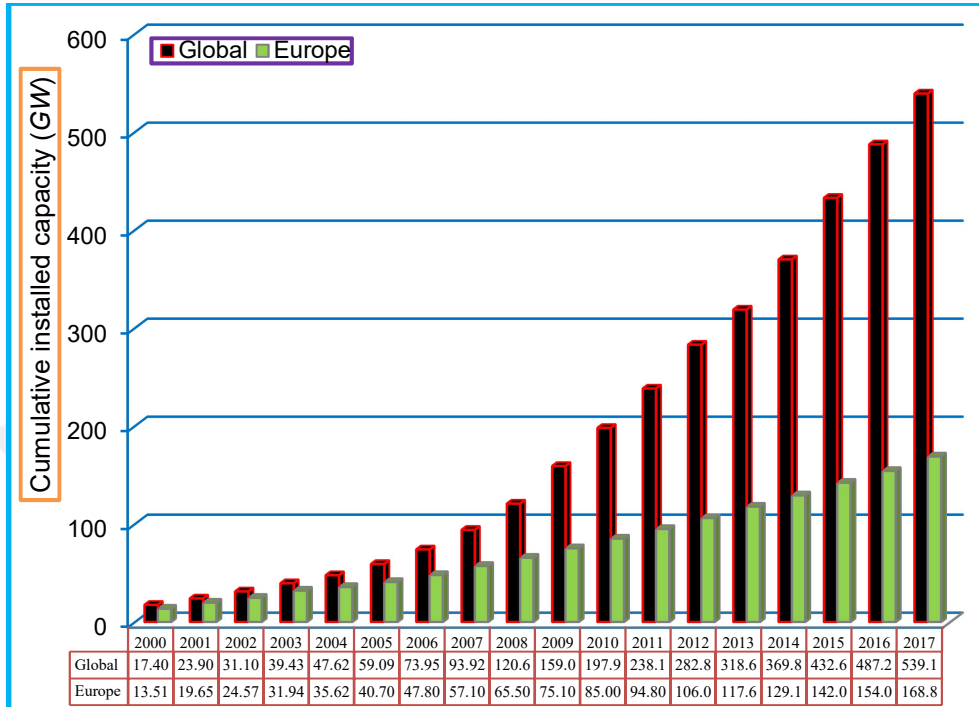


Figure 1.19. Statistical comparison of installed wind power capacity between Europe and the World (*GWEC, 2016; GWEC, 2017*)

Wind energy is an important part of the World's renewable energy sources as formerly expressed, and it nearly becomes the most economical energy source among other types. Thus, within the renewable energy resources of 432.680 GW installed total global capacity; i.e., wind applications, having a share of 23.4% of total renewable energy generations covered a great deal of World's energy demand, by 2015. On the other hand, a rapid increase of wind power plant installations by the wind energy industry in one year corresponding to 54,642 MW was reported constituting a rise of approximately 1% of new installations in this sector having finally a share of 24.2% in total renewable power plants. So, 487.279 GW of global wind power generation capacity eventuated by the end of 2016, presented in Figure 1.19. By 2017, a global installation corresponding to 52,492 MW of installations was realized. In these regards, 24.6% share of installed wind power with respect to

whole global renewable installations was actualized. Ultimately, total installed wind power by 2017 reached 539.123 MW of installations. (*REN21, 2016; REN21, 2017; REN21, 2018; GWEC, 2017*).

Wind energy involving a total installed capacity reaching 539 GW, has an important place in the World considering other renewable energy sources and it also has the pretty fast application advantage, and it is certainly one of the most economical type of renewable energy sources. On the other hand, considering the case of Turkey, by the end of the 2015 year, the cumulative number of operating wind power plants were exceeded 110 which corresponded to the total installed power capacity of 4.71830 GW (*TWEA, 2016*). Thus, 6.45% of total installed power which corresponds to 73.1467 GW was provided by wind energy sources for electrical energy generation by 2015 (*TEIAS, 2017*). However, a significant increase was reported in energy generation from wind power utilization in Turkey. Thus, Turkey had a record year of 2016, adding nearly 1.4 GW of wind energy installations and Turkey took place in top ten countries in wind energy production of the World in 2016 (*REN21, 2016*). The new total installed wind capacity of Turkey was reported to reach 6,106.05 MW by the end of 2016 among total installed power of 78,592 MW, achieving 7.8% of wind share in the total energy production (*EI, 2017*). Thus, considering the end of 2016, Turkey put 152 wind power plants into operation (*TWEA, 2017b*). On the other hand, this situation became 6,872.10 MW of wind power installations by 2017 with a total of 164 operational wind farms, achieving 8.07% of wind share in the total energy production of 85,200 MW in this year. Ultimately, Turkey has 180 wind power plants in operation by 2018 corresponding to an installed wind power of 7,369.35 MW of installations by this year. Additionally, Turkey has the objective of reaching the share of wind energy that is aimed to attain 20 GW for electric generation targeted by the year 2023. Also, within this period of time, to increase the utilization of wind energy applications further; especially in the regions where

interconnecting electrical lines cause problem, studies of research and development on small size diffuser augmented wind turbine technologies should also be executed in parallel to technological developments of large size wind turbines (Takahashi et al., 2012; Lawn, 2003; Poh et al., 2014; Nikolic et al., 2015; Bukala et al., 2015; Al-Sulaiman and Yilbas, 2015; Kesby et al., 2016; Balaji and Gnanambal, 2014).

Considering the importance of wind energy both in Turkey and the World globally, a comprehensive review of diffuser augmented vertical and horizontal wind turbine technologies, as well as recent technological development in wind turbines in general, and their related designs, performances, aerodynamic characteristics, and their efficiencies are aimed to be looked at comprehensively. The main aim of the present work is to investigate the casing system design characteristics in detail in terms of aerodynamic characteristics to focus on the importance of wind turbine performance improvement (Cetin et al., 2005; Amer et al., 2013; Watson et al., 2007; BoroumandJazi et al., 2013; Kannan et al., 2013; Maia, 2014; Kishore et al., 2013; Wang et al., 2015; Toshimitsu et al., 2008; Van Bussel, 2007; Gow et al., 2014; Gade and Abhang, 2016).

1.3.3. Main Wind Turbine Aerodynamic Parameters

Characterization of the wind turbine classification is significantly influenced by wind turbine aerodynamics (Shonhiwa and Makaka, 2016). In this context, the mechanical power output of a wind turbine, P and other main aerodynamic parameters including tip speed ratio, λ_R , thrust coefficient, C_T , power coefficient, C_p , theoretical estimation of the maximum power coefficient, C_{pmax}^* , power coefficient definition, C_p based on the axial flow induction factor, a , torque coefficient, C_Q , axial flow induction factor, a , pressure drop coefficient, C_{pr} , loading coefficient, C_t , and air velocity or maximum wind speed ratio, K

(maximum axial air velocity, U_{max} of diffuser divided by free-stream wind speed, U_∞) are presented by Eqs. (1.1), (1.2), (1.3), (1.4), (1.5), (1.6), (1.7), (1.8), (1.9), (1.10), and (1.11), respectively.

$$P = 1/2\rho A_d U_\infty^3 \eta_{mech} C_p \quad (1.1)$$

$$\lambda_R = \Omega R / U_\infty \quad (1.2)$$

$$C_T = T / 0.5\rho A_d U_\infty^2 \quad (1.3)$$

$$C_p = P / 0.5\rho A_d U_\infty^3 \quad (1.4)$$

$$C_{pmax}^* = \frac{16}{27} \lambda_R \left[\frac{n^{2/3}}{1.48 + (n^{2/3} - 0.04)\lambda_R + 0.0025\lambda_R^2} - \left(\frac{C_d}{C_l} \right) \frac{1.92n\lambda_R}{1 + 2\lambda_R n} \right] \quad (1.5)$$

$$C_p = 4a(1 - a)^2 \quad (1.6)$$

$$C_Q = Q / 0.5\rho A_d U_\infty^2 D_{rotor} \quad (1.7)$$

$$a = 1 - u / U_\infty \quad (1.8)$$

$$C_{pr} = (p - P_{atm}) / (0.5\rho U_\infty^2) \quad (1.9)$$

$$C_t = (P_1 - P_2) / (0.5\rho U_2^2) \quad (1.10)$$

$$K = U_{max} / U_\infty \quad (1.11)$$

The Betz limit indicating the upper limit of the available power that can be converted to useful energy by a wind turbine is presented by Eqs. (1.4) and (1.6), where the axial flow induction factor, a links the axial wind velocity, u with the free-stream wind speed, U_∞ by Eq. (1.8). Thus, the maximum possible attainable ideal power conversion is expressed by $C_{pmax} = 16/27 = 0.593$ obtained by the differentiation of power coefficient, C_p in Eq. (1.6) with respect to the axial flow induction factor, a , i.e., at $a = 1/3$ referred to be the Betz limit. Consequently, Figure

1.20 presents several conventional wind turbine designs which cannot generate power beyond this cited limit, i.e., not possible to exceed the limit since this theoretical limit can only be achieved in the case of a wind turbine involving infinite number of blades. And, this is not a possible situation in practical applications. Thus, ideal power coefficient, C_p obtained by the momentum theory can be approached by the theoretical case of infinite number of blades as shown in Figure 1.20 (Hau, 2006).

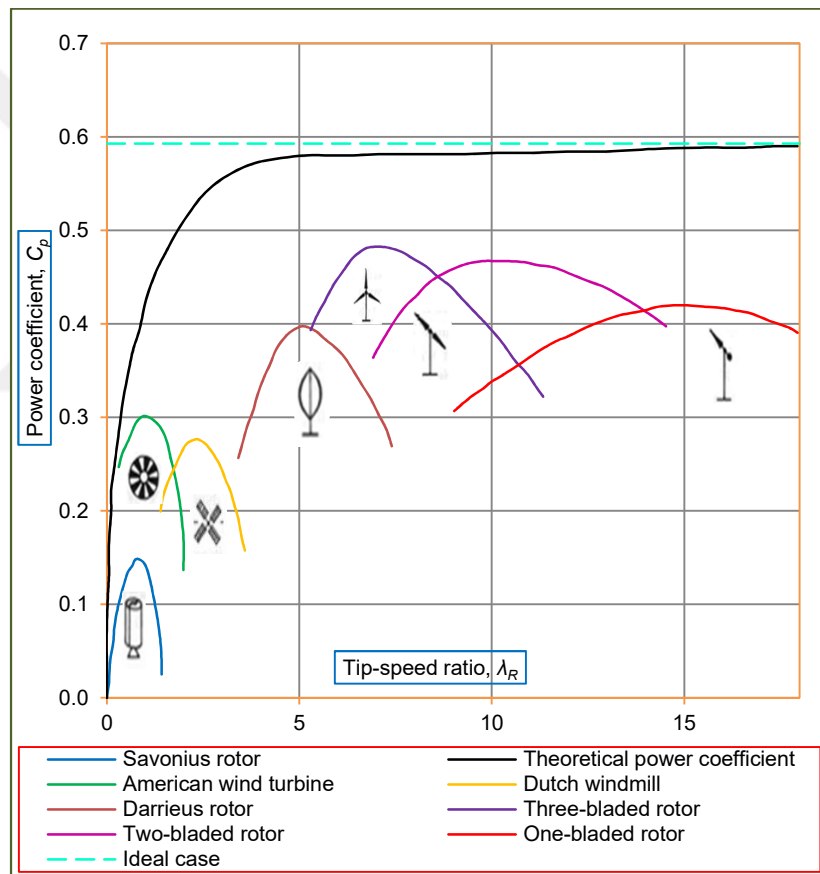


Figure 1.20. Power coefficient, C_p ranges of different wind turbine designs available in the practical applications (Hau, 2006)

1.3.4. Wind Turbine Casing Studies and Classifications of Wind Turbines

Efforts on the small scale wind turbine especially with horizontal axis were given onto the casing or diffuser applications starting from the beginning of the 2000s in the World. However, the development of small-capacity wind turbine technology, the establishment of research and development infrastructure, and related works play an important role in the enhancement of the dissemination and persuasion of the public to use such wind turbines in a wide range globally. A wind turbine generates power, P from the wind energy with the cube of the free-stream wind speed, U_∞ as expressed in Eq. (1.1). Namely, a minor rise in approaching wind speed can induce a large increase in wind power generation is the focus of this dissertation. For that reason, developing new technologies which can considerably accelerate the approaching wind speed, U_∞ before rotor contact is the main focus in wind turbine casing systems. In this respect, augmenting power output, P of wind turbines with a diffuser (*DAWT*) was first proposed in 1956 (Lilley and Rainbird, 1956). This work was later followed by many other experimental studies (Oman et al., 1975; Igra, 1977; Foreman et al., 1978; Gilbert et al., 1978; Igra, 1981; Gilbert and Foreman, 1983; Phillips et al., 2002). Furthermore, several theoretical and numerical works were also further conducted (Shonhiwa and Makaka, 2016; Hansen et al., 2000; Bet and Grassmann, 2003; Werle and Presz, 2008; Jamieson, 2009, Jafari and Kosasih, 2014). Different types of small scaled vertical and horizontal axis wind turbines were also reviewed, and it was also reported that the most of previous works focused on the effects of rotor speed and pitch angles of a specified airfoil, conducted due to the rapid development of the wind turbine technology (Tummala et al., 2016). However, influences originated due to wing gust, wind direction, and turbulence intensity deteriorating the overall turbine performances, unfortunately, were not considered in all of these studies. In fact, all these considered parameters actually have a

significant effect on the overall wind turbine performances, i.e., improvement of the wind turbine efficiency, C_p is directly linked to better analysis of these parameters. On the other hand, considering these expressed studies, classifications of wind turbines in different categories are reviewed, to be presented in this part of the dissertation, as shown in Table 1.14. It is also expected that increasing efficiency of a wind turbine by a casing shroud system results in a significant reduction of energy generation costs. In these respects, designing wind turbine running with higher efficiency and generating power under a lower wind speed certainly need further research and development both in industry and universities, and collaboration of both in future will be undoubtedly inevitable. The concentration of this dissertation is on the generation of electricity by wind turbines under a lower wind speed to obtain a higher power coefficient, C_p , i.e., improved efficiency of wind turbines is mainly focused in this work.

Table 1.14. Classification of horizontal axis wind turbines categorized by the rotor diameters and the power rating data (Tummala et al., 2016)

Type of wind turbine		Rotor diameter (m)		Swept area (m ²)		Standard power rating (kW)	
Small scale	Micro	0.5	1.25	0.2	1.2	0.004	0.25
	Mini	1.25	3	1.2	7.1	0.25	1.4
	Household	3	10	7.1	79	1.4	16
Small commercial		10	20	79	314	25	100
Medium commercial		20	50	314	1963	100	1000
Large commercial		50	100	1963	7854	1000	3000
Largest commercial		100	160	7854	20106	3000	8000
Under development		160	220	20106	38013	8000	20000

It is also anticipated that the demand to small-capacity wind turbines will increase in small businesses including agricultural locations, petrol stations, and various manufacturing firms; and especially in residential applications where there are no electric-powered lines to meet partial needs; all these will be actualized along with an increase in electricity consumption both in the World and Turkey. In

addition, it is expected that the need for small capacity wind turbines in small enterprises is expected to be enhanced even further. Thus, based on those reasons, the installed power limit for unlicensed electricity generation bound up with renewable energy sources in Turkey was increased from 500 kW to 1000 kW in accordance with the Electricity Market Law adopted on March 14 of 2013. However, studies on the design, modeling, optimization, manufacture, and increasing power generation, P ; and especially power coefficient, C_p of small-capacity wind turbine technologies in Turkey are further progressing. In this sense, it is substantially important for the global and domestic industrialists to produce wind turbines working efficiently even at low wind speeds, for the use of these wind turbines in residential buildings and small businesses both in urban and rural areas. Consequently, product operating principle and manufacturing improvements to increase wind turbine power coefficient, C_p , and product quality are the aimed issues to increase overall wind turbine performances.

1.3.5. Analysis of Casing Systems Applied to Horizontal Axis Wind Turbines

1.3.5.1. Horizontal Axis Wind Turbine with Exclusive Diffuser Components

The most applied wind turbine casing system found in the literature is the shrouding of horizontal axis wind turbines using only a diffuser component. Thus, wind turbine combined with a diffuser component increases the turbine efficiency, C_p , and starts electric generation at a lower free-stream wind speeds, U_∞ . Additionally, efficiency improvement of a wind turbine results in a significant reduction in the energy generation costs, thus exergy losses are significantly reduced in parallel. In this context, flow regime in the vicinity of a casing are analyzed and expressed in terms of the parameters including diffuser full-cone angle, 2θ , diffuser casing full body length, L , inlet diameter, D_I , and exit diameter,

D_2 which have significant influences on the wind flow characteristics, i.e. the power coefficient, C_p of a shrouded horizontal axis wind turbine.

1.3.5.2. Wind Turbine with Airfoil Shaped Diffuser Component

Innovative and original aspects of ongoing shrouding researches mainly focus on ensuring the optimization of casing systems also consisting airfoil structured diffuser components formed around the wind turbine; i.e., lens in order to enhance the performance of small scaled conventional wind turbines of moderate capacity which are eligible to use for the domestic purposes. It is certain that diffuser structures used as casing systems around the wind turbine reduce the vortices developed by the blade tips considerably which also attenuate aerodynamic noise substantially. In this context, numerical and experimental studies were performed to report the vorticities formed around the wind turbine rotor, and in the vicinity of the shrouding case (Abe et al., 2005; Abe et al., 2006). Additionally, diffuser augmented wind turbine performances are also possible to be evaluated theoretically as well, especially utilizing from the one-dimensional model is useful in theoretical analysis. The representation of a schematic airfoil structured diffuser presented in Figure 1.21 is studied using one dimensional model for the enhancement of air mass flow rate, \dot{m} passing through the rotor disc which effectuates the rise of the wind speed ratio, u/U_∞ and as well as the maximum wind speed ratio, K (Rio Vaz et al., 2014).

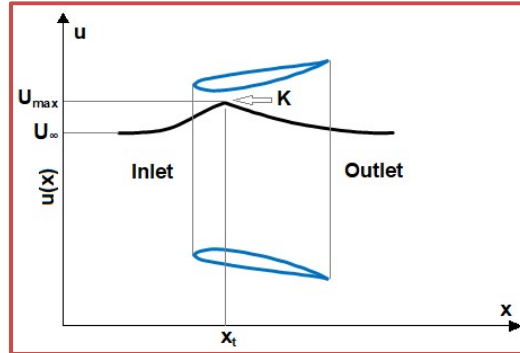


Figure 1.21. Illustration of the axial velocity distribution profile, $u(x)$ on the symmetry axis of an airfoil structured diffuser casing without an installed wind turbine (Rio Vaz et al., 2014)

On the other hand, several diffuser geometries found in the literature as seen in Figure 1.22 were also examined, under the utilization of numerical methods (Shives and Crawford, 2011), and also a double airfoil shaped diffuser casing system was also designed in the literature studies to be used for wind turbine shrouding as presented in Figure 1.22, shown with the 8th configuration (Bet and Grassmann, 2003). The design parameters of the airfoil casings are so influential in the power coefficient performance, C_p improvement of the wind rotors. Notably, the diffuser exit to inlet area ratio, μ^* or full-cone angles of the casing, 2θ significantly influence the degree of boundary layer separations from the surface of diffusers to deteriorate the performance of wind turbine which is characterized unfortunately by a considerable reduction in the overall diffuser casing efficiency.

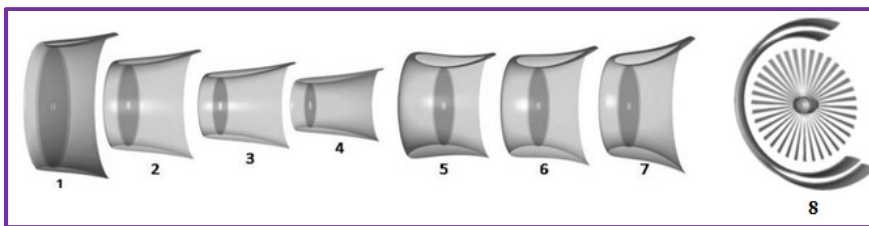


Figure 1.22. Blade profiled diffuser shrouding configurations (Shives and Crawford, 2011), and a double airfoil shaped diffuser casing system, 8th configuration (Bet and Grassmann, 2003)

A numerical study performed on the wind turbine shown in Figure 1.22, as the 8th configuration, has a rotor diameter of $D_{rotor}=1.12$ m corresponding to a rotor area of $A_{rotor}=0.98$ m². On the other hand, wind power rate, P_{rt} is 75 W/m² under 5 m/s free-stream wind speed, U_{∞} . This wind turbine generated 29 W of energy according to the numerical predictions under 5 m/s wind speed, U_{∞} , 0.98m² rotor swept area, A_{rotor} , and 190 rpm turbine rotor rotational speed, Ω . These results indicated that the wind turbine only converted 39% of the available wind energy into the electricity. However, according to the Betz limit, 59% of wind energy can be theoretically converted into useful electrical energy. In relation to the Betz limit, wind turbine efficiency is only around $39/59=66\%$, ideally. However, placing the wind turbine in a wing profiled diffuser casing system with an axial casing full-body length of $L=0.125D_I$, and an inlet diameter, D_I of 1.54 m corresponding to an inlet casing area, A_I of 1.7 m² as seen in the 8th configuration, increased the power coefficient, C_p of wind turbine by a factor of 1.6. Besides, adding a second wing profiled diffuser casing downstream of the first one, power generation increased further to a value of 58 W corresponding to a factor 2 was resulted, which also exceeded the Betz limit reaching, a final power coefficient, $C_p=0.79$ and wind turbine efficiency compared with respect to the Betz limit finally reached, $79/59=1.34$ (Bet and Grassmann, 2003).

1.3.5.3. Wind Turbine with a Flange Component Introduced to the Diffuser Structure

The turbine rotor blades which were initially placed inside a sole diffuser structure were then combined with an additional flange structure at downstream for the enhancement of the wind turbine power coefficient, C_p even more.

The flanged-diffuser shrouding concept is rather important to present a role of a device for collecting and accelerating the approaching free-stream wind, thus

improving the wind turbine power coefficient, C_p (Ohya et al., 2008). Namely, the flange component generates a low-pressure region in the exit neighborhood of the diffuser casing by vortex formations and draws enhanced air mass flow rate, \dot{m} through the wind turbine inside the diffuser shroud to increase approaching wind speed ratio, u/U_∞ by 1.6-2.4 times more.

Aerodynamic parameters discussed in Section 3 influencing the nature of wind power generation are significantly influenced by the designed casing configurations. The study of Matsushima et al. (2006) presents a diffuser structure involving only a flange component at downstream of the casing body as shown in Figure 1.23. In this context, Figure 1.24, Figure 1.25, and Figure 1.26 consider the predicted maximum wind speed ratio, K variations along the flanged diffuser axis depending on the diffuser casing full-body length, L , full-cone angle of the casing or also referred as included angle, 2θ and flange height, H , respectively, and studied numerically under 5 m/s of free-stream wind speed, U_∞ (Matsushima et al., 2006). As mentioned before, the geometrical optimization of the flanged diffuser, such as full-cone angle of the casing, 2θ , dimensionless casing full-body length, L/D , and flange height ratio, H/D as seen in these figures are very crucial parameters for magnifying axial wind speed, u at the immediate downstream of the casing measured axially according to the entry of the diffuser where the wind turbine is usually installed. As shown in Figure 1.24, the maximum wind speed ratio, K at this location enlarges while L/D increases resulting in that dimensionless casing full-body length should be lower than $L/D \leq 3$ because of wind loading in the case of wind turbine. On the other hand, the maximum wind speed ratio, K obtained at $\theta = 6^\circ$, as presented in Figure 1.25. These results suggest that it is more convenient for application of a cased wind turbine having the full cone angle of the casing, 2θ in between 8° and 16° . Lastly, Figure 1.26 suggests that the flange height ratio, H/D should be $H/D \geq 0.1$, because the maximum wind speed ratio, K remained essentially constant beyond $H/D \geq 0.1$ (Matsushima et al., 2006).

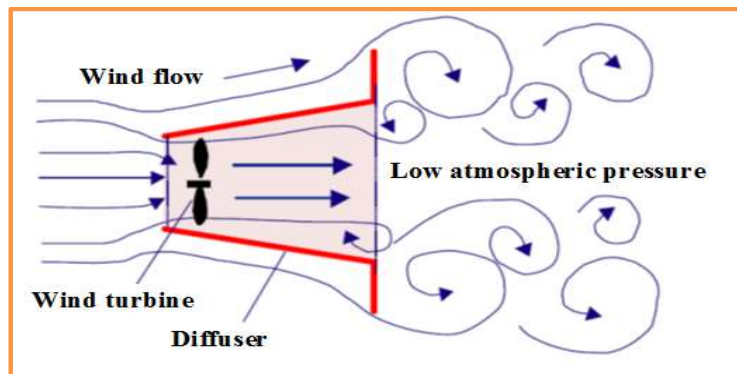


Figure 1.23. Diffuser casing configuration of (Matsushima et al., 2006), only including a flange component at downstream

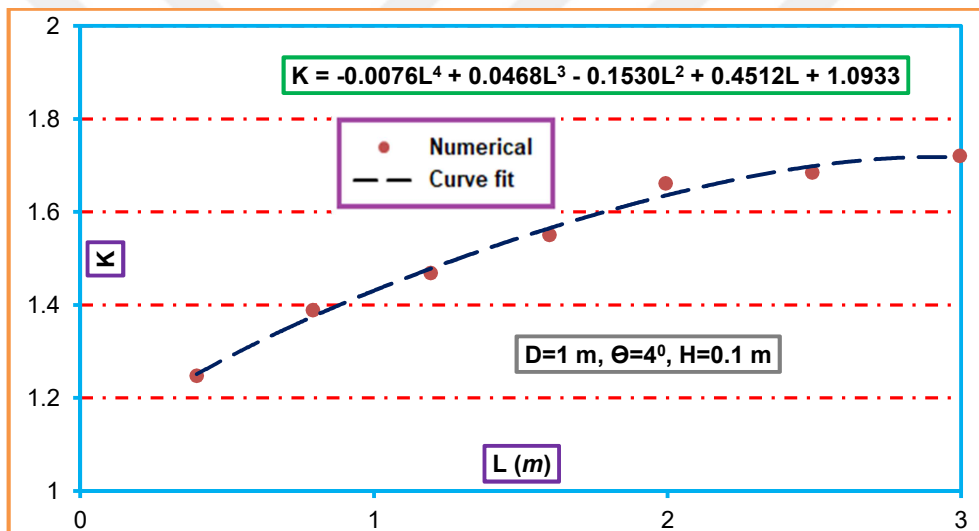


Figure 1.24. Variation of maximum wind speed ratio, K along the diffuser central axis as a function of diffuser casing full-body length, L/D studied under a free-stream wind speed of $U_\infty=5$ m/s, (Matsushima et al., 2006)

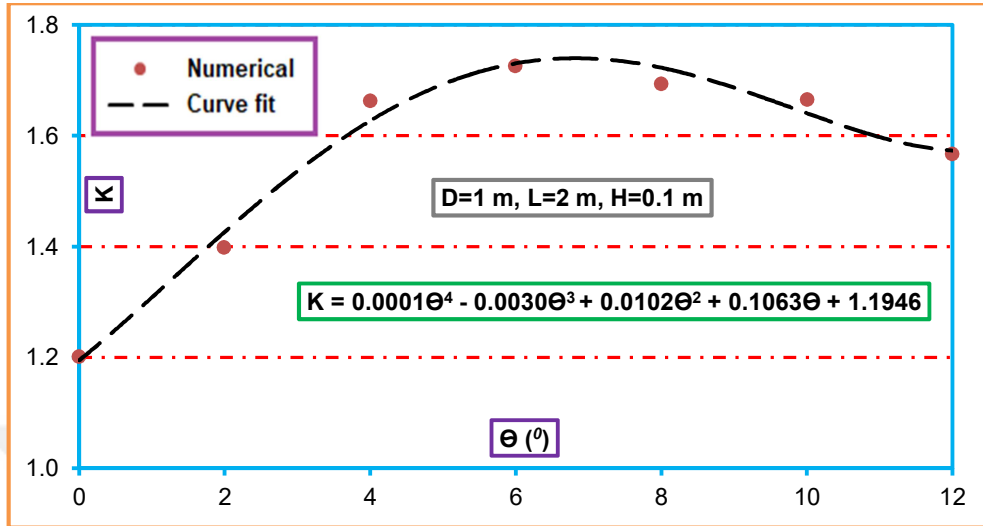


Figure 1.25. Variation of maximum wind speed ratio, K along the diffuser central axis as a function of diffuser casing full cone angle, 2θ studied under a free-stream wind speed of $U_\infty=5$ m/s, (Matsushima et al., 2006)

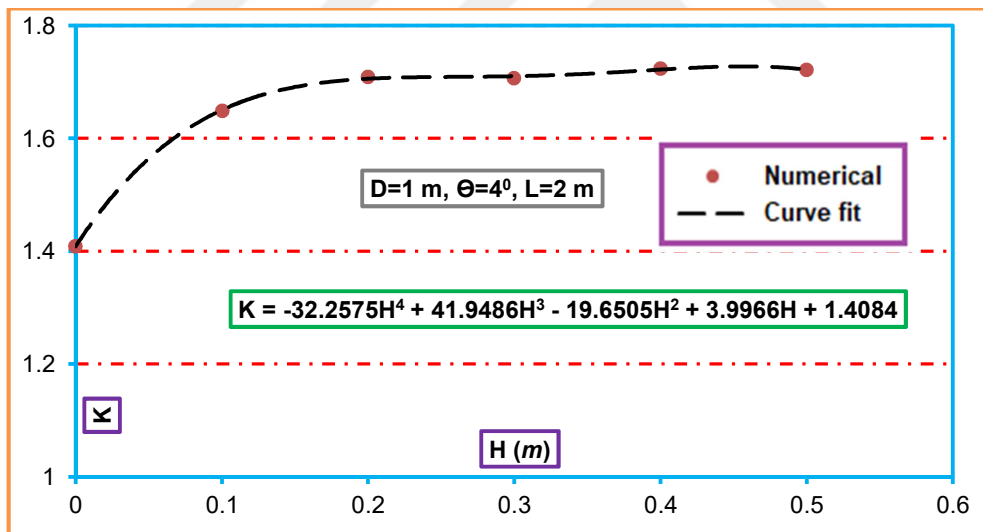


Figure 1.26. Variation of maximum wind speed ratio, K along the diffuser central axis as a function of flange height ratio, H/D studied under a free-stream wind speed of $U_\infty=5$ m/s, (Matsushima et al., 2006)

1.3.5.4. Wind Turbine Casing Including Nozzle, Diffuser, and Flange Components Together

In this innovation system, wind turbine rotor blades are initially placed in a sole diffuser, later a flange is combined with the diffuser, presently, a casing system consisted of a nozzle, diffuser, and flange components all together are used to further upgrade the wind turbine performance due to the increase of air mass flow rate, \dot{m} , and axial wind speed, u passing through the wind turbine rotor disc.

Thus, this part of the dissertation also reports that the most effective form of casing structure is usually the one having nozzle, diffuser, and flange components altogether. Thus, inlet shrouding component is so convenient to take over a task such as concentrating the free-stream wind flow, and directing this through the wind turbine casing shroud. Besides, the diffuser component functions in the enhancement of free-stream wind speed, U_∞ passing on the rotor disc as augmented. Finally, the flange component generates low pressure regions at its immediate downstream region to draw an increased amount of wind energy through the wind turbine rotor disc. For example, an optimized diffuser geometry with dimensions of $L/D=1.47$, and $H/D=0.5$ as schematically presented in Figure 1.27 is usually the one used for these purposes. Here, the optimized casing properties including L , D , and H are the full-body length of the casing main body, diameter of the casing where the wind turbine is installed and usually casing diameter at minimum cross-section, and height of the flange component, respectively. Also, a particular designed small nozzle component serving as inlet shroud is introduced to this casing system as presented in this figure (Ohya and Karasudani, 2010).

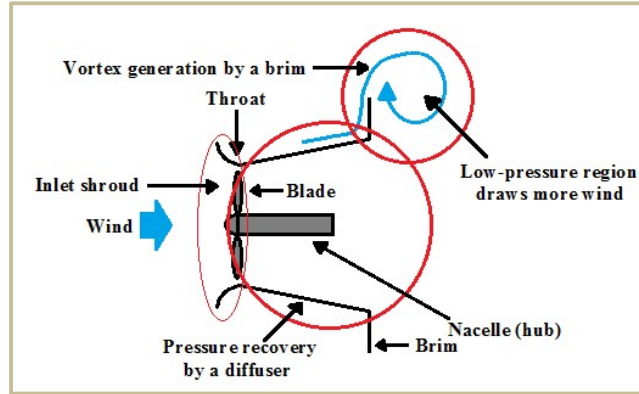


Figure 1.27. Flow structures around wind turbine with a nozzle, diffuser, and flange components, all together (Ohya and Karasudani, 2010)

Including both a flange to the diffuser as well as inlet shroud component introduced to the system as schematically shown in Figure 1.27, increase the maximum available wind power, P_{av} , by increasing free-stream wind speed significantly, and also significantly yields the wind turbine output power, P to be enhanced around 4-5 times more compared that of a conventional or bare wind turbine, as shown in Figure 1.28 (Ohya and Karasudani, 2010).

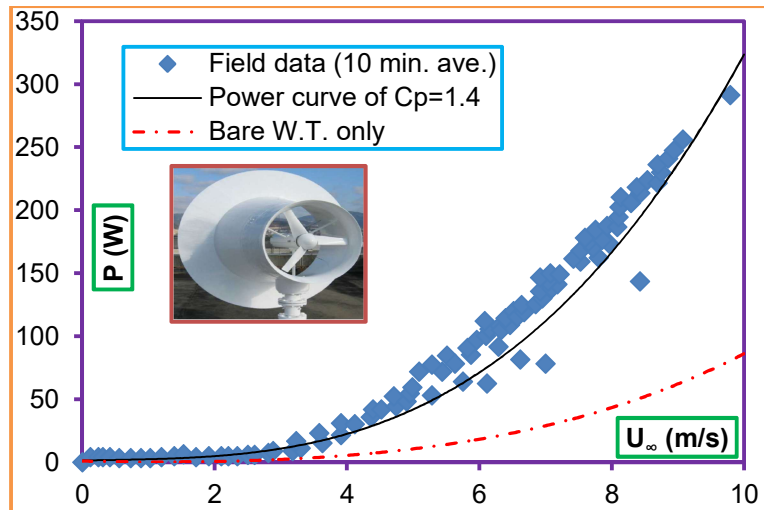


Figure 1.28. Wind turbine output power, P depending on free-stream wind speed, U_{∞} (Ohya and Karasudani, 2010)

1.3.5.5. Smart Solutions to Cased Wind Turbines

1.3.5.5.(1). Flexible Flange Idea

The drag force, F_D acting on a diffuser augmented wind turbine may cause damage, especially under high free-stream wind speeds, U_∞ . Considering this negative situation, a solution of a self-adaptive flange was proposed for the wind turbine located in a flanged diffuser inlet shrouded casing to lower the high drag force, F_D caused by extreme wind loads applied on the flanged casing (Hu and Wang, 2015).

Numerical results indicated that this drag force, F_D on the flanged casing can be alleviated to about 35% of the original, as seen in Figure 1.33 at 60 m/s free-stream wind speed because of the deformation of the smartly self-adaptive flange as the configuration seen in Figure 1.29b, and drag force, F_D results presented in Figure 1.33. Over a threshold value of free-stream wind speed (Figure 1.30), V_r , the self-adaptive flange enables the wind flow as in the case of the non-flanged situation. The corresponding dimensions of the self-adaptive flange and the casing shroud as well the drag force, F_D , and the drag coefficient, C_d results of the casing components are presented in Figures 1.32, 1.33, and 1.34, respectively.

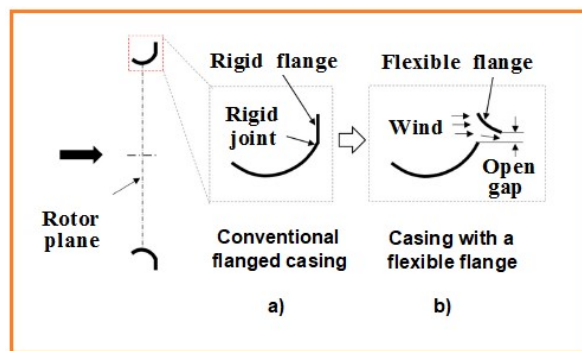


Figure 1.29. a) Conventional rigid flanged casing, b) general flexible flanged casing idea (Hu and Wang, 2015)

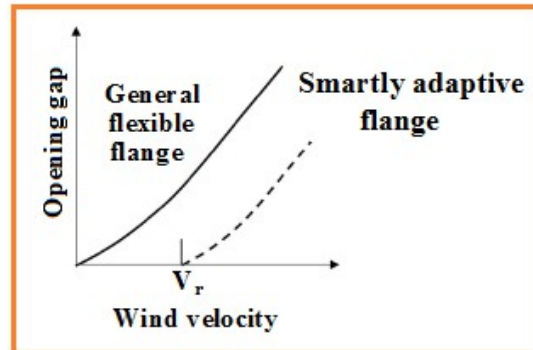


Figure 1.30. Curves of open gap with threshold of free-stream wind velocity, V_r (Hu and Wang, 2015)

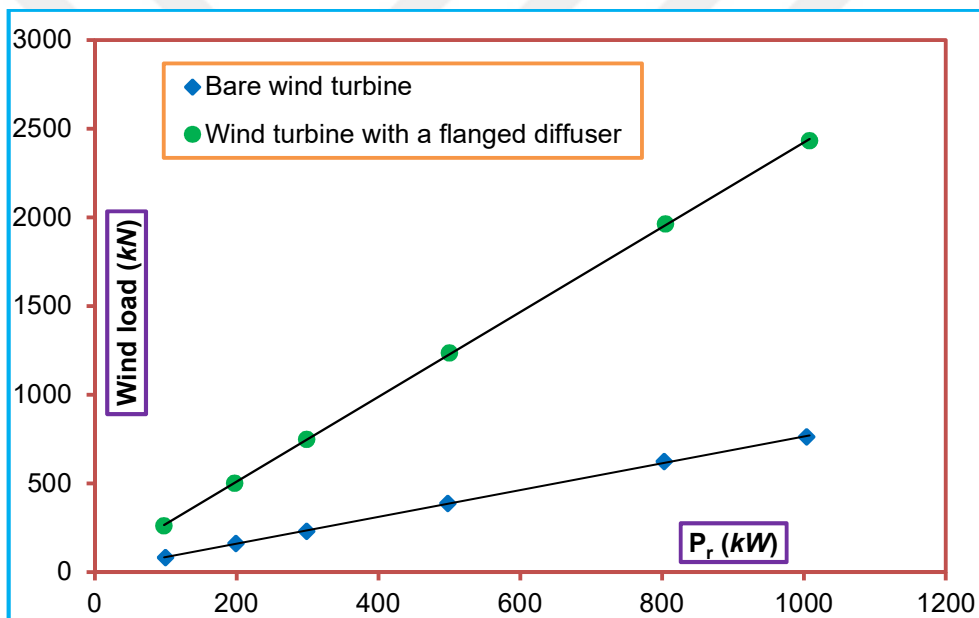


Figure 1.31. Wind loads acting on two kinds of wind turbines with and without a flanged casing at 60 m/s for various rated powers, P_r (Hu and Wang, 2015)

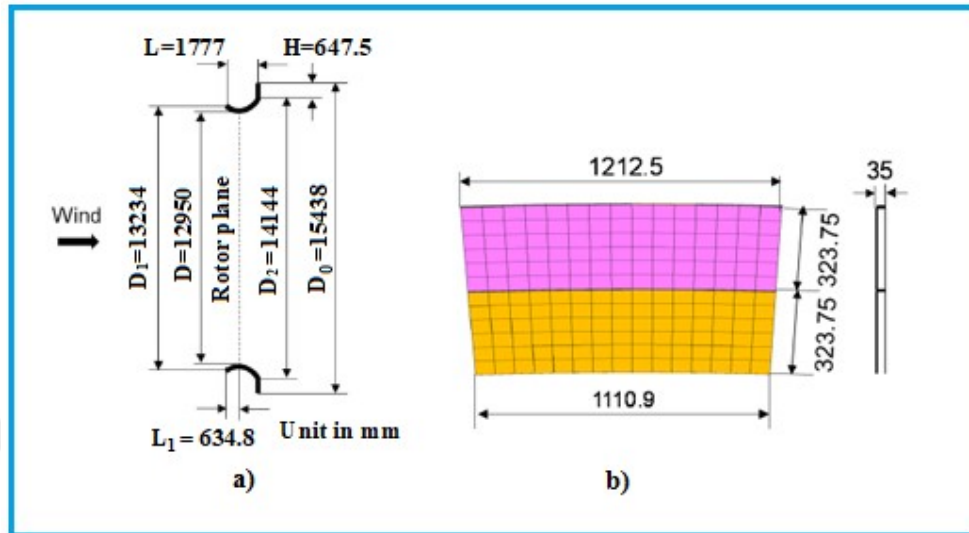


Figure 1.32. The casing configuration to conduct drag comparison based on casing components, a) dimensions of a smart flanged casing, b) side view of the flexible flange component and related dimensions (Hu and Wang, 2015)

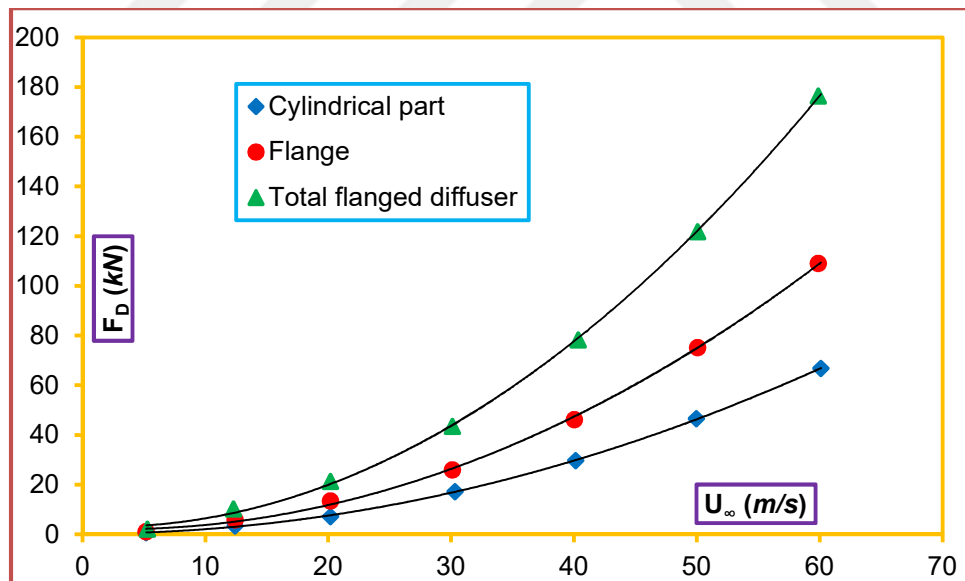


Figure 1.33. Drag forces, F_D of the casing components (Hu and Wang, 2015)

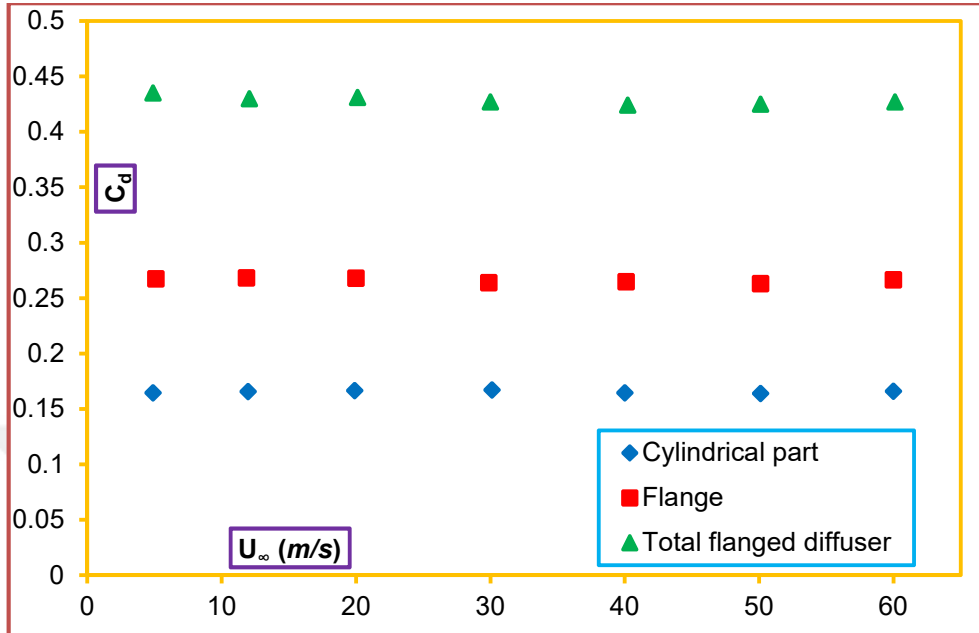


Figure 1.34. Drag coefficients, C_d of the casing components (Hu and Wang, 2015)

1.3.5.5.(2). Wind Turbine Casing by Passive Flow Control Devices in Airfoil Cross-Section

The axial full body length, L of the nozzle-diffuser-flange type casing was unfortunately constrained due to a high rate of drag force, F_D . However a solution was brought to this problem which encloses a nozzle-diffuser-flange component type shrouding with passive flow control devices in the form of a multi-airfoil structure to increase the mass flow rate of air, \dot{m} passing through the casing and rotor disc, and, reducing the corresponding drag force, F_D . Thus, air injection application created by the multi-airfoil structure was used to avoid or delay flow separations as seen in Figure 1.35. Nevertheless, the numerical and experimental results indicated that free-stream velocity, U_∞ was increased in the throat section of the casing by a factor of maximum wind speed ratio, up to $K=3.25$ (Coşoiu et al., 2013).



Figure 1.35. The airfoil type casing appropriate for small scale wind turbines with passive control devices (Coşoiu et al., 2013)

1.3.5.5.(3). Truncated Nozzle-Diffuser Shaped Wind Turbine Casing

Among the reviewed studies in the establishment of the present dissertation; the minimum value obtained for the maximum wind speed ratios, K vary from $K=1.16$ to 1.31 inside a truncated triangle form of a nozzle-diffuser shaped casing which is shown in Figure 1.36 (Setoguchi et al., 2004). The other conducted studies were comprehensively handled in Section 4.10 with the geometric parameters of casing configurations and relevant results in terms of free-stream wind speed, U_∞ enhancements inside the casings. However, although the casing configuration presented in Figure 1.36 is a smart solution of a case type of wind turbines, the wind speed enhancement inside this type of casing body was reported to stay at lower levels, as reported above.

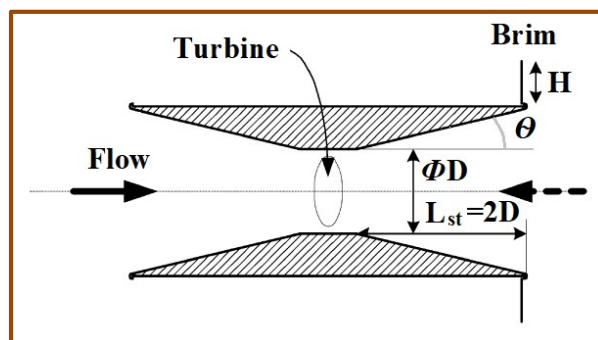


Figure 1.36. Cross-section of a truncated triangle used for wind turbine shrouding (Setoguchi et al., 2004)

1.3.5.5.(4). Scoop Type of Wind Turbine Casing Configuration

Eventually, the most appropriate design in wind turbine shrouding is usually the one in the form of a proper diffuser or an optimized scoop design including inlet shroud to concentrate the air flow and a flange to generate downstream vortices to speed up the mass flow rate, \dot{m} of air running through the wind turbine rotor disc. The scoop generating the highest maximum pressure drop ratio, C_{pmax} among the reviewed studies in the scope of the dissertation is schematically shown in Figure 1.37, has an entrance diameter, Φ_1 , exit diameter, Φ_2 , entrance axial length, L_1 , exit axial length, L_2 , the diameter of the cylindrical section, Φ_c (or R_c in terms of the radius dimension), and the axial length of the cylindrical section, L_c ; 6000 mm , 6000 mm, 2000 mm, 2000 mm, 4000 mm, and 2000 mm, respectively.

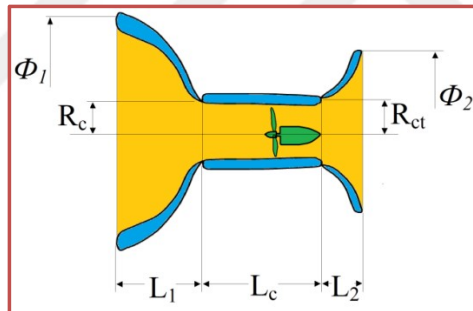


Figure 1.37. General schematic scoop optimization concept (Wang et al., 2008)

1.3.6. Casing Systems Applied to Vertical Axis Wind Turbines

A vertical axis wind turbine with concentrator in parallel to the horizontal casing augmented wind turbines were also reviewed in the concept of the dissertation. These wind turbines consisted of new innovated technologies stated above should become prevalent globally, particularly in developing countries. Presently, reviewed turbines are capable of producing electricity generation in

lower wind speeds and hence, they attain their maximum output power, i.e., they reach their rated power capacity, P_r with lower wind speeds, U_∞ , and eventually have a higher wind turbine power coefficient, C_p . A few sample types of vertical axis wind turbines are shown in Figure 1.38. However, it is worth to mention that the earliest known vertical axis windmills built by Persians in Nashtifan in the east of Khorasan of Iran, approximately around 2500-3000 years ago to only grind grains and those had concentrators as seen in Figure 1.39 (Sahin et al., 2017). On the other hand, the diffuser shaped shroud as seen in Figures 1.40a and b along with a few other changes, are able to significantly improve the power generated by the vertical axis wind turbine which corresponds to an increase of about 2.5 times the power coefficient, C_p in the case of vertical axis wind turbine applications placed at the exit of cooling towers. These wind turbines are used to smartly assess from the energy of air exhausted from the cooling tower. Also, the exhausted air speed, u is further accelerated by utilization of additional components including diffuser-plates and guide-vanes (Chong et al., 2014a; Chong et al., 2014b).

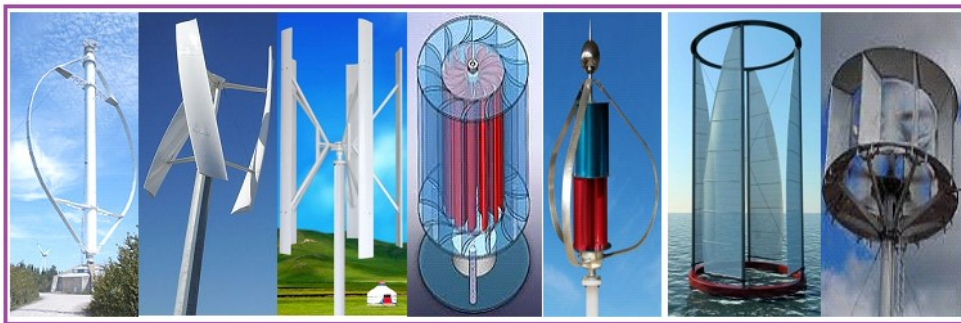


Figure 1.38. Samples of mostly used vertical axis wind turbines available in the industry

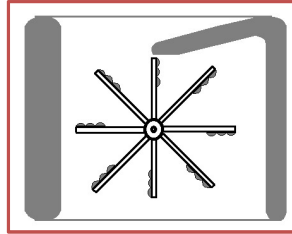


Figure 1.39. The earliest known vertical axis windmills built initially by Persians in Nashtifan region in the east province of Khorasan of Iran (Sahin et al., 2017)

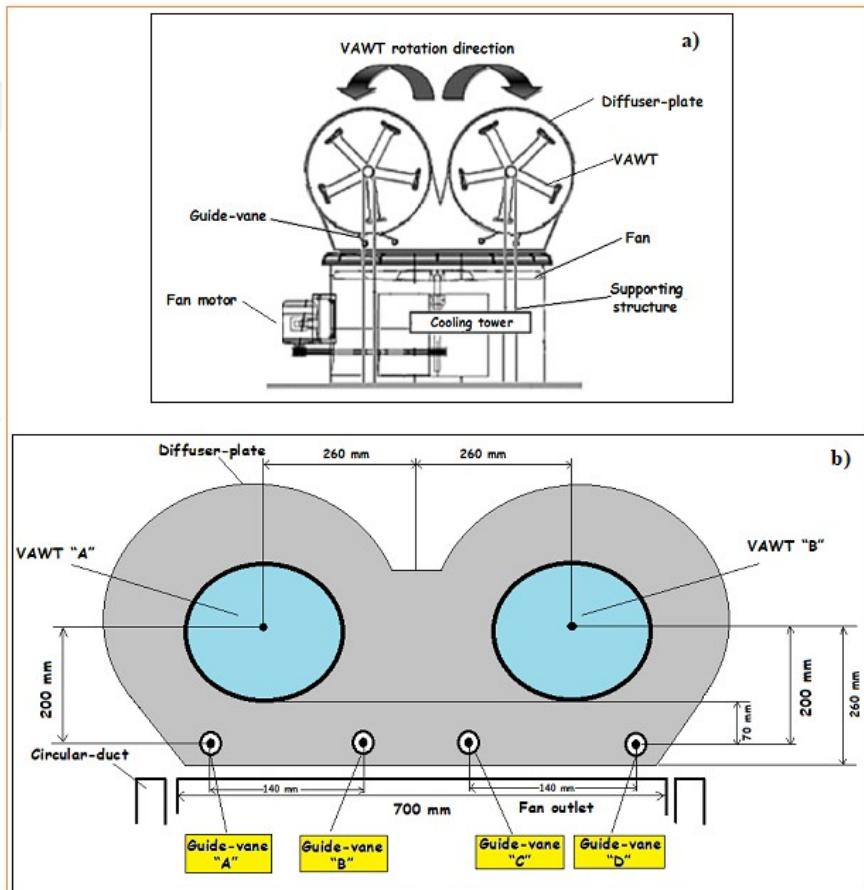


Figure 1.40. Vertical axis wind turbine shrouding application for the cooling tower, a) cooling tower with the other auxiliary equipment, b) dimensioning of VAWT settlement in diffuser shaped shroud and guide vane locations (Chong et al., 2014a; Chong et al., 2014b)

Table 1.15. The utilities of vertical axis wind turbine (VAWT) and enclosure applications placed at the cooling tower exit (Chong et al., 2014a; Chong et al., 2014b)

Test configuration	Intake wind speed (m/s)	Fan motor power input (W)	Fan rotational speed (rpm)	W.T. Rotational speed (rpm)		W.T. Response time (s)	
				VAWT 1	VAWT 2	VAWT 1	VAWT 2
Cooling tower only	1.90	203.84	1364.33	-	-	-	-
Cooling tower with VAWTs	2.15	200.20	1366.00	438.0	444.7	101.7	150.0
Cooling tower with VAWTs and enclosure	2.52	198.86	1369.67	472.2	475.3	59.6	87.8

Table 1.15 presents an increase of cooling tower intake wind speed based on vertical axis wind turbine application and furthermore due to shrouding of the wind turbines and one stage further regarding the guide vane applications to properly direct the exhaust air inside the wind turbine. The intake wind speed enhancements demonstrate the maximum available wind power, P_{av} , and wind turbine output power, P generation by the wind turbines can be increased by a factor of 2.33 during the utilization of enclosure application around the wind turbines. Also, the other benefits including reduction in cooling tower fan power consumption and improvement in the response times of wind turbines due to enclosure applications are the other two advantages of wind turbine shrouding as given in Table 1.15.

1.3.7. Shrouding of Savonius Wind Turbines

A recent type of wind concentrator arrangement in order to improve the power coefficient performance, C_p of Savonius type vertical wind turbines is also developed as presented in Figure 1.41. The diffuser type wind concentrator was located in front of the turbine rotor to prevent the negative torque opposite of the

rotor rotation. The geometrical parameters, including the guide vanes conveying the air flow into the *VAWT* were optimized to obtain an optimum wind turbine performance and turbine power coefficient, C_p . The turbine rotor with different geometrical parameters was tested, and the optimized dimensions of the entrance guide vane were determined to be, $\mu=45$ cm, $\lambda=52$ cm, $\xi=45^\circ$, and $\zeta=15^\circ$. Altan et al. (2008) found that the maximum power coefficient, C_p of the Savonius type vertical axis wind turbine is raised to about 38.5%, which is reported by them to be very low in the situation of conventional bare Savonius type.

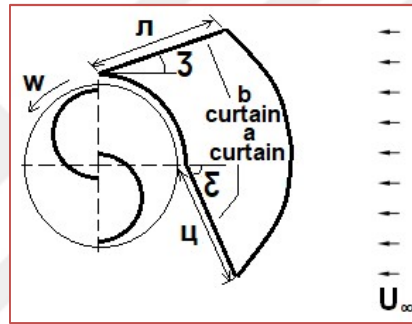


Figure 1.41. The concentrator arrangement optimization for *VAWT* ($\mu=45$ cm, $\lambda=52$ cm, $\xi=45^\circ$, and $\zeta=15^\circ$) (Altan et al., 2008)

While, the power coefficient, C_p of vertical axis Savonius wind turbine with optimized geometrical parameters of entrance arrangement of the guide vane which were taken as $\mu=45$ cm, $\lambda=52$ cm, $\xi=45^\circ$, and $\zeta=15^\circ$ approaches $C_p=0.39$; without utilizing guide vanes, this value of power coefficient, C_p is only around $C_p=0.16$ (Altan et al., 2008). A movable entrance guide vane was also used for similar vertical wind turbines to properly guide the wind flow through the rotor (Wahyudi et al., 2015).

1.3.8. Recent Methods in Wind Energy Generation

Recent concepts of wind energy generation beyond the traditional horizontal or vertical types of wind turbines mainly include *INVELOX*, Neodymium Magnetic Wind Turbines, and the Vortex Bladeless types. Those perform wind power generation very well under same wind conditions and tower-mounted turbines of the conventional type are eliminated in these new innovative wind turbines. On the other hand, manufacturing and assembly of the classic types are also so expensive; and unfortunately, operation of such wind turbines is usually inefficient.

1.3.8.1. Increased Velocity Wind Turbines (*INVELOX*)

The general design of the *INVELOX* type wind turbine includes the capability of capturing wind flow without the utilization of active or passive yaw control, since the wind stream is directed towards the wind turbine whichever direction it flows, as shown in Figure 1.42. On the other hand, the wind flow is further accelerated through the Venturi section and then expanded to be discharged into the environment through a diffuser. The power generation is obtained at the cross-section having a minimum area shown by the 4th location as seen in Figure 1.42a.

INVELOX type of wind turbines is possibly to capture and intensify the air to accelerate the approaching wind through the piping system. Consequently, *INVELOX* turbine accomplishes a significant boost of the wind turbine mechanical output power, P as reported by (Allaei and Andreopoulos, 2014).

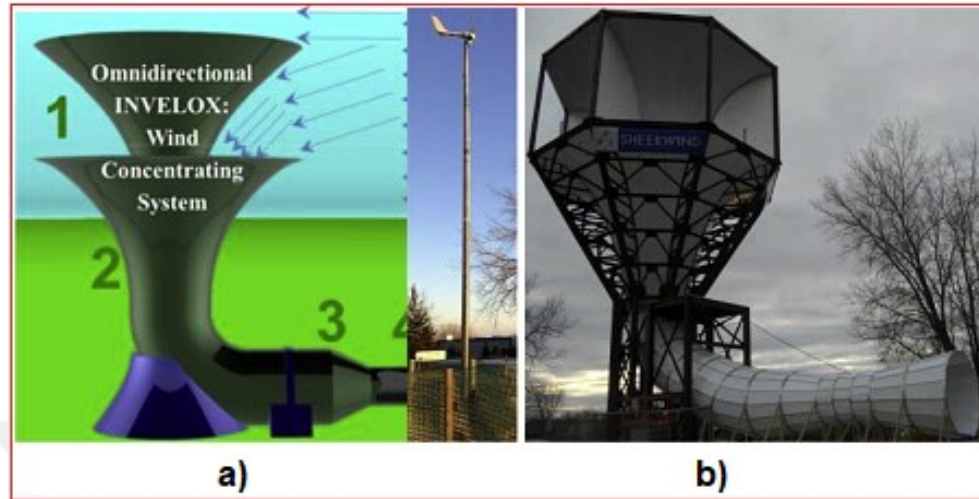


Figure 1.42. *INVELOX* type energy generation method, **a)** schematic view to represent the main components of the *INVELOX* body, **b)** an installed, energy generating *INVELOX* type of wind turbine (Allaei and Andreopoulos, 2014)

1.3.8.2. Neodymium Magnetic Wind Turbines

The miniature type of shrouding applied to the micro type of wind turbines is used to generate power for sensors located inside pipes or ducts is in the concept of this type of electrical power generation. The wind turbine rotor diameter, D_{rotor} is rather small around 2 cm as whole exploded components of this micro wind turbine are presented in Figure 1.43. The main advantage of the neodymium magnetic wind turbine is the elimination of the shaft and gear system; where the maintenance problems of such components cause serious problems in conventional wind turbines (Howey et al., 2011).

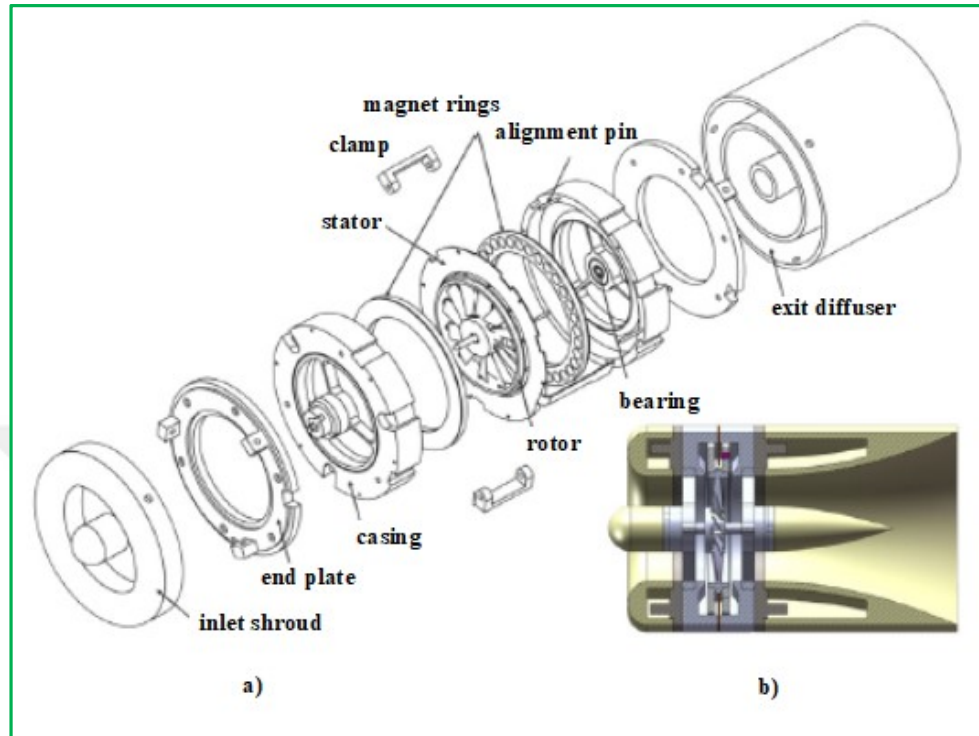


Figure 1.43. A miniature type of wind turbine, **a)** exploded components, and **b)** its shrouding (Howey et al., 2011)

Power generation is obtained by an axial-flux permanent magnet machine assembled into the shroud. This type of wind turbines usually operate at a range of free-stream wind speed, U_∞ , values including 3 - 7 m/s; and very small amounts of mechanical output power, P is aimed to be generated such as between $80 \mu\text{W}$ and 2.5 mW (Howey et al., 2011).

1.3.8.3. Vortex Bladeless Wind Turbines

The most recent type of wind turbine developed by the Spanish engineers involves 12 m long, hollowed poles mounted in series as shown in Figure 1.44. Free-stream wind flow induces the poles to vibrate as in the case of guitar strings

results in the generation of mechanical output power, P , thus electrical energy is obtained.



Figure 1.44. A view of vortex bladeless wind turbine generating power

The new technology using only the vibration energy is quite environment-friendly due to the non-bladed structure of wind turbine, in this way, the possibility of flying birds to strike to the wind turbines is almost zero. Additionally, there is no noise generation taking place in this type unlike the conventional bladed wind turbines saving the nearby villagers. On the other hand, the elegant structure of the wind turbine eliminates the negative visual impact originated by the blade structure of the conventional wind turbines.

Although this new technology is working with an efficiency, C_p corresponding to only 70% of the conventional wind turbines; due to the initial investment of such wind turbines being half of the conventional types compensates the negative effect of the efficiency, C_p . However, studies including the improvement of the efficiencies, C_p of vortex bladeless turbines still proceed.

The shaking energy, caused by the wind energy is directly obtained from the free-stream wind flow resulting shaking effect in nature. The flow swirling formed on circular cylinders as shown in Figure 1.44 generates a lift force, F_L . This lifting influence is directly proportional to the power of the vortex. Thus, a vortex

generator (VG) is used to create turbulence or vortex of fluid according to the design configuration and related optimization of the hollowed pole. Since the spinning motion of the wind turbine is eliminated by this method, energy generated from these wind farms consisting of vibrating turbines is rather cheap. On the other hand, the generated shaking movement, i.e., shaking energy is transformed into electrical energy by the utilization of an alternator. This method is a simple and smart way of extracting fluid energy firstly to shake energy and then to generate useful power (Demirbas and Andejany, 2017; Forster and White, 2014). On the other hand, one of the designed configurations found in literature and suitable for the sufficient deflection and displacement energy of the hollow structures is shown in Figure 1.45 (Cajas et al., 2017).

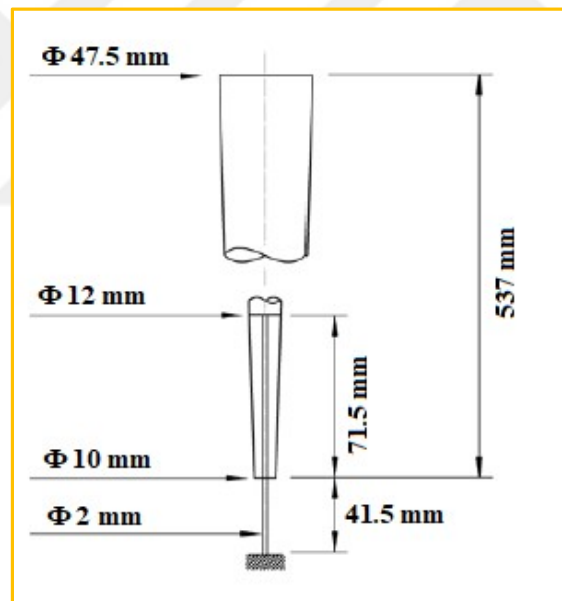


Figure 1.45. An optimized configuration and its dimensions for numerical and experimental testing (Cajas et al., 2017)

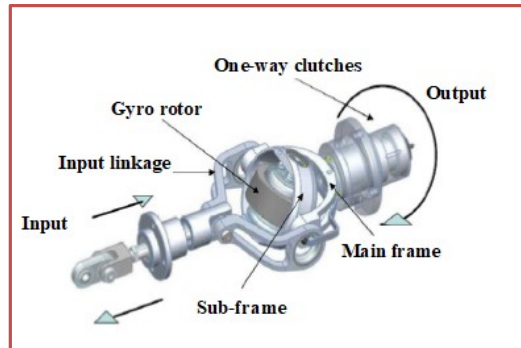


Figure 1.46. Gyroscopic electric generator (Mane et al., 2017)

The vibration energy is transformed to the electrical energy by a gyroscopic rotor, as the components of a gyroscopic rotor are shown in Figure 1.46. A gyroscopic rotor supported by an inner ring, i.e., sub-frame is set to rotate free in an outer ring, i.e., main-frame. Besides, the main-frame can also rotate freely in the transmission housing. The sub-frame is linked to a linkage, thus this pivot the sub-frame inside the mainframe. Eventually, all three mechanisms including main-frame, sub-frame, and linkage rotate together by the gyroscopic reaction influence. The output rotating shaft is connected to the mainframe and the rotating shaft is attached to the transmission housing by a one-way clutch (Mane et al., 2017).

On the other hand, Table 1.16 gives the superior and non-superior aspects of non-bladed wind turbines presented with respect to the conventional spinning bladed wind turbines, in order to handle recently developed technologies. The following equations numbered as Eqs. (1.12), (1.13), (1.14), (1.15), (1.16), and (1.17) give the physical concept of energy generation obtained from shaking and vibrating movements of non-bladed wind turbines (Demirbas and Andejany, 2017; Dresig and Dien, 2011).

Table 1.16. Comparison of bladeless wind turbine advantages and disadvantages (Demirbas and Andejany, 2017)

Advantages	Disadvantages
The shaking and vibrating oscillations of the turbine columns are used to generate energy using an alternator at the base, thus this is cheaper than conventional methods	Requires additional componential costs, especially in stormy weathers to cause quick shaking
The maintenance costs are only around 20% of the conventional wind turbines	Difficulties in skills, information, and as well as service facilities
No noise generation occurs, which do not scare animals and do not disturb the villagers	Generate less electricity when compared to conventional spinning bladed wind turbines
The initial investment is also so low compared to the conventional wind turbines	Lack of advanced technology
Appropriate for the utilization of individual homes	A poor market, thus lower industrial acceptance is encountered

One dimensional simple harmonic motion is defined by Eq. (1.12);

$$F_h = -ky \quad (1.12)$$

On the other hand, the second derivation of the displacement with respect to time yields;

$$d^2y/dt^2 = -(k/m)y \quad (1.13)$$

Solving the differential equation presented in Eq. (1.13) becomes (Eq. 1.14);

$$y(t) = C_1 \cos(\omega t) + C_2 \sin(\omega t) = A \cos(\omega t - \varphi) \quad (1.14)$$

Initial conditions determine the constants C_1 , and C_2 , presented in Eq. (1.14), respectively. And, the origin is fixed at the equilibrium position.

Besides, the angular frequency is defined by, $w = 2\pi\nu$. System's kinetic energy, KE considering an arbitrary time, t is,

$$KE = 0.5mv_{ob}^2 = kA^2 \sin^2(wt - \varphi)/2 \quad (1.15)$$

On the other hand, the potential energy, PE is defined by Eq. (1.16),

$$PE = 0.5ky^2 = kA^2 \cos^2(wt - \varphi)/2 \quad (1.16)$$

Finally, the system's total mechanical energy including kinetic and potential energy is shown in Eq. (1.17) (Demirbas and Andejany, 2017);

$$TE = KE + PE = 0.5kA^2 \quad (1.17)$$

2. LITERATURE SURVEY AND OUTLINE OF THE PRESENT STUDY

2.1. Literature Survey

2.1.1. Aerodynamic Characteristic Concept of Horizontal Axis Wind Turbines

2.1.1.1. Efficiency Analysis of Operating Wind Farms

[Bilgili et al. \(2004\)](#) researched wind energy potential in eastern regions of Turkey such as they took Iskenderun and Antakya regions into account. In this part of the dissertation; it was shown that they utilized the Wind Atlas Analysis and Application Program, *WAsP* software package in order to obtain a wind map for the related regions of Turkey. Whole wind map of this cited region was constructed by [\(Sahin et al., 2005\)](#) using this *Wasp* package program. In this context, data of hourly wind speeds and wind directions obtained in regions of Antakya, İskenderun, Karataş, Yumurtalık, Dörtyol, Samandağ, and Adana provinces of Turkey were used for this work. Also, wind characteristics and energy potential of Belen-Hatay regions of Turkey were researched by [\(Sahin and Bilgili, 2009\)](#), and statistical analyses were performed in these regards.

[Bilgili and Sahin \(2009\)](#) investigated wind energy density in the southern and southern west regions of Turkey through using Weibull and Rayleigh probability density functions, and also utilizing the Wind Atlas Analysis and Application Program (*WAsP*). Also, [Bilgili and Sahin \(2010b\)](#) investigated wind energy density in the western region of Turkey by using Weibull and Rayleigh probability density functions, and as well the Wind Atlas Analysis and Application Program (*WAsP*).

[Bilgili et al. \(2009\)](#) statistically analyzed wind energy potential in the provinces of Turkey considering the regions of Akhisar, Bababurnu, Belen, Datça, Foça, Gelendost, Gelibolu, Gökçeada, and Söke located in the south, south-west, and west coasts of Turkey.

On the other hand, an analysis conducted by means of an operating wind farm to reveal the efficiency performances of active wind turbines in the field can serve in the purpose of getting opinions of expansion of current wind farm, for the constructions of neighbor wind farms, and in order to execute studies to improve power generation efficiencies ([Ilhan, 2014](#)).

2.1.1.2. Aerodynamic Parameter Analysis

Wind power is predicted to have the greatest future prospects among the possibilities for renewable and sustainable energy ([Ilhan, 2014](#); [Lee et al., 2010](#); [Kishinami et al., 2005](#)). Without decisive action, energy-related greenhouse gas emissions could, unfortunately, go up more than double by 2050, and increased oil demand will heighten interest over the security of supplies. For this reason, an energy revolution is needed to achieve at least a 50% reduction of global CO_2 emissions relative to current levels by the 2050 year. In this revolution, energy efficiency, sustainable, and low-carbon energy technologies certainly play a crucial role in the energy sector. In addition, renewable energy plays a significant role in addressing global energy and environmental challenges ([Bilgili et al., 2015b](#)). Among all available renewable energy sources, the wind is the most advanced of the new renewable energy technologies. In a few countries, wind power already provides 15% to 30% of total electricity generations and consumptions. The wind technology has been growing rapidly, and the costs of electricity generation from the land-based wind installations have continued to fall ([TRWE, 2013](#)). There was around 370 GW of installed wind power capacity in the World, and a total of 129.1

GW was installed in the European Union by the 2014 year as seen in Figure 1.19 and as reported by (WPES, 2014). However, recently, this capacity has exceeded 530 GW by 2017 in a global speaking.

Production of energy affair in Turkey by recent years boosted dependency on abroad as in natural gas and consequently unbalances in energy productions, unfortunately, grew out. Wind energy which is a sub-category of renewable energy source has undoubtedly a great potential in Turkey; however we cannot presently benefit from this potential source sufficiently in reality (Ilhan, 2014).

A new installation of wind power with the capacity of 804 MW was installed in the 2014 year, increasing the total installed capacity in this sector to a value of 3,763 MW by the 2014 year in Turkey. Namely, Turkey's installed capacity has grown up with an amount of approximately 500 MW per year from 2010 to 2014. On the other hand, Turkey's National Transmission Company had declared that annual installations were expected to reach 1,000 MW per year starting from 2015 onwards. And, these expectations are almost satisfied reaching a total installed wind power of 6742.4 MW of power installations at the end of 2018. Turkey's best wind resources are located in the provinces of Çanakkale, İzmir, Balıkesir, Hatay, Osmaniye, and İstanbul. By the end of the 2014 year, the Aegean region had the highest installed wind capacity with a total of 1,486 MW installations, followed by Marmara region with 1,359 MW installations, and the Mediterranean region with 543 MW installations. However, in the following four years; same provinces had 2,832 MW, 2,449 MW, and 996 MW of installations, respectively, at the end of 2018. And, the Turkish Wind Energy Association who expected Turkey to reach an installed capacity of 5,000 MW by the end of the 2015 year and 6,200 MW by the 2016 year considering the reports of 2013; almost reached these goals of installations in the cited years (GWEC, 2013a). Since, considering both years, real installations were occurred as 4503.2 MW and 5751.3 MW, respectively for years 2015 and 2016. These installations indicated the results

were kept a little below the expected installation amounts decided in 2013. On the other hand, presently, Turkey is one of the biggest on-shore wind markets in Europe with an 11 GW capacity of wind power projects (GWEC, 2013a; TWEA, 2019).

Aerodynamic parameters including power, power coefficient, axial flow induction factor, thrust coefficient, and thrust provide answers to questions including the variations in the performances of operating identical wind turbines in a wind farm. In this context, Bilgili et al. (2015b) performed a study considering identical wind turbines of a wind farm located in Belen province in Hatay city of Turkey. Similarly, Ilhan et al. (2018a) performed a parallel study dealing with identical wind turbines of an installed wind farm to conduct aerodynamic explanations of these wind turbines. In this regard, the optimum rotational speed of these wind turbines, the probability density of rotational speed, and power generations and efficiencies of the considered wind turbines of the farm were clarified.

2.1.2. Estimation of Aerodynamic Characteristics for Horizontal Axis Wind Turbines

2.1.2.1. Wind Energy Density Forecast by Statistical Analysis

Renewable energy is the type of energy that is obtained from non-depletable sources which create relatively a low level of carbon-dioxide emissions. In this regard, renewable energy necessarily differs from the other types of energy sources such as fossil fuels; therefore, many countries all over the World including Turkey develop different incentives and subsidy schemes to promote its use (Ilkilic, 2012). In addition, renewable energy which is an important agent for the alleviation of the future's global climate change is certainly a promising method of

energy obtainment. Wind energy has attained a relatively better position among the other renewable energy sources, and it has demonstrated the highest growth throughout the World for the last years, as it has been used for quite a long period of time throughout the World. Thus, wind energy which is an environmentally friendly renewable energy source makes its usage to become rapidly widespread (Saidur et al., 2012).

Among the numerous advantages of wind power including low cost, purity, sustainability, and being abundance in anywhere in the World, establishes its position to become further stronger among other all available renewable sources. There is no transportation problem in wind energy, and high technology is not necessary for its employment. Wind energy is a clean energy resource, and it cannot be depleted ever in contrast to conventional fossil fuel sources. All types of energy production put some adverse effects on the environment; however, wind energy causes considerably low and local effects which are manageable and negligible compared to traditional energy resources. In fact, the importance of wind energy comes from its friendly effects on the environment. For this reason, wind power is demanded electricity production to reduce air pollution resulting from fossil fuels (Bilgili and Simsek, 2012).

In addition, wind power can be put into use more rapidly than the other energy technologies, which is another significant advantage of wind energy. While a conventional power plant takes 10 to 12 years or even more to be completely installed, the wind power plant can be put into operation in a few months; as well as a conventional power plant cannot produce power unless it is entirely built up; however, a wind power plant can start power generation as long as the installation of the first power plant in the wind farm is completed (GWEC, 2013b).

Wind power is currently the fastest growing sector for electricity production, and it has demonstrated the fastest growth among all available renewable energy sources for the past years (White, 2006). Turkey has a

considerable wind power potential, particularly in the regions of Marmara, western coasts, and southern Anatolia. However, wind energy potentials in the other regions of Turkey are also reported by (Yumak et al., 2012), (Yaniktepe et al., 2013), (Genc and Gokcek, 2009), (Bilgili et al., 2004), and (Sahin et al., 2005). On the other hand, Kose et al. (2014) performed a statistical analysis of wind energy potential in the vicinity of Selcuk University campus. They used the wind data of 2005, in which the statistical analysis was conducted by *WAsP* in their study. Yearly average wind velocities at a variety of heights were calculated to be 5.36 m/s, 5.40 m/s, and 6.05 m/s, respectively, for 10 m, 20 m, and 40 m of altitudes. Besides, the range of 260 - 308 W/m² of power density was determined at an altitude of 40 m. In their calculations for the statistical analysis; the wind speed frequency histogram, Rayleigh and Weibull distributions, wind direction, and temperature data were utilized. In this regard, this part of the dissertation was performed in order to report the wind power properties in Bababurnu-Çanakkale location in the Marmara region of Turkey. And, certain parameters including wind velocity probability or frequency distribution, the frequency distribution of the wind velocity directions, Weibull and Rayleigh parameters, average wind velocity, and variations of wind power potential were calculated in the context of the study. Each of these wind characteristics was separately investigated using seasonal, monthly, and hourly data (Ilhan et al., 2017a).

2.1.2.2. Wind Power Output and Aerodynamic Forecasts through Artificial Neural Networks (ANN)

2.1.2.2.(1). Wind Power Output Curve Determination by ANN

Evaluation of wind turbine efficiency requires the wind turbine capacity factor (Chang et al., 2014b). Additionally, the turbine performance specification

and an indication of wind turbine service life can be deduced from the power characteristics curve. Generally speaking, theoretical wind turbine power characteristics curves are based on ideal meteorological and topographical conditions. In reality, however, the ideal conditions for wind power generation are unfortunately never realized in practice. The factors including the location of wind turbines, air density, and the distribution of wind speed, and as well as wind direction can each significantly affect the power characteristics curve (Shokrzadeh et al., 2014). Estimation of the power curve equation and the related aerodynamic parameters have recently increased its validity (Carrillo et al., 2013). In addition, the forecasting of the wind power and the planning of wind farm expansions require an accurate computation of power characteristics curves (Lydia et al., 2014; Trivellato et al., 2012).

A number of methods have been mentioned in the literature for forecasting wind turbine performance parameters over different duration of time and including a variety of physical models, statistical methods, hybrid physical-statistical methods, artificial intelligence, and neuro-fuzzy processing, along with more recent methods (Morales et al., 2010; Fadare, 2010). Li and Shi (2010) have made a comparative study of three types of neural networks; these are the adaptive linear element, backpropagation, and the radial basis function, enabling the prediction of hourly wind speed. They have confirmed that no single neural network model is superior to the others in terms of its entire evaluation capability. The main advantage of the neuro-fuzzy model is in combining neural network and fuzzy logic systems, thus giving an increased capability in both areas. The fuzzy logic system enables better representation of the behavior of a given system by the use of a simple rule set, although it is unable to make use of the knowledge contained in the numerical data (Karray and De Silva, 2004). Besides, it has been shown that artificial neural networks (ANN) are in general capable of training virtually any smooth nonlinear function, and as well a high degree of accuracy generally results

from the application of *ANN*. Nevertheless, *ANN* has only a limited capability in dealing with linguistic information.

It has been demonstrated that artificial neural networks (*ANN*) are generally has the skill of training virtually any smooth nonlinear function, and a high degree of precision generally occurs from the application of an artificial neural network model. Nevertheless, an inconvenience of *ANN* is, unfortunately, the limited talent in proceeding with the linguistic information.

Horizontal axis wind turbines are the major type of large wind turbines quite in use today, and they have received a great deal of attention both among researchers and in commercial terms (Eriksson et al., 2008; Fadare, 2010). In this part of the dissertation; turbine power output values have been modeled in relation to the hub-height wind speed (U_D), local atmospheric air temperature measured at the nacelle (T_{atm}), and the turbine rotor rotational speed (Ω), using the *ANN* modeling approach. Power curves obtained by this modeling method can be used in the planning of new installations and for computation of total wind power generation for an existing wind farm. The main advantage of an *ANN* model is to operate with fewer variables in forecasting of mechanical output power extraction (P) from wind turbines. Wind turbine mechanical output power (P) can be predicted using required hub-height wind speed (U_D), local atmospheric air temperature (T_{atm}), and the rotational speed of the turbine rotors (Ω) without comprehensive knowledge of the turbine operation or its control scheme. Furthermore, wind turbine power (P) output can also be estimated satisfactorily without knowledge of the other turbine characteristics, or meteorological and topographical data is the desired process of wind turbine mechanical output power (P) computation with fewer input variables (Ilhan et al., 2017b).

2.1.2.2.(2). Determination of Aerodynamic Parameters by ANN

As reported by [Bilgili et al. \(2015b\)](#); if any precaution is not taken, greenhouse gas emissions will increase two times more reaching 2050, and concerns on the security of supplies will be enhanced due to the increase of oil demand. Thus, it is essential to reduce these excess amounts of CO_2 emissions possible to occur by 2050 to current levels, i.e., in order to obtain a 50% reduction in the emissions, an energy revolution is certainly required. The cited energy revolution should cover energy efficiency, sustainability, and low-carbon energy technologies; in which those perform a significant role. Besides, worldwide energy and environmental problems will be possibly solved by renewable energy utilization ([Bilgili et al., 2015b](#)). Among the renewable energy technologies, the wind is precisely the most advanced of the new renewable energy technologies. In a few countries, wind power already provides 15% to 30% of the total electricity. On the other hand, wind technology keeps rapidly improving, and as a result costs of energy generation from the land-based wind installations have continued to fall. There was 371 GW of installed wind power capacity in the World globally, and a total of 131 GW was installed in the European Union by the 2014 year based on the 2015 year wind reports ([GWEC, 2015a](#); [EWEA, 2015](#)). By 2015, global wind power installation attained 433 GW, whereas, Europe installation attained 142 GW ([GWEC, 2016](#); [EWEA, 2016b](#)). On the other hand, global and Europe wind power installations reached a total installation of 487 GW and 154 GW, respectively by 2016 based on 2017 year wind reports ([GWEC, 2017](#)). This situation is further enhanced reaching a total of 537 GW of wind power installations globally, reaching the end of the 2017 year ([REN21, 2018](#)). The related function of wind speed enhancement expressed with respect to the years was shown in Figures 1.1d and 1.19.

As seen, wind energy has been developing towards a mainstream, competitive, and reliable power technology. Globally, progress continues to be strong, with more participating countries, ambitious manufacturers, increasing annual installment capacity, and as well wide range of investments. According to the reports of International Energy Agency (IEA, 2013a), wind power could be generated up to 18% of the World's total electricity by the 2050 year, compared with 2.6% of the 2013 year's capacity and 3.4% of the 2016 year's capacity (WEC, 2016b). Technology improvements have continuously reduced energy costs; especially this is the case on land. In this context, wind turbine aerodynamic characteristics estimation is an important tool in monitoring the wind turbine performance, turbine control, and power forecasting (Shokrzadeh et al., 2014). Because, effective integration of the wind power into the power systems requires accurate estimation of the wind turbine power curve for operational management of wind energy as well as the monitoring of turbine performance. Additionally, accurate estimation of wind turbine power characteristic curve is required to more realistically size the storage capacity for wind energy integration (Shokrzadeh et al., 2014). In this manner, an equivalent power characteristic curve for the entire power plant can serve for the same purpose, for example, plant and system operators may use this curve to predict the plant output for a given wind speed (Wan et al., 2010).

The wind turbine capacity factor is an essential parameter in evaluating a wind turbine's efficiency (Chang et al., 2014b). In addition to this, the power characteristic curve is a wind turbine performance specification, and it is an indicator of overall wind turbine health. Theoretical wind turbine power characteristic curves are obtained by manufacturers, however under an assumption of ideal meteorological and topographical conditions. In practice, however, wind turbines are never used under ideal conditions; and the empirical wind turbine power characteristic curves could be substantially different from the theoretical

ones due to the location of the wind turbine, air density, wind velocity distributions, wind directions, mechanical and control issues, as well as possible uncertainties in the measurements (Shokrzadeh et al., 2014). In this context, the use of an equation for determining a power curve and the obtainment of its parameters become an important issue (Carrillo et al., 2013). Furthermore, accurate estimation of power characteristic curve serves as an essential tool in wind power forecasting and especially aid in wind farm expansion (Lydia et al., 2014; Trivellato et al., 2012).

Today, the most common design of wind turbines is definitely the horizontal axis wind turbine. In this part of the dissertation, horizontal axis wind turbine aerodynamic characteristics are modeled as a function of the hub-height wind speed, U_D (Ilhan et al., 2015). This turbine power curve and its aerodynamic characteristics model obtained for Belen Wind Farm in Turkey can be used for planning purposes and estimating total wind power production. Besides, the most advantage of this model is that as long as having the required hub-height wind speed, U_D ; wind turbine aerodynamic characteristics can be predicted without detailed knowledge of turbine operations and its control schemes. Furthermore, these aerodynamic characteristics can also be predicted straightaway and satisfactorily, without the use of other wind turbine characteristics, and without the requirement of the meteorological, and topographical data.

2.1.2.3. Wind Power Output Curve Determination by Adaptive Neuro-Fuzzy Inference System (ANFIS)

Wind energy is now regarded as a competitive and reliable source of power technology. The capacity of wind power plants and the level of investment in wind energy systems should, therefore, be increased in order to permit continued progress in wind energy sector. However, the current worldwide capacity of wind

energy power plants for electricity generation is, unfortunately, a mere 3.4% of the total (WEC, 2016b). On the other hand, it is glamorous to report that the International Energy Agency (IEA) has estimated that global output of wind power plants will generate about 18% of the World's electricity requirement by the year 2050. One of the main reasons for the increasing development of wind turbine technology, particularly onshore, is the declining cost of energy production.

The estimation of wind turbine aerodynamic characteristics, such as the wind turbine output power coefficient, C_p , has become an important factor in the monitoring of wind turbine performance, turbine control, and as well in the prediction of power extraction. Accurate estimation of the C_p curve for the operational management of wind energy, including the monitoring of wind turbine performance, is required for the effective integration of wind power into the power network systems. Realistic sizing of the storage capacity for wind energy integration can be obtained from the wind turbine power characteristics curve (Shokrzadeh et al., 2014). ANFIS forecasting structure can serve to obtain an equivalent power characteristics curve for the considered wind power plant as in the case of ANN application, for the predicted data to be used in the output power prediction at a given wind speed (Wan et al., 2010).

It is accepted that wind power is influenced significantly by environmental factors. In order to optimize wind power systems; new estimating methods are now being employed, including mostly fuzzy logic (FL), artificial neural networks (ANN), and neuro-fuzzy logic (NF) (Petković et al., 2013). One of the most effective types in the neural network system is the utilization of the adaptive neuro-fuzzy inference system (ANFIS) structure. Among the other conventional methods, ANFIS structure provides a better organized fuzzy inference system for given input/output data pairs (Petković et al., 2013). This technique uses the principle of formerly expressed FL, and has the ability to adapt the membership function parameters in the best manner to allow the associated inference system to track the

input and corresponding output data (Petković et al., 2013). The learning and the prediction capability of the *ANFIS* method have been shown to provide an effective tool for overcoming the uncertainties inherent in other methods. As a part of a hybrid intelligent system, *ANFIS* structure not only enables the adaptation, but it also increases the capability for automatic learning. *ANFIS* structure has therefore been used in a variety of engineering systems in recent years (Ghandoor and Samhouri, 2009), and the term implies the integration of the fuzzy inference system and a back-propagation learning algorithm of the neural network tool.

Dominant type of large wind turbines mainly in use today is reported by Eriksson et al. (2008) to be the horizontal axis wind turbines. Besides, this situation resulted them to receive a significant attention among researches and as well as in the commerciality (Eriksson et al., 2008). In this part of the dissertation; wind turbine power output values have been modeled concerning the hub-height wind speed (U_D), local atmospheric air temperature measured at the nacelle position (T_{atm}), and turbine rotor rotational speed (Ω), using the *ANFIS* tool approach. Power curves obtained by this modeling method can be used in the planning of new installations and for computation of total wind power generation for an existing wind farm. As well, the main advantage of this forecasting model is to operate with fewer variables in forecasting power extraction (P) from wind turbines. In this regards, wind turbine output power (P) can be predicted using the required hub-height wind speed (U_D), local atmospheric air temperature (T_{atm}), and the rotational speed of the rotors (Ω) without comprehensive knowledge of the wind turbine operation or its control scheme. Furthermore, wind power (P) output can also be estimated satisfactorily without knowledge of the other turbine characteristics, or meteorological and topographical data are even not required (Ilhan et al., 2016).

2.1.3. A Novel Concept of Wind Turbine Shrouding Systems

2.1.3.1. History of Wind Power Generation Systems and their Shroudings

Wind power generation systems have been in use more than 3000 years, and several different types of wind-mills have been invented as from 3000 years ago by the initial appearance of the ancient Persian vertical axis wind-mills. However, in a real sense, a starting point of wind power generation system started to be used in electrical power generation in years considering late 1800s and early 1900s. But, wind turbines mainly started to spread across the World in the last three decades as reported by (Sørensen, 2011). On the other hand, a wind turbine generates power from the wind with the cube of the wind speed, defined by the equation, $P_{av}=0.5\rho A_{rotor}U_D^3$. This equation of formerly expressed relation presents, maximum wind power that is available to be converted into electric power.

Namely, a minor rise in approaching wind speed can induce a large increase in wind power generation. For that reason, developing new technologies can considerably accelerate the approaching wind speed is the desired fact. In this respect, augmenting wind turbines with a diffuser (*DAWT*) was first proposed by Lilley and Rainbird (1956) in the 1956 year. This work was followed by many other studies such as Oman et al. (1975), Igra (1977), Foreman et al. (1978), Gilbert et al. (1978), Igra (1981), Gilbert and Foreman (1983), Phillips et al. (2002), Hansen et al. (2000), Bet and Grassmann (2003), Jafari and Kosasih (2014), and Shonhiwa and Makaka (2016).

According to the Betz limit, the maximum possible ideal conversion of wind power is given by $C_{Pmax} = 0.593$ (Bilgili et al., 2015b). There have been several different designs of conventional wind turbines which cannot generate power beyond exceeding the Betz limit as it was seen in Figure 1.20 (Hau, 2006). İlhan (2014) performed the processing of the real annual power output data of an

installed wind farm where in the case of bare wind turbines, the average monthly power coefficient, C_p of the identical wind turbines in the wind farm were calculated to be lower than the Betz limit, C_{pmax} .

2.1.3.2. Developments of Wind Turbine Capacity and Installations

The capacity of wind turbines increased significantly in the last two decades, and they were classified with different categories by (Tummala et al., 2016), as it was presented in Table 1.14. The leading companies have started to manufacture wind turbines with the capacities of 7.5-8 MW. It is also known that there are as well projects for developing wind turbines for the applications of offshore installations with the huger power capacities of 10-20 MW.

The global concentration of CO_2 increased from 277 ppm in the 1950 year to 398 ppm in the 2014 year which corresponds to a rise of 43.7% (REN21, 2016) due to mostly fossil fuel consumptions. On the other hand, this concentration further enhanced to 414.7 ppm by 2018, demonstrating an increase of 4.2% rise reported based on 2014 (CN, 2019). In this context, the whole World is very anxious about the impact of CO_2 emissions on the environment. One of the alternatives in the reduction of CO_2 generation is the utilization of wind power energy. In this respect, technological development, progress in energy efficiency, and considerable growth of energy generation from renewable energy sources are the three among several factors caused this percentage reduction in the increase of CO_2 emissions (GWEC, 2015b).

The global wind power capacity has been growing rapidly for the last ten years as it was shown in Figure 1.19 (GWEC, 2015b; GWEC, 2016; GWEC, 2017). It seems that wind energy generation is one of the most crucial alternatives of reducing fossil fuel consumption which is the primary source of the global CO_2 emissions (Bilgili et al., 2015a). In the last decade, the cost of initial investment of

wind turbines has been declined considerably due to the progress of manufacturing technologies, and a high rate of demand on wind turbines resulted in this reduction. As well, in connection with these reasons, global wind power cumulative capacity has grown up significantly. In the near future, the rate of wind power installations is going to be substantially increased considering the global situation.

2.1.3.3. Wind Turbines with Diffuser

Shrouding of wind turbines is one of the most important ways of increasing the generated output power and reducing the cost of power generation. That is to say, an important way of enhancing the wind turbine output power under low wind speed can be achieved through concentrating of airflow by a relevant shrouding geometry. This geometry configuration involves the rotor with diverging and converging ducts to convey the air mass flow rate through the wind turbine at a higher rate. Studies demonstrated that better performance under low free-stream wind speed, U_∞ was observed with concentrating shroud utilization compared to a conventional horizontal or vertical axis wind turbine (Shonhiwa and Makaka, 2016).

In the performance of diffuser augmented wind turbines; most effective design parameters are mainly casing full-cone angle, 2θ , casing full body length, L , and casing inlet diameter, D_1 , and casing exit diameter, D_2 . Three different geometric configurations of diffuser casing shrouds as shown in Figure 4.59a were selected by Disterfano et al. (2015), in which they measured the axial velocity distributions along the diffuser casing shrouds under variations of casing full-cone angles, 2θ , and casing full body lengths, L . Besides, as reported in Figure 4.59b, the maximum wind speed ratio, $U_{max}/U_\infty = 1.48$ takes place at a location very close to the diffuser entry for the smallest casing full-cone angle, $2\theta = 10^\circ$, and the longest diffuser length ratio, $L/D_1 = 2.32$, symbolized as diffuser 2 of this figure.

However, [Ohya and Karasudani \(2010\)](#) also obtained maximum wind speed ratio, $U_{max}/U_{\infty} = 1.79$ experimentally, at a location very close to the diffuser entry with diffuser opening angle $2\theta = 8^{\circ}$, and diffuser length ratio, $L/D_1 = 7.7$ as also seen in Figure 4.59a. On the other hand, the influences of either sole nozzle or diffuser casing applications result in opposite effects in terms of wind speed ratio inside and in the vicinity of casing, u/U_{∞} as demonstrated in Figure 2.1 ([Ohya and Karasudani, 2010](#)).

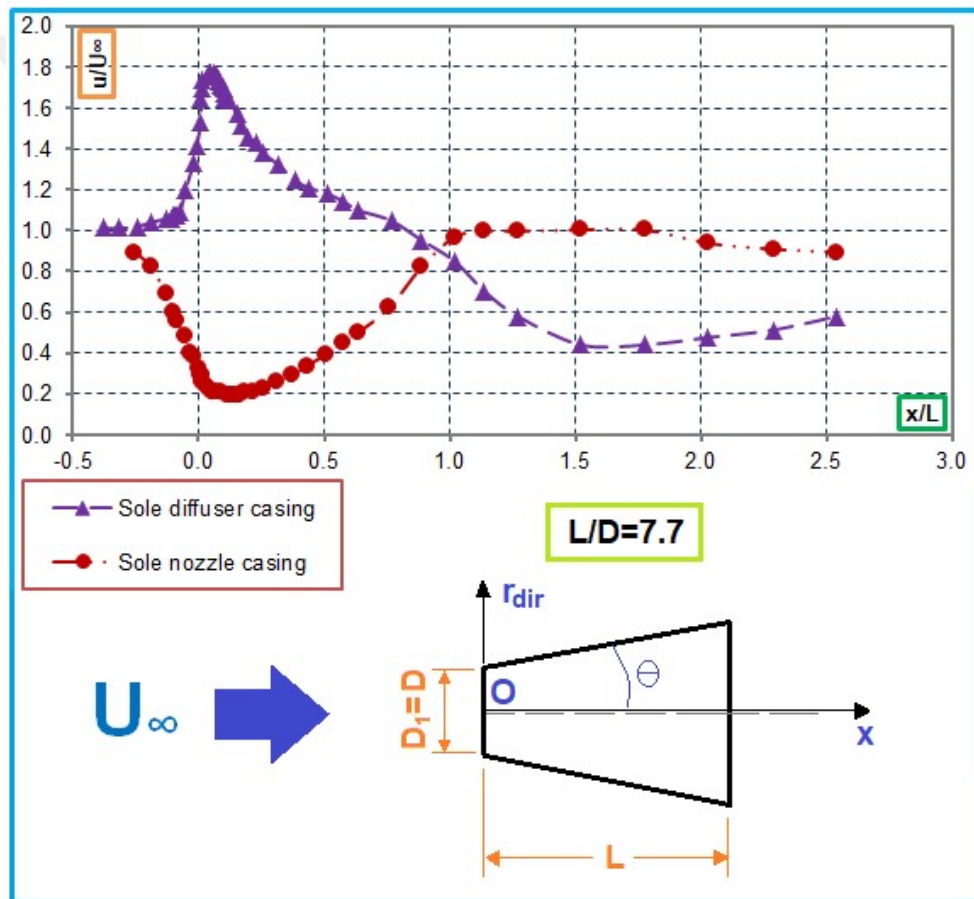


Figure 2.1. Opposite influences of either sole nozzle and diffuser casing applications ([Ohya and Karasudani, 2010](#))

Innovative and original aspects of ongoing research works focus on ensuring the optimization of a casing system around the wind turbine consisting of components including nozzle-diffuser-flange combination or lens is used in order to enhance the performance of small scaled conventional wind turbines having a moderate capacity.

In the case of nozzle-diffuser-flange applied casing system, instead of having a straight diffuser wall, it is better to have a curved wall like a geometric airfoil configuration as it was seen in Figure 1.21. This method also provides an inlet section as well as working in the form of an inlet nozzle to the contracting section. Illustration of the axial velocity profile along the central axis of the airfoil structured diffuser casing without wind turbine given by [Rio Vaz et al. \(2014\)](#) demonstrates that axial velocity is maximum close to the inlet section of the curved wall diffuser. This presents the importance of the curved shrouding on the velocity enhancement.

Conical diffusers as seen in Figure 2.2 have main parameters of dimensionless casing full body length, L/D , and dimensionless flange height, H/D which affect the power coefficient, C_p significantly. For example, having a small value of dimensionless casing axial full body length based on casing exit diameter, L/D_2 causes high full-cone angle of the casing, 2θ resulting in flow separation in the diffuser which can cause considerable reduction in the overall power coefficient, C_p as reported by [Jafari and Kosasih \(2014\)](#). Several diffuser geometry performances in terms of wind speed enhancement as it was presented in Figure 1.22 were examined by [Shives and Crawford \(2011\)](#), numerically. The diffuser exit to inlet area ratio, μ^* or full-cone angles of the casings, 2θ significantly influence the degree of the boundary layer separations from the surface of diffusers to deteriorate the performance of wind turbine which is characterized by a reduction in the diffuser efficiency. In summary, wind turbine rotor blades initially placed in a diffuser, later a flange was combined with the diffuser, presently, a casing system

consisted of a nozzle, diffuser, and a flange component all together are used to further upgrade the wind turbine performance by obtaining an increase of air mass flow rate and wind speed passing through the turbine blades. This topic is handled in the next section including a casing system includes a nozzle, diffuser, and a flange component. Diffuser augmented wind turbine improves the power coefficient, C_p significantly as it will be seen in Figure 4.61. Since the conical diffuser of [Disterfano et al. \(2015\)](#) is very lengthily, thus, it may not be practical to use for the high rate of wind loading due to receiving high wind loading. Considering these reasons; optimized casing full body length, L is to become shorter in commercially manufactured wind turbines.

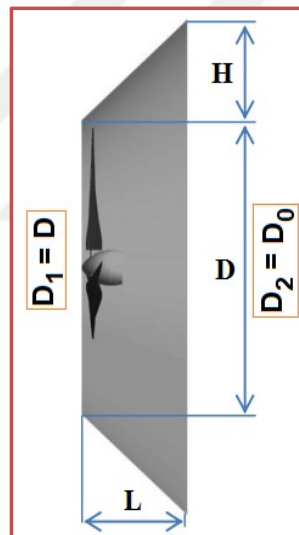


Figure 2.2. Diffuser geometry with straight wall ([Jafari and Kosasih, 2014](#))

2.1.3.4. Wind Turbine with a Nozzle-Diffuser-Flange Components

[Ohya and Karasudani \(2010\)](#) constructed a casing geometric configuration with optimized dimensions of $L/D = 1.47$, and $H/D = 0.5$ as shown in Figure 2.3. Here, abbreviations defined by, L is the full-body length of the casing, and D is the

casing diameter where the wind turbine is located, and H indicates the height of the flange.

As presented in Figure 2.3, [Ohya and Karasudani \(2010\)](#) reported that flange component inclusion to the diffuser component together increases the wind turbine output power around 4-5 times more that of a conventional bare wind turbine. Whereas, the experimental results of [Ohya et al. \(2008\)](#) presented that the power coefficient, C_p of the wind turbine combined with a flanged diffuser component is $C_p = 1.4$, but, the power coefficient, C_p for conventional bare wind turbines is only around $C_p = 0.35$.

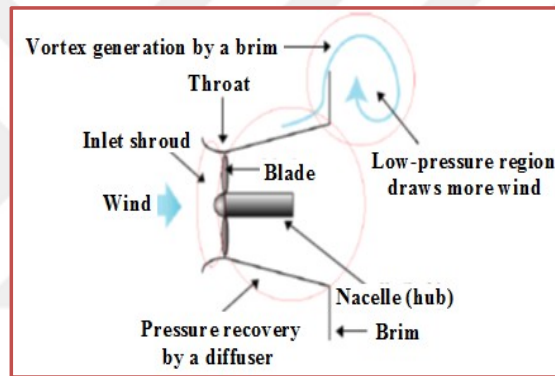


Figure 2.3. Flow around a wind turbine with a brimmed diffuser including nozzle-diffuser-flange components all together ([Ohya and Karasudani, 2010](#))

[Ohya and Karasudani \(2010\)](#) combined a shorter curved casing with a flange attached to the outlet periphery of the casing and also formed a curved nozzle as inlet shrouding attached to the entrance of the casing as well, as seen in Figure 2.4. This flange component also named as “brim” develops vortices and shedding of these vortices causes a low-pressure region downstream of the casing, and curved nozzle at the entrance results in a higher mass flow rate of air running through the wind turbine rotor blades, as desired ([Wang et al., 2015](#)).

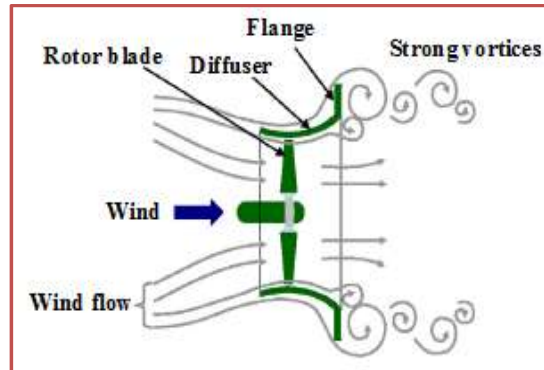


Figure 2.4. Illustration of a curved nozzle-diffuser casing structure including also a brim (Wang et al., 2015)

Because of the high rate of drag force, F_D , the axial length of the nozzle-diffuser-flange type casing was constrained.

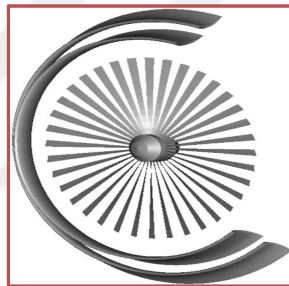


Figure 2.5. Propeller placed inside the shrouding form composed of double airfoil structures (Bet and Grassmann, 2003)

Bet and Grassmann (2003) concluded that one can increase turbine power generation by a factor of 2 times more comparing to the conventional bare wind turbine when an optimum length of casing consisted of a couple of wind profiles as shown in Figure 2.5 that has an area equal to the swept area of the rotor. Similarly, a numerical work was also conducted by Kannan et al. (2013) using two diffusers with straight walls as a casing for the wind turbine.

2.1.3.5. Vertical Axis Wind Turbines

Presently, reviewed shrouded horizontal axis wind turbines are capable of producing electricity generation in lower wind speeds; they attain to their maximum power values with lower wind speeds as well, and also result of generating higher efficiencies. On the other hand, a few samples of vertical axis wind turbines are shown in Figure 2.6a. However, it is worth to mention that the earliest known vertical axis windmills built by Persians in Nashtifan which is in the east of Khorasan of Iran, approximately 2500-3000 years ago to grind grains, and those windmills had a concentrator as shown in Figure 2.6b. The diffuser shaped shroud as it was seen in Figure 1.41, along with a few other changes, are able to significantly improve the power generated by the vertical axis wind turbine which corresponds to a rise of about 2.5 times the power coefficient, C_p of the conventional bare one (Altan et al., 2008).

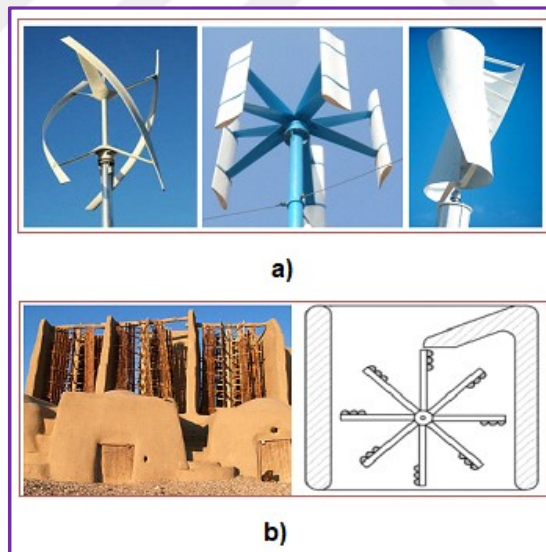


Figure 2.6. a) Samples of vertical axis wind turbines, b) The earliest known vertical axis windmills built by the Persians in Nashtifan located in the east provinces of Khorasan of Iran

In recent years; numerical, analytical, and all other experimental works are also performed by several other researchers to optimize design parameters of the vertical axis wind turbines.

The studies of Altan et al. (2008) introduce a new concentrator arrangement to improve the performance of Savonius type vertical axis wind turbines. The diffuser type concentrator was placed in front of the rotor preventing the negative torque opposite the rotor rotation. The geometrical parameters of guide vanes conveying the air flow into the *VAWT* rotor were optimized to generate an optimum performance of the wind turbine. They found that maximum power coefficient, C_p of the Savonius type vertical axis wind turbine is increased to about 38.5% in the case of a suitable shrouding application.

2.1.4. Numerical CFD Analysis of Wind Turbine Shrouding Systems

Limited studies are found in the literature regarding the low capacity wind turbine shrouding system designs, modeling, optimization, and their efficiencies. The theoretical power available in free-stream wind flow is expressed by the equation, ($P_{av}=0.5\rho A_d V_i^3$) indicating the extracted output power, P_{av} of the wind turbine is directly proportional with the rotor disc cross-sectional area, A_d , and more importantly with the third power of the wind speed, V_i . The international studies cover the ways to improve the speed of the wind touching the wind turbine rotor blades that result in output power, P_{av} to enhance significantly is an expected result. These studies include the rotor casing, namely wind turbine shrouding began in mid of the 1900s with a diffuser utilization surround the wind turbine rotor. Thus, the aim is to boost the air flow rate through the wind turbine rotor blades (Glauert, 1959; Oman and Foreman, 1975; Igra, 1981; Gilbert and Foreman, 1983; Rauh and Seelert, 1984, Nagai and Irabu, 1987; Ushiyama, 1997; Philips et al., 2000; Inoue et al., 2002; Ohya et. al., 2002; Ohya et al., 2004).

Numerical studies, mainly *CFD* constitute part of the literature studies in dealing with the performance analysis of the diffuser shrouded wind turbines. The main idea of the diffuser casing is to exceed Betz limit ($C_{pmax} = 16/27$) which is unfortunately not achievable by conventional bare wind turbines. For example, Franković and Vrsalović (2001) conducted that nozzle shrouded wind turbine at a capacity of 660 kW can generate 3.28 times more energy compared to a traditional unshrouded wind turbine. On the other hand, Abe and Ohya (2004) performed a numerical study with a casing structured wind turbine surrounding the wind turbine rotor blades to improve the power coefficient, C_p of the low capacity wind turbines. Geometrical parameters were optimized in their study including diameter, length, diffuser opening angle, and flange height to show the performance of the numerically tested flanged and shrouded wind turbines. Besides, Abe et al. (2005) performed both experimental and numerical studies for flanged and shrouded low capacity wind turbine located in a diffuser. Matsushima et al. (2006) experimentally described the low capacity wind turbine characteristics placed in a flanged diffuser shroud. In the study of Matsushima et al. (2006), the performance of a bare wind turbine at 62 W of rated power, P_r was compared to the diffuser shrouded wind turbine of same rated power having diffuser full body length, diffuser inlet diameter, half cone angle of the casing, flange height of $L=2$ m, $D_I=1$ m, $\Theta=4^\circ$, and $H=0.1$ m, respectively. Using a rotor diameter of $D_{rotor}=950$ mm, 2.4 times more of maximum energy generation was observed in the study.

A low capacity wind turbine in a flanged diffuser shroud manufactured by Ohya et al. (2008) was tested at rotor diameter, $D_{rotor}=0.7$ m, and rated power, $P_r=500$ W. The field tests indicated this low capacity wind turbine to show wind speed at the rotor disc, U_D to enhance by 1.6-2.4 times more compared to a traditional bare wind turbine. Additionally, the maximum power coefficient, C_p of the shrouded wind turbine was measured to be 1.38. Toshimitsu et al. (2008) used the *PIV* technique to deal with the flanged diffuser shrouded wind turbine

performance. Output wind power ratio was to increase by 2.6 times more was reported in their study. On the other hand, [Jamieson \(2009\)](#) showed the maximum power coefficient to increase by 1.5 times more based on the Betz limit when the diffuser structure was used for the casing of the bare wind turbine. A low capacity wind turbine was studied by [Ohya and Karasudani \(2010\)](#) for 2.5 m rotor diameter, D_{rotor} and 5 kW rated power, P_r tested in a casing which they determined output power, P_{av} to increase by 2.5 times more than that of the conventional wind turbine having the same technical properties. [Van Dorst \(2011\)](#) also designed flanged wind turbine with a casing structure. An experimental analysis was executed by [Kosasih and Tondelli \(2012\)](#) including the flanged wind turbine casing optimized in different geometries. In this study, the wind turbine was placed in a casing to report the enhancement of the power coefficient, C_p of the low capacity wind turbine that reached the value of 63%. On the other hand, an interesting study of a shrouded horizontal axis low capacity wind turbine for moving vehicle applications was developed by [Chen et al. \(2012\)](#). [Takahashi et al. \(2012\)](#) considered the wind turbine blade tip vortices in a casing study using the *CFD* model. [Chen et al. \(2013\)](#) dealt with the experimental study of low capacity flanged wind turbine aerodynamic characteristics in a casing structure. Cased rotor performances for a variety of blade numbers including $n=6$, $n=8$, and $n=12$ were tested in their study. The highest performance was reported from the $n=12$ bladed rotor in the conducted study. Also, the power coefficient, C_p of the $n=8$ bladed rotor was conducted to be $C_p=68\%$.

Numerical flow analysis of the inlet shrouded flanged diffuser casing used for the low capacity wind turbine was executed by [Adeel et al. \(2013\)](#). The inlet shrouded flanged diffuser casing properties in their study were $L_y=500$ mm length, $D=400$ mm diameter, and $\Theta=12^\circ$ of half cone angle of the casing. The influence of the flange height, H on the wind speed passing through the rotor was reported in their study. On the other hand, the optimization of 13 different casing types for

wind turbine shrouding was conducted by Coşoiu et al. (2013) to have the correct dimensions for low capacity wind turbines. Kale et al. (2013) reported the comparison of 3 different inlet shrouded flanged curved type of diffuser models with a numerical study also performed for low capacity wind turbines. The models they numerically tested included non-flanged, vertical-flanged, and as well as inclined-flanged diffuser casing models. The best they reported was determined to be the shrouded low capacity wind turbine with the inclined-flanged diffuser model. Besides, Kishore et al. (2013) executed the design of a low capacity wind turbine at a rated power of $P_r=0.83$ W positioned in a flanged diffuser casing with inlet shrouded component. Wind speeds, 2.7 m/s and 5 m/s were reported for this turbine as cut-in speed and nominal wind speed to extract power, respectively. Their study was validated both by experimental and numerical ways. Also, the power range enhancement in between 1.4-1.6 times more compared to the traditional wind turbine was obtained by the shrouding application. Mansour and Meskinkhoda (2014) evaluated the flow characteristics of a flanged diffuser casing for small type of wind turbines by using numerical *CFD* method. They as well inspected the influence of inlet shrouding component on wind speed enhancement and corresponding pressure drop. Additionally, they reported that the flanged diffuser casing increased the free-stream wind speed by 1.6-2.1 times enhanced. Blade Element Momentum (*BEM*) method was studied by Rio Vaz. et al. (2014) theoretically for flanged and diffuser cased wind turbines designed as low capacity. Experimental and numerical analyses were performed by Jafari and Kosasih (2014) considering the low capacity flanged and diffuser cased wind turbine at 1300 mm rotor diameter, D_{rotor} , and 300 W of power rating, P_r . Wind tunnel experiment was used by Wang et al. (2015) for the low capacity flanged and diffuser applied wind turbine having an inlet shroud component in the casing as well, in order to test the performance experimentally for the wind turbine of 3 kW rated power, P_r . Bukala et al. (2015) dealt on the estimation of power generation costs of modern small

type wind turbines. On the other hand, [Hu and Wang \(2015\)](#) proposed a smart solution of a self-adapting flange to reduce the wind resistance on the flanged diffuser structure. This type of flange was constructed to a curved type of casing structure having an inlet shrouding component as well. In these regards, a numerical study was conducted that reported wind resistance can be reduced to 35% of the original value, in a corresponding study of 60 m/s value of wind speed.

Other researches ([Lawn, 2003](#); [Van Bussel, 2007](#); [Scherrillo et al., 2011](#); [Nasution and Purwanto, 2011](#); [Amer et al., 2013](#); [Balaji and Gnanambal, 2014](#); [Bukala et al., 2015](#); [Disterfano et al., 2015](#); [Al-Sulaiman and Yilbas, 2015](#); [Bet and Grassmann, 2003](#); [Fletcher et al., 2007](#); [Grassmann et al., 2003](#); [Hjort and Larsen, 2014](#); [Kannan et al., 2013](#); [Kosasih et al., 2012](#); [Krishnan and Paraschivoiu, 2015](#); [Mahalakshmi et al., 2007](#); [Gow et al., 2014](#); [Nikolic et al., 2015](#); [Ohya et al., 2006](#); [Phillips et al., 1999](#); [Setoguchi et al., 2004](#); [Pinheiro Vaz et al., 2011](#); [Wang et al., 2008](#); [Watson et al., 2007](#)) also surveyed the wind turbine performance in shrouding and flanged conditions, both numerically and experimentally considering a variety of optimized casing profiles.

The casing and its all components such as a diffuser, inlet shroud, and flange design, i.e., shortly casing shroud design as a whole is essential for the development of low capacity wind turbine performance. On the other hand, still, some lacks in the literature are valid for the development and improvement of optimization and design situations of the low capacity wind turbines and their shrouding systems. In these regards, the design and modeling studies related to flanged and shrouded horizontal axis wind turbines to be used in residential purposes and as to give service for small businesses are reasonably low. Thus, this subject should be rapidly considered for the commerciality and the industry to involve the collaboration study of academicians and industrialists together to obtain optimum designed low capacity wind turbines and their shrouding structures.

2.1.5. Experimental PIV Analysis of Wind Turbine Shrouding Systems

Experimental *PIV* analysis studies for wind turbine shrouding systems mainly available in the literature include literature studies of (Ohya and Karasudani, 2010; Abe et al., 2005; Ohya et al., 2008; Chen et al., 2012; Kosasih et al., 2012; Kosasih and Tondelli, 2012; Chen et al., 2013; Wang et al., 2008; Hayashi et al., 2005; Rio Vaz et al., 2014; Chang et al., 2014a; Setoguchi et al., 2004; Fletcher et al., 2007; Coşoiu et al., 2013; Abe and Ohya, 2004; Mansour and Meskinkhoda, 2014; Ohya et al., 2006; Scherillo et al., 2011; Coiro et al., 2009). The *PIV* system is a very effective measurement method for separated and non-steady flows, since it can generally measure instantaneous velocity values within a given area at many points at the same time. Measurement of instantaneous velocity values and analysis of measured velocity values and turbulence statistics provide information about the physics of flow.

2.2. Outline, Objective, and Scope of the Dissertation

The literature in terms of scientific studies or dissertations is lacked dealing with energy and specifically wind energy as a whole including energy cases of World, Europe, and Turkey, also including wind energy applications such as horizontal axis wind turbine output power curve and aerodynamics, efficiency analysis, statistical analysis, *ANN* tool, *ANFIS* tool, shrouding of wind turbines for energy generation enhancement, and *CFD* analysis of shrouded horizontal axis wind turbines. Most importantly, this dissertation is unique in terms of dealing with shrouding horizontal axis of wind turbines in terms of conducting particle image velocimetry analysis (*PIV*).

Introduction part introduces the significance of energy briefly, and mainly focuses on renewable energy generation methods. Also, it includes World, Europe,

and Turkey energy situations; however more specifically wind energy status is handled.

Literature survey section summarizes the available studies found in the literature relating horizontal axis wind turbine aerodynamics, efficiency analysis of operating wind farms, wind power output curve and aerodynamic characteristic estimations utilizing statistical analysis, artificial neural network methods (*ANN*), adaptive neuro-fuzzy inference system methods (*ANFIS*), shrouding concept of horizontal and vertical axis wind turbines, and *CFD* and *PIV* analyses regarding performances, optimizations and flow characteristics of wind turbine shrouding systems.

Material and method part describes the general equations utilized in methods of statistical analysis, wind power and efficiency analysis, the aerodynamics of horizontal axis bare wind turbines, artificial neural networks (*ANN*) tool, adaptive neuro-fuzzy inference system (*ANFIS*) tool, the aerodynamics of horizontal axis shrouded wind turbines. On the other hand, this section also handles used equations in computational fluid dynamics (*CFD*) numerical analysis, and as well as required information on *PIV* image processing used in this dissertation is also taken into account. Also, the suitable casing configuration designed as the setup for *PIV* testing is described depending on the geometrical properties and experimental visualized images are also shown in this section.

Finally, results and discussions part of the dissertation is divided into eleven sub-parts.

- i. Section 4.1 involved statistical analysis forecasting of the wind energy density of a region located in Çanakkale province of Turkey. In this study, superior wind velocity direction parameters, average wind velocity, probability distribution, wind power potential of the considered zone, and Weibull and Rayleigh parameters were processed. These data were analyzed using

annual, seasonal, and monthly point of views. The study brought innovation to the literature by demonstrating that the province handled, has the acceptable wind energy potential to be reasonable for the planting of new wind turbines.

- ii. Section 4.2 conducted wind power and efficiency analysis of an operating wind farm located in the south province of Turkey in terms of examining processes of wind speed, wind direction, air temperature, and electricity generation data of the wind turbines in a chosen year. Aerodynamic characteristics of chosen wind turbines of the wind farm were also demonstrated in the study. The study brought innovation to the literature by demonstrating the parameters affecting turbine efficiency and as well as variations of energy generations between wind turbines in the same wind farm were explained.
- iii. Third sub-section of results and discussions part considered horizontal axis wind turbine aerodynamics mainly found in the literature as mechanical output power of wind turbines, P , power coefficient, C_p , axial flow induction factor, a , thrust coefficient, C_T , and thrust force, T . Study presented in Section 4.3 was conducted based on the data of an installed wind farm in Belen province of Hatay referred to be the Belen Wind Power Plant. The study taking the data of 5 wind turbines in the wind farm, brought innovation to the literature by indicating that 3 MW rated power of the identical wind turbines was achieved at the hub-height wind speed, U_D value of $U_D=15$ m/s. Besides, in terms of bare wind turbines, maximum power coefficient, C_p of the wind turbines was shown unfortunately to be in the range of only 30%-35%.

- iv. Section 4.4 dealt with the aerodynamic characteristics of horizontal axis wind turbines using the data measured in an existing onshore wind farm. Blade Element Momentum (*BEM*) was used in the calculation of aerodynamic parameters including axial flow induction factor, a , power coefficient, C_p , thrust force coefficient, C_T , thrust force, T , and tangential flow induction factor, a' . This part of the dissertation brought innovation to the literature by configuring wind turbines in the chosen wind farm generally rotate at the optimum rotational speed value of $\Omega=16.1$ rpm, and the maximum power coefficient value among the chosen wind turbines reached $C_p=30\%$ at the optimum blade tip speed ratio, λ_R of $\lambda_R=7.12$ was as well achieved.
- v. Fifth sub-section of results and discussions part demonstrated that utilizing of an artificial neural network (*ANN*) structure has the advantage of forecasting aerodynamic characteristics of wind turbines, as long as having the required hub-height wind speed, U_D , and atmospheric air temperature, T_{atm} . Additionally, no detailed other knowledge of wind turbine operations and control schemes required during the predictions of wind turbine aerodynamic characteristics is the innovation part of this section of the thesis for the literature. In this context, two models were used in the study including the predictions of the parameters utilizing the model of single hub-height wind speed, U_D ; and the model including hub-height wind speed, U_D and atmospheric air temperature, T_{atm} together. It was demonstrated in the study that inputs including both hub-height wind speed, U_D and atmospheric air temperature, T_{atm} together, resulted in better forecasting.
- vi. Section 4.6 involved *ANN* structure for the prediction of horizontal axis wind turbine output power, P using climatic data and wind

turbine rotor rotational speed, Ω . The method was constructed utilizing hub-height wind speed (U_D), atmospheric air temperature (T_{atm}), and the turbine rotor rotational speed (Ω) of wind turbines selected of an operating wind farm. The method indicated to be so convenient in the decision stage of new wind power plant installations - is the innovation part of this section of the thesis for the literature. Additionally, the *ANN* forecasting tool functioned the best during the optimum rotation of $\Omega=16.14$ rpm.

- vii. Similar to Section 4.6 of the dissertation, the results of Section 4.7 also indicated to be so convenient in the decision stage of new wind power plant installations is the innovation part of this section of the thesis for the literature. However, the method was changed in this section, shifting to *ANFIS* tool rather than the *ANN* structure. Again similar to Section 4.6, *ANFIS* construction was based on hub-height wind speed (U_D), atmospheric air temperature (T_{atm}), and the turbine rotor rotational speed (Ω) of wind turbines selected of an operating wind farm in the prediction of horizontal axis wind turbine output power, P . Similarly, *ANFIS* forecasting tool also functioned the best during the optimum rotation of $\Omega=16.1$ rpm.
- viii. Wind turbine aerodynamic characteristics were analyzed in Section 4.8, using currently operating selected types of wind turbines. Aerodynamic parameters were analyzed initially depending on the influence of rotor diameter, D_{rotor} keeping the rated power, P_r of the wind turbines constant, secondly, the influence of wind turbine rated power, P_r on them was analyzed when the rotor diameter, D_{rotor} was kept constant, thirdly, both rotor diameter, D_{rotor} and rated power, P_r of wind turbines are altered in order to analyze

influences of both on the formerly expressed four aerodynamic parameters, and finally, the influence of the air density, ρ for the chosen wind turbines on the cited aerodynamic parameters was analyzed. In this section, it is reported that the best parameter influencing the improvement of power coefficient, C_p is the rotor swept area, A_d decrease. Additionally, this part of the dissertation brought an innovation to the literature by yielding that increases of both turbine rated power, P_r and the rotor swept area, A_d do not continuously provide the increase of the power coefficient, C_p .

- ix. Section 4.9 covered the studies of wind turbine shrouding systems that are found in the literature. So, the comparison of power coefficient results conducted by theoretical and field data studies was executed in this part of the dissertation. General momentum theory of [Burton et al. \(2011\)](#), theoretical study of [Sørensen, \(2011\)](#) based on number of blades, n , and field data study of [Ilhan et al. \(2018\)](#) were compared in terms of power coefficient, C_p results of each study. On the other hand, this section also involved wind speed enhancement comparison in wind turbine casings influenced by diffuser geometry. So, three geometrical configurations designed by [Disterfano et al. \(2015\)](#) and one geometrical configuration designed by [Ohya and Karasudani \(2010\)](#) were compared with each other, in terms of wind speed ratio, u/U_∞ performances. Additionally, a comparison of airfoil structured casing system with respect to the conventional linear diffuser casing bodies is conducted considering three diffuser configurations of [Disterfano et al. \(2015\)](#) and a designed airfoil structured casing system (*AFSCS*) structure of [Hansen et al. \(2000\)](#). It was demonstrated that the results indicated the designed

airfoil structured shrouding gave outcomes exceeding power coefficient, C_p over 0.9 when compared to the designed configurations of [Disterfano et al. \(2015\)](#). Finally, in this section, again the performances of conventional linear diffuser casing body of [Ohya et al. \(2008\)](#) are compared according to the airfoil shrouded wind turbine of [Grassmann et al. \(2003\)](#). In this comparison, it was demonstrated that 6% enhanced value in the case of airfoil type shrouding ([Grassmann et al., 2003](#)) out coming power coefficient as $C_p=1.46$ in terms of maximum values of the power coefficients, C_p . These cited comparisons of power coefficient, C_p and wind speed ratio, u/U_∞ performances are the innovation parts of this section of the thesis for the literature.

- x. Section 4.10 brought innovation to the literature by executing the aerodynamic parameter comparisons of the experimental, *CFD*, and theoretical studies found in the literature. The conducted aerodynamic comparisons included power coefficient, C_p , wind speed ratio, u/U_∞ , pressure coefficient, C_{pr} , power coefficient, C_p , and torque coefficient, C_Q , and thrust coefficient, C_T parameters, expressed with respect to the tip speed ratio, λ_R , dimensionless axial coordinate system, x/D , dimensionless axial coordinate system, x/D , thrust coefficient, C_T , and tip speed ratio, λ_R , respectively, considering a variety of literature studies.
- xi. Section 4.11 brought innovation to the literature through conducting experimental *PIV* analysis of wind turbine shrouding systems. In the experimental *PIV* analysis; the study of a curved type of wind turbine shrouding structure was executed in terms of the flow visualization at downstream of the flange region; as well as water velocity, streamline, and vorticity analyses of the

designed curved shrouding body were also conducted. Besides, numerical *CFD* analysis of designed linear wind turbine shrouding structures was also executed in this sub-section of results and discussions part.

Finally, overall conclusions and recommendations section briefly summarizes the main findings formerly presented in results and discussions part, and as future studies; this section also provides suggestions for further and new investigations to be performed in future works.



3. MATERIALS AND METHODS

3.1. Statistical Analysis for the Determination of Wind Energy Density

The Weibull distribution function is considered in wind power applications to conform well with wind data (Eskin et al., 2008; Gokcek et al., 2007; Incecik and Erdogmus, 1995). A two-parameter distribution is defined as functionally indicated in Eq. (3.1) below;

$$f_w(v) = \left(\frac{k}{c}\right) \left(\frac{v}{c}\right)^{k-1} \exp\left[-\left(\frac{v}{c}\right)^k\right] \quad (3.1)$$

Considering all parameters of Eq (3.1); k , $f_w(v)$, and c are described as the dimensionless Weibull shape parameter, the probability of observing wind velocity v , and finally the Weibull scale parameter, respectively.

On the other hand, the cumulative probability function of the Weibull distribution is calculated as presented below:

$$F_w(v) = 1 - \exp\left[-\left(\frac{v}{c}\right)^k\right] \quad (3.2)$$

There are several methods of determining Weibull k and c parameters which are also used in Eqs. (3.1) and (3.2), such as utilizing the least-square fit to observe distribution method, mean wind speed-standard deviation method, the maximum likelihood method (Celik, 2004; Genc et al., 2005; Seguro and Lambert, 2000; Bilgili et al., 2016; Bilgili and Yasar, 2017; Akpinar and Akpinar, 2004a; Akpinar and Akpinar, 2004b; Akpinar and Akpinar; 2006). The dissertation includes the two parameters shown in Eqs. (3.1) and (3.2), i.e., k and c parameters,

are obtained using the mean wind speed-standard deviation method. According to this cited method, Weibull k and c parameters are expressed with Eqs. (3.3) and (3.4), respectively.

$$k = \left(\frac{\sigma}{v_m}\right)^{-1.086} \quad (1 \leq k \leq 10) \quad (3.3)$$

$$c = \frac{v_m}{\Gamma(1+1/k)} \quad (3.4)$$

Where v_m denoted in both above equations shows the mean wind speed, and it is calculated using Eq. (3.5). On the other hand, σ term indicated in Eq. (3.3) is the standard deviation and it is calculated using Eq. (3.6). And finally, $\Gamma()$ demonstrated in Eq. (3.4) is the Gamma function. For any y value, it is usually functionally written as demonstrated in Eq. (3.7).

$$v_m = \frac{1}{n} [\sum_{i=1}^n v_i] \quad (3.5)$$

$$\sigma = \left[\frac{1}{n-1} \sum_{i=1}^n (v_i - v_m)^2 \right]^{1/2} \quad (3.6)$$

$$\Gamma(y) = \int_0^{\infty} \exp(-x) x^{y-1} dx \quad (3.7)$$

Where n is the number of hours in the period of the considered time such as month, season, or year.

On the other hand, a simplified form of the Weibull function provides the Rayleigh function. It is necessary to consider the scale factor, c of the Weibull function equivalent to 2 for the conversion of the Weibull function to the Rayleigh

function. In this context, the Rayleigh probability density function is presented in Eq. (3.8) by (Gokcek et al., 2007),

$$f_R(v) = \frac{\pi v}{2v_m^2} \exp\left[-\left(\frac{\pi}{4}\right)\left(\frac{v}{v_m}\right)^2\right] \quad (3.8)$$

3.2. Calculation of Wind Power and Efficiency

The equation demonstrating the relation between wind speed and generated available output power is given in Eq. 3.9. Change of wind power potential, i.e., power per unit area expressed with respect to the wind speed is depicted in Figure 3.1 (Tanrioven, 2011).

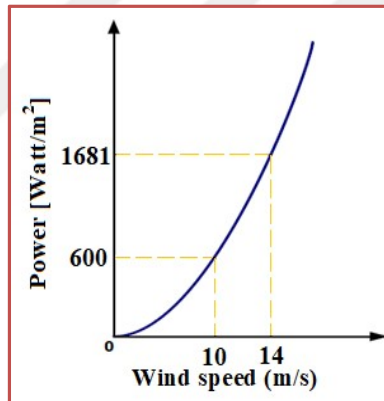


Figure 3.1. Relation of wind power potential with respect to the wind speed (Tanrioven, 2011)

Maximum wind power that is available to be converted into electric power is expressed by the following equation (Burton et al., 2011);

$$P_{av} = \frac{1}{2} \rho A_d V_i^3 \quad (3.9)$$

On the other hand, theoretical available power determined by Eq. (3.9) is multiplied by Betz-Limit in order to obtain maximum accessible turbine power (Burton et al., 2011);

$$P_{TH} = \frac{1}{2} \rho A_d V_i^3 \times 0.59 \quad (3.10)$$

3.3. Aerodynamics of Horizontal Axis Bare Wind Turbines

A schematic representation of an energy extracting actuator disc and stream-tube is illustrated in Figure 3.2. As shown in this figure, wind turbine power production depends on the interaction between the turbine rotor and the wind. Practical horizontal axis wind turbine designs need airfoils to transform the kinetic energy of the wind into useful energy. The wind turbine is represented by a uniform ‘*actuator disc*’ which creates a discontinuity of pressure in the stream tube of air flowing through it. Note that this analysis is not limited to any particular type of wind turbine. On the other hand, this analysis uses the following assumptions:

- continuous, homogenous, incompressible, and steady-state fluid flow;
- no frictional drag or resistance;
- turbine rotor having an infinite number of blades;
- uniform thrust over the disc or rotor area;
- a non-rotating wake;
- static pressure given at far upstream and far downstream of the rotor is equal to the undisturbed ambient static pressure.

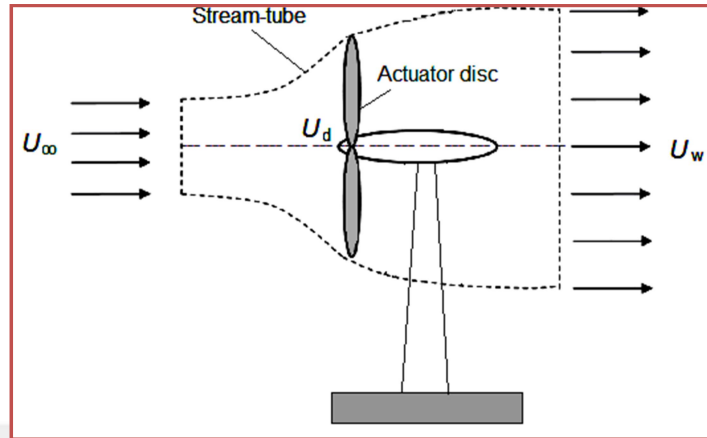


Figure 3.2. Actuator disc and stream-tube representation for a wind turbine

As seen from Figure 3.2, the disc upstream of the stream-tube has a cross-sectional area smaller than that of the disc, and a larger area at the disc far downstream is presented. During a steady-flow process of wind flow, the total rate of air mass entering a control volume is equal to the total rate of mass leaving the control volume. In this context, the conservation of mass principle can be expressed as defined by (Burton et al., 2011); utilizing the blade element momentum theory.

3.3.1. Blade Element Momentum Theory

Aerodynamical characteristics of horizontal axis wind turbines are determined using the basic momentum theory. Figure 3.3 gives the schematic representation definition of the rotor disc thrust force, F_{rotor} , and local definitions of the area, pressure, and wind speed defined on the stream tube. The rotor and wind interaction directly influence the generated power obtained from the wind turbine as shown in this figure (Burton et al., 2011).

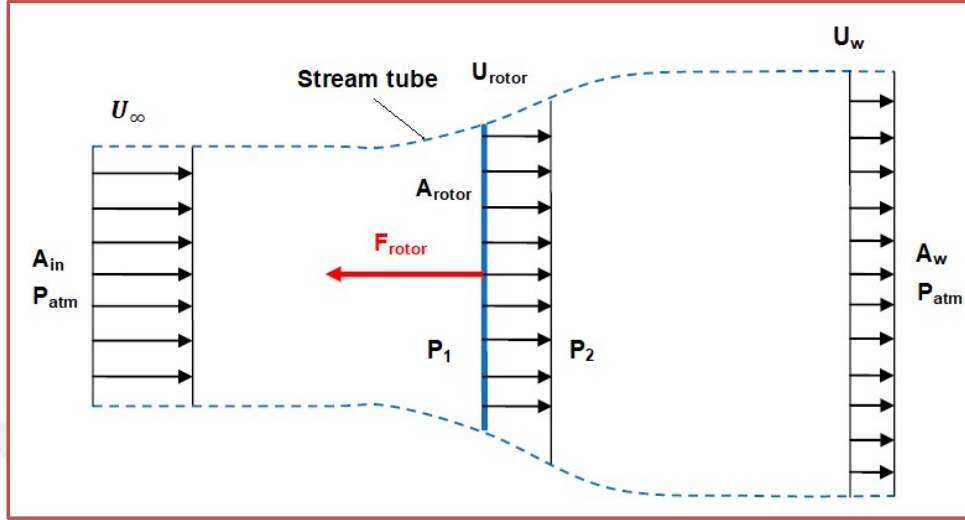


Figure 3.3. Energy interaction of the rotor disc that is rotating inside the stream tube (Burton et al., 2011)

Conservation of the mass principle regarding continuous flow system of the actuator disc model should satisfy the following relations,

$$\dot{m}_{in} = \dot{m}_{out} \quad (3.11)$$

$$\rho A_{in} U_{\infty} = \rho A_{rotor} U_{rotor} = \rho A_w U_w \quad (3.12)$$

Besides, conservation of the momentum theory is used inside and along the stream tube to obtain Eqs. (3.13), (3.14), and (3.15),

$$\Delta M = T \quad (3.13)$$

$$\Delta M = \rho A_{in} U_{\infty}^2 - \rho A_w U_w^2 \quad (3.14)$$

$$T = \rho A_{rotor} U_{rotor} (U_{\infty} - U_w) \quad (3.15)$$

On the other hand, the Bernoulli Equation is executed on the immediate upstream and downstream locations of the rotary disc under the assumption of equal wind speeds at these cited regions,

$$P_{atm} + \frac{1}{2}\rho U_{\infty}^2 = P_1 + \frac{1}{2}\rho U_{rotor}^2 \quad (3.16)$$

$$P_{atm} + \frac{1}{2}\rho U_w^2 = P_2 + \frac{1}{2}\rho U_{rotor}^2 \quad (3.17)$$

Pressure drop along the rotor disc is expressed by Eq. (3.18), which is derived using Eqs. (3.16) and (3.17) together;

$$(P_1 - P_2) = \frac{1}{2}\rho(U_{\infty}^2 - U_w^2) \quad (3.18)$$

Pressure drop shown in Eq. (3.18), i.e., the left side of Eq. (3.18) is the primary driving influence causing a thrust force, T on the rotor blade plane as shown in Figure 3.3. Thus, Eq. (3.19) is structured using Eq. (3.18) as follows;

$$T = (P_1 - P_2)A_{rotor} = \frac{1}{2}\rho A_{rotor}(U_{\infty}^2 - U_w^2) \quad (3.19)$$

On the other hand, thrust force, T parameter involving equations such as Eqs. (3.15) and (3.19) are considered together to structure Eqs. (3.20) and (3.21) as follows,

$$U_{rotor}(U_{\infty} - U_w) = \frac{1}{2}(U_{\infty}^2 - U_w^2) \quad (3.20)$$

$$U_{rotor} = \frac{1}{2}(U_{\infty} + U_w) \quad (3.21)$$

Rotor disc wind speed, U_{rotor} and free-stream wind speed, U_{∞} are related with each other on the axial flow induction factor, a parameter defined by Eq. (3.22),

$$a = 1 - \frac{U_{rotor}}{U_{\infty}} \quad (3.22)$$

Rotor disc or also referred as hub-height wind speed, U_{rotor} , and wind speed at far wake, U_w are defined depending on axial flow induction factor, a and free-stream wind speed, U_{∞} parameters expressed in Eqs. (3.23) and (3.24), respectively,

$$U_{rotor} = U_D = U_{\infty}(1 - a) \quad (3.23)$$

$$U_w = U_{\infty}(1 - 2a) \quad (3.24)$$

Wind speeds presented in Eqs. (3.23) and (3.24) are related to each other with a dimensionless number, λ as shown in Eq. (3.25),

$$\lambda = \frac{U_w}{U_{\infty}} \quad (3.25)$$

Thrust force, T and generated mechanical output power, P of the wind turbine are calculated using Eqs. (3.26) and (3.27), respectively,

$$T = 2\rho A_{rotor} U_{\infty}^2 a(1 - a) \quad (3.26)$$

$$P = 2\rho A_{rotor} U_{\infty}^3 a(1 - a)^2 \quad (3.27)$$

The power coefficient of a wind turbine, C_p is defined generally with Eqs. (3.28) and (3.29), expressed as well in a simplified expression depending only to axial flow induction factor, a parameter,

$$C_p = \frac{P}{\frac{1}{2}\rho U_\infty^3 A_{rotor}} \quad (3.28)$$

$$C_p = 4a(1 - a)^2 \quad (3.29)$$

The maximum value of the wind turbine power coefficient is determined by utilizing Eq. (3.30),

$$\frac{dC_p}{da} = 4(1 - a)(1 - 3a) = 0 \quad (3.30)$$

The axial flow induction factor, a is found as $a=1/3$ from Eq. (3.30) which yields the maximum value of power coefficient, C_{pmax} also referred to be the Betz limit, as calculated from Eq. (3.29) and expressed finally in Eq. (3.31),

$$C_{pmax} = 16/27 = 0.593 \quad (3.31)$$

In this context, the maximum value of the power coefficient, C_{pmax} shown in Eq. (3.31) above is the maximum achievable efficiency of a wind turbine. In conventional bare wind turbines, this is the upper limit of the power generation.

Eq. (3.28) presented the solution of power coefficient, C_p in the case of approaching free-stream wind speed, U_∞ is initially known. On the other hand, rotor disc wind speed, U_D to be given initially rather than wind speed at upstream (*free-stream wind speed*), U_∞ ; in this case, Eqs. (3.32) and (3.33) are used together to determine X coefficient initially and then finally axial flow induction factor, a .

$$a = \frac{X}{X+4} \quad (3.32)$$

Where, X parameter shown in Eq. (3.32) is determined by Eq. (3.33),

$$X = \frac{P}{0.98 \times 0.97 \times \frac{1}{2} \rho A_{rotor} U_D^3} \quad (3.33)$$

On the other hand, thrust force, T influencing the rotor disc is also defined according to the thrust coefficient, C_T , and expressed in Eq. (3.34);

$$C_T = \frac{T}{\frac{1}{2} \rho U_\infty^2 A_{rotor}} \quad (3.34)$$

Similarly, the thrust coefficient, C_T should also be calculated depending as a function of only axial flow induction factor, a parameter as expressed in Eq. (3.35);

$$C_T = 4a(1 - a) \quad (3.35)$$

3.3.2. Blade Element Angular Momentum Theory

Figure 3.4 presents the variation of turbine rotor angular speed, Ω on the rotary disc. The torque, Q originating on the rotor disc is equal to the ratio of the exchange of angular momentum caused by the air flow through the rotor disc.

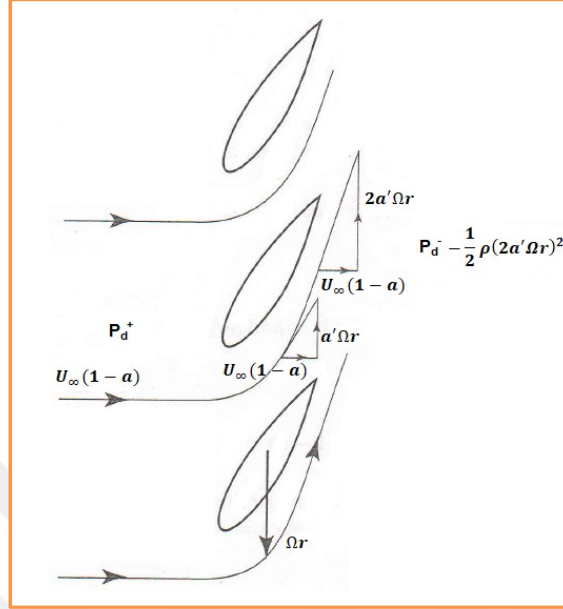


Figure 3.4. Variation of turbine rotor angular speed, Ω on the rotary disc

$$\delta Q = \rho \delta A_d U_\infty (1 - a) 2\Omega a' r^2 \quad (3.36)$$

Angular flow induction factor, a' given in Eq. (3.36) relates the torque output, Q defined with respect to the function of turbine rotor angular speed, Ω and as well axial flow induction factor, a . On the other hand, rotor shaft power, P originated on the wind turbine rotor disc is calculated according to the utilization of Eqs. (3.37) and (3.38).

$$\delta P = \delta Q \Omega \quad (3.37)$$

$$\delta P = \rho \delta A_d U_\infty (1 - a) 2\Omega^2 a' r^2 \quad (3.38)$$

Parameters of axial flow induction factor, a and angular flow induction factor, a' are related with each other on turbine rotor angular speed, Ω , radial radius of the rotor, r , and free-stream wind speed, U_∞ , when Eqs. (3.27) and (3.38)

are considered together to give Eq. (3.39). In this way, axial and angular flow induction factors are simply related by blade speed ratio, λ_r defined with respect to the radial radius of the rotor, r as shown in Eq. (3.40).

$$U_\infty^2 a(1-a) = \Omega^2 a' r^2 \quad (3.39)$$

On the other hand, the edge of the rotary disc results the radial radius of the rotor, r to be set equivalent to full radius of the rotor, R . Thus, the blade speed ratio, λ_r and blade edge speed ratio, λ_R ; and efficiency of blade element depending on radial radius, r and full radius, R , respectively are all calculated by the following equations;

$$\lambda_r = \frac{r\Omega}{U_\infty} \quad (3.40)$$

$$\lambda_R = \frac{R\Omega}{U_\infty} \quad (3.41)$$

$$\eta_r = 4a'(1-a)\lambda_r^2 \quad (3.42)$$

$$\eta_R = 4a'(1-a)\lambda_R^2 \quad (3.43)$$

3.3.3. Output Power Estimations of Bare Wind Turbines

3.3.3.1. Utilization of Artificial Neural Networks

Artificial neural networks are computational networks which attempt to simulate, in a gross manner, the networks of nerve cell of the biological central nervous system. The neural network is, in fact, a novel computer architecture and a

novel algorithmization architecture relative to the conventional computers. It allows using very simple computational operations to solve especially complex, mathematically ill-defined problems, and nonlinear problems or stochastic problems (Bilgili, 2010; Bilgili and Ozgoren, 2011).

The main contribution of *ANNs* structuring is that it allows for very low level programming to allow solving complex problems, especially those that are non-analytical and/or nonlinear and/or nonstationary and/or stochastic, and to do so in a self-organizing manner that applies to a wide range of problems with no re-programming or other interference in the program itself (Cobaner et al., 2014; Ay and Kisi, 2014).

In the literature; there are many types of *ANN* structuring such as utilizing Feed Forward Neural Networks (*FFNN*), Radial Basis Neural Networks (*RBNN*), and Generalized Regression Neural Networks (*GRNN*). On the other hand, the learning of *ANNs* is generally accomplished by a back-propagation algorithm. The back-propagation (*BP*) is the most commonly used supervised training algorithm in multilayered *FFNNs*. In back-propagation networks, information is processed in the forward direction from the input layer to the hidden layer and then to the output layer. The objective of a back-propagation network is to find the optimal weights which will generate an output vector as close as possible to the target values of the output vector with a selected accuracy by minimizing a predetermined error function (Bilgili, 2010; Bilgili and Ozgoren, 2011; Cobaner et al., 2014; Ay and Kisi, 2014).

The fundamental processing element of a neural network is a neuron. The *BP* algorithm starts, of necessity with computing the output layer, which is the only one where desired outputs are available, but the outputs of the intermediate layers are unavailable (Figure 3.5), presented as follows (Graupe, 2007):

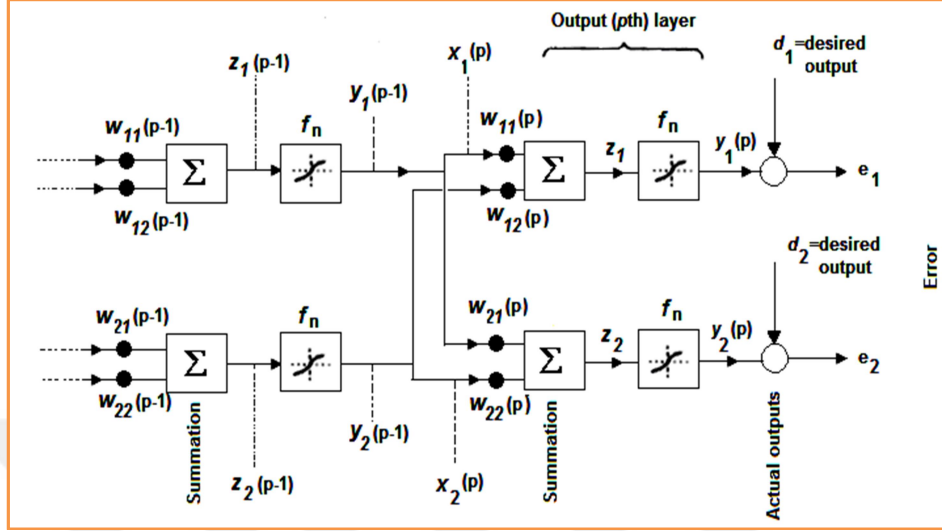


Figure 3.5. A multi-layer perceptron

Error-energy at the output layer is shown by the ε designation in order to define,

$$\varepsilon = \frac{1}{2} \sum_k (d_k - y_k)^2 = \frac{1}{2} \sum_k e_k^2 \quad (3.44)$$

The term “k” of the summation formula includes the subsequent numbers starting from number 1 to number N, where N is the total number of neurons in the output layer. Consequently, the gradient on the ε is considered, where:

$$\nabla \varepsilon_k = \frac{\partial \varepsilon}{\partial w_{kj}} \quad (3.45)$$

Here, with the consideration of the steepest gradient procedure, we have,

$$w_{kj}(m+1) = w_{kj}(m) + \Delta w_{kj}(m) \quad (3.46)$$

The j^{th} input to the output layer of the neuron involving in the series with the order of k^{th} , where, with the steepest descent procedure again, Δw_{kj} is defined as presented in Eq. (3.47) below.

$$\Delta w_{kj} = -\eta \frac{\partial \varepsilon}{\partial w_{kj}} \quad (3.47)$$

On the other hand, the k 's perceptron's node-output, z_k is defined with the multiplication of “ w_{kj} ” and “ x_j ” terms in the sigma formula as presented in Eq. (3.48);

$$z_k = \sum_j w_{kj} x_j \quad (3.48)$$

The j^{th} input to that neuron is x_j , and the perceptron's output is shown with y_k where a nonlinear function defines this output as shown in Eq. (3.49):

$$y_k = F_N(z_k) \quad (3.49)$$

The designation F presented in Eq. (3.49) is the nonlinear function. We can now substitute,

$$\frac{\partial \varepsilon}{\partial w_{kj}} = \frac{\partial \varepsilon}{\partial z_k} \frac{\partial z_k}{\partial w_{kj}} \quad (3.50)$$

And,

$$\frac{\partial z_k}{\partial w_{kj}} = x_j(p) = y_j(p - 1) \quad (3.51)$$

Considering formerly presented Eqs. (3.50) and (3.51) together structures Eq. (3.52) as follows;

$$\frac{\partial \varepsilon}{\partial w_{kj}} = \frac{\partial \varepsilon}{\partial z_k} x_j(p) = \frac{\partial \varepsilon}{\partial z_k} y_j(p-1) \quad (3.52)$$

Here, the output layer is indicated with p . Defining:

$$\Phi_k(p) = -\frac{\partial \varepsilon}{\partial z_k(p)} \quad (3.53)$$

$$\frac{\partial \varepsilon}{\partial w_{kj}} = -\Phi_k(p) x_j(p) = -\Phi_k y_j(p-1) \quad (3.54)$$

$$\Delta w_{kj} = \eta \Phi_k(p) x_j(p) = \eta \Phi_k(p) y_j(p-1) \quad (3.55)$$

J shows the j^{th} input to the neuron k of the output (p) layer. In addition;

$$\Phi_k = -\frac{\partial \varepsilon}{\partial z_k} = -\frac{\partial \varepsilon}{\partial y_k} \frac{\partial y_k}{\partial z_k} \quad (3.56)$$

$$\frac{\partial \varepsilon}{\partial y_k} = -(d_k - y_k) = y_k - d_k \quad (3.57)$$

And, for a sigmoid nonlinearity, Eq. (3.58) is considered:

$$y_k = F_N(z_k) = \frac{1}{1 + \exp(-z_k)} \quad (3.58)$$

$$\frac{\partial y_k}{\partial z_k} = y_k(1 - y_k) \quad (3.59)$$

Consequently, with the consideration of Eqs. (3.56), (3.57), and (3.59) altogether, Φ_k is simply given with the Eq. (3.60),

$$\Phi_k = y_k(1 - y_k)(d_k - y_k) \quad (3.60)$$

Additionally, at the output layer, the following expressions are written:

$$\Delta w_{kj} = -\eta \frac{\partial \varepsilon}{\partial w_{kj}} = -\eta \frac{\partial \varepsilon}{\partial z_k} \frac{\partial z_k}{\partial w_{kj}} \quad (3.61)$$

$$\Delta w_{kj}(p) = \eta \Phi_k(p) y_j(p - 1) \quad (3.62)$$

In Eq. (3.60), Φ_k term was given in order to complete the derivation of the setting of output layer weights.

If we propagate back for the hidden layer of r^{th} order with the consideration of i^{th} branch into the neuron of j^{th} order, we again have the same as before, and consequently in parallel to Eq. (3.50), we can now constitute Eqs. (3.63) and (3.64), as presented below;

$$\Delta w_{ji} = -\eta \frac{\partial \varepsilon}{\partial w_{ji}} \quad (3.63)$$

$$\Delta w_{ji} = -\eta \frac{\partial \varepsilon}{\partial z_j} \frac{\partial z_j}{\partial w_{ji}} \quad (3.64)$$

When Eq. (3.51) is noted and the definition of Φ_k term in Eq. (3.56) is defined, in parallel with these information; Eq. (3.65) can now be set up as follows:

$$\Delta w_{ji} = -\eta \frac{\partial \varepsilon}{\partial z_j} y_i(r - 1) = \eta \Phi_j(r) y_i(r - 1) \quad (3.65)$$

When the right-hand-side relation of Eq. (3.56) is considered, the definition of equation (3.66) can be obtained as presented below:

$$\Delta w_{ji} = -\eta \left[\frac{\partial \varepsilon}{\partial y_j(r)} \frac{\partial y_j}{\partial z_j} \right] y_i(r-1) \quad (3.66)$$

Here, $\partial \varepsilon / \partial y_j$ is inaccessible. Finally, $\Phi_j(r)$ can be given as:

$$\Phi_j(r) = y_j(r) [1 - y_j(r)] \sum_k \Phi_k(r+1) w_{kj}(r+1) \quad (3.67)$$

Finally, the mean absolute percentage error (*MAPE*) and the correlation coefficient (*R*) were used to see the convergence between the real target values and the predicted output values. Here, *MAPE* definition is defined as follows:

$$MAPE = \frac{1}{n} \sum_{i=1}^n \frac{|p_i - m_i|}{p_i} * 100 \quad (3.68)$$

3.3.3.2. Utilization of Adaptive Neuro-Fuzzy Inference System

Complex, analytically ill-defined, nonlinear, or stochastic problems can be tackled using basic computational operations (Bilgili, 2010; Bilgili and Ozgoren, 2011). Complex problems such as non-analytical, nonlinear, non-stationary, and stochastic types can be solved with limited programming knowledge when the *ANFIS* forecasting approach is used.

An adaptive network system is composed of a network structure involving nodes and as well as directional links connecting these nodes. In this construction, obtained outputs depend on the parameters belonging to these nodes, where the

learning rule determines how such parameters should be altered in order to reduce the error as much as possible.

An adaptive network consists of a multilayer feed-forward network in which a particular function is regulated for the oncoming signals. This particular function may be expressed as a node function in which a set of parameters are involved within the node. However, each function between the nodes may vary with each other. In order to construct the desired mapping of the input-output parameters, the given training data updates the related parameters, and a gradient-based learning format is produced.

This dissertation includes the Takagi and Sugeno's fuzzy if-then rules taken into consideration (Jang, 1993). In this context, the outputs obtained by each rule are formed by the linear combination of the input variables, and in addition, a constant term is added in the linear relation. And, the final output obtained is constructed from the weighted average of each rule obtained.

The formerly expressed general logic of these if-then rules in this part of the dissertation is given by Eq. (3.69). In this context,

Rule m: If turbine hub-height wind speed, U_D is A_m , atmospheric air temperature, T_{atm} is B_m , and turbine rotor rotational speed, Ω is C_m ; the related general function can be written as expressed in Eq. (3.69):

$$f_m = p_m x + q_m y + r_m \quad (3.69)$$

The designation of m indicated in Eq. (3.69) above corresponds to any rule number, and refers the total number of the equations that have to be constructed between 1 and m numbers.

Five layers can be defined with a general *ANFIS* structure to estimate an output with a given input and a smallest error value as much as possible.

First layer: Each node in the first layer is defined with $i = 1, 2, 3, \dots, k$, in which k is defined for each linguistic label (small, large, etc.). Linguistic labels are shown as A, B, C, \dots, X designations, where a node function defines the given input with the corresponding linguistic label and the node. Functions for each linguistic label and its node can generally be defined by Eq. (3.70). Node functions belonging to the same layer remain in the same function family.

$$O_i^j = \mu X_i^j(X) \quad (3.70)$$

Where, j designation denotes the number of the layer, i designation is the node number, and finally, X designation is the corresponding layer element. Similarly, Eq. (3.70) can be specialized for the first layer, in the form of Eq. (3.71). Thus, a square node having a node function is defined as expressed in Eq. (3.71) for the linguistic label, A :

$$O_i^1 = \mu A_i(x) \quad (3.71)$$

Similarly, node functions for the linguistic labels B and C of the first layer can be defined as presented in Eqs. (3.72) and (3.73), respectively, similarly to the formerly expressed Eq. (3.71):

$$O_i^1 = \mu B_i(y) \quad (3.72)$$

$$O_i^1 = \mu C_i(z) \quad (3.73)$$

On the other hand, Eq. (3.74) gives the general expression for the linkage of inputs. This part of the dissertation involves three inputs of hub-height wind

speed, U_D , atmospheric air temperature, T_{atm} , and wind turbine rotor rotational speed, Ω refer to the first layer (*premise*) for any node of i .

$$O_i^1 = \mu X_i(X) \quad (3.74)$$

On the other hand, the premise parameter is a term used in the literature to define the parameters of this layer. O_i^1 determines the membership function of the first label of consequent premise parameters, such as A_i , B_i , C_i , ..., X_i , where i depends on the structured node number of each premise sub-group.

Maximum and minimum values of a bell-shaped $\mu A_i(x)$ function are 1 and 0, respectively; and are described either by Eq. (3.75), or can also be expressed in the form of a Gaussian curve membership (*gaussmf*) function as presented in Eq. (3.76).

$$\mu A_i(x) = \frac{1}{1 + \left[\frac{(x-c_i)^2}{a_i} \right] b_i} \quad (3.75)$$

$$\mu A_i(x) = e^{\left\{ -\left(\frac{x-c}{a_i} \right)^2 \right\}} \quad (3.76)$$

A variety of bell-shaped or Gaussian curve membership functions (*gaussmf*) can be derived using different combinations of the coefficients involved within the set $\{a_i, b_i, c_i\}$ or only utilizing $\{a_i, c\}$, respectively. Consequently, linguistic labels A_i , B_i , C_i , ..., X_i can be defined by a variety of membership functions.

In this context, considering the cases for the linguistic labels B_i and C_i ; similarly to Eq. (3.76); Eqs. (3.77) and (3.78) use a general functional form for

these labels, and take the form of a Gaussian curve membership (*gaussmf*) function:

$$\mu_{B_i}(y) = e^{\left\{-\left(\frac{y-f'}{d_i}\right)^2\right\}} \quad (3.77)$$

$$\mu_{C_i}(z) = e^{\left\{-\left(\frac{z-j'}{g_i}\right)^2\right\}} \quad (3.78)$$

On the other hand, Eq. (3.79) gives the general form of the right-hand side of Eq. (3.70), depending on the first layer with an arbitrary linguistic label, X , and for any given node, i , defined by the Gaussian curve membership functions (*gaussmf*).

$$\mu_{X_i}(X) = e^{\left\{-\left(\frac{X-c_2}{c_{1i}}\right)^2\right\}} \quad (3.79)$$

Second layer: The PI symbol (π) in this layer is used to relate the incoming signals in a multiplied form, and the output product that will be sent out. In this context, for the second layer, Eq. (3.80) is simply written as follows:

$$w_i = \mu_{A_i}(x) \cdot \mu_{B_i}(y) \dots \quad (3.80)$$

Nodes of this layer are given in the form of a circle as presented in Figure 3.6. Besides, each output node exemplifies the firing strength of a rule.

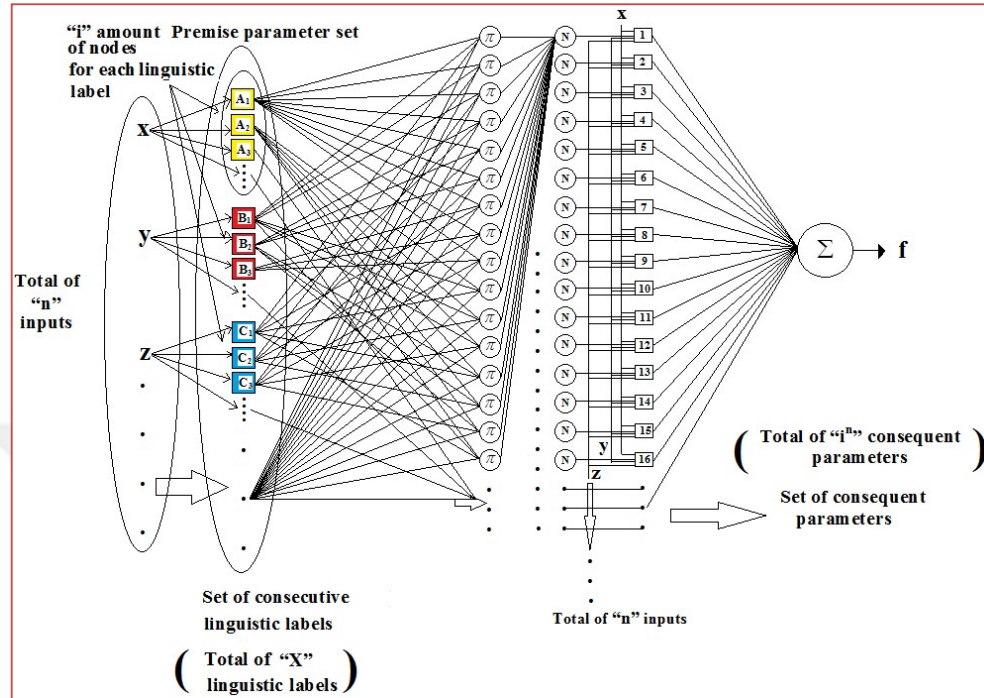


Figure 3.6. Schematic *ANFIS* structure representation with “ n ” inputs, “ X ” linguistic labels, and “ i ” nodes

Eq. (3.70) describes the general form of an instant *ANFIS* event, in which it includes the corresponding number of the layer, the node number, and the layer element, i.e., the specific linguistic label. A total of n inputs are shown with the input set, a total of linguistic labels starting from A, B, C, ..., X, defining three linguistic labels (A, B, C) plus a consecutive set of linguistic labels. A proper linguistic label designated with X is defined by the user for the proper configuration inside the figure, and a set of consecutive linguistic labels is shown like a single label in which links from the consecutive set are formed through the third layer that meets with the links coming from the linguistic labels A, B, and C.

Third layer: The designation N is used for this layer to reveal a computational step on the i^{th} node in terms of the ratio of the firing strength of the i^{th} rule to the sum of the firing strengths of all rules as shown in Eq. (3.81), below.

Consequently, the symbol shown as N designates the normalizing of the i^{th} rule in terms of the ratio of the firing strengths.

$$\bar{w}_i = \frac{w_i}{w_1 + w_2 + w_3 + \dots + w_m} \quad (3.81)$$

The total amount of multiplied incoming signals obtained by the product of premise parameters and ranging within the second layer is shown with the notation m to reveal all firing strengths as inputs to the third layer. Thus, the denominator of Eq. (3.81) gives the sum of the weights in the third layer, whereas the output of the third layer is the normalized firing strength used for input to the next layer, i.e., the obtained input to the fourth layer. Nodes of this layer are also denoted by circling similar to the second layer and are shown in Figure 3.6.

Fourth layer: Similarly, the remaining i^n-1 nodes of the fourth layer are obtained from the signals referred to in the third layer, as shown with Eq. (3.81), where the output of the third layer provides the input for the fourth layer. To prevent the complexity, only the first node of the third layer is shown in the figure as linked with the incoming signals, based on the ratio of the normalized firing strength signals obtained from the third layer, in which the general equation for the third layer is given by Eq. (3.81).

Fifth layer: Received signals by the fifth layer are defined concerning Eq. (3.82), in other words, they are defined by a normalized weight (\bar{w}_i), with inputs of x, y, z, \dots, n , and proper coefficients of p_i, q_i, \dots, r_i . The designation sigma, Σ is used for this layer to compute the overall output as the summation of all incoming signals, as shown in Eq. (3.83), and output of this layer is shown with O_i^5 for $j = 5$ to refer to the fifth layer and the i^{th} , referring the corresponding node. Similar to the second and the third layers, a circular node case is considered for this fifth layer.

Node function in the fourth layer is characterized by the node function for the i^{th} node, as given in Eq. (3.82). Thus, the representation with O_i^4 will functionally relate the multiplication of the normalized firing strength to the linear function as output of this layer for the i^{th} node, as shown below:

$$O_i^4 = \bar{w}_i f_i = \bar{w}_i (p_i x + q_i y + \dots + r_i) \quad (3.82)$$

On the other hand, Eq. (3.82) defines the output of this layer for the parameter set, $\{p_i, q_i, \dots, r_i\}$. Parameters of this layer are named the *consequent parameters* as shown in Figure 3.6. Similarly to the first layer, nodes of the fourth layer are square nodes as well. Finally; Eq. (3.83) gives the required output based on the ANFIS forecasting, as shown in Figure 3.6 for the final obtained function, f .

$$O_i^5 = \text{overall output} = \sum_i \bar{w}_i f_i = \frac{\sum_i w_i f_i}{\sum_i w_i} \quad (3.83)$$

3.4. Aerodynamics of Shrouded Horizontal Axis Wind Turbines

Literature search indicating mainly three different types of casing shroud types are generally used in wind turbine shrouding systems as presented in Figure 3.7. In the literature studies, the optimization of the given geometries in a variety of casing configurations to obtain a best performance in the concentration of the airflow running through the turbine rotor blade area is aimed. Thus, in this way, acceleration of wind speed on the rotor disc, U_D and enhancement of the air mass flow rate running through the turbine blades, \dot{m} are obtained. This method provides around 2.5 times enhancement of power generation measured with respect to a standard conventional bare wind turbine under the utilization of a wind turbine surrounded by an optimized casing shroud system. On the other hand, the

configurations involving a nozzle-diffuser structure and sometimes flange component mainly cause a significant pressure drop through the casing body, at downstream region of rotor blade plane, and especially at downstream region of flange sections which result in the boost of free-stream wind speed, U_∞ significantly. This increase of free-stream wind speed, U_∞ depends on the proper design of nozzle-diffuser and flange geometry. Besides, power generation of wind turbines start at lower values of free-stream wind speed, U_∞ . Especially introduction of a flange component attached to the nozzle-diffuser casing body results on the formations of separated flow regions in the vicinity of rotor blade plane and at downstream regions of the flange. These separated flow regions cause the static pressure to be decreased further. In these regards, this increase of wind speed is usually a function of casing full body length, L , nozzle length of the casing, L_1 , diffuser length of the casing, L_2 , flange height, H , casing inlet geometry, casing inlet diameter, D_1 , casing exit diameter, D_2 , diameter of the casing where the wind turbine is installed, D (also referred as D_t for the narrowest cross-sectional diameter of the casing), or in the case of airfoil structure, optimized airfoil structure play an important role of the casing performance. Also, the design of the optimum rotor diameter, D_{rotor} based on these cited parameters is important. So, the correct design of those parameters give an optimum designed wind turbine casing configuration causing this best optimized configuration resulting of the wind turbine to start power generations at a lower wind speed. A presentation of a such condition including the wind speed enhancement and corresponding pressure drop is shown in Figure 3.8 (Mansour and Meskinkhoda, 2014). In their study, utilizing a casing shroud system surrounding a wind turbine, a maximum enhancement value of 1.5 is obtained in free-stream wind speed, U_∞ on the turbine rotor blade region inside this casing body as shown in Figure 3.8a, similarly, a maximum value of corresponding pressure drop ratio along and inside the casing body of $C_{prmax}=1.5$ is also obtained, as this situation revealed in Figure 3.8b. Both parameters as

well as turbine performance should be even further improved during the utilization of a flange height, H in an optimum length which is attached to the nozzle-diffuser geometry. This situation was also proved by (Hu and Wang, 2015).

A theoretical sight applied to the casing shrouded wind turbines, in order to figure out the mutual variations of the aerodynamic parameters can also be derived using the *BEM* theory (Bilgili et al., 2015b; İlhan et al., 2018a).

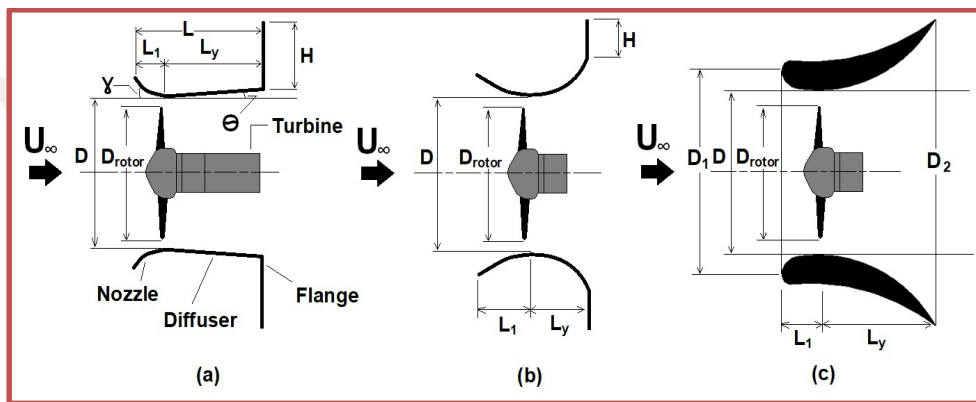
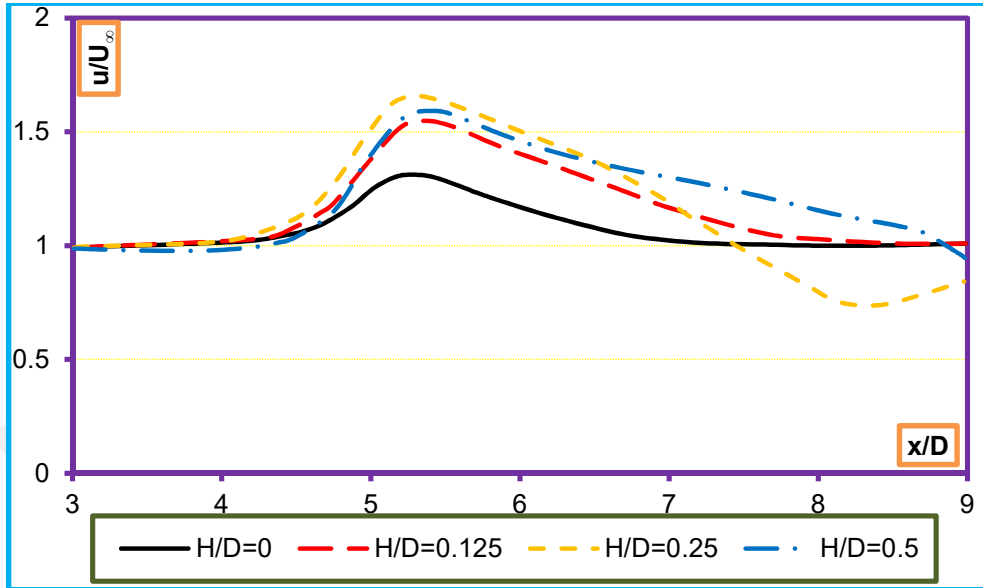
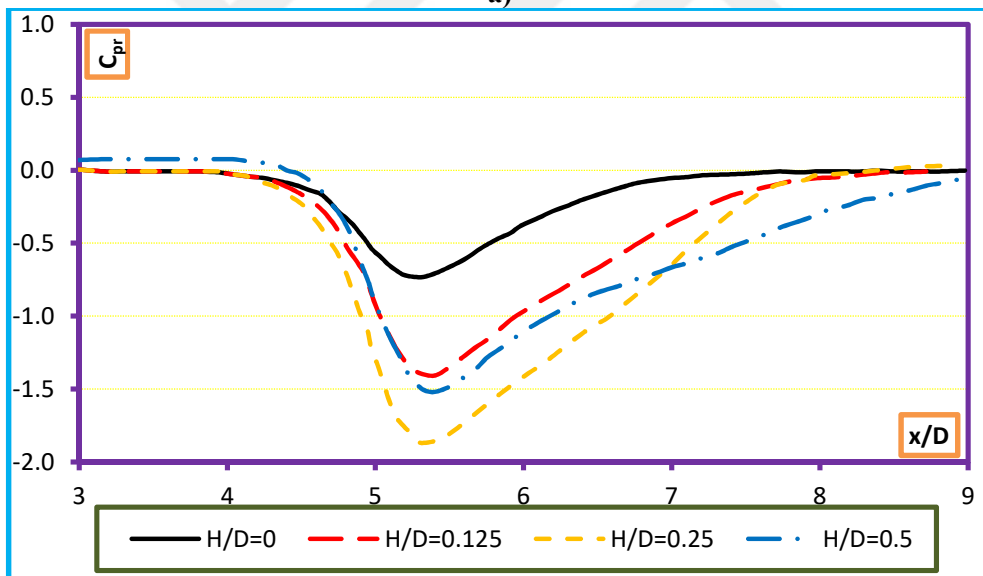


Figure 3.7. Wind turbine casings mainly available in the literature



a)



b)

Figure 3.8. Along with the casing dimensionless axial coordinate system defined with respect to the cross-sectional diameter of the wind turbine location, x/D ; **a)** increase of wind speed shown by wind speed ratio inside and in the vicinity of casing, u/U_∞ ; **b)** decrease of dimensionless pressure coefficient, C_{pr} (Mansour and Meskinkhoda, 2014)

3.4.1. Blade Element Momentum Theory for Wind Turbines with Diffuser Constructed

The control volume including a wind turbine with diffuser and its energy interaction inside this control volume are both shown in Figure 3.9. The wind turbine power generation is related to the interaction of the turbine rotor and wind, as clearly observed in this figure. In this context, the mass conservation principle is applied to continuous flow condition assuming the case of no rotary disc or rotor placed inside the diffuser. Thus, Eqs. (3.84) and (3.85) are derived based on these formerly expressed assumed conditions.

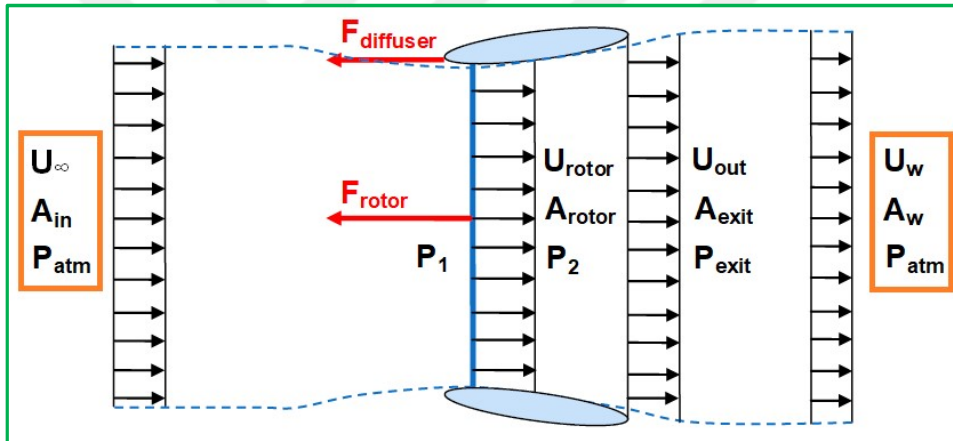


Figure 3.9. Energy interaction within the control volume obtained from the wind turbine with diffuser constructed

$$\dot{m}_{in} = \dot{m}_{out} \quad (3.84)$$

$$\rho A_{in} U_{\infty} = \rho A_{rotor} U_{rotor} = \rho A_{exit} U_{out} = \rho A_w U_w \quad (3.85)$$

In terms of the control volume assumption, the inlet area of the stream tube, area of the diffuser exit plane, and rotor disc cross-sectional areas are related

with each other and non-dimensionalized with Eqs. (3.86), (3.87), and (3.88) (Van Dorst, 2011),

$$\varepsilon = \frac{A_{exit}}{A_{rotor}} \quad (3.86)$$

$$\mu = \frac{A_{in}}{A_{exit}} \quad (3.87)$$

$$\mu\varepsilon = \frac{A_{in}}{A_{rotor}} \quad (3.88)$$

On the other hand, rotor blade plane immediate upstream pressure, P_1 is calculated when the condition $U_\infty = U_{out}$ is assumed and Bernoulli Equation is utilized;

$$P_{total} = P_1 + \frac{1}{2}\rho(\varepsilon U_\infty)^2 = P_{atm} + \frac{1}{2}\rho(U_\infty)^2 \quad (3.89)$$

$$P_1 = P_{atm} + \frac{1}{2}\rho(U_\infty)^2 - \frac{1}{2}\rho(\varepsilon U_\infty)^2 \quad (3.90)$$

$$P_1 = P_{atm} + (1 - \varepsilon^2)\frac{1}{2}\rho(U_\infty)^2 \quad (3.91)$$

Pressure drop occurred along the upstream and downstream of the rotor disc is obtained in the case of the dimensionless area ratio, ε formerly indicated in Eq. (3.86) to be higher than 1. In this case, wind speed at the diffuser exit plane, U_{out} , and wind speed at the rotor disc, U_{rotor} are expressed with Eqs. (3.92) and (3.93), respectively,

$$U_{out} = \mu U_{\infty} \quad (3.92)$$

$$U_{rotor} = \mu \varepsilon U_{\infty} \quad (3.93)$$

In these regards, Eqs. (3.90) and (3.91) will be turned into the following state with the above considerations,

$$P_1 = P_{atm} + (1 - \mu^2 \varepsilon^2) \frac{1}{2} \rho U_{\infty}^2 \quad (3.94)$$

On the other hand, wind speeds at the diffuser exit plane, dead flow region (*far wake*), and rotor blade plane (*rotor disc*) are calculated as functions of axial flow induction factor, a as presented in Eqs. (3.95), (3.96), and (3.97), respectively in the case of rotary disc or rotor placed inside the diffuser,

$$U_{out} = U_{\infty}(1 - a) \quad (3.95)$$

$$U_w = U_{\infty}(1 - 2a) \quad (3.96)$$

$$U_{rotor} = U_{\infty} \mu \varepsilon (1 - a) \quad (3.97)$$

Immediate upstream and downstream pressures of rotor disc are determined by the application of the Bernoulli Equation, given in Eqs. (3.98) and (3.99), respectively,

$$P_1 = P_{atm} + (1 - \mu^2 \varepsilon^2 (1 - a)^2) \frac{1}{2} \rho U_{\infty}^2 \quad (3.98)$$

$$P_2 = P_{atm} + ((1 - 2a)^2 - \mu^2 \varepsilon^2 (1 - a)^2) \frac{1}{2} \rho U_{\infty}^2 \quad (3.99)$$

On the other hand, pressure drop occurring through the immediate exit of the rotor caused by the rotary disc is estimated by considering Eqs. (3.98) and (3.99) together which constitute Eq. (3.100) shown below,

$$P_1 - P_2 = 4a(1 - a)\frac{1}{2}\rho U_\infty^2 \quad (3.100)$$

Thrust coefficient, $C_{T,rotor}$ of only rotor component in the case of casing utilization is expressed using Eq. (3.101),

$$C_{T,rotor} = 4a(1 - a) \quad (3.101)$$

Finally, Eqs. (3.102), (3.103), and (3.104) present power coefficient of the rotor with turbine placed in a casing shroud, $C_{p,rotor}$, total thrust coefficient of the casing and rotor system, $C_{T,total}$, and thrust coefficient of only diffuser casing shroud component in the case of rotor assembled inside the casing body, $C_{T,diffuser}$, respectively.

$$C_{p,rotor} = \mu\varepsilon 4a(1 - a)^2 \quad (3.102)$$

$$C_{T,total} = \mu\varepsilon 4a(1 - a) \quad (3.103)$$

$$C_{T,diffuser} = C_{T,total} - C_{T,rotor} = (\mu\varepsilon - 1)4a(1 - a) \quad (3.104)$$

3.4.2. CFD Analysis of Wind Turbine Casing Shrouds

3.4.2.1. Definition of CFD Parameters

The dissertation includes the *CFD* numerical analysis of wind turbine shrouding systems, containing definitions of dimensionless parameters including Reynolds number, Re , turbulence intensity, I , turbulent kinetic energy, k , turbulent

length scale, l , and turbulent kinetic energy dissipation rate, ε as defined in Eqs. (3.105), (3.106), (3.107), (3.108), and (3.109), respectively.

$$Re = \frac{\rho U_{\infty} D_t}{\mu} \quad (3.105)$$

$$I = 0.16xRe^{-0.125} \quad (3.106)$$

$$k = 1.5x(U_{\infty}I)^2 \quad (3.107)$$

$$l = 0.07D_t \quad (3.108)$$

$$\varepsilon = C_{\mu}^{3/4} x \frac{k^{3/2}}{l} \quad (3.109)$$

Intermediate abbreviations took part in above equations including μ and C_{μ} stand for dynamic viscosity of the approaching fluid to the cased wind turbine, i.e., in this case the fluid is air; and empirical constant that is specified in the turbulent model, respectively.

3.4.2.2. Standard k- ε Model

Two equation models comprise of two additional transport equations in order to represent turbulent characteristics of the numerically studied considered flows. In a more specialized form, i.e., in the case of the k - ε model; the first and second transported variables are generally turbulent kinetic energy, k and turbulent dissipation rate, ε , respectively. In this context, the turbulent kinetic energy, k and turbulent dissipation rate, ε stand for energy presented in the turbulent flow and the scale of turbulence, respectively ([CFD-Wiki, 2005](#)).

The *CFD - Wiki* reports that two-equation models are the most common referred turbulent models considering the whole numerical *CFD* history. The fundamental advantages of the k - ε model are providing of sturdiness, the economy in terms of computer logic, and most importantly high and reasonable accuracy obtained by the behavior of wide range of turbulent flows (*CFD-Wiki, 2005*).

3.4.2.3. Physics of Standard k - ε Model

The turbulence model initially proposed by ([Lauder and Spalding, 1972](#)) was named as the “standard k - ε turbulence model”. The following equations presented in this section are as well available in the *CFD-Wiki* source published in 2005, in [Fluent \(2005\)](#), and [Wilcox \(1994\)](#). On the other hand, the following transport equations shown in Eqs. (3.110) and (3.111) show the logic of turbulent kinetic energy, k , and the turbulent dissipation rate, ε of this kinetic energy, respectively (*CFD-Wiki, 2005; Fluent, 2005; Wilcox, 1994; Maia, 2014*).

$$\frac{\partial}{\partial t}(\rho k) + \frac{\partial k}{\partial x_i}(\rho k u_i) = \frac{\partial}{\partial x_j} \left[\left(\mu + \frac{\mu_t}{\sigma_k} \right) \frac{\partial k}{\partial x_j} \right] + G_k + G_b - \rho \varepsilon + S_k \quad (3.110)$$

$$\begin{aligned} \frac{\partial}{\partial t}(\rho \varepsilon) + \frac{\partial}{\partial x_i}(\rho \varepsilon u_i) &= \frac{\partial}{\partial x_j} \left[\left(\mu + \frac{\mu_t}{\sigma_\varepsilon} \right) \frac{\partial \varepsilon}{\partial x_j} \right] + C_{1\varepsilon} \frac{\varepsilon}{k} (G_k + C_{3\varepsilon} G_b) - \\ C_{2\varepsilon} \rho \frac{\varepsilon^2}{k} + S_\varepsilon & \end{aligned} \quad (3.111)$$

When the above equations are considered; G_k abbreviation presented in these equations refer to the turbulence kinetic energy generation occurred by the mean velocity gradients, and this situation is comprehensively explained in [Fluent \(2005\)](#). On the other hand, G_b is the turbulence kinetic energy formation depending on the buoyancy and calculated by the Fluent. The terms including $C_{1\varepsilon}$, $C_{2\varepsilon}$, and $C_{3\varepsilon}$

are given as first, second, and third constants, respectively in the standard k - ε model, as well, σ_k and σ_ε depend for the turbulent Prandtl numbers respectively for k and ε . And finally, sources terms defined by the users are S_k and S_ε , respectively, for k and ε in order of partial differential equations.

On the other hand, modeling of turbulent/eddy viscosity ($kgm^{-1}s^{-1}$) is executed through the consideration of Eq. (3.112) as follows;

$$\mu_t = \rho C_\mu \frac{k^2}{\varepsilon} \quad (3.112)$$

In the standard k - ε defined in Eqs. (3.110), (3.111), and (3.112); the definitions are closed down by the five essential assigned values presented in Eq. (3.113);

$$C_{1\varepsilon}=1.44, C_{2\varepsilon}=1.92, C_\mu=0.09, \sigma_k = 1.0, \text{ and } \sigma_\varepsilon = 1.3 \quad (3.113)$$

Where $C_{1\varepsilon}$ and $C_{2\varepsilon}$ define first and second constants, respectively in the standard k - ε model without the utilization of third constant $C_{3\varepsilon}$ presented in Eq. (3.111), for the current study. Besides, C_μ , σ_k , and σ_ε refer to turbulent/eddy viscosity constant, turbulent kinetic energy Prandtl number, and turbulent kinetic energy dissipation rate Prandtl number, respectively, as formerly defined or presented in Eqs. (3.109) and (3.112) for C_μ , and Eq. (3.110) for σ_k , and finally Eq. (3.111) for σ_ε , respectively.

3.4.3. PIV Analysis of Wind Turbine Shrouds

3.4.3.1. Particle Image Velocimetry (*PIV*) Channel System

Particle Image Velocimetry (*PIV*) experiments of the thesis were conducted in a free-surface water channel of Fluid Mechanics Laboratory of Çukurova University. The used water channel for this purpose has dimensions 8000 mm x 1000 mm x 750 mm. On the other hand, it is manufactured of 15 mm thick transparent plexiglass sheet including upstream and downstream fiberglass reservoirs. The water was pumped through a settling chamber and traveled through a honeycomb section of 2:1 channel contraction just before arriving the test chamber at downstream. The turbulence intensity was kept below 0.1% by the utilization of the reservoirs and honeycomb screen arrangements. The pumping of water was executed by an electric motor including a variable speed controller. A schematic of the test chamber used for *PIV* analysis of this dissertation is demonstrated in Figure 3.10.

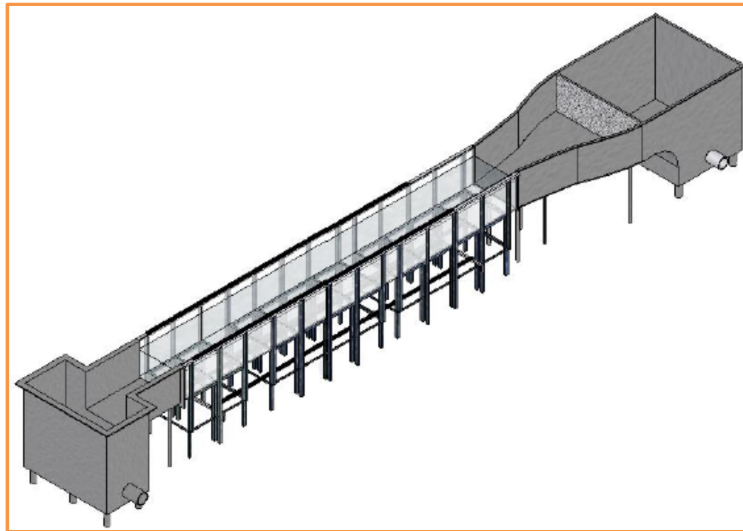


Figure 3.10. Schematic representation of the water channel used for *PIV* analysis

3.4.3.2. Experimental Aperture

In the present study, the designed wind turbine shrouding configuration was maintained as stable in the water channel by utilizing a specially designed aperture which the whole system is shown in Figures 3.11 and 3.12. While this aperture kept wind turbine shrouding stationary, the four sticks placed at downstream of the configuration kept casing configuration and the hub as a single rigid body. The sticks were manufactured as small as possible for them not to inhibit water flow inside the casing body.

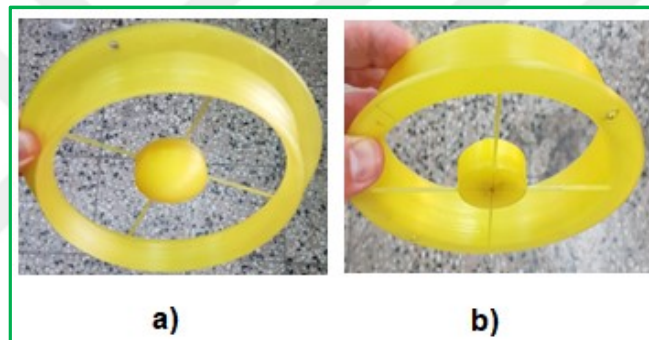


Figure 3.11. Designed wind turbine shrouding configuration **a)** upstream side of configuration **b)** downstream side of the configuration

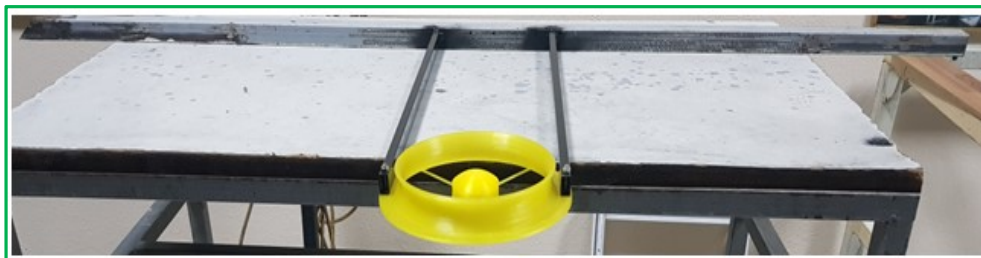


Figure 3.12. Fixing equipment of designed wind turbine shrouding configuration

On the other hand, Figure 3.13 presents the casing system and its fixing equipment placed inside the *PIV* water channel.

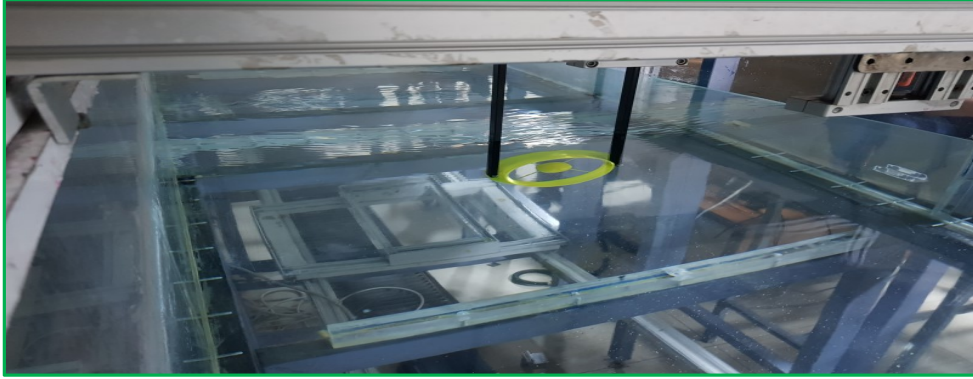


Figure 3.13. Wind turbine casing system located inside the *PIV* water channel

3.4.3.3. Dye for Particle Image Velocimetry (*PIV*) Experiments

3.4.3.3.(1). Dye Visualization Experiments

In the case of dye experiments, flow characteristics over the wind turbine casing were visualized using a fluorescent dye. This dye shines under the laser sheet, and it is utilized in creating color alterings of water. Dye was placed in a small sized container which was arranged in a place of 500 mm above the water channel free surface. Dye was injected at downstream region of wind turbine casing body. In order to capture video images obtained for vortex flow configurations, SONY HD-SR1 video camera was utilized. The software of this video camera was used for capturing of these images, referred as frame grabber. On the other hand, although visualizations obtained by dye utilizations give no numerical information about vorticity flow structure, it presents a brief and rough idea about the structure of the water flow over the wind turbine casing body. Figure 3.14 presents the representation of *PIV* water channel and its working and dye mechanisms.

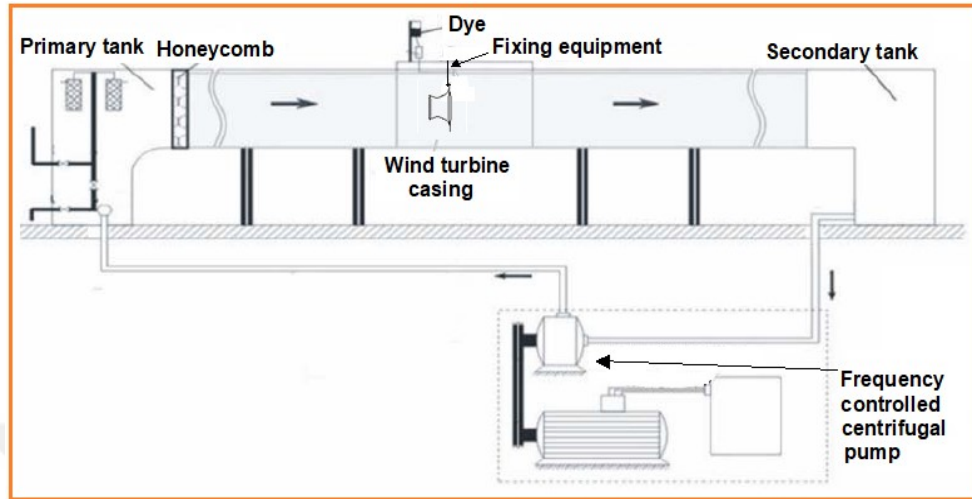


Figure 3.14. Channel schematics and its working mechanism

3.4.3.4. Particle Image Velocimetry (*PIV*) Experiments

3.4.3.4.(1). Measurement Principle

Particle Image Velocimetry (*PIV*) is a technique of flow measurement utilized to acquire time-dependent field velocity distributions of single or multi-phase flows. A velocity field in the form of two-dimensional outputs can be obtained using this method. It as well provides a proper view of instantaneous flow region described in a quantitative fashion. In these regards, the user is allowed well to examine small flow structures occurred in the flow region and their influences are also analyzed. On the other hand, vorticity fields can also be quantitatively analyzed.

PIV works in a principle of determining the distance that used particles moved in a time interval between laser illuminations. A *PIV* system generally involves components including illumination, image acquisition, particle seeding, image processing and data analysis sub-systems. The illumination source of *PIV* is frequently obtained by a laser light. From this point, the particles are lighted up by

light pulsed sheets at accurate time intervals. The lighted up particles generate images which are then recorded onto a photographic film. Particles used for ideal tracing are required to be so small, and those should follow the flow field. Common methods utilized in the determination of the distance are correlation methods and particle tracking. The dominant distance between each particle is demonstrated by the correlation field and as well each other particle within the interrogation spot. The maximum intensity spot, representing each particle image correlation with itself, is situated in the center. On the other hand, the positive displacement peak corresponds to the dominant particle spacing which is the second peak. The flow field velocity cannot be found after calculation of particle displacements at a certain time. So, the instantaneous velocity vector field, vorticity, streamline topology, and turbulent statistics are used for this purpose to configure them by this technique. Besides, the average velocity field, vorticity contours, streamline topology, and turbulent statistics can be determined utilizing instantaneous data. The 3D stereoscopic measurement principle of a *PIV* system is demonstrated in Figure 3.15.

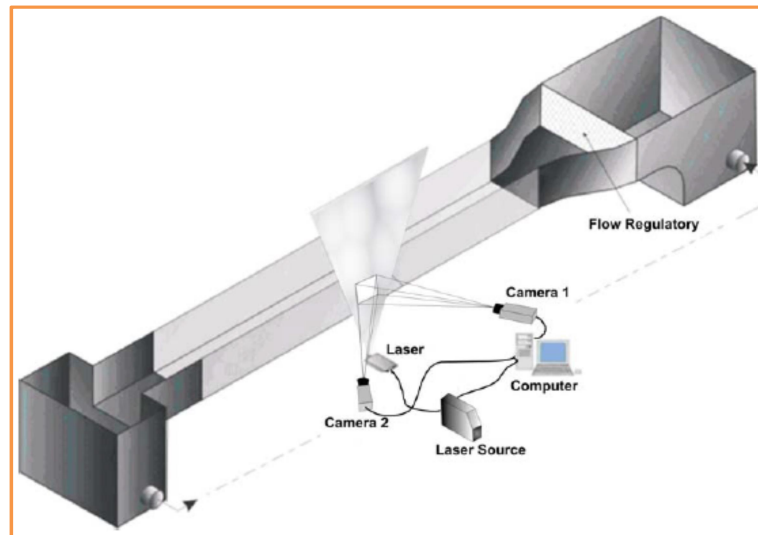


Figure 3.15. 3D *PIV* representation of illumination and camera system

3.4.3.5. Illumination

The illumination of a *PIV* system is actualized by an Nd. YAG Laser which is presented in Figure 3.16. Generally, the laser is chosen for this intent in order to effectively take images. On the other hand, in gas flow applications, to obtain a better and proper illumination, a high light source is ordinarily required. Tracer particles scatter the light, thus better capturing of images by the camera is executed. High scattering effectiveness is attained by large tracer particles, so they are more appropriate for this target. Particles move with fluid flow simultaneously. In this context, selecting the correct type of tracer particles is an extremely important parameter in *PIV* experiments. Small particles gain this parameter so easily compared with respect to the large tracer particles. However, this situation is generally decided in researcher experiments. Image haziness is avoided by keeping illumination light pulse duration as short as possible. Time retardation is always occurred between the illumination pulses. However, this time delay must be long enough to obtain tracer particle displacement between images with a high resolution. Additionally, it is needed to be short enough to avoid particles with an out-of-plane velocity component leaving the light sheet between subsequent illuminations. Measurement plane's location and its dimensions should also be well characterized (Canpolat, 2008).



Figure 3.16. Source of a Nd. YAG Laser used in *PIV* experiments

3.4.3.6. Adaptive Cross-Correlation Technique and Further Analysis

Auto-correlation has been the most used conventional type of method, since initial and final particle positions on separate camera frames were not probable to be separated in the past. In these regards, one camera image map was exposed to consecutive light-sheet pulses. Naturally, this situation resulted in uncertainty with the measurements, because it was impossible to declare initial and final positions of two recorded particle images corresponding to which of two. However, recently, developments of camera technology enabled initial and final particle positions to be recorded on different camera frames. For this reason, cross-correlation is required to be used excluding the directional ambiguity of auto-correlation, then utilizing adaptive correlation is performed ([Dantec Dynamics Software Manual](#)).

An adaptive correlation includes a fundamental principle in terms of an iterative procedure. Considering a preliminary guessed offset value, an offset is given initially from the first window to the second window. The obtained output vector is then validated and later utilized for a new forecast for the window offset. Subsequently, a new run is performed; however the new run is executed with a smaller window (interrogation area). The primary benefit obtained during the usage of the shifted window includes capturing the particle images leaving the interrogation area, which occurred during the interval between two light pulses. On the other hand, particle image loss is referred to be “in-plane dropout”, and this situation diminishes signal strength and consequently, successful vectors as much as possible can be obtained. When an enhanced number of particle images is captured for each vector, this situation allows the interrogation area to be refined and enough amounts of successful vectors are still obtained while keeping seeding density in the flow constant. The images that were received from *CCD* camera having a pixel resolution of 1600x1186 and the rate of camera receiving was 15

frames/second. Time retardation between frames alters between 2 ms and 3 ms. Next, FLOWMAP software was used in the analyses of a digital image. And, the image was chained on a CDD array. The camera image from CCD camera was read by the Frame Grabber in the computer. These read data then were stored in TIFF file format in the RAM in a digital image file format. Later, FLOWMAP software was used for the processing and analyzing of this digital image. For each continuous run, 350 images totally were taken. Finally, for the velocity field determination, cross-correlation technique of 32x32-interrogation window was operated with an overlap of 50% ([Dantec Dynamics Software Manual](#)).

3.4.3.7. Experimental System

The *PIV* test section consists of a wind turbine shrouding body set in parallel to the water flow. The thickness of the shrouding body was 3.5 mm. The casing hub center was placed in a location 500 mm down measured by the upper side of the channel. And, it was also located 265 mm down from the free-surface of the flow. Besides, the total height of the flowing water along the shrouding body was adjusted to a level of 530 mm; in which the wind turbine casing body was positioned just in the middle of the water body. On the other hand, it was placed at a far distance to downstream of the water channel in order to prevent problems that may arise during the development of the flow. Free-stream water flow velocity was adjusted at the value of 0.2 m/s generating a Reynolds number corresponding to $Re=29757$ presented for the wind turbine location diameter, D . The free-stream water flow velocity and Reynolds number were both kept constant in *PIV* and dye experiments. Using the *PIV* technique, two-dimensional laser sheet lighted up the zone where the velocity vectors were measured. Dantec *PIV* system was utilized for the velocity vector measurement executions. The illumination of the flow field was obtained by two Nd: Yag pulsed laser sources of 532 nm wavelength. Each

laser source had a 120 mJ maximum energy output. Besides, Dantec Flow Map Processor was utilized for camera synchronizing and laser unit control, as well as data acquisition timing was obtained. A CCD camera of a resolution 1600x1186 pixels recorded the particle movements. And, 60 mm focal-length lens equipped the camera. On the other hand, the frame-to-frame adaptive correlation technique was employed by a Dantac flow grabber digital PIV software in order to count raw displacement vector field obtained from particle image velocity data. In order to obtain image processing, 32x32 pixels having rectangular effective interrogation windows was utilized. To satisfy the Nyquist criterion, 50% overlap was operated for the interrogation process (Karasu, 2015). On the other hand, the flow camera inspecting the nature of the flow is located in a direction as shown in Figure 3.17.

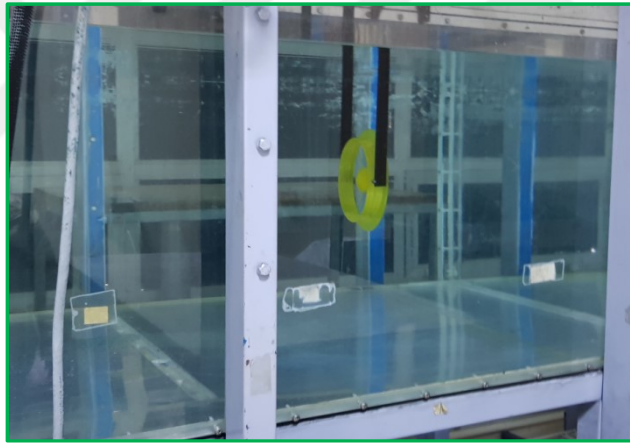


Figure 3.17. The location side of the flow viewer camera, i.e., at the right-hand side of the upstream flow direction

The designed curved type of configuration configured for *PIV* experiments has casing inlet diameter, D_1 , casing exit diameter, D_2 , wind turbine location diameter, D , flange height, H , turbine hub diameter, D_h , and turbine axial length including whole mechanical mechanism, L_s 159.243, 170.023, 149.533, 14.988, 48.501, and 23.441 mm, respectively. On the other hand, the hub component

located inside the casing body is shifted by 9.232 mm measured with respect to the plane of inlet diameter, D_i of wind turbine casing body, thus constituting a casing full body length, L of $L=32.672$ mm. The final aspect of the wind turbine shrouding configuration manufactured at these dimensions, its fixing equipment, its location in the water channel, and flow viewer camera are shown in Figure 3.18.

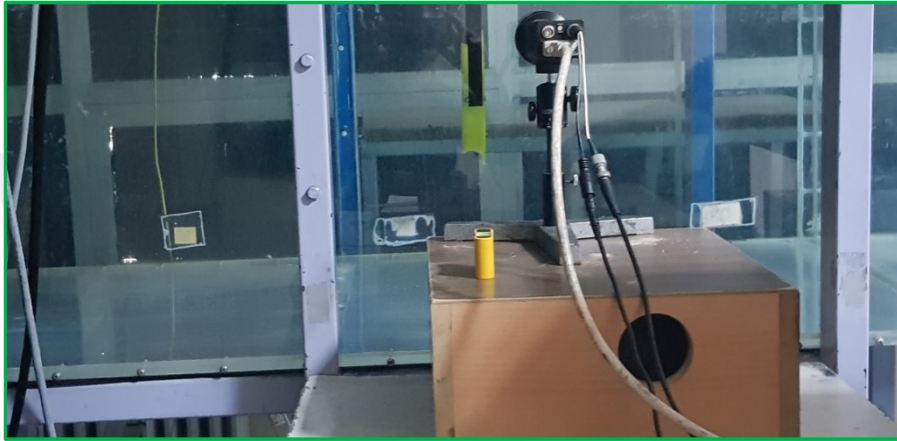


Figure 3.18. Wind turbine shrouding system and flow monitoring camera



4. RESULTS AND DISCUSSIONS

4.1. Statistical Analysis of Wind Energy Density in the Babuburnu – Çanakkale Region of Turkey

4.1.1. Introduction

The total of available wind energy potential including wind speed values over 7 m/s is estimated to be around 47 GW in Turkey, and especially Çanakkale, İzmir, Balıkesir and Hatay basins are excellent wind resources for wind farm installations. Therefore, the capability of the wind power potential of Bababurnu-Çanakkale province in the Marmara region of Turkey was reported in the context of this study as an example of a statistical analysis of wind energy density forecasting. Parameters including the superior wind velocity direction, average wind velocity, Weibull and Rayleigh parameters, probability distribution, and wind power potential of this province were processed and analyzed in terms of annual, seasonal and monthly point of view. Finally, at a level of 10 m over the ground surface, the average wind velocity and average wind energy potential in this site were determined as 6.01 m/s and 257 W/m², respectively according to the whole processed data. These data indicated that Bababurnu-Çanakkale region has an acceptable wind energy potential, which is quite reasonable for the planting of wind power turbines.

4.1.2. The Objective of the Present Work

The results considered in the present work were received from Bababurnu-Çanakkale station situated in the Marmara region of Turkey. This meteorological station was constructed by the Renewable Energy General Directorate (REGD,

2017). The location of the station presented in Figure 4.1 presents the map of the region. The long-term wind data consists of hourly wind velocities and their corresponding wind directions considering three different years. Monthly, annually and diurnal average wind velocities were determined through processing of hourly wind velocities. Anemometer positioned at the wind velocity measuring station is located at the height of 10 m over the ground surface. The station of wind observation is located at the coordinates of $39^{\circ}30'03''$ N latitude and $26^{\circ}12'39''$ E longitude. The altitude of this station is 348 m above the sea level. There is no obstacle around the wind velocity measuring area that would negatively influence wind velocities and their corresponding wind directions. The models of the Weibull and Rayleigh are employed in this dissertation for the investigation of the wind characteristics in this site.

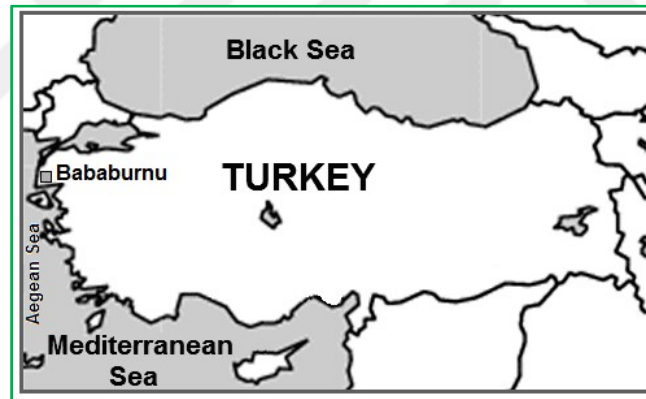


Figure 4.1. Map of the region and location of the station (REGD, 2017)

Wind direction has decisive importance in evaluating the possible utilization of wind power. Therefore, statistics of wind direction have a significant task for determining the right position of wind turbines according to the roughness of the terrain. It is known that wind direction and speed are also affected by the topography.

This part of the dissertation mainly deals with the statistical forecasting of the frequency distribution of yearly mean wind speeds and their values for the considered years predicted by Weibull and Rayleigh models. Furthermore, monthly distributions of mean wind speed and wind power values for the considered years are also predicted using these statistical models.

4.1.3. Results and Discussions

The wind direction and frequency distribution in the Bababurnu site are presented in Figure 4.2. Results of three years reveal that the dominant wind direction of Bababurnu site is obtained to be NE (30°) as clear from this figure.

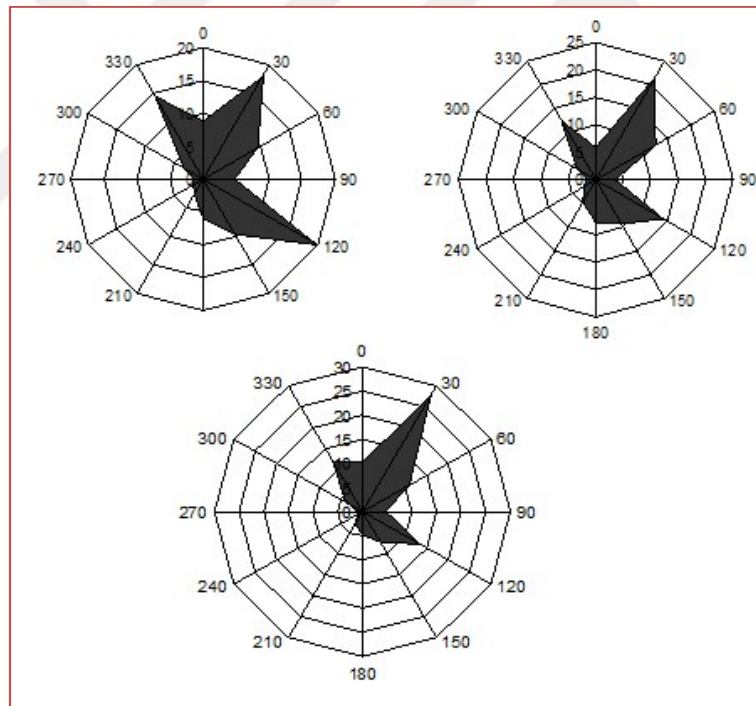


Figure 4.2. Wind direction and frequency distribution for Bababurnu station, considering (a) 1st (Top - left), (b) 2nd (Top - right), and (c) 3rd years of measurement time (Bottom)

The diurnal wind velocity in terms of the hourly variation of the mean wind speed obtained from the first year data of Bababurnu site is indicated in Figure 4.3. In consideration of the summer season, the diurnal wind velocity obtained in this study varies from 4.83 m/s to 8.16 m/s, and this speed interval indicates to be quite high for high capacity wind turbine generations and wind energy conversion systems. While the minimum level of diurnal wind speed occurs in the morning hours, it was shown that maximum wind speed occurs in the afternoon hours. Namely, after 12 o'clock and 11 o'clock, rapidly increased values of wind speeds for the time ranges including 14-16 o'clock and 14-17 o'clock were reported for the autumn and summer seasons, respectively.

Maximum enhancements of wind speeds for both seasons were calculated to be 41% and 69% for autumn and summer seasons, respectively, according to the maximum and minimum values of the average daily results depending on the mean hourly variation of the wind speeds of first-year data. Also, maximum enhancements of wind speeds for spring and winter seasons according to the maximum and minimum values of the average daily results of first-year data were reported to be 24% and 19%, respectively. These results are attributed to the high level of solar intensity throughout the afternoon times of the day. Namely, wind can be defined as a motion of air masses. Air masses move because of different thermal conditions of the air masses. This motion of the air masses can be stated as global and regional airflow phenomenon. During the day, the ground solar heating causes thermal mixing resulting in the downward transfer of momentum. As a result of these different thermal conditions, generally, maximum wind velocity is observed after midday. On the other hand, after sunset, usually, wind velocities are relatively calm near the surface (Incecik and Erdogmus, 1995).

During a typical day in Bababurnu site, the difference between the highest and lowest average hourly wind velocity is considerable which is much influenced by the seasonal weather variation. For instance, average diurnal ranges determined

according to the maximum and minimum average hourly values of winter and summer seasons are observed to be 1.16 m/s and 3.33 m/s, respectively. Namely, this comparison indicates that the diurnal variation is more pronounced in the summer season compared to the winter season. Thus, diurnal fluctuation in spring and winter seasons is less with respect to the autumn and summer seasons. Peak values of wind speed which were 6.36 m/s at 14 o'clock; and 7.17 m/s and 7.24 m/s at 4 o'clock and 15 o'clock were obtained considering spring and winter seasons, respectively.

Especially the results of summer seasons occur due to surface heating, which increases mixing of the faster-moving air at the higher levels with the air near the surface. As long as the surface heating effect is diminished like in winter seasons, the wind velocity decreases and significant variation cannot be observed from hour to hour during the night. Also, the diurnal variation is the greatest on sunny days and least on dull days.

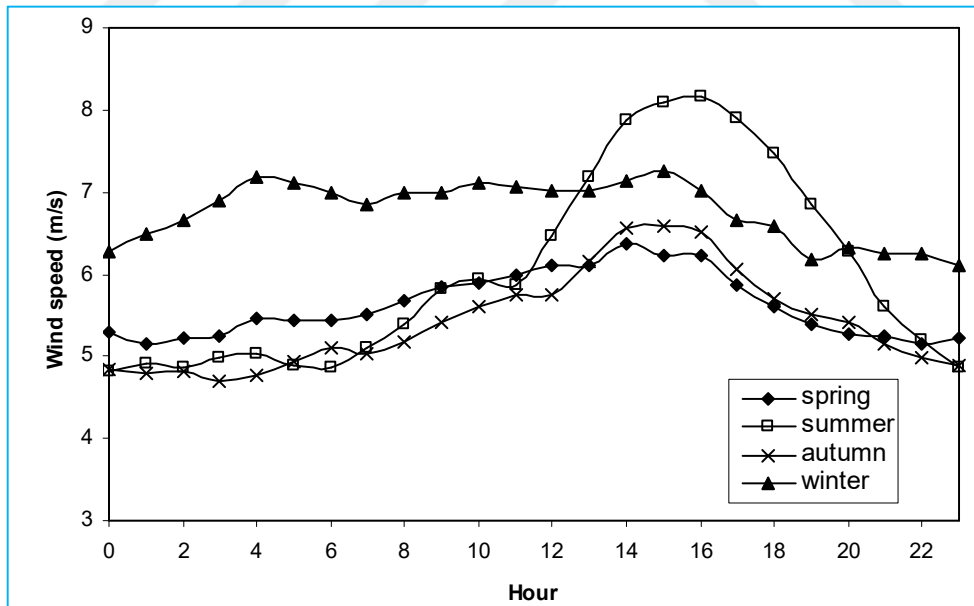


Figure 4.3. Hourly variation of the mean wind speed for Bababurnu station

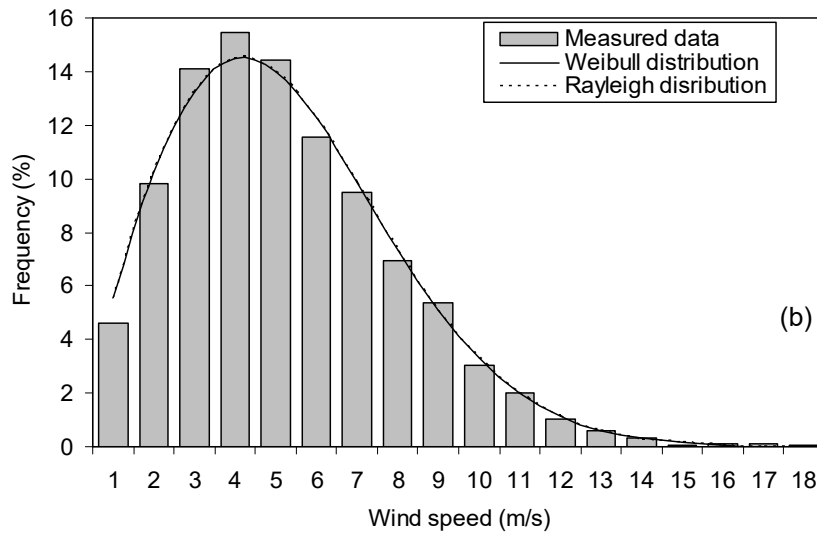
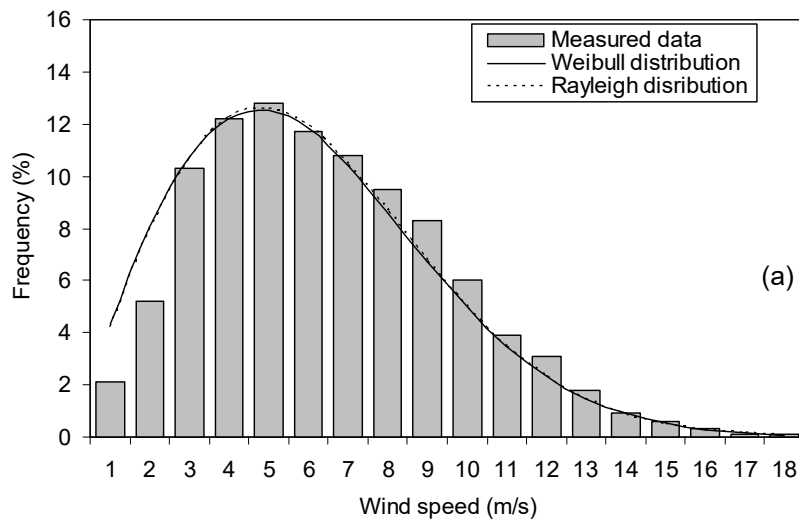
The seasonal and yearly average Weibull parameters for Bababurnu - Çanakkale station are indicated in Table 4.1. The value of Weibull shape parameters, k and Weibull scale parameters, c vary within the range of $1.78 \leq k \leq 2.14$ and $6.1 \text{ m/s} \leq c \leq 7.8 \text{ m/s}$, respectively according to the processed data of the first year as indicated in Table 4.1. Here, the maximum value of the c parameter is seen in winter season as 7.8 m/s. However, the minimum value of the c parameter is observed in autumn season corresponding to 6.1 m/s. Also, while the biggest value of k parameter is seen in summer season as 2.14, the smallest value of k parameter is seen in the autumn season which is equal to 1.78.

Table 4.1. Seasonal and yearly Weibull parameters for Bababurnu station

Season	Weibull scale parameters (c), m/s			Weibull shape parameters (k)		
	1 st year	2 nd year	3 rd year	1 st year	2 nd year	3 rd year
Spring	6.4	5.95	5.62	2.09	2.12	1.61
Summer	6.7	6.37	6.72	2.14	2.26	2.22
Autumn	6.1	5.12	6.10	1.78	1.98	1.79
Winter	7.8	6.21	7.22	2.09	1.81	1.89
Yearly average	6.8	5.92	6.42	1.98	2.00	1.84

Due to its convenience in statistical analysis, time series of wind velocity data is generally organized in the form of the frequency distribution. The frequency distribution and probability density of wind velocities provide answers to specific questions including duration of wind turbine that generates electricity. In this context, common questions that can be addressed during new wind power plant installments usually involve the duration of wind shortages, the most frequent wind

velocity ranges and how frequently wind turbines attain their maximum efficiencies. Considering these reasons, the available times-series of wind data were transformed into a form of a frequency distribution in the scope of this part of the dissertation. The Mathematical representation of the wind velocity probability distributions and the corresponding functions are principal tools used in the wind-related literature.



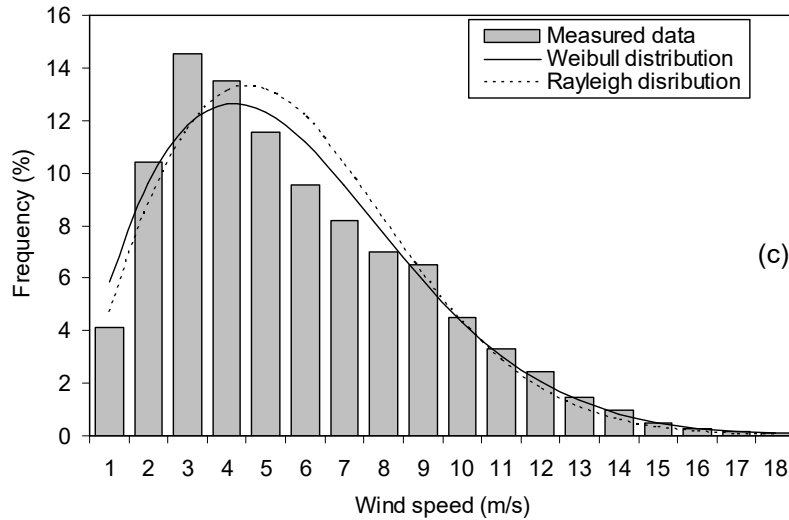


Figure 4.4. Wind speed frequency distributions for Bababurnu station, considering (a) 1st, (b) 2nd, and (c) 3rd years of measurement time

Annual wind velocity frequency variations considering the data of three years taken into consideration for Bababurnu-Çanakkale station are presented in Figures 4.4a, 4.4b, and 4.4c, respectively. These figures clearly show that the distributions of Weibull and Rayleigh parameters indicate the same variations for the considered years, however small discrepancies occurred according to two functional results especially within the range of speed $3 \text{ m/s} < V \leq 9 \text{ m/s}$ considering the third year as shown in Figure 4.4c. On the other hand, the even small discrepancy is valid between both functions; taking measured data into account reveals that Weibull function generally generates better results concerning the Rayleigh distribution within the considered wind speeds range. According to the wind speed frequency distributions during the third year, except values of wind speeds; $V=1 \text{ m/s}$, $V=3 \text{ m/s}$, $V=4 \text{ m/s}$, $V=9 \text{ m/s}$, and $V=10 \text{ m/s}$; the Weibull function provides predicted results that are more compatible with the measured data. At wind speed values of $V=3 \text{ m/s}$ and $V=10 \text{ m/s}$, both functions produced the same

result. But, at wind speeds of $V=1$ m/s, $V=4$ m/s, and $V=9$ m/s, the Rayleigh distribution function provides better results.

Considering this wind speed interval, it is clear from Figure 4.4c that Rayleigh distribution exceeded Weibull distribution with a maximum discrepancy percentage around 7.4% for a wind speed of 5 m/s. Beyond this limit, i.e., at smaller wind speed values, exceeding of Weibull distribution over Rayleigh distribution was observed. Beyond the wind speed of $V<3$ m/s, discrepancies were also observed between Rayleigh and Weibull functions. But this is not distinct as much as the wind speed interval of $3 \text{ m/s}<V\leq 9 \text{ m/s}$. Furthermore, very small discrepancies are also observed considering the first year of the data. However, it was reported that the best-fitted model curves with each other according to the frequency results of both functions were obtained for the second year of the data.

Designers and researchers working on wind energy conversion systems should take two parameters, i.e., the speed and power potential of wind into account which are the most two significant parameters for these systems.

Wind power production is basically depended on the level and stability of wind velocities. In this regard, monthly variations of the average wind velocity and wind power potential of Bababurnu-Çanakkale station are presented in Figures 4.5 and 4.6, respectively. According to Figure 4.5, considering the monthly variations including mean wind speeds for 1st, 2nd, and 3rd years, Weibull and Rayleigh models yielded similar data based on the measured data. About 79%, 52%, and 84% of wind speeds increments were measured for 1st, 2nd, and 3rd years of data. It is interesting to note that considering monthly variations of the wind power potential of three years in Figure 4.6; the Weibull distribution is seen to be better compared with the distribution of Rayleigh parameter, also for the third year where Weibull distribution is also better. Furthermore, the wind speed and power density demonstrate rapid changes each month. Thus, there is a general trend for the power density not to exceed 300 W/m^2 is observed, when the first eleven months of 1st-

year data is taken into account. However, this value is observed to be exceeded more than two times in December. Also, again according to 1st-year data, the monthly average wind velocities with the highest values are mainly seen in December and August as 8.3 m/s and 6.5 m/s, respectively. But, the smallest magnitudes of wind velocities are observed in September and May having 4.6 m/s and 4.9 m/s, respectively. In parallel with this, while the highest monthly average wind energy potentials are mainly seen in December and August having 603 W/m² and 290 W/m² wind energy, respectively; the smallest values of wind energy potential are observed in September and May such as 103 W/m² and 152 W/m², respectively according to the 1st year data.

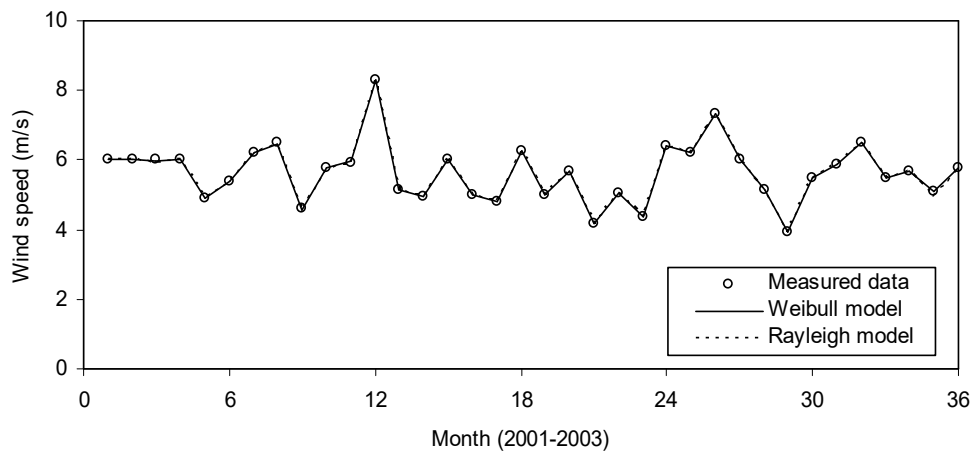
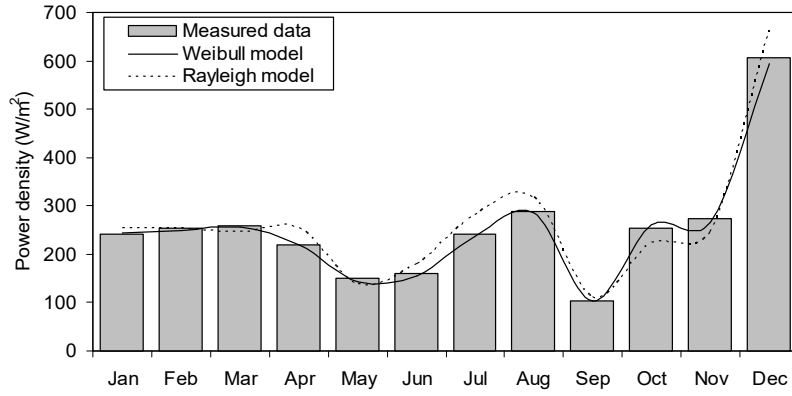
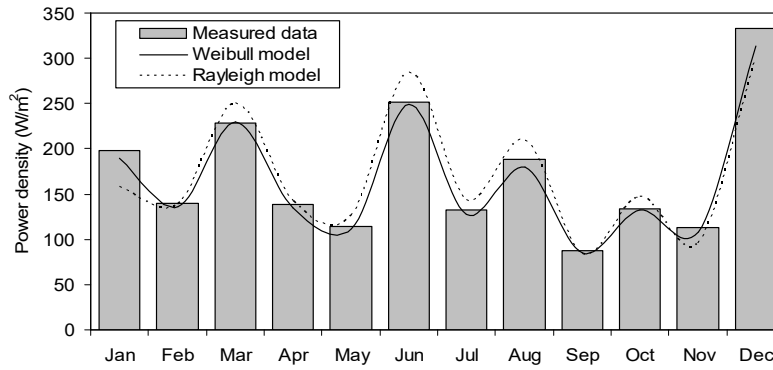


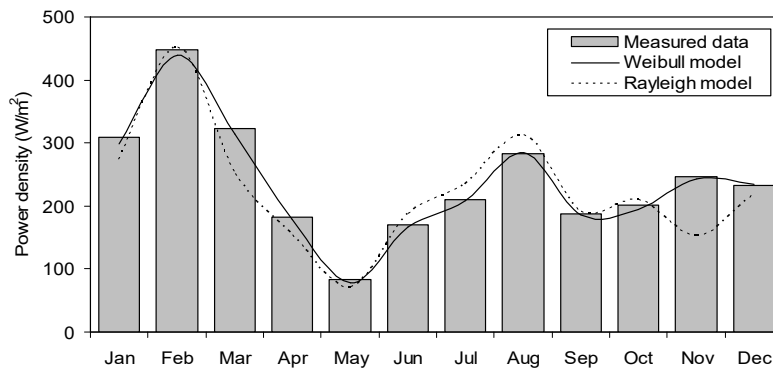
Figure 4.5. Monthly variations of mean wind speed values for Bababurnu station, considering (a) 1st, (b) 2nd, and (c) 3rd years of measurement time



(a)



(b)



(c)

Figure 4.6. Monthly variations of wind power potential for Bababurnu station, considering (a) 1st, (b) 2nd, and (c) 3rd years of measurement time

Table 4.2. Seasonal and yearly average wind speed and wind energy potential for the Bababurnu station

Season	Wind speed, m/s			Wind energy potential, W/m ²		
	1 st year	2 nd year	3 rd year	1 st year	2 nd year	3 rd year
Spring	5.71	5.27	5.04	209	161	196
Summer	5.96	5.64	5.95	232	187	222
Autumn	5.44	4.54	5.43	214	112	212
Winter	6.93	5.52	6.41	374	226	325
Yearly Average	6.01	5.24	5.7	257	171	239

Table 4.2 presents the annual average and seasonal mean wind speed and wind power potential of the Bababurnu site. According to the 1st year of data, the annual average wind velocity is demonstrated to be 6.01 m/s corresponding to annual average wind energy potential of 257 W/m². Wind energy potential can be utilized for new installations of wind power plants since these wind properties are shown to be acceptable in this part of the dissertation dealing with the statistical analysis of wind energy density in the Bababurnu region of Turkey.

4.1.4. Concluding Remarks

In Turkey, the total of available wind energy potential is estimated to reach 47 GW especially considering wind speeds higher than 7 m/s. There are also excellent wind resources in Turkey, particularly in Çanakkale, İzmir, Balıkesir and Hatay basins to be addressed for incoming wind farm installations. Based on the results of this part of the dissertation, the territory of Bababurnu-Çanakkale is shown to have an acceptable wind power potential. The hourly wind velocity magnitude was found to be bigger than 5 m/s around 70% of the total duration at a level of 10 m over the ground surface in this region. But, the monthly average wind velocities according to the 1st year of data were determined to be higher than 5 m/s throughout ten months of the year, and the monthly average wind energy potentials

also considering the 1st year of data were higher than 200 W/m² throughout nine months of the year. The yearly mean wind speed was measured as 6.01 m/s, and this gave a corresponding yearly mean wind energy potential which was calculated as 257 W/m². These values in this part of the dissertation are shown to be acceptable for the generation of the wind power in this region; thus new power plants are required to be installed in this region.

4.2. Efficiency Analysis of an Installed Wind Farm Located in South of Turkey

4.2.1. Introduction

In this study, efficiency study of five wind turbines of a wind farm located in southern region of Turkey was performed using data of wind speed, wind direction, air temperature, and electric generation of five turbines selected. Parameters affecting turbine efficiency were also examined.

Analysis of monthly and yearly dominant wind directions for selected turbines was as well performed. Performed analysis of turbines was also conducted considering the measured wind speed and direction. Aerodynamic characteristics of wind turbines were defined according to the variation of measured wind speeds. Finally, in this part of the dissertation; annual energy production of turbines were calculated in order to obtain the most productive and efficient months.

4.2.2. The Objective of the Present Work

Energy usage is vital in enhancing the quality of life besides providing physical comfort and surviving of life. Most of the energy used by humans was obtained from the sun until the discovery of nuclear energy. The solar energy is

absorbed and stored up by plants with the specific activity named photosynthesis in order to provide energy found in foodstuffs. Fossil fuels, whose energy source was ultimately the sun, were also produced from decayed plants that lived a million years ago. On the other hand, energy generated by the sun develops wind formation in the atmosphere. This wind formation operates wind rotors for years. Nowadays, the World demand of energy grows rapidly, and this demand will continue to grow substantially in coming years because of the high growth of populations, social, economic and industrial developments. A high rate of energy demand, the rapid increase of oil price and the negative impact of fossil fuels on the environment gave tremendous attention to wind energy all over the World. In order to convert wind energy into electricity, one needs to use a wind turbine. Wind is an indirect product of solar energy. There are lots of variations in wind speed from stagnant velocities to hurricanes.

This part of the dissertation aims to study the performance of installed wind turbines in a chosen wind farm in order to see the power produced on the feasibility basis.

The increase of the petrol cost and limitations in traditional energy sources enhanced interest in wind energy again. By the encouragements and formal research studies, lots of new turbine designs were accomplished. In this context, wind turbine aerodynamical studies play an essential role in new designs. This part of the dissertation presents a sight of dealing the whole aerodynamic parameters of the chosen wind turbines of the farm.

4.2.3. Results and Discussions

4.2.3.1. Identification of Wind Directions for Considered Wind Turbines

Figure 4.7 was constructed according to the considered wind data presented in Tables 4.3, 4.4, 4.5, and 4.6. This figure demonstrates yearly wind blowing directions for all selected wind turbines. Monthly distributions of wind direction for turbines T01, T02, T03, T04, and T05 are presented in Figures 4.8 and 4.9. During the procurement of these figures, numbers of hourly wind direction data used in these directional estimations are numbered on these figures.

Data determined in Tables 4.3, 4.4, 4.5, and 4.6 refer the processed wind speed, power generation, wind direction, and air temperature, respectively, by eliminating wind speeds below cut-in speed (4 m/s) where turbine starts power generation, eliminating error values of power generation including zero and negative values and unrecorded wind direction data.

Table 4.3. Monthly average wind speed data (*Considering the boundary values*)

Turbine no	Hourly Wind Data (m/s)				
	T01	T02	T03	T04	T05
Date	Hourly Average Wind Speed (m/s)	Hourly Average Wind Speed (m/s)	Hourly Average Wind Speed (m/s)	Hourly Average Wind Speed (m/s)	Hourly Average Wind Speed (m/s)
January	8.15	8.97	8.82	10.00	9.25
February	9.10	9.94	9.65	10.85	10.03
March	7.75	8.28	7.97	8.57	8.18
April	6.99	7.64	6.98	8.01	7.43
May	7.80	9.05	7.87	8.91	8.33
June	8.82	10.02	9.03	10.09	9.49
July	10.70	12.60	11.26	12.88	12.05
August	8.62	10.02	8.75	9.73	9.23
September	7.98	9.15	8.30	9.41	8.91
October	6.54	7.25	6.66	7.26	6.80

November	6.18	6.79	6.22	7.26	6.69
December	8.12	9.05	8.31	9.65	8.76
Yearly	8.06	9.06	8.32	9.38	8.76

Table 4.4. Monthly average electricity generations per hour (*Considering the boundary values*)

Turbine no	Hourly Generation Data (kWh)				
	T01	T02	T03	T04	T05
Date	Hourly Average Generation (kWh)	Hourly Average Generation (kWh)	Hourly Average Generation (kWh)	Hourly Average Generation (kWh)	Hourly Average Generation (kWh)
January	934.99	1129.00	1044.95	1336.83	1163.70
February	1130.39	1407.07	1237.43	1564.24	1334.85
March	787.02	919.22	838.46	966.28	860.72
April	604.97	745.74	615.47	801.98	668.22
May	813.02	1144.56	907.04	1070.66	909.49
June	1083.59	1393.10	1241.85	1431.59	1231.07
July	1605.48	2094.98	1922.58	2136.12	1934.50
August	1019.48	1375.24	1161.50	1303.19	1142.37
September	878.57	1190.30	1058.07	1298.62	1119.85
October	513.03	645.44	549.92	678.96	543.78
November	392.67	508.15	412.73	658.33	506.74
December	881.44	1054.35	922.99	1250.19	1033.13
Yearly	887.05	1133.93	992.75	1208.08	1037.37

Table 4.5. Monthly average wind direction data (*Considering the boundary values*)

Turbine no	Hourly Wind Direction Data (°)				
	T01	T02	T03	T04	T05
Date	Hourly Average Wind Dir. (°)	Hourly Average Wind Dir. (°)	Hourly Average Wind Dir. (°)	Hourly Average Wind Dir. (°)	Hourly Average Wind Dir. (°)
January	161.65	187.76	164.64	187.26	214.10
February	174.15	177.18	136.97	185.52	209.32
March	129.55	100.63	98.83	110.54	162.64
April	73.83	74.18	70.41	74.70	146.54
May	163.21	38.20	42.38	43.33	136.26

June	315.84	1000.00	39.08	39.57	151.12
July	329.80	1000.00	27.29	20.48	196.88
August	326.25	1000.00	24.05	20.92	202.14
September	212.78	1000.00	36.07	33.71	183.73
October	80.85	1000.00	90.86	78.76	160.32
November	191.47	1000.00	188.49	190.34	184.65
December	215.40	1000.00	206.07	203.94	197.49
Yearly	197.90	115.59	93.76	99.09	178.77

Table 4.6. Monthly average air temperature data (*Considering the boundary values*)

Turbine no	Hourly Temperature Data (°C)				
	T01	T02	T03	T04	T05
Date	Hourly Average Temp. (°C)	Hourly Average Temp. (°C)	Hourly Average Temp. (°C)	Hourly Average Temp. (°C)	Hourly Average Temp. (°C)
January	7.51	7.55	8.14	8.15	7.38
February	7.89	7.93	8.70	8.61	7.87
March	12.08	12.06	12.70	12.15	11.82
April	14.15	14.21	14.63	13.93	13.67
May	17.38	16.17	17.88	17.02	16.75
June	20.06	20.23	20.75	19.58	19.48
July	21.91	21.67	22.58	21.13	21.03
August	27.04	25.42	25.52	24.49	24.34
September	25.67	22.39	22.73	21.70	21.77
October	21.66	18.42	19.52	18.04	18.00
November	20.21	16.80	17.37	16.96	16.86
December	12.08	9.74	10.28	10.41	9.74
Yearly	17.30	16.05	16.73	16.02	15.73

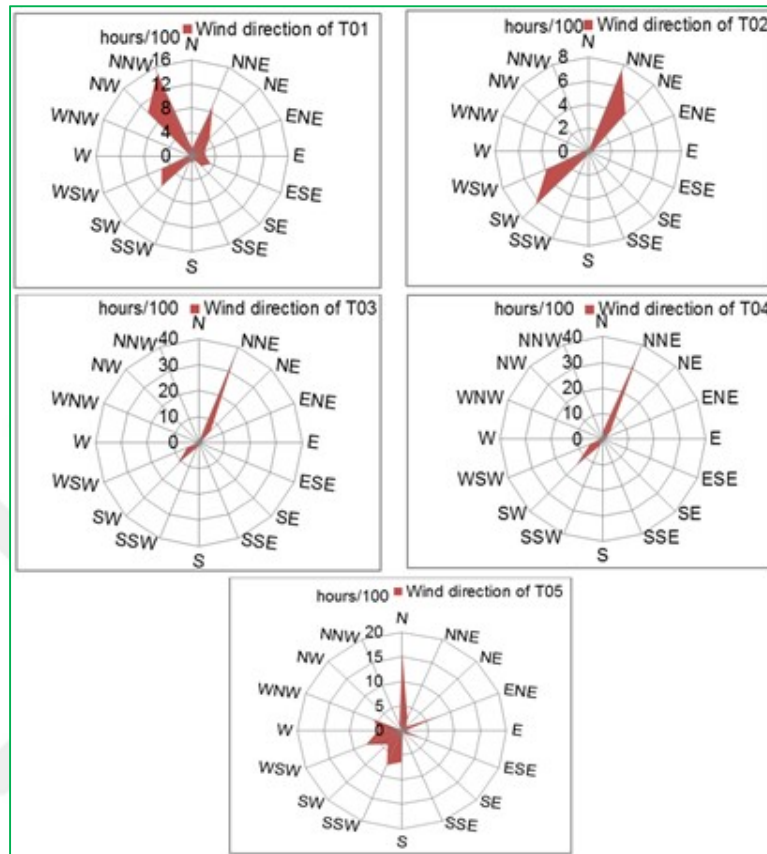


Figure 4.7. Distributions of wind directions for turbines T01, T02, T03, T04, and T05

Figures 4.8 and 4.9 involve average wind directions of wind turbines T01, T02, T03, T04; and T05, respectively, for each month shown with blue numbers. Green patterns inside the figures indicate the amount of data used in determining the monthly wind direction for each discrete wind turbines. Considering wind turbine T02; all hourly wind directions measured for months between June and December were, unfortunately, unrecorded and indicated by the claret red color. Similarly, these unrecorded wind directions were also designated with bluish color in Table 4.5. On the other hand, the other month data were also shown with bluish color in Tables 4.3, 4.4, and 4.6, including monthly average wind speed, monthly

average electricity generations per hour, and monthly average air temperature data, and corresponding to these unrecorded monthly average wind direction data. Since, many suitable data of these cited months for these cited parameters in the cited tables were processed, unlike the unrecorded monthly average wind direction data; processed suitable data for these parameters gave reasonable calculations as presented in these tables.

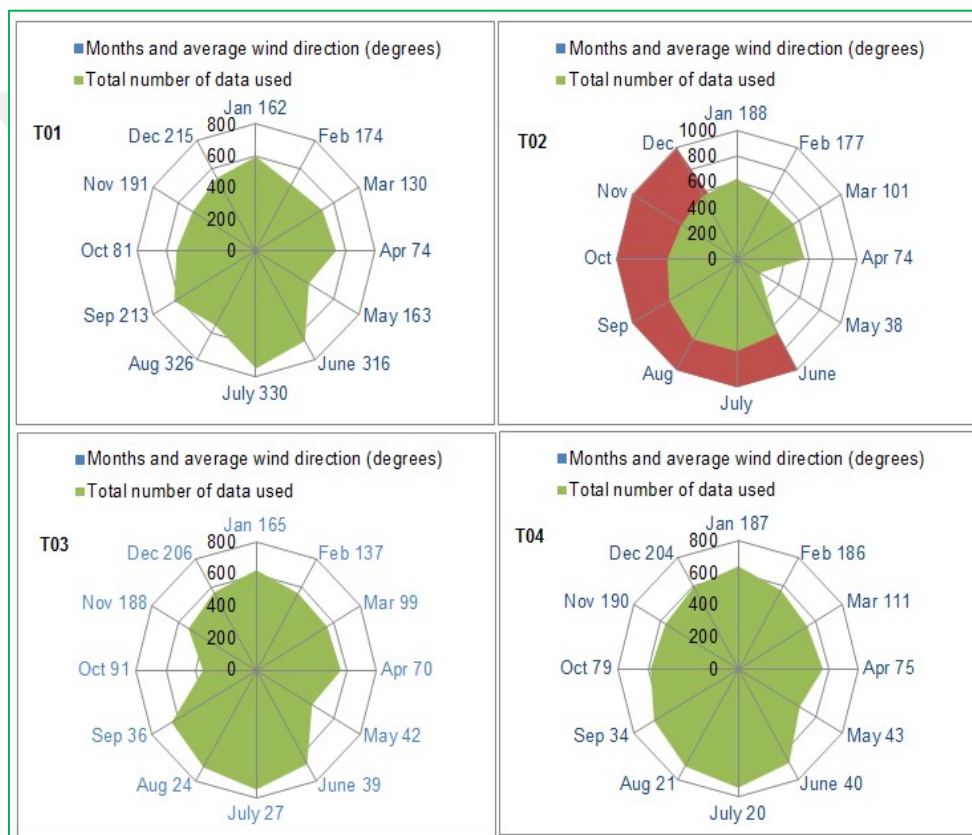


Figure 4.8. Monthly distributions of wind direction for wind turbines T01, T02, T03, and T04

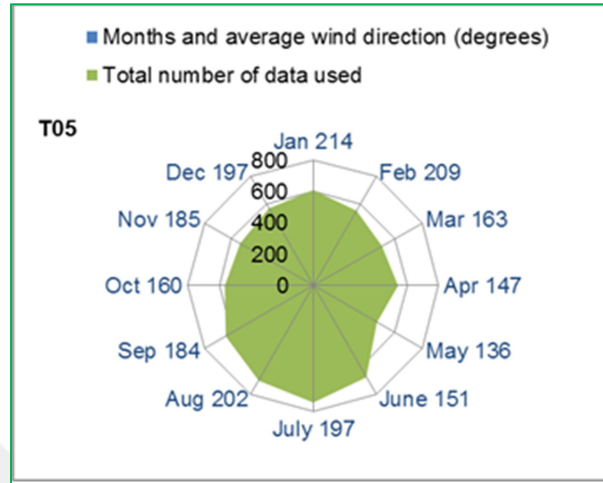


Figure 4.9. Monthly distributions of wind direction for wind turbine T05

4.2.3.2. Introduction of Cut-in and Cut-out Speeds

Average data presented in Tables 4.3, 4.4, 4.5, and 4.6 are acquired with the consideration of cut-in and cut-out speeds of wind turbines, elimination of error power generation values including zero and negative values, and elimination of unrecorded wind directions (using boundary values). Maximum wind powers were obtained using wind speeds presented in Table 4.3 and Eq. 3.9 was used for the calculations. Theoretical wind powers were determined according to the wind speed data given in Table 4.3 with the utilization of Eq. 3.10. Efficiency calculations were performed by Eq. 3.28. Real powers were directly taken from Table 4.4 which were computed by taking average values of hourly data.

These estimations were given for each discrete wind turbines distributed for each month of the 2010 year. Table 4.7 contains related computed data for wind turbines T01, T03, T04, and T05.

Distribution of expression $C_p - \tau$ for four turbines regarding Eqs. (3.28) and (3.25) is given in Figure 4.10; whereas, $C_T - \tau$ variation of the same wind turbines is shown in Figure 4.11 with using Eqs. (3.34) and (3.25).

Figure 4.12 presents the change of power efficiency, C_p for the flow induction factor, a by considering Eqs. (3.33), (3.32), and finally (3.29), respectively.

As it is mentioned above, thrust coefficient (C_T) and flow induction factor (a) are related by Eq. (3.35). This relation considering four turbines is given in Figure 4.13.

Wind speed far on the wake, (U_w) and free-stream wind speed at upstream of the rotor, U_∞ are related through the exploitation of Eq. (3.24) as demonstrated in Figure 4.14.

For determination of data presented in Figure 4.15, Eq. (3.23) was used in order to relate wind speed on the rotor (U_D) and free-stream wind speed, U_∞ upstream of the rotor.

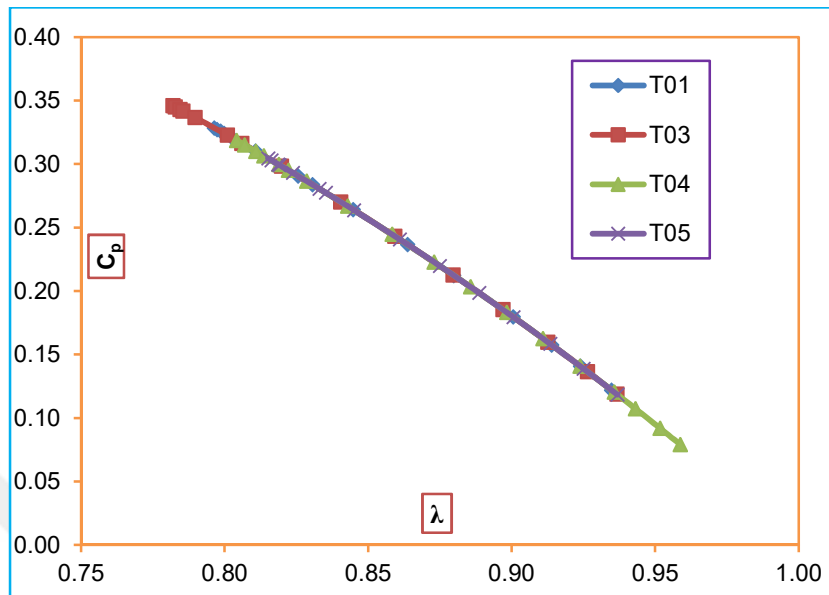
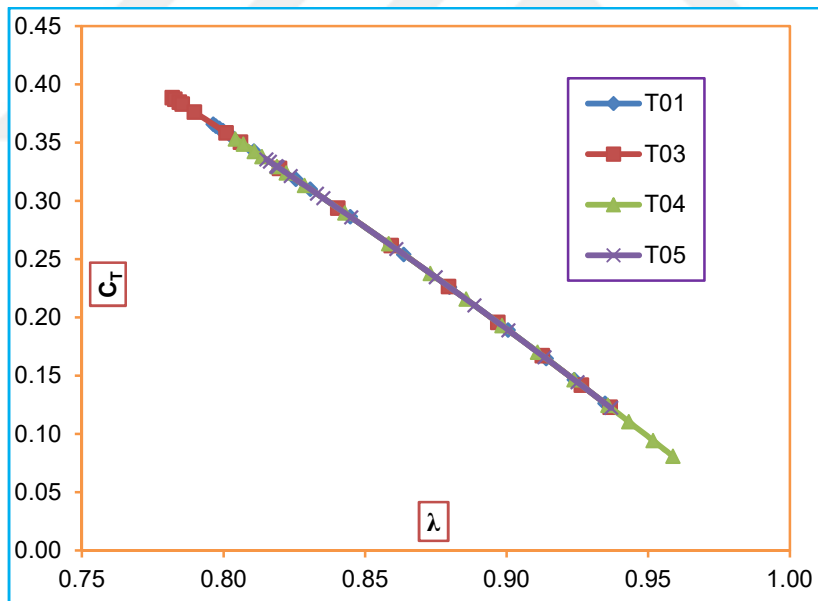
By using Eq. (3.23), free-stream velocity, U_∞ was estimated; since the given wind speed values were measured at a rotor plane. On the other hand, generated real power values are already presented in Table 4.7. Consequently, the variation of real power generation with free-stream velocity, U_∞ are presented in Figure 4.16. When this figure is carefully analyzed, it is observed that through approaching cut-in and cut-out speeds, power generations either stop or approach to a maximum limit. Eq. (3.26) gives the relation between thrust force, T and free-stream wind speed, U_∞ for all turbines considering twelve months and obtained results are shown in Figure 4.17.

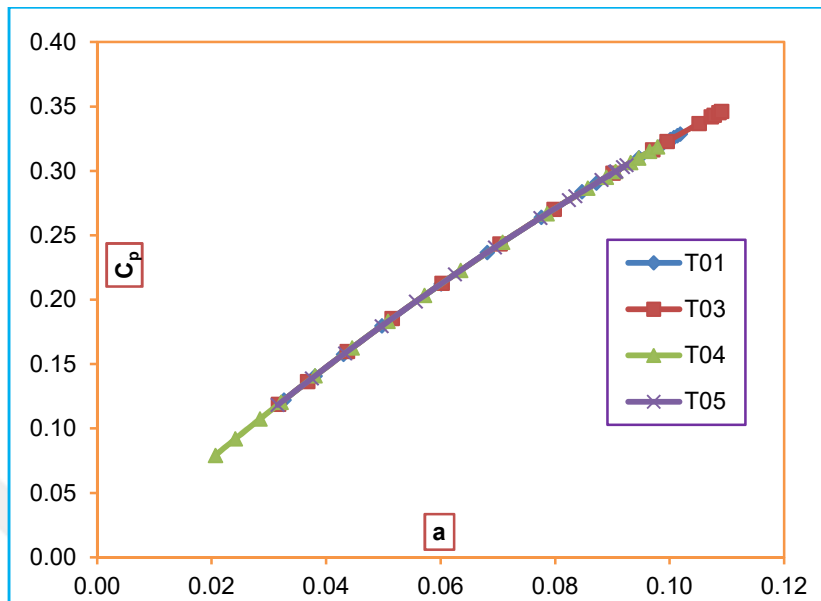
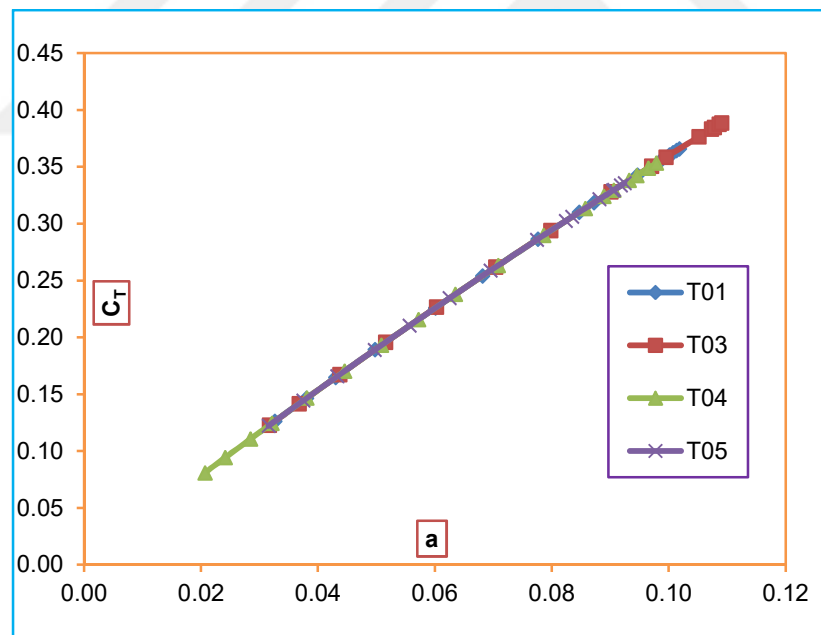
Variations of actual power generation and thrust force, T with free-stream wind speed, U_∞ for all wind turbines presented in Figures 4.16 and 4.17 throughout twelve months are more or less the same.

Table 4.7. Power efficiencies of wind turbines including T01, T03, T04, and T05

Turbine no	Wind speed (m/s)	Maximum power (kW)	Theoretical power (kW)	Real power (kW)	Efficiency
T01	4.8542	445.6982	264.1174	115.8390	0.2599
	6.0351	856.5000	507.5556	251.3872	0.2935
	7.1572	1428.5968	846.5759	426.2730	0.2984
	8.2743	2207.3699	1308.0710	661.6781	0.2998
	9.4016	3238.0499	1918.8444	974.3245	0.3009
	10.4749	4478.5340	2653.9461	1329.9973	0.2970
	11.5412	5990.0773	3549.6754	1701.8768	0.2841
	12.4639	7544.7621	4470.9701	2008.2902	0.2662
	13.4355	9450.2355	5600.1395	2285.4070	0.2418
	14.3531	11521.6548	6827.6473	2497.6512	0.2168
	15.2248	13751.0976	8148.7986	2673.9116	0.1945
	16.1984	16561.4152	9814.1720	2724.9523	0.1645
	17.0716	19386.5748	11488.3406	2798.0730	0.1443
	17.8630	22209.8284	13161.3798	2864.3308	0.1290
18.7791	25805.0456	15291.8789	2884.7340	0.1118	
T03	4.9233	464.9877	275.5483	134.7493	0.2898
	6.0929	881.3775	522.2978	276.0047	0.3132
	7.2370	1476.8998	875.1999	464.1775	0.3143
	8.3490	2267.7116	1343.8291	718.9983	0.3171
	9.4530	3291.4989	1950.5179	1040.5259	0.3161
	10.5174	4533.2110	2686.3473	1398.1634	0.3084
	11.5628	6023.8053	3569.6624	1780.7973	0.2956
	12.5354	7675.2377	4548.2890	2097.2404	0.2732
	13.4731	9529.8545	5647.3212	2359.2805	0.2476
	14.4110	11661.7551	6910.6697	2598.4248	0.2228
	15.3588	14117.2667	8365.7877	2751.5994	0.1949
	16.2030	16575.5669	9822.5582	2815.4732	0.1699
	17.2275	19922.5552	11805.9586	2917.2658	0.1464
	18.1135	23157.4471	13722.9316	2894.9068	0.1250
19.0480	26929.7331	15958.3603	2930.7750	0.1088	
T04	4.8807	453.0365	268.4661	122.4706	0.2703
	6.0234	851.5431	504.6181	248.5066	0.2918
	7.1199	1406.3880	833.4151	405.8159	0.2886
	8.2053	2152.6312	1275.6333	611.2681	0.2840
	9.3222	3156.7560	1870.6702	886.1574	0.2807
	10.3743	4350.6705	2578.1751	1193.7902	0.2744

	11.4162	5797.5271	3435.5716	1521.2887	0.2624
	12.4037	7435.9902	4406.5127	1817.1450	0.2444
	13.3638	9299.6407	5510.8982	2083.4820	0.2240
	14.3495	11513.0491	6822.5476	2348.4563	0.2040
	15.2871	13920.4128	8249.1335	2591.5827	0.1862
	16.2272	16650.0439	9866.6927	2792.9743	0.1677
	17.1461	19641.7550	11639.5585	2925.3417	0.1489
	18.0498	22913.7882	13578.5411	2957.9491	0.1291
	19.0750	27044.1911	16026.1873	2982.0494	0.1103
	19.8078	30282.4839	17945.1757	2977.9515	0.0983
	20.8706	35423.2427	20991.5512	2983.6730	0.0842
	21.9236	41059.6220	24331.6278	2978.8525	0.0725
T05	4.8353	440.4980	261.0359	111.9293	0.2541
	6.0091	845.4752	501.0223	235.7734	0.2789
	7.0869	1386.9045	821.8693	384.7237	0.2774
	8.1803	2133.0148	1264.0088	585.6881	0.2746
	9.2691	3103.0995	1838.8738	850.4058	0.2741
	10.3372	4304.1979	2550.6358	1155.1794	0.2684
	11.3677	5723.9545	3391.9730	1470.3233	0.2569
	12.3900	7411.3334	4391.9013	1789.1887	0.2414
	13.3765	9326.2484	5526.6657	2055.6961	0.2204
	14.3002	11394.7150	6752.4237	2293.1810	0.2012
	15.2531	13827.9953	8194.3676	2514.0166	0.1818
	16.1750	16489.7061	9771.6777	2711.1743	0.1644
	17.0856	19434.4234	11516.6953	2821.0584	0.1452
	18.0232	22812.7127	13518.6446	2901.7680	0.1272
19.1645	27426.6182	16252.8108	2971.9598	0.1084	

**Figure 4.10.** $C_p - \lambda$ distribution**Figure 4.11.** $C_T - \lambda$ distribution

Figure 4.12. $C_p - a$ distributionFigure 4.13. $C_r - a$ distribution

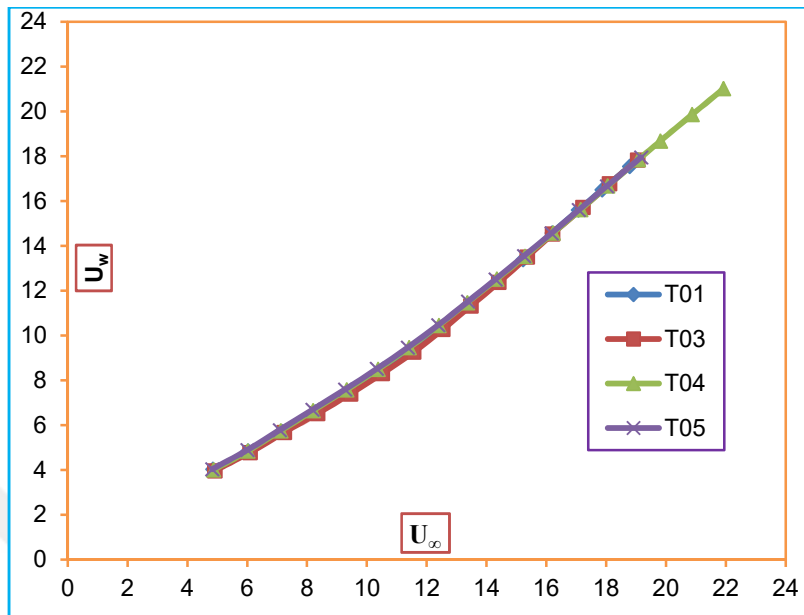


Figure 4.14. $U_w - U_\infty$ distribution

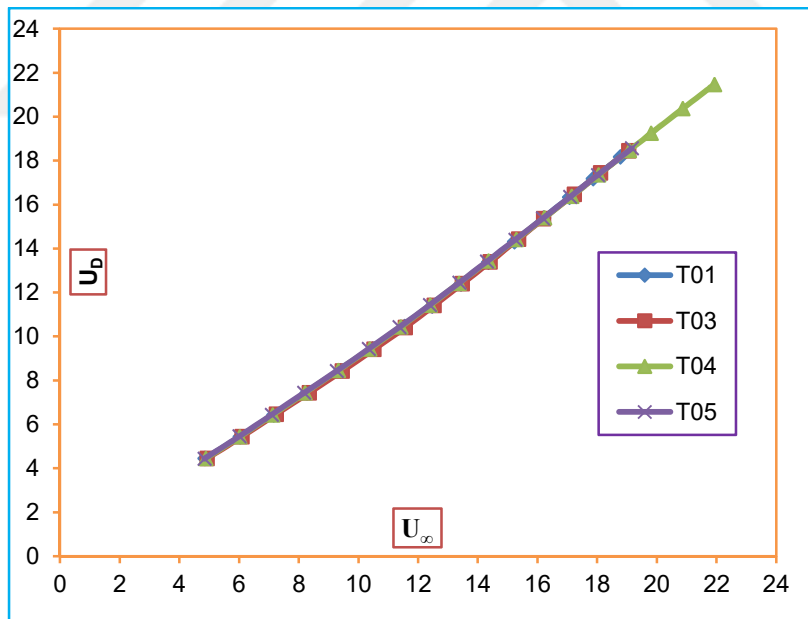


Figure 4.15. $U_D - U_\infty$ distribution

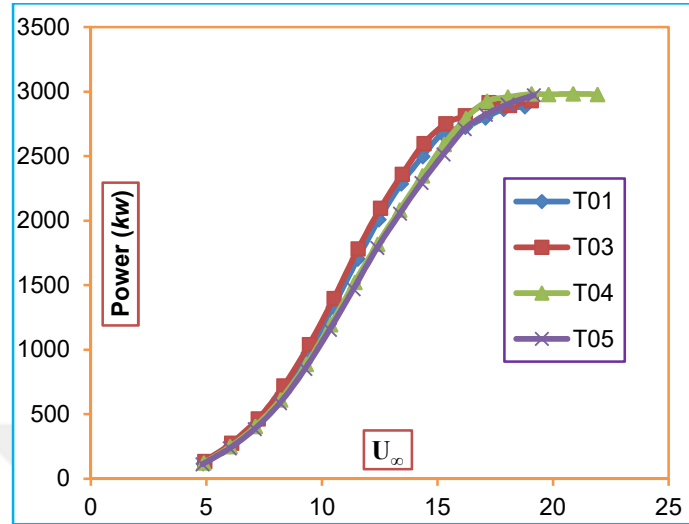


Figure 4.16. Power - U_∞ distribution

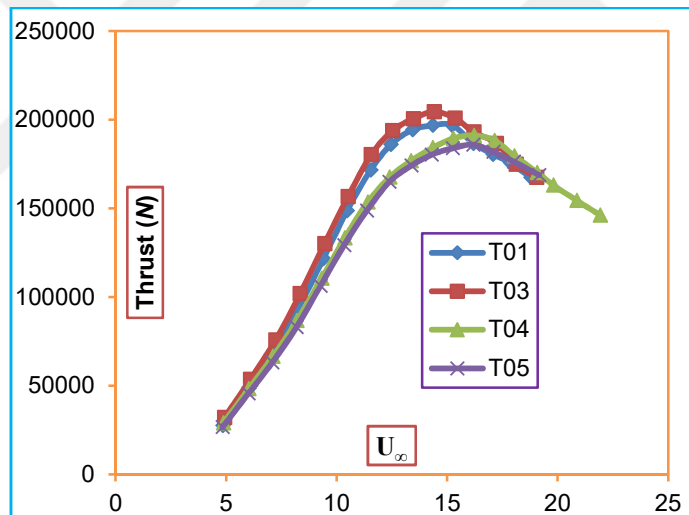


Figure 4.17. Thrust - U_∞ distribution

Figure 4.18 refers to total energy generation of five wind turbines with an average wind speed presented throughout twelve months. It can be seen that all turbines generate electricity throughout twelve months. However, the highest power generation occurs in July with a highest mean wind speed. It was concluded

that 11.90 m/s and 7.15 GWh of mean wind speed and generated power, respectively were reported in this month.

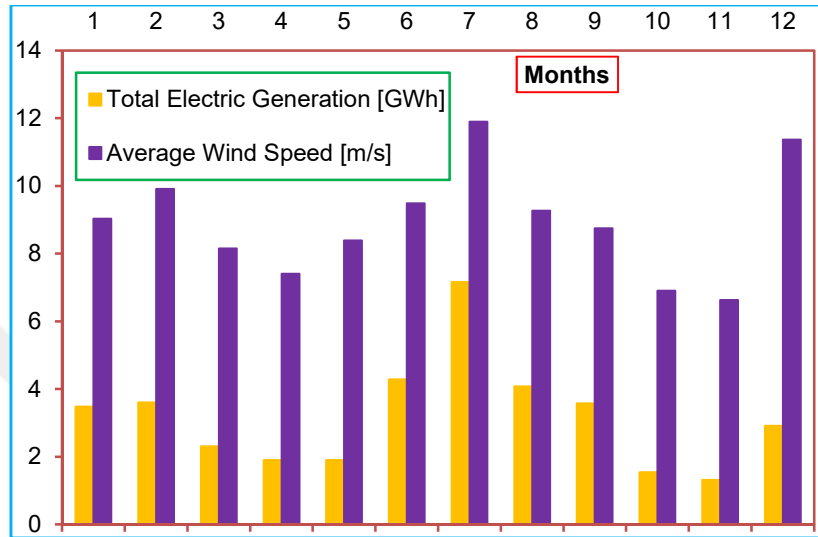


Figure 4.18. Monthly total electric generations and average wind speeds

4.2.4. Concluding Remarks

According to the data obtained from the wind farm, firstly analyses were performed without taking cut-in and cut-out speeds into consideration. Monthly averages wind data were used in the estimations of related parameters. At very low speeds, a wind turbine cannot generate electricity where it is expressed in its specifications as cut-in speed. Maximum power and real power generally increase with increasing free-stream wind speeds (U_{∞}) when cut-in speeds are considered, however efficiencies decreases to meaningful values.

It is observed that maximum power generations occur in July for all wind turbines, when average wind speed (U_{∞}) is maximum, and air temperature is also high compared with other months for all turbines. In addition, almost non-stop generations take place this month for all wind turbines.

The total electric generation of five turbines was 38.09 GWh in the year of 2010. Wind turbine T04 generated 9.03 GWh of electricity. The maximum power was generated by turbine T04; on the other hand, wind turbine T01 generated 6.12 GWh electricity. Although both wind turbines are installed in the same wind farm, the difference in electric production in between turbine T01 and T04 is 33% in the year of 2010. This wind farm is situated in the valley containing many hills, crests, and roughness. This topographic condition of the farm effects wind directions and magnitude of wind speed, U_{∞} , thus the generated output power.

4.3. Aerodynamic Characteristics of a Horizontal Axis Wind Turbine in Belen-Hatay, Turkey

4.3.1. Introduction

Wind turbine aerodynamic characteristics play a vital role in condition monitoring and control of wind turbines in a wind power plant. Today, the most common design of a wind turbine is the horizontal axis wind turbine. In this part of the dissertation; horizontal axis wind turbine aerodynamic characteristics including wind power (P), power coefficient (C_p), axial flow induction factor (a), thrust coefficient (C_T), and thrust (T) were determined as a function of the hub-height wind speed. The data used in this part of the dissertation were measured from the Belen Wind Power Plant which is located in Belen province in Hatay, Turkey and the total installed capacity of that power plant is 48 MW which is composed of 16 identical wind turbines. The selected 5 of 16 wind turbines were evaluated by means of aerodynamic characteristics in detail. As a result, for five turbines, the maximum wind power capacity reached 3 MW when the hub-height wind speed was 15 m/s. Also, the maximum power coefficient of all turbines was calculated to be in the range 30% - 35%.

4.3.2. The objective of the Present Work

As seen, wind energy is developing towards mainstream, competitive, and reliable power technology. Globally, the progress of wind power technology continues to be strong in further involved countries and increases annual installed capacity having more investments. According to the (IEA, 2013b), wind power could generate up to 18% of the World's electricity by 2050. Technology improvements have continuously reduced energy costs, especially on land. Many wind turbines are being constructed to obtain energy from wind. However, regions which have high wind energy density are finite. Therefore, many researches make an effort to increase the energy efficiency of the wind turbines. In this context, wind turbine aerodynamic characteristics are important tools in turbine performance monitoring, turbine control and power forecasting (Bilgili et al., 2015b). Generally, horizontal axis wind turbines (*HAWT*) having a single rotor is used for conventional wind turbine systems. In this study, aerodynamic characteristics of *HAWT* including P , C_p , a , C_T , and T were determined as a function of the hub-height wind speed.

Definition and understanding of aerodynamic parameters clearly, especially wind turbine output power, P and power coefficient, C_p provide answers to questions including correct settlements of wind turbine installations in a considered wind zone. Considering the regions possible to be used for power generations are not infinite, the efficiency and aerodynamic concept of wind turbines are required to be well understood for the most effective power generations.

4.3.3. The Technique of the Study

4.3.3.1. Study Area and Data Description

The data used in this study were measured from Belen Wind Power Plant (*WPP*). Belen *WPP* was put into operation in 2009 and situated in Hatay region of Turkey. In the first phase, the installed capacity of the plant was only 30 MW. In 2010, the 6-MW capacity expansion provided with temporary admission, thus Belen *WPP* has later reached 36 MW by 2010. The total installed capacity of Belen *WPP* increased to 48 MW with four additional turbines in 2012, and annual production amounts to about 150 million kWh. Belen *WPP* includes 16 identical wind turbines with each having the rated capacity of 3 MW and the hub height of 80 m. The cut-in speed, rated speed, and cut-out speed of the turbines are 4 m/s, 15 m/s, and 25 m/s, respectively. Turbines of *WPP* are the Vestas V90-3 MW wind turbine types. The VESTAS V90-3 MW wind turbine is a pitch regulated upwind turbine with active yaw and a three-blade rotor. It has a rotor diameter of 90 m with a generator rated at 3.0 MW. Five VESTAS V90-3 MW wind turbines (*T1*, *T2*, *T3*, *T4*, and *T5*) were selected to investigate the aerodynamic characteristics of these wind turbines. On the other hand, the important specifications of the three-bladed identical wind turbines having a hub-height of 80 m are provided in Table 4.8. The rotor swept area considering 90 m of rotor diameter corresponds to an area of 6362 m². Nominal revolutions of the wind turbines are 16.1 rpm. Operation period of wind turbines is ranged from 8.6 rpm to 18.4 rpm. Wind turbines operate in a speed interval of $4m/s \leq U_D \leq 25m/s$. However, the nominal speed of wind turbines is 15 m/s. Rated output power generation, P of a single wind turbine is 3000 kW.

Table 4.8. Wind turbine technical specifications

Equipment	Properties
Rotor	
Diameter	90 m
Area swept	6,362 m ²
Nominal revolutions	16.1 rpm
Operational interval	8.6-18.4 rpm
Number of blades	3
Power regulation	Pitch/OptiSpeed
Air brake	Full blade pitch by three separate hydraulic pitch cylinders
Tower	
Hub height	80 m
Operational data	
Cut-in wind speed	4 m/s
Nominal wind speed	15 m/s
Cut-out wind speed	25 m/s
Generator	
Type	Asynchronous with OptiSpeed
Rated output	3,000 kW
Operational data	50 Hz, 1000 V
Gearbox	
Type	Two planetary and one helical stage
Control	
Type	Microprocessor-based control of all the turbine functions with the option of remote monitoring. Output regulation and optimization via OptiSpeed and OptiTip pitch regulation

4.3.3.2. Aerodynamic Concept

The energy extracting actuator disc and stream-tube concept which was illustrated in Figure 3.2 and the analysis including the assumptions of continuous, homogenous, incompressible, steady state, no frictional drag, infinite number of blades, uniform thrust, non-rotating wake, far upstream and downstream static

pressure being equal to atmospheric pressure situation which are as well defined in Section 3.3 are used as the aerodynamic concept for this part of the dissertation.

4.3.4. Results and Discussions

The variation of wind turbine output power, P values as a function of hub-height, U_D wind speeds are shown in Figure 4.19. As seen in this figure, obtained results for whole turbines are in a similar trend based on rotor wind speed, U_D . For whole wind turbines, the maximum wind output power was obtained at a wind speed of 15 m/s. On the other hand, it was concluded that the best results were taken from the second wind turbine, $T2$.

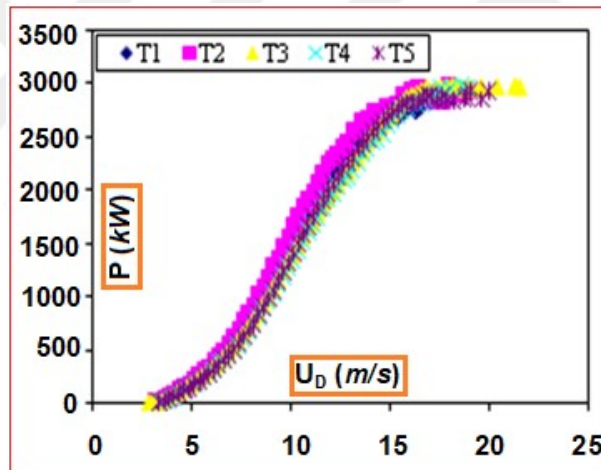


Figure 4.19. Distribution of power generation, P with hub-height wind speed, U_D

Moreover, Figure 4.20 presents the variation of flow induction factor, a versus hub-height wind speed, U_D on the rotor. Maximum flow induction factor values are existed with U_D in the range of $5 \text{ m/s} \leq U_D \leq 11 \text{ m/s}$. Besides, flow induction factor values increase rapidly for $U_D \geq 5 \text{ m/s}$. Similarly, the values decrease rapidly for $U_D \geq 10 \text{ m/s}$.

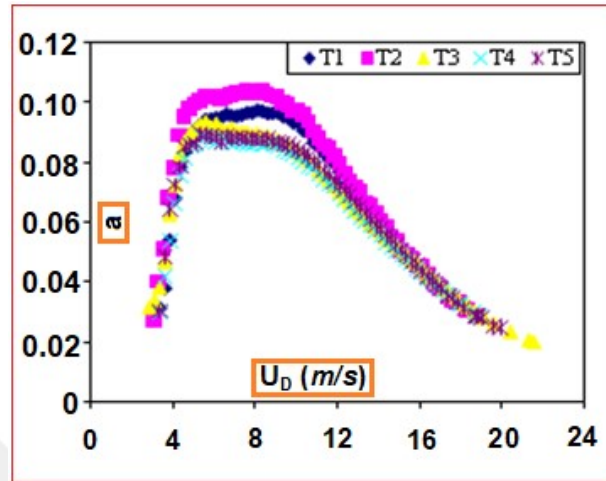


Figure 4.20. Variation of flow induction factor, a with hub-height wind speed, U_D

Comparisons of the power coefficient, C_p with hub-height wind speed, U_D for five turbines are given in Figure 4.21 and relations between thrust coefficient, C_T and hub-height wind speed, U_D on the rotor were analyzed for five turbines, and calculated results were also presented in Figure 4.22. Power coefficient, C_p and thrust coefficient, C_T are maximum with velocities in the range of $5 \text{ m/s} \leq U_D \leq 11 \text{ m/s}$. These results indicate that the design of the blade is capable of getting maximum power capacity for existing wind speed. But, there is a power variation between turbines. For example, while turbine $T2$ generates maximum peak power with a power coefficient percentage of 34%; turbine $T4$ produces minimum peak power with a power coefficient percentage of 29 considering the same hub-height wind speed, U_D .

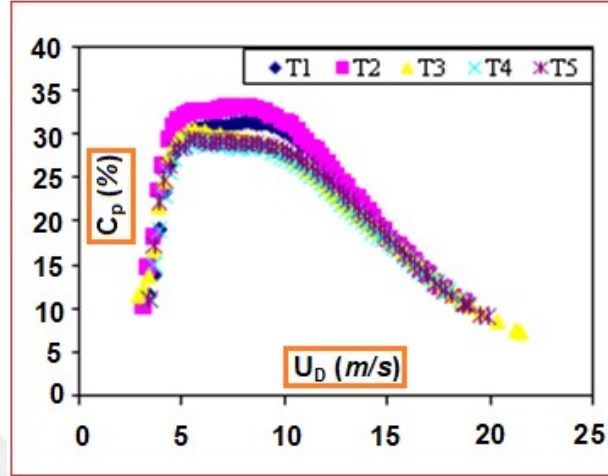


Figure 4.21. Relation of power coefficient, C_p with hub-height wind speed, U_D

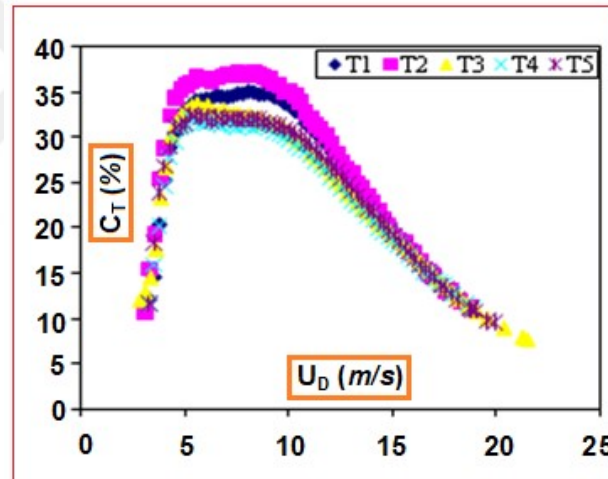


Figure 4.22. Distribution of thrust coefficient, C_T with hub-height wind speed, U_D on the impeller

Variations between thrust force, T with respect to hub-height wind speed, U_D are presented in Figure 4.23. It is seen that the thrust force, T is extremely important for the performance of a wind turbine. Linear variations of the thrust forces depending on the hub-height wind speed, U_D are similar for all turbines considering $U_D \leq 7.5 \text{ m/s}$. For higher values of hub-height wind speed, U_D , it is

obvious that wind turbine, $T2$ generates maximum peak thrust reaching at approximately a value of $T=200$ kN, whereas turbine, $T4$ generates minimum peak thrust force about $T=170$ kN. The peak values of the thrusts are generally obtained at approximately hub-height wind speed, U_D corresponding to 14 m/s. In additions, there is a rapid decrease of thrust forces for whole wind turbines considering hub-height wind speeds, U_D which is greater than 14 m/s. Thrust force is presented as a function of hub-height wind speed, U_D with the expression of $T = 2\rho A_d U_d^2 (a/(1-a))$. Consequently, increasing hub-height wind speed, U_D above 14.86 m/s, this U_D^2 term can no longer suppress the decreasing trend of flow induction factor, a and the expression $a/(1-a)$; where the decreasing trend of both terms start over the values of 8.10 m/s. As a result, hub-height wind speed, U_D equivalent to 14.86 m/s for wind turbine $T2$ is the breaking point where thrust force, T with respect to U_D rapidly falls down.

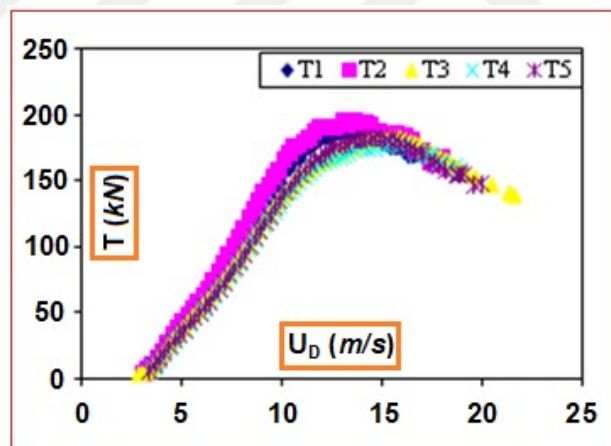


Figure 4.23. Variation of thrust force, T with hub-height wind speed, U_D

4.3.5. Concluding Remarks

Wind power is playing a more significant role in energy supply systems and as well in more sustainable environmental conditions. In this part of the dissertation, aerodynamic characteristics of horizontal axis wind turbines such as wind power, power coefficient, axial flow induction factor, thrust coefficient, and thrust force were determined as a function of the hub-height wind speed, U_D . The results obtained can be given and summarized as follows;

Generated power increases with increasing hub-height wind speed, U_D . Maximum flow induction factors, a are determined for hub-height wind speed, U_D in the range of $5 \text{ m/s} \leq U_D \leq 11 \text{ m/s}$. This is also the case in power coefficient, C_p and thrust coefficient, C_T parameters. Through exceeding the rotor wind speed that is greater than 11 m/s, related parameters of flow, such as flow induction factor, a , power coefficient, C_p , and thrust coefficient, C_T decrease rapidly. Finally, thrust force, T is maximum with hub-height wind speed, U_D in the range of $12 \text{ m/s} \leq U_D \leq 14 \text{ m/s}$. Turbine, $T2$ generates maximum peak power efficiency with a percentage of 34%; whereas turbine, $T4$ produces minimum peak power efficiency with a percentage of 29%.

Although identical wind turbines are used in the considered wind farm, there are at approximately 15% differences between maximum and minimum values of the power coefficients. The differences in power coefficient values that occur between turbines in this wind farm are due to the obstacles, roughness, wind directions, and topographical effects.

4.4. Analysis of Aerodynamic Characteristics of 2 MW Horizontal Axis Large Wind Turbine

4.4.1. Introduction

In this part of the dissertation, aerodynamic characteristics of horizontal axis wind turbines (*HAWT*) were evaluated and discussed in terms of measured data in the existing onshore wind farm. Five wind turbines (*T1*, *T2*, *T3*, *T4*, and *T5*) were selected, and hub-height wind speed, U_D , wind turbine power output, P , and turbine rotational speed, Ω data measured from these turbines were used for the evaluation. In order to obtain characteristics of axial flow induction factor, a , power coefficient, C_p , thrust force coefficient, C_T , thrust force, T , and tangential flow induction factor, a' ; the Blade Element Momentum (*BEM*) theory was used. According to the results obtained, during a year, the probability density of turbines at a rotational speed of 16.1 rpm was determined as approximately 45%. Optimum tip speed ratio was calculated to be $\lambda_R=7.12$ for the most efficient wind turbine. On the other hand, the maximum power coefficient, C_p was found to be 30% corresponding to this tip speed ratio, λ_R .

4.4.2. The Objective of this Part of the Work

Monitoring of operating wind turbine aerodynamic characteristics and dealing with the efficiency of an operating wind farm provides a vision of new wind turbine or farm installations in the considered location. In this way, the consisting foresight in this subject can result in the increase of the effectiveness of new installations, since the high-speed windy regions in the World are not infinite.

Selected wind turbines of the farm symbolized as *T1*, *T2*, *T3*, *T4*, and *T5* were used to evaluate the performance of wind turbines using parameters such as power output, P , hub-height wind speed, U_D , and turbine rotational speed, Ω . The

performance analysis of these wind turbines was revealed in terms of presenting whole turbine aerodynamic parameters including output power values as well as wind turbine efficiencies.

4.4.3. Examination of the Location of the Wind Farm and Analysis of the Working Efficiency of the Turbines

The data used for this part of the dissertation was provided from the Sebenoba Wind Energy Power Plant (*WEPP*), as the map location, altitude, and the density distribution of the average free-stream wind speed are presented in Figure 4.24. By the year 2008, this *WEPP* was initially put into operation including 17 identical wind turbines, and the rated capacity of each turbine was 2 MW. The hub height of the identical wind turbines is 67 m, and the rotor diameter corresponds to 80 m. Consequently, the total swept area of a single wind turbine is approximately 5027 m². These and the other technical specifications of the identical wind turbines are provided in Table 4.9. The wind turbines operate with wind speeds within the speed range of $4 \text{ m/s} \leq U_{\infty} \leq 25 \text{ m/s}$, and the nominal speed of the turbines corresponds to 15 m/s. Wind turbines are the pitch regulated upwind turbines with an active yaw and a three-bladed rotor.

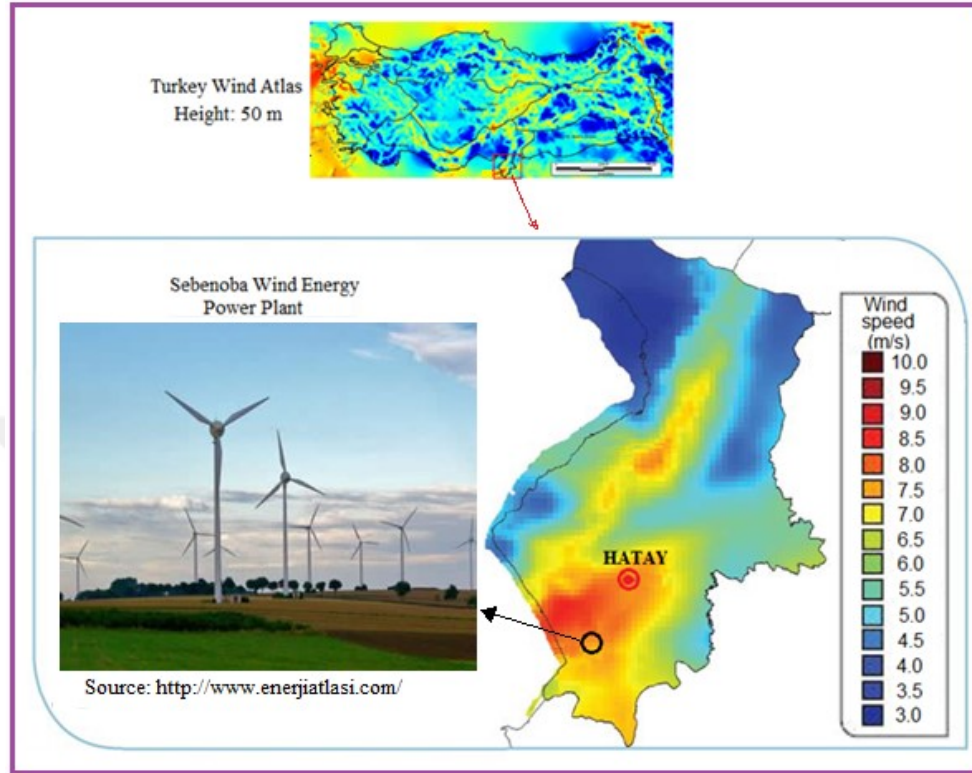


Figure 4.24. Sebenoba wind power plant in Hatay province (REGD, 2017)

The existing data belongs to the whole year of 2013 with measurements taken in a period of every 10 minutes. Initially, 52560 ($365 \times 24 \times 6$) original data of hub-height wind speed, U_D , turbine rotational speed, Ω , and generated output power, P were categorized into a suitable number of classes. For the probability distribution of rotational speed, Ω ; class limits were determined as 1.00-2.99 rpm, 3.00-4.99 rpm, 5.00-6.99 rpm, 7.00-8.99 rpm, 9.00-10.99 rpm, 11.00-12.99 rpm, 13.00-14.99 rpm, and 15.00-16.99 rpm. The average value in terms of rotational speed, Ω considering five turbines taking the average observation values of each turbine into account was computed. In this way, considering all turbines, average values of observations for all classes were calculated to be 2.02 rpm, 4.10 rpm, 6.05 rpm, 8.08 rpm, 10.10 rpm, 12.44 rpm, 13.94 rpm, and 16.14 rpm as a function

of rotational speed, Ω . Since average values of observations contain multi-data, a secondary operation is performed for all wind turbines where parameters such as hub-height wind speed, U_D , and output power, P are defined concerning the average observation values of rotational speed, Ω .

Table 4.9. Technical properties of wind turbines (*VESTAS 2017*)

Equipment	Properties
Rotor	
Diameter	80 m
Area swept	5,027 m ²
Nominal revolutions	16.7 rpm
Operational interval	9-19 rpm
Number of blades	3
Power regulation	Pitch/OptiSpeed
Air brake	Full blade pitch by three separate hydraulic pitch cylinders
Tower	
Hub height	67 m
Operational data	
Cut-in wind speed	4 m/s
Nominal wind speed	15 m/s
Cut-out wind speed	25 m/s
Generator	
Type	Asynchronous with OptiSpeed
Rated output	2,000 kW
Operational data	50 Hz, 690 V
Gearbox	
Type	Planet / parallel axles
Control	
Type	Microprocessor-based control of all the turbine functions with the option of remote monitoring. Output regulation and optimization via OptiSpeed and OptiTip pitch regulation

The probability density of rotational “speed, Ω over a year is presented in Figure 4.25. As seen from the figure, the rotational probability of wind turbines at the rotational speed, Ω of 0 rpm is approximately 22%. This data was probably formed for the cases of no wind case or sudden change of the rotor position because of rapid alterations in wind speed, vortices forcing to change the position of the rotor, and these results may also be obtained due to the breakdowns or maintenance of the wind turbines. In additions, for certain reasons such as maintenance and cut-out wind speed (beyond 25 m/s), no electric energy production can happen. On the other hand, the rotation probability of the turbines over a year is approximately 45% having a rotational speed, Ω of 16.11 rpm, at which the wind turbines have a nominal power production. Furthermore, all wind turbines operate at a nominal and close to nominal rotational speeds, Ω over half of the year. On the other hand, the rotation probability of wind turbines is very low (2%) at rotational speeds, Ω between 2.07 rpm and 10 rpm over a year.

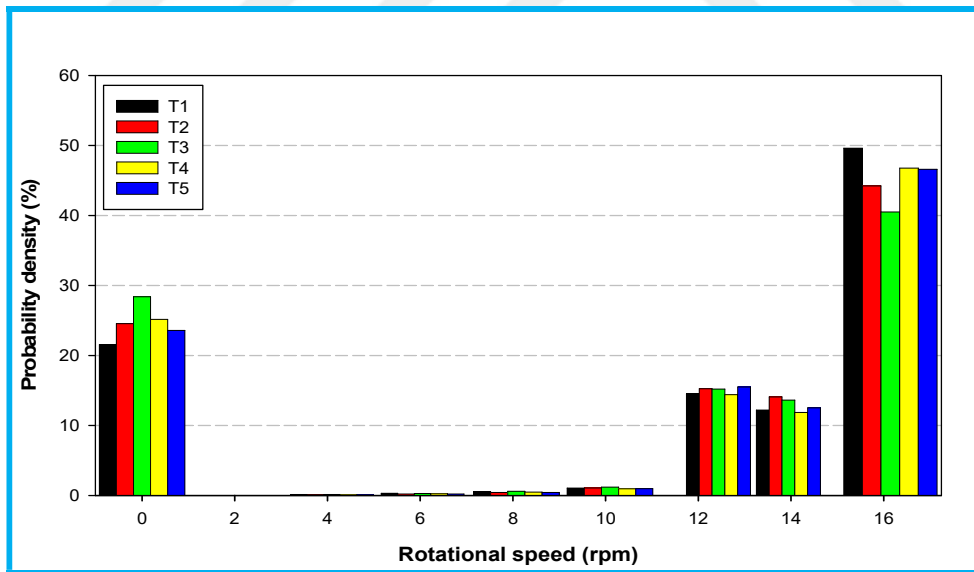


Figure 4.25. Probability density of rotational speed, Ω

4.4.4. Results and Discussions

Figure 4.26 reveals the variation of the extracted output power, P depending on the hub-height wind speed, U_D for different rotational speeds, Ω considering wind turbine TI . It is also clear from this figure that enhancement of power, P can generally be achieved by the increase of hub-height wind speed, U_D , or wind turbine rotational speed, Ω . However, in terms of power, P , and hub-height wind speed, U_D depending on a constant rotational speed, Ω ; it is observed that this increase of power, P is seen only up to a particular value of hub-height wind speed, U_D . This value of the turbine output power, P at certain rotation speed, Ω is the threshold value of generated power, and thus it is a design property of the wind turbine. On the other hand, the rapid increase of turbine output power, P with respect to the hub-height wind speed, U_D is more apparent in the case of the optimum rotational speed, Ω .

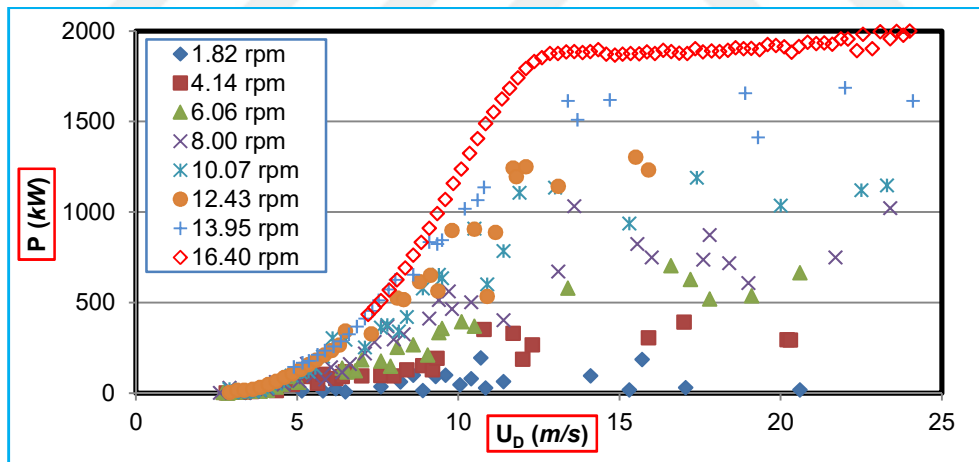


Figure 4.26. Variation of turbine output power, P with hub-height wind speed, U_D at varied rotational speeds, Ω considering wind turbine TI

It is not possible to have the optimum wind power characteristic curve continuously as desired due to wind gusts as seen in Figure 4.26. Sudden and

continuous fluctuations of wind speeds vary between 30% and 50% above or below the average of wind speeds due to the wind gusts. The complex wind structure and gusty wind rapidly alter the wind direction and the magnitude of the wind speed resulting in a large scale vorticity concentration that avoids wind turbines to have optimal wind power generation as seen in Figure 4.26. Consequently, the resultant power output, P of wind turbines are mostly affected by gusty wind characteristics, the incoming wind direction, and as well as terrain roughness characteristics ([Emejemara et al. 2015](#)). In consideration of the effectiveness of the wind speed, and its direction on the wind turbine performances; the topographic conditions must also carefully be taken into account. Namely, orographic elements exert an additional influence on the characteristics of wind. For example, having turbine rotational speed, Ω of 16.40 rpm, the power curve is well defined as the function of hub-height wind speed, U_D . However, having rotational speed, Ω in the range of $1.82 \text{ rpm} \leq \Omega \leq 13.95 \text{ rpm}$ for turbine $T1$ cannot precisely match with the optimized power characteristic curve obtained at a nominal rotational speed of $\Omega = 16.40 \text{ rpm}$. But, they can be designed to simulate this curve near the target range of wind speeds as discussed elsewhere. As mentioned before, the maximum power output rate of wind turbines over a year is approximately 45% under an optimum rotational speed, Ω . However, in the case of rotational speed, Ω ranging from 12.43 rpm to 13.95 rpm, power generation rate occurs at around 30% over a year. Although, there are occasionally high values of hub-height wind speed, U_D varying between 15 m/s and 25 m/s which corresponds to the rotational speeds, Ω in the range of $1.82 \text{ rpm} \leq \Omega \leq 16.40 \text{ rpm}$, a wind power generation rate is very low with fluctuations as seen in Figure 4.26. These rotational speed variations happen due to the complexity of wind. That is to say; it is known that in the atmosphere, catastrophic large scale vortices are developed and, these vortices, unfortunately, alter the direction of wind speed frequently. Because of these reasons, it is not possible for wind turbines to follow the flow direction using a yaw mechanism in a

short period of time. Namely, there is a phase shift between the change of flow direction and yaw mechanism of the wind turbine frequently.

Distributions of wind turbine output power, P , axial flow induction factor, a , power coefficient, C_P , thrust coefficient, C_T , thrust force, T , and tangential flow induction factor, a' based on the dimensionless tip speed ratio, λ_R at an optimum rotational speed ($\Omega=16.4$ rpm) are presented in Figures 4.27-4.32, respectively. Generally, the variation of wind turbine output power, P against tip speed ratio, λ_R reveals that power extracted from a wind turbine is inversely related with tip speed ratio, λ_R . Eq. (3.41) demonstrates that an increase of free-stream wind speed, U_∞ adversely affects the tip speed ratio, λ_R . It is also valid from Eq. (3.27) that free-stream wind speed, U_∞ positively affects the extracted power increase. Thus, under constant rotational speed, Ω , turbine output power, P and the tip speed ratio, λ_R are inversely altered. Regarding this information, for the average of tip speed ratio, 2.90 of five wind turbines corresponds to the average power extraction, P of 2000 kW as seen in Figure 4.27. According to the average data of five wind turbines, power generation rate does not change much for the range of tip speed ratio of $3.2 \leq \lambda_R \leq 5.12$. On the other hand, the power generation rate decreases rapidly for the average tip speed ratio of $\lambda_R > 5.12$. The power extracted at this average tip speed ratio, λ_R value of 5.12 corresponds to a power extraction of $P=1781.41$ kW as an average value of five wind turbines. Power generation results of wind turbines are in a good agreement for the whole range of tip speed ratio as seen in Figure 4.27. It is observed from the data of five wind turbines, the tip speed ratio value of $\lambda_R=5.12$ is the critical value for variation of the power extraction which is altered from a lower slope of curve to a higher slope of curve.

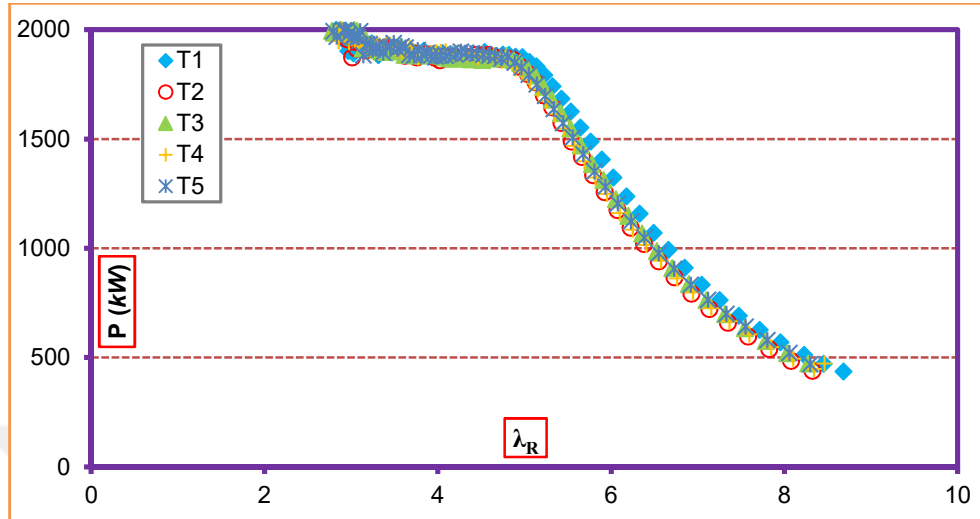


Figure 4.27. Variation of turbine output power, P with the tip speed ratio, λ_R for five wind turbines

Variation of axial flow induction factor, a depending on the tip speed ratio, λ_R for five wind turbines is shown in Figure 4.28. Based on the average data of five wind turbines, a rapid increase of axial flow induction factor, a is observed for the tip speed ratio of $2.81 \leq \lambda_R \leq 6.10$. Here, the range of the average flow induction factor, a was determined to be $0.0124 \leq a \leq 0.0894$. On the other hand, considering this average range of tip speed ratio, λ_R , for example, at $\lambda_R = 2.81$, corresponding free-stream wind speed, U_∞ , and hub-height wind speed, U_D are reported as 24.07 m/s and 23.77 m/s, respectively. However, U_∞ and U_D are reported to be 11.10 m/s and 10.11 m/s, respectively for the tip speed ratio of $\lambda_R = 6.10$.

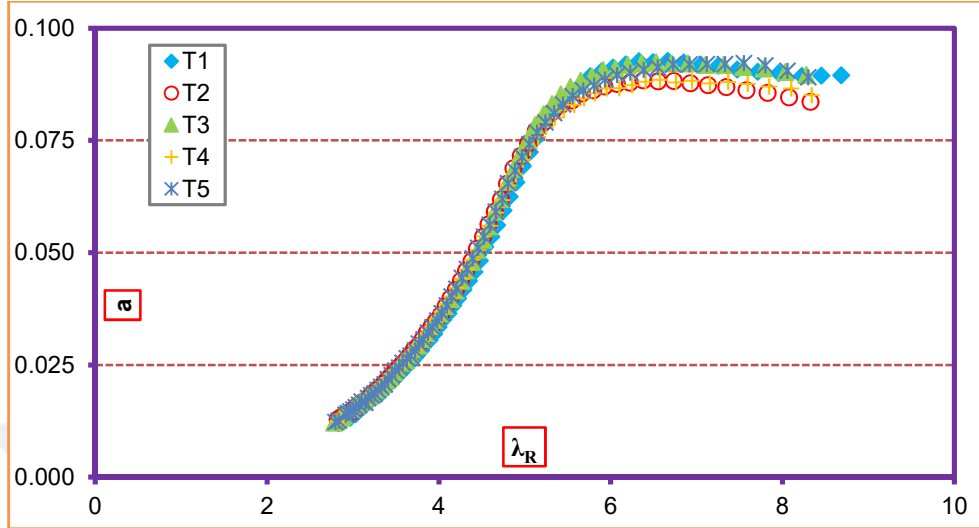


Figure 4.28. Variation of flow induction factor, a with the tip speed ratio, λ_R for five wind turbines

Variation of power coefficient, C_p depending on the tip speed ratio, λ_R is presented in Figure 4.29. An increase of power coefficient, C_p is observed at lower free-stream wind speeds, U_∞ corresponding to higher values of tip-speed ratio, λ_R . According to the average data of five wind turbines considered; a rapid increase of power coefficient, C_p is valid for the average range of tip speed ratio of $2.81 \leq \lambda_R \leq 6.04$. The power coefficient, C_p is computed to be $0.0482 \leq C_p \leq 0.2961$ for the range, $2.81 \leq \lambda_R \leq 6.04$. Thus, power coefficients, C_p of wind turbines are agreed well. In summary, a higher power coefficient values, C_p are obtained at lower free-stream wind speeds, U_∞ ; whereas, lower power coefficient values, C_p are obtained at a higher free-stream wind speeds, U_∞ in this range of tip speed ratio, λ_R . Considering the average data of five wind turbines, maximum power coefficient, C_p was computed as 30.03% at the tip speed ratio of $\lambda_R = 7.12$.

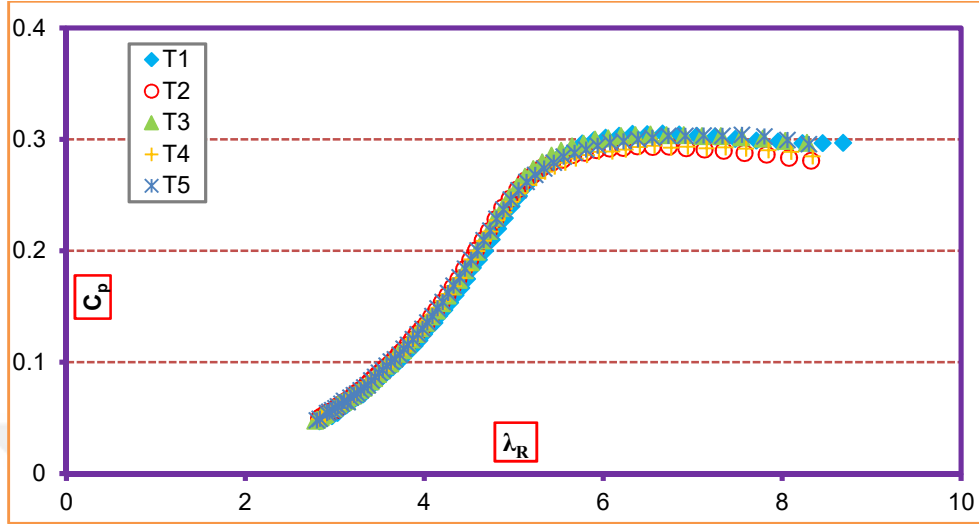


Figure 4.29. Variation of power coefficient, C_p with the tip speed ratio, λ_R for five wind turbines

Considering data of five wind turbines, variation of the thrust force coefficient, C_T depending on the tip speed ratio, λ_R is shown in Figure 4.30. In the range of tip speed ratio of $2.81 \leq \lambda_R \leq 5.31$, the thrust coefficient, C_T shows a rapid increase as the tip speed ratio increases, λ_R . A good agreement is obtained between the thrust coefficient, C_T values of the considered wind turbines.

On the other hand, the variation of thrust force, T depending on the tip speed ratio, λ_R is presented in Figure 4.31. The maximum thrust force, T corresponding to 150 kN occurs at the tip speed ratio of $\lambda_R = 5.21$. The final aerodynamic parameter analysis in this part of the dissertation includes Figure 4.32 indicating the relationship between the angular flow induction factor, a' , and the tip speed ratio, λ_R . Angular flow induction factor, a' for all wind turbines takes a maximum value of $a' = 0.0027$ at the tip speed ratios, λ_R of 5.21. At this condition, a related free-stream wind speed, U_∞ , and a hub-height wind speed, U_D are calculated to be 13.35 m/s and 12.36 m/s, respectively.

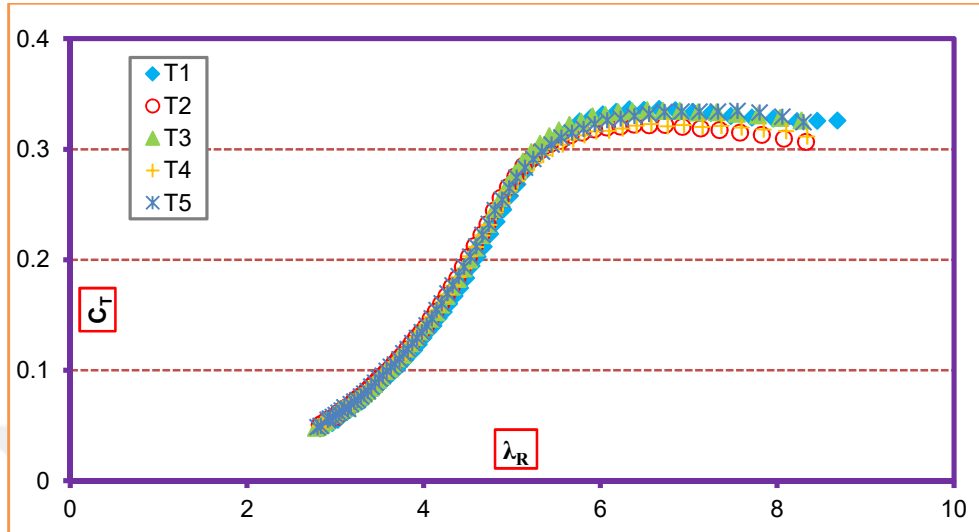


Figure 4.30. Variation of thrust coefficient, C_T with the tip speed ratio, λ_R for five wind turbines

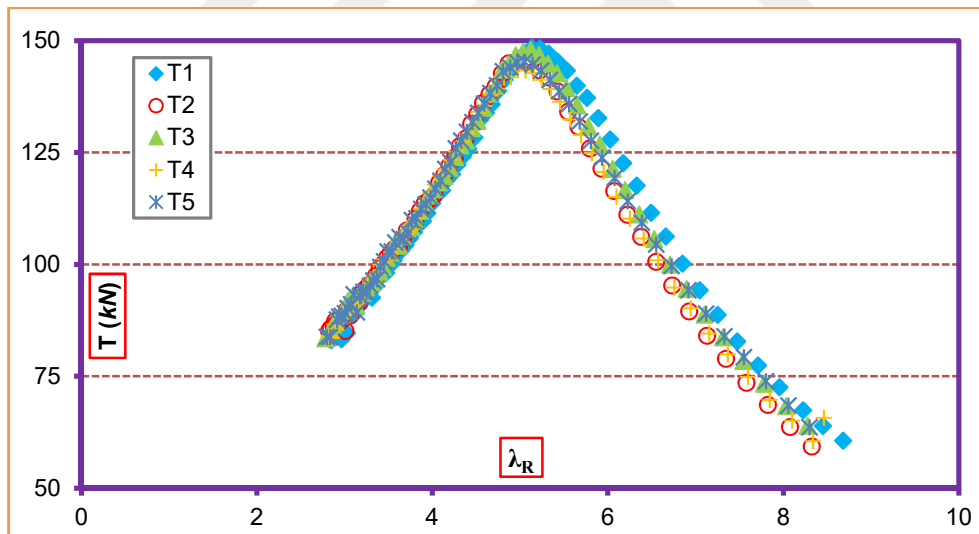


Figure 4.31. Variation of thrust force, T with the tip speed ratio, λ_R for five wind turbines

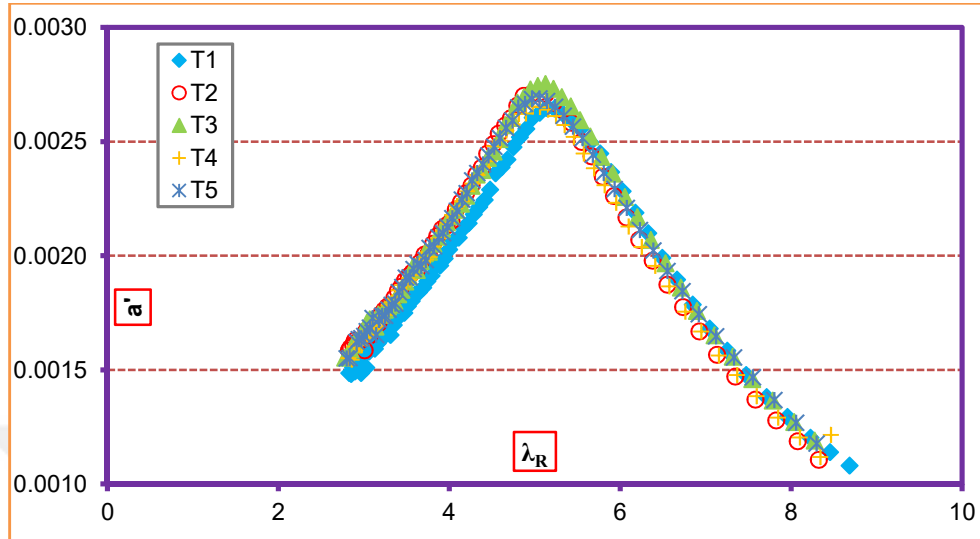


Figure 4.32. Variation of angular flow induction factor, a' with the tip speed ratio, λ_R for five wind turbines

4.4.5. Concluding Remarks

Wind turbine aerodynamic characteristics are quite crucial in the development of wind turbine technology. This part of the dissertation involved proper explanations of wind turbine aerodynamic parameters. Also, among the analyzed aerodynamic data of five wind turbines, well agreement is reached between each wind turbine data in terms of the aerodynamic parameters. The results obtained are summarized as follows:

- A wind turbine can rotate at different rotational speed, Ω during the year. However, optimum rotational speed, Ω is very important for the maximum turbine efficiency. According to the obtained results, during a year, operating percentage of wind turbines at an optimum rotational speed of $\Omega=16.40$ rpm is determined as 45%.
- Very low wind speeds or low rotational speeds cannot exert enough torques to the wind turbine blades to force them to rotate, in the case of preventive

maintenance and fault detection, the wind turbine does not generate power. It is observed that wind turbines do not, unfortunately, generate power approximately for one-fourth of a year in the Sebenoba Wind Energy Power Plant.

- Initially, power output remains almost constant between the tip speed ratios of $\lambda_R=2.81$ and $\lambda_R=5.0$, and then decreases with increasing tip speed ratio, λ_R . On the other hand, the maximum wind power output of 2000 kW occurs at a tip-speed ratio, λ_R of 2.81 and a rotational speed of $\Omega=16.40$ rpm.
- According to the present results obtained in this part of the dissertation, wind turbine efficiency rapidly increases with increasing tip speed ratio, λ_R , and then remains approximately constant, or decreases slightly. Maximum wind turbine efficiency is found to be 30%. Optimum tip speed ratio, λ_R which turbines operate most efficiently, is calculated to be $\lambda_R=7.12$.
- Variations of the axial flow induction factor, a , and the wind turbine efficiency presented as a function of the tip speed ratio, λ_R have the same tendency. Minimum and maximum flow induction factors, a are determined as 0.0124 and 0.0924 at corresponding tip speed ratio values of $\lambda_R=2.81$ and $\lambda_R=7.12$, respectively.
- Thrust force, T on the rotor is an essential factor for the performance of wind turbines, and it is directly applied to the tower on which the rotor is attached. Firstly, the thrust force, T rises rapidly with increasing tip speed ratio, λ_R , and then decays down sharply. Maximum thrust force, T is computed to be $T=150$ kN at a corresponding tip speed ratio of $\lambda_R=5.21$.

4.5. Estimation of Aerodynamic Characteristics for a Horizontal Axis Wind Turbine

4.5.1. Introduction

Wind turbine aerodynamic characteristics play an important role in the monitoring of condition and control of wind turbines in any wind power plant. Accurate estimation of these wind turbine aerodynamic characteristics is required to obtain a more realistic prediction of the size of the storage capacity for wind energy integration. Aerodynamic characteristics of the horizontal axis wind turbine are modeled as a function of hub-height wind speed (U_D) and atmospheric air temperature (T_{am}) using artificial neural networks (*ANNs*). Hub-height wind speed, U_D and atmospheric air temperature, T_{am} are used as the input variables, and wind turbine output power (P), power coefficient (C_p), axial flow induction factor (a), thrust coefficient (C_T), and thrust force (T) are computed as the output layer. The measured wind farm data values are compared versus those data predicted by the *ANN* model and as well as the data obtained by the manufacturer. The results obtained indicate that the *ANN* model can be a useful tool for accurate forecasting of the wind turbine aerodynamic characteristics. The most advantage of this model is that as long as having the required hub-height wind speed, U_D , and atmospheric air temperature, T_{am} ; wind turbine aerodynamic characteristics can be predicted without detailed knowledge of turbine operations and its control schemes.

4.5.2. The Objective of the Present Work

Obtaining aerodynamic characteristics, especially power generations to be defined concerning a single or two parameters provide quick and straightforward answers to questions including output power of new wind turbine installations and

capacity enhancements of wind farms in the considered region. So, the most critical advantage of forecasting output power and other aerodynamic parameters is the elimination of complex handling or approach to the problem.

4.5.3. The Technique of the Study

4.5.3.1. Feasibility of Wind Farm Locations and Technical Specifications of Wind Turbines

The data used in this study were measured from Belen Wind Power Plant (*WPP*). Belen *WPP* is located in the Hatay province of Turkey. The location of Belen *WPP* in Turkey is shown in Figure 4.33. This *WPP* lay on the geographical coordinates of 36°12'N, 36°28'E, latitude and longitude, respectively. On the other hand, it is located at an altitude of 474 m above sea level. It was put into operation in 2009. In the first phase, the installed capacity of the plant was 30 MW. In 2010, the 6-MW capacity expansion provided with temporary admission, thus Belen *WPP* has subsequently reached 36 MW. Finally, the total installed capacity of Belen *WPP* has increased reaching 48 MW with 4 new turbines in 2012, and annual production amounts to about 150 million kWh. Belen *WPP* includes 16 identical wind turbines with the rated capacity of 3 MW, the hub height of 80 m, and the rotor diameter of 90 m. A summary of these cited and other technical specifications for the identical wind turbines is given in Table 4.10. The cut-in speed, rated speed, and cut-out speed of the wind turbines are 4 m/s, 15 m/s, and 25 m/s, respectively. Turbines of *WPP* are the VESTAS V90-3 MW wind turbine types. The VESTAS V90-3 MW wind turbine is a pitch regulated upwind turbine with active yaw and has a three-blade rotor. The turbine utilizes the OptiTip and the variable speed concepts. Due to these features, rated power will be maintained even in high wind speeds, regardless of air temperature, and air density, and the

wind turbine can operate the rotor at variable speed (RPM). At low wind speeds, the OptiTip system and variable speed operation maximizes the power output, P by giving the optimal RPM and pitch angle, which also minimizes the sound emission from the turbine.



Figure 4.33. The location of Belen WPP in Hatay province of Turkey

Five wind turbines ($T1$, $T2$, $T3$, $T4$, and $T5$) of this wind farm were selected to evaluate the performance of the presented forecasting method. For each wind turbine, the collected data from the anemometer on top of the nacelle includes power output, P (kW), nacelle position ($degree$), hub-height wind speed, U_D (m/s), and atmospheric air temperature, T_{atm} . The existing hourly data cover a period of 1 year (2011). From this extensive dataset, the distributions of U_D , T_{atm} , and P of all wind turbines are analyzed over a wide range of wind speeds.

Table 4.10. Wind turbine technical properties

Equipment	Properties
Rotor	
Diameter	90 m
Area swept	6,362 m ²
Nominal revolutions	16.1 rpm
Operational interval	8.6-18.4 rpm
Number of blades	3
Power regulation	Pitch/OptiSpeed

Air brake	Full blade pitch by three separate hydraulic pitch cylinders
Tower	
Hub height	80 m
Operational data	
Cut-in wind speed	4 m/s
Nominal wind speed	15 m/s
Cut-out wind speed	25 m/s
Generator	
Type	Asynchronous with OptiSpeed
Rated output	3,000 kW
Operational data	50 Hz, 1000 V
Gearbox	
Type	Two planetary and one helical stage
Control	
Type	Microprocessor-based control of all the turbine functions with the option of remote monitoring. Output regulation and optimization via OptiSpeed and OptiTip pitch regulation

4.5.3.2. ANN Forecasting Model Concept

For the development of forecasting models, the hourly data records were collected in 2011 for five selected wind turbines ($T1$, $T2$, $T3$, $T4$, and $T5$). However, some turbine aerodynamic characteristic data including missing values were removed from the data set. From the extensive data set, distributions of hub-height wind speed, U_D , atmospheric air temperature, T_{am} , and wind turbine output power, P of all turbines were analyzed over a wide range of wind speeds. Other wind turbine aerodynamic characteristics such as power coefficient, C_p , axial flow induction factor, a , thrust coefficient, C_T , and thrust force, T were calculated using

hub-height wind speed, U_D , and wind turbine output power, P parameters. First, the total 298 data records were divided into two subsets such as training and testing data set. The training data set includes 236 data covered the turbines of $T1$, $T3$, $T4$, and $T5$ which are approximately 80% of the total data. On the other hand, the testing data set covered the turbine of $T2$ consists of 62 data which corresponds to 20% of the total data. So, formerly expressed turbine aerodynamic characteristics including (P , C_p , a , C_T , and T) can be characterized as the function of hub-height wind speed, U_D , and atmospheric air temperature, T_{atm} . The relationship between the turbine aerodynamic characteristics and independent variables can be functionally expressed as;

$$(P, a, C_p, C_T, T) = f(U_D, T_{atm}) \quad (4.1)$$

The selected independent variables determine the structure of the forecasting model and affect the results of the model and the weighted coefficient. For this reason, the selection of the most suitable independent variables is an essential tool in the forming of a satisfactory forecasting model. The *ANN* architecture used in this part of the dissertation is schematically shown in Figure 4.34. As seen in this figure, hub-height wind speed, U_D , and atmospheric air temperature, T_{atm} were used as the input variables. Two different input combinations (Model 1 and Model 2) were used for estimating wind power (P), power coefficient (C_p), axial flow induction factor (a), thrust coefficient (C_T), and thrust force (T). In Model 1, there is one input parameter into the network, which purely consisted of hub-height wind speed, U_D . On the other hand, there are two input parameters (U_D and T_{atm}) for Model 2. The chosen parameters of hub-height wind speed, U_D , and atmospheric air temperature, T_{atm} are the most important climatic factors influencing the performance of turbine aerodynamic characteristics. As well, these parameters are more readily available in this region

and all over the World. Moreover, they can be measured and obtained easily in any regions of the World.

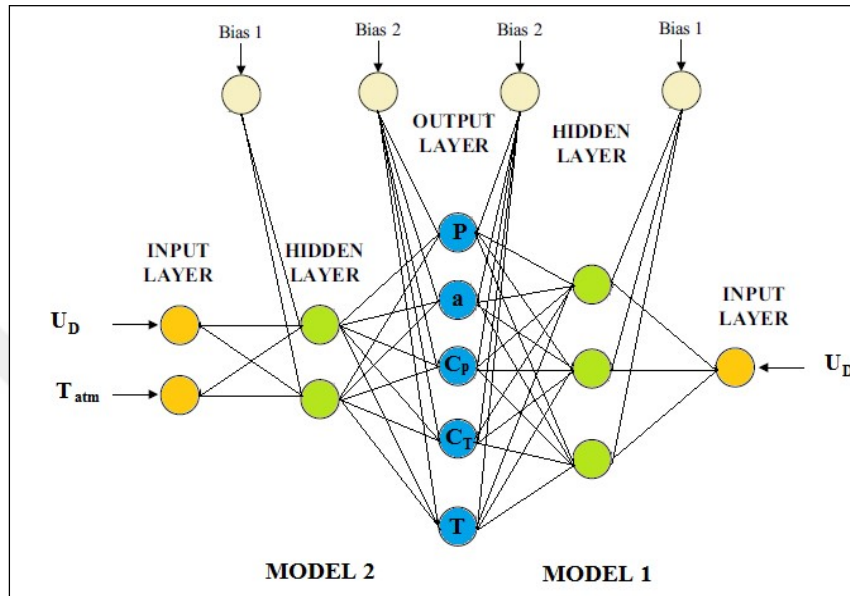


Figure 4.34. ANN architecture used in this part of the dissertation

In order to determine the optimal network architecture, various structures of forecasting models were designed under *MATLAB* software. For this reason, the predictions were performed by taking a different number of hidden layer neurons between 1 and 10. Models 1 and 2 were tested by testing data set, which was not used during the training process. Different training algorithms were used, and the best fit result was obtained. In these models, the Levenberg–Marquardt (*LM*) learning algorithm was used. Neurons in the input layer have no transfer function. The logistic sigmoid transfer function (*logsig*) and linear transfer function (*purelin*) were applied in the hidden layers and the output layer of the network as an activation function, respectively. The ANN architecture consists of an input layer, an output layer, and one hidden layer with three and two neurons for Models 1 and

2, respectively. In the training procedure, the maximum epoch's number was set to 300, and the mean square error goal was set to 5×10^{-5} .

4.5.4. Results and Discussions

Models 1 and 2 demonstrated in Figure 4.34 were trained and tested to compare and evaluate the performances of *ANNs*. The input combinations of both models and obtained equations of *ANN* models are given in Table 4.11. These mathematical expressions can be used for the prediction of aerodynamic characteristics of the VESTAS V90-3 MW wind turbines. On the other hand, the training and testing results in terms of *MAPE* and *R* of Models 1 and 2 are given in Table 4.12. Comparing the results of these models, it is seen that the performance values of Model 2 are generally better than Model 1. According to the derived results, based on the testing data set; the *MAPE* and *R* ranged from 2.62% to 3.86% and 0.9950–0.9995, respectively. These results indicate that artificial intelligence models can be a useful tool for accurate forecasting wind turbine aerodynamic characteristics based on hub-height wind speed, U_D , and atmospheric air temperature, T_{atm} .

The scatter diagrams of the network predictions compared concerning the actual values and manufacturer curves were drawn in order to indicate the performance of the used *ANN* forecasting models. As seen in Figures 4.35–4.39, the results of predictions have a reasonably close agreement with the corresponding actual values.

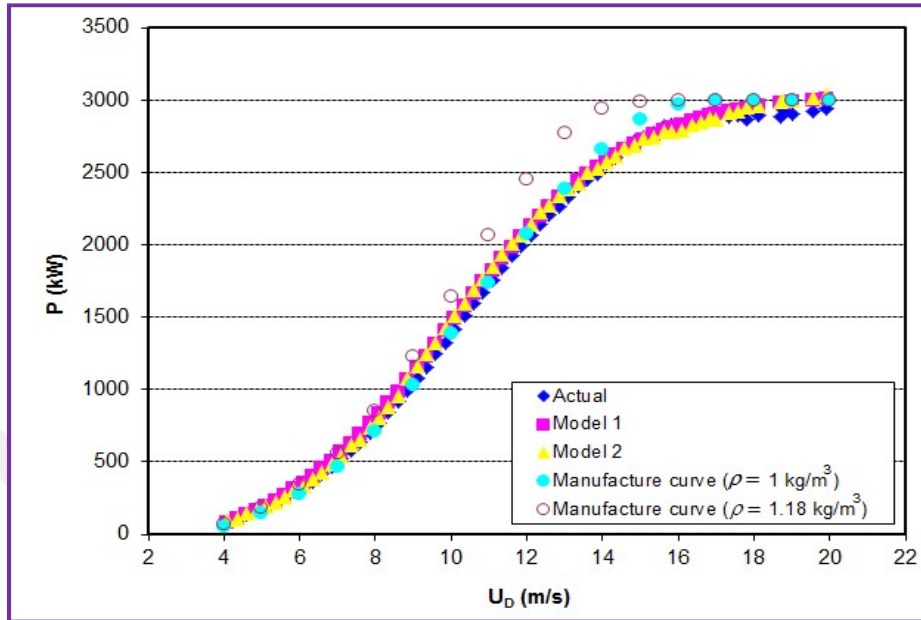


Figure 4.35. Comparison between prediction and actual results for power, P

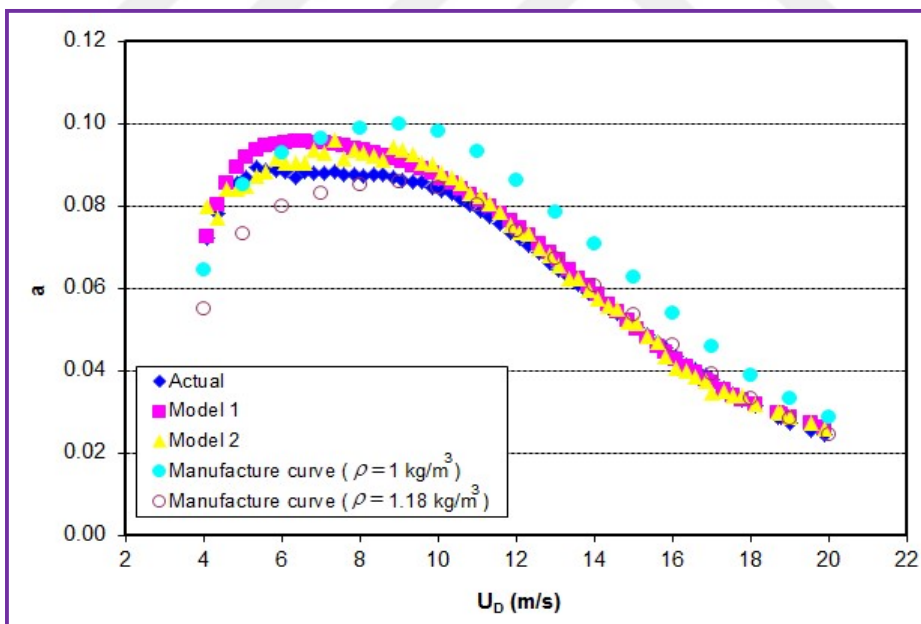


Figure 4.36. Comparison between prediction and actual results for axial flow induction factor, a

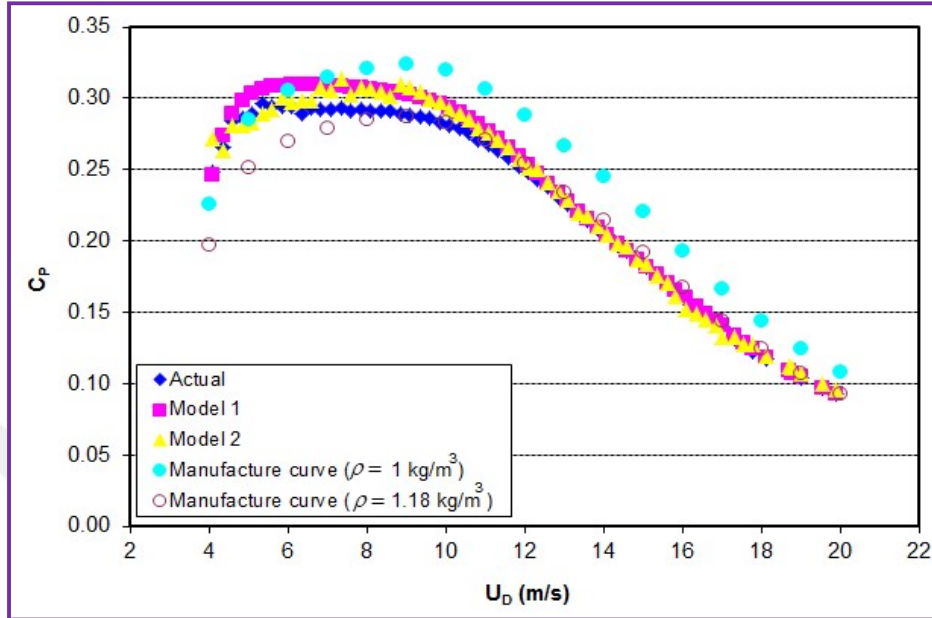


Figure 4.37. Comparison between prediction and actual results for power coefficient, C_p

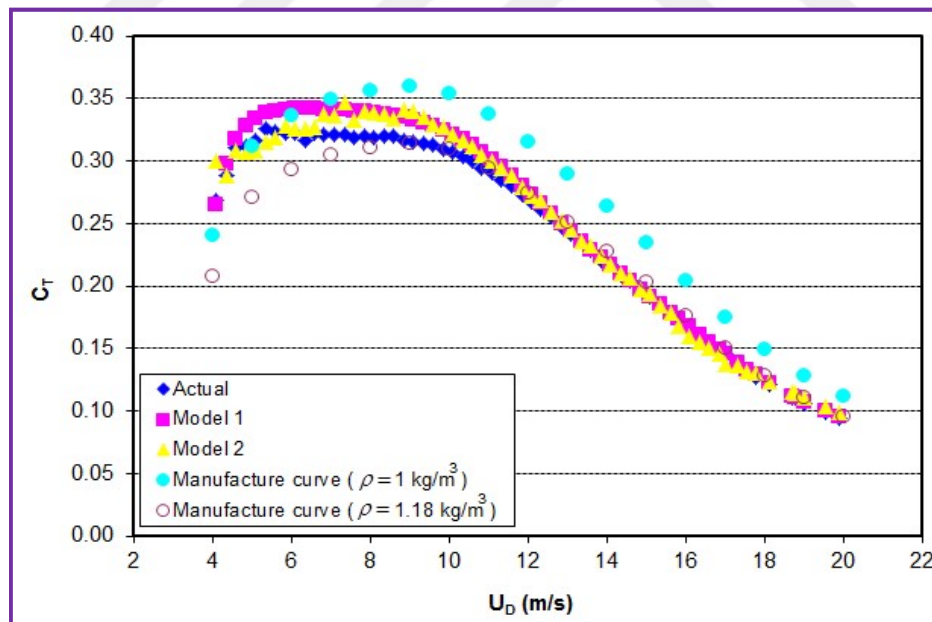


Figure 4.38. Comparison between prediction and actual results for thrust coefficient, C_T

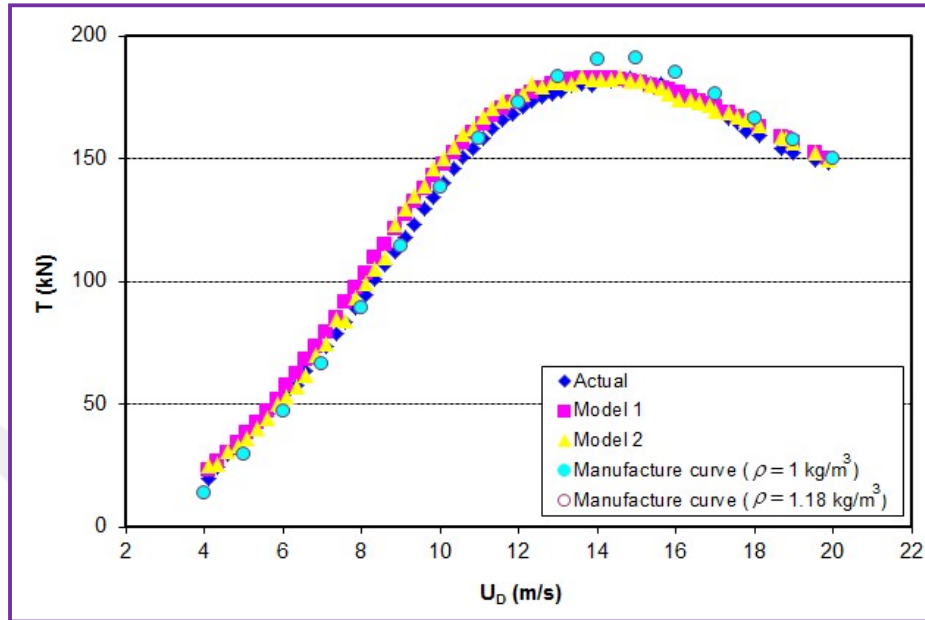


Figure 4.39. Comparison between prediction and actual results for thrust force, T

Table 4.11. The input combinations and obtained equations of ANN models

Output	Input	Model	Equation
P	U _D	Model 1	$P = \frac{1511.118}{1 + e^{-949.732U_D - 98.65}} - \frac{3209.861}{1 + e^{0.427U_D - 4.266}} - \frac{48.206}{1 + e^{-3122.747U_D + 1394.805}} + 1588.875$
	U _D and T _{atm}	Model 2	$P = \frac{3210.86}{1 + e^{-0.416U_D - 0.025T_{atm} + 4.627}} - \frac{867.528}{1 + e^{-708.578U_D - 611.768T_{atm} + 236.175}} + 746.762$
a	U _D	Model 1	$a = \frac{0.079}{1 + e^{-0.008U_D + 20.64}} - \frac{0.078}{1 + e^{0.434U_D - 6.028}} - \frac{24.019}{1 + e^{-1.464U_D - 0.835}} - 23.998$
	U _D and T _{atm}	Model 2	$a = \frac{17.106}{1 + e^{-0.199U_D - 0.0004T_{atm} - 2.62}} - \frac{8.915}{1 + e^{-0.16U_D + 0.007T_{atm} - 2.026}} - 8.194$
C _p	U _D	Model 1	$C_p = -\frac{0.074}{1 + e^{-0.947U_D + 11.345}} + \frac{0.173}{1 + e^{0.475U_D - 7.817}} + \frac{11.082}{1 + e^{-2.214U_D + 3.95}} - 10.943$
	U _D and T _{atm}	Model 2	$C_p = \frac{3.804}{1 + e^{0.126U_D - 0.001T_{atm} + 0.474}} - \frac{6.605}{1 + e^{0.186U_D + 0.015T_{atm} + 1.162}} - 0.047$
C _T	U _D	Model 1	$C_T = -\frac{0.19}{1 + e^{-0.477U_D + 7.771}} + \frac{0.088}{1 + e^{0.963U_D - 11.441}} + \frac{8.677}{1 + e^{-2.187U_D + 4.276}} - 8.421$
	U _D and T _{atm}	Model 2	$C_T = -\frac{0.703}{1 + e^{-0.196U_D + 0.003T_{atm} + 1.945}} + \frac{0.957}{1 + e^{-0.249U_D - 0.067T_{atm} + 0.793}} - 0.239$
T	U _D	Model 1	$T = -\frac{139.356}{1 + e^{35.882U_D + 96.786}} + \frac{175.726}{1 + e^{0.227U_D - 3.645}} + \frac{288.232}{1 + e^{0.403U_D + 3.318}} - 187.64$
	U _D and T _{atm}	Model 2	$T = \frac{130.309}{1 + e^{0.355U_D + 0.022T_{atm} - 6.443}} + \frac{264.079}{1 + e^{-0.339U_D - 0.054T_{atm} + 3.692}} - 146.342$

Table 4.12. The training and testing results of Models 1 and 2

Charact.	Training procedure				Testing procedure			
	MAPE (%)		R		MAPE (%)		R	
	Model 1	Model 2	Model 1	Model 2	Model 1	Model 2	Model 1	Model 2
P	4.88	4.63	0.9965	0.9967	3.71	3.54	0.9995	0.9991
a	4.82	4.61	0.9787	0.9811	3.86	3.84	0.9977	0.995
C _p	3.73	3.67	0.9839	0.9842	2.62	2.82	0.9987	0.9959
C _T	4.13	4.07	0.9818	0.982	2.93	3.15	0.9986	0.995
T	5.12	4.71	0.9896	0.9909	3.85	3.43	0.9983	0.9972

4.5.5. Concluding Remarks

The primary objective of this part of the dissertation is to develop *ANN* models for estimating wind turbine aerodynamic characteristics so that the wind plant performance can be characterized with a few measured or predicted input variables such as hub-height wind speed, U_D , and atmospheric air temperature, T_{atm} values. Equivalent wind plant aerodynamic characteristic curves obtained in this part of the dissertation become highly desirable and useful in predicting plant output for a given wind forecast. According to the derived results, based on the testing data set, the *MAPE* and *R* values ranged from 2.62% to 3.86% and from 0.9950 to 0.9995 as minimum and maximum results, respectively. These results indicate that artificial intelligence models can be a useful tool for accurate forecasting wind turbine aerodynamic characteristics based on hub-height wind speed, U_D , and atmospheric air temperature, T_{atm} . On the other hand, the most advantage of this model is that as long as having the required hub-height wind speed, U_D , and atmospheric air temperature, T_{atm} ; wind turbine aerodynamic characteristics can be predicted without detailed knowledge of turbine operations and its control schemes with high accuracy.

4.6. Estimation of Wind Power Output Curve using Artificial Neural Network

4.6.1. Introduction

Accurate estimation of wind turbine power curve has an essential role in the monitoring of conditioning and controlling of wind turbines in wind power plants. Artificial neural network (*ANN*) was used in this part of the dissertation in the prediction of horizontal axis wind turbine output power (P) in terms of climatic data and wind turbine rotational speed (Ω). The method of artificial neural network

(*ANN*) involved the input parameters including the hub-height wind speed (U_D), atmospheric air temperature (T_{atm}) and the rotational speed (Ω) of wind turbines which they were obtained from an operating wind power plant. According to the derived results for the testing process, minimum mean absolute percentage of error (*MAPE*) and maximum correlation coefficient (*R*) values were determined for an optimum turbine rotational speed (Ω). Namely, *MAPE* and *R* values were respectively determined as 1.47%, and 0.9991 in the case of the *ANN* study. These results well indicated that the *ANN* approach provided accurate and straightforward forecasting in the determination of wind turbine output power (*P*). This part of the dissertation showed that wind turbine power curve of a considered site can be rapidly predicted in a successful way with a little error under the utilization of the *ANN* method when the parameters of the climatic data including the hub-height wind speed (U_D), and the atmospheric air temperature (T_{atm}); and as well rotational speed (Ω) of wind turbines in a wind farm are available. Thus, this method is rather convenient during the decision stage of new wind power plant installations.

4.6.2. The Objective of the Present Work

4.6.2.1. Regional Feasibility Study for the Installation of the Wind Farm and Technical Specifications of Wind Turbines

The data used in the present study were taken from a wind power plant (*WPP*) which is currently in operation. The altitude of this wind farm is 400 m above the sea level. By 2008; the wind farm was in operation, and it comprised 17 identical wind turbines, each having an equal rated capacity of 2 MW. The hub height of the identical wind turbines is 67 m, and the rotor diameter is 80 m. The total swept area of a single wind turbine is thus 5027 m². The technical specifications of identical wind turbines are presented in Table 4.13. The turbines

operate at a cut-in speed of 4 m/s, a cut-out speed of 25 m/s, and a nominal wind speed of 15 m/s. The present wind turbines are pitch-regulated upwind turbines with active yaw and have a three-bladed rotor.

Table 4.13. Technical properties of wind turbines

Equipment	Properties
Rotor	
Diameter	80 m
Area swept	5,027 m ²
Nominal revolutions	16.7 rpm
Operational interval range	9-19 rpm
Number of blades	3
Power regulation	Pitch/OptiSpeed
Air brake	Full blade pitch by three separate hydraulic pitch cylinders
Tower	
Hub-height	67 m
Operational data	
Cut-in wind speed	4 m/s
Nominal wind speed	15 m/s
Cut-out wind speed	25 m/s
Generator	
Type	Asynchronous with OptiSpeed
Rated power output	2,000 kW
Operational data	50 Hz, 690 V
Gearbox	
Type	Planet / parallel axles
Control	
Type	Microprocessor-based control of all the turbine functions with the option of remote monitoring. Output regulation and optimization via OptiSpeed and OptiTip pitch regulation

The turbines employ the OptiTip and variable speed functions, making it possible to maintain the rated power at very high wind speeds, regardless of air temperature and density. The OptiSpeed generator allows the turbine rotor speed to run at rotational speeds ranging from 9 rpm to 19 rpm of the rotational speed. The OptiTip system can be employed at low free-stream wind speeds, and the variable speed function can, therefore, maximize the output generated power (P) by optimizing the rotational speed (Ω), and pitch angle.

Five wind turbines of the wind farm; $T1$, $T2$, $T3$, $T4$, and $T5$ were selected for this part of the dissertation. For each of the wind turbines, the data set taken from the WPP included wind power output (P , kW), hub-height wind speed (U_D , m/s), atmospheric air temperature (T_{am} , $^{\circ}C$), and turbine rotational speed (Ω , rpm). Table 4.14 illustrates the relationship between the three input and one output parameters which are described in Figure 4.41 and correlation of these parameters with the output parameter, i.e., the wind power output (P).

Table 4.14. Variation range of variables and related to statistical parameters

Input and output variables	Unit	Min	Max	Mean	Standard deviation	Correlation with P
P	kW	2.63	2000.63	1187.23	679.32	1.000
U_D	m/s	2.87	24.50	12.48	5.57	0.896
T	$^{\circ}C$	6.00	27.00	17.08	4.47	-0.640
Ω	rpm	12.43	16.40	14.67	1.58	0.703

It is evident from the table that hub-height wind speed, U_D , is the most effective factor in wind power output (P) forecasting. Besides, U_D has a directly proportional relationship to wind power output (P). On the other hand, an increase in atmospheric air temperature (T_{am}) inversely affects wind power output (P), since an increase in T_{am} results in expansion of the atmospheric air. So, this increase in atmospheric air temperature (T_{am}) means that a lower mass flow rate (\dot{m}) of air interacts with the rotor blades. In this sense, this situation is already expressed in

Table 4.14, since negative sign implies this case. Furthermore, the absolute correlation ratio of the atmospheric air temperature (T_{atm}) with respect to the generated output power, P is lower in comparison with the correlation ratio of the hub-height wind speed (U_D) presented with respect to the P . The absolute magnitude of the correlation ratio of turbine rotational speed (Ω) with the wind power output (P) is smaller when compared to the hub-height wind speed (U_D), but greater than the absolute value of the atmospheric air temperature, T_{atm} correlation ratio. As can be seen from Table 4.14, when the minimum value of the wind power output (P) was 2.63 kW, the maximum output power (P) obtained was 2000.63 kW according to the processed data. Besides, the minimum and maximum values of hub-height wind speed (U_D) were 2.87 m/s, and 24.50 m/s, respectively. The data also revealed that while the average minimum atmospheric air temperature (T_{atm}) for the five wind turbines was 6.00 °C, the maximum value was reported as 27.00 °C. On the other hand, the average rotational speed (Ω) of five turbines varied, with a minimum value of 12.43 rpm, and a maximum of 16.40 rpm.

The data was accumulated for the entire year of 2013. Measurements were taken over periods of 10 minutes. The data were initially composed of 52560 measurements ($365 \times 24 \times 6$ quantities) for each parameter related to hub-height wind speed, U_D , atmospheric air temperature, T_{atm} , wind turbine rotational speed, Ω , and generated output power, P . Initially, original data for turbine rotational speed, Ω was classified within the limit ranges such as 1.00–2.99 [rpm], 3.00–4.99 [rpm], 5.00–6.99 [rpm], 7.00–8.99 [rpm], 9.00–10.99 [rpm], 11.00–12.99 [rpm], 13.00–14.99 [rpm], and 15.00–16.99 [rpm]. The probability distribution of the rotational speed, Ω was calculated as shown in Figure 4.40. Subsequently, the average value in terms of the rotational speed, Ω corresponding to each class mark of the probability distribution for five wind turbines was calculated. Hence, average class marks of probability distribution considering all turbines were calculated as 2.02 [rpm], 4.10 [rpm], 6.05 [rpm], 8.08 [rpm], 10.10 [rpm], 12.44

[rpm], 13.94 [rpm], and 16.14 [rpm] in terms of rotational speed, Ω . Accordingly, designated class marks, including multi-data, were then performed for all wind turbines, and parameters such as U_D , T_{atm} , and P were defined for each class mark of rotational speed, Ω . In this way, in terms of turbine rotational speed (Ω), an average value corresponding to each class mark involved variation in the values of parameters such as hub-height wind speed, U_D , atmospheric air temperature, T_{atm} , and generated output power, P .

Pre-filtering was performed in order to eliminate inexact power data given as zero or negative wind output power (P) values. These improper data probably arose from rapid alterations in hub-height wind speed (U_D), vortices forcing a change in position of the turbine rotor, or maintenance of the wind turbines. For these reasons, power generation could not be assessed at high wind speeds. Thus, the probability density of rotational speed, Ω , corresponding to a value of 0, i.e., the non-rotational case was reported as 22%. It should be observed that these data were omitted from the present computations.

As shown in Figure 4.40, a half of the data set was observed, corresponding to a nominal rotational speed (Ω) of the turbine rotor of 16.14 rpm. Also, pre-filtered data involving rotational speeds (Ω) below 12.44 rpm were filtered for a second time, since the data within the rotational speed range $2.02 \text{ rpm} \leq \Omega \leq 10.10 \text{ rpm}$ (Ω) corresponded to only 2% of the total data. Finally, the remaining 76% of the data were used for the forecasting *ANN* model in this part of the dissertation.

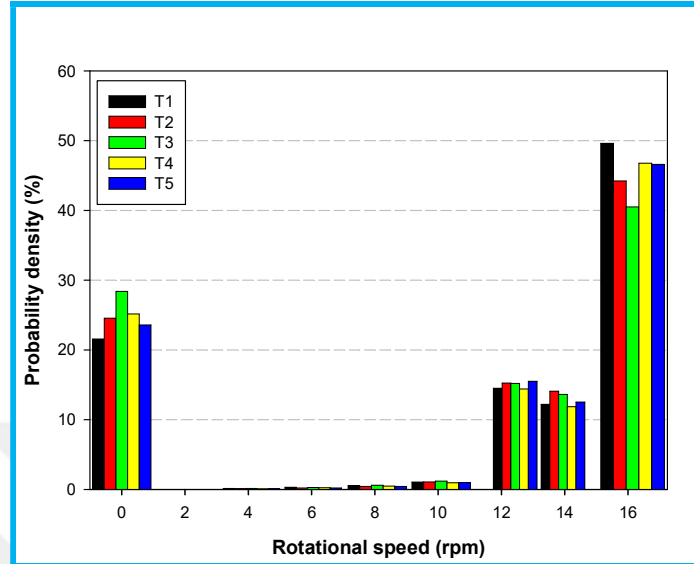


Figure 4.40. Probability density representation of rotational speed (Ω)

4.6.2.2. ANN Forecasting Method

For the development of forecasting *ANN* model, the total of 660 data for each parameter was used. This data set was divided into two subsets described as the training and testing groups. The training data set included 532 data covering wind turbines *T1*, *T2*, *T3*, and *T4*, representing approximately 80% of the total data. The testing data set included only wind turbine *T5*, consisting of 128 data representing approximately 20% of the total data. So, wind turbine power output (P) can be characterized as a function of hub-height wind speed, U_D , atmospheric air temperature, T_{atm} , and turbine rotational speed, Ω . The relationship between wind turbine power output (P) and these independent variables can be functionally expressed as:

$$P = f(U_D, T_{atm}, \Omega) \quad (4.2)$$

The selected independent variables determined the structure of the forecasting *ANN* model and this situation influenced the results of the model and the weighted coefficient, W . For this reason, the selection of the most suitable independent variables becomes a significant factor in forming a satisfactory forecasting *ANN* model. The *ANN* architecture used in this part of the dissertation is shown schematically in Figure 4.41. As seen in this figure; U_D , Ω , and T_{atm} were used as input variables. The parameters U_D and T_{atm} are the most important climatic factors influencing the performance of wind turbine power output (P); thus it is the reason that they considered. Additionally, these parameters are readily available both in this region and all over the World. Moreover, they can easily be obtained and measured in any considered region of the World.

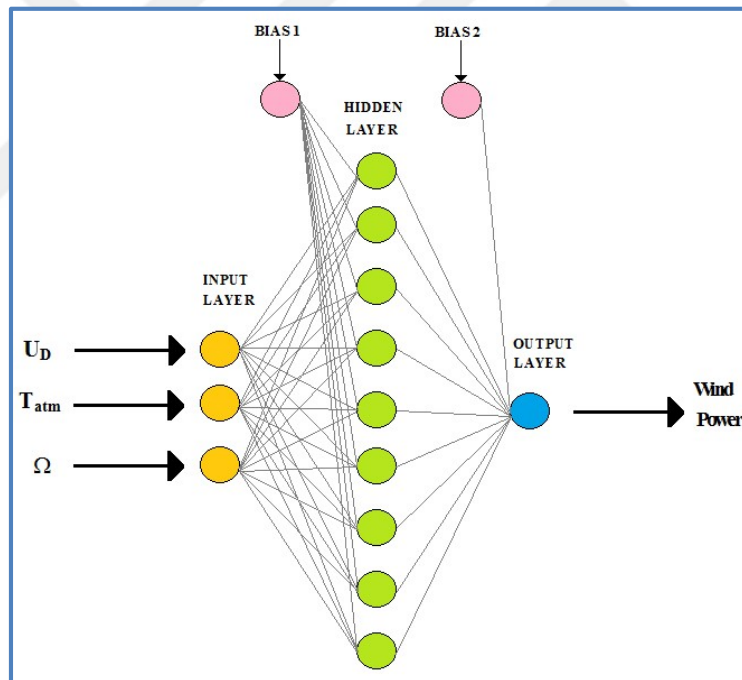


Figure 4.41. Schematic representation of the *ANN* framework used in the present study denoting of layers and nodes

In order to determine the optimal network architecture; various structures of forecasting models were designed using the *MATLAB* software. For this reason, the predictions were performed by considering a different number of hidden layer neurons between 1 and 15. The *ANN* model was assessed by testing a data set not used during the training process. The best result was obtained by working with different training algorithms, and leading to the adoption of the Levenberg–Marquardt (*LM*) learning algorithm. In the model of *ANN* formed, neurons in the input layer have no transfer function. However, the logistic sigmoid transfer function (*logsig*) and linear transfer function (*purelin*) were applied in the hidden layer and output layer of the network as an activation function, respectively. The *ANN* architecture schematically shown in Figure 4.41 consists of an input layer, an output layer, and one hidden layer with the hidden layer involving nine neurons. In the training procedure, the maximum epoch number was set to 200, and the mean square error goal was set at 5×10^{-5} .

The determined structure used in this part of the work had an input layer, a hidden layer, and an output layer consisting of 3, 9, and 1 nodes, respectively. While four turbines were used for training the *MATLAB* simulation, data from one wind turbine was considered adequate for testing the results. The general construction of the *MATLAB* codes, consisting of Levenberg–Marquardt back-propagation algorithm and logic (*logistic function*), and *purelin* (*linear transfer*) functions, were used in this part of the dissertation.

4.6.3. Results and Discussions

4.6.3.1. ANN Results

The prediction model was trained and tested to compare and evaluate the performance of the utilized *ANNs*. Figures 4.42 and 4.43 present the comparison

between the prediction of *ANN* and measured results for the training data set. According to the results derived, based on the testing data set, the scatter diagrams of the network predictions presented with respect to the actual values of power output (P) were drawn in order to evaluate the performance of the utilized *ANN* model. As seen in Figures 4.44-4.46, the results of the prediction were in reasonably close agreement with the actual values of turbine power output (P), especially in the case of optimum 16.14 rpm rotational speed. These agreed predictions indicated that the use of the *ANN* artificial intelligence model can be a useful tool for accurate forecasting wind turbine power output (P); based on the hub-height wind speed (U_D), atmospheric air temperature (T_{am}), and turbine rotational speed, Ω .

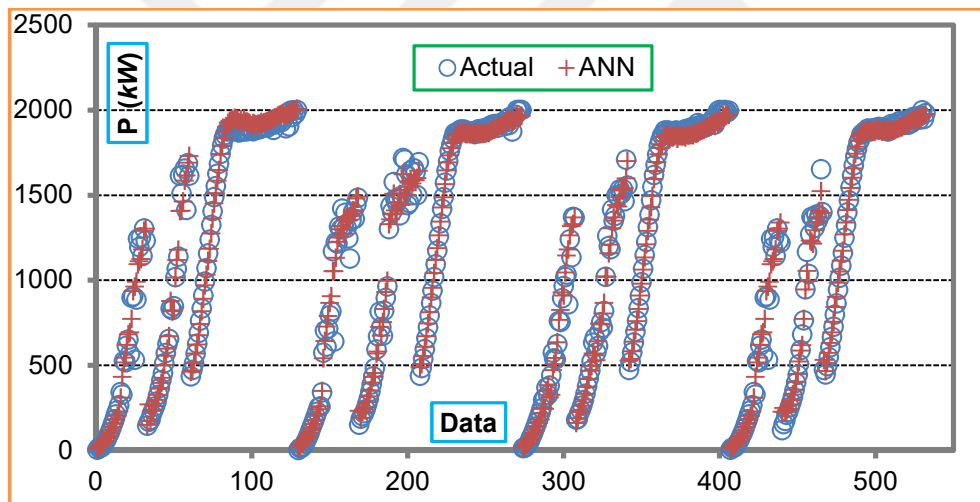


Figure 4.42. Comparison between the prediction of *ANN* forecasting method and measured results for the training data set in terms of studied data

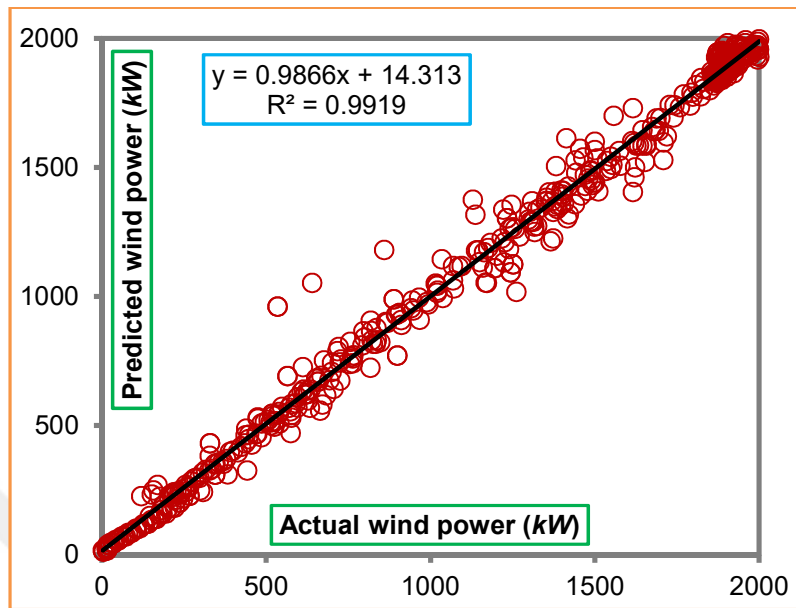


Figure 4.43. Comparison of actual and predicted output power, P values for the training data set

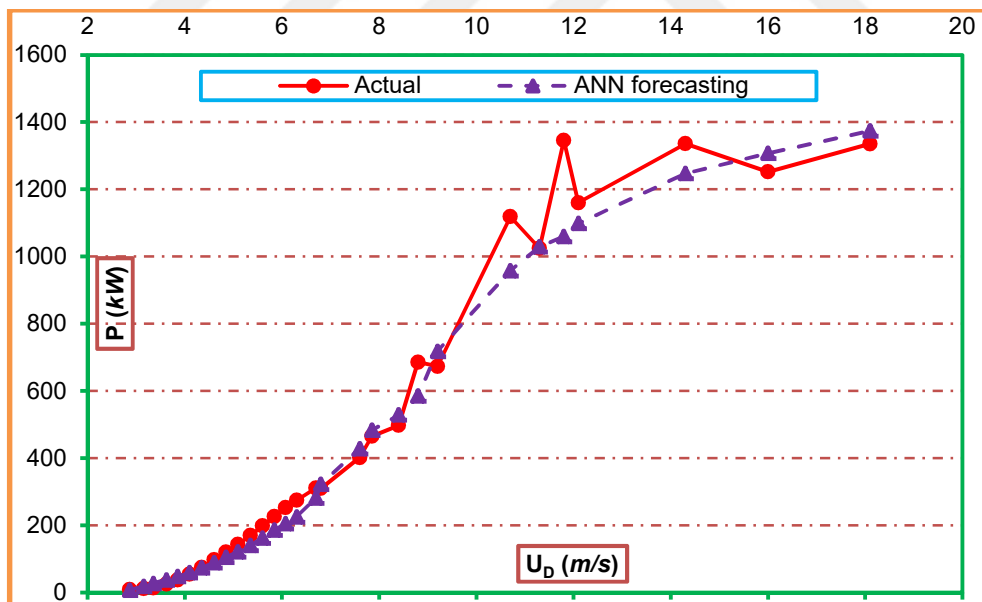


Figure 4.44. Comparison of the actual output power (P) and the forecasted computational results at 12.44 rpm

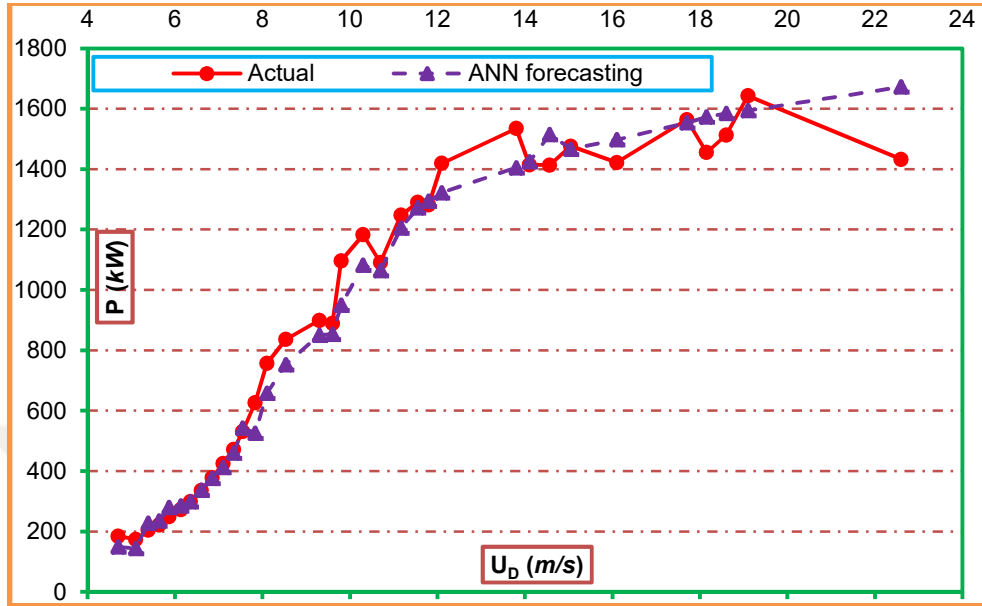


Figure 4.45. Comparison of the actual output power (P) and the forecasted computational results at 13.94 rpm

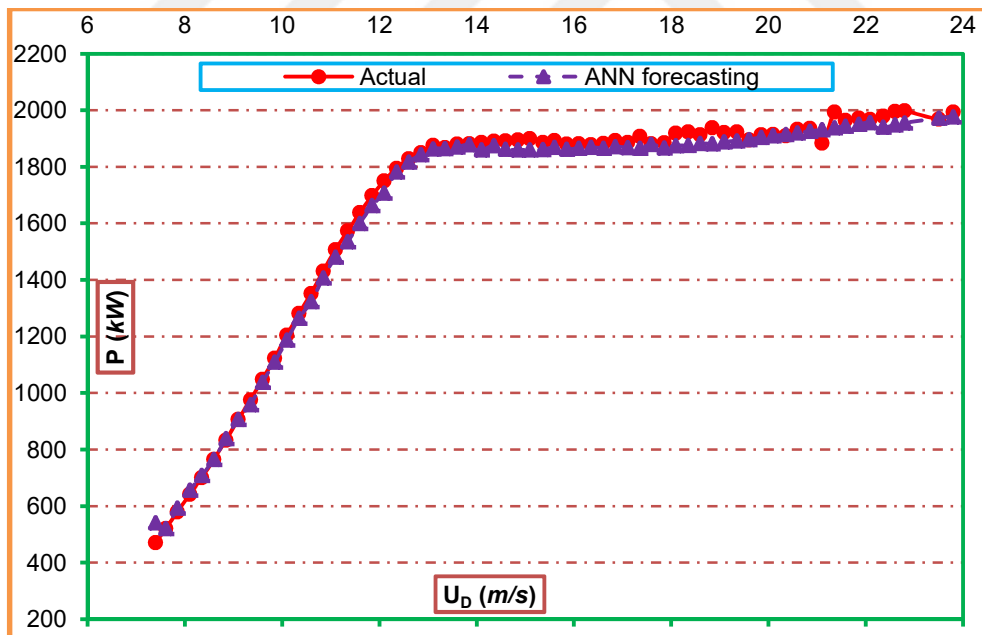


Figure 4.46. Comparison of the actual output power (P) and the forecasted computational results at 16.14 rpm

4.6.3.2. Errors in the Results of ANN Method with Reference to the Actual Power Output (P)

Table 4.15 gives the mean absolute percentage error ($MAPE$), and the correlation coefficient (R) results of the training and testing processes depending on the forecasting computations compared to the actual data set of power output (P). According to the results obtained from the testing process, the range of $MAPE$ varied from 1.47% to 16.94% for rotational speeds (Ω) in the range of 12.44 rpm \leq (Ω) \leq 16.14 rpm. On the other hand, the corresponding range of correlation coefficient, R values for this rotational speed (Ω) range was $0.9898 \leq R \leq 0.9991$. The $MAPE$ and R results for turbine rotational speeds (Ω) over the whole data of 12.44 rpm, 13.94 rpm, and 16.14 rpm rotational speeds were determined as 6.31% and 0.9970, respectively.

Table 4.15. $MAPE$ and R results of the forecasting model estimations

Ω (rpm)	Training process								Testing process	
	$MAPE$ (%)				R				$MAPE$ (%)	R
	T1	T2	T3	T4	T1	T2	T3	T4	T5	T5
12.44	21.35	30.00	13.88	21.00	0.9762	0.9866	0.9863	0.9775	16.94	0.9901
13.94	6.37	6.63	4.83	10.56	0.9901	0.9928	0.9914	0.9951	6.48	0.9898
16.14	2.05	1.44	1.83	1.54	0.9980	0.9994	0.9993	0.9995	1.47	0.9991
whole	7.78	10.58	5.68	8.57	0.9958	0.9958	0.9967	0.9963	6.31	0.9970

Table 4.15 reveals that accurate forecasting estimates were obtained especially, with 16.14 rpm of the optimum rotation (Ω). When the whole data set of the three rotational cases is taken into consideration, it is seen that the $MAPE$ result was insufficient in the forecasting ANN model. This insufficiency is due to the insufficiencies that occurred in between 12.44 rpm and 13.94 rpm. However, in terms of the optimum rotational speed class, i.e., at 16.14 rpm, $MAPE$ results are quite acceptable. On the other hand, in terms of the correlation coefficient (R), the

values showed quite acceptable results for each classes of rotational speed (Ω) as well considering whole classes of rotational speeds, Ω . For instance, the overall correlation coefficient (R) result of the estimations was determined a value of 0.9970, when whole classes of rotational speeds, Ω are taken into account.

During training of the program, *MAPE* values were higher for the presented rotational speed values, apart from $\Omega = 16.14$ rpm when compared with the actual power values of the wind turbines studied as presented in Table 4.15. Considering the results of the testing stage in terms of three rotational speed cases and whole case of *MAPE* values; *ANN* forecasting results clearly revealed that the *MAPE* values of the estimated power output (P) values of testing stage were all among the lower and upper values of *MAPE* according to the training forecasting results obtained from four different turbines. On the other hand, there was a slight difference between the testing results of the correlation coefficient (R) in *ANN* estimations according to different classes of rotational speed (Ω) referenced with respect to the training R values. Namely, both training and testing data indicated higher results of the correlation coefficient (R). The executed comments were therefore based on the *MAPE* results.

The *MAPE* results did not indicate the same degree of success of the utilized method, regardless of its value during the training stage, since the aim of the training was to obtain the actual logic in terms of the computer program to present good estimates at the testing stage. *MAPE* values remained higher in the training stage of estimations at $\Omega=12.44$ rpm; on the other hand, at 13.94 rpm, and 16.14 rpm resulted in *MAPE* with lower values during the training process. Besides, when whole classes of rotational speeds (Ω) are considered, *ANN* estimations of *T3* turbine during the training stage performed the best forecasting result based on the *MAPE*. Estimation of *T3* turbine also showed the best performance compared to others in terms of the overall correlation coefficient (R) taking whole classes of turbine rotational speeds (Ω) into account.

These results indicated that the performance of the *ANN* forecasting model was generally useful tool for accurate forecasting of wind turbine power output, P estimation. Estimations concerning the actual power output (P) values were illustrated in Figures 4.44-4.46 using scatter diagrams. Thus, in these figures, it is demonstrated that the results of predictions based on the *ANN* model especially for optimum rotational (Ω) case were in fairly close agreement with the corresponding actual wind turbine power output (P) data.

4.6.4. Concluding Remarks

In this part of the dissertation, the power output (P) of a horizontal axis wind turbine referred as T5 was predicted using the *ANN* forecasting tool and compared the results with the actual average values obtained from five turbines. The results obtained from this forecasting model compared to the actual data of power output, P were in good agreement especially for the optimum rotational speeds (Ω). According to the prediction model, the *MAPE* values at rotational speeds (Ω) of 13.94 rpm and 16.14 rpm were found to be 6.48% and 1.47%, respectively. For the testing process, the maximum value of the correlation coefficient (R) was obtained for the optimal rotational speed (Ω) conditions of the turbine, estimated as $R=0.9991$. Similarly, the *MAPE* values obtained at the optimum rotational speed (Ω) of 16.14 rpm were better than those results obtained at rotational speeds of 12.44 and 13.94 rpm. Consequently, the advantage of this forecasting *ANN* model is that wind turbine power output (P) can be predicted, regardless of detailed knowledge of turbine operations and topographical data, and can provide successful results when the required hub-height wind speed (U_D), atmospheric air temperature (T_{atm}), and turbine rotational speed (Ω) data are available. Furthermore, the wind turbine power curve of any site can be successfully estimated with a high degree of accuracy using this *ANN* estimation

model suggested utilizing the wind speed (U_D), atmospheric air temperature (T_{atm}), and turbine rotational speed (Ω).

4.7. Wind Power Curve Estimation by Adaptive Neuro-Fuzzy Inference System

4.7.1. Introduction

Sensitive forecasting of wind turbine output power curve has a significant role in tracing of conditioning and controlling of wind turbines in wind power plants. This part of the work involves the adaptive neuro-fuzzy inference system (*ANFIS*) in the forecasting of horizontal axis wind turbine output power (P) in terms of the climatic data and turbine rotational speed (Ω). Adaptive neuro-fuzzy inference system (*ANFIS*) is based on the input parameters covering the hub-height wind speed (U_D), atmospheric air temperature (T_{atm}), and the wind turbine rotational speed (Ω). These parameters were obtained from an operating wind power plant located in Turkey. Derived results of the testing process reveal that the minimum mean absolute percentage of error (*MAPE*), and the maximum correlation coefficient (R) values were determined for an optimum rotational speed (Ω). Namely, *MAPE* and R values were evaluated to be 1.18% and 0.9992, respectively when the *ANFIS* approach was applied to the wind farm data. These results indicated well that *ANFIS* approach presented a basic and a precise estimation in the wind turbine output power (P) determination. A wind farm's turbine power curve can be quickly forecasted in an accomplished way under little error through the utilization of the *ANFIS* forecasting method when the parameters of hub-height wind speed (U_D), atmospheric air temperature (T_{atm}), and rotational speed (Ω) of wind turbines in a wind farm are known. It is concluded that this technique is rather suitable in the decision-making process of new wind power

plant installations of a considered zone, or during the construction of totally a new wind farm.

4.7.2. The Objective of the Present Work

4.7.2.1. Study Region, Data, and Turbine Technical Specifications

The data used in this part of the dissertation were taken from a wind power plant (*WPP*) which is in current operation. The altitude of this wind farm is 400 m above the sea level. By the year 2008; the wind farm was in operation, and it comprised 17 identical wind turbines, each having a rated capacity of 2 MW. The hub height of the identical wind turbines is 67 m, and the rotor diameter is 80 m. The total swept area of a single wind turbine is thus 5027 m². The technical specification of identical wind turbines is given in Table 4.16. The wind turbines operate at a cut-in speed of 4 m/s, a cut-out speed of 25 m/s, and a nominal wind speed of 15 m/s. The present wind turbines are pitch-regulated upwind turbines with active yaw, and they have a three-bladed rotor.

Table 4.16. Technical properties of the considered wind turbines

Equipment	Properties
Rotor	
Diameter	80 m
Swept area	5,027 m ²
Nominal rotational	16.7 rpm
Operational interval range	9-19 rpm
Number of blades	3
Power regulation	Pitch/OptiSpeed
Air brake	Full blade pitch by three separate hydraulic pitch cylinders
Tower	
Hub-height	67 m
Operational data	

Cut-in wind speed	4 m/s
Nominal wind speed	15 m/s
Cut-out wind speed	25 m/s
Generator	
Type	Asynchronous with OptiSpeed
Rated output	2,000 kW
Operational data	50 Hz, 690 V
Gearbox	
Type	Planet/parallel axles
Control	
Type	Microprocessor-based control of all the turbine functions with the option of remote monitoring. Output regulation and optimization via OptiSpeed and OptiTip pitch regulation

The turbines employ the OptiTip and variable speed functions, making it possible to maintain the rated power even at very high wind speeds, regardless of the air temperature and the density. Also, the rotor rotation can be controlled to a range of speeds. The OptiSpeed generator allows the turbine rotor speed to run at rotational speeds (Ω) ranging between $\Omega = 9$ rpm and $\Omega = 19$ rpm. Additionally, the OptiTip system can also be employed at low free-stream wind speeds, and the variable speed function can, therefore, maximize the turbine output power (P) by optimizing the turbine rotational speed (Ω) and as well pitch angle.

In this part of the dissertation; five wind turbines, $T1$, $T2$, $T3$, $T4$, and $T5$, were selected for the present study. For each of the selected wind turbines, the data taken from the WPP included the turbine power output (P , kW), hub-height wind speed (U_D , m/s), atmospheric air temperature (T_{atm} , °C), and turbine rotational speed (Ω , rpm). Table 4.17 illustrates the relationship between these input and output parameters, and their correlation with wind power output (P) is presented.

Table 4.17. Variation of variables and related statistical parameters

Inputs and output	Unit	Min	Max	Mean	St. dev.	Cor. with P
P	kW	2.63	2000.63	1187.23	679.32	1.000
U_D	m/s	2.87	24.50	12.48	5.57	0.896
T_{atm}	°C	6.00	27.00	17.08	4.47	-0.640
Ω	rpm	12.43	16.40	14.67	1.58	0.703

It is obvious from Table 4.17 that hub-height wind speed, U_D , is the most effective factor in wind power output (P). In addition, hub-height wind speed, U_D has a directly proportional relationship to wind power output (P). On the other hand, an increase in the atmospheric air temperature (T_{atm}) inversely affects wind power output (P), since an increase in the air temperature, T_{atm} results in the expansion of the atmospheric air. This, unfortunately, means that a lower mass flow rate of air interacts with the turbine rotor blades. Furthermore, the absolute correlation ratio with atmospheric air temperature (T_{atm}) is lower in comparison with the hub-height wind speed (U_D). On the other hand, the absolute magnitude of the correlation ratio of turbine rotational speed (Ω) with the wind power output (P) is smaller when compared to the hub-height wind speed (U_D) correlated with power output (P), but greater than the absolute value of the atmospheric air temperature, T_{atm} correlated with power output (P). As can be seen from Table 4.17; among the studied and observed variables, when the minimum value of the wind power output (P) was 2.63 kW, the maximum output power (P) obtained was 2000.63 kW. The minimum and maximum values of the hub-height wind speed (U_D) were 2.87 m/s and 24.50 m/s, respectively. Besides, the data also revealed that the average minimum atmospheric air temperature (T_{atm}) for the five wind turbines was 6.00 °C, with a maximum value of 27.00 °C. And finally, the average rotational speed (Ω) of five turbines varied, with a minimum value of 12.43 rpm, and a maximum value of 16.40 rpm was observed.

The data was accumulated in the year 2013 and included the data for the

entire year. Measurements were taken over periods of every 10 minutes. The data were initially composed of 52560 measurements ($365 \times 24 \times 6$) in total, for each parameter related to hub-height wind speed, U_D , air temperature, T_{atm} , wind turbine rotational speed, Ω , and generated power, P . Initially, original data for rotational speed, Ω was classified within the limit ranges such as $1.00-2.99$, $3.00-4.99$, $5.00-6.99$, $7.00-8.99$, $9.00-10.99$, $11.00-12.99$, $13.00-14.99$, and $15.00-16.99$ [rpm]. The probability distribution of turbine rotational speed, Ω was calculated as shown in Figure 4.47. The average value in terms of turbine rotational speed, Ω corresponding to each class mark of the probability distribution for five wind turbines was calculated. Hence, the average class marks of probability distribution considering all wind turbines were calculated as 2.02 , 4.10 , 6.05 , 8.08 , 10.10 , 12.44 , 13.94 , and 16.14 [rpm] in terms of turbine rotational speed, Ω . Accordingly, designated class marks, including multi-data, were then performed for all wind turbines, and parameters such as hub-height wind speed, U_D , air temperature, T_{atm} , and turbine generated power, P were defined with respect to each class mark of rotational speed, Ω . In this way, in terms of turbine rotational speed (Ω), an average value corresponding to each class mark involved the variation in the values of parameters such as U_D , T_{atm} , and P .

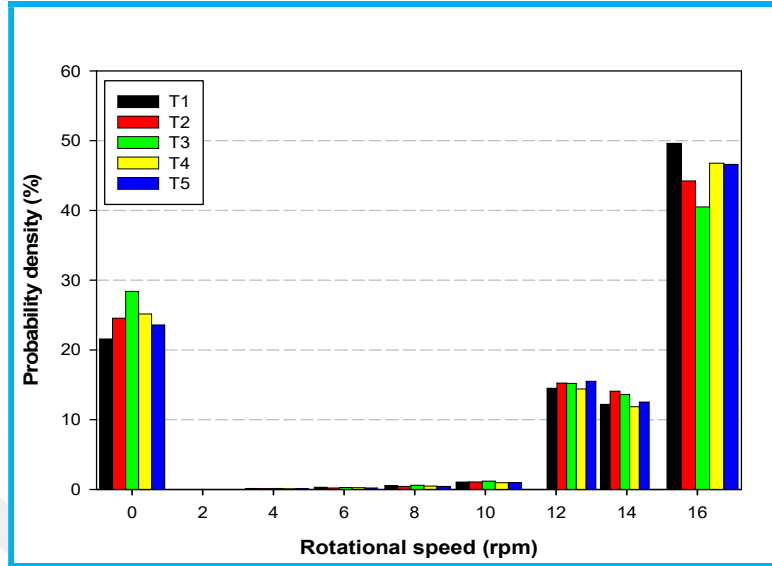


Figure 4.47. Probability density representation of the rotational speed (Ω)

Pre-filtering was performed in order to eliminate power data given at zero or negative erroneous wind power (P) values. These improper data probably arose from the rapid alterations in hub-height wind speed (U_D), vortices forcing a change in position of the rotor, or possible maintenance of the wind turbines. For these reasons, power generation could not be assessed at high wind speeds. Thus, the probability density of turbine rotational speed, Ω , corresponding to a value of the non-rotational case, i.e., 0 [rpm] was observed to be 22%. It should be observed that these data as presented in Figure 4.47 to correspond 0 [rpm] were omitted from the present computations, in this part of the work.

As shown in Figure 4.47, it was satisfactory that half of the data were observed, corresponding to a nominal rotational speed (Ω) of the rotor of 16.14 rpm. Also, pre-filtered data involving turbine rotational speeds (Ω) below 12.44 rpm were then filtered for the second time, since data within the rotational speed range of $2.02 \leq \Omega \leq 10.10$ rpm corresponded to only 2% of the total data. Finally, the remaining 76% of the total data were used for the forecasting *ANFIS* models.

4.7.2.2. ANFIS Forecasting Method

In this part of the dissertation, three inputs (hub-height wind speed (U_D), atmospheric air temperature (T_{atm}), and turbine rotational speed (Ω)), and one output (wind turbine output power, P) were considered. The complete set of 27 fuzzy architectural “if-then” rules were architecturally related below, and are summarized in Figure 4.48.

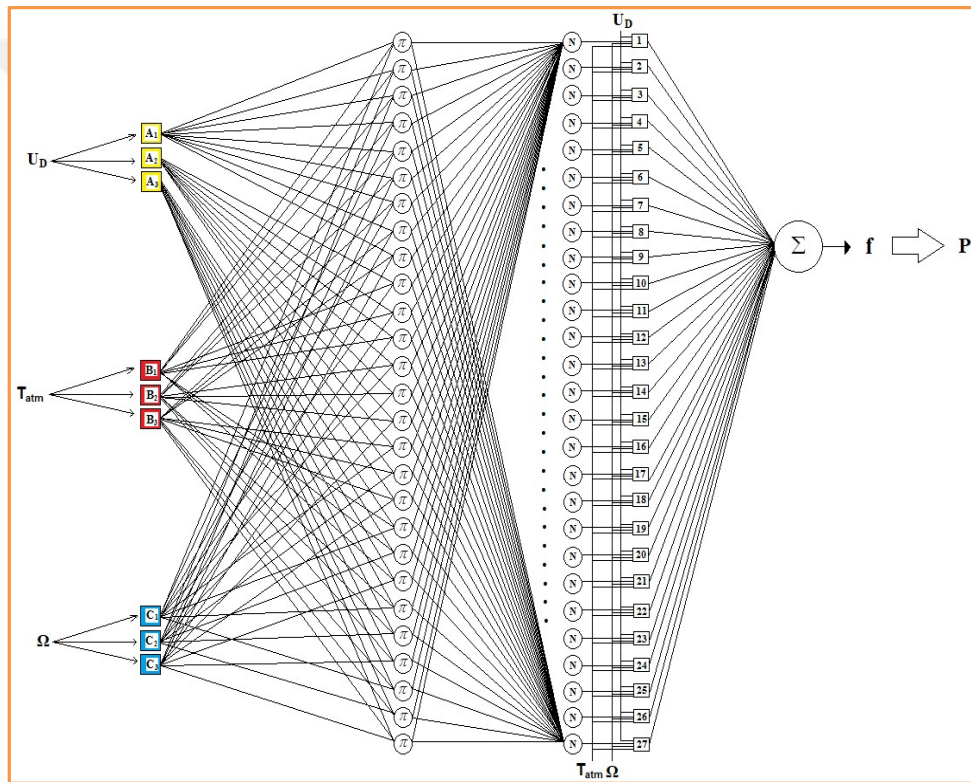


Figure 4.48. Schematic ANFIS representation with three inputs, three linguistic labels, and a total of 27 nodes

In this part of the dissertation, m given in Eq. (3.69) denotes 27, indicating that 27 consequent parameters equal to the total amount of rules were obtained, as given in Figure 4.48. The ANFIS architecture obtained in this part of the

dissertation is shown based on the Takagi and Sugeno's fuzzy if-then rules (Jang, 1993).

The logic of the if-then rules considered in this part of the dissertation is derived as follows, ranging from 1 to 27, however, only four rules are summarized as shortly:

Rule 1: If U_D is A_1 , T_{atm} is B_1 , and Ω is C_1 , then the *ANFIS* function can be written as $f_1 = p_1x + q_1y + r_1$.

Rule 2: If U_D is A_1 , T_{atm} is B_1 , and Ω is C_2 , then the *ANFIS* function can be written as $f_2 = p_2x + q_2y + r_2$.

Rule 3: If U_D is A_1 , T_{atm} is B_1 , and Ω is C_3 , then the *ANFIS* function can be written as $f_3 = p_3x + q_3y + r_3$.

·
·

Finally,

Rule 27: If U_D is A_3 , T_{atm} is B_3 , and Ω is C_3 , then the *ANFIS* function can be written as $f_{27} = p_{27}x + q_{27}y + r_{27}$.

Similarly to the three rules given above, an additional 23 further rules can be constructed, making a total of 27 rules, covering three premise parameters belonging to every input ($3 \times 3 \times 3 = 27$). In this context, the other equations can be constructed covering Rule 3 to Rule 27. The general equation given with Eq. (3.69) can similarly form the other rules, as in the case of Rules 1, 2, 3, and 27, shown above.

In this part of the dissertation, estimations of *ANFIS* depending on the variables hub-height wind speed, U_D , atmospheric air temperature, T_{atm} , and turbine rotational speed, Ω were performed to demonstrate three linguistic labels. These can be illustrated with Eqs. (4.3), (4.4), and (4.5), which are similar to Eqs. (3.71),

(3.72), and (3.73), respectively. However, atmospheric air temperature (T_{atm}), and turbine rotational speed (Ω) are shown with the functions, P and R , respectively.

$$O_i^1 = \mu A_i(U_D) \quad (4.3)$$

$$P_i^1 = \mu B_i(T_{atm}) \quad (4.4)$$

$$R_i^1 = \mu C_i(\Omega) \quad (4.5)$$

The present study involved $i = 3$ amount of nodes for each linguistic label of A , B , and C . Thus, Eqs. (4.3), (4.4), and (4.5) can be modified by considering three nodes for each linguistic label, A , B , and C ; as presented in Table 4.18.

Table 4.18. Basic linkage relations to the first layer (i.e., *premise*) using three inputs (U_D , T_{atm} , and Ω)

$O_1^1 = \mu A_1(U_D)$	$O_2^1 = \mu A_2(U_D)$	$O_3^1 = \mu A_3(U_D)$
$P_1^1 = \mu B_1(T_{atm})$	$P_2^1 = \mu B_2(T_{atm})$	$P_3^1 = \mu B_3(T_{atm})$
$R_1^1 = \mu C_1(\Omega)$	$R_2^1 = \mu C_2(\Omega)$	$R_3^1 = \mu C_3(\Omega)$

Transformation of a_i , d_i , and g_i with $2\sigma_i$ was carried out considering Eqs. (3.76), (3.77), and (3.78); since the *ANFIS* gives parameter outputs were based on the parameter, σ_i . Thus, the referred equations are considered to set the best proper parameter set of $\{\sigma_i, c\}$, where related members were arranged to allow values structuring the set to be; $\{4.867, 3.34\}$; $\{4.781, 13.8\}$; $\{4.246, 24.58\}$ for the linguistic labels of $A_i(U_D)$, where $i = 1, 2$, or 3 , respectively. Thus, appropriate specific Gaussian curve membership function was determined from the general membership function in order to express it in a form for specific to the present study. Consequently, a specialized functional form of the linguistic label A_i regarding this part of the dissertation on the hub-height wind speed, U_D was given with this parameter set.

Similarly, parameter sets of {4.654, 6.069}; {4.363, 16.4}; {4.228, 27.13}, and {0.4564, 12.27}; {0.4333, 14.3}; {0.8023, 16.37}, for linguistic labels $B_i(T_{atm})$ and $C_i(\Omega)$ and for nodes $i = 1, 2$, and 3 were chosen, respectively. Consequently, considering the general form of the Eqs. (3.76), (3.77), and (3.78), and special forms of linguistic labels A_i , B_i , and C_i for this part of the study, the following equations were set up and these are presented in Table 4.19.

Table 4.19. Gaussian curve membership (i.e., *gaussmf*) functional relations of the first layer (i.e., *premise*)

$\mu A_1(U_D) = e^{-\frac{1}{2} \left(\frac{U_D - 3.34}{4.867} \right)^2}$	$\mu A_2(U_D) = e^{-\frac{1}{2} \left(\frac{U_D - 13.8}{4.781} \right)^2}$	$\mu A_3(U_D) = e^{-\frac{1}{2} \left(\frac{U_D - 24.58}{4.246} \right)^2}$
$\mu B_1(T_{atm}) = e^{-\frac{1}{2} \left(\frac{T - 6.069}{4.654} \right)^2}$	$\mu B_2(T_{atm}) = e^{-\frac{1}{2} \left(\frac{T - 16.4}{4.363} \right)^2}$	$\mu B_3(T_{atm}) = e^{-\frac{1}{2} \left(\frac{T - 27.13}{4.228} \right)^2}$
$\mu C_1(\Omega) = e^{-\frac{1}{2} \left(\frac{\Omega - 12.27}{0.4564} \right)^2}$	$\mu C_2(\Omega) = e^{-\frac{1}{2} \left(\frac{\Omega - 14.3}{0.4333} \right)^2}$	$\mu C_3(\Omega) = e^{-\frac{1}{2} \left(\frac{\Omega - 16.37}{0.8023} \right)^2}$

A specialized form of Eq. (3.80) can be written in terms of the hub-height wind speed, U_D ; air temperature, T_{atm} ; and turbine rotational speed, Ω , as shown in Eq. (4.6).

$$w_i = \mu A_i(U_D) \cdot \mu B_i(T_{atm}) \cdot \mu C_i(\Omega) \quad (4.6)$$

The present study consisted of 27 ($m = 27$) amounts which were included in all rules' firing strengths to calculate the denominator of Eq. (3.81). Thus, for the given i^{th} node, the firing strength, depending on the node over the denominator, presents the ratio of the firing strengths for that node. Consequently, Eq. (4.7) may be derived as a specialized form of Eq. (3.81) for use:

$$\bar{w}_i = \frac{w_i}{w_1 + w_2 + w_3 + \dots + w_{27}} \quad (4.7)$$

During the normalization by Eq. (4.7); the node i here is given for the range $i = 1, 2, 3, 4, \dots, 27$. A specialized form of the output layer presented in Eq. (3.81) depends on the normalized firing strength (\bar{w}_i) for the i^{th} node being dependent on the input parameters of hub-height wind speed (U_D), atmospheric air temperature (T_{atm}), and turbine rotational speed (Ω). Moreover, the parameter set given in Eq. (3.82) as $\{p_i, q_i, \dots, r_i\}$ is also dependent on the same input variables. However, a new additional parameter is required within the parameter set of Eq. (3.82); since three inputs were used for the present study. A modified parameter set can therefore be constructed; as $\{p_i, q_i, l_i, r_i\}$. Thus, Eq. (4.8) can be constructed as follows, taking Eq. (3.82) into consideration:

$$O_i^4 = \bar{w}_i f_i = \bar{w}_i(U_D, T_{atm}, \Omega) f_i(U_D, T_{atm}, \Omega) = \bar{w}_i(U_D, T_{atm}, \Omega) [p_i(U_D, T_{atm}, \Omega)x + q_i(U_D, T_{atm}, \Omega)y + l_i(U_D, T_{atm}, \Omega) + r_i(U_D, T_{atm}, \Omega)] \quad (4.8)$$

Sub- and superscripts, i and 4 presented in Eq. (4.8) represent the i^{th} node number and the fourth layer, respectively.

Similarly and finally; for the fifth layer, the overall output of the layer is written as Eq. (4.9), based on Eq. (3.83).

$$O_i^5 = \text{overall output} = \sum_i \bar{w}_i(U_D, T_{atm}, \Omega) f_i(U_D, T_{atm}, \Omega) = \frac{\sum_i w_i(U_D, T_{atm}, \Omega) f_i(U_D, T_{atm}, \Omega)}{\sum_i w_i(U_D, T_{atm}, \Omega)} \quad (4.9)$$

In addition, sub- and superscripts i and 5 in Eq. (4.9) represent the i^{th} node number and the fifth layer, similarly.

4.7.3. Results and Discussions

The prediction model was trained and as well tested to compare and evaluate the *ANFIS* forecasting performance. Figures 4.49 and 4.50 illustrate the comparison between the prediction of *ANFIS* model and measured results for the training data set. On the other hand, using the results based on the testing data set, the scatter diagrams of the *ANFIS* model predictions against the actual power output (P) values were extracted in order to indicate the performance of the *ANFIS* forecasting model. As seen in Figures 4.51-4.53, the prediction results were in fairly close agreement with the corresponding actual turbine power output (P) values. These predictions confirmed that the *ANFIS* forecasting model could be a useful tool for accurately forecasting wind turbine aerodynamic characteristics based on only the hub-height wind speed, U_D , atmospheric air temperature, T_{atm} , and wind turbine rotational speed, Ω .

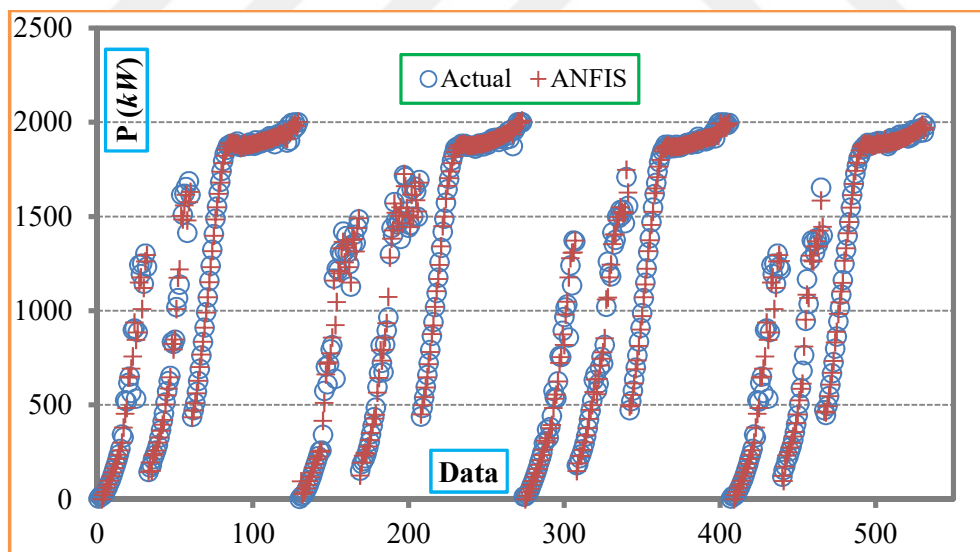


Figure 4.49. Comparison between the prediction of *ANFIS* forecasting model and actual measured results for the training data set

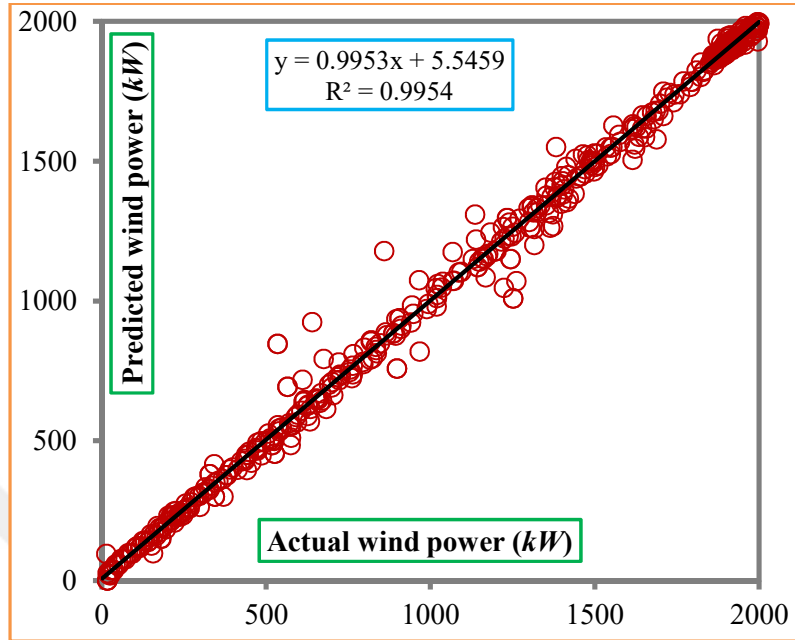


Figure 4.50. Comparison of actual and predicted generated power, P values for the training data set

Comparison of the *ANFIS* approach forecasting model estimations concerning the actual turbine power output (P) values is illustrated using the scatter diagrams. Figures 4.51-4.53 demonstrate that results of predictions based on the *ANFIS* approaching model especially for optimum rotational (Ω) cases are in reasonably close agreement with the corresponding actual wind turbine power output (P) data.

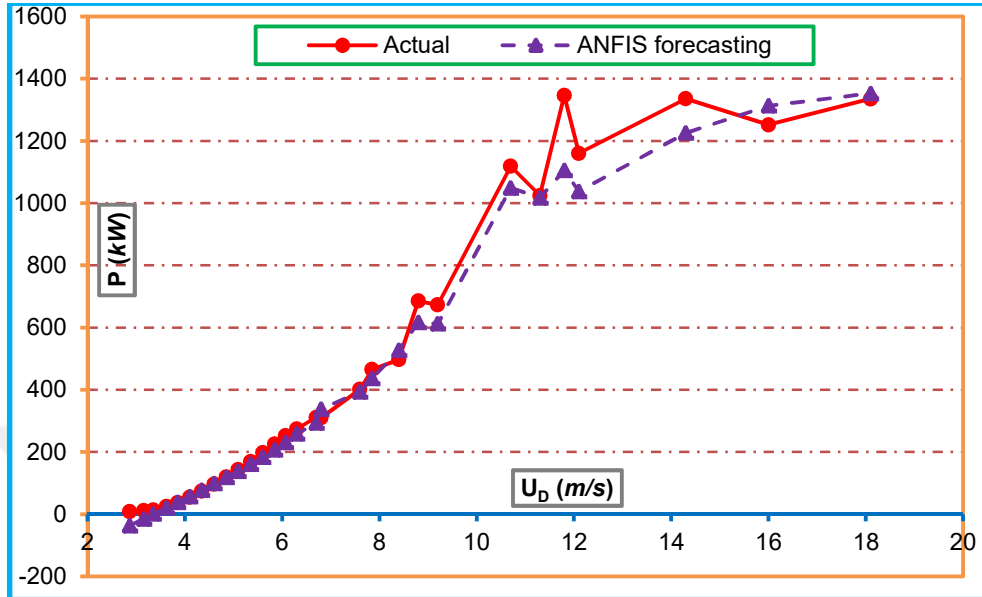


Figure 4.51. Comparison of output power (P) to the hub-height wind speed (U_D) at $\Omega=12.44$ rpm using ANFIS forecasting model

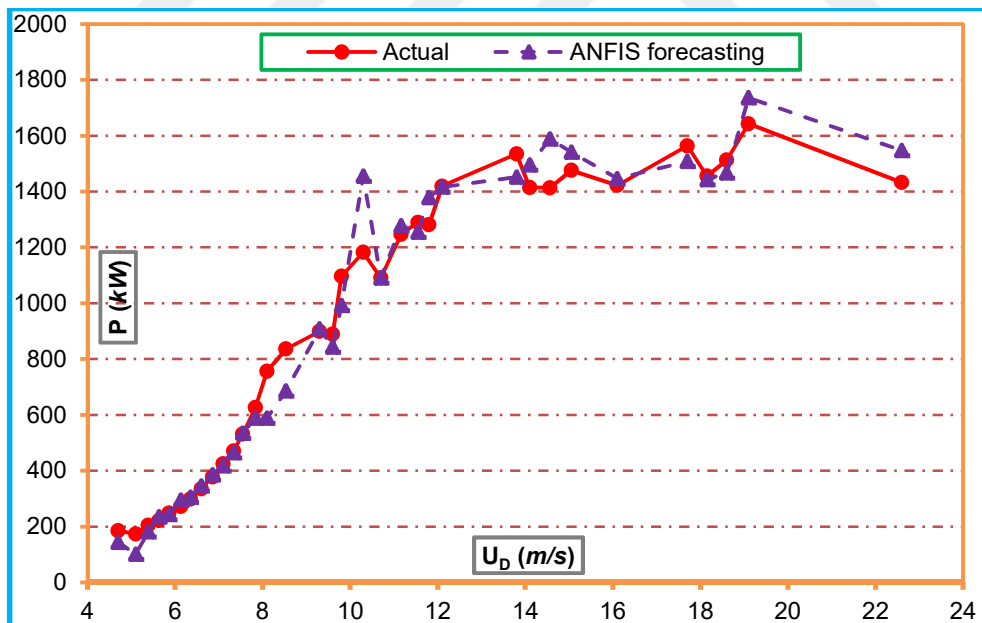


Figure 4.52. Comparison of power (P) to the hub-height wind speed (U_D) at $\Omega=13.94$ rpm using ANFIS forecasting model

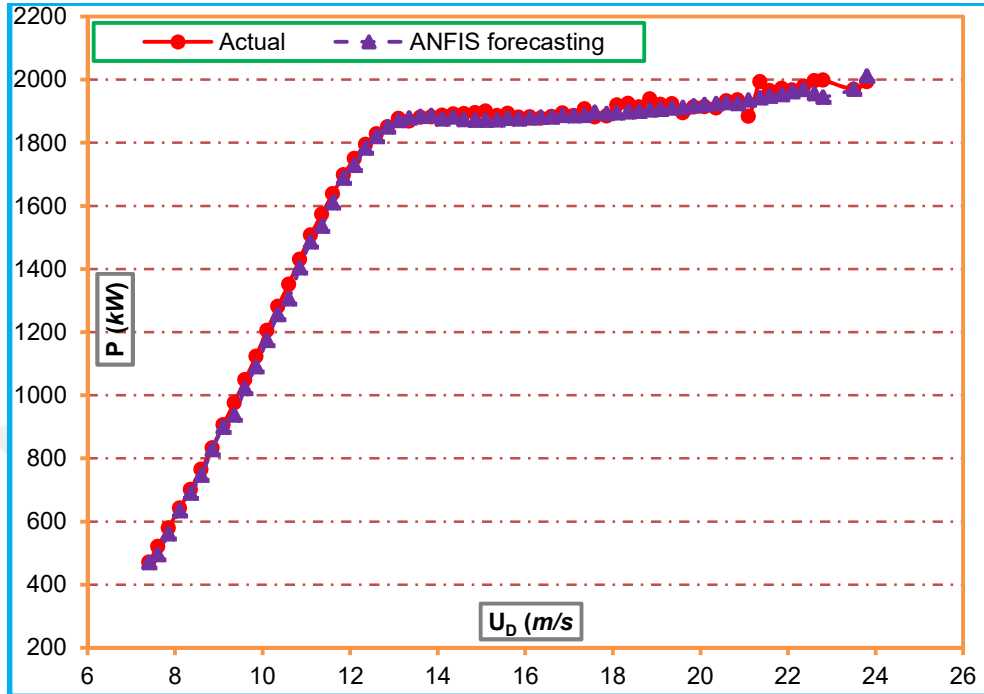


Figure 4.53. Comparison of power (P) to the hub-height wind speed (U_D) at $\Omega=16.1$ rpm using *ANFIS* forecasting model

Table 4.20 gives the *MAPE* and *R* statistical results of the training and testing data set depending on the *ANFIS* forecasting model computations with respect to the actual data set of power output (P).

In this context, during training of the program, the *MAPE* values were observed to be higher apart from the optimum rotational speed, $\Omega = 16.10$ rpm, in the *ANFIS* forecasting approach, when compared with the actual power output values of the wind turbines studied. On the other hand, considering the results of the testing stage; the *ANFIS* results also clearly revealed that the *MAPE* values of the estimated power output (P) values were generally among the lower and upper values of the *MAPE* according to the training results obtained from the four turbines.

Table 4.20. *MAPE* and *R* statistical results of the *ANFIS* forecasting model estimations

Ω (rpm)	Training process								Testing process	
	MAPE (%)				R				MAPE (%)	R
	T1	T2	T3	T4	T1	T2	T3	T4	T5	T5
12.44	39.53	37.41	15.80	38.44	0.9819	0.9928	0.9860	0.9831	34.40	0.9938
13.94	4.49	4.28	3.89	5.56	0.9964	0.9964	0.9958	0.9963	7.40	0.9888
16.10	0.52	0.7197	0.8966	0.8415	0.9996	0.9995	0.9995	0.9996	1.18	0.9992
whole	11.06	11.62	5.47	11.70	0.9977	0.9978	0.9978	0.9976	10.36	0.9970

However, in the rotational speeds of the *ANFIS* estimation of optimum rotational speed, i.e., $\Omega = 16.10$ rpm, the *MAPE* value of the power output (*P*) estimations of the testing stage was outside the lower and upper values of the training *MAPE* results. On the other hand, training and testing data both indicated in the *ANFIS* forecasting approach that higher statistical results of the correlation coefficient (*R*) were obtained.

On the other hand, *MAPE* statistical results did not indicate the same degree of success of the method, regardless of its value during the training stage, since the aim of the training was to obtain the true logic in terms of the computer program to present good estimates at the testing forecasting stage. Therefore, the conducted comments were based on the *MAPE* statistical results.

4.7.4. Concluding Remarks

In this part of the dissertation, the power output (*P*) of a horizontal axis wind turbine was predicted using the *ANFIS* forecasting approach and compared this approach with the actual average values obtained from five wind turbines. The results obtained from the *ANFIS* forecasting model were reported to have good

agreement with the actual values of the power output data. According to the prediction model for the *ANFIS*, the *MAPE* statistical values at turbine rotational speeds (Ω) of *13.94 rpm* and *16.10 rpm* were found to be *7.40%* and *1.18%*, respectively. For the testing process, the maximum statistical value of the correlation coefficient (*R*) was obtained for the optimal rotational speed (Ω) conditions of the turbine, i.e., at $\Omega=16.10$ rpm. In this context, the *R* value for the *ANFIS* model was determined as *0.9992* at this rotational speed of $\Omega=16.10$ rpm. On the other hand, the *MAPE* statistical values obtained at the optimum rotational speed (Ω) of *16.10 rpm* were better than those at rotational speeds of *12.44* and *13.94 rpm*. Consequently, the advantage of this forecasting model is that wind turbine power output (*P*) can be predicted, regardless of detailed knowledge of wind turbine operations and topographical data, and can provide the required hub-height wind speed (U_D), atmospheric air temperature (T_{atm}), and wind turbine rotational speed (Ω). Furthermore, the wind turbine power curve of any site can be successfully estimated with a high degree of accuracy utilizing the forecasting model suggested using the hub-height wind speed (U_D), atmospheric air temperature (T_{atm}), and turbine rotational speed (Ω).

4.8. Theoretical Analysis of Different Capacity Wind Turbines Using the Blade Element Momentum Theory

4.8.1. Introduction

It is known that the contribution rate of fossil fuels to air pollution is substantially high. For example, carbon dioxide, CO_2 emissions are unfortunately projected to rise from 35.9 Gt in 2014 to 42 Gt by the year of 2030. In this regard, renewable energy sources certainly play a significant role in electricity generation. Wind power presently compensates 3.7% of the global electricity demand.

However, by the year 2050, wind power is projected to contribute approximately 18% of the World's total electricity demand. In recent years, wind energy has attracted the attention of most energy producers. As a result of the increased demand for wind power globally, wind turbine technology has been progressing significantly.

In this part of the dissertation, an analysis and a comparison of the aerodynamic parameters for different capacity wind turbines are conducted. According to the power level of wind turbines produced by the manufacturers, a variety of different wind turbines are chosen with different capacities in order to examine parameters of rated power, P_r , power coefficient, C_p , axial flow induction factor, a , and thrust force, T defined with respect to the approaching free-stream wind speed, U_∞ having different level. In this context, in the first group of study, formerly expressed aerodynamic parameters are analyzed depending on the influence of diameter, D_{rotor} keeping the rated power, P_r of the wind turbines constant. On the other hand, the second group of study includes the influence of wind turbine rated power, P_r when the rotor diameter, D_{rotor} is kept constant. Thirdly, both rotor diameter, D_{rotor} and rated power, P_r of wind turbines are altered in order to analyze formerly expressed four aerodynamic parameters. Finally, the influence of the air density, ρ for the chosen wind turbine capacity was analyzed in order to configure these cited aerodynamic parameters. The results are compared in terms of the rated power and other aerodynamic outputs to reveal the performances of the chosen wind turbines.

4.8.2. The Objective of the Present Work

The data of the chosen wind turbines used was provided from the catalogs of a wind turbine manufacturer company (WP, 2018). Thus, the chosen wind turbine properties are given in Tables 4.21 and 4.22. In this part of the work, the

chosen wind turbines were initially classified in order to reveal the influence of the rotor diameter, D_{rotor} during keeping rated power, P_r of the wind turbines constant. On the other hand, the second operation involved the alteration of the rated power, P_r of the wind turbines under the same rotor diameter, D_{rotor} . Thirdly, both cited parameters are varied to analyze the influence of both in the aerodynamic inspection. Finally, only the air density, ρ is changed to observe the influence of this parameter on the wind turbine aerodynamics.

The performance parameters were analyzed for wind turbines including the types named as V80-2 MW, V90-2 MW, V100-2 MW, and V110-2 MW to reveal the influence of rotor diameter, D_{rotor} effect in the first part of the study. On the other hand, the second group of study involved wind turbines of type V90-1.8 MW, V90-2 MW, and V90-3 MW for the observation of turbine rated power, P_r alteration influences on power generations and rotor blade aerodynamics of those wind turbines. These selected wind turbines as a third group were V39-0.5 MW, V52-0.85 MW, V80-2 MW, V90-3 MW, and V112-3.3 MW, in order to consider both wind turbine capacity and rotor diameter enhancement influences on power generations and rotor blade aerodynamics of the cited wind turbines. Finally, in the last group of the performed study, the chosen wind turbine from the catalog is the type V90-3 MW. This cited wind turbine having a corresponding rotor diameter of $D_{rotor}=90$ m, and a turbine rated power of $P_r=3$ MW was examined in the fourth group to indicate the air density influences under the air densities, ρ of 1, 1.06, 1.12, 1.18, and 1.225 kg/m³.

Table 4.21. Wind turbines considered for the analysis of aerodynamic parameters (WP, 2018)

Variable	VESTAS TURBINE MODEL				
	V80-2 MW	V90-2 MW	V100-2 MW	V110-2 MW	V90-1.8 MW
Operating data					
Rated power, P_r	2,000 kW	2,000 kW	2,000 kW	2,000 kW	1,800 kW
Cut-in wind speed	3.5 m/s	3 m/s	3.5 m/s	4 m/s	3 m/s
Rated wind speed	14.5 m/s	13.5 m/s	12 m/s	12 m/s	13 m/s
Cut-out wind speed	25 m/s	25 m/s	22 m/s	20 m/s	25 m/s
Operational interval	9-19 rpm	8.2-17.3 rpm	13.4 rpm max		9-15 rpm
Wind class	IEC Ia (DIBt III)	IEC IIa/IIa	IEC IIb	IEC IIIa	IEC IIa/IIa
Offshore model	No	No	No	No	No
Power control	Pitch	Pitch	Pitch	Pitch	Pitch
Weights					
Nacelle	68 tons	68 tons	78 tons		68 tons
Tower	122-198 tons	206-335 tons	250 tons		148-245 tons
Rotor + hub	37 tons	36 tons	45 tons		38 tons
Total	227-303 tons	310-439 tons	373 tons		254-351 tons
Rotor					
Diameter, D_{rotor}	80 m	90 m	100 m	110 m	90 m
Swept Area, A_d	5,027 m ²	6,362 m ²	7,854 m ²	9,504 m ²	6,362 m ²
Power density	2.52 m ² /kW	3.19 m ² /kW	3.93 m ² /kW	4.76 m ² /kW	3.54 m ² /kW
Number of blades	3	3	3	3	3
Manufacturer	Vestas	Vestas	Vestas	Vestas	Vestas
Gearbox					
Gearbox	Yes	Yes	Yes	Yes	Yes
Stages	3	3	3	3	3
Gear ratio	100.5	112.8			112.8
Generator					
Type	ASYN	ASYN	DFIG	DFIG	ASYN
Number	1	1	1	1	1
Maximum speed	1,909 rounds/min	1,680 rounds/min			1,680 rounds/min
Voltage	690 V	690 V			690 V
Tower					
Minimum hub-height	60 m	95 m	80 m	80 m	80 m
Maximum hub-height	100 m	125 m	120 m	125 m	105 m
Manufacturer	Vestas	Vestas	Vestas	Vestas	Vestas

Table 4.22. Wind turbines considered for the analysis of aerodynamic parameters
(Continuing) (WP, 2018)

Variable	VESTAS TURBINE MODEL			
	V90-3 MW	V39-0.5 MW	V52-0.85 MW	V112-3.3 MW
Operating data				
Rated power, P_r	3,000 kW	500 kW	850 kW	3,300 kW
Cut-in wind speed	3.5 m/s	4.5 m/s	3 m/s	2.5 m/s
Rated wind speed	16.5 m/s	15.5 m/s	14 m/s	14 m/s
Cut-out wind speed	25 m/s	25 m/s	25 m/s	25 m/s
Operational interval	8.6-18.4 prm	30 rpm max	14-31.4 rpm	6.2-17.7 rpm
Wind class	IEC Ia/Ila		IEC I/II	IEC Ib/Ila
Offshore model	No	No	No	Yes
Power control	Pitch	Pitch	Pitch	Pitch
Weights				
Nacelle	68 tons	18 tons	22 tons	
Tower	155-235 tons	58 tons	77-111 tons	
Rotor + hub	28 tons	3.5 tons	10 tons	
Total	251-331 tons	79.5 tons	109-143 tons	
Rotor				
Diameter, D_{rotor}	90 m	39 m	52 m	112 m
Swept Area, A_d	6,362 m ²	1,195 m ²	2,124 m ²	9,852 m ²
Power density	2.13 m ² /kW	2.39 m ² /kW	2.5 m ² /kW	2.99 m ² /kW
Number of blades	3	3	3	3
Manufacturer	Vestas	Vestas	Vestas	Vestas
Gearbox				
Gearbox	Yes	Yes, Made by Hansen	Yes, Made by Hansen	Yes
Stages	3	3	3	3
Gear ratio	104.5	50	62	94.4
Generator				
Type	ASync	ASync, Made by Siemens	ASync, Made by Weier, ABB	
Number	1	1	1	
Maximum speed	1,680 rounds/min	1,255 rounds/min	1,947 rounds/min	1,550 rounds/min
Voltage	1000 V	690 V	690 V	650 V
Tower				
Minimum hub-height	65 m	40 m	65 m	84 m
Maximum hub-height	105 m	53 m	86 m	140 m
Manufacturer	Vestas		Vestas	Vestas

The four groups determined from the available manufacturer catalogs were used in the analysis of aerodynamic parameters including variations of output power, P of the wind turbines, power coefficients, C_p , axial flow induction factors, a , and thrust values, T . Whole of these conducted aerodynamic expressions are compared with each other in order to determine the superior wind turbine performances.

4.8.3. Results and Discussions

Wind turbine output power, P is analyzed to reveal wind turbine rotor diameter, D_{rotor} , rated power, P_r , both rotor diameter and rated power, and air density, ρ influences presented in Figures 4.54a, 4.54b, 4.54c, and 4.54d, respectively.

Wind turbine output power generation, P depending on the influence of the turbine rotor diameter, D_{rotor} , thus the rotor swept area, A_d considering wind turbines of constant rated power, P_r is shown in Figure 4.54a. In this figure, turbine power generation, P generally increases with increasing rotor swept area, A_d . On the other hand, the influence of the increase of wind turbine rated capacity, P_r on turbine power generation, P considering constant rotor swept area, A_d is presented in Figure 4.54b. Power curves considering the effects of both rotor swept area, A_d and wind turbine rated power, P_r are given in Figure 4.54c. Finally, Figure 4.54d demonstrates the influence of the air density, ρ on the generated turbine power, P in the case of V90-3 MW wind turbine.

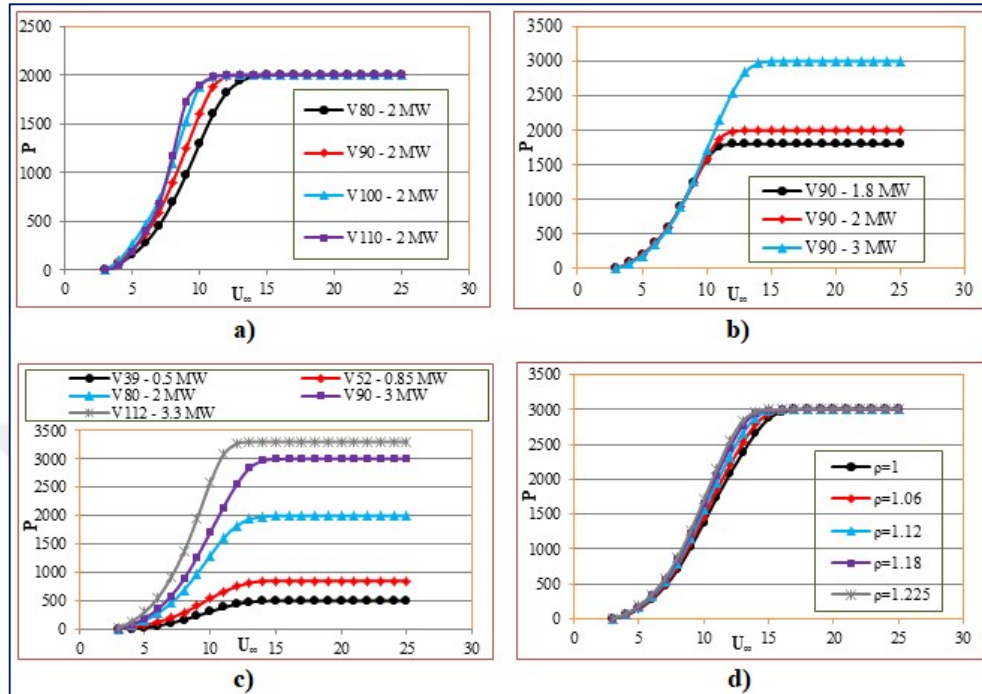


Figure 4.54. Wind turbine output power, P defined by the free-stream wind speed, U_∞ , according to the influences of **a)** wind turbine rotor diameter, D_{rotor} , **b)** turbine rated power, P_r , **c)** both rotor diameter and turbine rated power, and **d)** air density, ρ

On the other hand, axial flow induction factor, a of the wind turbines was studied with respect to the free-stream wind speed, U_∞ to analyze formerly expressed influences of the wind turbine rotor diameter, D_{rotor} , turbine rated power, P_r , both rotor diameter and rated power, and air density, ρ as shown in Figures 4.55a, 4.55b, 4.55c, and 4.55d, respectively.

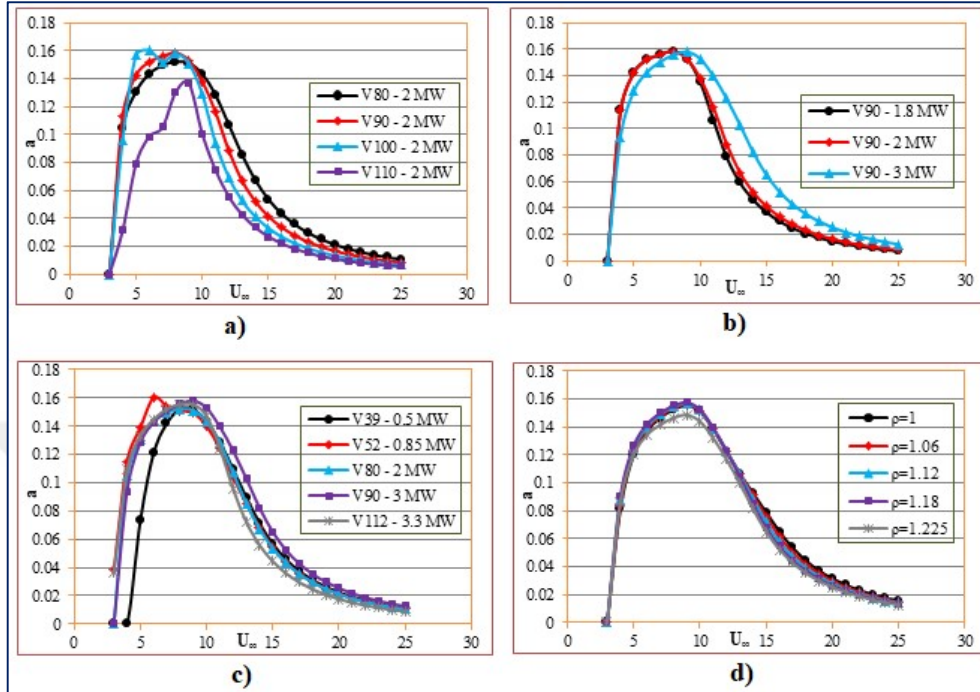


Figure 4.55. Axial flow induction factor, a expressed by free-stream wind speed, U_∞ , according to the influences of **a)** wind turbine rotor diameter, D_{rotor} , **b)** turbine rated power, P_r , **c)** both rotor diameter and turbine rated power, and **d)** air density, ρ

Figures 4.56a, 4.56b, 4.56c, and 4.56d demonstrate the influence of the similar cited parameters in the presentation of the wind turbine power coefficients, C_p expressed depending on the free-stream wind speed, U_∞ . Finally, wind turbine output thrust force values, T are defined depending as the function of free-stream wind speed, U_∞ shown in Figures 4.57a, 4.57b, 4.57c, and 4.57d.

In the case of wind turbines of 2 MW constant rated power, P_r ; wind turbine efficiency, C_p generally decreases with increasing rotor swept area, A_d as shown in Figure 4.56a. This situation is especially valid for the condition of the free-stream wind speed, $U_\infty \geq 10$ m/s. However, when the wind turbine of 90 m constant rotor diameter, D_{rotor} considered as presented in Figure 4.56b, the increase of the wind turbine capacity, P_r results in the efficiency, C_p increase. Similarly, this

situation is valid for the free-stream wind speed, U_∞ exceeding 10 m/s as well. On the other hand, the results are interesting as seen in Figure 4.56c. Since, the highest wind turbine efficiency values are obtained in V90-3 MW type wind turbine as demonstrated in Figure 4.56c. Thus, this part of the dissertation reports that the moderate capacity of turbine rated power, P_r and turbine rotor swept area, A_d results in the highest wind turbine efficiency, C_p . Finally, it is observed that the wind turbine efficiency, C_p slightly decreases with the increasing air density, ρ as presented in Figure 4.56d.

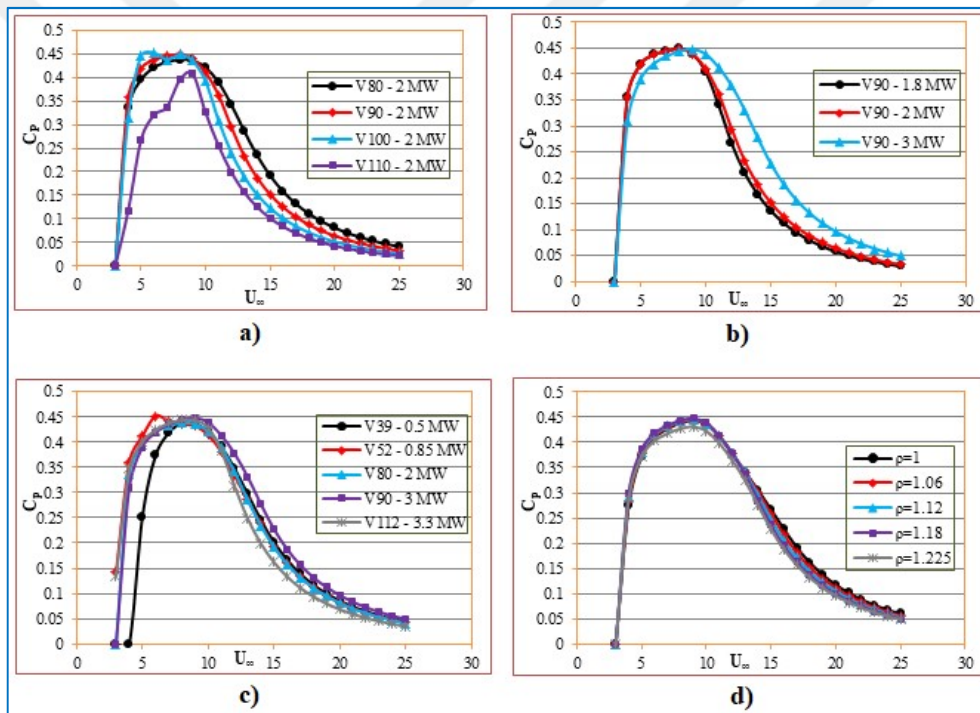


Figure 4.56. Power coefficient, C_p presented as a function of free-stream wind speed, U_∞ , for the analysis of **a)** wind turbine rotor diameter, D_{rotor} , **b)** turbine rated power, P_r , **c)** both rotor diameter and turbine rated power, and **d)** air density, ρ

The calculated thrust force, T values of the wind turbines indicated that the thrust values of 2 MW same capacity wind turbines generally increases with

increasing rotor swept area, A_d . On the other hand, when the free-stream wind speed, U_∞ is especially above 15 m/s, this increasing effect is being observed to drift away as shown in Figure 4.57a. Exceeding free-stream wind speed, U_∞ over 10 m/s results in the thrust force, T values to increase with increasing wind turbine capacity, P_r in the case of 90 m wind turbine rotor diameter as indicated in Figure 4.57b. However, below 10 m/s of free-stream wind speed, U_∞ , almost no difference between the thrust forces, T of different capacity wind turbines is observed. Figure 4.57c presents the variation of thrust force, T defined according to the free-stream wind speed, U_∞ considering a variety of chosen wind turbines at different turbine capacities and rotor diameters. The thrust force, T generation was observed to be highest in the V112-3.3 MW wind turbine of greatest swept area, A_d and highest rated power, P_r as expected. This cited wind turbine generated a corresponding thrust force, T value of 319 kN at an 11 m/s free-stream wind speed, U_∞ as seen in Figure 4.57c. Finally, thrust force values, T of the considered wind turbines taken into account were reported to generally increase with increasing air density, ρ as shown in Figure 4.57d. On the other hand, the influence of the air density, ρ on the thrust force, T especially exceeding free-stream wind speed, U_∞ of 15 m/s is so weak. Thus, beyond this cited value of the free-stream wind speed, U_∞ the influence of the air density function over the thrust force, T is not clear in the free-stream wind speed range of $15 \text{ m/s} \leq U_\infty \leq 25 \text{ m/s}$. Especially, the influence of the air density, ρ function is so specific for the free-stream wind speed in the range of $10 \text{ m/s} \leq U_\infty \leq 15 \text{ m/s}$.

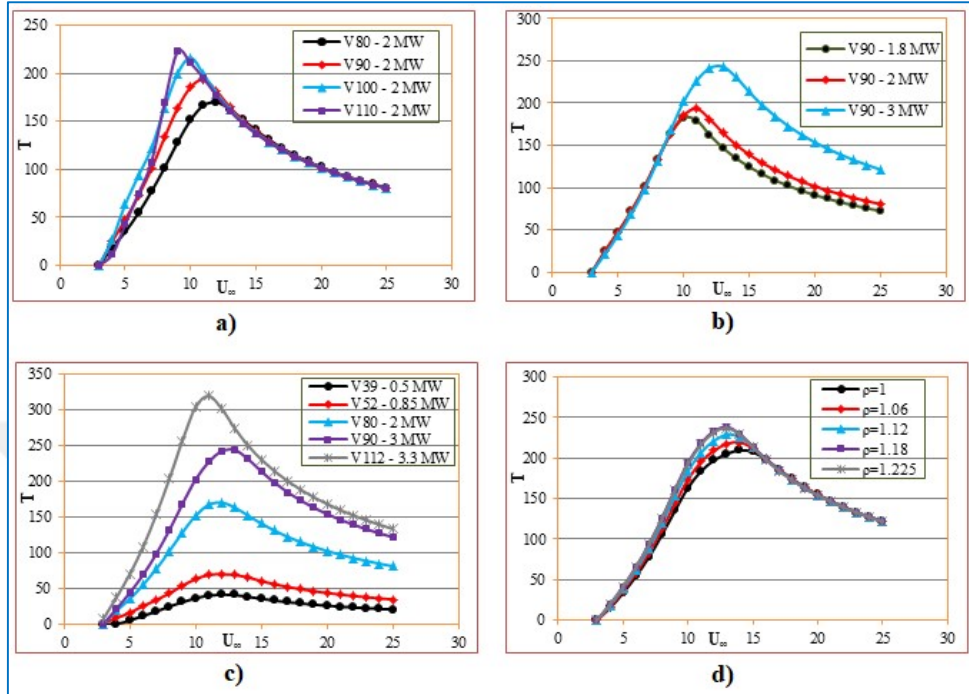


Figure 4.57. Thrust force, T values of the chosen wind turbines shown depending to free-stream wind speed, U_{∞} , in the analysis of **a)** wind turbine rotor diameter, D_{rotor} , **b)** turbine rated power, P_r , **c)** both rotor diameter and turbine rated power, and **d)** air density, ρ

4.8.4. Concluding Remarks

Wind turbine technology development indeed requires the understanding of the turbine aerodynamics in terms of the aerodynamic parameters. In this context, this part of the thesis provides a good description of wind turbine aerodynamics by comparisons of turbine aerodynamic parameters between selected wind turbine types shown in Tables 4.21 and 4.22. In these regards, nine different types of wind turbines were chosen to conduct the comparison of their wind turbine output power, P , axial flow induction factors, a , power coefficients, C_p , and finally thrust forces, T . The results obtained are given as follows:

- Output power generation, P is weakly influenced by the increase of rotor swept area, A_d , however much more influenced depending on the increase of turbine rated power, P_r . On the other hand, higher power generations, P are obtained in proportion to the increase of both parameters.
- The influence of air density, ρ on the generated wind turbine output power, P under the same rotor swept area, A_d and turbine rated power, P_r was observed to be weak.
- In terms of power coefficient, C_p speaking; it was observed that the best parameter influencing the improvement of the power coefficient, C_p was reported to be rotor swept area, A_d decrease. It is interesting to note that an increase of both rotor swept area, A_d and turbine rated power, P_r does not provide an increase of power coefficient, C_p . A moderate capacity wind turbine of 90 m rotor diameter, D_{rotor} and 3 MW of rated capacity, P_r generally provides the highest wind turbine efficiency, C_p especially in the case of exceeding 10 m/s free-stream wind speed, U_∞ .
- Again the influence of air density, ρ on the wind turbine power coefficient, C_p under the same rotor swept area, A_d and the turbine rated power, P_r was observed to be weak, as well. On the other hand, uncertainties in the influence of air density, ρ on power coefficient, C_p are especially much more evident in the free-stream wind speed, U_∞ in the range of $3 \text{ m/s} \leq U_\infty \leq 14 \text{ m/s}$.
- Finally, the increase of three parameters including air density, ρ , wind turbine rotor swept area, A_d , and turbine rated power, P_r functions resulted in the increase of thrust force, T . In this context, among the chosen wind turbines, the highest thrust force, T value was obtained in the V112-3.3 MW wind turbine corresponding to a thrust force of $T=319 \text{ kN}$, corresponding to a free-stream wind speed of $U_\infty=11 \text{ m/s}$.

4.9. Wind Turbine Shrouding Systems

4.9.1. Comparison of Theoretical and Actual Power Coefficients

To achieve a rapid forecast of maximum power coefficient obtained at a considered configuration of a rotor and a given wind property, the basic formula presented in Eq. (1.5) is used (Wilson et al., 1976).

Under the light of this information, comparison of the power coefficient, C_p definition designated with respect to the tip speed ratio, λ_R , handled according to the studies of Sørensen and the general momentum theory (*G.M.T.*) adopted from Burton et al. (Sørensen, 2011; Burton et al., 2011); and the data of an installed wind farm was processed by (Ilhan et al., 2018a), as shown in Figure 4.58. Although the theoretical results (Sørensen, 2011; Burton et al., 2011) and the installed onshore wind farm results (Ilhan et al., 2018a) are shown to be in a good agreement, in the case of three-bladed rotor configuration consideration, it is clear from this figure that theoretical estimation of the power coefficient exceeds the installed wind farm result by 90%. The comments performed of the field study and theoretical outputs were conducted based on three-bladed rotor case, since considered wind turbines of the wind farm involved three-bladed rotors. Although the theoretical maximum power coefficient, C_p is equal to $C_p=0.57$ (Sørensen, 2011; Burton et al., 2011) in the range of $14.86 < \lambda_R < 15$, in the case of installed wind farm (Ilhan et al., 2018a), the actual maximum power coefficient, C_p is equal to $C_p=0.30$ in the range of tip speed ratio, $6.5 < \lambda_R < 7.5$. Five wind turbines designated as *T1*, *T2*, *T3*, *T4*, and *T5* were also examined, and it was observed to outcome similar results of power coefficient, C_p based on whole processed data (Ilhan et al., 2018). On the other hand, another important point to be underlined is that the *G.M.T.* (Burton et al., 2011) generates similar results to the case of the

infinite number of blades (Sørensen, 2011) with very small discrepancies as shown in this figure.

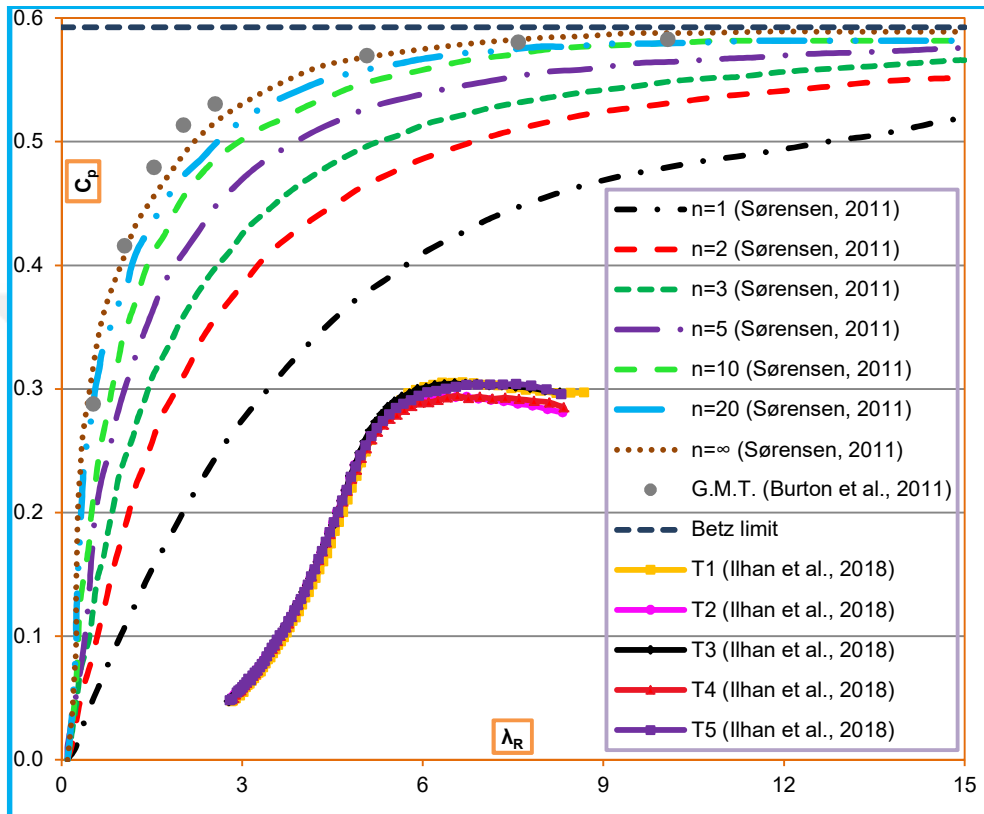
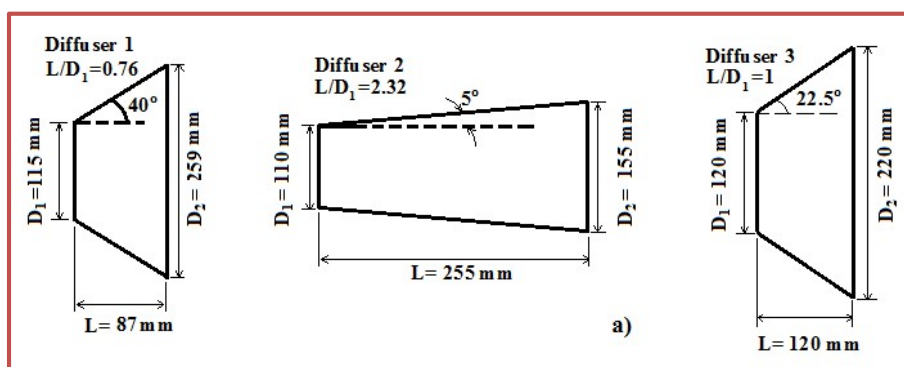


Figure 4.58. Theoretical expressions of power coefficient, C_p compared to an installed wind farm results (Sørensen, 2011; Burton et al., 2011; İlhan et al., 2018a)

4.9.2. Variation of Wind Speed through the Rotor Cross-Section Placed in Diffuser with Different Geometrical Parameters

Four different geometric configurations of diffusers as shown in Figure 4.59a are considered for the performance of different casing configurations (Disterfano et al., 2015). Those configurations were selected to measure the axial

wind velocity distributions, $u(x)$ along with the diffuser under variations of diffuser casing full-cone angles, 2θ and diffuser casing full-body axial lengths, L . Thus, in this way, wind speed ratios, u/U_∞ inside the casing bodies are configured, and wind speed enhancements are defined with respect to the dimensionless axial coordinate, x/L normalized on the casing full body length, L . As the related results reported in Figure 4.59b, the highest wind speed ratio, $K=U_{max}/U_\infty=1.48$ takes place at a location very close to the diffuser entry for the smallest full-cone angle, $2\theta=10^\circ$, and the longest diffuser length ratio, $L/D_1=2.32$ symbolized as Diffuser 2 in Figure 4.59a (Disterfano et al., 2015). In general, especially boundary layer separations originate in the diffuser body according to the considered full-cone angles, 2θ in Diffusers 1 and 3 deteriorating the performance, thus resulting in lower acceleration at the entry of those cited diffusers. On the other hand, maximum wind speed ratio exceeding, $K=1.79$ was obtained at a location very close to the diffuser entry with an opening angle $2\theta=8^\circ$ and diffuser length ratio, $L/D_1=7.7$ (Figure 4.59a, Diffuser 4) studied experimentally as seen in Figure 4.59b. This result fairly exceeded the others due to the high dimensionless casing axial full-body length normalized on inlet diameter, L/D_1 . Thus, this configuration's geometrical dimensions kept diffuser exit to inlet area ratio at $\mu^*=4$ for Diffuser 4 in a similar range usually found in the literature (Ohya and Karasudani, 2010).



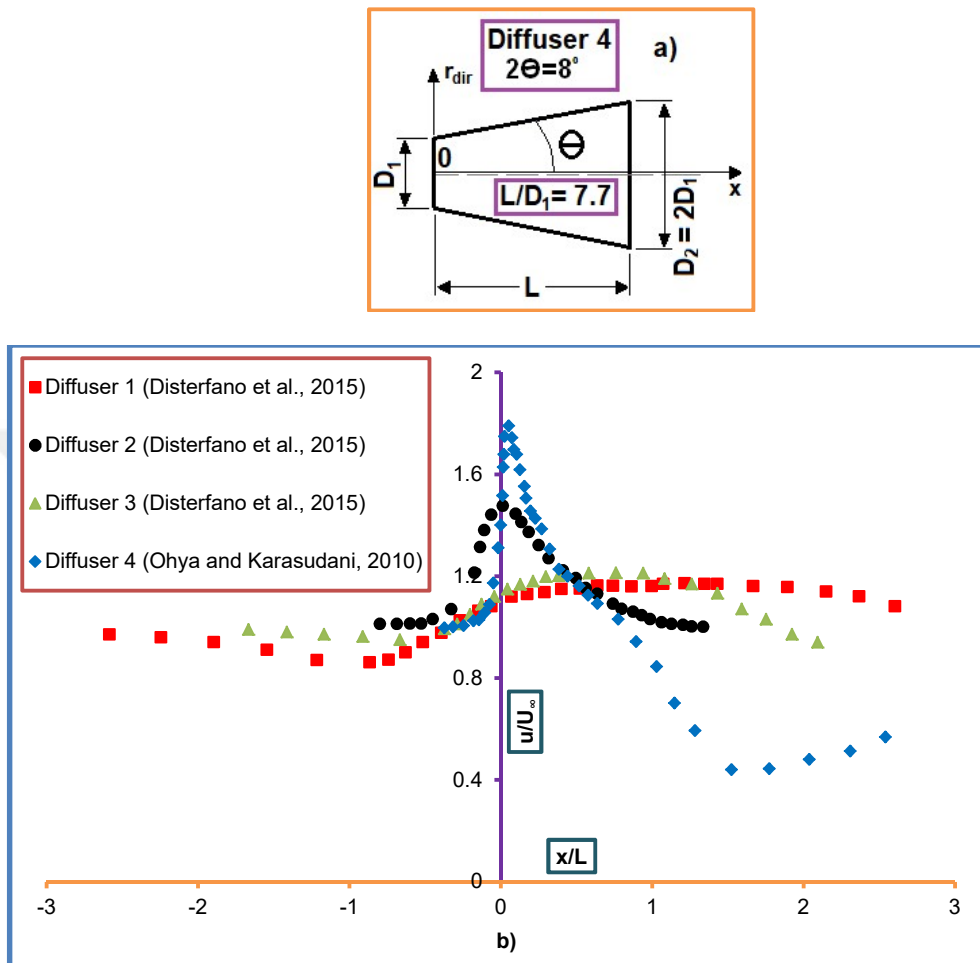


Figure 4.59. Distributions of wind speed ratio, u/U_∞ in four different diffuser configurations, **a)** four different diffuser configurations, **b)** corresponding wind speed ratio, u/U_∞ (Disterfano et al., 2015; Ohya and Karasudani, 2010)

4.9.3. The Progress of Wind Speed in the Airfoil Structured Casing System

An increase of axial wind speed distribution, $u(x)$ with respect to the free-stream wind speed, U_∞ within the airfoil structured shroud casing is undoubtedly quite essential (Nasution and Purwanto, 2011). Their experimental results measured by a hot wire can serve for this purpose to both measure the axial wind

speed, u and radial wind speed, v as both are shown in Figure 4.60. Considering the shrouding system presented in this figure, maximum wind speed augmentation of $K=1.41$ was obtained inside the casing system. One of the most important advantages of this airfoil structured shrouding system resulted in maximum enhanced wind speed, U_∞ to be both increased and shifted further towards the downstream of the casing shroud as well as seen in Figure 4.60. In this way, the correct position of the turbine rotor can be settled inside the casing body especially to prevent the boundary layer separations. Additionally, according to the results compared with conventional diffuser shrouding systems and the one in the form of airfoil structure presented that 1.29 times more enhancement in maximum axial wind speed, U_{max} and as well maximum radial wind speed, V_{max} inside the casing were obtained. The boost of wind speed is simply obtained by altering internal curvature of casing shroud to obtain an airfoil structure in place of a plain surface configuration as both configurations shown in Figure 4.60.

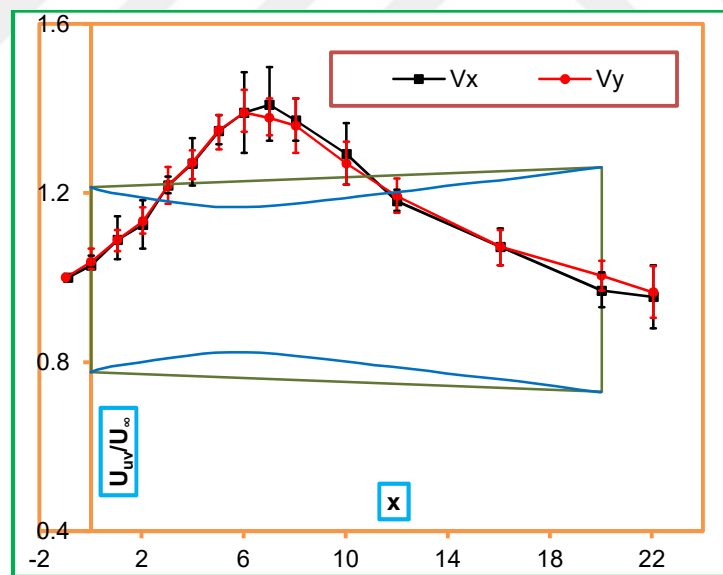


Figure 4.60. Axial, u and radial, v experimental wind speed measurements inside the casing shroud bodies (Nasution and Purwanto, 2011)

4.9.4. Comparison of Airfoil Structured Casing System with respect to the Conventional Linear Diffuser Casing Systems

4.9.4.1. Case Study 1

The first configuration of Table 4.27, shown below, is the designed configuration of (Hansen et al., 2000) presenting the mass flow rate of the air, \dot{m} running through the rotor induced by the airfoil structured casing system (AFSCS) which rises the extracted power, P for the same thrust coefficient, C_T compared with respect to the conventional bare wind turbine (Hansen et al., 2000). Placing a deformed NACA0015 airfoil shaped casing shroud system around the wind turbine generates a higher lift force comparing to the bare wind turbine that produces higher circulated ring vortices. The angle between the central line of airfoil and diffuser central axis at the inlet is zero degree, but since the trailing edge of the airfoil is gradually bent outward, the outlet included angle is therefore set to 15.6 degree. The results of this airfoil study are compared with respect to the results of diffuser casing structures which the configurations are available in Figure 4.59a, and the comparisons of results are shown in Figure 4.61. This study of comparison is quite important to point out the superior performance of the airfoil casing utilization over a conventional diffuser shrouding in terms of the obtained power coefficient, C_p results. Thus, the results of an airfoil shrouding gives outcomes exceeding power coefficient, C_p over 0.9 as presented in this figure (Hansen et al., 2000; Disterfano et al., 2015).

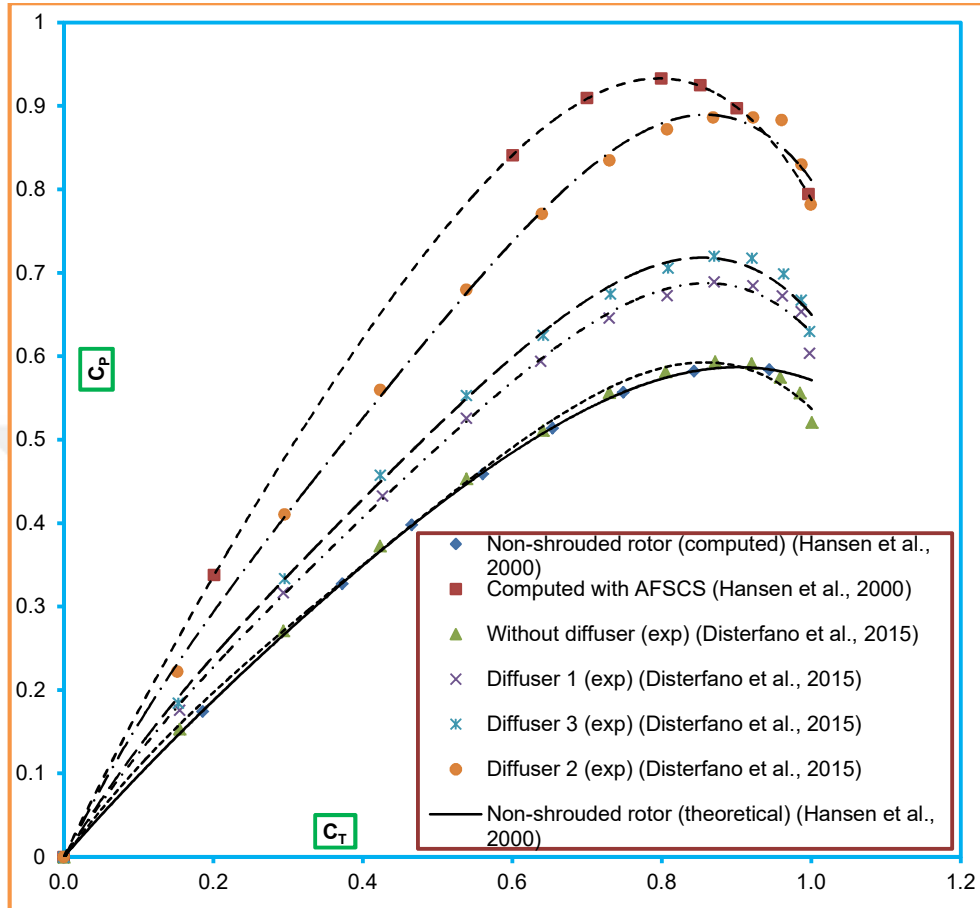


Figure 4.61. Rotor power coefficients, C_p expressed as the function of thrust coefficients, C_T (Hansen et al., 2000; Disterfano et al., 2015)

4.9.4.2. Case Study 2

On the other hand, experimental studies conducted the power coefficient of the wind turbine under the conditions of casing configurations including nozzle, diffuser, and flange components all together resulted, power coefficient in the vicinity of $C_p=1.4$. However, power coefficient, C_p for conventional bare wind turbines is very low, i.e., only around $C_p= 0.35$ as shown in Figure 4.62 (Ohya et al., 2008). It is also aimed in this part of the dissertation to reveal the second case

study performance comparisons of a flanged diffuser shroud with respect to an airfoil shrouding as also presented in the same figure. It is evident from this figure that although both types of casings generated the similar maximum power coefficient, C_p results, the tip speed curve range determined for flanged diffuser shroud is greater than that of airfoil type casing. Besides, the maximum power coefficient, C_p results are obtained at higher values of tip speed ratios, λ_R in the case of flanged diffuser and airfoil shrouding utilizations (Ohya et al., 2008; Grassmann et al., 2003). And, considering the tip speed ratio, λ_R values corresponding to the maximum power coefficient, C_p values for bare wind turbines are reported to be higher in the study of (Ohya et al., 2008), since the blade tip speed ratio, λ_R is a function of wind turbine rotor rotational speed which is higher due to high free-stream wind speed, U_∞ . On the other hand, considering the blade tip speed ratio, λ_R values corresponding to the maximum power coefficient, C_p values for shrouded wind turbines are conducted to be also higher in the study of (Ohya et al., 2008). Additionally, the discrepancy range of blade tip speed ratios, λ_R considering both studies are larger in the case of shrouding utilizations mostly influenced by the augmented wind speed, u through the casing where the wind turbine is located, x_t . Besides, maximum values of the power coefficients, C_p demonstrate a larger result is obtained in the case of airfoil shrouding with a percentage of 6% enhanced value in the case of airfoil type shrouding (Grassmann et al., 2003) out coming power coefficient as $C_p=1.46$.

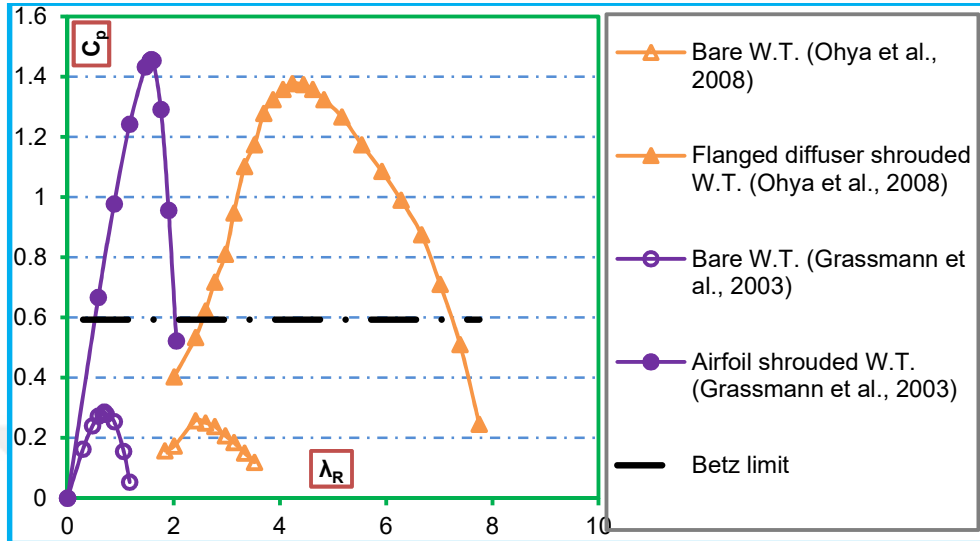


Figure 4.62. Power coefficient, C_p comparisons for the wind turbines equipped with and without shrouding utilizations, and application of shroudings utilizing a flanged diffuser and an airfoil casing types (Ohya et al., 2008; Grassmann et al., 2003)

4.10. Comparison of the Casing Advantages Described by the main Aerodynamic Characteristics

Power coefficients, C_p defined depending on the tip speed ratio, λ_R considering a variety of studies in literature is presented in Figure 4.63; whereas, the used configurations with the main wind turbine properties regarding those studies and related symbols are shown in Tables 4.23. It is evident from this figure that the maximum power coefficient, C_p values were achieved in an airfoil cased study (Grassmann et al., 2003), reaching $C_p=1.46$; and secondly in a flanged diffuser inlet shrouded casing (Ohya et al., 2008), reaching $C_p=1.38$; on the other hand the minimum power coefficient, C_p values among the considered studies regarding the peak values of the reviewed studies was observed to be at a diffuser shaped shroud for Savonius type rotors, reaching only $C_p=0.14$ (Larin et al., 2015) as shown in Figure 4.63. The properties of this ideal airfoil cased shroud in a

similar form of a sail include a configuration having a throat diameter, $D_f=1.52$ m. And this section is reported to be the narrowest section of the casing shroud, i.e., at the turbine location, x_t . On the other hand, this airfoil casing shroud enlarges through an outer casing exit diameter, $D_2=2.6$ m. Besides, the axial full-body length of the shroud casing was designed to be set at, $L=1.1$ m, long (Grassmann et al., 2003).

Energy and momentum balance was observed to be not provided sufficiently in conventional diffuser casing systems, thus brought alternative shrouding system optimizations to the literature studies including especially airfoil type of shrouding applications. However, the fluid dynamic simulation program, namely Star-CD was utilized in the correct optimization of the airfoil shrouding dimensions which ultimately propagated a proper sizing as above mentioned (Grassmann et al., 2003).

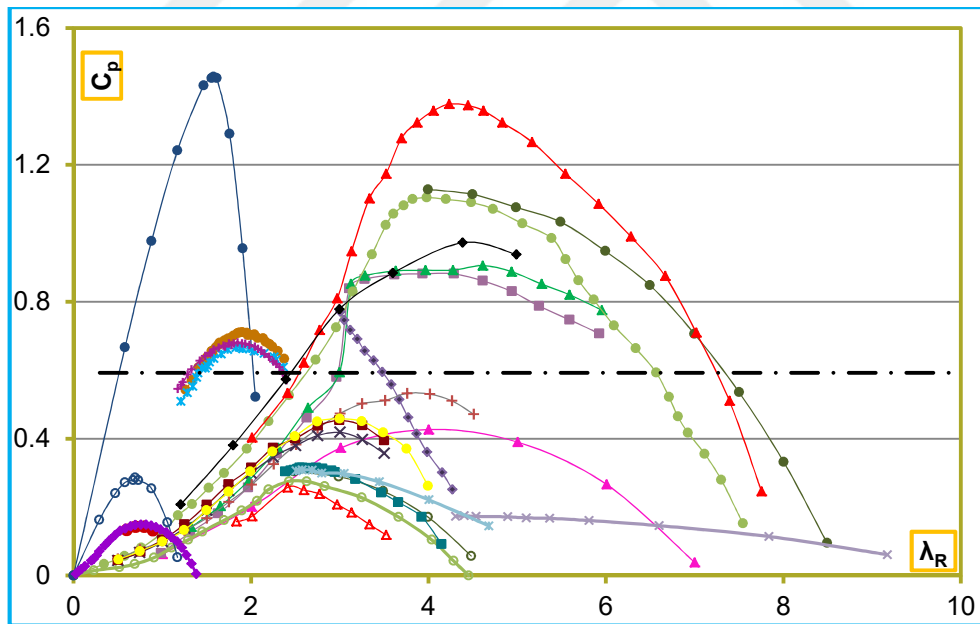

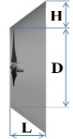







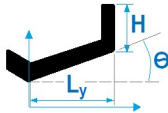

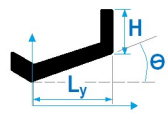


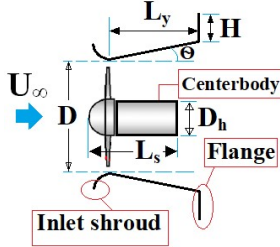


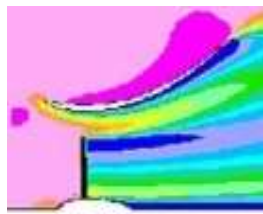

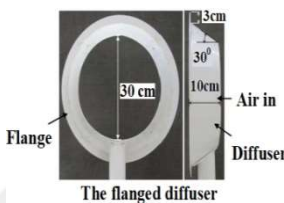








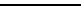
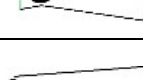

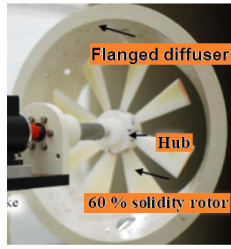

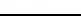

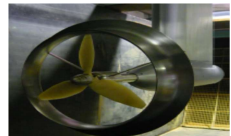

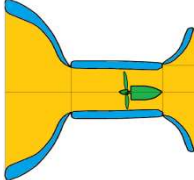


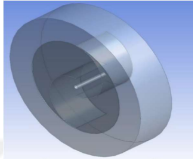

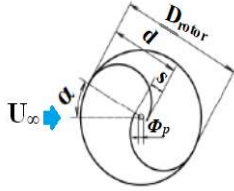



Figure 4.63. Power coefficient, C_p expressions against tip speed ratio, λ_R for different literature studies of wind turbines with and without a casing shroud utilization, reviewed in Table 4.23

Table 4.23. Related reference names, the symbols relating to the results given in Figure 4.63, the relevant casing geometries of wind turbines, the type of studies, related other data and information

Ref.	Symbol	Study type	U_∞ (m/s)	D_{rotor} (m)	Casing type	Conf.
(Jafari and Kosasih, 2014)		Num.	10	0.65	Flanged diffuser	
(Ohya and Karasudani, 2010)		Exp.	8	1	Flanged diffuser shroud	
(Ohya and Karasudani, 2010)		Exp.	8	1	Flanged diffuser shroud	
(Abe et al., 2005)		Num.	11	0.39	None	-----
(Abe et al., 2005)		Exp.	11	0.39	None	-----
(Abe et al., 2005)		Num.	6.8	0.39	Flanged diffuser shroud	
(Abe et al., 2005)		Exp.	6.8	0.39	Flanged diffuser shroud	
(Ohya et al., 2008)		Exp.	6	0.59	None	-----
(Ohya et al., 2008)		Exp.	6	0.59	Flanged inlet shrouded diffuser casing	
(Grassmann et al., 2003)		Num.	5	1.12	None	-----

(Grassman et al., 2003)		Num.	5	1.12	Airfoil cased	
(Chen et al., 2012)		Exp.	14	0.30	Flanged diffuser	
(Chen et al., 2012)		Exp.	14	0.30	None	
(Kosasih et al., 2012)		Exp.	7	0.19	Brimmed diffuser shroud	
(Kosasih et al., 2012)		Exp.	7	0.19	Diffuser augmented	
(Kosasih and Tondelli, 2012)		Exp.	6	0.19	Nozzle-diffuser shrouded	
(Kosasih and Tondelli, 2012)		Exp.	6	0.19	Diffuser shrouded	
(Chen et al., 2013)		Exp.	12	0.3	Diffuser augmented	
(Chen et al., 2013)		Exp.	12	0.3	Flanged diffuser	
(Chen et al., 2013)		Exp.	12	0.3	Flanged diffuser	
(Sun and Kyoazuka, 2011)		Num.	1	0.3	Brimmed diffuser shroud	

(Wang et al., 2008)		Exp.	13.9	0.57	Divergent, convergent, and cylindrical scoop	
(Wang et al., 2008)		Exp.	13.9	0.57	No scoop	-----
(Larin et al., 2015)		Num.	4.4	2.44	Diffuser shaped shroud for Savonius	
(Hayashi et al., 2005)		Exp.	12	0.42	Diffuser shaped shroud for Savonius	
Betz		-----	-----	-----	-----	-----

Moreover, presently used configurations taken into account with the main wind turbine properties regarding these studies which are considered in Figure 4.64, are reviewed in Table 4.24. In this figure, numerical predictions and experimental measurements of the wind speed ratios, u/U_∞ for different literature studies are expressed depending on the dimensionless axial coordinate system, x/D , i.e., according to the chosen coordinate system and the throat area, D of the considered literature studies. It is clear from this figure that the maximum wind speed ratio, K is obtained in the study of flanged diffuser casing with an appropriate inlet shroud configuration design optimized in a linear form (Mansour and Meskinkhoda, 2014), attaining a maximum wind speed ratio of $K=1.67$. Considering another study of flanged diffuser casing with an inlet shroud configuration (Owis et al., 2015), the maximum wind speed ratio has become $K=1.66$, reaching almost the previously mentioned. On the other hand, according to

the peak values of the reviewed literature studies; minimum value among the maximum wind speed ratios, K was observed to be at a two-way diffuser shroud which was tested for flanged and non-flanged cases, reaching only $K=1.16$ as the peak value (Setoguchi et al., 2004), the optimized configuration shown in Figure 1.36 of Section 1.3.5.5.(3), whereas the related wind speed performance demonstrated in Figure 4.64. It is important to note the properties of the ideal casing structure generating the highest maximum wind speed ratio, K owns a particular design configuration including half cone angle, $\Theta=4^\circ$, dimensionless casing full body length, $L/D=1.5$, dimensionless flange height, $H/D=0.25$, and tested at a loading coefficient of $C_l=0$. The casing profile generating a similar result of maximum wind speed ratio, such as $K=1.66$ which has also the similar design properties of configuration including dimensionless casing full body length, $L/D=1.5$, half cone angle, $\Theta=4^\circ$, no loading case, $C_l=0$, and dimensionless flange height, $H/D=0.5$ (Owis et al., 2015). However the small discrepancy observed between both results corresponding to a value of 0.01 of maximum wind speed ratio, K is probably due to the different casing inlet shroud design configurations both constructed in the former study of (Mansour and Meskinkhoda, 2014), and (Owis et al., 2015). Also, the result may also be dependent to the dimensionless flange height, H/D variation given in Mansour and Meskinkhoda as $H/D=0.25$ (Mansour and Meskinkhoda, 2014), and slightly different in Owis et al. designed at $H/D=0.5$ (Owis et al., 2015). However, the lowest value among the considered maximum wind speed ratio, K values was seen in a two-way diffuser system including the shrouding type having a cross-section in a similar form of a truncated triangle configuration, thus it was designed to have some cylindrical structure for a small part of axial length in the middle, as it was shown in Figure 1.36. Additionally, it has also concentrating and diffusing sections in upstream and downstream of flows, respectively (Setoguchi et al., 2004). This designed configuration generating the lowest value among the considered maximum wind

speed ratio, K values had the condition of the non-flanged case, i.e., at dimensionless flange height condition of $H/D=0$. Thus, this configuration was observed to be unfortunately insufficient in maximum wind speed ratio, K enhancement among whole considered designs also including other parameters such as dimensionless casing full body length, $L/D=2$, and casing full-cone angle, $2\theta=20^\circ$, resulting $K=1.16$ (Setoguchi et al., 2004).

Comparison of available numerical analysis and numerical and experimental studies of (Abe and Ohya, 2004), especially those who had initiated the studies regarding wind turbine shrouding systems, when outcome indications of good agreements generate correct flow fields, thus by this way accurate dimensioning of wind turbine casing systems are designed. Their studies and others found in the literature adopting their studies have shown that flanged diffuser casing performance is strongly influenced by casing half cone angle, θ and the flange height, H . Additionally, constructing a proper design of an inlet shrouding presented a remarkable enhancement in axial wind speed, u by 1.6-2.1 times more than that of the approaching free-stream wind speed, U_∞ (Mansour and Meskinkhoda, 2014). This increase is due to the introduction of a flange structure and an inlet component generating a low pressure region in the downstream area of the diffuser through vortex formation and allowing extra wind flowing onto the rotor disc.

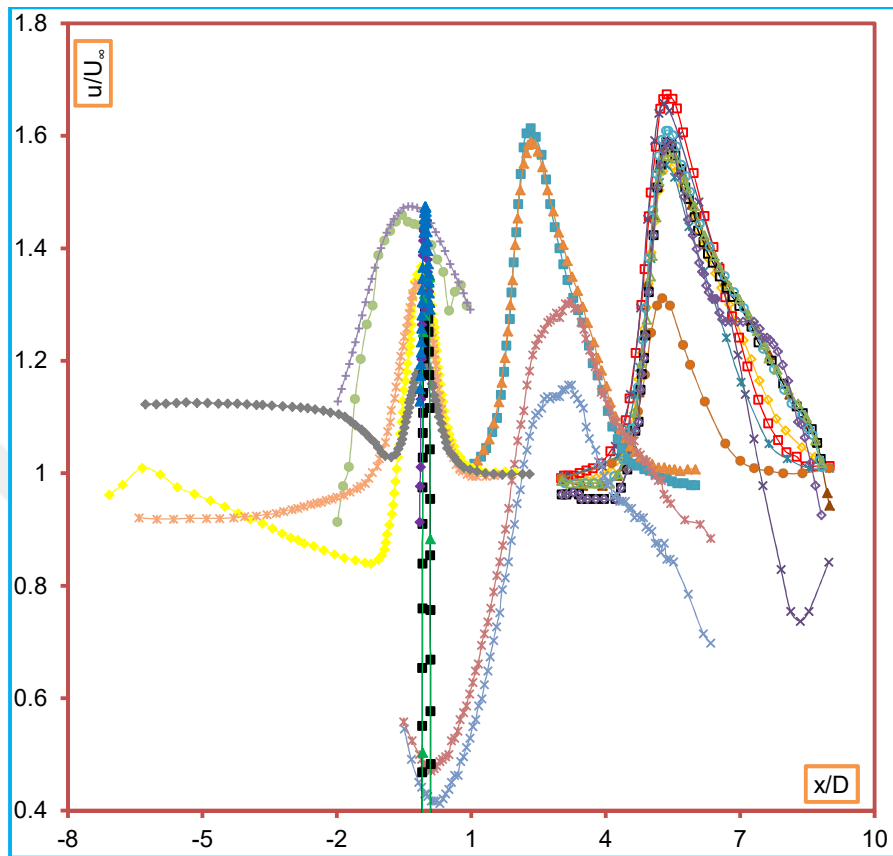

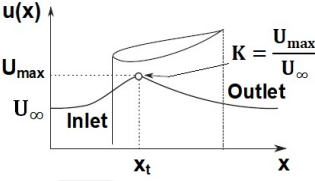


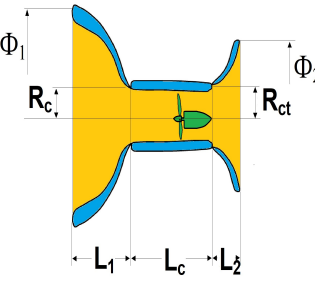




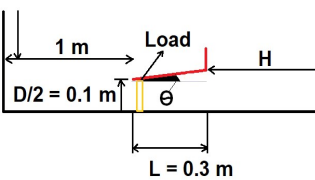


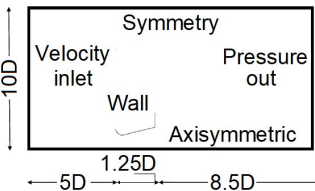




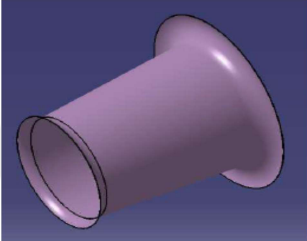




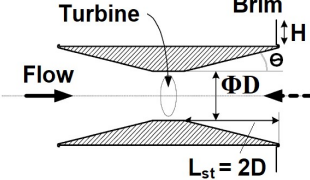




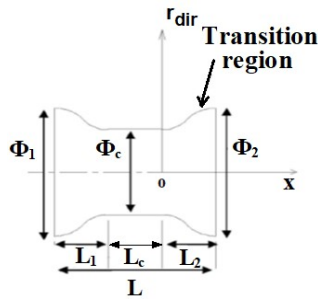


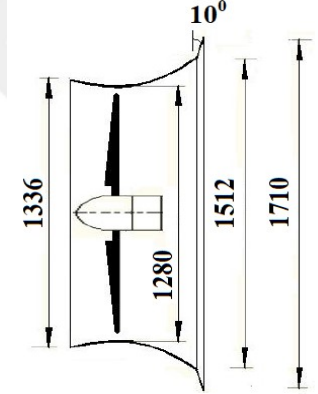


Figure 4.64. Wind speed ratio, u/U_∞ distributions along the central axis of the casing for different literature studies, reviewed in Table 4.24

Table 4.24. Related reference names, the symbols relating to the results given in Figure 4.64, the relevant casing geometries of wind turbines, the type of studies, related other data and information

Ref.	Symbol	Study type	U_∞ definition	Rotor dia. def.	Casing type	Conf.
(Rio Vaz et al., 2014)		Exp.	$U_\infty = 5 \text{ m/s}$	0.2 m	Flanged diffuser	
(Rio Vaz et al., 2014)		Theo.	$U_\infty = 7 \text{ m/s}$	4 m	Airfoil cased	
(Wang et al., 2008)		Num.	$U_\infty = 11.25 \text{ m/s}$	4 m	Scoop cased with long axial cylindrical section	
(Wang et al., 2008)		Exp.	$U_\infty = 11.25 \text{ m/s}$	4 m	Scoop cased with long axial cylindrical section	
(Wang et al., 2008)		Exp.	$U_\infty = 11.25 \text{ m/s}$	4 m	Scoop cased with long axial cylindrical section	
(Wang et al., 2008)		Num.	$U_\infty = 11.25 \text{ m/s}$	4 m	Scoop cased with long axial cylindrical section	

(Mansour and Meskin khoda, 2014)		Num.	$U_{max}/U_{\infty}=1.6-2.1$	$L/D=1.5$	Linear type of shroud with a flange component	
(Mansour and Meskin khoda, 2014)		Num.	$U_{max}/U_{\infty}=1.6-2.1$	$L/D=1.5$	Linear type of shroud with a flange and small inlet shroud later introduced to the casing	
(Owis et al., 2015)		Num.	$U_{\infty}=5 \text{ m/s}$	$L/D=1.5$	Linear type of casing with inlet shroud and flange components	
(Owis et al., 2015)		Num.	$U_{\infty}=5 \text{ m/s}$	$L/D=1.5$		
(Owis et al., 2015)		Num.	$U_{\infty}=5 \text{ m/s}$	$L/D=1.5$		
(Owis et al., 2015)		Num.	$U_{\infty}=5 \text{ m/s}$	$L/D=1.5$		

(Chang et al., 2014a)		Exp.	$U_{max}/U_{\infty}=1.33-2.1$	L/D=1.5 L=600 mm	Linear type of casing with inlet shroud and flange	
(Chang et al., 2014a)		Exp.	$U_{max}/U_{\infty}=1.33-2.1$	L/D=2 L=600 mm	Linear type of casing with inlet shroud and flange	
(Chang et al., 2014a)		Exp.	$U_{max}/U_{\infty}=1.33-2.1$	L/D=2.5 L=600 mm	Linear type of casing with inlet shroud and flange	
(Chang et al., 2014a)		Num.	$U_{max}/U_{\infty}=1.33-2.1$	L/D=3 L=600 mm	Linear type of casing with inlet shroud and flange	
(Setoguchi et al., 2004)		Exp.	$U_{max}/U_{\infty}=1.16$	D=30 mm	Truncated triangle type of nozzle-diffuser casing without a flange component	
(Setoguchi et al., 2004)		Exp.	$U_{max}/U_{\infty}=1.3$	D=30 mm	Truncated triangle type of nozzle-diffuser casing with a flange component	

(Fletcher et al., 2007)		Exp.	$U_\infty=11.25$ m/s	D=305 mm	Scoop type of shroud including contractor and diffuser	
(Fletcher et al., 2007)		Num.	$U_\infty=11.25$ m/s	D=305 mm	Scoop type of shroud including contractor and diffuser	
(Kale et al., 2013)		Num.	$U_\infty=7$ m/s	D=1200 mm	Curved type of casing with inlet contracting and an inclined flange	
(Kale et al., 2013)		Num.	$U_\infty=7$ m/s	D=1200 mm	Curved type of casing with inlet contracting and a vertical flange	
(Kale et al., 2013)		Num.	$U_\infty=7$ m/s	D=1200 mm	Curved type of casing with inlet contracting and without a flange	

The main reason of the maximum wind speed ratio, K increase inside the casing, i.e. caused by the pressure drop, C_{pr} occurred among the reviewed literature studies was observed to be the highest in a designed configuration having passive control devices type of shrouding (Figure 4.65 (Coşoiu et al., 2013)), i.e. the maximum pressure drop ratio, corresponding to $C_{prmax}=-4.76$, as shown in Figure

4.66. Sensitive dimensioning of the relevant casing structure is presented in Figure 4.65. On the other hand, Figure 4.66 demonstrates the maximum pressure drop locations for different literature studies are expressed depending on the dimensionless axial coordinate normalized on wind turbine location diameter, x/D , i.e., according to the chosen coordinate system and the diameter where the wind turbine is installed, D , i.e. usually the casing throat cross-sectional area of the reviewed studies taken into account. On the other hand, the used configurations with the other aerodynamical properties considering these literature studies are summarized in Table 4.25. The configuration corresponding to the highest pressure drop, i.e. the optimized passive control devices including five separate different airfoil configurations in a variety of cross-sectional areas attached with each other, reveals a good design example to enhance the free-stream wind speed, U_∞ in the benefit of the highest power generation, P . The shrouding structure formed of five precise airfoil structures in various design forms and attached with each other presents the maximum pressure-drop, shown in Figure 4.66; as well optimized by dimensionless casing full body length, $L/D=1$, dimensionless casing inlet diameter normalized on turbine location diameter, $D_1/D=1.3$, and dimensionless casing exit diameter normalized by turbine location diameter, $D_2/D=2.6$.

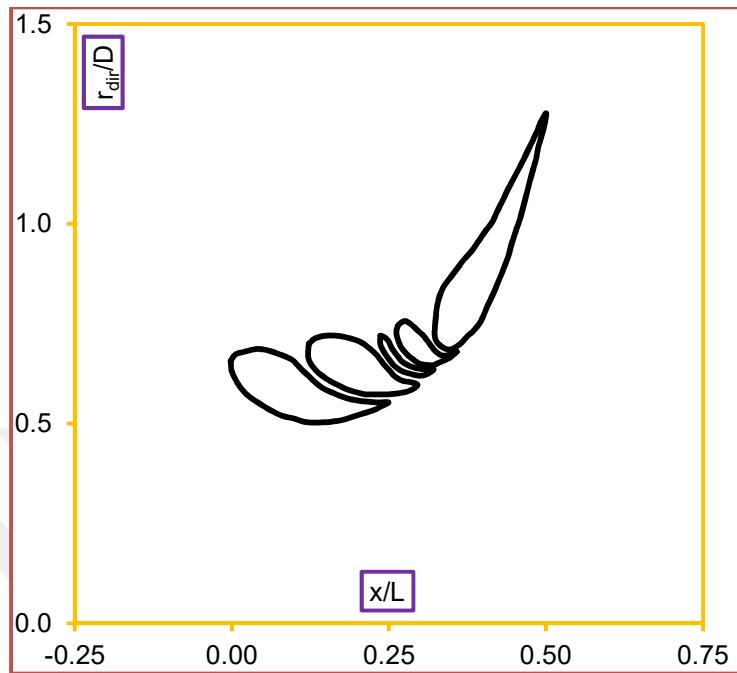


Figure 4.65. Passive control devices including five separate airfoil sections attached to allow the air injection inside (Coşoiu et al., 2013)

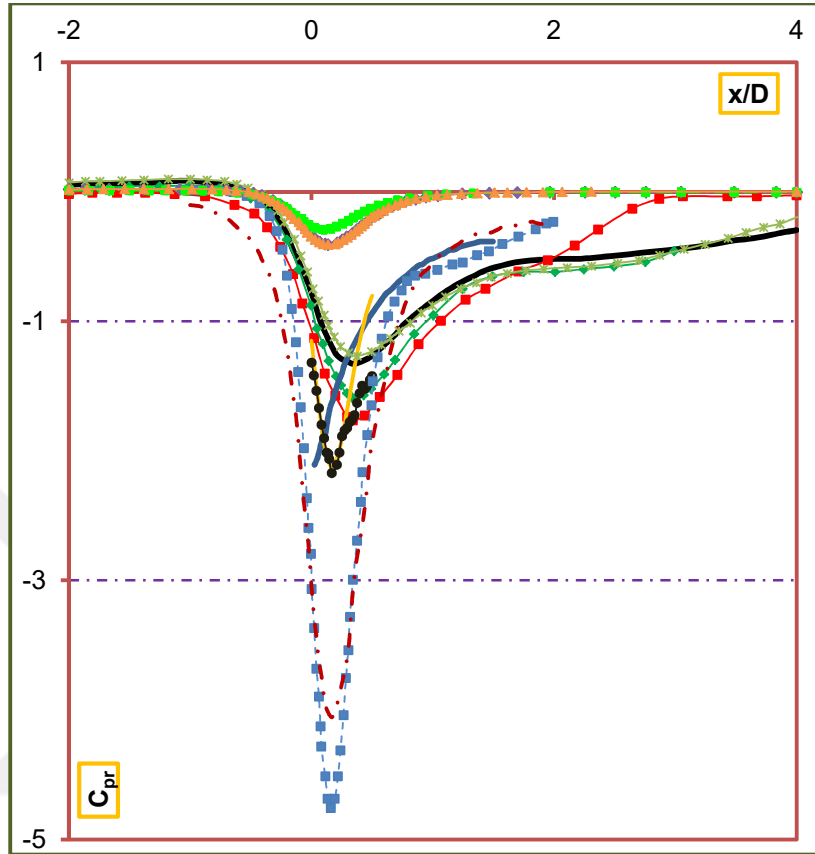



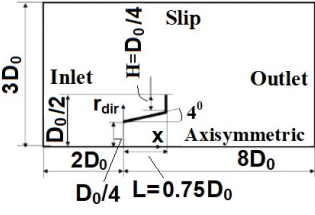

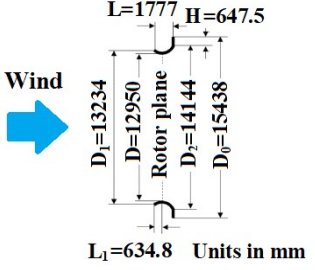



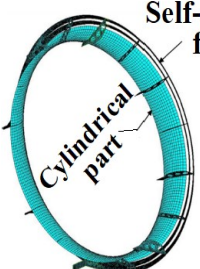

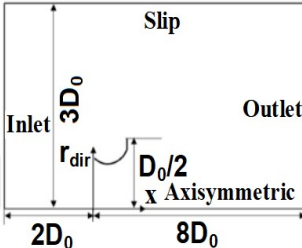

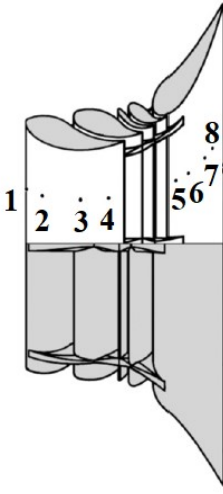

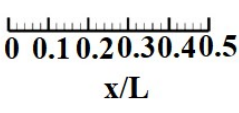
Figure 4.66. Distributions of dimensionless pressure coefficient, C_{pr} expressions along the central axial axis of the casing for different literature studies, reviewed in Table 4.25


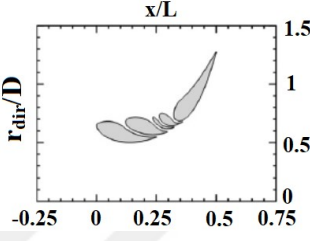


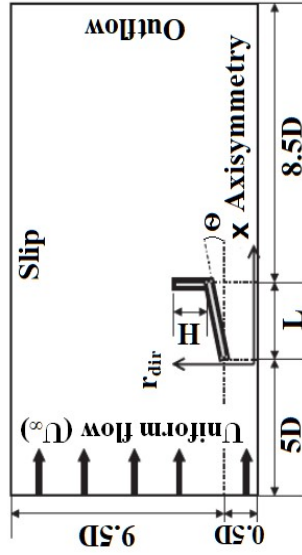

The optimization of casings especially those working under small wind turbine systems requires ultimate alternative methods of shrouding optimizations including active transversal circular sections. In these systems, since the axial length of the casing are constrained due to small energy generation systems, passive flow control devices, i.e., circular injection slots are used to operate shrouding of wind turbines, also overlapping of many aerodynamic effects are supplied. Such researches are verified also utilizing from numerical investigational tools and as well as experimental tests are also conducted in a wind tunnel to test


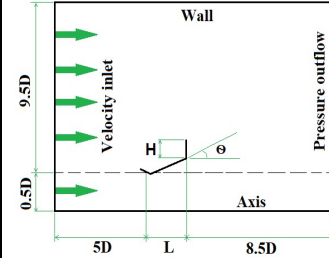
for the comparisons of both. Flow mechanisms are well understood by numerical post-processing in order to investigate a total of 13 casing configurations to obtain the optimal one ensuring the highest maximum pressure drop ratio, C_{prmax} resulting the highest maximum wind speed ratio, K (Coşoiu et al., 2013).

Table 4.25. Related reference names, the symbols relating to the results given in Figure 4.66, the relevant casing geometries of wind turbines, the type of studies, related other data and information

Ref.	Symbol	Study type	U_∞ definition	D_{rotor}	Casing type	Conf.
(Ohya and Karasudani, 2010)		Exp. in wind tunnel and field test	$U_\infty=8$ m/s	1020 mm	Linear type of shrouding with curved inlet shroud and flange	
(Hu and Wang, 2015)		Num.	$U_\infty=5$ m/s	200 mm	Linear type of casing with flange and no inlet shroud	
(Hu and Wang, 2015)		Num.	$U_{max}/U_\infty=1.2$	13 m	Curved type of shrouding with a rigid and flat flange	

(Hu and Wang, 2015)		Num.	$U_{max}/U_{\infty}=1.15$	13 m	Curved type of shrouding with a flexible flange application	
(Hu and Wang, 2015)		Num.	$U_{max}/U_{\infty}=1.5$	13 m	Curved type of shrouding with a rigid flange	
(Coşoiu et al., 2013)		Num.	$U_{\infty}=3.5$ m/s	2.27 m	Casing type in the form of passive control devices in airfoil cross-sections attached in series	
(Coşoiu et al., 2013)		Exp.	$U_{\infty}=13$ m/s	0.11 m	Casing type in the form of passive control devices in airfoil cross-sections attached in series	

(Coşoïu et al., 2013)		Num.	$U_{\infty}=3.5$ m/s	2.27 m	Casing type in the form of circular injection slots in airfoil cross-section attached in series	
(Coşoïu et al., 2013)		Num.	$U_{\infty}=3.5$ m/s	2.27 m	Casing type in the form of circular injection slots in airfoil cross-section attached in series	
(Abe and Ohya, 2004)		Exp.	$U_{\infty}=5$ m/s	0.2 m	Shrouding with flange and no inlet shroud ($L/D=1.5$, $H/D=0.25$, $C_f=0$, $\Theta=4^\circ$)	
(Abe and Ohya, 2004)		Num.	$U_{\infty}=5$ m/s	0.2 m	Shrouding with flange and no inlet shroud ($L/D=1.5$, $H/D=0.5$, $C_f=0$, $\Theta=4^\circ$)	

(Adeel et al., 2013)		Num.	$U_{\max}/U_{\infty}=2.2$	0.4 m	Conventional type of casing with flange and inlet shroud components	
----------------------	---	------	---------------------------	-------	---	--

A group of other reviewed studies was also taken into account to report the pressure drops, C_{pr} originated inside the casing shrouds as presented in Figure 4.67. As well as, the other aerodynamical properties of the used configurations in the considered literature studies are presented in Table 4.26. Among the considered literature studies, it was observed that the highest maximum pressure drop ratio was observed to correspond $C_{prmax}=-4.07$ in a scoop design type of shroud, in this group of studies (Wang et al., 2008). On the other hand, it is interesting to note in this group of studies, the dimensionless pressure coefficient, C_{pr} is almost constant in the cylindrical shrouding (Ohya et al., 2006), and presented the inverse influence unfortunately, thus adverse effect in the nozzle shrouding (Ohya et al., 2006).

The objective of studies regarding casing studies is to investigate the possibility of upgrading wind energy capturing; thus domestic utilization in built-up areas absolutely require correct sizing appropriate for purpose and place. In this context, both experimental and numerical studies are performed to optimize scoop designs proper according to the desired characteristics. The utilization of a scoop maintains increased reliability of energy generations in locations of lower wind speed and more turbulent environment. Along with the scoop design, blade design as well completes the structure of the best power curve resulting in the acceptable

configuration to be selected. The accurate scoop design including a contractor at upstream, a cylindrical section just in the middle and an expanding region at downstream was tested until a maximum wind speed ratio, K of 1.5 got. Thus this results in the boost of available wind energy in the vicinity of the disc to be increased by a factor reaching 2.25 measured concerning the free-stream wind energy selected as the reference. This case was acquired by the dimensionless pressure coefficient to fall below $C_{pr} < -4.00$ (Wang et al., 2008). The optimized configuration of (Wang et al., 2008) was demonstrated in Figure 1.37.

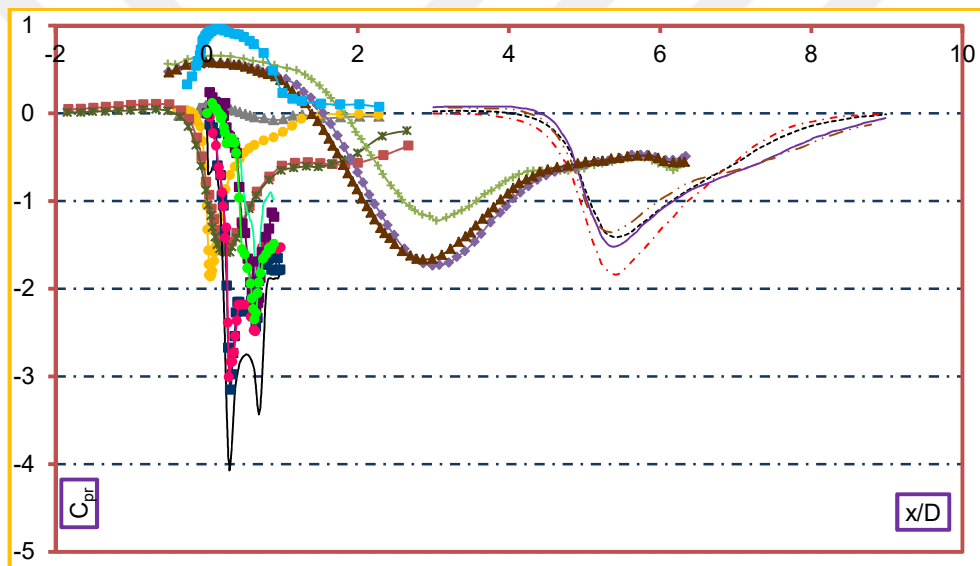

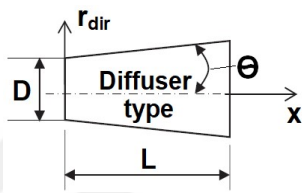

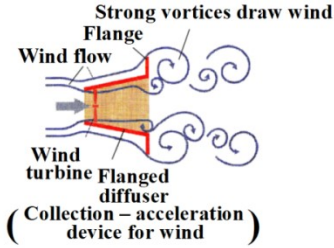

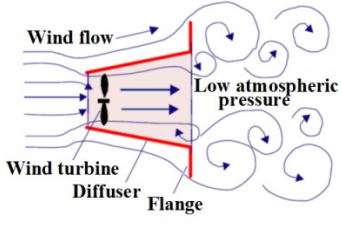

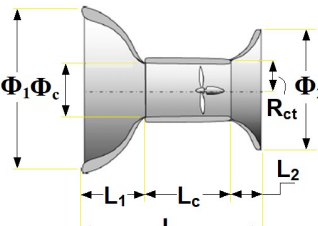

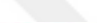

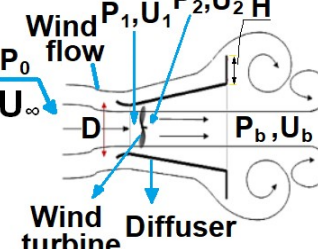


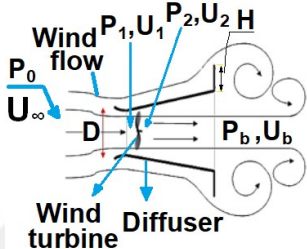

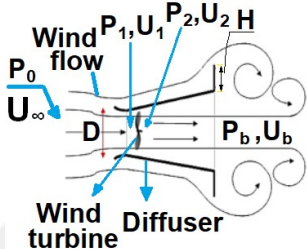

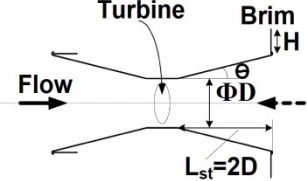



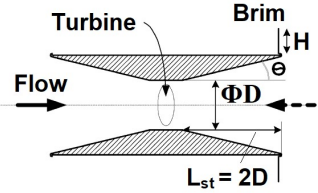

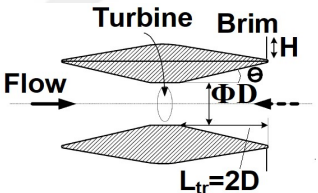

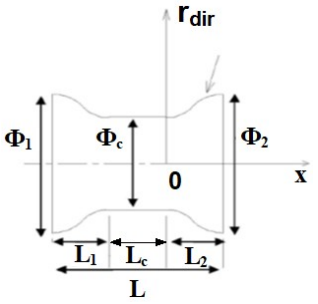
Figure 4.67. Distributions of dimensionless pressure coefficient, C_{pr} values along the central axis of the casing for different literature studies, reviewed in Table 4.26


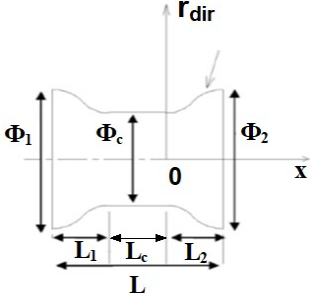


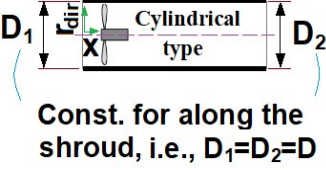
Table 4.26. Related reference names, the symbols relating to the results given in Figure 4.67, the relevant casing geometries of wind turbines, the type of studies, related other data and information


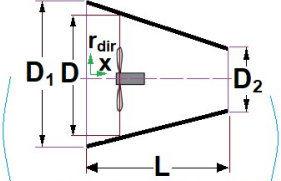
Ref.	Symbol	Study type	U_∞ definition	D_{rotor} def.	Casing type	Conf.
(Ohya et al., 2008)		Wind Tunnel	$U_\infty=5$ m/s	$D=12$ cm	Conventional type of diffuser casing, $\mu^*=4$, $L/D=7.7$, and $\theta=3.7^\circ$	
(Ohya et al., 2008)		Wind tunnel	$U_\infty=5$ m/s	$D=40$ cm	Conventional type of diffuser used to test the flange influence; $\mu^*=1.44$, $L/D=1.5$, and $H/D=0.625$	
(Ohya et al., 2008)		Wind Tunnel	$U_\infty=5$ m/s	$D=40$ cm	Conventional type of diffuser used to test the flange influence; $\mu^*=1.44$, $L/D=1.5$, and $H/D=0.5$	

(Wang et al., 2008)		Num.	$U_{\infty}=11.25$ m/s	0.91 in	Scoop type of wind turbine shrouding; $\Phi_1=6000$ mm, $\Phi_c=4000$ mm, $\Phi_2=6000$ mm, and $L=6000$ mm	
(Wang et al., 2008)		Wind Tunnel	$U_{\infty}=11.25$ m/s	0.91 in		
(Wang et al., 2008)		Wind Tunnel	$U_{\infty}=11.25$ m/s	0.91 in		
(Mansour and Meskin khoda, 2014)		Num.	$U_{max}/U_{\infty}=1.55$	D=0.2 m	Conventional type of shrouding with flange and without inlet, $\theta=4^\circ$, $L/D=1.5$, $H/D=0.25$, $C_t=0$	
(Mansour and Meskin khoda, 2014)		Num.	$U_{max}/U_{\infty}=1.70$	D=0.2 m	Conventional type of shrouding with flange and inlet, $\theta=4^\circ$, $L/D=1.5$, $H/D=0.25$, $C_t=0$	

<p>(Mansour and Meskin khoda, 2014)</p>		<p>Exp.</p>	<p>$U_{max}/U_{\infty}=1.6$</p>	<p>D=0.2 m</p>	<p>Conventional type of shrouding with flange and without inlet, $\theta=4^\circ$, $L/D=1.5$, $H/D=0.5$, $C_t=0$</p>	
<p>(Mansour and Meskin khoda, 2014)</p>		<p>Num.</p>	<p>$U_{max}/U_{\infty}=1.5$</p>	<p>D=0.2 m</p>	<p>Conventional type of shrouding with flange and without inlet, $\theta=4^\circ$, $L/D=1.5$, $H/D=0.5$, $C_t=0$</p>	
<p>(Setoguchi et al., 2004)</p>		<p>Wind tunnel</p>	<p>$U_{max}/U_{\infty}=1.25$</p>	<p>D=30 mm</p>	<p>Truncated triangle type of shrouding with an inlet flow smoother and having components of concentrating, cylindrical, and diffusing sections; $H/D=2$</p>	

<p>(Setoguchi et al., 2004)</p>		<p>Wind tunnel</p>	<p>$U_{max}/U_{\infty}=1.30$ D= 30 mm</p>	<p>Truncated triangle type of shrouding having components of concentrating, cylindrical, and diffusing sections; $H/D=2$</p>	
<p>(Setoguchi et al., 2004)</p>		<p>Wind Tunnel</p>	<p>$U_{max}/U_{\infty}=1.30$ D= 30 mm</p>	<p>Diamond type of shrouding having components of concentrating, cylindrical, and diffusing sections; $H/D=2$</p>	
<p>(Fletcher et al., 2007)</p>		<p>Exp.</p>	<p>$U_{max}/U_{\infty}=1.47$ D= 305 mm</p>	<p>Casing shroud having components of concentrating, cylindrical, and diffuser sections</p>	

<p>(Fletcher et al., 2007)</p>		<p>Exp.</p>	<p>$U_{max}/U_{\infty}=1.47$</p>	<p>D=305 mm</p>	<p>Casing shroud having components of concentration,</p>	
<p>(Fletcher et al., 2007)</p>		<p>Num.</p>	<p>$U_{max}/U_{\infty}=1.47$</p>	<p>D=305 mm</p>	<p>cylindrical, and diffuser sections</p>	
<p>(Ohya et al., 2006)</p>		<p>Exp.</p>	<p>$U_{\infty}=5$ m/s</p>	<p>12 cm</p>	<p>Shrouding of non-conventional type, i.e., cylindrical turbine casing of constant cross-section along the axial axis; $L/D=7.7$</p>	 <p>Const. for along the shroud, i.e., $D_1=D_2=D$</p>

(Ohya et al., 2006)		Exp.	$U_\infty = 5 \text{ m/s}$ 21 cm	Shrouding of non-conventional type, i.e., nozzle casing of contracting cross-section along the axial axis; $D_1 = 24 \text{ cm}$, $D_2 = 12 \text{ cm}$, $L/D_2 = 7.7$, and $\theta = 3.7^\circ$	 <p>Contracting along the axial axis, x, i.e. $D_1 > D > D_2$</p>
---------------------	---	------	-------------------------------------	---	---

Studies demonstrated that in the case of shrouding gave the power coefficient, C_p to reach around 1.835 as shown in Figure 4.68, which is defined according to the thrust coefficient, C_T ; and this maximum peak value of the power coefficients, C_p corresponded to a thrust coefficient, $C_T = 0.919$ (Owis et al., 2015). On the other hand, the reviewed literature studies presented that the minimum peak value among the considered power coefficient, C_p curves was observed to only slightly exceed 0.394, corresponding to a thrust coefficient value of $C_T = 0.596$ (Rio Vaz et al., 2014). On the other hand, taking the whole reviewed literature studies into account, the used configurations of this group are shown in Table 4.27.

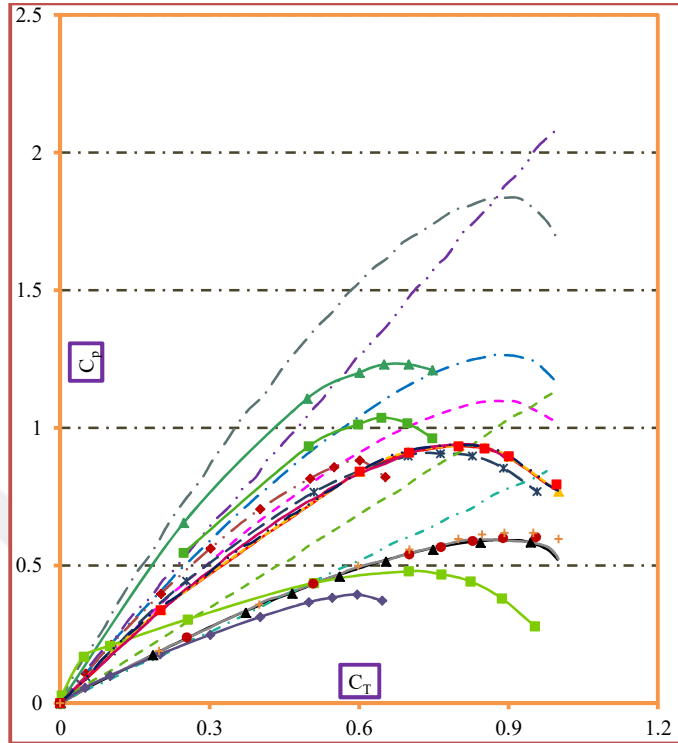

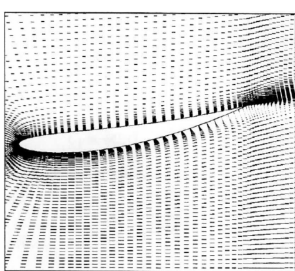



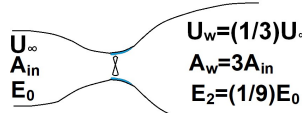


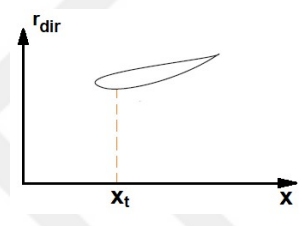



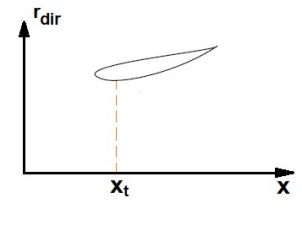

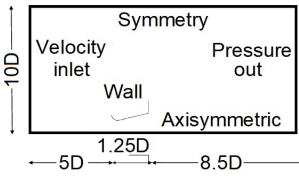




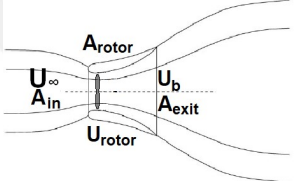

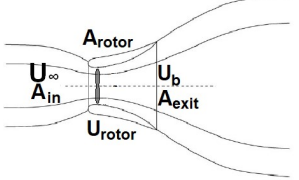






Figure 4.68. Distributions of power coefficient, C_p to the thrust coefficient, C_T values considering different studies in the literature, indicated in Table 4.27

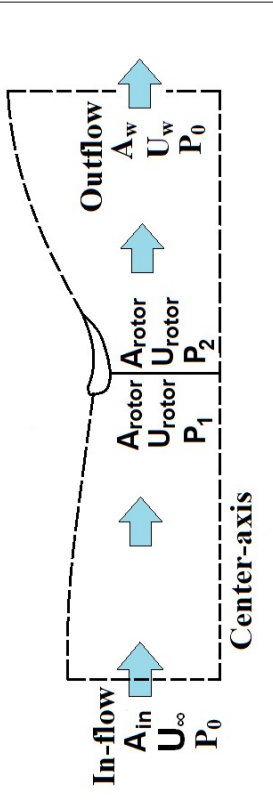
Table 4.27. Related reference names, the symbols relating to the results given in Figure 4.68, the relevant casing geometries of wind turbines, the type of studies, related other data and information


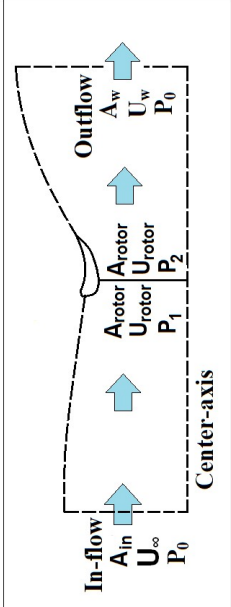

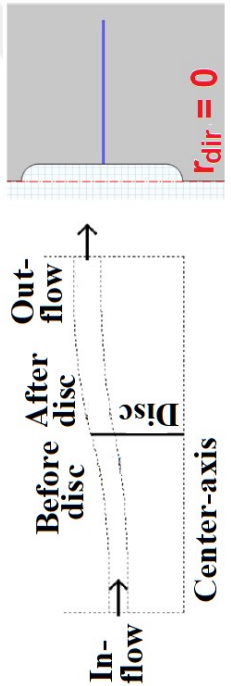
Ref.	Symbol	Study type	U_∞ (m/s)	Rotor dia. def.	Casing type	Conf.
(Hansen et al., 2000)		Num.	5	0.62 m	Conventional bare wind turbine	
(Hansen et al., 2000)		Num.	5	0.62 m	Airfoil type of casing configuration	


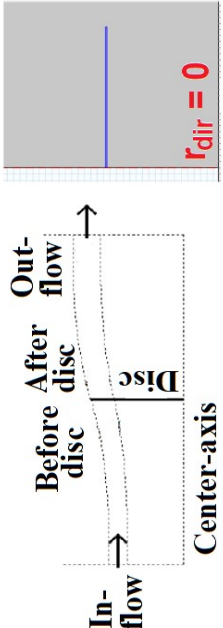

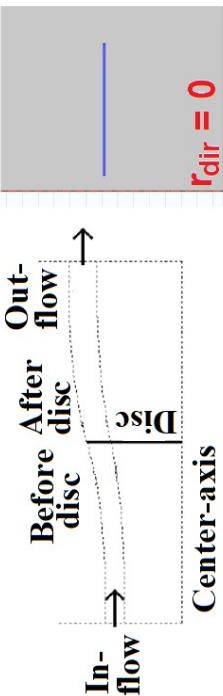
(Jamieson, 2009)		Theo.	-----		Theory according to the constrained flow concept	
(Jamieson, 2009)		Num.	-----		CFD comparison with the theory of constrained flow concept	$U_{rotor} = U_\infty(1-a)$ $A_{rotor} = A_{in}/(1-a)$
(Rio Vaz et al., 2014)		Theo.	1	1.5 m	Airfoil type of casing studied under classical 1D momentum theory regarding the shrouding concept	
(Rio Vaz et al., 2014)		Theo.	1	1.5 m		
(Rio Vaz et al., 2014)		Theo.	1	1.5 m	Airfoil type of casing with a diffuser efficiency, $n_d=0.4$	$n_d=(P_b-P_2)/(0.5\rho(U_2^2-U_b^2))$
(Rio Vaz et al., 2014)		Theo.	1	1.5 m	Airfoil type of casing with a diffuser efficiency, $n_d=0.2$	 $n_d=(P_b-P_2)/(0.5\rho(U_2^2-U_b^2))$

(Owis et al., 2015)		Num.	5	L/D= 1.5	Linear type of casing with optimized inlet shroud and flange components	
(Owis et al., 2015)		Num.	5	L/D= 1.5		
(Owis et al., 2015)		Num.	5	L/D= 1.5		
(Owis et al., 2015)		Num.	5	L/D= 1.5		
(Pinheiro Vaz et al., 2011)		Theo.	3	3 m	Airfoil type of turbine shrouding studied under Glauert's model, theoretically; turbine shrouding is initially not used	
(Pinheiro Vaz et al., 2011)		Theo.	3	3 m	Airfoil type of turbine shrouding studied under Glauert's model, theoretical ly; turbine shrouding is later used	

(Hjort and Larsen, 2014)		Theo.	10	2 m	Airfoil type of shrouding studied under 1D momentum theory (<i>RANS</i>)
(Hjort and Larsen, 2014)		Theo.	10	2 m	Airfoil type of shrouding studied under 1D momentum theory (<i>panel</i>)
(Hjort and Larsen, 2014)		Num.	10	2 m	Airfoil type of shrouding studied under <i>RANS CFD</i>
(Hjort and Larsen, 2014)		Num.	10	2 m	Airfoil type of shrouding studied under <i>Panelcode</i>



<p>(Hjort and Larsen, 2014)</p>		<p>Num.</p>	<p>10</p>	<p>2 m</p>	<p>Airfoil type of shrouding studied under <i>RANS CFD</i></p>	 <p>The diagram shows a cross-section of an airfoil shrouding. The flow enters from the left as 'In-flow' with parameters A_{in}, U_{∞}, and P_0. It passes through two rotor stages, each with area A_{rotor} and velocity U_{rotor}, at pressures P_1 and P_2. The flow exits as 'Outflow' with parameters A_w, U_w, and P_0. The 'Center-axis' is indicated at the bottom.</p>
<p>(Hjort and Larsen, 2015)</p>		<p>Num.</p>	<p>10</p>	<p>2 m</p>	<p>Center body assumption</p>	 <p>The diagram illustrates the center body assumption. It shows a 'Disc' with flow 'Before disc' and 'After disc'. The flow enters as 'In-flow' and exits as 'Out-flow'. A boundary condition is specified as $r_{dir} = 0$. The 'Center-axis' is indicated at the bottom.</p>

<p>(Hjort and Larsen, 2015)</p>		<p>Num. 10</p>	<p>2 m</p>	<p>Full disc rotor assumption</p>	 <p>The diagram shows a vertical center-axis. Below the axis, an arrow labeled 'In-flow' points upwards. Above the axis, an arrow labeled 'Out-flow' points upwards. A horizontal line labeled 'Disc' is positioned between the flow regions. The region below the disc is labeled 'Before disc' and the region above is 'After disc'. A vertical blue line is drawn at the center axis, with the text $r_{dir} = 0$ written in red to its right.</p>
<p>(Hjort and Larsen, 2015)</p>		<p>Num. 10</p>	<p>2 m</p>	<p>Center hole assumption</p>	 <p>The diagram is identical in structure to the one above, showing a vertical center-axis, 'In-flow' and 'Out-flow' arrows, a 'Disc' line, and 'Before disc'/'After disc' regions. A vertical blue line is drawn at the center axis, with the text $r_{dir} = 0$ written in red to its right.</p>

Finally, Figure 4.69 gives the thrust coefficient, C_T , and torque coefficient, C_Q relations expressed depending on the functions of dimensionless tip speed ratio, λ_R . In this group of study, the twelve considered studies presented in Table 4.28 include only the torque coefficients, C_Q , whereas; in the same table, the remaining other six studies (Scherrillo et al., 2011; Coiro et al., 2009) include curves of thrust coefficients, C_T . Among these whole reviewed literature studies, the maximum peak value of the thrust coefficients, C_T was seen to exceed 1.47 as shown in this figure, at a corresponding tip speed ratio value of $\lambda_R=4.05$ (Scherrillo et al., 2011). The thrust coefficient, C_T results were obtained in a shrouded turbine designed to work as a hydro turbine; however, the results presented in Figure 4.69 were obtained in a wind tunnel experiment (Scherrillo et al., 2011). Moreover, in order to extract marine current energy, a designed turbine of (Coiro et al., 2009), was also tested under the utilization of wind tunnel experiments. On the other hand, Figure 4.69 also presents the positive influence of turbine shrouding application on the torque coefficient, C_Q enhancement from $C_Q=0.06$ to $C_Q=0.15$, at corresponding tip speed ratios, $\lambda_R=2.23$ and $\lambda_R=3.60$, respectively. In this respect, utilization of a casing shroud on a wind turbine was shown to increase both the torque coefficient, C_Q , as well as, the corresponding tip speed ratio, λ_R generating this torque coefficient, C_Q (Abe et al., 2005) are as well reported in the context of this dissertation.

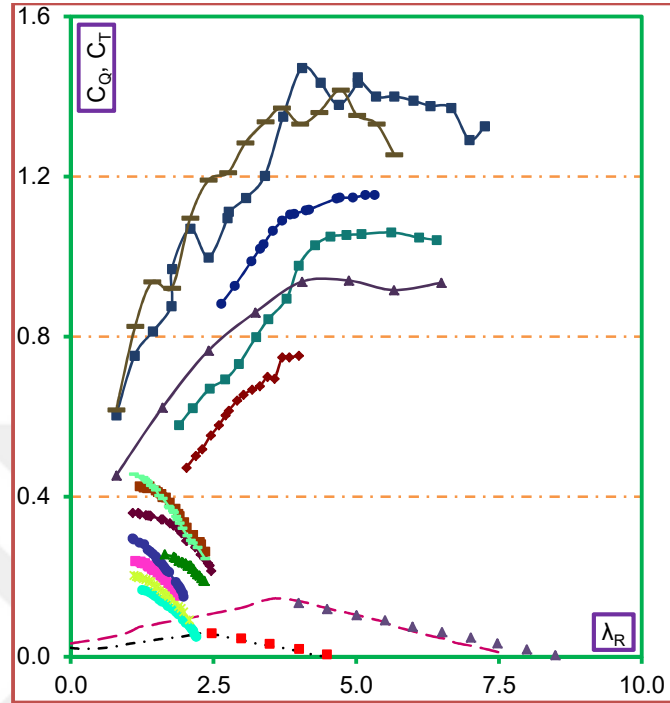

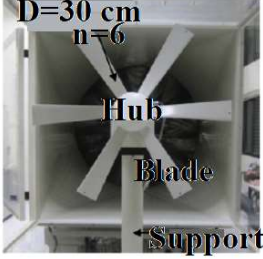

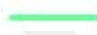








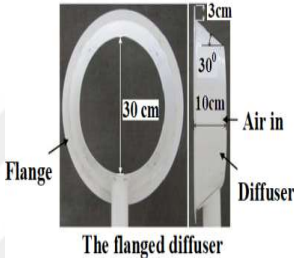

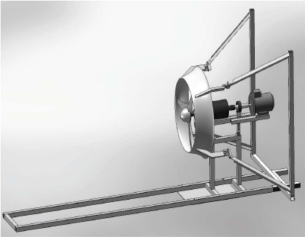





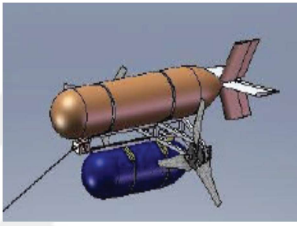


Figure 4.69. Variations of torque, C_Q and thrust coefficients, C_T defined to the tip speed ratio, λ_R values considering different literature studies found in the scientific studies, reviewed in Table 4.28

Table 4.28. Related reference names, the symbols relating to the results given in Figure 4.69, the relevant casing geometries of wind turbines, the type of studies, related other data and information

Ref.	Symbol	Study type	U_{∞} (m/s)	D_{rotor}	Casing type	Conf.
(Abe et al., 2005)	— •	Num.	11	388 mm	Conventional bare wind turbine	
(Abe et al., 2005)	—	Num.	6.8	388 mm	Casing shroud application in the form of linear shrouding as well including inlet shroud and a flange	
(Abe et al., 2005)	■	Exp.	11	388 mm	Conventional bare wind turbine	
(Abe et al., 2005)	▲	Exp.	6.8	388 mm	Casing shroud application in the form of linear shrouding as well including inlet shroud and a flange component	

(Chen et al., 2012)		Exp.	16	28 cm	Flanged diffuser shroud having properties of $L/D=0.33$, $H/D=0.1$, and having 6 bladed rotor disc, and 30% solidity	
(Chen et al., 2012)		Exp.	18	28 cm		
(Chen et al., 2012)		Exp.	20	28 cm		
(Chen et al., 2013)		Exp.	12	28 cm	Bare wind turbine of unused $L/D=0.33$ and $H/D=0.1$ shroud, and having 8 bladed rotor and 40% solidity	
(Chen et al., 2013)		Exp.	12	28 cm	Bare wind turbine of unused $L/D=0.33$ and $H/D=0.1$ shroud, and having 8 bladed rotor and 50% solidity	
(Chen et al., 2013)		Exp.	12	28 cm	Bare wind turbine of unused $L/D=0.33$ and $H/D=0.1$ shroud, and having 8 bladed rotor and 60% solidity	-----

(Chen et al., 2013)		Exp.	12	28 cm	Bare wind turbine of unused $L/D=0.33$ and $H/D=0.1$ shroud, and having 8 bladed rotor and 70% solidity	
(Chen et al., 2013)		Exp.	12	28 cm	Flanged diffuser shroud of $L/D=0.33$, $H/D=0.1$, and having 8 bladed rotor and 40% solidity	
(Scherillo et al., 2011)		Exp.	2.49	0.6 m	3 bladed rotor of conventional bare wind turbine	
(Scherillo et al., 2011)		Exp.	2.49	0.6 m	$\theta=23^\circ$ shrouding applied to smoothly curved type of turbine shroud casing	
(Scherillo et al., 2011)		Exp.	2.49	0.6 m	$\theta=26^\circ$ shrouding applied to smoothly curved type of turbine shroud casing	

(Coiro et al., 2009)		Exp.	2.49	-----	Bare type of wind turbine, at the non-axial position of $\beta=10^0$	
(Coiro et al., 2009)		Exp.	2.49	-----	Bare type of wind turbine, at the axial position of $\beta=0^0$	
(Coiro et al., 2009)		Exp.	2.49	-----	Bare type of wind turbine, at the non-axial position of $\beta=5^0$	

4.10.1. A Short Review of the Influence of Wind Turbine Shrouding Systems

In the case of energy-related CO_2 emissions to continue along with this current trend, emissions on a trajectory are expected unfortunately to raise the average global temperature considerably. Thus, renewable energy technologies play a significant role in contributing to global energy demand, and also conservation of the environment can thus be obtained by these technologies. Besides, energy is a strategic issue which also influences universal affairs, for example, political debates, as well as the military conflicts, are strongly affected by

energy. One of the latest technologies that enables the small size of low capacity wind turbines to operate most efficiently is the diffuser augmented wind turbine system utilization. Thus, researchers have realized that wind turbines that are combined with a diffuser casing not only increase the overall efficiency of the wind turbine, but also those wind turbines start generating electricity at lower wind speeds. It is also expected that increasing efficiency of a wind turbine as well results in a reduction of energy generation costs. In these respects, designing wind turbine running with higher efficiency and generating power under a lower wind speed need further research and development both in universities and industries. The generation of electricity by wind turbines under a lower wind speed to obtain a higher power coefficient, i.e., improved efficiency of wind turbines obviously possible with diffuser casing utilizations. For this reason, in this work, concentrators involving systems including components of nozzle-diffuser-flange and optimization studies of those components were aimed to be reviewed thoroughly by studying the variety of casing geometries that are mostly available in the literature. Furthermore, the latest type of wind turbine is the system, whichever direction the wind travels, the entire wind is forced to be collected in a channel, in these regards, i.e., *INVELOX* type is a new type of wind turbine technology. Within this channel, a venturi effect is created, and wind turbines are installed at the ground level where this effect occurs to obtain the best turbine performance. Other new developments such as a wind turbine rotor is combined with an alternator which is called the Blade Tip Power System (*BTPS*). Additionally, the most recent type of energy generation method is the vortex bladeless generator, where the blades are eliminated, as the name implies. Thus, this is the most environmental friendly and the cheapest energy-generating wind turbine, also reviewed in the content of the study. On the other hand, comparison of the aerodynamic parameters of wind turbines, especially the efficiency of the shrouded turbines presents the proper wind turbine casing to be installed. At the same time, the maximum wind

speed enhancement or the corresponding pressure drop obtained inside the turbine casing are the other two influential aerodynamic parameters in energy generation from shrouded wind turbines to be taken into consideration in terms of comparing the designed casing configurations. In this context, through handling of these cited aerodynamic parameters, optimizations on the best casing configuration for obtaining mass production of the optimized casing shrouds can be successfully achieved in the industry.

The reviewed literature studies presented the highest power coefficient, C_p values were observed to correspond $C_p=1.46$ in an airfoil type of casing having the throat diameter, $D_1=1.52$ m, casing exit diameter, $D_2=2.6$ m, and casing full body length, $L=1.1$ m. Besides, designed wind turbine rotor diameter was set at a diameter value of $D_{rotor}=1.12$ m. And, the numerical study was conducted at a free stream wind speed, U_∞ of $U_\infty=5$ m/s, and the outer walls of the designed model were kept at ambient atmospheric pressure, P_{atm} . On the other hand, the attempts of energy extractions utilizing conventional diffuser shrouding systems have not been successful due to the failures of insufficient energy and momentum conversion. However, an airfoil structure can go beyond the Betz limit quite much compared to other conventional wind turbine shrouding systems (Grassmann et al., 2003). Additionally, maximum enhancement of free-stream wind speed, K as much as possible is also a desired situation similar to the power coefficient, C_p increase. It was observed that the maximum wind speed enhancement; K among the considered literature studies was monitored in an optimized linear type of shroud designed in a linear form also has a flange and an inlet shroud components. The free-stream wind speed was increased maximum by a factor of $K=1.67$ in this study. The highest boost of maximum wind speed ratio, K among the scanned literature showed that this amount of increase was obtained in a particular designed configuration comprising a casing half cone angle, $\Theta=4^\circ$, dimensionless casing full body length, $L/D=1.5$, dimensionless flange height, $H/D=0.25$, and worked at a loading

coefficient of $C_f=0$ (Mansour and Meskinkhoda, 2014). This study as well reported that a significant increase of maximum wind speed ratio, K was obtained during the utilization of the inlet shroud component.

Similar to these two considered former situations of power coefficient and wind speed enhancements; it is also essential to obtain a sufficient pressure drop along with the casing full body length, L of a casing structure. This pressure drop provides the maximum wind speed ratio, K as well as power coefficient, C_p , rise allowing them to reach ample rates. In this context, reviewed studies demonstrated a maximum pressured drop obtained in a passive control device type of turbine casing constructed by attaching five separate airfoil sections yielding a corresponding maximum pressure drop ratio of $C_{pmax}=-4.76$. This study reported that this system was optimized by a special designed shrouding configuration set at a dimensionless casing full body length, $L/D=1$, dimensionless casing inlet diameter normalized on turbine location diameter, $D_1/D=1.3$, and dimensionless casing exit diameter normalized on turbine location diameter, $D_2/D=2.6$. Besides, dimensionless nozzle axial length, L_1/D , and dimensionless diffuser axial length, L_2/D for this study were reported to correspond 0.25 and 0.75, respectively (Coşoio et al., 2013). Moreover, scoop design type of wind turbine casing shrouds was also shown to increase the pressure drop along with the center axis, for instance, an optimized scoop design was observed to change the maximum pressure drop ratio down to $C_{pmax}=-4.07$ among the considered literature studies (Wang et al., 2008). This type of wind turbine shrouding systems were absolutely monitored to be quite successful in reducing the pressure drop since they comprise constricting, cylindrical, and expanding casing components serving as inlet shroud, minimum throat area to locate the wind turbine for maximum energy generation, and a flange-like component to create vortices at far downstream, respectively, enhancing the mass flow rate touching the wind turbine rotor blades. The scoop casing configuration optimized in the current study revealed that an appropriate

wind turbine shrouding structure was determined to have an entrance diameter, Φ_1 , exit diameter, Φ_2 , entrance axial length, L_1 , exit axial length, L_2 , the diameter of the cylindrical section, Φ_c , and the axial length of the cylindrical section, L_c ; reported as, 6000, 6000, 2000, 2000, 4000, and 2000 mm, respectively. The sensitively designed wind turbine casing scoop body was tested numerically under a free-stream wind speed, U_∞ value of $U_\infty=11.25$ m/s which generated this performance of cited pressure drop. And, wind turbine rotor decided to be placed inside the scoop casing system was set to have a rotor diameter, D_{rotor} corresponding to $D_{rotor}=0.91$ in (Wang et al., 2008).

4.11. Numerical and Experimental Performance Analyze of Wind Turbine Shrouding Systems

4.11.1. Introduction

Modeling of wind turbine shrouding systems plays a vital role in power extraction from these optimized casing structures in terms of wind speed enhancement and output power increase. Thus, this part of the dissertation involves modeling of linear and curved types of numerically studied wind turbine casings to choose the proper shrouding dimensions for obtaining the most effective shrouding to be used in the micro wind turbine power generation enhancement. Chosen wind turbine casing structures include the conventional type of linear shrouding systems to reveal the influences of flange height, casing shroud body length, casing shroud expansion angle, and inlet shrouding effects through the analysis of computational fluid dynamics (CFD) flow modeling. In this context, wind speed enhancements and corresponding pressure drops inside the modeled casings, velocity vectors, velocity and pressure contours, and streamline analysis are performed for these systems. On the other hand, a selected curved structure of a wind turbine casing

shroud system compatible with the literature studies is studied both numerically, and the Particle image velocimetry (*PIV*) performance is as well demonstrated. Thus the former expressed flow characteristics and energy generation capacity in terms of both utilized models are compared.

4.11.2. The Objective of the Present Work

Three different configurations for turbine shrouding are generally available in the literature to be used for low capacity wind turbine energy generation systems. These are schematically indicated in Figure 3.7. The diameter of the casing where the wind turbine is installed, turbine rotor diameter, dimensionless nozzle axial length, dimensionless diffuser axial length, dimensionless flange height, half cone angle of the casing, nozzle contraction angle and free stream wind speed are assigned with the abbreviations; D , D_{rotor} , L_1/D , L_2/D , H/D , Θ , γ , and U_∞ , respectively. The main aim of the schematic geometries presented in Figure 3.7 is to concentrate wind flow on the turbine rotor blade cross-sectional area; thus, enhancement of the mass flow rate through the rotor blades will be obtained is the intended issue. Namely, an average increase on the power extraction by 2.5 times more measured according to the conventional wind turbines can be acquired as shown in Figure 4.70b. Additionally, pressure drop just downstream of the rotor and blade plane will result in a considerable wind speed enhancement which is also a function of the optimized geometrical structure dimensions. The power generation, P will be improved, i.e., the cut-in speed could be reduced to lower values of free-stream wind speed, U_∞ . Optimum design of the flange configuration at the exit periphery of the casing structure will provide separated flow regions in the vicinity of the rotor blade plane and downstream of the flange, thus causing the pressure drop to increase even more. The schematic representation of this phenomenon was indicated in Figure 3.8 similar to the study conducted by

(Mansour and Meskinkhoda, 2014). Wind speed is enhanced on the turbine rotor blade area with a factor around 1.5 defined with respect to the free stream wind speed, U_∞ as demonstrated in Figure 3.8a. Similarly, this is caused by the reduction of pressure with a factor of 1.5 drop compared to the free flow region conditions as shown in Figure 3.8b. Thus, both alterations of wind speed and pressure with the utilization of nozzle-diffuser geometry and a flange component will undoubtedly enhance the power coefficient, C_p of the turbine, consequently the overall wind turbine performance will be positively influenced. This part of the dissertation includes the nozzle-diffuser and flange system optimization of linear and curved shrouding models to improve the pressure drop by the separated flows formed at downstream of the flange and in the vicinity region of the rotor blade plane. Thereby, a corresponding fluid speed increase will be resulted by this low pressure region. Hu and Wang (2015) performed scientific studies to show the proof of this case. The scope of the study contains the separated flow and the low pressure regions to be increased by the optimization of a flanged and a nozzle-diffuser shrouded wind turbine geometry to accelerate the mass flow rate passing on the rotor.

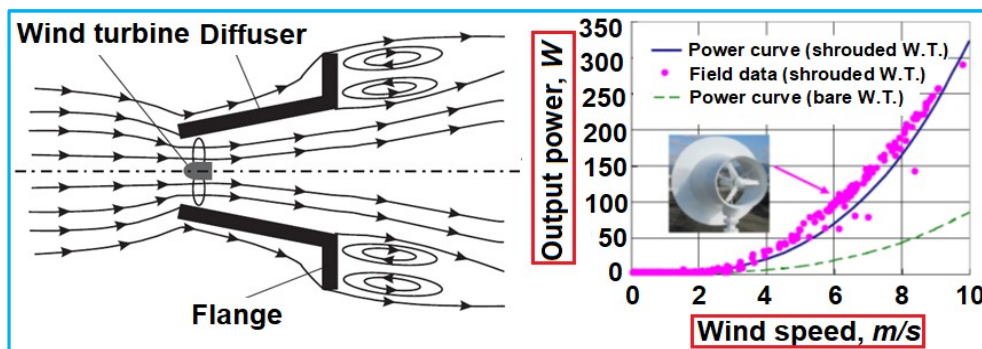


Figure 4.70. The schematic representation of a shrouded wind turbine and its performance analysis (a) a model of a micro wind turbine located in a shroud having a diffuser and a flange component (b) The performance of a shrouded micro wind turbine in terms of power generation enhancement (Ohya and Karasudani, 2010)

The optimized linear shrouding models that are presented schematically in Figure 3.7b are presented in Table 4.29. Fluent commercial software was used in the velocity vector, contour, and pressure analysis for these determined models. The casing systems, as the dimensions shown in Table 4.29 are gone through by computational fluid dynamics to reveal the flow characteristics in the vicinity of the obtained shrouding models.

The dimensions of casing diameter where the wind turbine is installed, D , rotor diameter, D_{rotor} , dimensionless nozzle axial length, L_1/D , dimensionless diffuser axial length, L_2/D , dimensionless flange height, H/D , half cone angle of the casing, θ , and nozzle contraction angle, γ , were optimized as given in Table 4.29 and Table 4.30 to determine the proper casing structure. Besides, the variation of maximum wind speed enhancements, U_{max}/U_∞ and maximum pressure drops, C_{pmax} depending on the casing shroud optimizations were identified. As well these parameters were held in a variety of dimensions for the analysis of the separated flow region behind flange, and the increment influences of those parameters on wind speed were as well observed.

The configuration of the models was performed based on the configuration of the casing inlet and exit diameters, D_1 and D_2 , respectively; diffuser length of the casing, L_2 , and the flange height, H for linear type; and the configuration of the model was performed based on the configuration of the casing inlet and exit diameters, D_1 and D_2 , respectively; casing full body length, L , and flange height, H for the curved type. However, for the curved type of modeling, the casing body structure is composed of initially a nozzle structure for directing flow inside the casing body, and subsequently a diffuser structure letting outflow of the wind. So, nozzle and diffuser lengths of the curved modeling are defined with L_1 and L_2 , abbreviations, respectively. And, the studied models involve the casing wind turbine location diameter, D , at a constant value of $D=1$ m for linear types of shrouds in order to present enough room of micro wind turbine rotors. On the other

hand, in terms of the curved type of modeling, diameter of the casing where the wind turbine is located, D was planned both to involve enough room for micro wind turbine location as well whole structure of casing was decided to be appropriate for *PIV* study. Thus, the final value of the turbine location diameter, D was set at a value of 149.533 mm for the conduction of *PIV* analysis. Additionally, a particular designed hub structure of turbine hub-diameter, D_h and turbine axial length including whole mechanical mechanism, L_s were configured as 48.501 mm and 23.111 mm, respectively.

4.11.2.1. Linear Optimized Configurations

Normalized casing shroud inlet diameter, D_1 with respect to the casing wind turbine location diameter, D , i.e., dimensionless casing inlet diameter, D_1/D is defined in the value range,

$$D < D_1 < 2D \quad (4.10)$$

The diffuser length of the casing, L_y is defined in the value range,

$$1.25D < L_y \leq 1.5D \quad (4.11)$$

On the other hand, flange height, H is signified in between the range expressed in Eq. (4.12),

$$0.2D \leq H < 0.5D \quad (4.12)$$

Finally, half cone angle of the casing, θ is given in the range demonstrated in Eq. (4.13),

$$3^{\circ} \leq \theta \leq 12^{\circ} \quad (4.13)$$

Thus, outcome values of casing exit diameter, D_2 is expressed as the functions of diffuser opening angle, and diffuser length, 2θ , and L_y , respectively. The schematic linear shrouding profile structure without an inlet shroud component used in this part of the dissertation is shown in Figure 4.71a. On the other hand, the inlet shrouded wind turbine casing system is as well shown in Figure 4.71b.

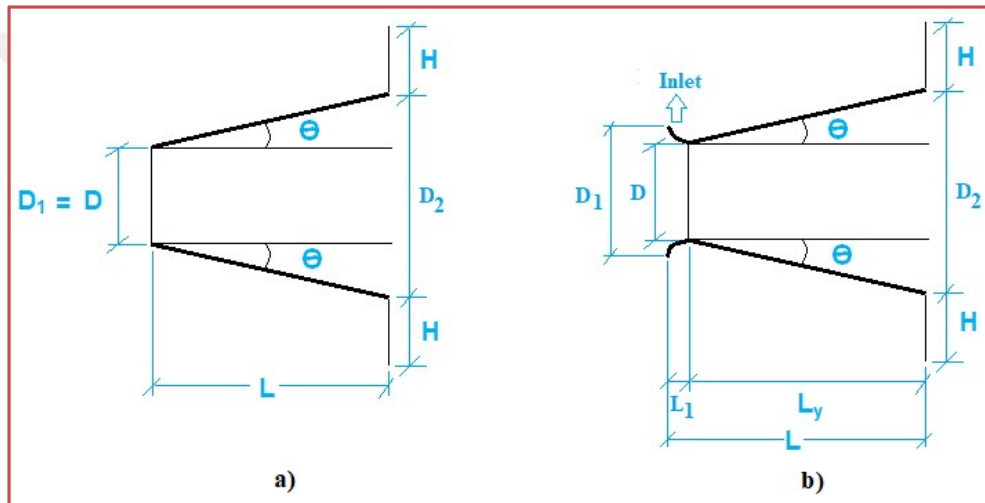


Figure 4.71. Linear shrouding profile structure

4.11.2.2. Curved Type Optimization

Curved type casing shroud systems are most widely used as wind turbine augmenting components. For instance, Wang et al. (2015) used a curved type optimized casing system in their study under the utilization of a 3 kW shrouded wind turbine. In this study, casing inlet diameter, D_1 , casing exit diameter, D_2 , diameter of the casing where the wind turbine was installed, D , exit diameter of the casing including the flange heights, D_0 , casing full body length, L , nozzle length of the casing, L_1 , diffuser length of the casing, L_y , and flange height, H were

optimized to be set at corresponding values of 2735.4 mm, 2910.8 mm, 2560 mm, 3424 mm, 565 mm, 225.9 mm, 339.1 mm, 256.6 mm, respectively. A curved profile used in this part of the dissertation for computational analysis and as well in *PIV* analysis also conducted in this part of the dissertation was inspired taking the study of Wang et al. (2015) into account. In this context, a scale factor of 17.12 was used for the profile to be properly set in the utilized *PIV* channel.

The scaled configuration by a factor of 17.12 used in this study is shown in Figure 4.72. So, the geometric configuration designed for *PIV* analysis including wind turbine casing and hub is shown in this figure. This curved configuration has inlet diameter, D_1 , casing exit diameter, D_2 , wind turbine location diameter, D , flange height, H , turbine hub diameter, D_h , and turbine axial length including whole mechanical mechanism, L_s corresponding to 159.243, 170.023, 149.533, 14.988, 48.501, and 23.441 mm, respectively. On the other hand, the hub component located inside the casing body is placed by 9.232 mm shifted measured with respect to the plane of inlet diameter, D_1 of wind turbine casing body. Besides, the casing full body length, L was set at $L=32.672$ mm.

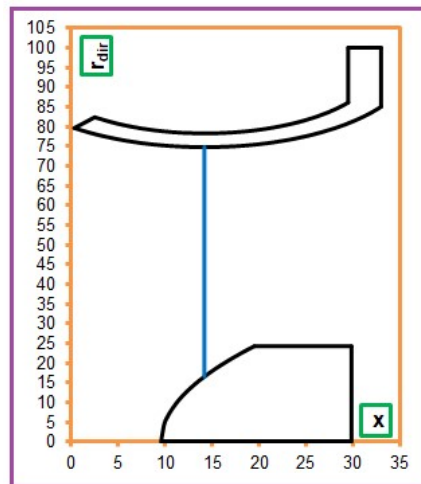


Figure 4.72. The curved type of casing geometric configuration used for *PIV* analysis

4.11.3. Results and Discussions

4.11.3.1. Results of Linear Optimizations

Study of Abe and Ohya (2004) was chosen to validate their results as the computational conditions, and the comparison of the results are shown in Figures 4.73 and 4.74, respectively. On the other hand, in Figure 4.74 presenting the steady and unsteady *CFD* solutions of the validation for (Abe and Ohya, 2004) resulted in similar computational outcomes. Considering both *CFD* studies including steady and unsteady cases, and as well study of (Abe and Ohya, 2004); maximum discrepancy occurred for steady solution as 3.9% at $x/D=1.41$ inside the shroud body as presented in Figure 4.74, on the other hand, maximum discrepancy occurred for unsteady solution as 2.12% at $x/D=1.30$ inside the shroud body as also presented in the same figure. In these regards, the computations were continued based on unsteady solvent due to the lower error as stated above.

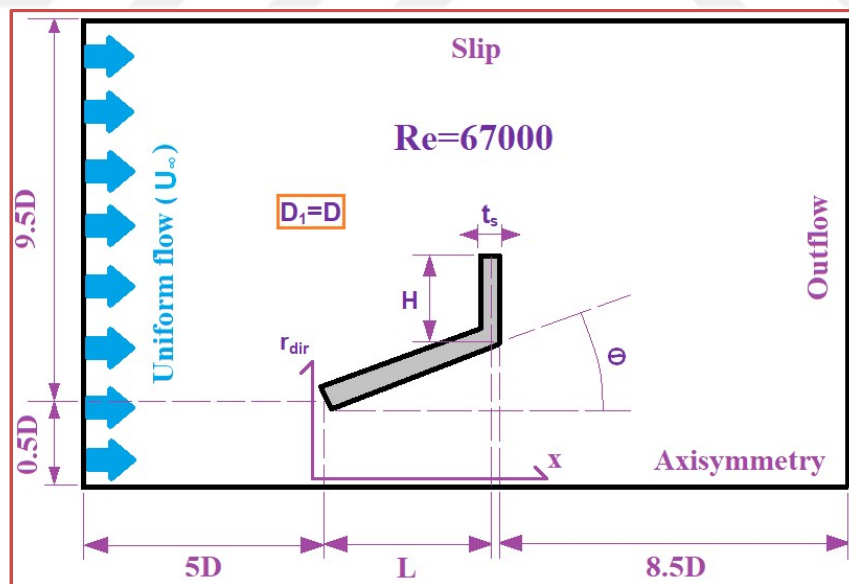


Figure 4.73. Computational conditions (Abe and Ohya, 2004)

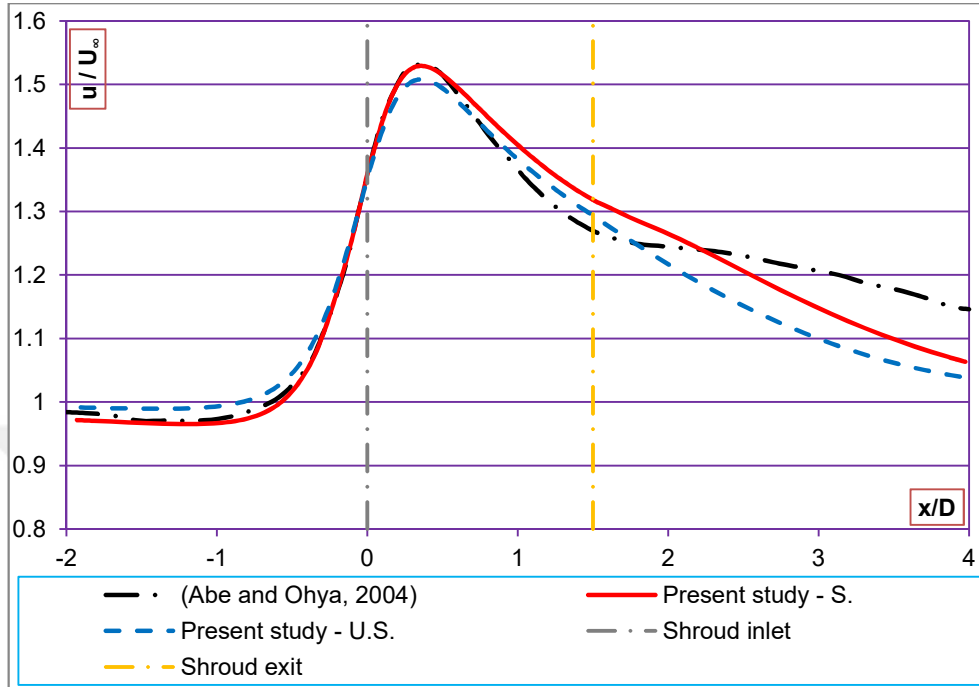


Figure 4.74. Steady and unsteady state validation of the *CFD* study in this part of the dissertation and comparison with the study of (Abe and Ohya, 2004)

Figure 4.75 demonstrates the vertex point representation of the non-flanged and flanged shrouding case as presented in Figure 4.75a and Figure 4.75b, respectively. Besides, Table 4.29 offers the optimized models of the cases for linear shrouding systems (Figure 3.7a) to be studied in *CFD*. On the other hand, Table 4.30 presents the coordinates of the optimized shrouding profiles. The designed setup configurations in which the properties of each shown in Table 4.29 includes the Case 1 divided to 26364 elements of meshes, whereas, other 16 cases presented in this table were optimized at 30956 elements of meshes. Additionally, similar to the study of Abe and Ohya (2004), Reynolds number was set at the value of $Re=67000$ for the validation. In these regards; since no-inlet shrouding was used in the study of Abe and Ohya (2004), this validation study does not also include inlet shrouding, and, free-stream wind speed, U_∞ value and the diameter of the

casing where the wind turbine is installed, D were set at the values of $U_\infty=5$ m/s and $D_I=D=0.2$ m, respectively. Besides, values of flange-height ratio, H/D and dimensionless casing full body length, L/D were designed at $H/D=0.5$ and $L/D=1.5$, respectively, as similar in the case of [Abe and Ohya \(2004\)](#) study. And, half cone angle of the casing, Θ validation configuration was also set to $\Theta=4^\circ$ as also in the case of the cited reference study. Finally, the kinematic viscosity, ν from the cited Reynolds number of $Re=67000$ was obtained as $\nu=1.4925 \times 10^{-5}$ generating an ambient atmospheric absolute air temperature of $T_{am}=290.6^\circ$ K is used in the validation as well. Moreover, for the *CFD* tested first 16 cases demonstrated in Table 4.29, same kinematic viscosity, ν , and free-stream wind speed, U_∞ are used as $\nu = 1.4925 \times 10^{-5}$ and $U_\infty=5$ m/s; however, the diameter of the casing where the wind turbine is installed, D is chosen as distinct as $D_I=D=1$ m. These conditions generated a Reynolds number of $Re=335,000$ which are consistent with literature studies of ([Abe et al., 2005](#); [Ohya et al., 2008](#)). Since, those studies considered Reynolds number as $Re=290,000$ and $Re=240,000$, respectively. Eventually, Reynolds number of both studies and the current study are shown to be compatible.

Considering 17 cases, the thicknesses of the casing shroud, t_s profiles are set to $t_s=8$ mm. Besides, air density, ρ studied in whole profiles as well as the validation was entered to Fluent *CFD* as $\rho=1.21471$ kg/m³. On the other hand, other cited features determined so far were set similar for Case 17, however except for casing inlet diameter, D_I which was determined as $D_I=1.102$ m, i.e. distinct from diameter of the casing where the wind turbine is installed, D of $D=1$ m, since Case 17 requires the utilization of an inlet shrouding component. Similarly, dimensionless casing full body length, L/D requires being distinct when compared to Case 16, because of again inlet utilization in Case 17. In these regards; dimensionless casing full body length, L/D for Case 17 was determined to be $L/D=1.677$, i.e., distinct from $L/D=1.5$ of Case 16, as also presented in Table 4.29. As mentioned, the discrepancies eventuated in dimensionless casing inlet diameter

normalized on turbine location diameter, D_t/D and dimensionless casing full body length, L/D values between Cases 16 and 17 of Table 4.29 result from an optimum designed of an inlet shrouding component shown in Figure 4.71b, in which this inlet shrouding component allow augmented mass flow rate of the air passing through the rotor disc, \dot{m} .

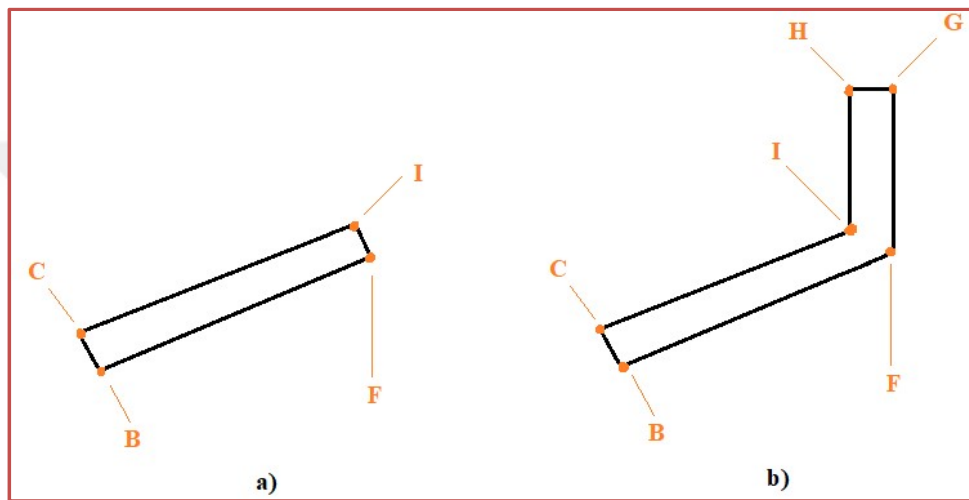


Figure 4.75. Coordinate representation of the vertex points of the shrouding cases; **a)** shroud without a flange and **b)** shroud having the flange component

Table 4.29. Optimized linear casing shrouds

Case analysis	Case number	Inlet shroud	L/D	H/D	θ (Degree)	D_2/D
Flange influence	1	No	1.40	0	9	1.437
	2	No	1.40	0.20	9	1.437
	3	No	1.40	0.30	9	1.437
	4	No	1.40	0.40	9	1.437
Expansion	5	No	1.35	0.20	3	1.134

angle influence	6	No	1.35	0.20	4	1.181
	7	No	1.35	0.20	5	1.229
	8	No	1.35	0.20	6	1.277
	9	No	1.35	0.20	9	1.421
	10	No	1.35	0.20	12	1.567
Diffuser length influence	11	No	1.30	0.20	6	1.266
	12	No	1.35	0.20	6	1.277
	13	No	1.40	0.20	6	1.287
	14	No	1.45	0.20	6	1.298
	15	No	1.50	0.20	6	1.308
Inlet shroud influence	16	No	1.50	0.30	5	1.255
	17	Yes	1.677	0.30	5	1.255

Table 4.30. Coordinates of the optimized casing shroud cases

Case	Coord.	B	F	G	H	I	C
1	x	5.000626	6.404	----	----	6.403442	4.999374
	r _{dir}	0.496049	0.718322	----	----	0.726302	0.503951
2	x	5.000626	6.404	6.404	6.396	6.396	4.999374
	r _{dir}	0.496049	0.718322	0.918322	0.918322	0.725155	0.503951
3	x	5.000626	6.404	6.404	6.396	6.396	4.999374
	r _{dir}	0.496049	0.718322	1.018322	1.018322	0.725155	0.503951
4	x	5.000626	6.404	6.404	6.396	6.396	4.999374
	r _{dir}	0.496049	0.718322	1.118322	1.118322	0.725155	0.503951
5	x	5.000209	6.354	6.354	6.346	6.346	4.999791
	r _{dir}	0.496005	0.566955	0.766955	0.766955	0.574546	0.503995
6	x	5.000279	6.354	6.354	6.346	6.346	4.999721
	r _{dir}	0.496010	0.590671	0.790671	0.790671	0.598131	0.503990
7	x	5.000349	6.354	6.354	6.346	6.346	4.999651
	r _{dir}	0.496015	0.614444	0.814444	0.814444	0.621775	0.503985

8	x	5.000418	6.354	6.354	6.346	6.346	4.999582
	r_{dir}	0.496022	0.638289	0.838289	0.838289	0.645492	0.503978
9	x	5.000626	6.354	6.354	6.346	6.346	4.999374
	r_{dir}	0.496049	0.710403	0.910403	0.910403	0.717235	0.503951
10	x	5.000832	6.354	6.354	6.346	6.346	4.999168
	r_{dir}	0.496087	0.783712	0.983712	0.983712	0.790190	0.503913
11	x	5.000418	6.304	6.304	6.296	6.296	4.999582
	r_{dir}	0.496022	0.633034	0.833034	0.833034	0.640237	0.503978
12	x	5.000418	6.354	6.354	6.346	6.346	4.999582
	r_{dir}	0.496022	0.638289	0.838289	0.838289	0.645492	0.503978
13	x	5.000418	6.404	6.404	6.396	6.396	4.999582
	r_{dir}	0.496022	0.643544	0.843544	0.843544	0.650748	0.503978
14	x	5.000418	6.454	6.454	6.446	6.446	4.999582
	r_{dir}	0.496022	0.648800	0.848800	0.848800	0.656003	0.503978
15	x	5.000418	6.504	6.504	6.496	6.496	4.999582
	r_{dir}	0.496022	0.654055	0.854055	0.854055	0.661258	0.503978
16	x	5.000349	6.504	6.504	6.496	6.496	4.999651
	r_{dir}	0.496015	0.627568	0.927568	0.927568	0.634898	0.503985
17	x	5.000349	6.504	6.504	6.496	6.496	4.999651
	r_{dir}	0.496015	0.627568	0.927568	0.927568	0.634898	0.503985

4.11.3.1.(1). Analysis of the Flange Component Influence

Figures 4.76 and 4.77 given below presents the influence of the flange component in the unsteady condition considering the cases 1, 2, 3, and 4 handled in Table 4.29. The shroud full body length, L normalized with respect to the turbine location diameter, D , and the half cone angle of the casing, θ for these cases are optimized as 1.40 and 9° , respectively. Taking the flange component influences into account, the *CFD* computations were performed to test both the steady and unsteady influences, however during taking far downstream of the casing shrouds into account, especially behind the flanges, it was observed that vortices might

result in the unsteady condition in these regions. However, for the non-flanged situation, i.e., the case of $H/D=0$, it was observed that the cases of steady and unsteady didn't cause any significant discrepancy; thus it was decided to deal with only the results of unsteady computations, and the rest of the computations considering the unsteady cases in this section were handled.

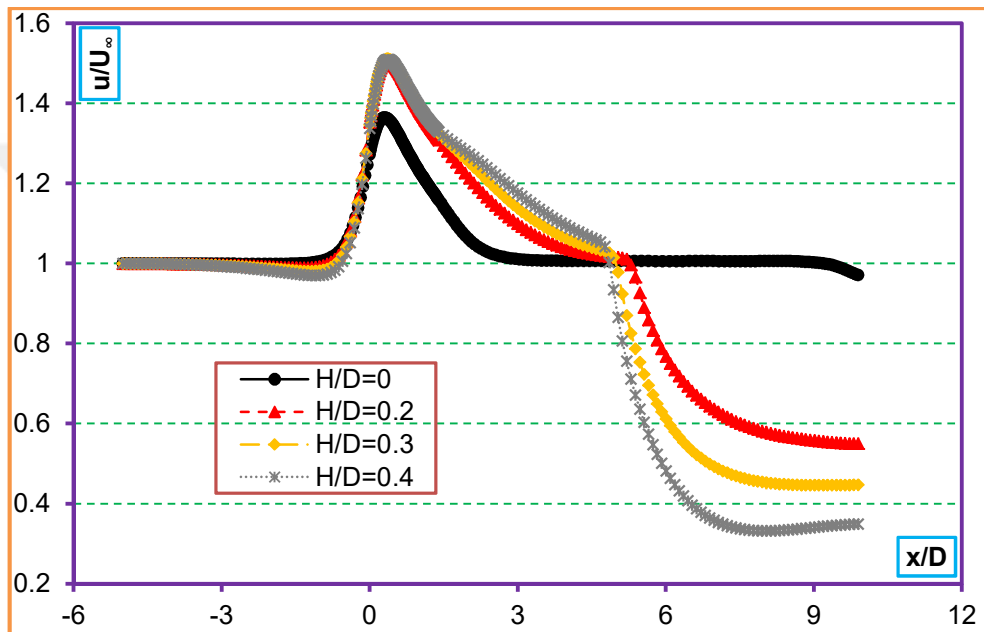


Figure 4.76. Flange component performance analysis in the unsteady case revealing wind speed ratio, u/U_∞ in the vicinity of the casing shroud profiles

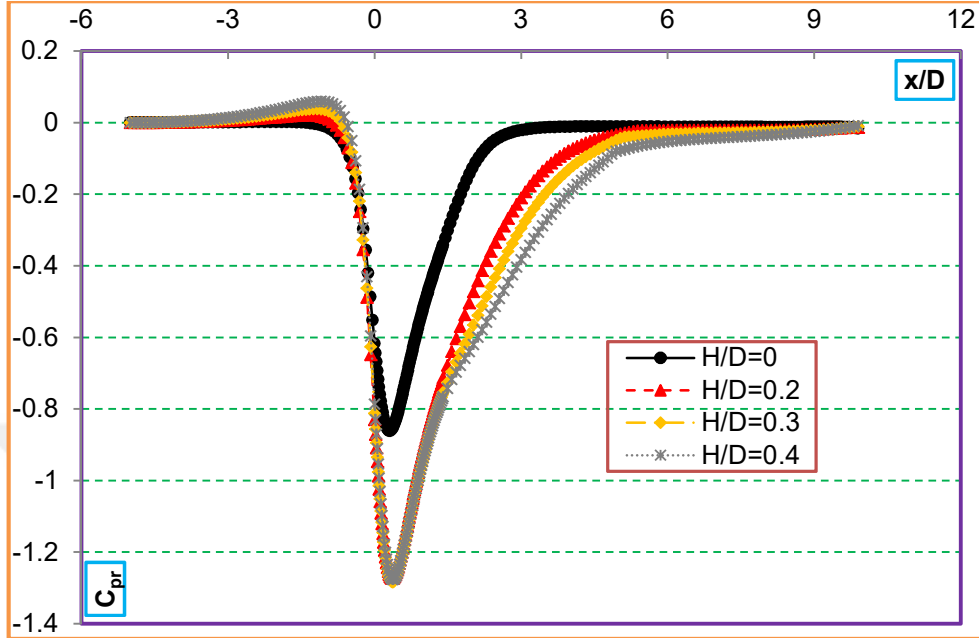


Figure 4.77. Flange component performance analysis in the unsteady case revealing pressure drop, C_{pr} in the vicinity of the casing shroud profiles

It is obvious from Figure 4.76, the introduction of a flange component to the casing body results in a significant boost of the wind speed ratio, u/U_∞ corresponding to 10.5% of maximum wind speed enhancement along the casing body, U_{max}/U_∞ . On the other hand, further increase of the flange height ratio, H/D does not cause any significant increase of the wind speed ratio, u/U_∞ especially inside the casing body. Highest maximum wind speed enhancement along the casing body, U_{max}/U_∞ was obtained in the flange height ratio of $H/D=0.3$ corresponding to $U_{max}/U_\infty=1.511$. Similarly, Figure 4.77 as well presents similar results. In this context, while the minimum pressure coefficient for the non-flanged case and $H/D=0.2$ flanged case are $C_{prmax}=-0.861$ and $C_{prmax}=-1.273$, respectively; this situation exhibits a pressure drop of 48% more in the case of flange utilization. Further increase of the flange height ratio, H/D to 0.3 does not, however, cause any significant pressure drop along the casing body. In these regards, flange height

ratio, $H/D=0.3$ resulted in the maximum pressured drop ratio, C_{pmax} to reach -1.284. However, this flange height ratio of $H/D=0.3$ was reported to be the highest pressure drop among the tested cases, similarly to the wind speed enhancement computations.

Besides, analysis of the velocity vectors for the optimized casing bodies are demonstrated in Figures A1, A2, A3, and A4 of Annex Section corresponding to the non-flanged case, flanged cases of $H/D=0.2$, $H/D=0.3$, and $H/D=0.4$, respectively. The highest wind speed increase inside the shrouding body shown in Figure A1 reached 7.85 m/s in the turbine location diameter for the non-flanged case exhibiting an increase of 1.57 more compared to free-stream wind speed, U_{∞} . On the other hand, this wind speed was increased by 8% in the case of an $H/D=0.2$ flange application reaching 8.5 m/s as shown in Figure A2. This situation was absolutely resulted by the vorticity formations at the immediate downstream of the flange. These vortices drew in a higher mass flow rate of air through the casing body which also increase mass flow rate of the air passing through the rotor disc, \dot{m} .

Velocity contours for the first four cases defined in Table 4.29 are as well shown in Figures A5, A6, A7, and A8 of Annex Section. Addition of a flange component results in the low pattern regions in terms of wind velocity behind the flange region as presented in these eight figures. Similarly, pressure drop occurs in the same trend in the case of a flange application as shown in Figures A9, A10, A11, and A12. The maximum pressure drop region is the location of the micro wind turbine installation referred to be unquestionably the throat area.

On the other hand, Figures A13, A14, A15, and A16 present the streamlines considering the first four cases. Finally, vorticity presented for the non-flanged case, and flanged cases of $H/D=0.2$, $H/D=0.3$, and $H/D=0.4$ are demonstrated in Figures A17, A18, A19, and A20 of Annex Section, respectively. It is also valid from these figures that the higher the flange height, H , the broader

region of vortex formation behind the flange resulting more air mass flow inside the shrouding case.

4.11.3.1.(2). Analysis of the Diffuser Opening Angle Influence

The influence of diffuser opening angle on wind speed enhancement and as well pressure drop are demonstrated in Figures 4.78 and 4.79, respectively. The *CFD* results are taken based on casing axial axis, as the schematic drawing and the axisymmetry axis were shown in Figure 4.73. The cases used in this part of the dissertation and indicated as 5, 6, 7, 8, 9, and 10 in Table 4.29 correspond to half-cone angles, Θ of 3° , 4° , 5° , 6° , 9° , and 12° , respectively. Among the tested cases, maximum wind speed enhancements, U_{max}/U_∞ along the axial axis of casing bodies were reported to be highest for half-cone angle, Θ of 5° , corresponding to 1.567. On the other hand, the results were quite interesting that an increase of maximum wind speed enhancement, U_{max}/U_∞ along the casing bodies was reported between 3° and 5° half cone angles, Θ in parallel with the half cone angle, Θ increase. However, especially exceeding half cone angle, Θ value of 6° , i.e., wind speed enhancements obtained for 9° and 12° of half cone angles were observed to be even lower than the wind speed enhancement obtained at 3° of half cone angle, Θ .

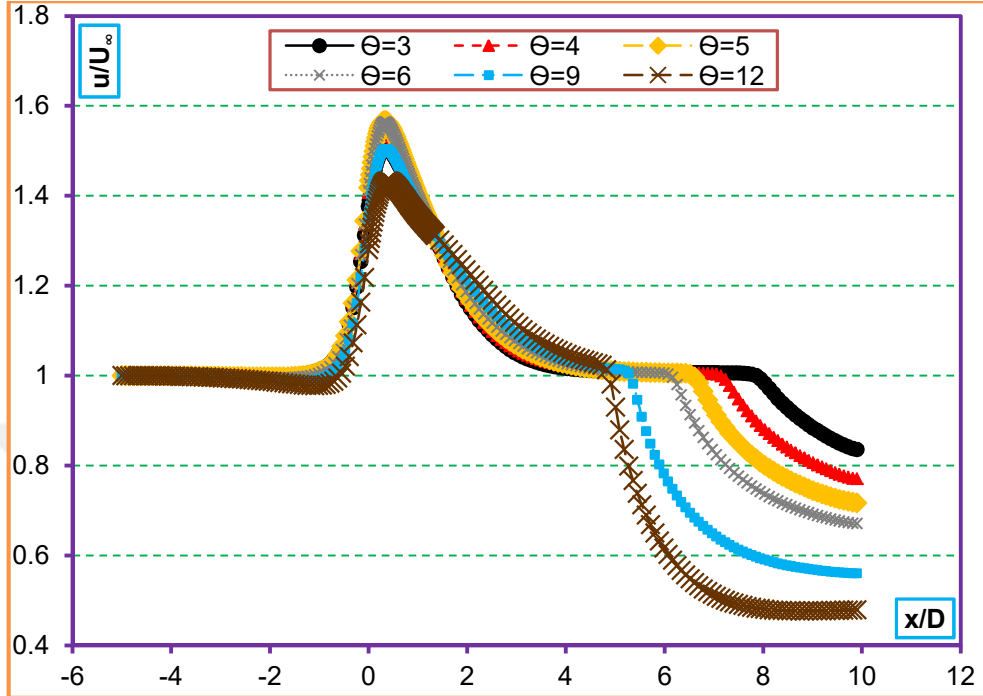


Figure 4.78. Diffuser opening angle performance analysis in the unsteady case revealing wind speed ratio, u/U_∞ in the vicinity of the casing shroud profiles

Among the considered cases of cone angles, Θ of 3° , 4° , 5° , 6° , 9° , and 12° , situation of pressure drop along the studied casing bodies, C_{pr} demonstrate that maximum pressure drop ratio, C_{prmax} among these cases was observed for half-cone angle, Θ of 5° , having the value of $C_{prmax} = -1.456$, similar to the above explained wind speed enhancement situations. Besides, again as similar to the wind speed enhancements, an improvement in maximum pressure drop ratio, C_{prmax} was reported between 3° and 5° half cone angles, Θ in parallel with the half cone angle, Θ increase. However, maximum pressure drop ratio, C_{prmax} becomes also worse especially exceeding half cone angle, Θ value of 6° , i.e., maximum pressure drop ratio, C_{prmax} obtained for 9° and 12° of half cone angles were observed to be even worse than the maximum pressure drop ratio obtained at 3° of half cone angle, Θ .

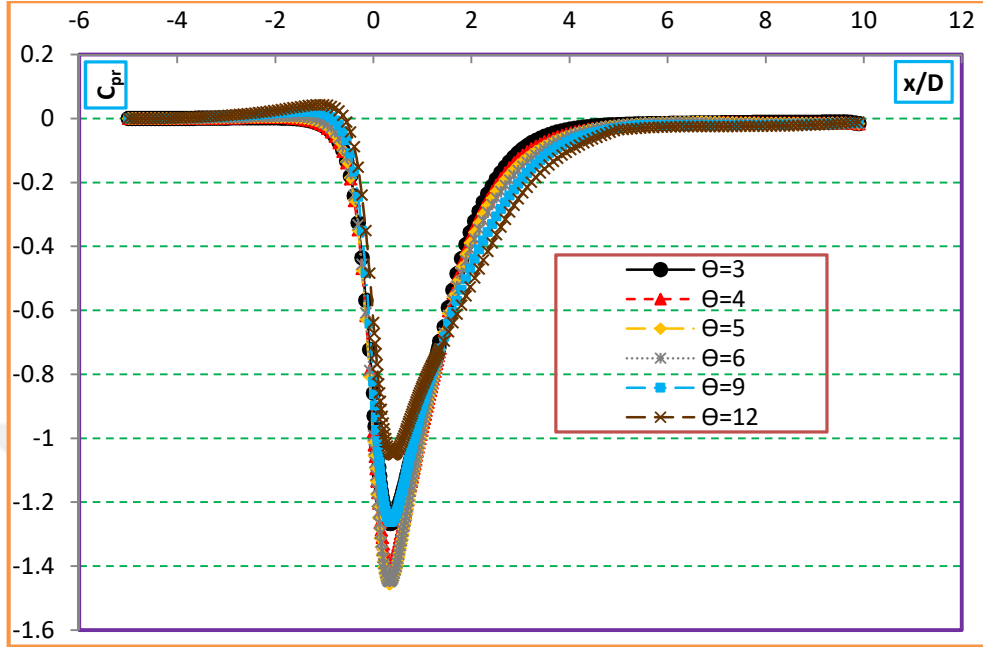


Figure 4.79. Diffuser opening angle performance analysis in the unsteady case revealing pressure drop, C_{pr} in the vicinity of the casing shroud profiles

4.11.3.1.(3). Analysis of the Casing Length Influence

Figures 4.80 and 4.81 reveal wind speed ratio, u/U_∞ and pressure drop, C_{pr} distribution in the vicinity of the casing shroud profiles for the considered cases of dimensionless casing full body length, L/D of 1.30, 1.35, 1.40, 1.45, and 1.50, which were shown as Cases 11, 12, 13, 14, and 15 in Table 4.29. It is interesting to note here that both parameters are not so influenced by the alteration of dimensionless casing full body length, L/D . On the other hand, maximum wind speed enhancements, U_{max}/U_∞ along the axial axis of casing bodies were obtained as highest for the Case 15 of Table 4.29, i.e., for the dimensionless casing full body length, L/D of 1.50, corresponding to 1.584 of maximum wind speed enhancement, U_{max}/U_∞ . Additionally, a small incremental increase is reported in this part of the

dissertation dealing that maximum wind speed enhancement, U_{max}/U_{∞} along the axial axis of casing bodies occur with dimensionless casing full body length, L/D increase.

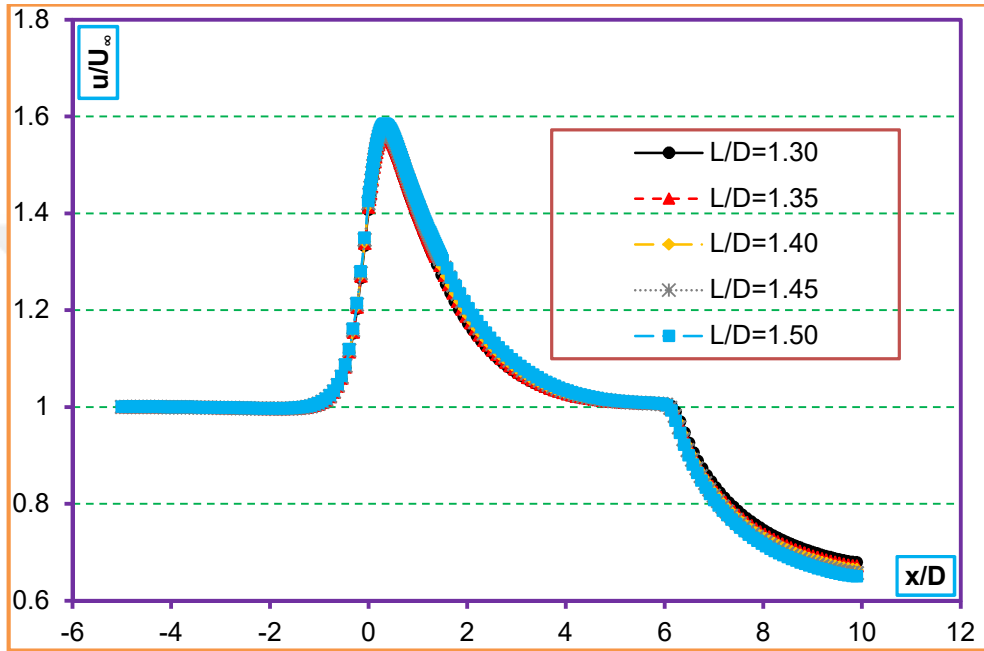


Figure 4.80. Casing length performance analysis in the unsteady case revealing wind speed ratio, u/U_{∞} in the vicinity of the casing shroud profiles

When the cases shown in Table 4.29 including the Cases 11, 12, 13, 14, and 15 are taken into account, similar to the situation of highest maximum wind speed enhancement, U_{max}/U_{∞} along the axial axis of casing bodies which was obtained for the longest dimensionless casing full body length, L/D of 1.50; in parallel to this situation, corresponding highest maximum pressure drop ratio, C_{prmax} was observed as well in the longest dimensionless casing full body length, L/D of 1.50. This value of dimensionless casing full body length generated the maximum pressure drop ratio, C_{prmax} to have the value of -1.509. Maximum pressure drop ratio, C_{prmax} which not influenced much by the alteration of

dimensionless casing full body length, L/D reveals that a small incremental increase in maximum wind speed enhancements, U_{max}/U_{∞} along the axial axis of casing bodies occurring with casing dimensionless full body length, L/D increase.

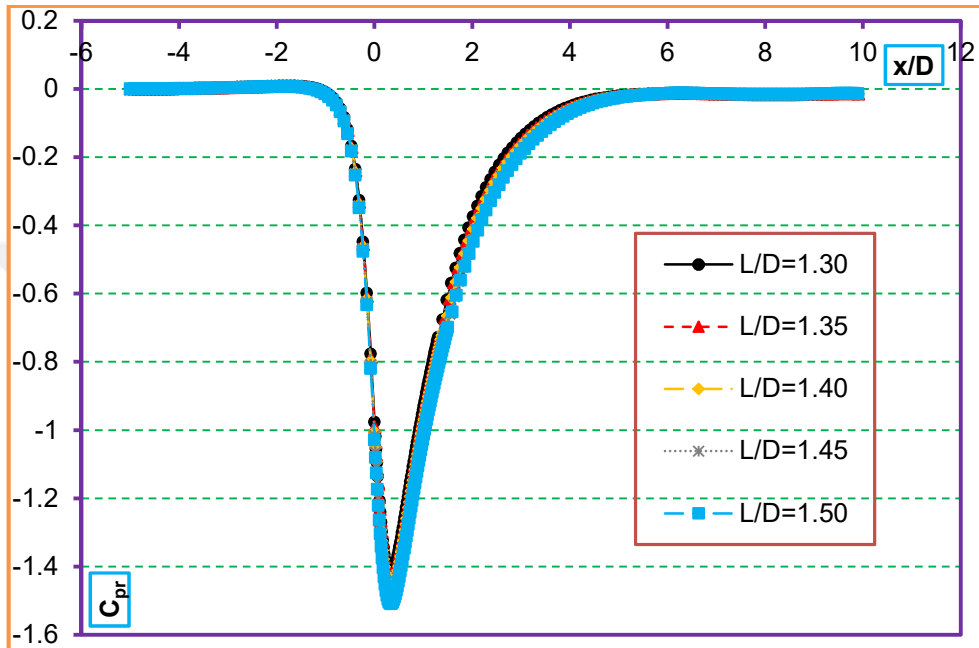


Figure 4.81. Casing length performance analysis in the unsteady case revealing pressure drop, C_{pr} in the vicinity of the casing shroud profiles

4.11.3.1.(4). Analysis of the Inlet Shrouding Component Influence

Figures 4.82 and 4.83 present the proper designed inlet shrouding component influence in terms of wind speed ratio, u/U_{∞} and pressure drop, C_{pr} distribution in the vicinity of the casing shroud profiles. The cases as demonstrated in Table 4.29 as 16 and 17 provide us a comparison of both cited parameters during the situations of non-inlet shrouded casing and inlet shrouded casing.

When Figure 4.82 is taken into account, it is observed that along the axial axis of casing profiles, a properly designed inlet shrouding presents a 16% of increase in maximum wind speed enhancement, U_{max}/U_{∞} along the axial axis of

casing bodies, resulting an initial value of maximum wind speed enhancement, U_{max}/U_{∞} value of 1.602 raised to 1.853, in the case of inlet utilization.

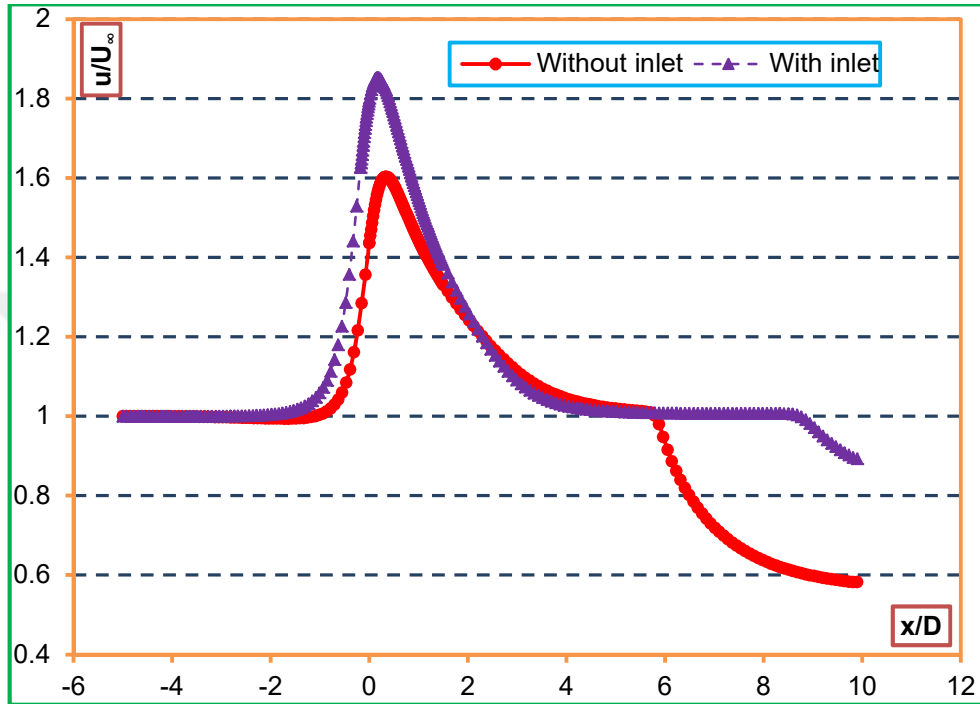


Figure 4.82. Casing inlet shrouding component performance analysis in the unsteady case revealing wind speed ratio, u/U_{∞} in the vicinity of the casing shroud profiles

On the other hand, a significant pressure drop in maximum pressure drop ratio, C_{prmax} of 55% during the utilization of inlet shrouding component was observed as seen in Figure 4.83. Based on this figure, it is seen that an initial value of maximum pressure drop ratio, C_{prmax} of -1.567 in non-inlet shrouded casing was further decreased to a value of maximum pressure drop ratio, C_{prmax} of -2.432.

In this context, Figures 4.82 and 4.83 both show the positive influence of an optimum designed inlet shrouding component that can play a role of significant increase of power generation in a wind turbine located in the casing.

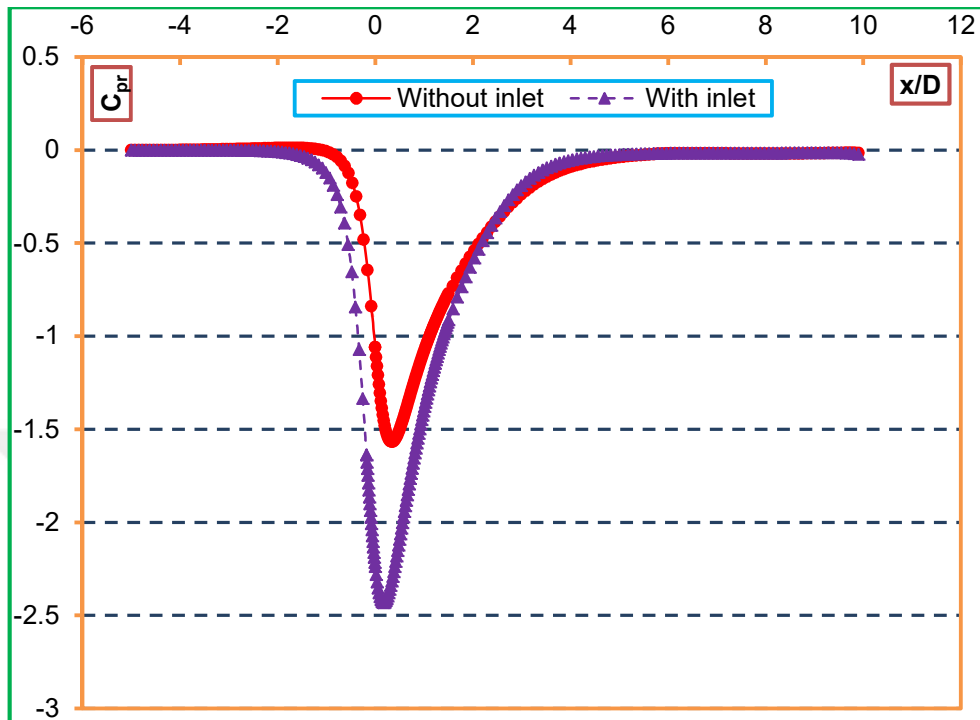


Figure 4.83. Casing inlet shrouding component performance analysis in the unsteady case revealing pressure drop, C_{pr} in the vicinity of the casing shroud profiles

4.11.3.2. Results of Curved Optimizations

Ohya et al. (2004) demonstrated vortex formation at downstream regions of the flange. Figures 4.84 and 4.85 indicate low pressure zones resulting in enhanced mass flow rate through the rotor plane and generated vortices at up radial and down radial regions at a chosen variety of instances, respectively.



Figure 4.84. Low pressure zone resulting enhanced mass flow rate of [Ohya et al. \(2004\)](#) study

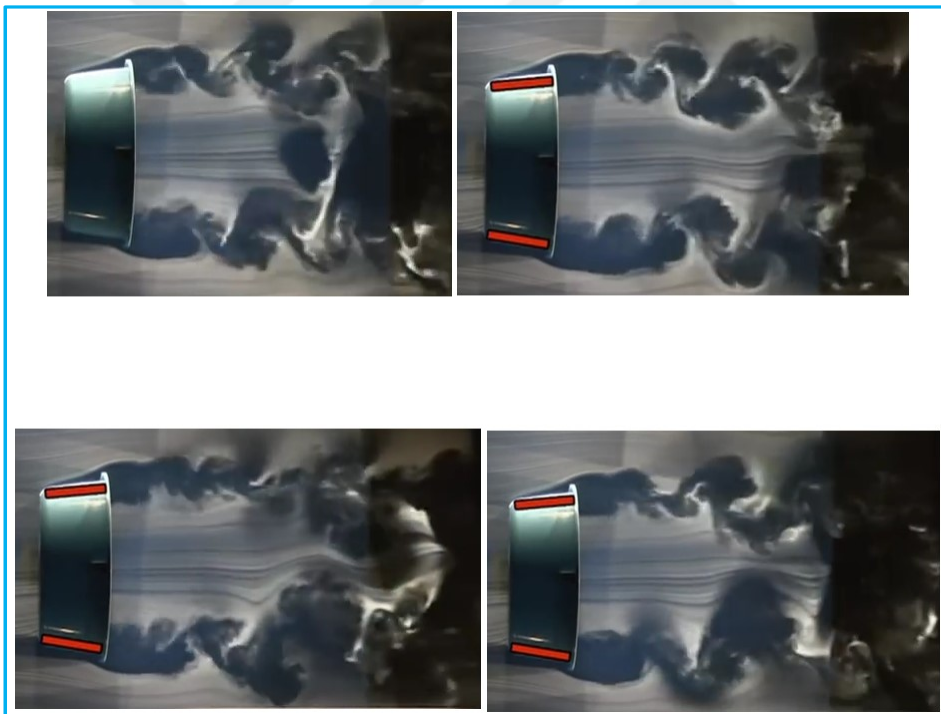


Figure 4.85. Vortices generations at up radial and down radial regions at a chosen variety of instances ([Ohya et al., 2004](#))

Dye experiments were conducted in the *PIV* laboratory of Çukurova University. The photographic views were obtained considering up flange side images, up flange wake side images, and hub side images. On the other hand, experiments of Ohya and Karasudani (2010), Ohya et al. (2002), Ohya et al. (2008), and Ohya et al. (2006) were taken into account to present the similarity of the results obtained from the current study with the results found in the literature. In these regards, Figures 4.86 and 4.87 present low pressure concept of up flange side images of Ohya et al. (2008) and Ohya and Karasudani (2010), respectively. Besides, up flange side images of the current study are also shown in Figures 4.86b, 4.86c, and 4.86d; and 4.87b, 4.87c, and 4.87d.

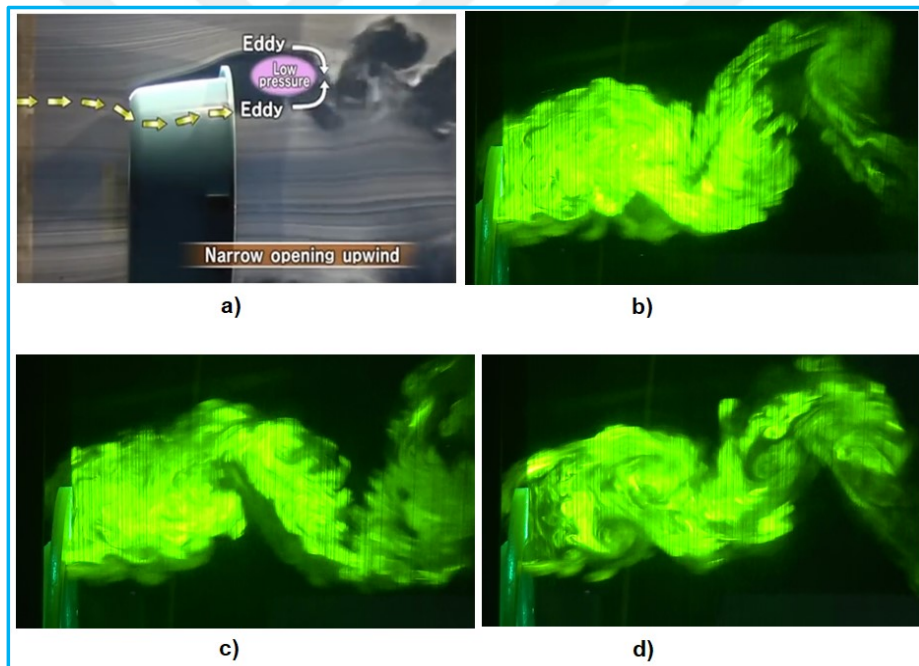


Figure 4.86. Low pressure concept of up flange side images of Ohya et al. (2008) and the current study, **a)** Ohya et al. (2008) up flange dye visualization, **b)** first view of current study up flange dye visualization, **c)** the second view of current study up flange dye visualization, **d)** the third view of current study up flange dye visualization

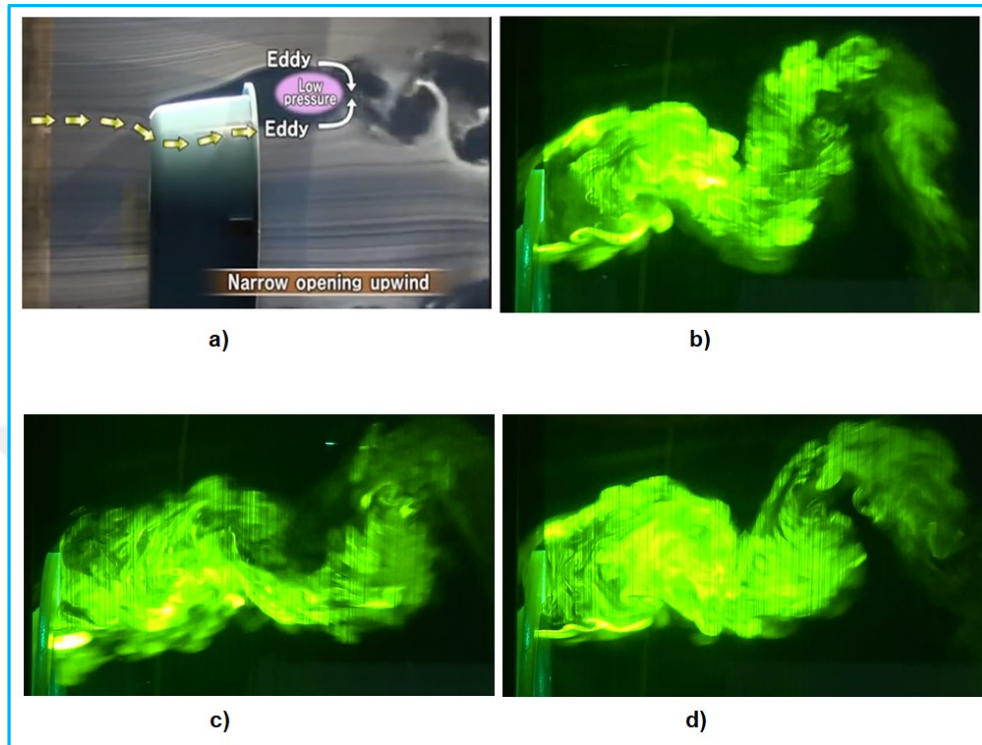


Figure 4.87. Low pressure concept of up flange side images of [Ohya and Karasudani \(2010\)](#) and the current study, **a)** [Ohya and Karasudani \(2010\)](#) up flange dye visualization, **b)** first view of current study up flange dye visualization, **c)** the second view of current study up flange dye visualization, **d)** the third view of current study up flange dye visualization

On the other hand, Figures 4.88 and 4.89 demonstrate up flange wake images of this study compared concerning the up flange wake visualizations of [Ohya et al. \(2002\)](#) and [Ohya et al. \(2006\)](#), respectively.

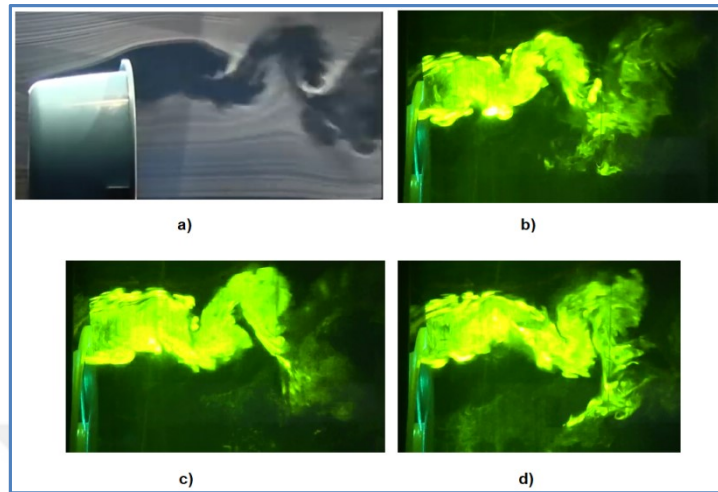


Figure 4.88. Up flange wake side images of [Ohya et al. \(2002\)](#) and the current study, **a)** [Ohya et al. \(2002\)](#) up flange wake dye visualization, **b)** first view of current study up flange wake dye visualization, **c)** the second view of current study up flange wake dye visualization, **d)** the third view of current study up flange wake dye visualization

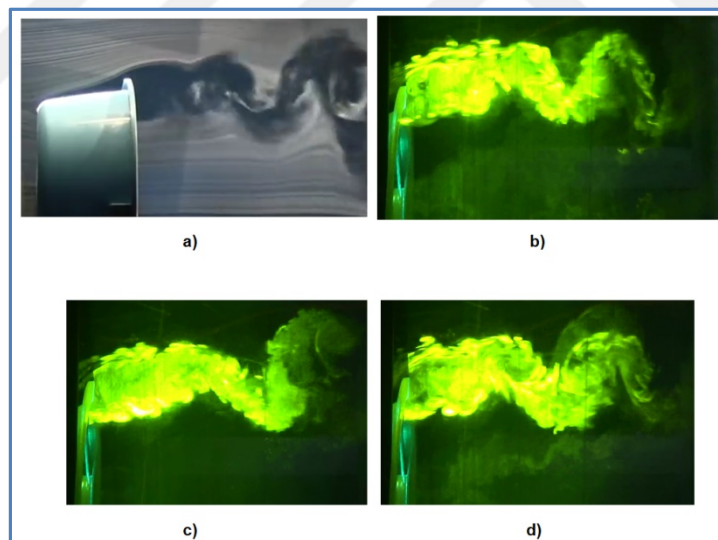


Figure 4.89. Up flange wake side images of [Ohya et al. \(2006\)](#) and the current study, **a)** [Ohya et al. \(2006\)](#) up flange wake dye visualization, **b)** first view of current study up flange wake dye visualization, **c)** the second view of current study up flange wake dye visualization, **d)** the third view of current study up flange wake dye visualization

Finally, the hub side *PIV* photographic images of the current study are presented in Figures 4.90 for a variety of instances. Besides, Figures 4.91 demonstrate hub side *PIV* photographic images for the developed flow.

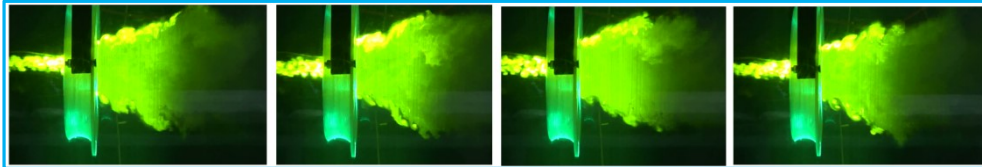


Figure 4.90. Hub side images of the current study at a chosen variety of instances

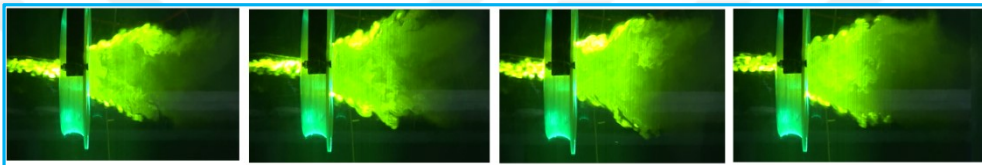


Figure 4.91. Hub side images of the current study at a chosen variety of instances for the developed flow

Figures 4.92, 4.93, and 4.94 demonstrate half shroud downstream axisymmetric flow visualizations. Figure 4.92 indicates streamlines formed at the downstream and up radial zone of the designed curved type of casing configuration which was shown in Figure 4.72. Besides, it is presented in this figure that two large vorticity formations at the downstream regions of the designed curved type of casing configuration were obtained. These two demonstrated vorticities are the main driving factors of enhancing mass flow rate running through the wind turbine blades. The proper location of the wind turbine location inside the casing body is shown in Figure 4.72 designated by the blue color.

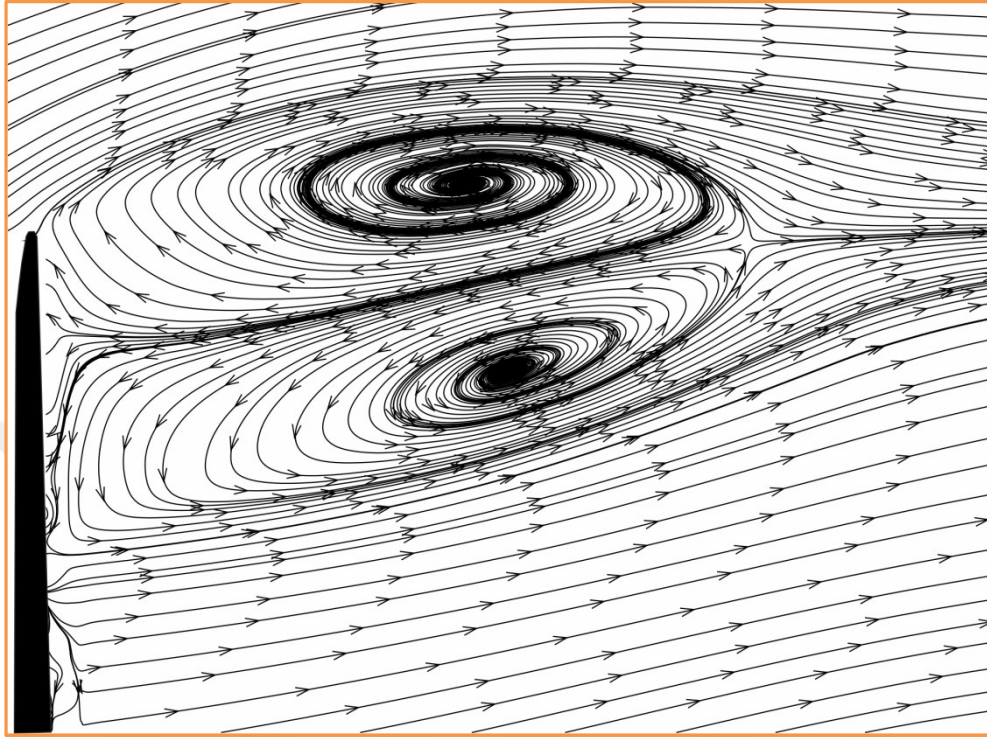


Figure 4.92. Streamlines shown at downstream and up radial regions of the curved type of wind turbine casing configuration

On the other hand, vortex formations at downstream and up radial regions of the configuration are demonstrated in Figure 4.93. This figure indicates that at both regions although strong vortices were obtained, rotational directions of both were reported as the inverse. Likewise, wind speed ratio inside and in the vicinity of casing, u/U_∞ is shown by dimensionless magnitude of the resultant velocity, $|V|/U_\infty$ in Figure 4.94. It is obvious in this figure that at downstream of up radial regions intersecting with casing exit diameter, D_2 and exit diameter of the casing including the flange heights, D_0 , although low wind speed ratio results were obtained; higher wind speed ratio results were obtained at downstream regions intersection with turbine location diameter, D due to the functionality of the wind turbine casing system. Additionally, at up radial regions of the flange, higher

dimensionless magnitude of the resultant velocity, $|V|/U_\infty$ results were also obtained. These increased wind velocity in these zones were observed to decrease at further downstream.

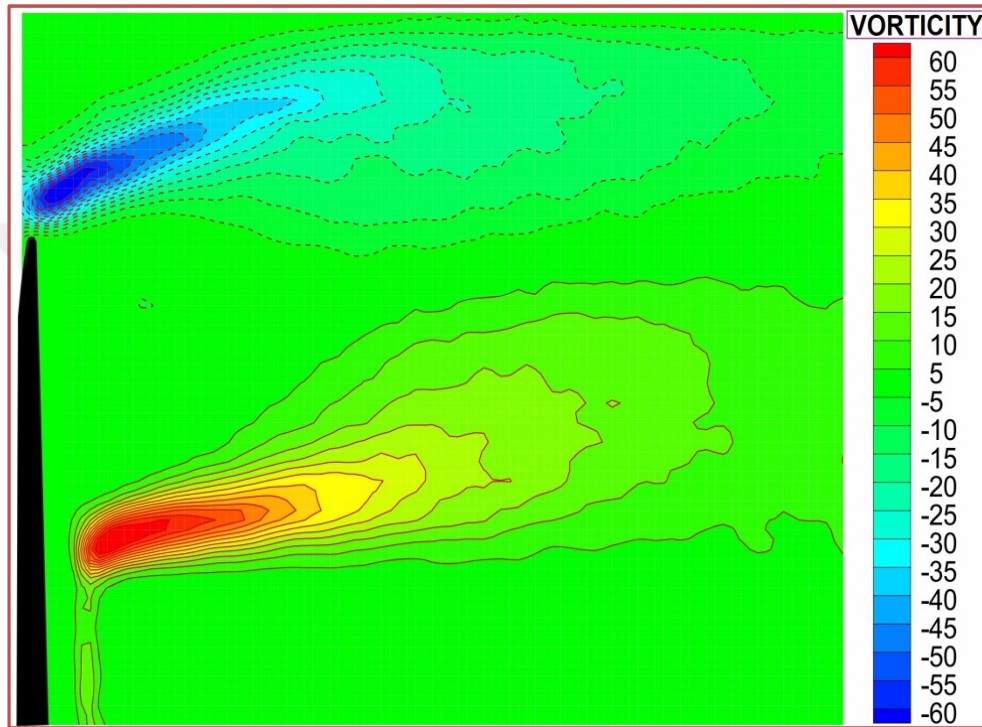


Figure 4.93. Vorticity results shown at downstream and up radial regions of the curved type of wind turbine casing configuration ($1/s$)

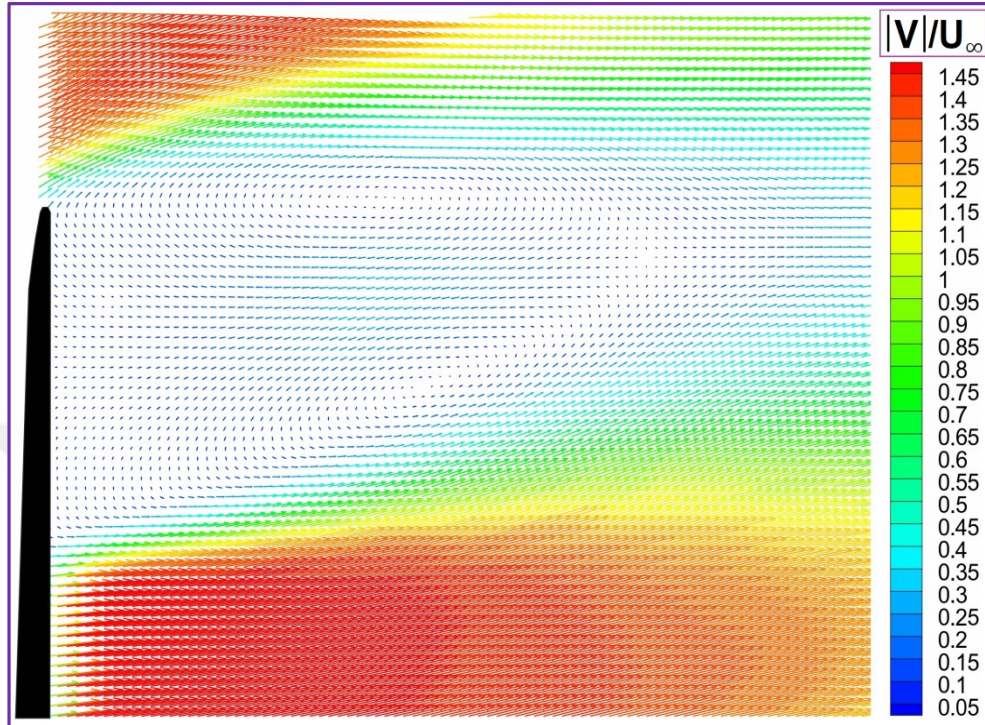


Figure 4.94. The dimensionless magnitude of the resultant velocity, $|V|/U_\infty$ outputs shown at downstream and up radial regions of the curved type of wind turbine casing configuration

Figures 4.95, 4.96, and 4.97 indicate flange downstream axisymmetric flow visualizations. In these regards, better focused flow visualizations in a specific study of an area are shown standing for flange downstream streamline, vorticity, and dimensionless magnitude of the resultant velocity, $|V|/U_\infty$ visualizations presented in Figures 4.95, 4.96, and 4.97, respectively.

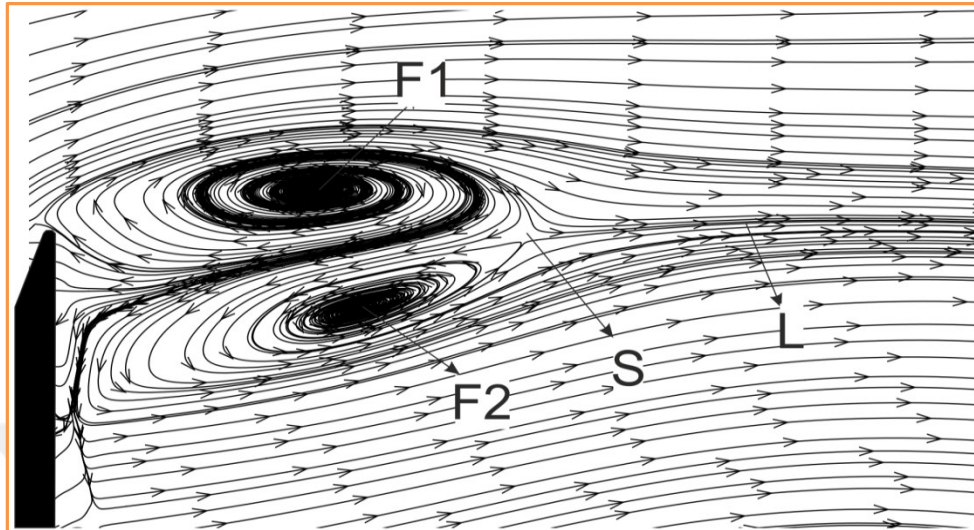


Figure 4.95. Streamlines shown at flange downstream of the curved type of wind turbine casing configuration

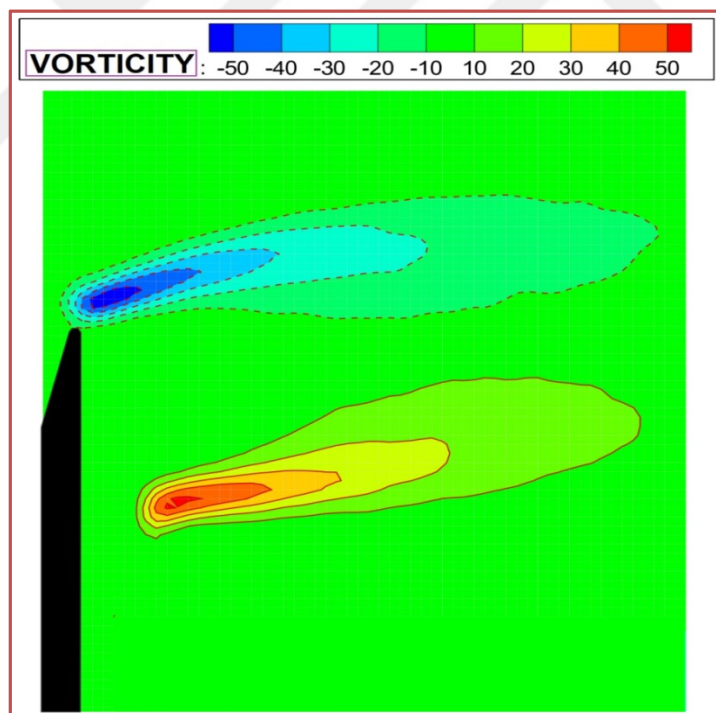


Figure 4.96. Vorticity results shown at flange downstream of the curved type of wind turbine casing configuration ($1/s$)

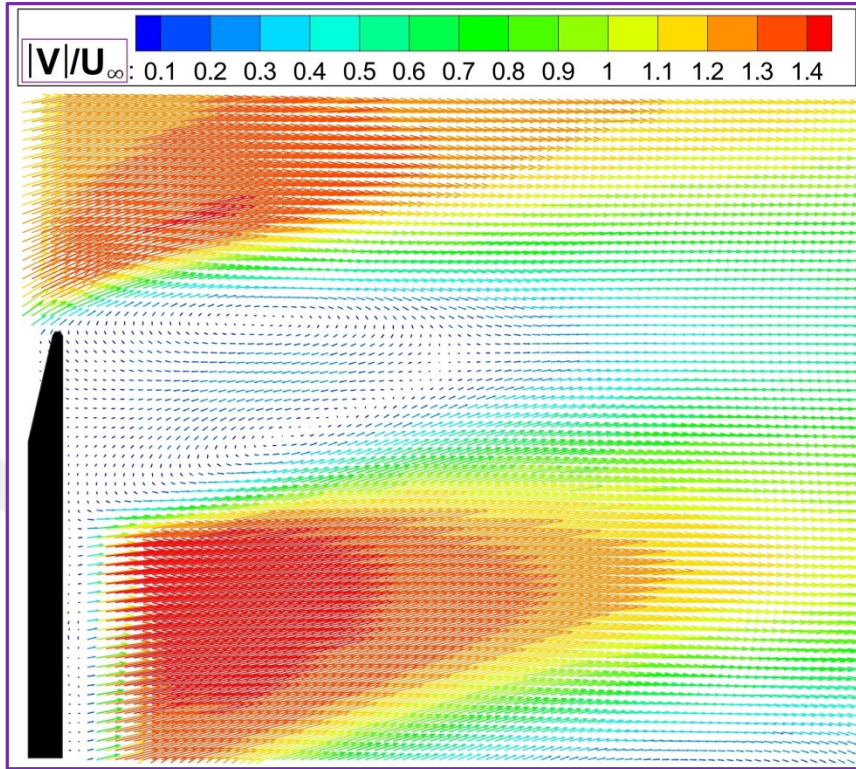


Figure 4.97. The dimensionless magnitude of the resultant velocity, $|V|/U_\infty$ outputs shown at flange downstream of the curved type of wind turbine casing configuration

4.11.4. Concluding Remarks

Casing applications in wind turbine systems play a significant role in enhancing wind speed touching turbine rotor blades; thus a substantial enhancement in energy generation can be obtained by this method. This part of the dissertation has set the following outcomes to forth:

- Among the *CFD* tested configurations in terms of flange height ratio, H/D and presented in Table 4.29 as Cases 1, 2, 3, and 4, reveals that highest maximum wind speed enhancement along the casing body, U_{max}/U_∞ was

obtained in the flange height ratio of $H/D=0.3$ corresponding to $U_{max}/U_{\infty}=1.511$. Similarly, the highest maximum pressure drop ratio, C_{prmax} to reach -1.284 was as well acquired at the flange height ratio of $H/D=0.3$.

- Among the *CFD* tested structures shown as Cases 5, 6, 7, 8, 9, and 10 in Table 4.29 demonstrates that for half-cone angle, θ of 5° , highest maximum wind speed enhancement along the casing body, U_{max}/U_{∞} corresponding to 1.567 was achieved. On the other hand, again in half-cone angle, θ of 5° , the value of $C_{prmax} = -1.456$ has come off as the highest maximum pressure drop ratio, C_{prmax} , among the numerically tested configurations.
- Among the *CFD* tested cases in terms of dimensionless casing full body length, L/D and shown in Table 4.29 as Cases 11, 12, 13, 14, and 15, indicates that highest maximum wind speed increase along the casing body, U_{max}/U_{∞} was attained in dimensionless casing full body length, L/D of 1.50, corresponding to 1.584 of maximum wind speed increase along the casing body, U_{max}/U_{∞} . Besides, the same value of dimensionless casing full body length, L/D also generated the maximum pressure drop ratio, C_{prmax} to have the value of -1.509.
- Finally, for the *CFD* studies, it was observed that utilizing of a proper inlet shrouding configuration exhibiting a significant increase both in wind speed ratio, u/U_{∞} and pressure drop, C_{pr} distributions in the vicinity of the casing shroud profiles. In this context, among the tested *CFD* designs in terms of inlet shrouding applications and pointed in Table 4.29 as Cases 16 and 17, signifies that a 16% of increase in maximum wind speed enhancement, U_{max}/U_{∞} along the axial axis of casing bodies as well a

significant pressure drop in maximum pressure drop ratio, $C_{p_{max}}$ of 55% were obtained, during the inlet utilization.

- On the other hand, in terms of the *PIV* studies, the designed curved type of wind turbine shrouding system was compared with the studies of [Ohya and Karasudani \(2010\)](#), [Ohya et al. \(2002\)](#), [Ohya et al. \(2008\)](#), [Ohya et al. \(2006\)](#) to reveal up flange side images and up flange side images. During the comparison of whole studies, it was observed that vorticity formations at downstream of casing bodies were shown to be similar.
- Hub side images at a variety of instances were also demonstrated for the designed curved type of wind turbine shrouding body. Vorticities were also formed in the vicinity of hub zone and at downstream resulted by the hub construction in which the blades are attached.
- The dimensionless magnitude of the resultant velocity, $|V|/U_{\infty}$ outputs shown at downstream and up radial regions of the curved type of wind turbine casing configuration and as well as dimensionless magnitude of the resultant velocity, $|V|/U_{\infty}$ outputs shown at flange downstream of the curved type of wind turbine casing configuration revealed that resultant velocity, $|V|/U_{\infty}$ was increased by a factor reaching $|V|/U_{\infty}=1.5$. Besides, it was also observed that two big vorticities were formed at the downstream region of flange rotating at the opposite direction.



5. OVERALL CONCLUSIONS AND RECOMMENDATIONS

5.1. Overall Conclusions

The main purpose of the dissertation is to investigate utilities of casing shrouds in performances of wind turbines. In this context, *CFD* and *PIV* performance analysis were conducted in linear and curved types of wind turbine shrouding systems to reveal wind speed enhancements, corresponding pressure drops, and as well flow visualizations including velocity contours, pressure contours, velocity vectors, streamlines, and vortices were handled. Additionally, flow visualizations at downstream region of the casing and flange component were studied using *PIV* method. These visualized views are compared with the views obtained by the findings obtained from the studies conducted by [Ohya and Karasudani \(2010\)](#), [Ohya et al. \(2002\)](#), [Ohya et al. \(2008\)](#), [Ohya et al. \(2006\)](#), [Ohya et al. \(2004\)](#).

5.2. Resultant Outputs of the Conducted Studies in the Dissertation

5.2.1. Conclusions for Wind Energy Density Statistical Analysis

The study had set forth Bababurnu region located in Çanakkale province of Turkey having enough wind energy potential to be utilized for new wind power plant installations, since the study had indicated that wind properties in this province shown to be acceptable. Among the derived results, this location of Turkey was observed to have an annual average wind velocity and annual average wind energy potential of 6.01 m/s and 257 W/m², respectively. Additionally, in this part of the dissertation, Weibull and Rayleigh statistical forecasting methods were

demonstrated to be significantly sufficient in revealing frequency, wind speed and power density distributions of the processed wind data.

5.2.2. Conclusions for Installed Wind Farm Efficiency Analysis

The study handled efficiency analysis of an installed wind farm in South province of Turkey. Five wind turbines were considered in this wind farm which these turbines were named as T01, T02, T03, T04, and T05 wind turbines. It was determined that based on hourly average wind speed data, initially monthly average wind speed values were determined revealing yearly average wind speed for corresponding wind turbines found as 8.06, 9.06, 8.32, 9.38, and 8.76 m/s, respectively. Similarly, hourly average generations for these cited wind turbines were also determined as 887.07, 1133.93, 992.75, 1208.08, and 1037.37 kWh, respectively. Additionally, based on the processed wind value data, wind direction status was reported as 197.90° , 115.59° , 93.76° , 99.09° , and 178.77° , for T01, T02, T03, T04, and T05 wind turbines, respectively. And finally, based on the study of air temperature data in the context of this part of the dissertation, it was observed that 17.30, 16.05, 16.73, 16.02, and 15.73°C of air temperature values were obtained, respectively.

On the other hand, based on the yearly average processed data formed of hourly wind data, efficiencies of the wind turbines were determined. Considering wind turbine named T01, in the range of free-stream wind speed values, $4.8542 \leq U_\infty \leq 18.7791$, the average power coefficient, C_p of the cited wind turbine was found to be $C_p=23.35\%$. On the other hand, T03 operated in the range of free-stream wind speed values of $4.9233 \leq U_\infty \leq 19.0480$ and had a corresponding average power coefficient, C_p of $C_p=24.29\%$. Besides, operation conditions of T04 wind turbine revealed that a free-stream wind speed value range of $4.8807 \leq U_\infty \leq 21.9236$ generated a corresponding average power coefficient, C_p of

$C_p=20.12\%$. And finally, wind turbine T05 was calculated to have a power coefficient, C_p value of $C_p=21.83\%$ in the range of free-stream wind speed value of $4.8353 \leq U_\infty \leq 19.1645$.

Aerodynamical understanding of horizontal axis wind turbines was configured through obtaining distributions of power coefficient, C_p , and thrust coefficient, C_T with respect to the wake and free-stream wind speed relation coefficient, λ , similarly power coefficient, C_p , and thrust coefficient, C_T distributions defined based on the axial flow induction factor, a , wind speed at far wake, U_w and hub height wind speed, U_D presented according to the free-stream wind speed, U_∞ values, and finally, mechanical output power of wind turbines, P , and thrust forces, T of wind turbines defined according to the free-stream wind speed, U_∞ values.

Finally, in this part of the dissertation, it is reported that based on the wind data of the 2010 year and considering five cited wind turbines; wind farm located in South part of Turkey generated 7.15 GWh of power at the corresponding mean wind speed value of 11.90 m/s in July. This value of electricity generation in this summer month was reported to be the peak value of the whole year 2010. On the other hand, considering the whole year of 2010, a total of 38.09 GWh of generations were obtained from five wind turbines. However, the yearly highest energy generation was obtained from wind turbine T04 and lowest from T01 corresponding to 9.03 and 6.12 GWh of generations, respectively. Although both wind turbines are installed in the same wind farm, the difference in electric production in between turbine T01 and T04 is 33% in the year of 2010. In other words, wind turbine T01 generated 33% less electricity when compared to wind turbine T04. This wind farm is situated in the valley containing many hills, crests, and roughness. This topographic condition of the farm effects wind directions and magnitude of free-stream wind speed, U_∞ , thus the generated turbine output power.

5.2.3. Conclusions for Horizontal Axis Wind Turbine Aerodynamic Characteristics

In this study, five identical wind turbines of a considered wind farm located in Belen province of Turkey were studied by means of aerodynamic parameters. The installed capacity of the chosen wind farm was reported to be 48 MW, composed of 16 identical wind farms having turbine rotor diameter of 90 m each. The distributions of aerodynamic functions were determined based on hub-height wind speed, U_D including outputs of mechanical output power of wind turbines, P , axial flow induction factor, a , power coefficient, C_p , thrust coefficient, C_T , and finally thrust force, T .

This part of the dissertation reports that generated wind turbine output power, P increases with increasing hub-height wind speed, U_D , until it is delimited by rated power of wind turbines, in this case, 3.0 MW of rated power, P_r . This delimitation situation is the case for whole wind turbines, since they are identical. On the other hand, maximum axial flow induction factor, a values, for all wind turbines, were reported to be in the range of hub-height wind speed, U_D , $5 \text{ m/s} \leq U_D \leq 11 \text{ m/s}$. These corresponding values of axial flow induction factor, a values reach their peak values after exceeding hub-height wind speed values of $U_D \geq 5 \text{ m/s}$. However, the values rapidly decrease for $U_D \geq 10 \text{ m/s}$ considering all wind turbines. This value range of hub-height wind speed, U_D having $5 \text{ m/s} \leq U_D \leq 11 \text{ m/s}$ also generates highest peak values for power coefficients, C_p , and thrust coefficients, C_T for whole wind turbines. It was observed that a significant difference occurred between wind turbine T2 and T4, namely, while wind turbine T2 generated a peak power coefficient, C_p value corresponding to 34%, T4 generated a peak power coefficient, C_p value corresponding to only 29%, at the same value of hub-height wind speed, U_D . Similarly, this is also the case for thrust force, T values. At a constant value of hub-height wind speed, U_D generating

highest thrust force, T values; it is reported that T2 wind turbine reached maximum peak thrust force, T of $T=200$ kN, however, T4 wind turbine reached minimum peak thrust force, T of only $T=170$ kN.

5.2.4. Conclusions for 2.0 MW Horizontal Axis Large Wind Turbine Aerodynamic Characteristics

The study focused on aerodynamic characteristics of horizontal axis wind turbines located in an existing wind farm, named as Sebenoba *WPP* and located in Hatay province of Turkey. Five identical wind turbines of the farm were selected in terms of aerodynamic performance analysis, and those were named as T1, T2, T3, T4, and T5. The configured aerodynamic parameters included the distributions of mechanical output power of wind turbines, P , axial flow induction factor, a , power coefficient, C_p , thrust force coefficient, C_T , thrust force, T , and tangential flow induction factor, a' , whole expressed with respect to the blade tip speed ratio, λ_R . The technique of the study utilized was the Blade Element Momentum Theory (*BEM*). On the other hand, the rotor diameter of identical wind turbines and rated power were reported to be 80 m and 2000 kW, respectively.

According to the derived results of the study, the aerodynamic output results cited above presented a good agreement, i.e., five identical wind turbines did not result in any significant discrepancy. Besides, it was observed that during almost half of the operating percentage of wind turbines for the considered year, they were reported to operate at the optimum turbine rotor rotational speed, Ω of $\Omega=16.40$ rpm. On the other hand, unfortunately during one-fourth of the year, wind turbines did not generate any power due to reasons of preventive maintenance and fault detections.

Maximum wind turbine output power was reported to occur at a tip-speed ratio, λ_R of 2.81 and a rotational speed of $\Omega=16.40$ rpm, generating an output power

of 2000 kW. On the other hand, maximum wind turbine efficiency, C_p was obtained to be 30% at a corresponding tip speed ratio, λ_R of $\lambda_R=7.12$. Since power coefficient, C_p is a derived function obtained from axial flow induction factor, a , distributions of axial flow induction factor, a with respect to the tip speed ratio, λ_R present the similar tendency as in the case of power coefficient, C_p . Besides, the lowest and highest flow induction factors, a are determined as 0.0124 and 0.0924 at corresponding tip speed ratio, λ_R values of $\lambda_R=2.81$ and $\lambda_R=7.12$, respectively. Finally, thrust force, T on the rotor plays an essential factor for the performance of wind turbines, and it is directly applied to the tower on which the turbine rotor is attached. In this context, the thrust force, T rises rapidly with increasing tip speed ratio, λ_R , and then decays down rather sharply. In this study, maximum thrust force, T is computed to be $T=150$ kN at a corresponding tip speed ratio, λ_R of $\lambda_R=5.21$.

5.2.5. Conclusions for Horizontal Axis Wind Turbine Aerodynamic Characteristics Estimation

The study covered the prediction of wind turbine aerodynamical parameters including mechanical output power of wind turbines, P , axial flow induction factors, a , power coefficients, C_p , thrust coefficients, C_T , and thrust forces, T using Artificial Neural Network (ANN) prediction models. The used wind turbines in the study include an identical type of wind turbines of rated power, P_r of $P_r=3000$ kW, and turbine rotor diameter, D_{rotor} of $D_{rotor}=90$ m, and these wind turbines are named as wind turbine T1, T2, T3, T4, and T5. These wind turbines are located in a wind farm located in South province of Turkey, referred as Belen WPP. The study reported the advantage of the utilized models to predict wind turbine aerodynamic characteristics, only having the required hub-height wind speed, U_D , and atmospheric air temperature, T_{atm} given as inputs. Thus, these

parameters can be predicted without detailed knowledge of wind turbine operations and their control schemes.

First utilized *ANN* prediction model included only hub-height wind speed, U_D given as input to the forecasting tool. On the other hand, the other model included hub-height wind speed, U_D , and additionally atmospheric air temperature, T_{am} given as inputs to the second model. The *MAPE* and *R* results of two utilized models indicated that Model 2 is generally more successful than Model 1, when both training and testing procedures of the models are taken into account. For instance, in terms of mechanical output power of wind turbines, P , *MAPE* values for Model 1 and Model 2 were recorded as 4.88% and 4.63%, respectively, and, *R* values for Model 1 and Model 2 were recorded as 0.9965 and 0.9967, respectively, during the training procedure. On the other hand, again in terms of mechanical output power of wind turbines, P , *MAPE* values for Model 1 and Model 2 were obtained as 3.71% and 3.54%, respectively, and, *R* values for Model 1 and Model 2 were obtained as 0.9995 and 0.9991, respectively, during the testing procedure. Similarly, *MAPE* and *R* results obtained for axial flow induction factor, a , power coefficient, C_p , thrust coefficient, C_T , and thrust force, T are in parallel with the *MAPE* and *R* results of mechanical output of wind turbines, P ; i.e., Model 2 generated better results than Model 1.

However, the results indicated that artificial intelligence models could be a useful tool for accurate forecasting wind turbine aerodynamic characteristics based on only hub-height wind speed, U_D , and atmospheric air temperature, T_{am} . On the other hand, the most advantage of these modes is that as long as having the required hub-height wind speed, U_D , and atmospheric air temperature, T_{am} ; wind turbine aerodynamic characteristics can be predicted without detailed knowledge of wind turbine operations and its control schemes with high accuracy.

5.2.6. Artificial Neural Network Estimation of Wind Power Output Curve

The study covered the prediction of wind turbine aerodynamical parameter of mechanical output power of wind turbines, P using an Artificial Neural Network (*ANN*) prediction model. The used wind turbines in the study include an identical type of wind turbines of rated power, P_r of $P_r=2000$ kW, and turbine rotor diameter, D_{rotor} of $D_{rotor}=80$ m, and these wind turbines are as well named as wind turbine T1, T2, T3, T4, and T5. These wind turbines are as well located in a wind farm also located in South province of Turkey. The study reported the advantage of the utilized model to predict wind turbine aerodynamic characteristics, only having the required hub-height wind speed, U_D , atmospheric air temperature, T_{atm} , and turbine rotor rotational speed, Ω given as inputs. Thus, these parameters can be predicted without detailed knowledge of wind turbine operations and their control schemes.

Prediction of mechanical output power of wind turbines, P was executed based on turbine rotor rotational speed, Ω values including 12.44 rpm, 13.94 rpm, and optimum of 16.14 rpm. The mechanical output power values of these cited rotational speeds were drawn concerning the turbine hub-height wind speed, U_D . It was concluded that best fitting *ANN* forecasting results were obtained in the optimum turbine rotor rotational speed, Ω of $\Omega=16.14$ rpm, when compared to actual energy generation data. Thus, *MAPE* and *R* values for the optimum turbine rotor rotational speed, Ω of $\Omega=16.14$ rpm are minimized and maximized, respectively.

5.2.7. Adaptive Neuro-Fuzzy Inference System Estimation of Wind Power Curve

The study included the prediction of wind turbine aerodynamical parameter of mechanical output power of wind turbines, P using an Adaptive Neuro-Fuzzy Inference System (*ANFIS*) prediction model. The used wind turbines in the study include identical type of wind turbines of rated power, P_r of $P_r=2000$ kW, and turbine rotor diameter, D_{rotor} of $D_{rotor}=80$ m, and these wind turbines are as well named as wind turbine T1, T2, T3, T4, and T5. These wind turbines are as well located in a wind farm also located in South region of Turkey. The study reported the advantage of the utilized model to predict wind turbine aerodynamic characteristics, only having the required hub-height wind speed, U_D , atmospheric air temperature, T_{atm} , and turbine rotor rotational speed, Ω given as input parameters.

Prediction of mechanical output power of wind turbines, P was executed based on turbine rotor rotational speed, Ω values including 12.44 rpm, 13.94 rpm, and optimum rotation of 16.10 rpm. The mechanical output power values of these cited rotational speeds were drawn for the turbine hub-height wind speed, U_D . It was concluded that best fitting *ANFIS* forecasting results were obtained in the optimum turbine rotor rotational speed, Ω of $\Omega=16.10$ rpm, when compared to actual energy generation data.

5.2.8. Blade Element Momentum Theory Analysis Applied to Different Capacity Wind Turbines

This study included the influences of turbine rotor diameter, D_{rotor} , turbine rated power, P_r , turbine rotor diameter and rated power together, and finally air density, ρ on wind turbine aerodynamics covering mechanical output power of wind turbines,

P , axial flow induction factor, a , power coefficient, C_p , and thrust force, T values. On the other hand, conducted study in this part of the dissertation handled wind turbines of types named to be V80-2 MW, V90-2 MW, V100-2 MW, V110-2 MW, V90-1.8 MW, V90-3 MW, V39-0.5 MW, V52-0.85 MW, and V112-3.3 MW.

The influence of wind turbine rotor diameter, D_{rotor} was tested for the constant type of 2 MW rated power, P_r . In this context, V80-2 MW, V90-2 MW, V100-2 MW, and V110-2 MW types of wind turbines were analyzed in terms of rotor diameter, D_{rotor} ; thus rotor swept area, A_d . It is observed that wind turbine output power generation, P shown concerning the free-stream wind speed, U_∞ is weakly influenced based on the alteration of rotor diameter, D_{rotor} . In terms of axial flow induction factor, a and power coefficient, C_p analysis, especially exceeding free-stream wind speed, U_∞ of $U_\infty \geq 10$ m/s, both parameters decrease with increasing rotor swept area, A_d at a constant value of free-stream wind speed, U_∞ . On the other hand, especially for free-stream wind speed, U_∞ values below 15 m/s, it is reported that thrust force, T values of 2 MW same capacity wind turbines generally increase with increasing rotor swept area, A_d , under keeping the value of free-stream wind speed, U_∞ constant.

Wind turbine rated power, P_r effect on the above-cited turbine aerodynamics during constant rotor diameter, D_{rotor} of $D_{rotor}=90$ m was tested considering wind turbines V90-1.8 MW, V90-2 MW, and V90-3 MW. Turbine output power generation, P is significantly influenced during the alteration of rated power, P_r , under keeping free-stream wind speed, U_∞ constant. In this context, a general trend of enhancement in output power generation, P with the rated power, P_r increase. This behavior is as well valid for the parameters including axial flow induction factor, a , power coefficient, C_p , and thrust force, T . Namely, output power generation, P , axial flow induction factor, a , power coefficient, C_p , and thrust force, T values increase with increasing rated power, P_r , during constant free-stream wind speed, U_∞ value and this is the case especially for free-stream wind speed values exceeding $U_\infty \geq 10$ m/s.

Influence of two parameters on the cited wind turbine aerodynamics was also considered. These parameters include the alteration of wind turbine rotor diameter, D_{rotor} and wind turbine rated power, P_r . For this group of the study, V39-0.5 MW, V52-0.85 MW, V80-2 MW, V90-3 MW, and V112-3.3 MW types of wind turbines were chosen for the testing. It is reported that highest output power generations, P were obtained during the increase of both parameters, when a constant free-stream wind speed, U_∞ is considered. Similarly, thrust force, T values are also significantly influenced by the alteration of both parameters, i.e., highest thrust force, T values were obtained during the increase of both parameters, when a constant free-stream wind speed, U_∞ is considered. On the other hand, in terms of axial flow induction factor, a , and power coefficient, C_p ; the moderate capacity of turbine rated power, P_r and turbine rotor swept area, A_d of V90-3 MW results in the highest axial flow induction factor, a , and wind turbine efficiency, C_p

Finally, V90-3 MW named type of wind turbine was chosen in order to reveal the influence of air densities, ρ of 1, 1.06, 1.12, 1.18, and 1.225 kg/m³ on parameters of output power of wind turbines, P , axial flow induction factor, a , power coefficient, C_p , and thrust force values, T . These parameters are similarly shown with respect to free-stream wind speed, U_∞ . In this context, output power generations, P , axial flow induction factor, a , power coefficient, C_p are not much influenced by the air density, ρ alterations. However, in terms of thrust force, T , especially for the free-stream wind speed, U_∞ values of $U_\infty \leq 15$, thrust force, T generally increases with increasing air density, ρ .

Among the observed studied situations, highest thrust force, T value was obtained in the V112-3.3 MW type of wind turbine corresponding to a thrust force of $T=319$ kN, corresponding to a free-stream wind speed of $U_\infty=11$ m/s. Finally, the most crucial aerodynamic parameter of wind turbines, i.e., power coefficient, C_p is mostly influenced and improved by rotor swept area, A_d decrease.

5.2.9. Wind Turbine Shrouding System Flow and Performance Analyses through Utilizations of Numerical CFD and Experimental PIV Methods

Wind speed enhancement and power generation of horizontal axis wind turbines are significantly enhanced by the utilization of wind turbine shrouding systems. Thus, using this method provides the acceleration of wind speed toughing the wind turbine rotor blades.

This study provides numerical and *PIV* performance analysis of wind turbine shrouding systems. In literature, three types of shrouding systems are mainly available including linear, curved, and airfoil type of systems. In this context, 17 designed cases for linear shrouding systems are tested numerically in terms of wind speed enhancement and corresponding pressure drops inside these systems. On the other hand, a curved type designed shrouding system was tested by *PIV* for flow visualization at downstream of the flange region.

Among the linear shrouding systems tested by *CFD* analysis, considering the first four cases revealing flange height ratio, H/D influence, it was reported that highest maximum wind speed enhancement along the casing body, U_{max}/U_{∞} was obtained in the flange height ratio of $H/D=0.3$ corresponding to $U_{max}/U_{\infty}=1.511$. In parallel, a highest maximum pressure drop ratio, C_{prmax} reached -1.284 as well at the flange height ratio, H/D of $H/D=0.3$.

Besides, Cases 5, 6, 7, 8, 9, and 10 were structured in order to configure half-cone angle, Θ influences on wind speed ratio, u/U_{∞} and pressure drop, C_{pr} distributions in the vicinity of the casing shroud profiles. Half-cone angle, Θ of 5° was observed to generate the highest maximum wind speed enhancement along the casing body, U_{max}/U_{∞} corresponding to 1.567. Similarly, again this value of half cone angle, Θ resulted in the value of $C_{prmax}=-1.456$ which came off as the highest maximum pressure drop ratio, C_{prmax} , among the five numerically tested configurations.

On the other hand, Cases 11, 12, 13, 14, and 15 indicated dimensionless casing full body length, L/D influence obtained through *CFD* analysis. This analysis demonstrated highest maximum wind speed increase along the casing body, U_{max}/U_{∞} obtained in dimensionless casing full body length, L/D of 1.50, corresponding to 1.584 of maximum wind speed increase along the casing body, U_{max}/U_{∞} . In the same way, this dimensionless casing full body length, L/D as well produced the maximum pressure drop ratio, C_{prmax} to have the value of $C_{prmax}=1.509$.

A proper design of an inlet shrouding component attached to the linear shrouding body results in a significant enhancement both in wind speed ratio, u/U_{∞} and pressure drop, C_{pr} distributions in the vicinity of the casing shroud profiles. So, considering Cases 16 and 17, *CFD* performance testing demonstrated a 16% increase and 55% drop in maximum wind speed enhancement, U_{max}/U_{∞} and maximum pressure drop ratio, C_{prmax} along the axial axis of the casing body, respectively, when an inlet component is utilized.

5.3. Recommendations for Future Work

The present study focused on linear and curved type of wind turbine shrouding systems. In these regards, linear type of wind turbine casing systems was studied utilizing *CFD* analysis. On the other hand, the curved type of wind turbine shrouding systems was executed using *PIV* analysis. As future works, it was decided to continue the scientific studies considering the comparisons of *CFD* analysis performed in linear shrouding systems concerning the *PIV* analysis, as well, *PIV* analysis performed in curved shrouding systems concerning *CFD* analysis, in order to test further validity of the results. Additionally, airfoil types of shrouding studies mainly found in the literature will be studied by *CFD* and *PIV* analysis in order to reveal the influences of airfoil types of casings in terms of

power and wind speed enhancements compared to conventional linear and curved types of wind turbine shrouding systems.

Also, as a future study, it is recommended to work on flexible wind turbine blades. Furthermore, the novel flow control techniques for preventing the separated flow region around the wings are also worth exploring. Both experimental and numerical studies should be performed to demonstrate the rotor blade and the casing performance with all flow parameters. In addition, the performance of single and multiple wind turbines augmented with diffusers located on the ground receiving the air mass flow rate from the air delivery pipe. This pipe should be connected to the vertical wind tunnel which collect wind flow from any direction and convey this air mass flow rate towards wind turbine/turbine.

REFERENCES

- Abe, K., Kihara, H., Sakurai, A., Nishida, M., Ohya, Y., Wada, E., and Sato, K., 2006. An Experimental Study of Tip-Vortex Structures behind a Small Wind Turbine with a Flanged Diffuser. *Wind and Structures*, 9(5):413-417.
- Abe, K., Nishida, M., Sakurai, A., Ohya, Y., Kihara, H., Wada, E., and Sato, K., 2005. Experimental and Numerical Investigations of Flow Fields behind a Small Wind Turbine with a Flanged Diffuser. *Journal of Wind Engineering and Industrial Aerodynamics*, 93(12):951-970.
- Abe, K., and Ohya, Y., 2004. An Investigation of Flow Fields around Flanged Diffusers Using CFD. *Journal of Wind Engineering and Industrial Aerodynamics*, 92:315-330.
- Adeel, A., Zaidi, M., and Uddin, N., 2013. Numerical Investigations of Subsonic Flow through a Convergent-Divergent Duct with Varying Flange Heights at Exit. *Proceedings of International Conference on Energy and Sustainability*, Ned University of Engineering & Technology, Karachi, Pakistan, 15-19.
- Ageze, M.B., Hu, Y., and Wu, H., 2017. Wind Turbine Aeroelastic Modeling: Basics and Cutting Edge Trends. *International Journal of Aerospace Engineering*, ID:5263897.
- Ağçay, M., 2007. Türkiye'nin Elektrik Enerjisi Arz Talep Dengesinin Tespiti, Üretim Projeksiyonuna Yönelik Rüzgar Elektrik Santrali Tasarımı RES'in Kurulum Maliyetlerinin ve Üretim Parametrelerinin Analizinin Matlab&Simulink ile Yazılan Programda Yapılması. Graduation Thesis – EMO Project Competition, Yıldız Technical University, Electric Electronic Faculty, Electric Engineering Department, İstanbul.
- Akpınar, E.K., and Akpınar, S., 2004a. Determination of the Wind Energy Potential for Maden-Elazığ, Turkey. *Energy Conversion and Management*, 45:2901-2914.

- _____, 2004b. Statistical Analysis of Wind Energy Potential on the Basis of the Weibull and Rayleigh Distributions for Agin-Elazığ, Turkey. *Journal of Power and Energy*, 218:557-565.
- Akpınar, E.K., and Akpınar, S., 2006. An Investigation of Wind Power Potential Required in Installation of Wind Energy Conversion Systems. *Journal of Power and Energy*, 220:1-13.
- Allaei, D., and Andreopoulos, Y., 2014. INVELOX: Description of a New Concept in Wind Power and its Performance Evaluation. *Energy*, 69:336-344.
- Al-Sulaiman, F.A., and Yilbas, B.S., 2015. Thermoeconomic Analysis of Shrouded Wind Turbines. *Energy Conversion and Management*, 96:599-604.
- Altan, B.D., Atılgan, M., and Özdamar, A., 2008. An Experimental Study on Improvement of a Savonius Rotor Performance with Curtaining. *Experimental Thermal and Fluid Science*, 32:1673-1678.
- Amer, A., Ali, A.H.H., ElMahgary, Y., and Ookawara, S., 7-9 March 2013. Effect of Diffuser Configuration on the Flow Field Pattern Inside Wind Concentrator. *IEEE Renewable and Sustainable Energy Conference (IRSEC)*, International, Ouarzazate, Morocco, 212-217.
- Argin, M., and Yerci, V., 26-28 November 2015. The Assessment of Offshore Wind Power Potential of Turkey. 9th International Conference on Electrical and Electronics Engineering (*ELECO*), Bursa, Turkey, 966-970.
- Ashrafi, Z.N., Ghaderi, M., and Sedaghat, A., 2015. Parametric Study on Off-Design Aerodynamic Performance of a Horizontal Axis Wind Turbine Blade and Proposed Pitch Control. *Energy Conversion and Management*, 93:349-356.
- Atılgan, B., and Azapagic, A., 2016. Renewable Electricity in Turkey: Life Cycle Environmental Impacts. *Renewable Energy*, 89:649-657.
- Austvik, O.G., and Rzayeva, G., 2017. Turkey in the Geopolitics of Energy. *Energy Policy*, 107:539-547.

- Ay, M., and Kisi, O., 2014. Modelling of Chemical Oxygen Demand by Using ANNs, ANFIS and k-Means Clustering Techniques. *Journal of Hydrology*, 511:279-289.
- Bai, C.J., and Wang, W.C., 2016. Review of Computational and Experimental Approaches to Analysis of Aerodynamic Performance in Horizontal-Axis Wind Turbines (HAWTs). *Renewable and Sustainable Energy Reviews*, 63:506-519.
- Balaji G., and Gnanambal, I., 2014. Wind Power Generator Using Horizontal Axis Wind Turbine with Convergent Nozzle. *Journal of Scientific and Industrial Research*, 73:375-380.
- Barbounis, T.G., and Theocharis, J.B., 2006. Locally Recurrent Neural Networks for Long-Term Wind Speed and Power Prediction. *Neurocomputing*, 69:466-496.
- Baris, K., 2011. The Role of Coal in Energy Policy and Sustainable Development of Turkey: Is It Compatible to the EU Energy Policy? *Energy Policy*, 39:1754-1763.
- Baris, K., and Kucukali, S., 2012. Availability of Renewable Energy Sources in Turkey: Current Situation, Potential, Government Policies and the EU Perspective. *Energy Policy*, 42:377-391.
- Bavanish, B., and Thyagarajan, K., 2013, Optimization of Power Coefficient on a Horizontal Axis Wind Turbine Using Bem Theory. *Renewable and Sustainable Energy Reviews*, 26:169-182.
- Beskirli, M., Koc, İ., Haklı, H., and Kodaz, H., 2018. A New Optimization Algorithm for Solving Wind Turbine Placement Problem: Binary Artificial Algae Algorithm. *Renewable Energy*, 121:301-308.
- Bet, F., and Grassmann, H., 2003. Upgrading Conventional Wind Turbines. *Renewable Energy*, 28: 71-78.

- Bilgili, M., 2009. A Global Review of Wind Power Installations and Their Development in Turkey. *Clean: Soil Air Water*, 37(3):195-202.
- Bilgili, M., 2010. Prediction of Soil Temperature Using Regression and Artificial Neural Network Models. *Meteorology and Atmospheric Physics*, 110(1-2):59-70.
- Bilgili, M., and Ozgoren, M., 2011. Daily Total Global Solar Radiation Modeling from Several Meteorological Data. *Meteorology and Atmospheric Physics*, 112:125-138.
- Bilgili, M., and Sahin, B., 2009. Investigation of Wind Energy Density in the Southern and Southwestern Region of Turkey. *Journal of Energy Engineering*, 135(1):12-20.
- Bilgili M., and Sahin B., 2010a. Electric Power Plants and Electricity Generation in Turkey. *Energy Sources, Part B: Economics, Planning, and Policy*, 5:81-92.
- _____, 2010b. Statistical Analysis of Wind Energy Density in the Western Region of Turkey. *Energy Sources, Part A: Recovery, Utilization, and Environmental Effects*, 32(13):1224-1235.
- Bilgili, M., Hassanzadeh, R., Sahin, B., Ozbek, A., Yasar, A., and Simsek, E., 2016. Investigation of Wind Power Density at Different Heights in the Gelibolu Peninsula of Turkey. *Energy Sources, Part A: Recovery, Utilization, and Environmental Effects*, 38:512-518.
- Bilgili, M., Ozbek, A., Sahin, B., and Kahraman, A., 2015a. An Overview of Renewable Electric Power Capacity and Progress in New Technologies in the World. *Renewable and Sustainable Energy Reviews*, 49:323-334.
- Bilgili, M., Sahin, B., and Kahraman, A., 2004. Wind Energy Potential in Antakya and İskenderun Regions, Turkey. *Renewable Energy*, 29(10):1733-1745.
- Bilgili, M., Simsek, E., 2012. Wind Energy Potential and Turbine Installations in Turkey. *Energy Sources Part B*, 7:140-151.

- Bilgili, M., Şahin, B., and Şimşek, E., 2009. Wind Energy Density in the Southern, Southwestern and Western Region of Turkey. *Journal of Thermal Science and Technology*, 30(1):1-12.
- Bilgili, M., and Yasar, A., 2017. Performance Evaluation of a Horizontal Axis Wind Turbine in Operation. *International Journal of Green Energy*, 14(12):1048-1056.
- Bilgili, M., Yasar, A., Ilhan, A., and Sahin, B., 2015b. Aerodynamic Characteristics of a Horizontal Axis Wind Turbine in Belen-Hatay, Turkey. *International Journal of Natural and Engineering Sciences*, 9(1):54-58.
- Bilgili, M., Yasar, A., and Simsek, E., 2011. Offshore Wind Power Development in Europe and Its Comparison with Onshore Counterpart. *Renewable and Sustainable Energy Reviews*, 15:905-915.
- Bloomberg New Energy Finance (BNEF), 2014. Renewable Power of Turkey, Alternative Electric Energy Supply Scenarios for Turkey. <http://awsassets.wwft.panda.org/>
- BoroumandJazi, G., Rismanchi, B., and Saidur, R., 2013. Technical Characteristic Analysis of Wind Energy Conversion Systems for Sustainable Development. *Energy Conversion and Management*, 69:87-94.
- Breton, S.P., and Moe, G., 2009. Status, Plans and Technologies for Offshore Wind Turbines in Europe and North America. *Renewable Energy*, 34:646-654.
- British Electricity Generation (BEG), 2017. <http://www.mygridgb.co.uk/>
- Bukala, J., Damaziak, K., Karimi, H.R., Kroszczyński, K., Krzeszowiec, M., and Malachowski, J., 2015. Modern Small Wind Turbine Design Solutions Comparison in terms of Estimated Cost to Energy Output Ratio. *Renewable Energy*, 83:1166-1173.
- Burton, T., Sharpe, D., Jenkins, N., and Bossanyi, E., 2001. *Wind Energy Handbook*. 1st edition, John Wiley and Sons, LTD, England.

- Burton, T., Jenkins, N., Sharpe, D., and Bossanyi, E., 2011. Wind Energy Handbook. 2nd edition, John Wiley and Sons, Ltd., United Kingdom.
- Cajas, J.C., Houzeaux, G., Yanez, D.J., and Mier-Torrecilla, M., 2017. Shape Project Vortex Bladeless: Parallel Multi-Code Coupling for Fluid-Structure Interaction in Wind Energy Generation. Partnership for Advanced Computing in Europe, 1-6.
- Canpolat, Ç., Vortex Formation over a Nonslender Delta Wing. MSc Thesis, Cukurova University, Institute of Natural and Applied Sciences, Adana, 2008.
- Cao, S., Tamura, Y., Kikuchi, N., Saito, M., Nakayama, I., and Matsuzaki, Y., 2009. Wind Characteristics of a Strong Typhoon. Journal of Wind Engineering and Industrial Aerodynamics, 97:11-21.
- Carrillo, C., Montano, A.F.O., and Diaz-Dorado, J.C.E., 2013. Review of Power Curve Modelling for Wind Turbines. Renewable and Sustainable Energy Reviews, 21:572-581.
- Celik, A.N., 2004. On the Distributional Parameters Used in Assessment of the Suitability of Wind Speed Probability Density Functions. Energy Conversion and Management, 45, 1735-1747.
- Central Intelligence Agency (CIA), 2017. Electricity - Installed Generating Capacity. <https://www.cia.gov/library/publications/the-world-factbook/rankorder/2236rank.html>
- Cetin, N.S., Yurdusev, M.A., Ata, R., and Ozdamar, A., 2005. Assessment of Optimum Tip Speed Ratio of Wind Turbines. Mathematical and Computational Applications, 10(1):147-154.
- Chang, S.H., Lim, Q.H., and Lin, K.H., 27-29 January 2014a. Design of a Wind Energy Capturing Device for a Vehicle. 5th International Conference on Intelligent Systems, Modelling and Simulation, Langkawi, Malaysia.

- Chang, T.P., Liu, F.J., Ko, H.H., Cheng, S.P., Sun, L.C., and Kuo, S.C., 2014b. Comparative Analysis on Power Curve Models of Wind Turbine Generator in Estimating Capacity Factor. *Energy*, 73:88-95.
- Chen, F., Lu, S.M., Wang, E., and Tseng, K.T., 2010. Renewable Energy in Taiwan. *Renewable and Sustainable Energy Reviews*, 14:2029-2038.
- Chen, T.Y., Hung, C.W., and Liao, Y.T., 2013. Experimental Study on Aerodynamics of Micro-Wind Turbines with Large-Tip Non-Twisted Blades. *Journal of Mechanics*, 29(3):15-20.
- Chen, T.Y., Liao, Y.T., and Cheng, C.C., 2012. Development of Small Wind Turbines for Moving Vehicles: Effects of Flanged Diffusers on Rotor Performance. *Experimental Thermal and Fluid Science*, 42:136-142.
- Chong, W.T., Hew, W.P., Yip, S.Y., Fazlizan, A., Poh, S.C., Tan, C.J., and Ong, H.C., 2014a. The Experimental Study on the Wind Turbine's Guide-Vanes and Diffuser of an Exhaust Air Energy Recovery System Integrated with the Cooling Tower. *Energy Conversion and Management*, 87:145-155.
- Chong, W.T., Yip, S.Y., Fazlizan, A., Poh, S.C., Hew, W.P., Tan, E.P., and Lim, T.S., 2014b. Design of an Exhaust Air Energy Recovery Wind Turbine Generator for Energy Conservation in Commercial Buildings. *Renewable Energy*, 67:252-256.
- Climate News (CN), 2019. Carbon Emissions for 2019. <https://www.iklimhaber.org/>
- Cobaner, M., Citakoglu, H., Kisi, O., and Haktanir, T., 2014. Estimation of Mean Monthly Air Temperatures in Turkey. *Computers and Electronics in Agriculture*, 109:71-79.
- Coiro, D.P., De Marco, A., Scherillo, F., Maisto, U., Familio, R., and Troise, G., 09-11 June 2009. Harnessing Marine Current Energy with Tethered Submerged Systems: Experimental Tests and Numerical Model Analysis of

- an Innovative Concept. IEEE International Conference on Clean Electrical Power (*ICCEP*), Capri, Italy.
- Computer Fluid Dynamics - Wiki (*CFD-Wiki*), 2005. Accessed on June 2014.
<http://www.cfd-online.com>
- Coşoiu, C.I., Georgescu, A.M., Degeratu, M., and Hlevca, D., 2013. Numerical Predictions of the Flow around a Profiled Casing Equipped with Passive Flow Control Devices. *Journal of Wind Engineering and Industrial Aerodynamics*, 114:48-61.
- Danish Energy Association (DEA), 2017. <https://stateofgreen.com/en/profiles/>
- Dantec Dynamics v4.71 Flowmap Software Manual
- Demirbas, A., and Andejany, M.I., 2017. Optimization of Wind Power Generation Using Shaking Energy. *Energy Sources, Part B: Economics, Planning, and Policy*, 12(4):326-331.
- Disterfano, L.M.B., Jerson, R.P.V., Savio, W.O.F., Marcelo De, O.E.S., Erb, F.L., and Andre L.A.M., 2015. An Investigation of a Mathematical Model for the Internal Velocity Profile of Conical Diffusers Applied to DAWTs. *Annals of the Brazilian Academy of Sciences*, 87(2):1133-1148.
- Dresig, H., and Dien N.P., 2011. Complete Shaking Force and Shaking Moment Balancing of Mechanisms Using a Moving Rigid Body. *Technische Mechanik*, 31(2):121-131.
- Durham Energy Institute (DEI), 2017. Energy, Science, and Society.
<https://www.dur.ac.uk/dei/>
- Elsland, R., Divrak, C., Fleiter, T., and Wietschel, M., 2014. Turkey's Strategic Energy Efficiency Plan - An Ex Ante Impact Assessment of the Residential Sector. *Energy Policy*, 70:14-29.
- Emejamara, F.C., Tomlin, A.S., and Millward-Hopkins, J.T., 2015. Urban Wind: Characterisation of Useful Gust and Energy Capture. *Renewable Energy*, 81:162-172.

Energy Institute (EI), 2017. <http://enerjiensitüsü.com/>

Energy Log (EL), 2018. <https://enerjigunlugu.net/>

Energy Map (EM), 2017a. List of Installed Power of Solar Energy Plants in the World Expressed According to the Countries. <http://www.enerjiatlasi.com/>

_____, 2017b. Biogas, Biomass, Waste Heat and Pyrolytic Oil Power Plants, <http://www.enerjiatlasi.com/biyogaz/>

_____, 2017c. Electricity Distribution Companies of Turkey. <http://www.enerjiatlasi.com/>

_____, 2017d. Turkish Wind Energy Potential Map. <http://www.enerjiatlasi.com/>

_____, 2018. Turkish Wind Energy Potential Map. <http://www.enerjiatlasi.com/>

Energy Panorama (EP), 2017. Energy Foundation of Turkey, Report of December 2017. www.tenva.org/

Energy Portal (EPR), 2018. Renewable Energy Status in Turkey. <https://www.enerjiportali.com/>

Energy Portal (EPR), 2019. China in Wind Energy. <https://www.enerjiportali.com/>

Eriksson, S., Bernhoff, H., and Leijon, M., 2008. Evaluation of Different Turbine Concepts for Wind Power. Renewable and Sustainable Energy Reviews, 12:1419-1434.

Eskin, N., Artar, H., Tolun, S., 2008. Wind Energy Potential of Gokceada Island in Turkey. Renewable and Sustainable Energy Reviews, 12:839-851.

European Wind Energy Association (EWEA), 2015. Wind in Power 2014, European Statistics. <http://www.ewea.org>

European Wind Energy Association (EWEA), 2016a. Interview with Energia and Empresa, www.ewea.org/

_____, 2016b. Wind in Power: 2016, European Statistics. <http://www.ewea.org/>

- Fadare, D.A., 2010. The Application of Artificial Neural Networks to Mapping of Wind Speed Profile for Energy Application in Nigeria. *Applied Energy*, 87:934-942.
- Fletcher, J., Wang, F., Bai, L., Whiteford, J., and Cullen, D., 12-14 April 2007. Wind Tunnel Tests on a Wind Turbine with Contractor and Diffuser Arrangement. International Conference on Power Engineering, Energy and Electrical Drives, Setubal, Portugal, 1-5.
- Fluent, 2005. *Fluent 6.2, Documentation, Modeling Turbulence*.
- Foreman, K. M., Gilbert, B., and Oman, R. A., 1978. Diffuser Augmentation of Wind Turbines. *Solar Energy*, 20:305-311.
- Forster K.J., and White T.R., 2014. Numerical Investigation into Vortex Generators on Heavily Cambered Wings. *American Institute of Aeronautics and Astronautics*, 52(5):1059-1071.
- Franković, B., and Vrsalović, I., 2001. New High Profitable Wind Turbines. *Renewable Energy*, 24: 491-499.
- Gade, S.T., and Abhang, L.B., 2016. Design and Analysis of Diffuser Augmented Wind Turbine. *International Engineering Research*, 226-237.
- Genc, A., Erisoglu, M., Pekgor, A., Oturanc, G., and Hepbasli, A., 2005. Estimation of Wind Power Potential Using Weibull Distribution. *Energy Sources*, 27:809-822.
- Genc, M.S., and Gokcek, M., 2009. Evaluation of Wind Characteristics and Energy Potential in Kayseri, Turkey. *Journal of Energy Engineering-ASCE*, 135:33-43.
- General Directorate of Mineral Research and Exploration (MTA), 2017. <http://www.mta.gov.tr/v3.0/>
- General Directorate of Renewable Energy (GDRE), 2017. <http://www.eie.gov.tr/>
- German Fraunhofer Institute (GFI), 2017. Energy and Resources-Renewable Energy. <https://www.fraunhofer.de/en/>

- Ghandoor, A.Al., and Samhour, M., 2009. Electricity Consumption in the Industrial Sector of Jordan: Application of Multivariate Linear Regression and Adaptive Neuro-Fuzzy Techniques. *Jordan Journal of Mechanical and Industrial Engineering*, 3:69-76.
- Gilbert, B.L., and Foreman, K.M., 1983. Experiments with a Diffuser-Augmented Model Wind Turbine. *Trans. ASME, Journal of Energy Resources Technology*, 105(1):46-53.
- Gilbert, B.L., Oman, R.A., and Foreman, K.M., 1978. Fluid Dynamics of Diffuser-Augmented Wind Turbines. *Journal of Energy*, 2:368-374.
- Glauert, H., 1959. *The Elements of Airfoil and Airscrew Theory*. Cambridge University Press., Cambridge.
- Global Wind Energy Council (GWEC), 2013a. <http://decarboni.se/publications/global-wind-report-annual-market-update-2013/Turkey>
-
- _____, 2013b. <http://www.gwec.net> (last viewed June 25, 2013).
- Global Wind Energy Council (GWEC), 2015a. *Global Wind Report, 2015*. <http://www.gwec.net>
-
- _____, 2015b. *Global Wind Statistics, 2015*. http://www.gwec.net/wp-content/uploads/vip/GWEC-PRstats-2015_LR.pdf
- Global Wind Energy Council (GWEC), 2016. *Global Wind Report, 2016*. <http://www.gwec.net>
- Global Wind Energy Council (GWEC), 2017. *Global Wind Report, 2017*. <http://www.gwec.net>
- Gokcek, M., Bayulken, A., and Bekdemir, S., 2007. Investigation of Wind Characteristics and Wind Energy Potential in Kirklareli, Turkey. *Renewable Energy*, 32(10):1739-1752.

- Gow, S.M., Jamieson, P., and Graham, J.M.R., 2014. Ducted Turbine Theory with Right Angled Ducts. The Science of Making Torque from Wind. Journal of Physics: Conference Series, 524(012083):1-10.
- Grassmann, H., Bet, F., Ceschia, M., and Ganis, M.L., 2003. On the Physics of Partially Static Turbines. Renewable Energy, 29:491-499.
- Graupe, D., 2007. Principles of Artificial Neural Networks. 2nd Edition, World Scientific Publishing Co. Pte. Ltd., USA.
- Green Economy (GE), 2017. Climate Change, Atmospheric CO₂ Concentration. <http://yesilekonomi.com/>
- Green Economy (GE), 2018. Renewable Energy, Wind Power Status of China. <http://yesilekonomi.com/>
- Green Economy (GE), 2019a. Renewable Energy, Capacity Allocation for Sun Energy in Denmark. <http://yesilekonomi.com/>
- _____, 2019b. Renewable Energy, Wind and Solar Power Status of Germany. <http://yesilekonomi.com/>
- Hansen, M.O.L., Sørensen, J.N., Voutsinas, S., Sørensen, N., and Madsen, H.A., 2006. State of the Art in Wind Turbine Aerodynamics and Aeroelasticity. Progress in Aerospace Sciences, 42(4):285-330.
- Hansen, M.O.L., Sørensen, N.N., and Flay, R.G.J., 2000. Effect of Placing a Diffuser around a Wind Turbine. Wind Energy, 3(4):207-213.
- Hau, E., 2006. Wind Turbines: Fundamentals, Technologies, Application, Economics. Springer, Germany.
- Hayashi, T., Li, Y., and Hara, Y., 2005. Wind Tunnel Tests on a Different Phase Three-Stage Savonius Rotor. JSME International Journal, Series B, 48(1).
- He, Y., Chan, P., and Li, Q., 2013. Wind Characteristics over Different Terrains. Journal of Wind Engineering and Industrial Aerodynamics, 20:51-69.
- Hjort, S., and Larsen, H., 2014. A Multi-Element Diffuser Augmented Wind Turbine. Energies, 7:3256-3281.

- Hjort, S., and Larsen, H., 2015. Rotor Design for Diffuser Augmented Wind Turbines. *Energies*, 8: 10736-10774.
- Hossain, M.E., 17-19 September 2017. Application of Gaussian Mixture Regression Model for Short-Term Wind Speed Forecasting. Power Symposium (NAPS), 2017 North American, Morgantown, WV, USA.
- Howey, D.A., Bansal, A., and Holmes, A.S., 2011. Design and Performance of a Centimetre-Scale Shrouded Wind Turbine for Energy Harvesting. *Smart Materials and Structures*, 20:1-12.
- Hu, J.F., and Wang, W.X., 2015. Upgrading a Shrouded Wind Turbine with a Self-Adaptive Flanged Diffuser. *Energies*, 8:5319-5337.
- Igra, O., 1977. Compact Shrouds for Wind Turbines. *Energy Conversion and Management*, 16:149-157.
- Igra, O., 1981. Research and Development for Shrouded Wind Turbines. *Energy Conversion and Management*, 21:13-48.
- Ilhan, A., 2014. Efficiency Analysis of an Installed Wind Farm. MSc Thesis, Cukurova University, Institute of Natural and Applied Sciences, Adana, 2014.
- Ilhan, A., and Bilgili, M., 2016. An Overview of Turkey's Offshore Wind Energy Potential Evaluations. *Review - Turkish Journal of Scientific Reviews*, 9(2):55-58.
- Ilhan, A., Bilgili, M., and Sahin, B., 2017a. Statistical Analysis of Wind Energy Density in the Bababurnu-Çanakkale Region of Turkey. 3rd International Congress on Natural and Engineering Sciences (*ICNES*), Çukurova and Tetova University, Belgrade/Serbia.
- Ilhan, A., Bilgili, M., and Sahin, B., 2018a. Analysis of Aerodynamic Characteristics of 2 MW Horizontal Axis Large Wind Turbine. *An International Journal of Wind and Structures*, 26(3):187-197.

- Ilhan, A., Bilgili, M., and Sahin, B., 2018b. Statistical Analysis of Wind Energy Density in the Bababurnu-Çanakkale Region of Turkey. Cukurova University Journal of Engineering and Architecture, 33(1):17-26.
- Ilhan, A., Bilgili, M., Ozbek, and Yasar, A., 2016. Wind Power Curve Estimation by Adaptive Neuro Fuzzy Inference System. International Journal of Natural and Engineering Sciences, 10(2):55-62.
- Ilhan, A., Bilgili, M., Sahin, B., and Akilli, H., 2015. Estimation of Aerodynamic Characteristics for a Horizontal Axis Wind Turbine. International Journal of Natural and Engineering Sciences, 9(2):51-57.
- Ilhan, A., Bilgili, M., Sahin, B., Yasar, A., and Ozbek A., 2017b. Estimation of Wind Power Output Curve using Artificial Neural Network. International Journal of Natural and Engineering Sciences, 11(1):40-45.
- Ilkilic, C., 2012. Wind Energy and Assessment of Wind Energy Potential in Turkey. Renewable and Sustainable Energy Reviews, 16:1165-1173.
- Incecik, S., and Erdogmus, F., 1995. An Investigation of the Wind Power Potential on the Western Coast of Anatolia. Renewable Energy, 6:863-865.
- Inoue, M., Sakurai, A., and Ohya, Y., 2002. A Simple Theory of Wind Turbine with a Brimmed Diffuser. Turbomachinery, 30:497-502 (In Japanese).
- International Energy Agency (IEA), 2013a. Energy Statistics Manual, 2013. <https://www.iea.org>
- _____, 2013b. <https://www.iea.org/newsroomandevents/news/2013/october/wind-power-seen-generating-up-to-18-of-global-power-by-2050.html>
- International Energy Agency (IEA), 2015. Carbon Capture and Storage: The Solution for Deep Emissions Reductions. <https://www.iea.org>
- International Energy Agency (IEA), 2017a. Deploying Renewables. <https://www.iea.org/>
- _____, 2017b. World Energy Statistics.

- https://www.iea.org/bookshop/752-World_Energy_Statistics_2017
_____, 2017c. World's Monthly Electricity Statistics. <https://www.iea.org/>
- International Hydropower Association (IHA), 2017. Hydropower Status Report, 2017. <https://www.hydropower.org/sites/default/files/publications-docs/2017%20Hydropower%20Status%20Report.pdf>
- International Renewable Energy Agency (IRENA), 2016. Wind Power Technology Brief, 2016. <http://www.irena.org>
- International Solar Energy Association (Solarist, 2018). Solar Power of USA, 2018. <https://www.solar.ist/>
- Jafari, S.A.H., and Kosasih, B., 2014. Flow Analysis of Shrouded Small Wind Turbine with a Simple Frustum Diffuser with Computational Fluid Dynamics Simulations. *Journal of Wind Engineering and Industrial Aerodynamics*, 125:102-110.
- Jamieson, P.M., 2009. Beating Betz: Energy Extraction Limits in a Constrained Flow Field. *Journal of Solar Energy Engineering*, 131(031008):1-6.
- Jang, J.S.R., 1993. ANFIS: Adaptive-Network-Based Fuzzy Inference System. *IEEE Transactions on Systems, Man, and Cybernetics*, 23(3):665-685.
- Jeon, S., Kim, B., and Huh, J., 2015. Comparison and Verification of Wake Models in an Onshore Wind Farm Considering Single Wake Condition of the 2 MW Wind Turbine. *Energy*, 93:1769-1777.
- Kale, S.A., Gunjal, Y.R., Jadhav, S.P., and Tanksale, A.N., 10-12 April 2013. CFD Analysis for Optimization of Diffuser for a Micro Wind Turbine. *International Conference on Energy Efficient Technologies for Sustainability (ICEETS)*, Nagercoil, India, 257-260.

- Kannan, T.S., Mutasher, S.A., and Lau, Y.H.K., 2013. Design and Flow Velocity Simulation of Diffuser Augmented Wind Turbine Using CFD. *Journal of Engineering Science and Technology*, 8(4):372-384.
- Karaca, V., Çoban, H., Onal, S., and Altunok, M.T., 2017. Supplying the Energy Demand for a Home with a Wind Turbine in the City Center of Tokat. *International Journal of Engineering Innovation and Research* Volume, 6(6):2277-5668.
- Karagöl, E.T., and Kavaz, İ., 2017. Renewable Energy in the World and Turkey. <https://setav.org/assets/uploads/2017/04/YenilenebilirEnerji.pdf>
- Karasu, İ., 2015. Effect of Yaw Angle on Vortex Formation over a Slender Delta Wing. PhD Thesis, Cukurova University, Institute of Natural and Applied Sciences, Adana, 2015.
- Karray, F.O., and De Silva, C., 2004. *Soft Computing and Tools of Intelligent Systems Design: Theory, Tools and Applications*. 1st Edition, Pearson, United Kingdom.
- Karthikeyan, N., Murugavel, K.K., Kumar, S.A., and Rajakumar, S., 2015. Review of Aerodynamic Developments on Small Horizontal Axis Wind Turbine Blade. *Renewable and Sustainable Energy Reviews*, 42:801-822.
- Kesby, J.E., Bradney, D.R., and Clausen, P.D., 2016. Determining Diffuser Augmented Wind Turbine Performance Using a Combined CFD/BEM Method, *The Science of Making Torque from Wind (Torque 2016)*. *Journal of Physics: Conference Series* 2016, 753(082033):1-10.
- Khanjari, A., Sarreshtehdari, A., and Mahmoodi, E., 2017. Modeling of Energy and Exergy Efficiencies of a Wind Turbine Based on the Blade Element Momentum Theory under Different Roughness Intensities. *Journal of Energy Resources Technology*, 139(022005).
- Khosravi, A., Koury, R.N.N., Machado, L., and Pabon, J.J.G., 2018. Prediction of Wind Speed and Wind Direction Using Artificial Neural Network, Support

- Vector Regression and Adaptive Neuro-Fuzzy Inference System. *Sustainable Energy Technologies and Assessments*, 25:146-160.
- Kishinami, K., Taniguchi, H., Suzuki, J., Ibano, H., Kazunou, T., and Turuhami, M., 2005. Theoretical and Experimental Study on the Aerodynamic Characteristics of a Horizontal Axis Wind Turbine. *Energy*, 30:2089-2100.
- Kishore, R.A., Coudron, T., and Priya, S., 2013. Small-Scale Wind Energy Portable Turbine (*SWEPT*). *Journal of Wind Engineering and Industrial Aerodynamics*, 116:21-31.
- Kokturk, G., and Tokuc, A., 2017. Vision for Wind Energy with a Smart Grid in Izmir. *Renewable and Sustainable Energy Reviews*, 73:332-345.
- Kosasih B., and Tondelli A., 2012. Experimental Study of Shrouded Micro-Wind Turbine. *Procedia Engineering*, 49:92-98.
- Kosasih, P.B., Bryce, N., Tondelli, A., and Beazley, A., 3-7 December 2012. Experimental Study of the Performance of Bare and Nozzle-Diffuser Shrouded Micro Wind Turbine Under Axial and Non-Axial Inflow Condition. 18th Australasian Fluid Mechanics Conference, Launceston, Australia.
- Kose, F., Aksoy, M.H., Ozgoren, M., 2014. An Assessment of Wind Energy Potential to Meet Electricity Demand and Economic Feasibility in Konya, Turkey. *International Journal of Green Energy*, 11:559-576.
- Kramer, O., Gieseke, F., and Satzger, B., 2013. Wind Energy Prediction and Monitoring with Neural Computation. *Neurocomputing*, 109:84-93.
- Krishnan, A., and Paraschivoiu, M., 2015. 3D Analysis of Building Mounted VAWT with Diffuser Shaped Shroud. *Sustainable Cities and Society*, 29:1-7.
- Lanzafame, R., and Messina, M., 2010. Horizontal Axis wind Turbine Working at Maximum Power Coefficient Continuously. *Renewable Energy*, 35:301-306.
- Larin, P., Aygun, C., and Paraschivoiu, M., 2015. CFD Based Analysis of High Efficiency Savonius Turbine in Synergy with Flow on Top of a Building,

- Montreal: EIC Climate Change Technology Conference 2015.
www.cctc2015.ca
- Launder, B.E., and Spalding, D.B., 1972. Lectures in Mathematical Models of Turbulence. Academic Press, London, England.
- Lawn, C.J., 2003. Optimization of the Power Output from Ducted Turbines. Proceedings of the Institution of Mechanical Engineers, Part A: Journal of Power and Energy, 217:107-117.
- Lee, S, Kim, H, and Lee, S., 2010. Analysis of Aerodynamic Characteristics on a Counter-Rotating Wind Turbine. Current Applied Physics. 10:339-342.
- Li, G., and Shi, J., 2010. On Comparing Three Artificial Neural Networks for Wind Speed Forecasting. Applied Energy, 87:2313-2320.
- Lilley, G.M., and Rainbird, W.J., 1956. A Preliminary Report on the Design and Performance of Ducted Windmills. Report 102; The College of Aeronautics Cranfield: Cranfield, UK.
- Lydia, M., Kumar, S.S., Selvakumar, A.I., and Kumar, G.E.P., 2014. A Comprehensive Review on Wind Turbine Power Curve Modeling Techniques. Renewable and Sustainable Energy Reviews, 30:452-460.
- Mahalakshmi, N.V., Krithiga, G., Sandhya, S., Vikraman, J., and Ganesan V., 2007. Experimental Investigations of Flow through Conical Diffusers with and without Wake Type Velocity Distortions at Inlet. Experimental Thermal and Fluid Science, 32:133-157.
- Maia, L.A.B., 2014. Experimental and Numerical Study of a Diffuser Augmented Wind Turbine - DAWT. The Master's Degree of Renewable Energies and Energy Efficiency, Escola Superior de Tecnologia e de Gestao, Instituto Politecnico de Bragança, Portugal.
- Maleki, M., and Sarhangzadeh, M., 2017. Wind Resource Assessment and Wind Power Potential of Tabriz Region in East Azerbaijan Province, Iran. Electronics Engineering Letters, 1:1-23.

- Mane, A., Kharade, M., Sonkambale, P., Tapase, S., and Kudte, S.S., 1-2 April 2017. Design and Analysis of Vortex Bladeless Turbine with Gyro E-Generator. 7th International Conference on Recent Trends in Engineering, Science and Management, Balewadi-Baner, Pune, 590-597.
- Mansour, K., and Meskinkhoda, P., 2014. Computational Analysis of Flow Fields around Flanged Diffusers. *Journal of Wind Engineering and Industrial Aerodynamics*, 124:109-120.
- Manwell, J.F., McGowan, J.G., and Rogers, A.L., 2009. *Wind Energy Explained: Theory, Design and Application*. 2nd edition, John Wiley and Sons, Ltd., United Kingdom.
- Mathew, S., 2006. *Wind Energy: Fundamentals, Resource Analysis and Economics*. Springer-Verlag Berlin Heidelberg, Netherlands.
- Matsushima, T., Takagi, S., and Muroyama, S., 2006. Characteristics of a Highly Efficient Propeller Type Small Wind Turbine with a Diffuser. *Renewable Energy*, 31(9):1343-1354.
- Mauna Loa, 2016. Report of Hawaii Observatory Station. <https://www.esrl.noaa.gov/gmd/obop/mlo/>
- Melikoglu, M., 2016. The Role of Renewables and Nuclear Energy in Turkey's Vision 2023 Energy Targets: Economic and Technical Scrutiny. *Renewable and Sustainable Energy Reviews*, 62:1-12.
- Milli Eğitim Bakanlığı, 2012. Yenilenebilir Enerji Teknolojileri, Rüzgâr Türbinlerinde Üretilen Alternatif Akımın Temelleri. [http://www.megep.meb.gov.tr/mte_program_modul/moduller_pdf/Rüzgar Türbinlerinde Üretilen Alternatif Akımın Temelleri.pdf](http://www.megep.meb.gov.tr/mte_program_modul/moduller_pdf/Rüzgar_Türbinlerinde_Üretilen_Alternatif_Akımın_Temelleri.pdf)
- Ministry of Energy and Natural Resources of Turkey Republic (MENR), 2015a. Turkey's Renewable Energy Strategy and Policies. General Directorate of Renewable Energy, <http://www.tepav.org.tr/>

- _____, 2015b.
Legal Regulations on Unlicensed Production of Electricity and Renewable Energy in Turkey, 6. Energy Efficiency, Quality, Symposium and Exhibition, <http://www.emo.org.tr/>
- Ministry of Energy and Natural Resources of Turkey Republic (MENR), 2017a.
Geothermal Energy. <http://www.enerji.gov.tr/>
- _____, 2017b.
Natural Gas. <http://www.enerji.gov.tr/>
- _____, 2017c.
General Directorate of Renewable Energy, Carbon Capture and Storage. <http://www.eie.gov.tr/>
- _____, 2017d.
General Directorate of Renewable Energy. <http://www.eie.gov.tr/>
- _____, 2017e.
Strategic Plan for 2020. <https://sp.enerji.gov.tr/>
- Morales, J.M., Mínguez, R., and Conejo, A.J., 2010. A Methodology to Generate Statistically Dependent Wind Speed Scenarios. *Applied Energy*, 87:843-855.
- Nagai, M., and Irabu, K., 1987. Momentum Theory for Diffuser Augmented Wind Turbine. *Transactions of the Japan Society of Mechanical Engineers Series B*, 53(489):1543-1547 (In Japanese).
- Nasution, A., and Purwanto, D.W., 27-29 June 2011. Optimized Curvature Interior Profile for Diffuser Augmented Wind Turbine (*DAWT*) to Increase Its Energy-Conversion Performance. *IEEE First Conference on Clean Energy and Technology CET*, Kuala Lumpur, Malaysia, 315-320.
- Nikolic, V., Petkovic, D., Shamshirband, S., and Cojbasic, Z., 2015. Adaptive Neuro-Fuzzy Estimation of Diffuser Effects on Wind Turbine Performance. *Energy*, 89:324-333.

- Offshore Wind Energy (OWE), 2009. Technology of OWE.
<http://www.offshorewindenergy.org/>
- Ohunakin, O.S., and Akinnawonu, O.O., 2012. Assessment of Wind Energy Potential and the Economics of Wind Power Generation in Jos, Plateau State, Nigeria. *Energy for Sustainable Development*, 16:78-83.
- Ohya, Y., and Karasudani, T., 2010. A Shrouded Wind Turbine Generating High Output Power with Wind-Lens Technology, *Energies*, 3:634-649.
- Ohya, Y., Karasudani, T., and Sakurai, A. 2002. Development of High-Performance Wind Turbine with Brimmed Diffuser. *Journal of the Japan Society for Aeronautical and Space Sciences*, 50:477-482 (In Japanese).
- Ohya, Y., Karasudani, T., Sakurai, A., Abe, K., and Inoue, M., 2008. Development of a Shrouded Wind Turbine with a Flanged Diffuser. *Journal of Wind Engineering and Industrial Aerodynamics*, 96:524-539.
- Ohya, Y., Karasudani, T., Sakurai, A., and Inoue, M., 2006. Development of a High-Performance Wind Turbine Equipped with a Brimmed Diffuser Shroud. *Transactions of the Japan Society for Aeronautical and Space Sciences*, 49(163):18-24.
- Ohya, Y., Karasudani, T., Sakurai, A., and Inoue, M., 2004. Development of High-Performance Wind Turbine with a Brimmed-Diffuser: Part 2. *Journal of the Japan Society for Aeronautical and Space Sciences*, 52(604):210-213 (In Japanese).
- Oman, R.A., and Foreman, K.M., 9-11 June 1975. Cost Effective Diffuser Augmentation of Wind Turbine Power Generators. Grumman Aerospace Corporation, Bethpage, New York 11714 Second Workshop on Wind Energy Conversion Systems, Washington, D.C.
- Oman, R.A., Foreman, K.M., and Gilbert, B.L., 1975. A Progress Report on the Diffuser Augmented Wind Turbine. In *Proceedings of the 3rd Biennial*

- Conference and Workshop on Wind Energy Conversion Systems, Washington, DC, USA, 8(12):829-826.
- Overview of Worldwide Installed Geothermal Energy Generation Capacity, 2017.
<http://www.jeotermalhaberler.com/dunya-capinda-kurulu-jeotermal-enerji-uretim-kapasitesine-genel-bakis/>
- Owis, F., Badawy, M.T.S., Abed, K.A., Fawaz, H.E., and Elfeky, A., 2015. Numerical Investigation of Loaded and Unloaded Diffuser Equipped with a Flange. *International Journal of Scientific and Engineering Research*, 6(11):312-341.
- Ozcan, M., 2018. The Role of Renewables in Increasing Turkey's Self-Sufficiency in Electrical Energy. *Renewable and Sustainable Energy Reviews*, 82:2629-2639.
- Ozgoren, M., Bilgili, M., and Sahin, B., 2012. Estimation of Global Solar Radiation Using ANN over Turkey. *Expert Systems with Applications*, 39:5043-5051.
- Palensky, P., 2011. Demand Side Management: Demand Response, Intelligent Energy Systems, and Smart Loads. *IEEE Transactions on Industrial Informatics*, 7(3):381-388.
- Petković, D., Čojbašić, Ž., and Nikolić, V., 2013. Adaptive Neuro-Fuzzy Approach for Wind Turbine Power Coefficient Estimation. *Renewable and Sustainable Energy Reviews*, 28:191-195.
- Phillips, D.G., Flay, R.G.J., and Nash, T.A., 1999. Aerodynamic Analysis and Monitoring of the Vortec 7 Diffuser-Augmented Wind Turbine. *IPENZ Transactions*, 26:13-19.
- Phillips, D.G., Richards, P.J., and Flay, R.G.J., 2000. CFD modelling and the Development of the Diffuser Augmented Wind Turbine. *Proceedings of the Computational Wind Engineering, Birmingham*, 189-192.

- Phillips, D.G., Richards, P.J., and Flay, R.G.J., 2002. CFD Modelling and the Development of the Diffuser Augmented Wind Turbine. *Wind and Structures*, 5:267-276.
- Pinheiro Vaz, J.R., Lins, E.F., and Rio Vaz, D.A.T.D.D., 24-28 October 2011. An Extended Glauert's Model Applied to Design of Wind Turbines with Diffusers. 21st International Congress of Mechanical Engineering, Natal, RN, Brazil.
- Pinto, R.L.U.F., and Gonçalves, B.P.F., 2017. A Revised Theoretical Analysis of Aerodynamic Optimization of Horizontal-Axis Wind Turbines Based on BEM Theory. *Renewable Energy*, 105:625-636.
- Poh, S.C., Sim, S.Y., Chong, W.T., Fazlizan, A., Yip, S.Y., Hew, W.P., Omar, W.Z.W., and Zain, Z.M., 2014. Computational Fluid Dynamics Simulation of the Effect of Guide-Vane Angles on the Performance of the Exhaust Air Energy Recovery Turbine Generator. The 6th International Conference on Applied Energy – ICAE2014, *Energy Procedia*, 61:1286-1289.
- Rauh, A., and Seelert, W., 1984. The Betz Optimum Efficiency for Windmills. *Applied Energy*, 17:15-23.
- Renewable Energy General Directorate (REGD), 2017. Wind Energy Technical Potential for the Provinces of Turkey. <http://www.eie.gov.tr/>.
- Renewable Energy Policy Network for the 21st Century (REN21), 2016. Renewables, Global Status Report, 2016. <http://www.ren21.net/status-of-renewables/global-status-report/>
- Renewable Energy Policy Network for the 21st Century (REN21), 2017. Renewables, Global Status Report, 2017. http://www.ren21.net/wp-content/uploads/2017/06/17-8399_GSR_2017_Full_Report_0621_Opt.pdf.
- Renewable Energy Policy Network for the 21st Century (REN21), 2018. Renewables, Global Status Report, 2018. <http://www.ren21.net/>

- Republic of Turkey Energy Market Regulatory (TEMR), 2017.
<http://www.emra.org.tr/en/home>
- Rio Vaz, D.A.T.D., Mesquita, A.L.A., Vaz, J.R.P., Blanco, C.J.C., and Pinho, J.T., 2014. An Extension of the Blade Element Momentum Method Applied to Diffuser Augmented Wind Turbines. *Energy Conversion and Management*, 87:1116-1123.
- Rodriguez-Hernandez, O., del Río, J.A., and Jaramillo, O.A., 2016. The Importance of Mean Time in Power Resource Assessment for Small Wind Turbine Applications. *Energy for Sustainable Development*, 30:32-38.
- Sahin, A.D., 2004. Progress and Recent Trends in Wind Energy. *Progress in Energy and Combustion Science*, 30(5):501-543.
- Sahin, A.D., 2008. A Review of Research and Development of Wind Energy in Turkey. *Clean: Soil Air Water*, 36(9):734-742.
- Sahin, B., and Bilgili, M., 2009. Wind Characteristics and Energy Potential in Belen-Hatay, Turkey, *International Journal of Green Energy*, 6(2):157-172.
- Sahin, B., Bilgili, M., and Akilli, H., 2005. The Wind Power Potential of the Eastern Mediterranean Region of Turkey. *Journal of Wind Engineering and Industrial Aerodynamics*, 93(2):171-183.
- Sahin, B., Ilhan, A., and Bilgili, M., 2017. Investigation of Diffuser Augmented Wind Turbine Technologies. *Cukurova University Journal of Engineering and Architecture*, 32(1):147-154.
- Saidur, R., Islam, M.R., Rahim, N.A., and Solangi, K.H., 2012. A Review on Global Wind Energy Policy. *Renewable and Sustainable Energy Reviews*, 14:1744-1762.
- Scherillo, F., Maisto, U., Troise, G., Coiro, D.P., and Miranda, S., 14-16 June 2011. Numerical and Experimental Analysis of a Shrouded Hydroturbine. *IEEE International Conference on Clean Electrical Power (ICCEP)*, Ischia, Italy, 216-222.

- Sedaghat, A., Assad, M.E.H., and Gaith, M., 2014. Aerodynamics Performance of Continuously Variable Speed Horizontal Axis Wind Turbine with Optimal Blades. *Energy*, 77:752-759.
- Seguro, J.V., and Lambert, T.W., 2000. Modern Estimation of the Parameters of the Weibull Wind Speed Distribution for Wind Energy Analysis. *Journal of Wind Engineering and Industrial Aerodynamics*, 85:75-84.
- Setoguchi, T., Shiomi, N., and Kaneko, K., 2004. Development of Two-Way Diffuser for Fluid Energy Conversion System. *Renewable Energy*, 29:1757-1771.
- Shahsavari, M., 2015. Effect of Shroud on the Performance of Horizontal Axis Hydrokinetic Turbines, PhD Thesis.
- Shives, M., and Crawford, C., 2011. Developing an Empirical Model for Ducted Tidal Turbine Performance Using Numerical Simulation Results. *Proceedings of the Institution of Mechanical Engineers, Part A: Journal of Power and Energy*, 226(1):112-125.
- Shokrzadeh, S., Jozani, M.J., and Bibeau, E., 2014. Wind Turbine Power Curve Modeling Using Advanced Parametric and Nonparametric Methods. *IEEE Transactions on Sustainable Energy*, 5(4):1262-1269.
- Shonhiwa, C., and Makaka, G., 2016. Concentrator Augmented Wind Turbines: A Review. *Renewable and Sustainable Energy Reviews*, 59:1415-1418.
- Simsek, H.A., and Simsek, N., 2013. Recent Incentives for Renewable Energy in Turkey. *Energy Policy*, 63:521-530.
- Sørensen, J.N., 2011. Aerodynamic Aspects of Wind Energy Conversion. *Annual Review of Fluid Mechanics*, 43:427-448.
- Sun, H., and Kyojuka, Y., 27-29 June 2011. Analysis of Performances of a Shrouded Horizontal Axis Tidal Turbine. *IEEE First Conference on Clean Energy and Technology CET*, Kuala Lumpur, Malaysia.

- Sun, Z., Chen, J., Shen, W.Z., and Zhu, W.J., 2016. Improved Blade Element Momentum Theory for Wind Turbine Aerodynamic Computations. *Renewable Energy*, 96:824-831.
- Takahashi, S., Hata, Y., Ohya, Y., Karasudani T., and Uchida, T., 2012. Behavior of the Blade Tip Vortices of a Wind Turbine Equipped with a Brimmed-Diffuser Shroud. *Energies*, 5:5229-5242.
- Tan, E., 02 March 2015. Offshore Wind Energy Potential of Turkey. 5th International Conference on Meteorology and Climatology of the Mediterranean, Istanbul, Turkey.
- Tanrioven, K., Yasarbas, S., and Cengiz, H., 5-7 October 2011. Future's Electricity Distribution Network Smart Grid. In: Symposium of Electric-Electronic and Computer, Elazığ, Turkey, 52-55.
- Tanrioven, M., 2011. Rüzgâr ve Güneş Enerjili Güç Sistemleri.
<http://www.yildiz.edu.tr/~tanriov/RG1.pdf>
- Tao, T., Wang, H., and Wu, T., 2017. Comparative Study of the Wind Characteristics of a Strong Wind Event Based on Stationary and Nonstationary Models. *ASCE Journal of Structural Engineering*, 143(5), 04016230.
- Technology Roadmap Wind Energy, 2013.
<https://www.iea.org/publications/freepublications/publication/Wind>
- Tenguria, N., Mittal, N.D., and Ahmed, S., 2010. Investigation of Blade Performance of Horizontal Axis Wind Turbine Based on Blade Element Momentum Theory (BEMT) Using NACA Airfoils. *International Journal of Engineering, Science and Technology*, 2(12):25-35.
- The European Bank for Reconstruction and Development (EBRD), 2017.
<http://www.ebrd.com/turkey.html>
- The Windpower, Wind Energy Market Intelligence.
https://www.thewindpower.net/manufacturer_en_14_vestas.php

- The World Bank in Turkey (WB), 2017. Report of Financing Products and Advisory Services. <http://www.worldbank.org/>
- Toshimitsu, K., Nishikawa, K., Haruki, W., Oono, S., Takao, M., and Ohya, Y., 2008. PIV Measurements of Flows around the Wind Turbines with a Flanged-Diffuser Shroud. *Journal of Thermal Science*, 17(4):375-380.
- Trivellato, F., Battisti, L., and Miori, G., 2012. The Ideal Power Curve of Small Wind Turbines from Field Data. *Journal of Wind Engineering and Industrial Aerodynamics*, 107-108:263-273.
- Tummala, A., Velamati, R.K., Sinha, D.K., Indraja, V., and Krishna, V.H., 2016. Review on Small Scale Wind Turbines. *Renewable and Sustainable Energy Reviews*, 56:1351-1371.
- Turkey's Electricity Transmission Corporation (TEIAS), 2017. <https://www.teias.gov.tr/>
- Turkey's Electricity Transmission Corporation (TEIAS), 2018. <https://www.teias.gov.tr/>
- Turkish Statistical Institute (TUIK), 2017. <http://www.tuik.gov.tr/>
- Turkish Statistical Institute (TUIK), 2018. <http://www.tuik.gov.tr/>
- Turkish Wind Energy Association (TWEA), 2016. <http://www.tureb.com.tr/bilgi-bankasi/turkiye-res-durumu>
- Turkish Wind Energy Association (TWEA), 2017a. <http://www.tureb.com.tr/files/>, 2017b. http://www.tureb.com.tr/files/tureb_sayfa/duyurular/2017_duyurular/subat/turkiye_ruzgar_enerjisi_istatistik_raporu_ocak_2017.pdf
- Turkish Wind Energy Association (TWEA), 2018. <https://www.tureb.com.tr/>
- Turkish Wind Energy Association (TWEA), 2019. <https://www.tureb.com.tr/>
- Union of Turkish Engineers and Architects (EMO), 2017. Chamber of Electrical Engineers, Turkish Electrical Energy Statistics. <http://www.emo.org.tr/>

- Unlu, M.A., 2012. Offshore Wind Power Economics, Analysis on the Economic Utilization of Turkey's Offshore Wind Power Potential under the Current Support Mechanisms. Master's Thesis in Energy, Natural Resources and the Environment.
- Ushiyama, I., 1997. Introduction of Wind Turbine. Sanseido Press, Tokyo, 77-84 (In Japanese).
- Van Bussel, G.J.W., 2007. The Science of Making More Torque from Wind: Diffuser Experiments and Theory Revisited. Journal of Physics: Conference Series, 75(012010):1-12.
- Van Dorst, F.A., 2011. An Improved Rotor Design for a Diffuser Augmented Wind Turbine. Master's Thesis, Delft University, Netherlands.
- VESTAS Global Energy Company, 2017. V80-2.0 MW Brochure. <https://www.vestas.com/>
- Wahyudi, B., Soeparman, S., and Hoeijmakers, H.W.M., 2015. Optimization Design of Savonius Diffuser Blade with Moving Deflector for Hydrokinetic Cross Flow Turbine Rotor. Energy Procedia, 68:244-253.
- Wan, Y.H., Ela, E., and Orwig, K., 23-26 May 2010. Development of an Equivalent Wind Plant Power-Curve. National Renewable Energy Laboratory, Dallas, Texas.
- Wang, F., Bai, L., Fletcher, J., Whiteford, J., and Cullen, D., 2008. The Methodology for Aerodynamic Study on a Small Domestic Wind Turbine with Scoop. Journal of Wind Engineering and Industrial Aerodynamics, 96:1-24.
- Wang, H., Wu, T., Tao, T., Li, A., and Kareem, A., 2016. Measurements and Analysis of Non-Stationary Wind Characteristics at Sutong Bridge in Typhoon Damrey. Journal of Wind Engineering and Industrial Aerodynamics, 151:100-106.

- Wang, W.X., Matsubara, T., Hu, J., Odahara, S., Nagai, T., Karasutani, T., and Ohya, Y., 2015. Experimental Investigation into the Influence of the Flanged Diffuser on the Dynamic Behavior of CFRP Blade of a Shrouded Wind Turbine. *Renewable Energy*, 78:386-397.
- Watson, S.J., Infield, D.G., Barton J.P., and Wylie, S.J., 2007. Modelling of the Performance of a Building-Mounted Ducted Wind Turbine. *The Science of Making Torque from Wind, Journal of Physics: Conference Series* 2007, 75(012001):1-10.
- Wekesa, D.W., Wang, C., and Wei, Y., 2016. Empirical and Numerical Analysis of Small Wind Turbine Aerodynamic Performance at a Plateau Terrain in Kenya. *Renewable Energy*, 90:377-385.
- Werle, M.J., and Presz, W.M., 2008. Ducted Wind/Water Turbines and Propellers Revisited. *Journal of Propulsion and Power*, 24(5):1146-1150.
- White, S.W., 2006. Net Energy Payback and CO₂ Emissions from Three Midwestern Wind Farms: An Update. *Natural Resources Research*, 15:271-281.
- Wilcox, D.C., 1994. *Turbulence Modeling for CFD*. Second edition, DCW Industries, La Canada, California.
- Wilson, R.E., Lissaman, P.B.S., and Walker, S.N., 1976. *Aerodynamic Performance of Wind Turbines*. Rep. ERDA/NSF/04014-76/1, Washington, DC: Dep. Energy.
- Wind in Power, 2014. *European Statistics*, 2014.
<http://www.ewea.org/fileadmin/files/library/publications/statistics/EWEA-Annual-Statistics-2014.pdf>
- Windpower Intelligence (WI), 2017. <http://www.windpowerintelligence.com/>
- Wood, D., 2011. *Small Wind Turbines Analysis, Design, and Application*. Springer, New York.

- World Energy (WE), 2018. Renewable Energies 2018 Global Status Report.
<https://www.dunyaenerji.org.tr/>
- World Energy Council (WEC), 2016a. World Energy Resources.
<https://www.worldenergy.org/>
- _____, 2016b. World Energy Resources, 2016.
<https://www.worldenergy.org/wp-content/uploads/2016/10/World-Energy-Resources-Full-report-2016.10.03.pdf>
- Yan, J., Li, K., Bai, E., Yang, Z., and Foley, A., 2016. Time Series Wind Power Forecasting Based on Variant Gaussian Process and TLBO. *Neurocomputing*, 189:135-144.
- Yaniktepe, B., Koroglu, T., and Savrun, M.M., 2013. Investigation of Wind Characteristics and Wind Energy Potential in Osmaniye, Turkey. *Renewable and Sustainable Energy Reviews*, 21:703-711.
- Yumak, H., Uçar, T., and Yayla, S., 2012. Wind Energy Potential on the Coast of Lake Van. *International Journal of Green Energy*, 9(1):1-12.
- Zheng, C.W., Li, C.Y., Pan, J., Liu, M.Y., and Xia, L.L., 2016. An Overview of Global Ocean Wind Energy Resource Evaluations. *Renewable and Sustainable Energy Reviews*, 53:1240-1251.
- Zidong, X., Hao, W., Teng, W., Tianyou, T., and Jianxiao, M., 2017. Wind Characteristics at Sutong Bridge Site using 8-Year Field Measurement Data. *Wind and Structures*, 25(2):195-214.

CURRICULUM VITAE

Akın İLHAN was born in Şanlıurfa by the year of 1983. His mother is teacher, father is civil engineer. He completed his elementary and secondary education in Tarsus/Mersin. He graduated from Tarsus American College (Tarsus/Mersin) in 2001. Akın İLHAN fulfilled higher education in Çukurova University Mechanical Engineering Department by the year of January 2008. He served for his military service in Konya - Karapınar Atış Poligon Grup Komutanlığı until January 2009.

After January 2009, Akın İLHAN took charge in various private sector companies. He started his career in Doğu İnşaat ve Ticaret A.Ş., as mechanical engineer in the project of Boyabat Dam and Hydro Electrical Plant Construction in Sinop/Turkey. He continued with this job through the ends of 2010 year. By the year of 2011, he worked as Machine Supply and Maintenance Chief (Azerbaijan - Xaçmaz and Azerbaijan - Baku Cities, respectively) in the company of Azer İnşaat Servis LLC in road construction projects. At the start of 2012 year, for a short time he worked in Volvo Group Automotive Ltd. Şti. (İstanbul) as Service Area Manager of Volvo Trucks for southern cities of Turkey. By the ends of 2012 year, Akın İLHAN took charge in Lilpar İnşaat Tur. Loj. Gıda San. ve Tic. Ltd. Şti. as corporate executive and shareholder of the same company. He quitted from this job through the ends of 2013. Later, he continued with his career as academic personnel in Amasya University Technology Faculty Mechanical Engineering Department in Amasya/Turkey (as Research Assistant - from September 2013 to June 2015).

Akın İLHAN started his M.Sc. Education in September 2012, at the department of Mechanical Engineering of Çukurova University Natural and Applied Sciences Institute in Adana/Turkey. He completed the MSc studies by

September 2014 and started the Ph.D. education same year. And, his Ph.D. education is completed by February of 2019.





APPENDICES



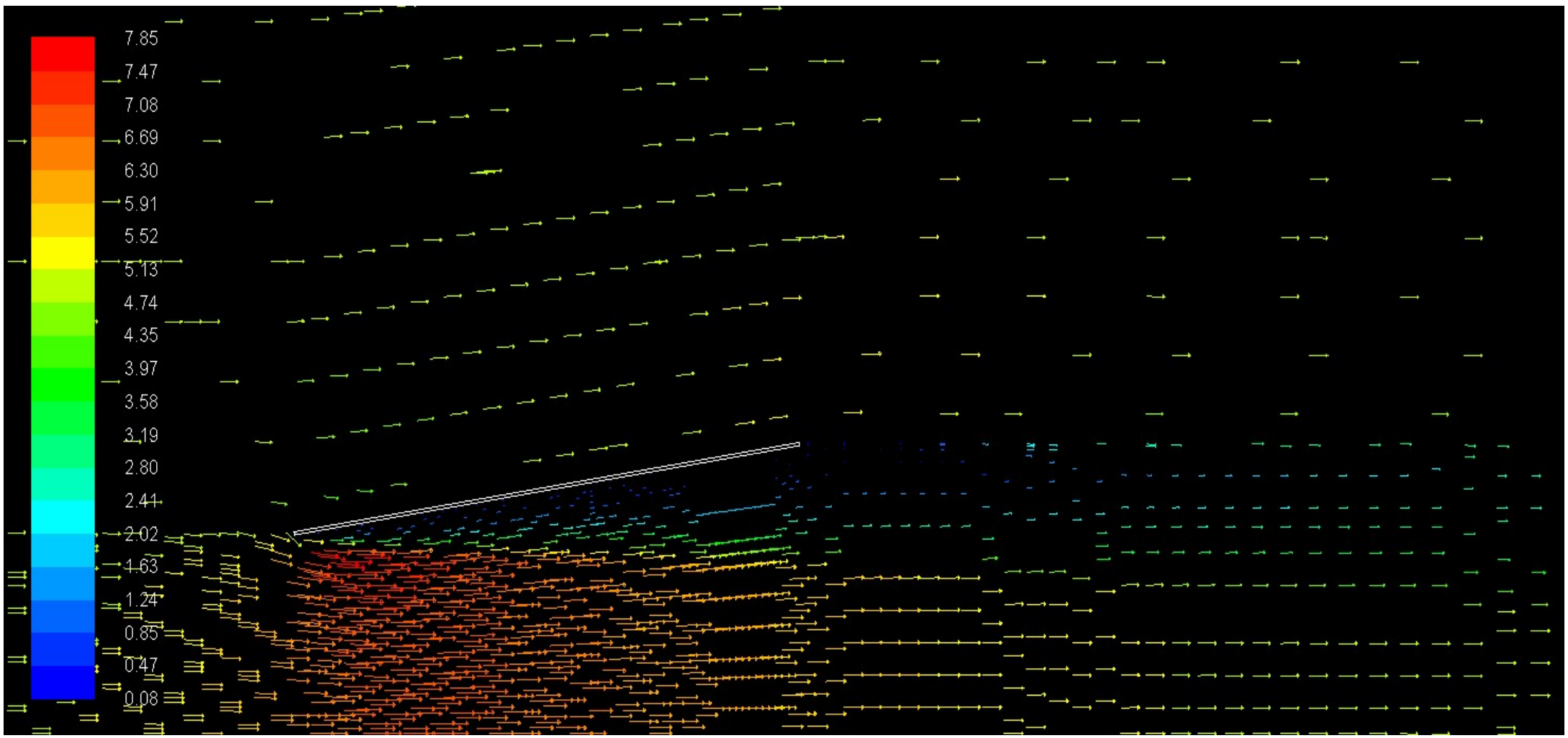


Figure A1. Velocity vectors [m/s] for Case 1 of Table 4.29, i.e., $H/D=0$

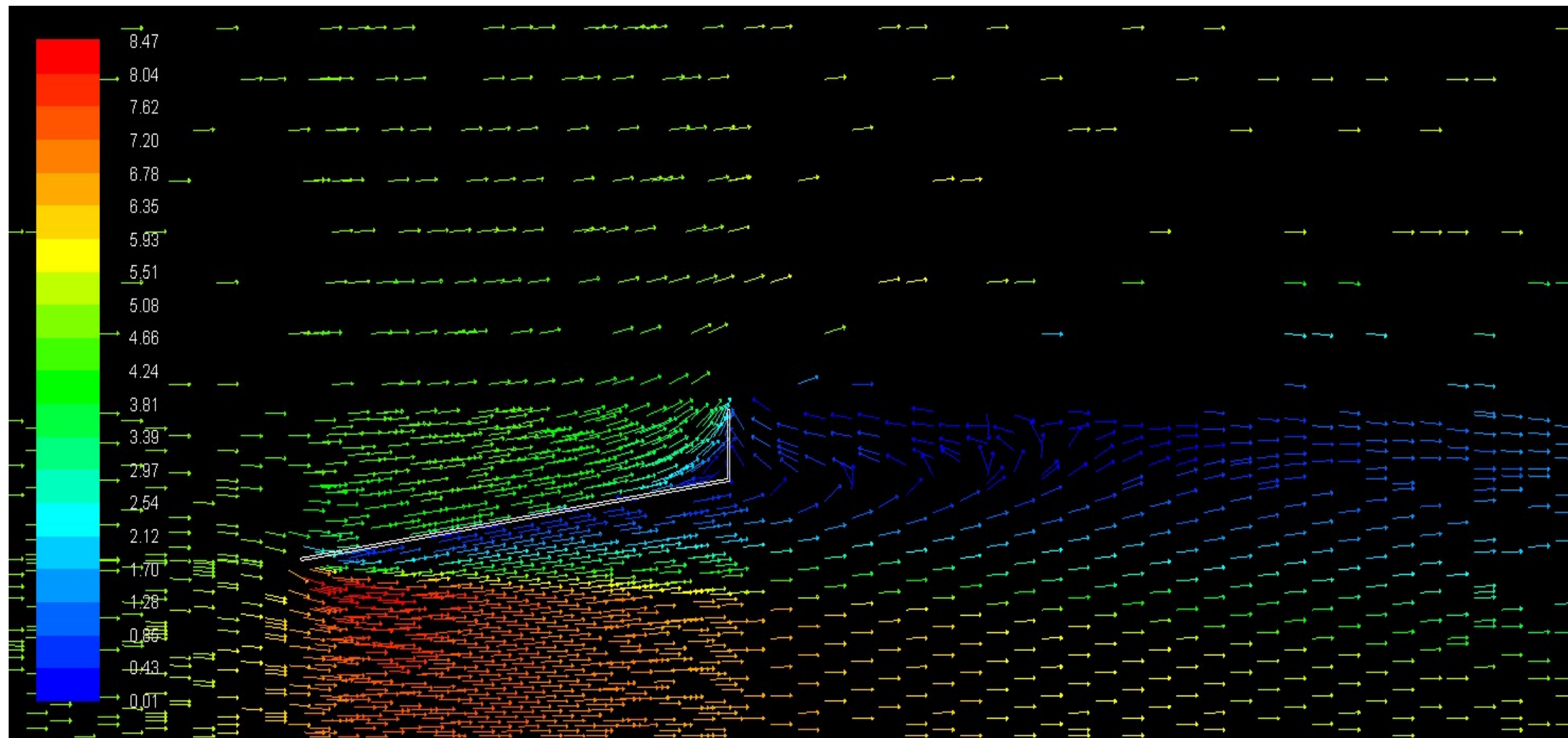


Figure A2. Velocity vectors [m/s] for Case 2 of Table 4.29, i.e., $H/D=0.2$

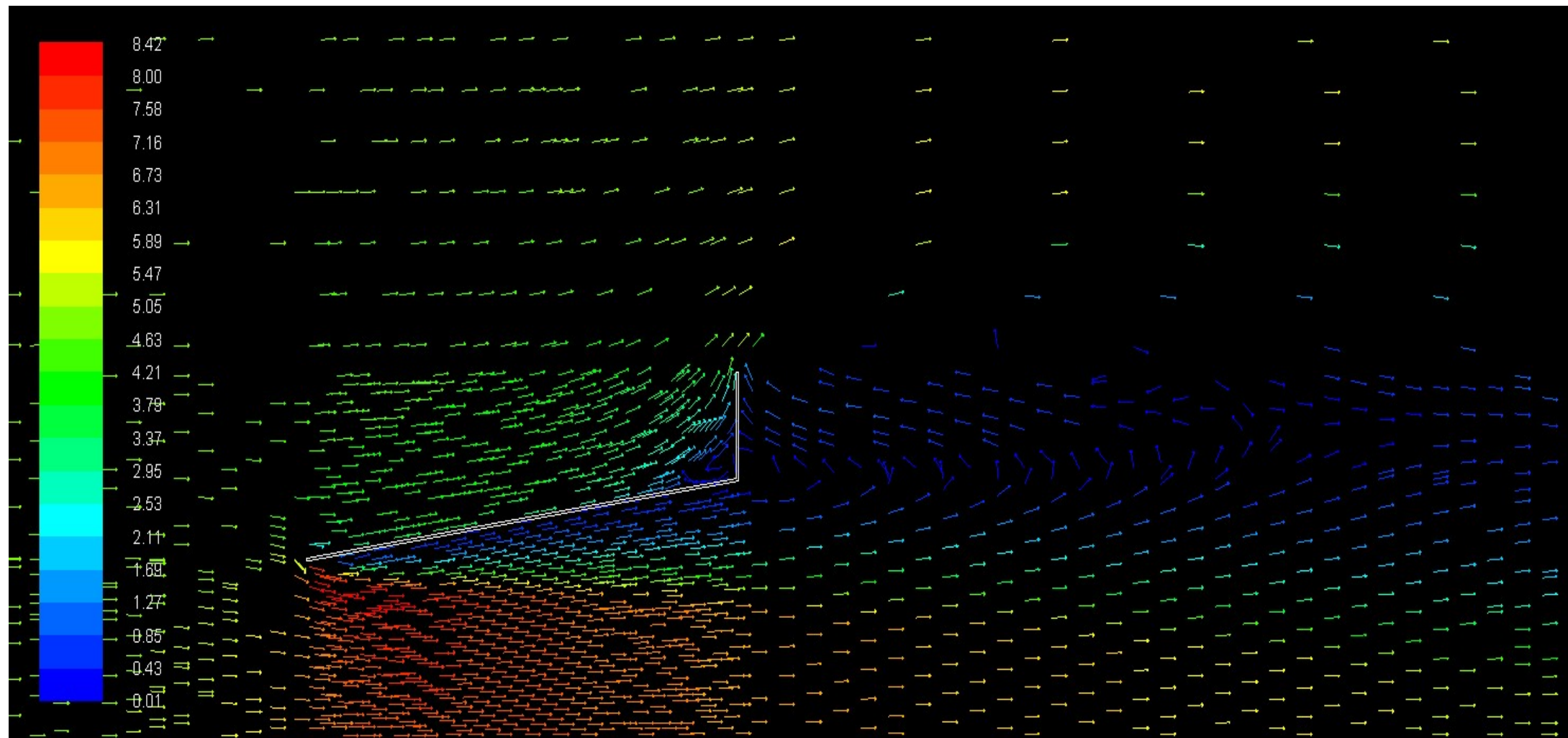


Figure A3. Velocity vectors [m/s] for Case 3 of Table 4.29, i.e., $H/D=0.3$

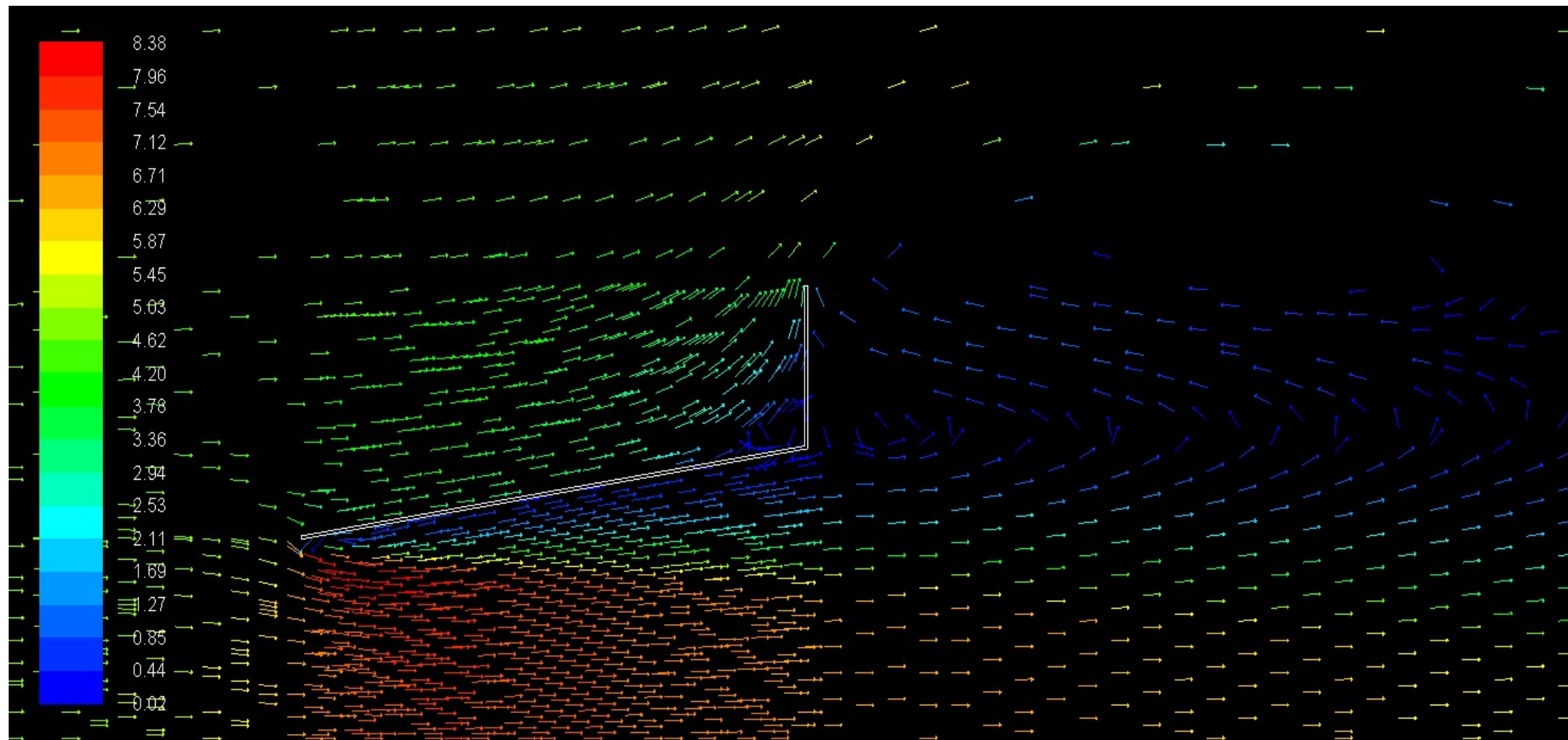


Figure A4. Velocity vectors [m/s] for Case 4 of Table 4.29, i.e., $H/D=0.4$

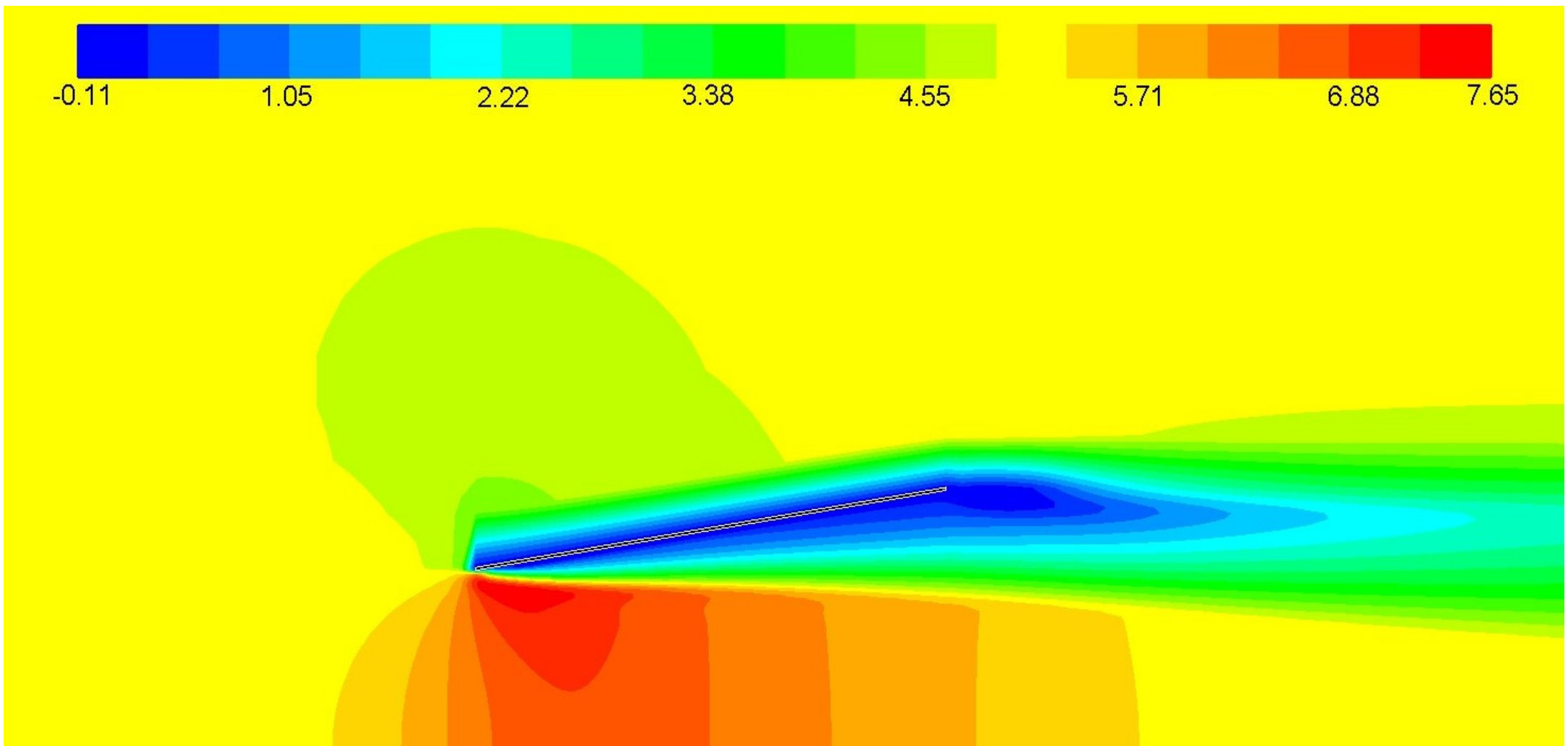


Figure A5. Velocity contours [m/s] for Case 1 of Table 4.29, i.e., $H/D=0$

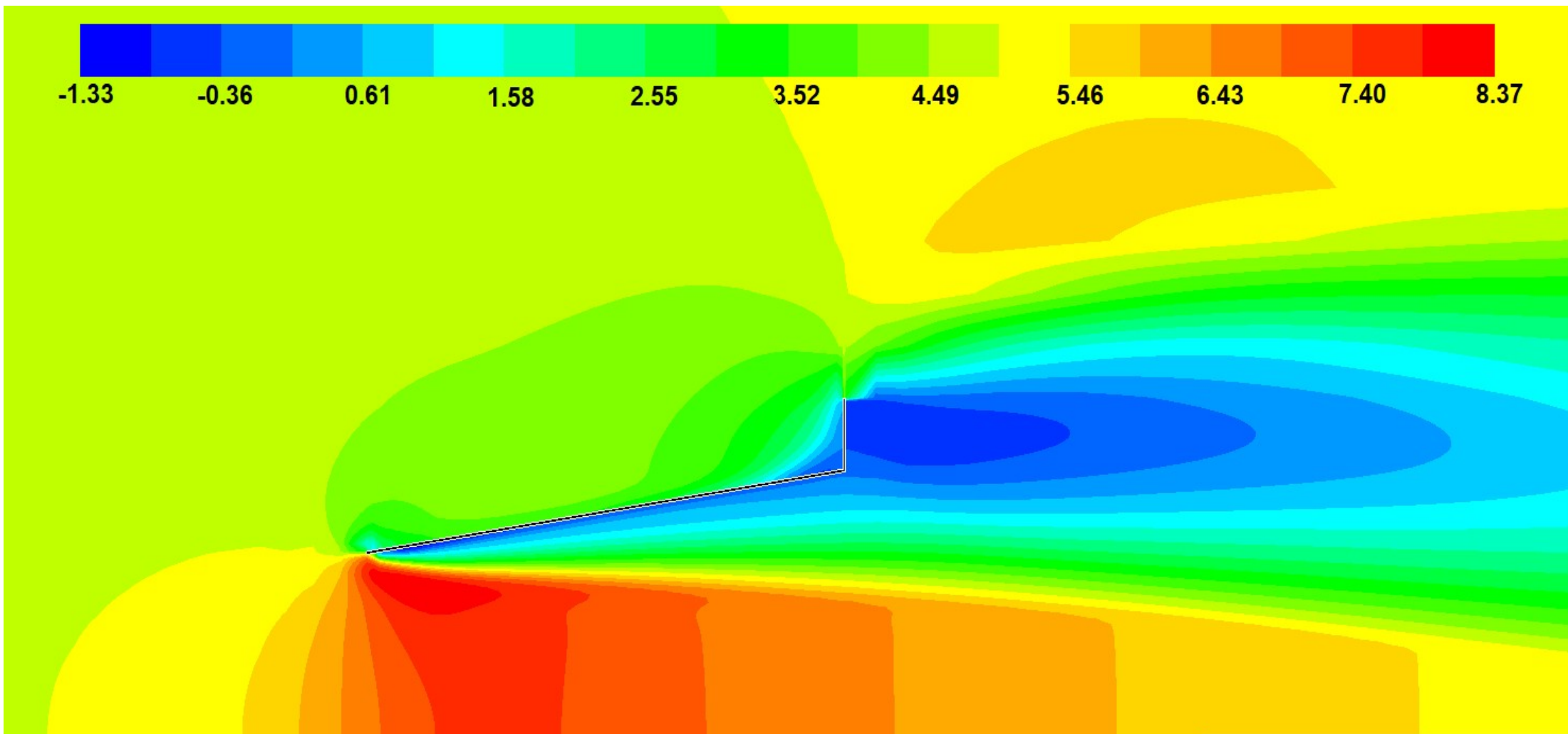


Figure A6. Velocity contours [m/s] for Case 2 of Table 4.29, i.e., $H/D=0.2$

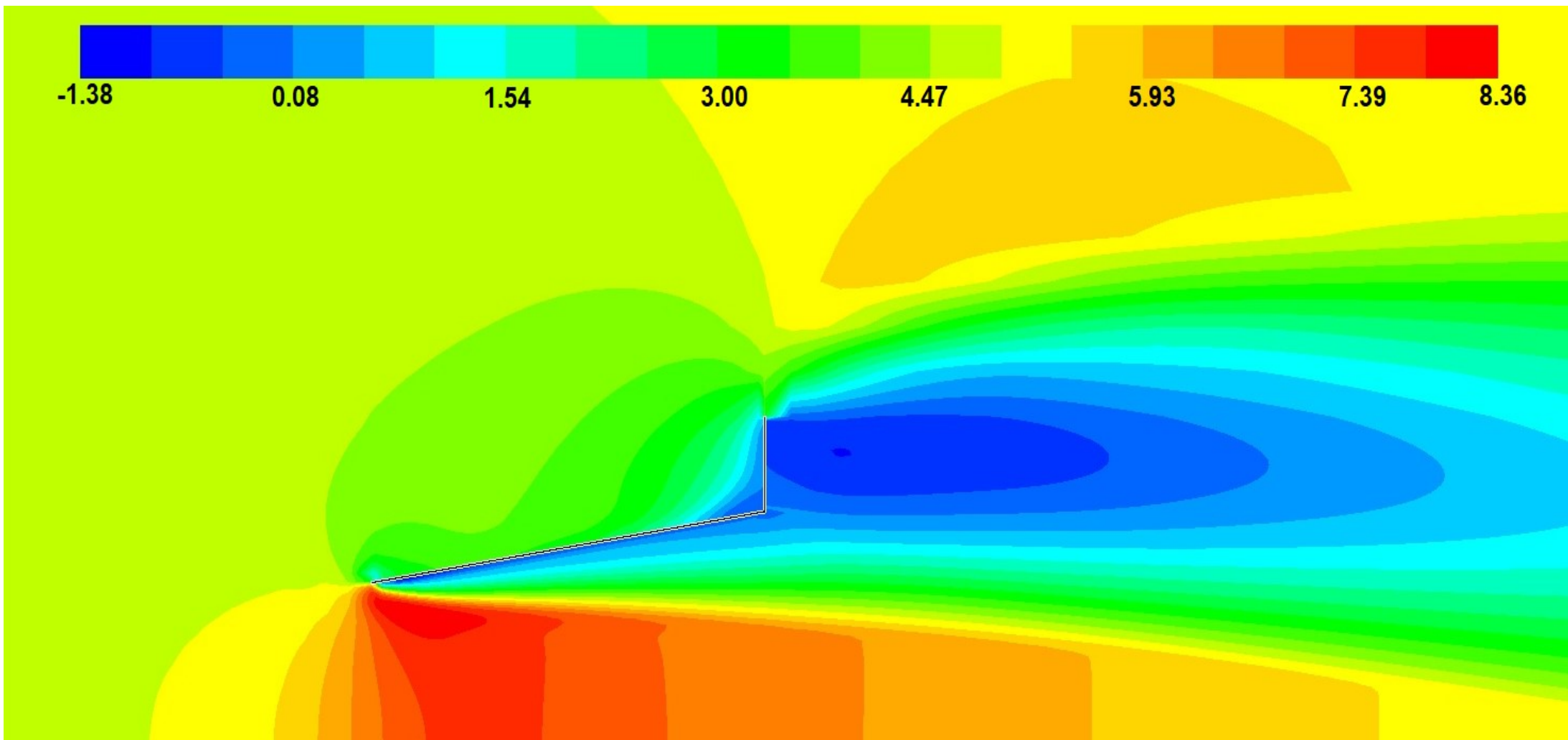


Figure A7. Velocity contours [m/s] for Case 3 of Table 4.29, i.e., $H/D=0.3$

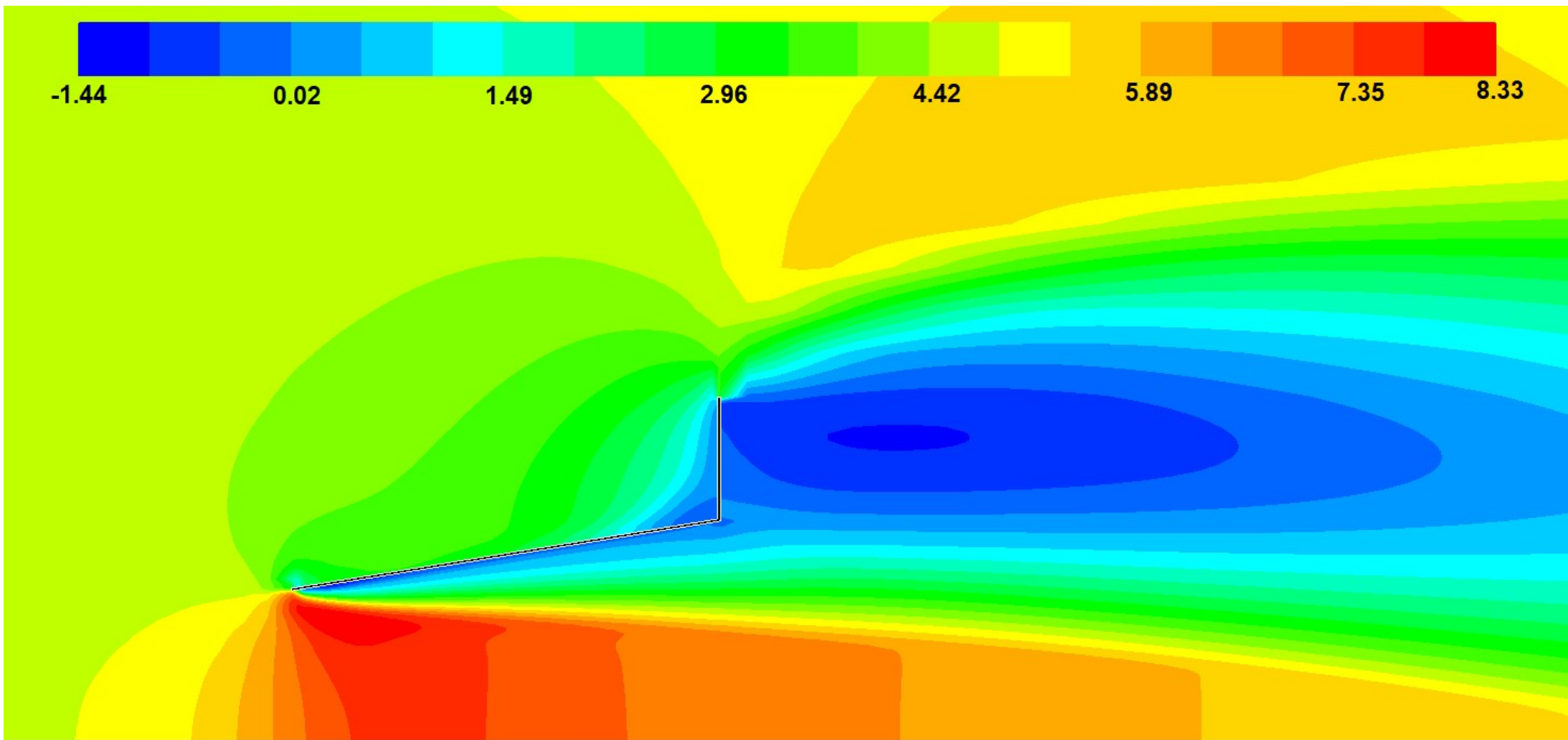


Figure A8. Velocity contours [m/s] for Case 4 of Table 4.29, i.e., $H/D=0.4$

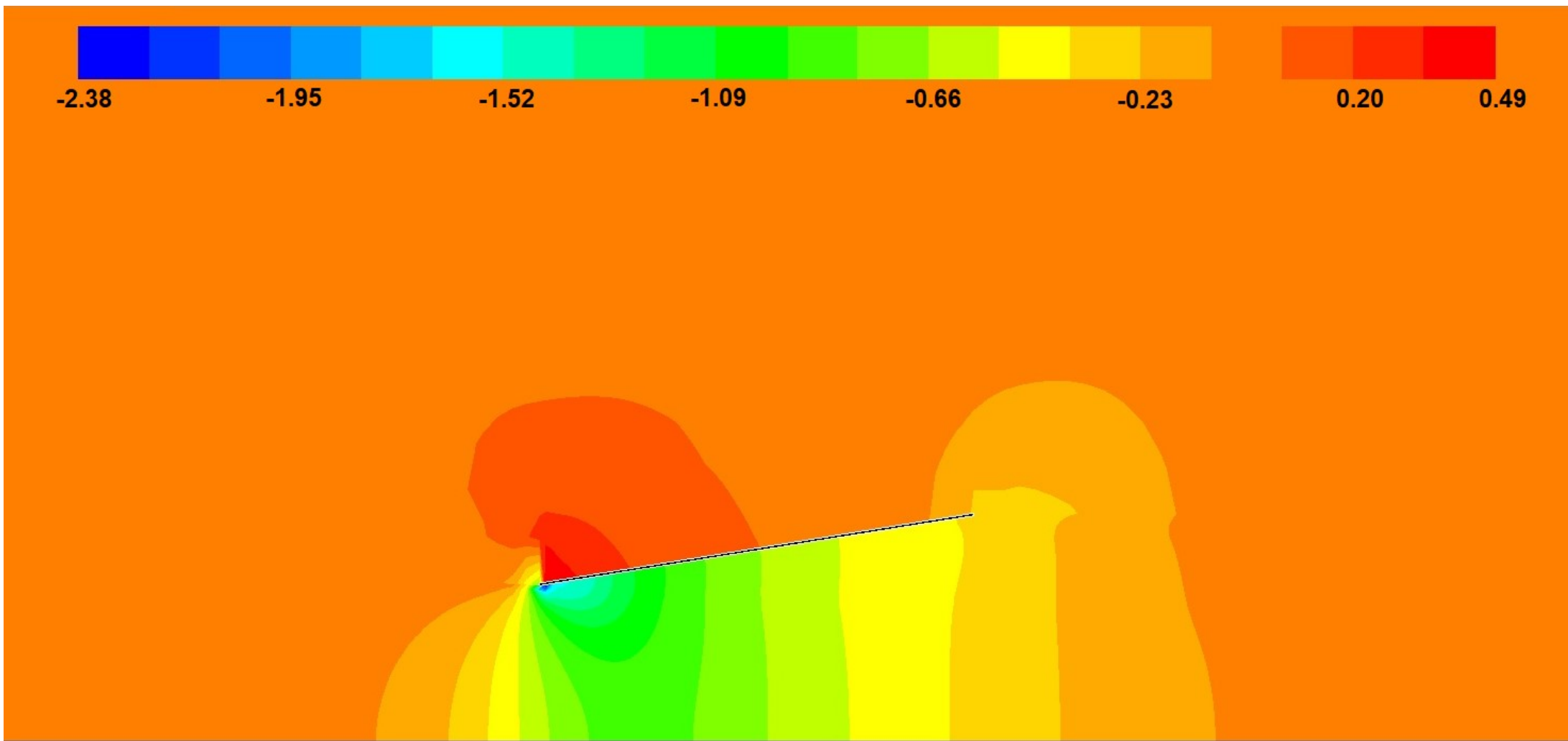


Figure A9. Pressure contours [*Patterns for dimensionless pressure coefficient, C_{pr}*] for Case 1 of Table 4.29, i.e., $H/D=0$

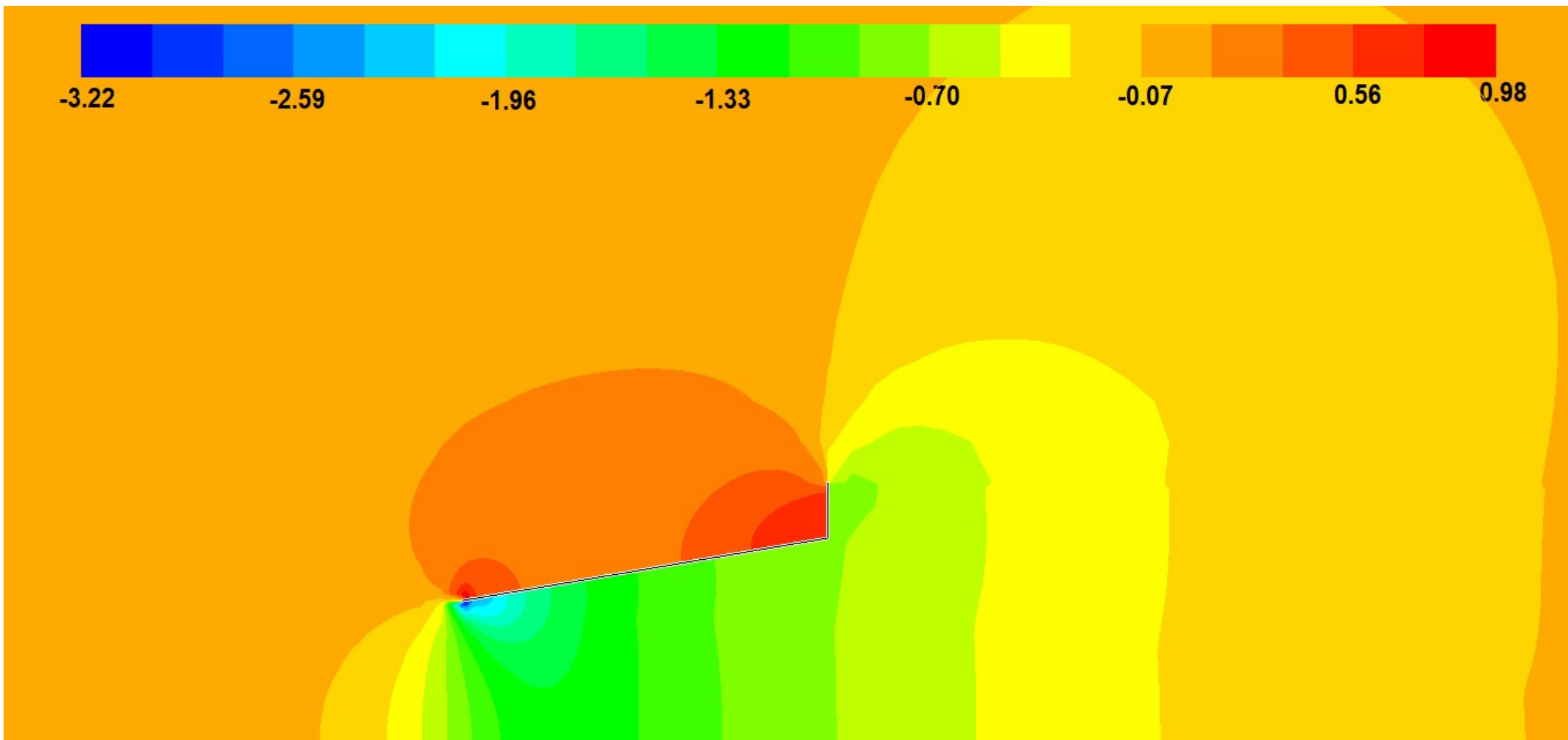


Figure A10. Pressure contours [*Patterns for dimensionless pressure coefficient, C_{pr}*] for Case 2 of Table 4.29, i.e., $H/D=0.2$

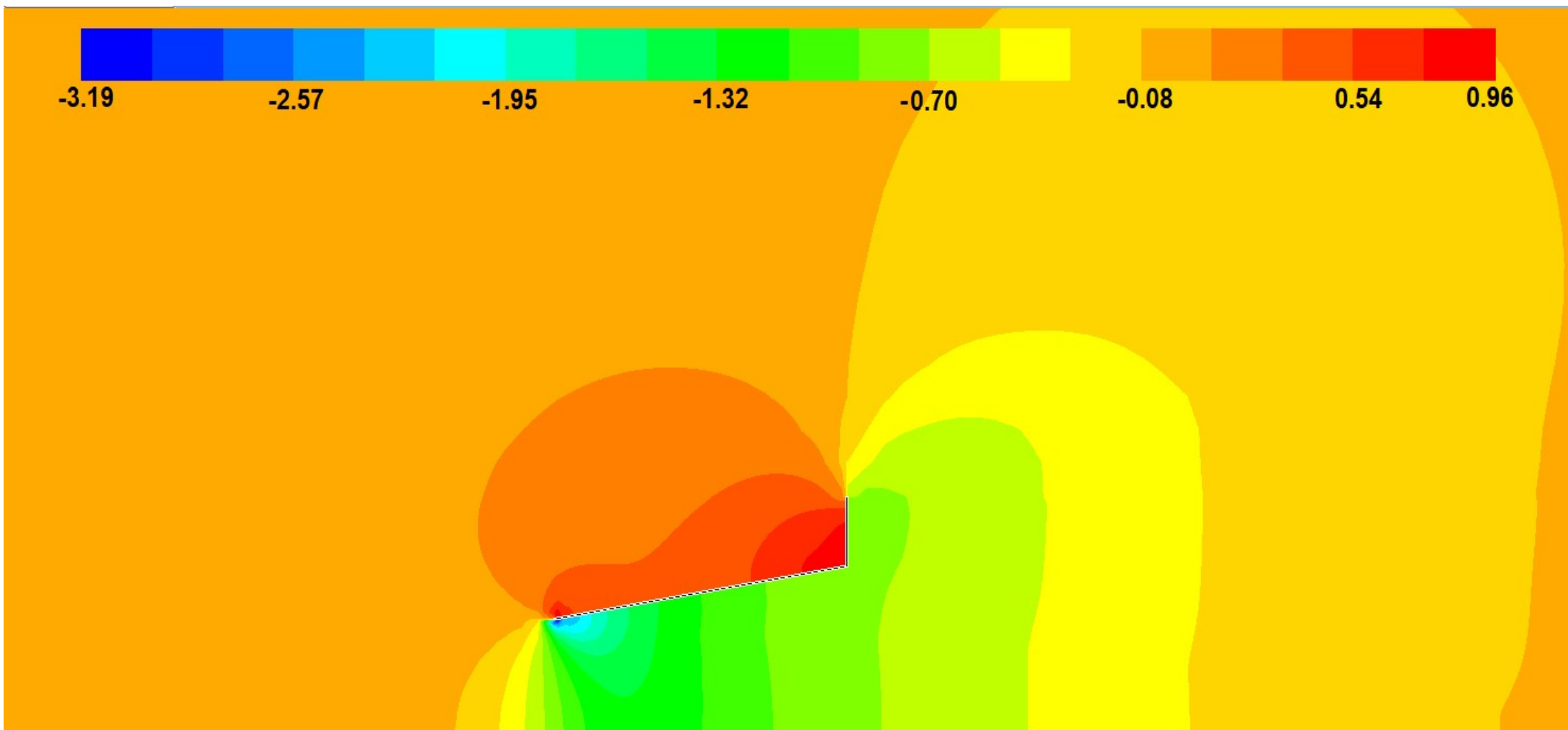


Figure A11. Pressure contours [*Patterns for dimensionless pressure coefficient, C_{pr}*] for Case 3 of Table 4.29, i.e., $H/D=0.3$

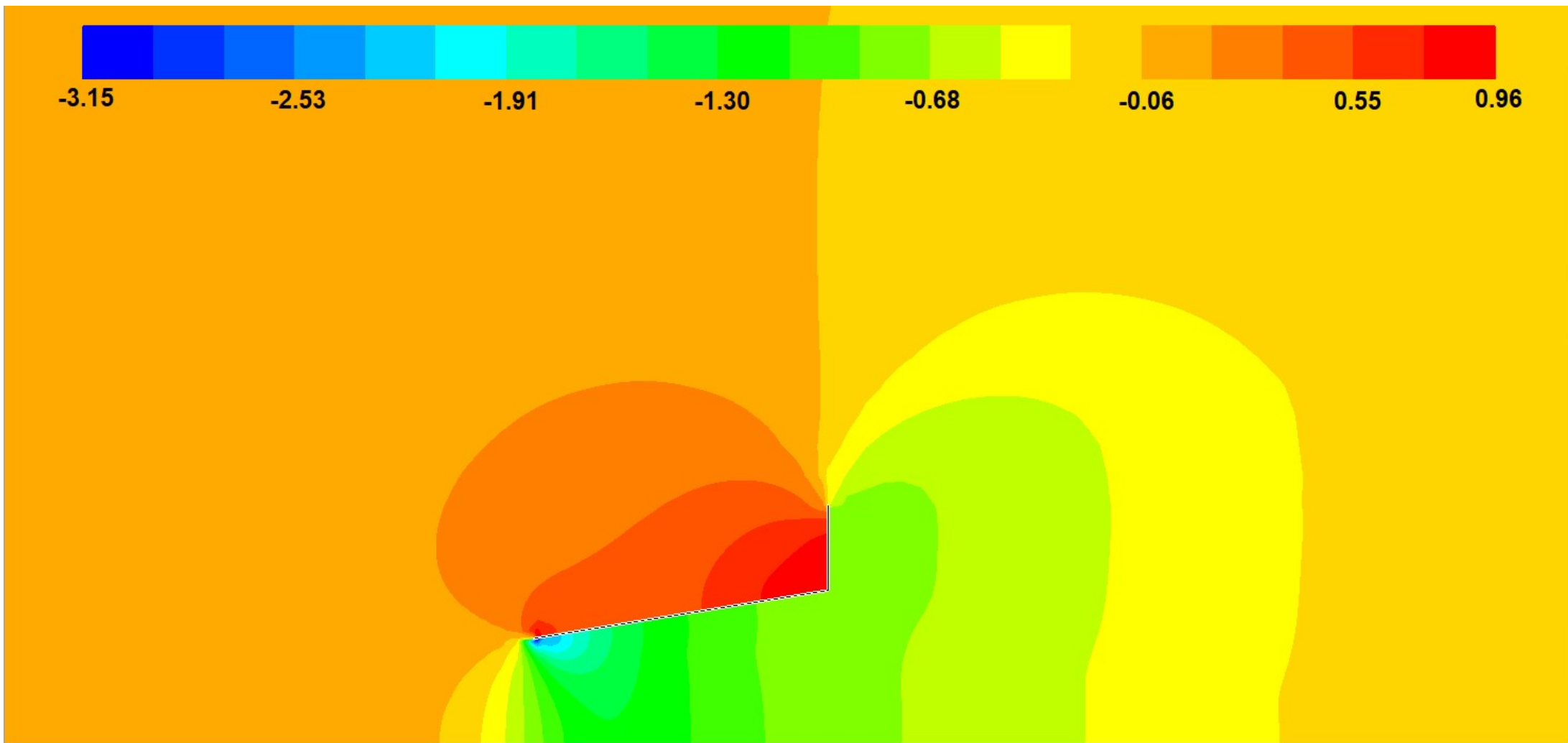


Figure A12. Pressure contours [*Patterns for dimensionless pressure coefficient, C_{pr}*] for Case 4 of Table 4.29, i.e., $H/D=0.4$

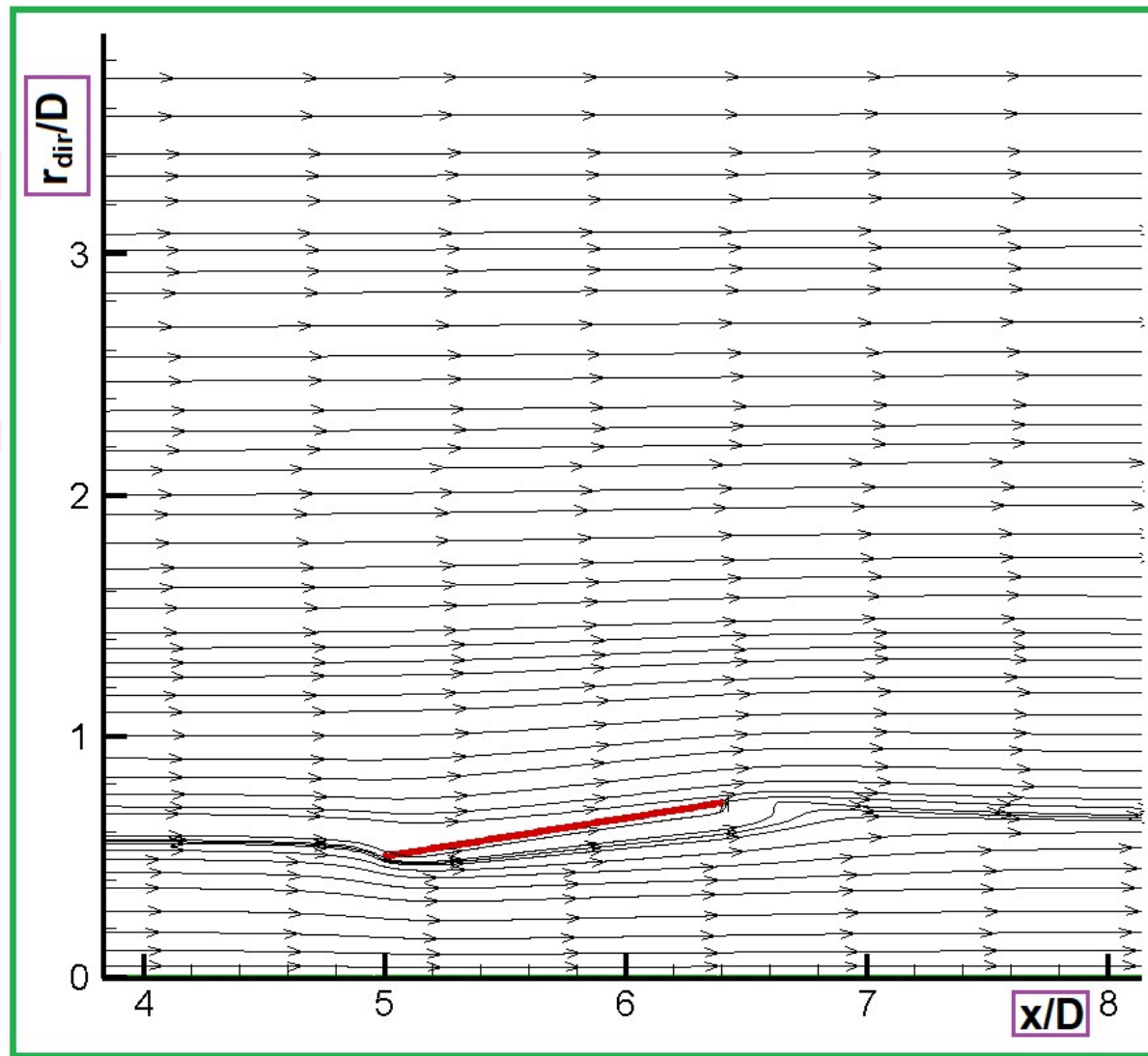


Figure A13. Streamlines [m^2/s] for Case 1, i.e., $H/D=0$

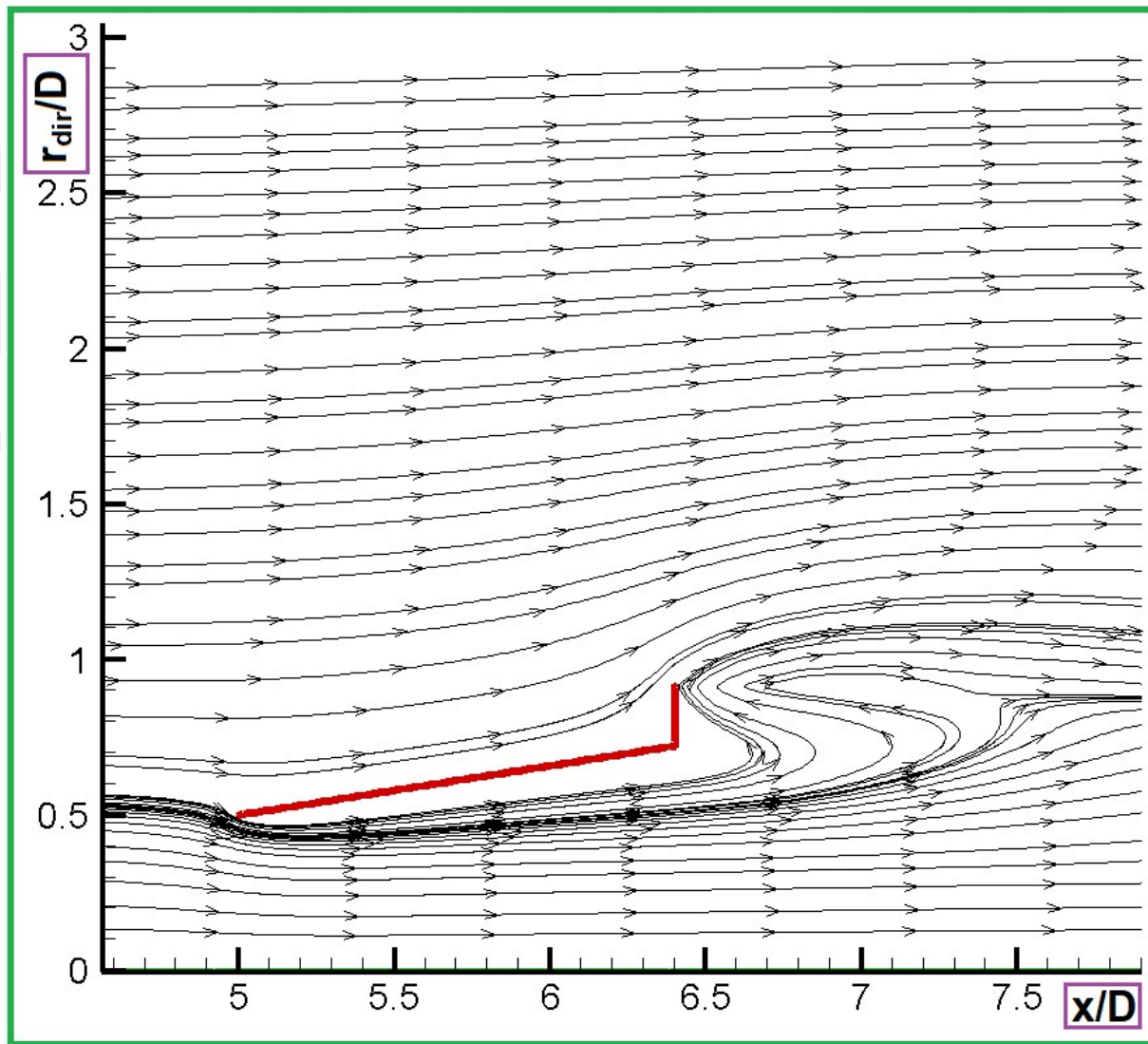


Figure A14. Streamlines [m^2/s] for Case 2, i.e., $H/D=0.2$

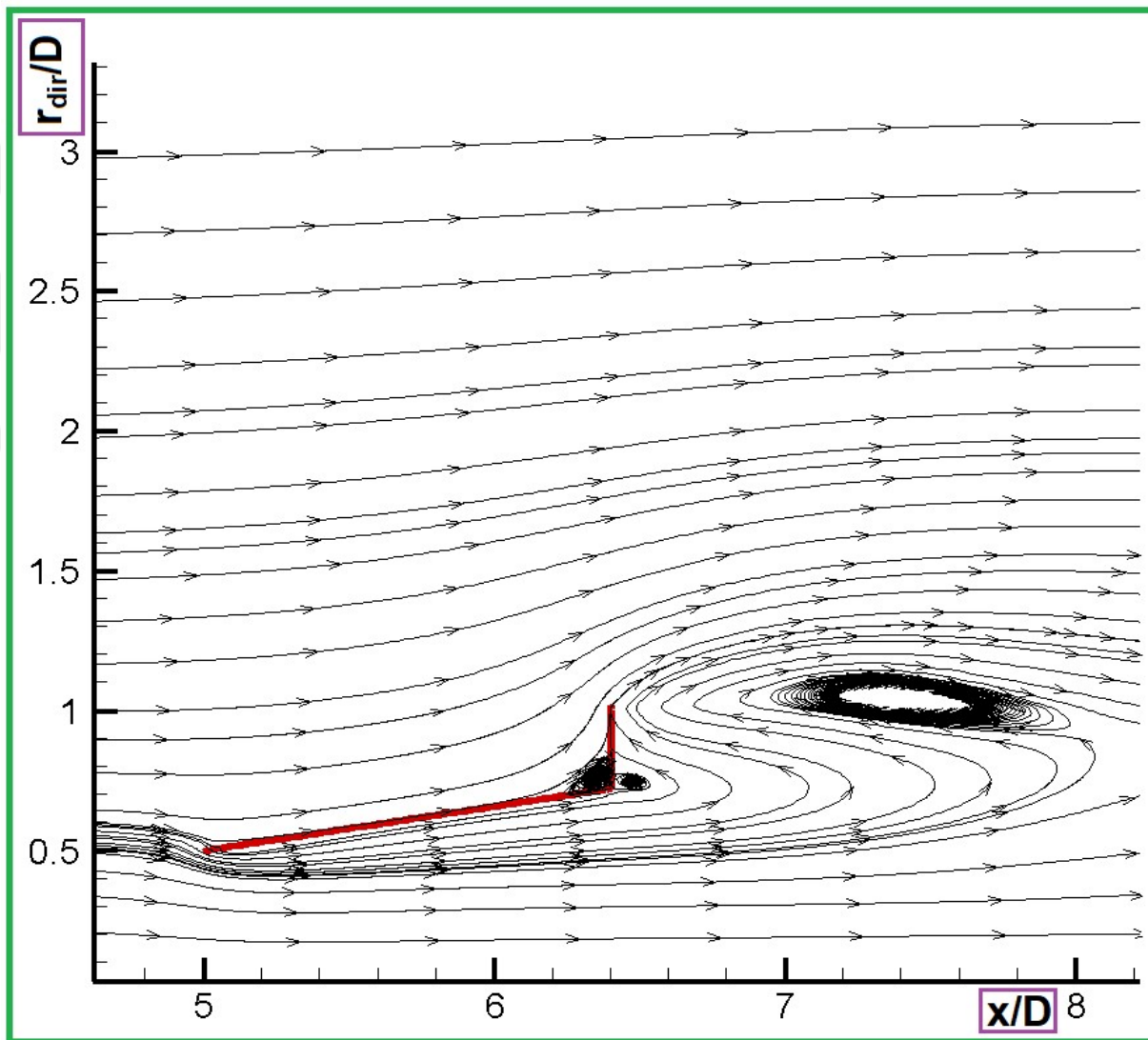


Figure A15. Streamlines [m^2/s] for Case 3, i.e., $H/D=0.3$

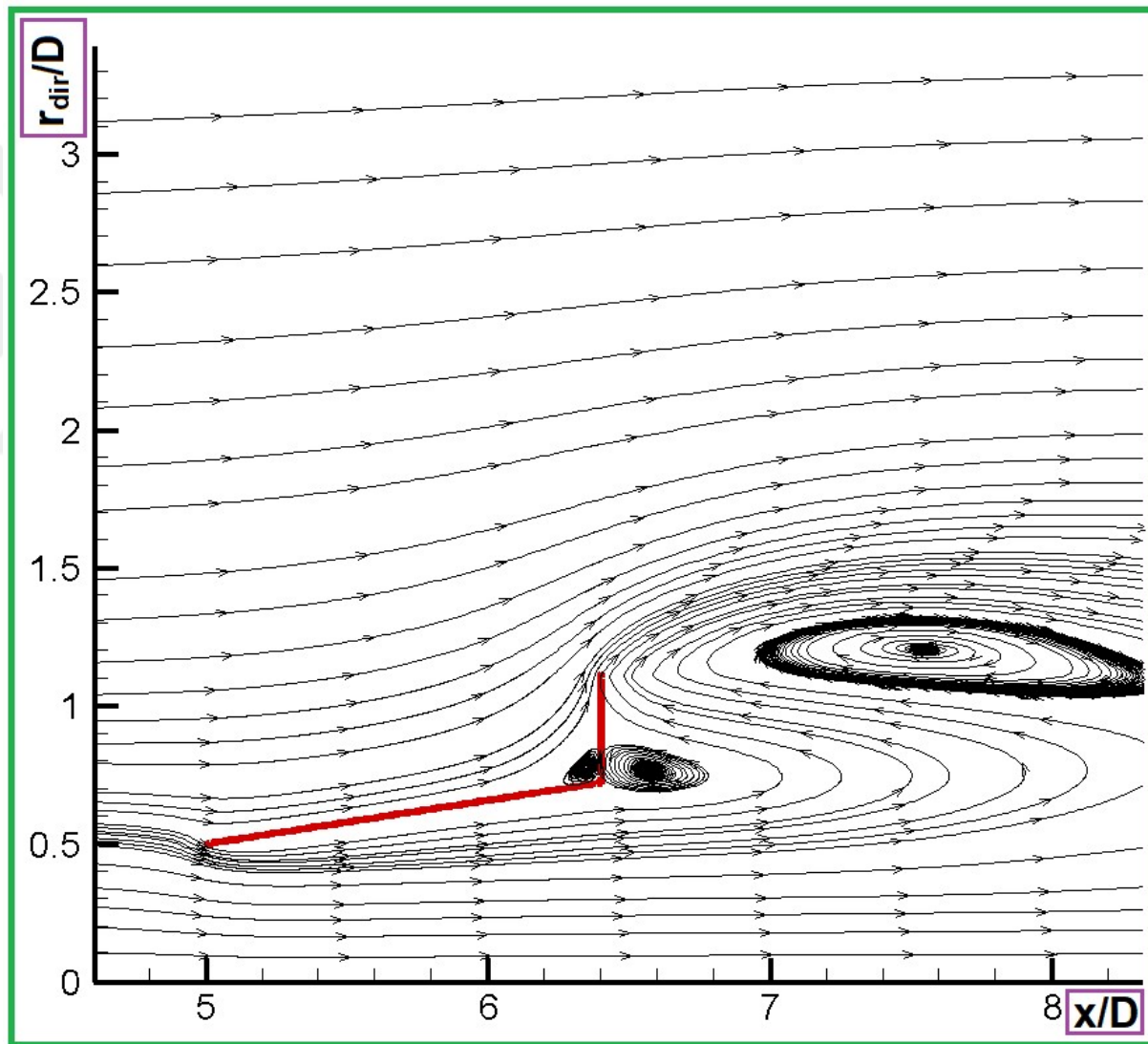


Figure A16. Streamlines [m^2/s] for Case 4, i.e., $H/D=0.4$

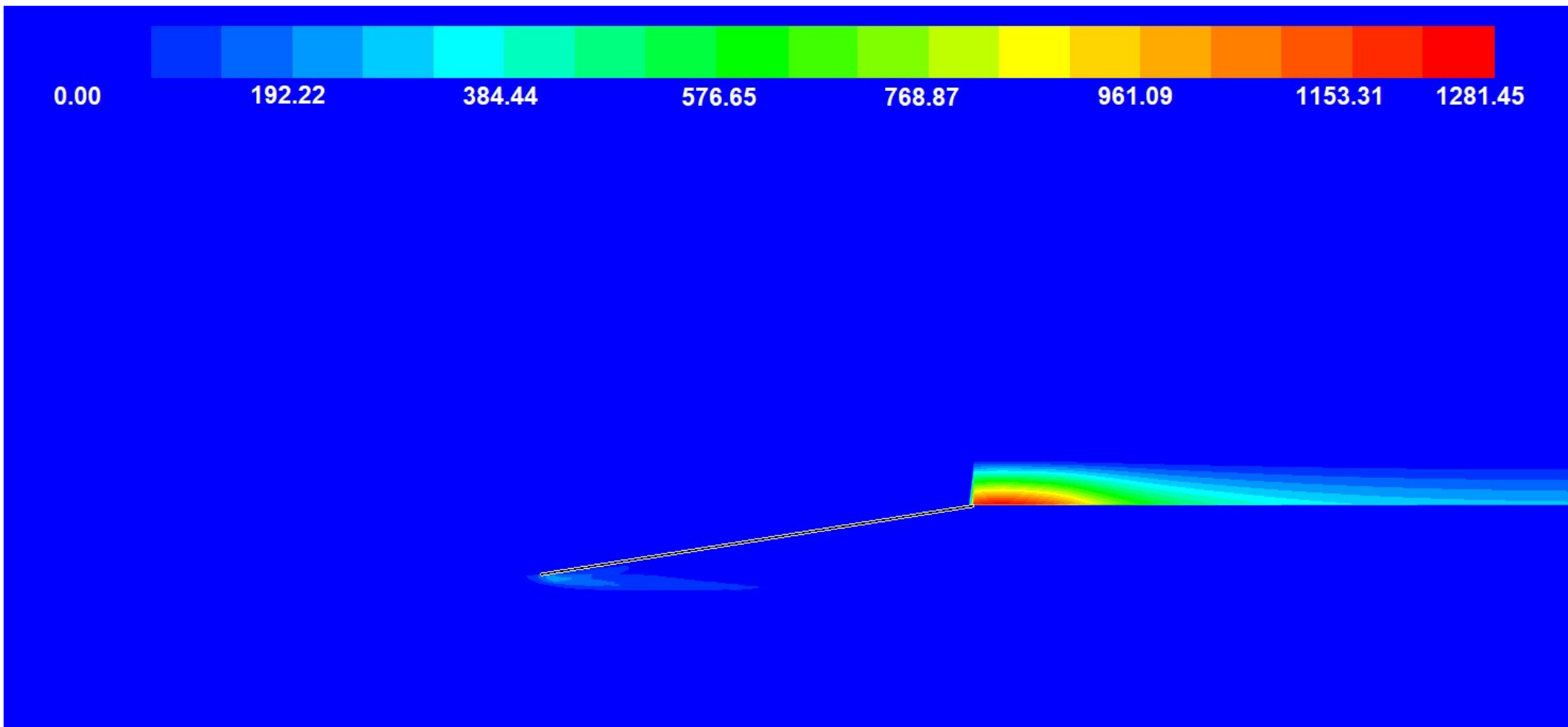


Figure A17. Vorticity [$1/s$] for Case 1, i.e., $H/D=0$

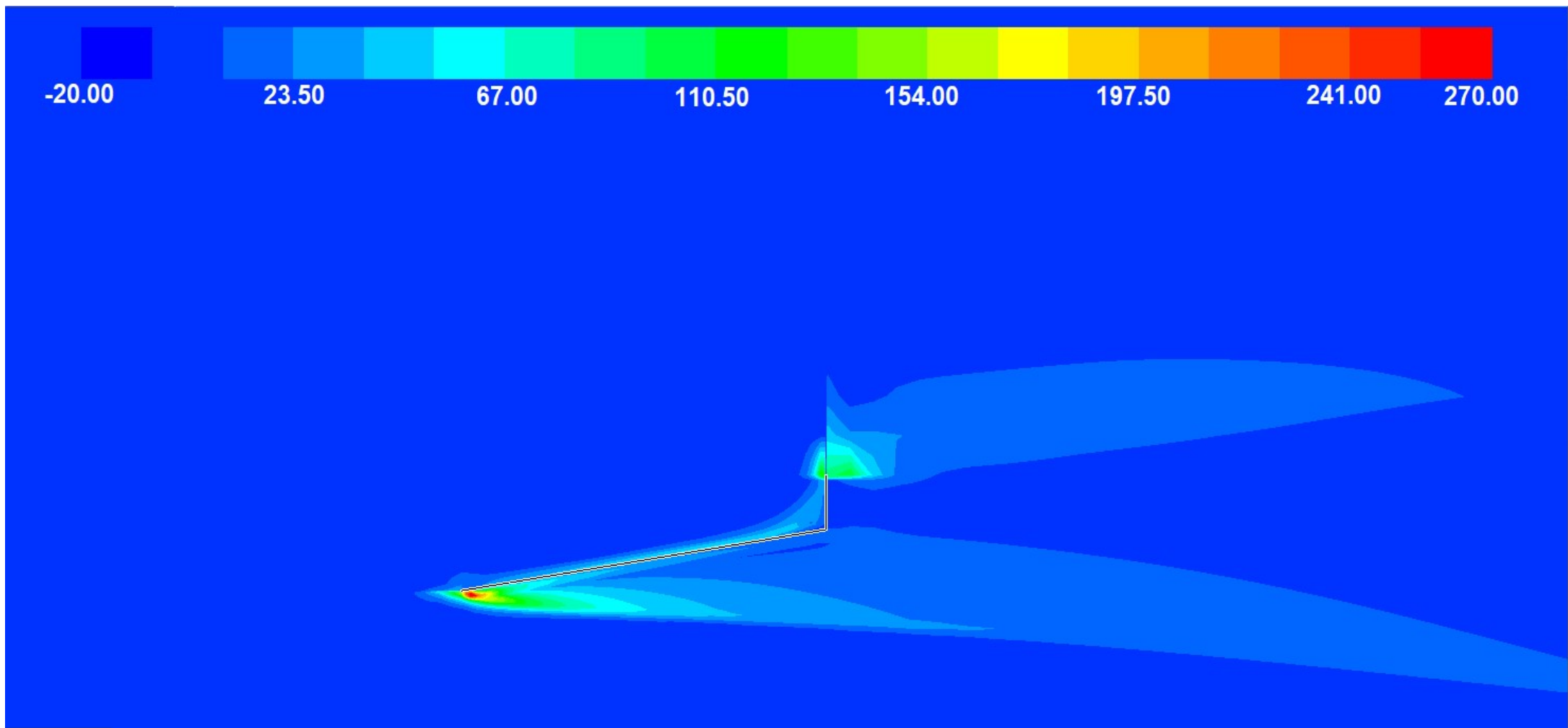


Figure A18. Vorticity [$1/s$] for Case 2, i.e., $H/D=0.2$

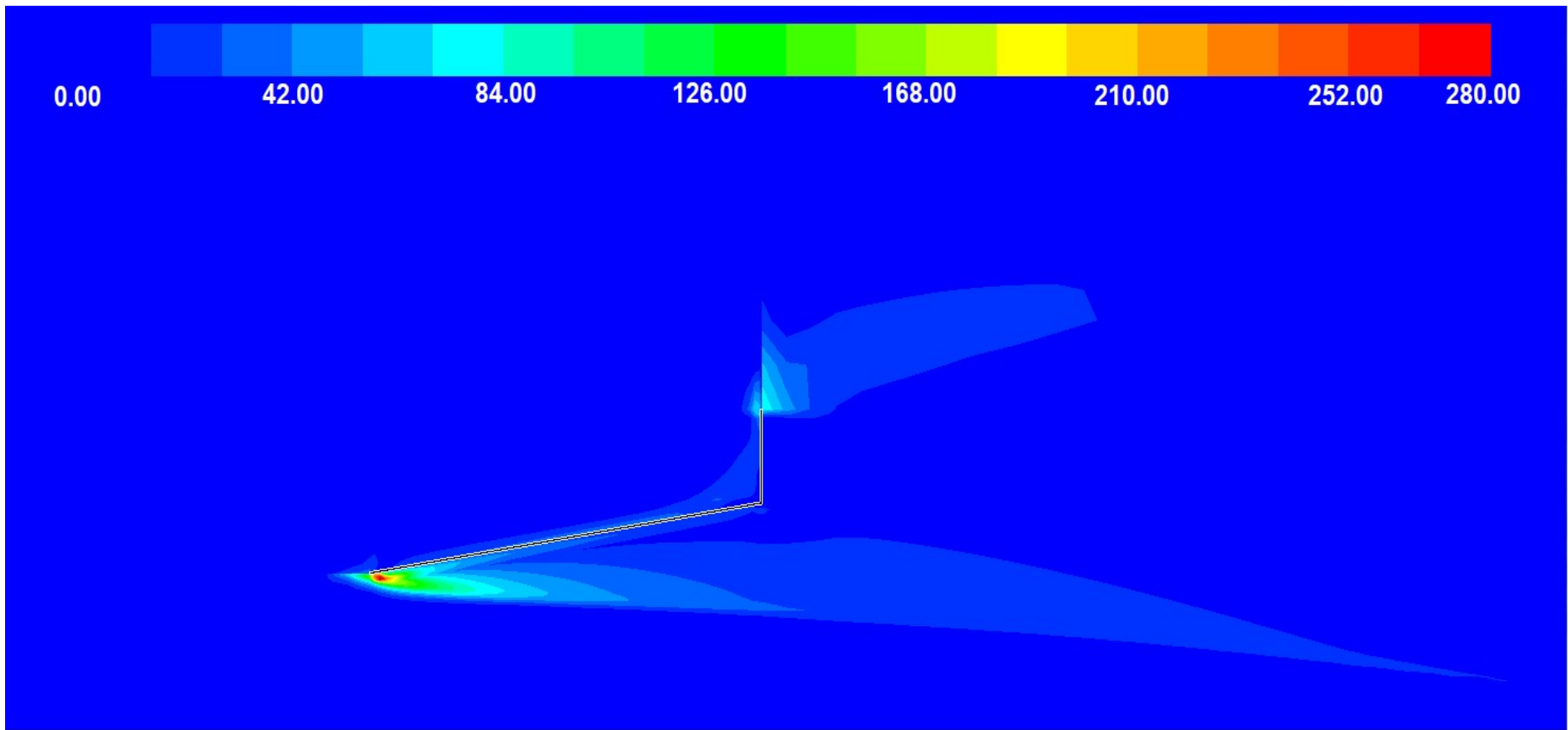


Figure A19. Vorticity [$1/s$] for Case 3, i.e., $H/D=0.3$

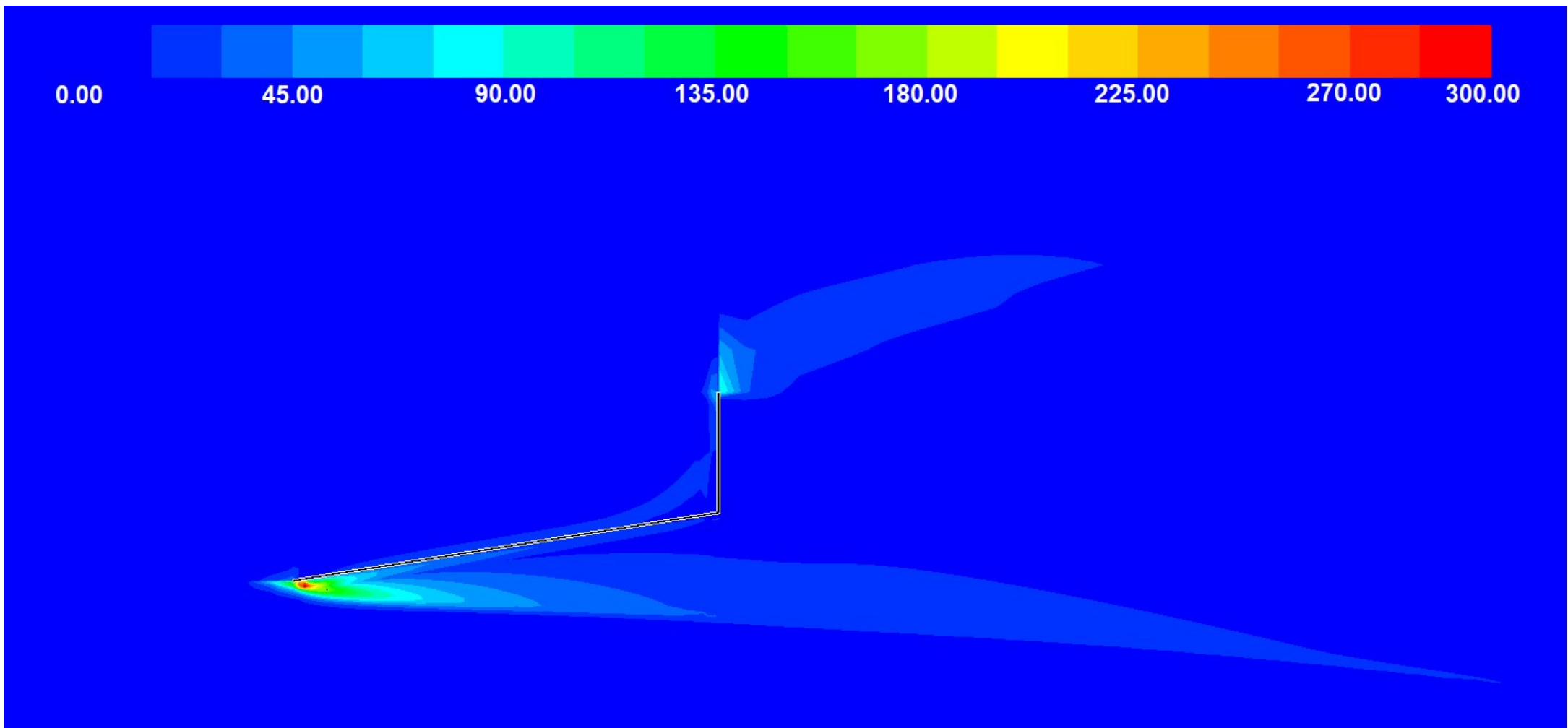


Figure A20. Vorticity [$1/s$] for Case 4, i.e., $H/D=0.4$